

K.A. Gschneidner, Jr.,
J.-C.G. Bünzli and V.K. Pecharsky
Editors



HANDBOOK ON THE
PHYSICS AND CHEMISTRY OF
RARE EARTHS

Volume 39

North-Holland

HANDBOOK ON THE PHYSICS AND CHEMISTRY OF RARE EARTHS

Advisory Editorial Board

G.-y. ADACHI, *Kobe, Japan*

W.J. EVANS, *Irvine, USA*

S.M. KAUZLARICH, *Davis, USA*

G.H. LANDER, *Karlsruhe, Germany*

M.F. REID, *Christchurch, New Zealand*

Editor Emeritus

LeRoy EYRING[‡], *Tempe, USA*

[‡]Deceased.

North-Holland is an imprint of Elsevier
Radarweg 29, PO Box 211, 1000 AE Amsterdam, The Netherlands
The Boulevard, Langford Lane, Kidlington, Oxford OX5 1GB, UK

First edition 2009

Copyright © 2009 Elsevier B.V. All rights reserved.

No part of this publication may be reproduced, stored in a retrieval system or transmitted in any form or by any means electronic, mechanical, photocopying, recording or otherwise without the prior written permission of the publisher.

Permissions may be sought directly from Elsevier's Science & Technology Rights Department in Oxford, UK: phone (+44) (0) 1865 843830; fax (+44) (0) 1865 853333; email: permissions@elsevier.com. Alternatively you can submit your request online by visiting the Elsevier web site at <http://elsevier.com/locate/permissions>, and selecting, *Obtaining permission to use Elsevier material*.

Notice

No responsibility is assumed by the publisher for any injury and/or damage to persons or property as a matter of products liability, negligence or otherwise, or from any use or operation of any methods, products, instructions or ideas contained in the material herein. Because of rapid advances in the medical sciences, in particular, independent verification of diagnoses and drug dosages should be made.

British Library Cataloguing in Publication Data

A catalogue record for this book is available from the British Library

Library of Congress Cataloging-in-Publication Data

A catalog record for this book is available from the Library of Congress

ISBN: 978-0-444-53221-3

ISSN: 0168-1273

For information on all North-Holland publications
visit our website at books.elsevier.com

Printed and Bound in Hungary

08 09 10 11 12 10 9 8 7 6 5 4 3 2 1

Working together to grow
libraries in developing countries

www.elsevier.com | www.bookaid.org | www.sabre.org

ELSEVIER

BOOK AID
International

Sabre Foundation

PREFACE

**Karl A. Gschneidner Jr., Jean-Claude G. Bünzli,
Vitalij K. Pecharsky**

These elements perplex us in our rearches [sic], baffle us in our speculations, and haunt us in our very dreams. They stretch like an unknown sea before us – mocking, mystifying, and murmuring strange revelations and possibilities.

Sir William Crookes (February 16, 1887)

This volume of the *Handbook on the Physics and Chemistry of Rare Earths* adds three new chapters to the series, describing three different aspects of rare-earth science. The volume opens with an overview of the dual nature of 4f states in the lanthanides (Chapter 241). It is followed by a review of the temperature-dependent behaviors of aluminates and gallates, the structures of which are based on the simple, yet flexible, cubic perovskite model (Chapter 242). The last chapter describes the current state-of-the-art in luminescence of polyoxometallolanthanoates and their photochemistry leading to the formation of highly colored nano-rings (Chapter 243).

CHAPTER 241. THE DUAL, LOCALIZED OR BAND-LIKE, CHARACTER OF THE 4f STATES

By W. M. TEMMERMAN

Daresbury Laboratory, Warrington, UK

L. PETIT AND A. SVANE

University of Aarhus, Aarhus, Denmark

Z. SZOTEK AND M. LÜDERS

Daresbury Laboratory, Warrington, UK

P. STRANGE

University of Kent, Canterbury, Kent, UK

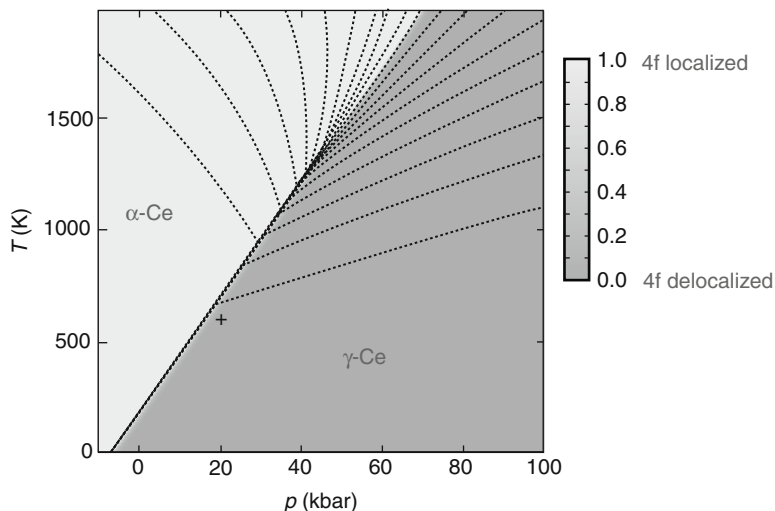
J. B. STAUNTON AND I. D. HUGHES

University of Warwick, Coventry, UK, and

B. L. GYORFFY

University of Bristol, Bristol UK

The opening chapter describes the dual character of the 4f core electrons that may either be part of the valence states or be inert and form part of the core using first principles theory. Here, W. M. Temmerman and coauthors begin with a review of the relevant physical, electronic, and magnetic properties of lanthanide materials.



They then give a brief overview of the applicable theoretical methods based on the density functional theory, with the focus on the self-interaction-corrected local spin density approximation method, and, in particular, the full implementation of self-interaction correction, involving repeated transformations between Bloch and Wannier representations. The main part of the chapter deals with the application of these methods to understanding the valence and valence transitions of the lanthanides. By introducing the notion of nominal valence, which defines the number of remaining band-like states as the valence of the lanthanide ion, a better understanding of the physical properties of the lanthanides and their compounds, and in particular, magnetism, was achieved as demonstrated by numerous examples. Later, the authors turn their attention to two spectroscopic techniques applicable to lanthanides and some of their compounds in order to study some of the properties of the localized 4f states. An important issue—how to calculate the finite temperature properties of the lanthanide metals and their compounds—is discussed and illustrated by the study of finite temperature magnetism of the heavy lanthanides and the finite temperature diagram of the Ce α - γ phase transition. The chapter concludes with the outline on how to include dynamical quantum fluctuations to further improve modeling precision.

CHAPTER 242. PEROVSKITE-TYPE ALUMINATES AND GALLATES

By **L. VASYLECHKO**

Lviv Polytechnic National University, Lviv, Ukraine

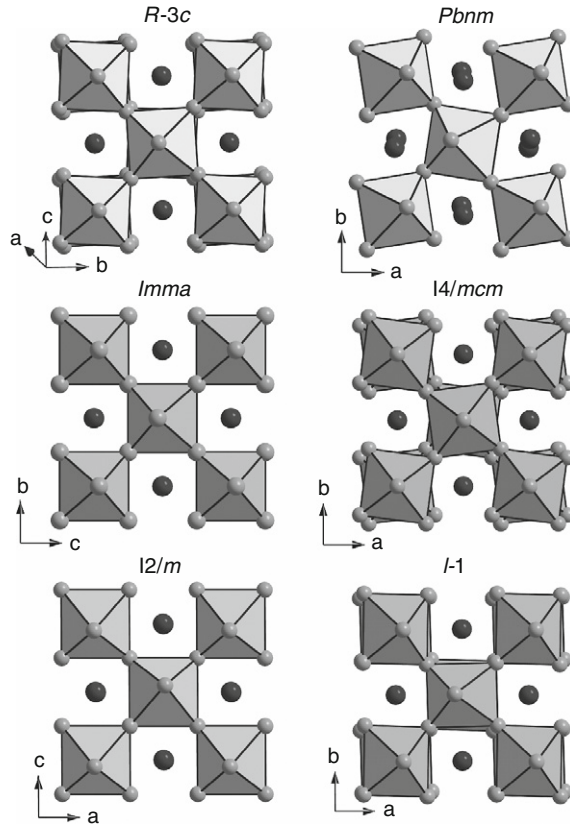
A. SENYSHYN

Darmstadt University of Technology, Darmstadt, Germany, and

U. BISMAYER

Hamburg University, Hamburg, Germany

The perovskite family is a typical representative of complex oxides. Many of the perovskites exhibit interesting physics that includes ferro- and piezoelectricity, high electronic and ionic conductivities, diverse magnetism, colossal



magnetoresistance, paraelectricity, and superconductivity. In this chapter L. Vasylechko, A. Senyshyn, and U. Bismayer are concerned with aluminates (RAlO_3) and gallates (RGaO_3) that adopt perovskite-derived structures and find use as substrate materials for epitaxy of high temperature superconductors, colossal magnetoresistive materials, and GaN films; and as active and passive laser media, scintillators, and microwave dielectric materials. Structural details are critical to understand how these important properties emerge, and therefore, this chapter reviews numerous experimental data about crystal structures, their thermal evolution and transformations of over a hundred of RAlO_3 and RGaO_3 compounds and their solid solutions. The authors use crystal chemistry to study and analyze perovskite structures and distortions over a wide temperature range in terms of bond-length distortions, tilting angles between octahedra, polyhedral volume ratios, tolerance factors, and individual and average cation–cation distances. Experimental data are supplemented by bond-valence calculations. The influence of isovalent substitutions in the rare-earth sublattice on the average structure, its thermal behavior, and phase transformations have been reviewed. Especially important are phase diagrams of $\text{RAlO}_3\text{--R}'\text{AlO}_3$ and $\text{RGaO}_3\text{--R}'\text{GaO}_3$ systems as functions of average radii of the R-cations. Common features of the thermal expansion of rare earth aluminates and gallates, as well as the observed

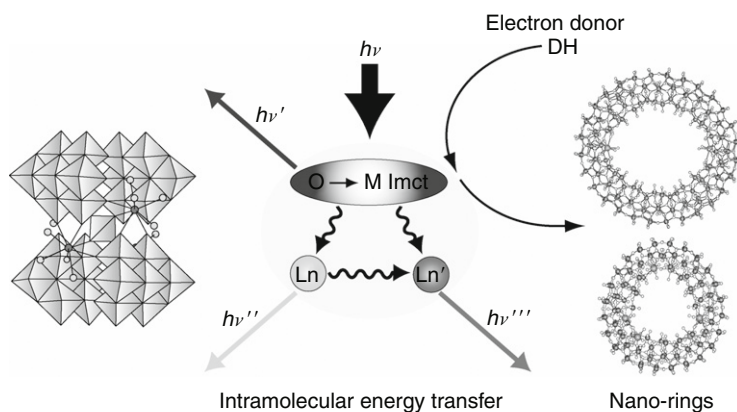
anomalies, including the negative thermal expansion observed in RGaO_3 containing praseodymium, are also discussed.

CHAPTER 243. LUMINESCENCE OF POLYOXOMETALLOLANTHANOATES AND PHOTOCHEMICAL NANO-RING FORMATION

By **TOSHIHIRO YAMASE**

Tokyo Institute of Technology, Nagatsuta, Midori-ku, Yokohama, Japan

Toshihiro Yamase's chapter is focused on the chemistry of polyoxolanthanoates—a special class of metal-oxide cluster compounds—which may be considered as models for lanthanide-doped metal-oxide phosphors. The emphasis of the chapter is on the understanding of the molecular mechanisms of energy transfer processes in metal-oxide phosphors, which often remain unclear mainly because the luminescence centers are insufficiently characterized. The author outlines energy transfer from $\text{O} \rightarrow \text{M}$ ($\text{M} = \text{Nb}, \text{V}, \text{Mo}, \text{and } \text{W}$) ligand-to-metal charge-transfer (lmct) states (donor) to luminescent Ln^{3+} centers (acceptor) processes in polyoxometalloylanthanoates, particularly in polyoxometalloyeuropates. The sensitized Ln^{3+} -emission is governed by a Förster–Dexter dipole–dipole type of coupling between the donor and the acceptor, and the $\text{O} \rightarrow \text{M}$ lmct triplet states are involved not only in energy transfers, but also in electron transfer during the photoredox reaction with proton and electron donors. Such a photoredox reaction enables the photochemical design of Mo-blue nano-rings by a novel “bottom-up” approach. These Mo-blue species are $\text{Mo}^{\text{V}}/\text{Mo}^{\text{VI}}$ mixed-valence polyoxomolybdates and they favor the highly delocalized systems with characteristic dark-blue color due to the intervalence charge-transfer transitions. Lanthanide ions not only open a novel method for the preparation of these nano-ring derivatives, but also provide a tool for the mechanistic investigation of their self-assembly. This is a beautiful example of lanthanide ions contributing to both nano-science and nanotechnology.



CONTENTS OF VOLUMES 1–38

VOLUME 1: Metals

1978, 1st repr. 1982, 2nd repr. 1991; ISBN 0-444-85020-1

1. Z.B. Goldschmidt, *Atomic properties (free atom)* 1
 2. B.J. Beaudry and K.A. Gschneidner Jr, *Preparation and basic properties of the rare earth metals* 173
 3. S.H. Liu, *Electronic structure of rare earth metals* 233
 4. D.C. Koskenmaki and K.A. Gschneidner Jr, *Cerium* 337
 5. L.J. Sundström, *Low temperature heat capacity of the rare earth metals* 379
 6. K.A. McEwen, *Magnetic and transport properties of the rare earths* 411
 7. S.K. Sinha, *Magnetic structures and inelastic neutron scattering: metals, alloys and compounds* 489
 8. T.E. Scott, *Elastic and mechanical properties* 591
 9. A. Jayaraman, *High pressure studies: metals, alloys and compounds* 707
 10. C. Probst and J. Wittig, *Superconductivity: metals, alloys and compounds* 749
 11. M.B. Maple, L.E. DeLong and B.C. Sales, *Kondo effect: alloys and compounds* 797
 12. M.P. Dariel, *Diffusion in rare earth metals* 847
- Subject index 877

VOLUME 2: Alloys and intermetallics

1979, 1st repr. 1982, 2nd repr. 1991; ISBN 0-444-85021-X

13. A. Iandelli and A. Palenzona, *Crystal chemistry of intermetallic compounds* 1
 14. H.R. Kirchmayr and C.A. Poldy, *Magnetic properties of intermetallic compounds of rare earth metals* 55
 15. A.E. Clark, *Magnetostrictive RFe₂ intermetallic compounds* 231
 16. J.J. Rhyne, *Amorphous magnetic rare earth alloys* 259
 17. P. Fulde, *Crystal fields* 295
 18. R.G. Barnes, *NMR, EPR and Mössbauer effect: metals, alloys and compounds* 387
 19. P. Wachter, *Europium chalcogenides: EuO, EuS, EuSe and EuTe* 507
 20. A. Jayaraman, *Valence changes in compounds* 575
- Subject index 613

VOLUME 3: Non-metallic compounds – I

1979, 1st repr. 1984; ISBN 0-444-85215-8

21. L.A. Haskin and T.P. Paster, *Geochemistry and mineralogy of the rare earths* 1
22. J.E. Powell, *Separation chemistry* 81
23. C.K. Jørgensen, *Theoretical chemistry of rare earths* 111
24. W.T. Carnall, *The absorption and fluorescence spectra of rare earth ions in solution* 171
25. L.C. Thompson, *Complexes* 209
26. G.G. Libowitz and A.J. Maeland, *Hydrides* 299
27. L. Eyring, *The binary rare earth oxides* 337

28. D.J.M. Sevan and E. Summerville, *Mixed rare earth oxides* 401
29. C.P. Khattak and F.F.Y. Wang, *Perovskites and garnets* 525
30. L.H. Brixner, J.R. Barkley and W. Jeitschko, *Rare earth molybdates (VI)* 609
Subject index 655

VOLUME 4: Non-metallic compounds – II

1979, 1st repr. 1984; ISBN 0-444-85216-6

31. J. Flahaut, *Sulfides, selenides and tellurides* 1
32. J.M. Haschke, *Halides* 89
33. F. Hulliger, *Rare earth pnictides* 153
34. G. Blasse, *Chemistry and physics of R-activated phosphors* 237
35. M.J. Weber, *Rare earth lasers* 275
36. F.K. Fong, *Nonradiative processes of rare-earth ions in crystals* 317
37A. J.W. O'Laughlin, *Chemical spectrophotometric and polarographic methods* 341
37B. S.R. Taylor, *Trace element analysis of rare earth elements by spark source mass spectroscopy* 359
37C. R.J. Conzemius, *Analysis of rare earth matrices by spark source mass spectrometry* 377
37D. E.L. DeKalb and V.A. Fassel, *Optical atomic emission and absorption methods* 405
37E. A.P. D'Silva and V.A. Fassel, *X-ray excited optical luminescence of the rare earths* 441
37F. F.W.V. Boynton, *Neutron activation analysis* 457
37G. S. Schuhmann and J.A. Philpotts, *Mass-spectrometric stable-isotope dilution analysis for lanthanides in geochemical materials* 471
38. J. Reuben and G.A. Elgavish, *Shift reagents and NMR of paramagnetic lanthanide complexes* 483
39. J. Reuben, *Bioinorganic chemistry: lanthanides as probes in systems of biological interest* 515
40. T.J. Haley, *Toxicity* 553
Subject index 587

VOLUME 5

1982, 1st repr. 1984; ISBN 0-444-86375-3

41. M. Gasgnier, *Rare earth alloys and compounds as thin films* 1
42. E. Gratz and M.J. Zuckermann, *Transport properties (electrical resistivity, thermoelectric power thermal conductivity) of rare earth intermetallic compounds* 117
43. F.P. Netzer and E. Bertel, *Adsorption and catalysis on rare earth surfaces* 217
44. C. Boulesteix, *Defects and phase transformation near room temperature in rare earth sesquioxides* 321
45. O. Greis and J.M. Haschke, *Rare earth fluorides* 387
46. C.A. Morrison and R.P. Leavitt, *Spectroscopic properties of triply ionized lanthanides in transparent host crystals* 461
Subject index 693

VOLUME 6

1984; ISBN 0-444-86592-6

47. K.H.J. Buschow, *Hydrogen absorption in intermetallic compounds* 1
48. E. Parthé and B. Chabot, *Crystal structures and crystal chemistry of ternary rare earth–transition metal borides, silicides and homologues* 113
49. P. Rogl, *Phase equilibria in ternary and higher order systems with rare earth elements and boron* 335
50. H.B. Kagan and J.L. Namy, *Preparation of divalent ytterbium and samarium derivatives and their use in organic chemistry* 525
Subject index 567

VOLUME 7

1984; ISBN 0-444-86851-8

51. P. Rogl, *Phase equilibria in ternary and higher order systems with rare earth elements and silicon* 1
52. K.H.J. Buschow, *Amorphous alloys* 265
53. H. Schumann and W. Genthe, *Organometallic compounds of the rare earths* 446
Subject index 573

VOLUME 8

1986; ISBN 0-444-86971-9

54. K.A. Gschneidner Jr and F.W. Calderwood, *Intra rare earth binary alloys: phase relationships, lattice parameters and systematics* 1
55. X. Gao, *Polarographic analysis of the rare earths* 163
56. M. Leskelä and L. Niinistö, *Inorganic complex compounds I* 203
57. J.R. Long, *Implications in organic synthesis* 335
Errata 375
Subject index 379

VOLUME 9

1987; ISBN 0-444-87045-8

58. R. Reisfeld and C.K. Jørgensen, *Excited state phenomena in vitreous materials* 1
59. L. Niinistö and M. Leskelä, *Inorganic complex compounds II* 91
60. J.-C.G. Bünzli, *Complexes with synthetic ionophores* 321
61. Zhiquan Shen and Jun Ouyang, *Rare earth coordination catalysis in stereospecific polymerization* 395
Errata 429
Subject index 431

VOLUME 10: High energy spectroscopy

1987; ISBN 0-444-87063-6

62. Y. Baer and W.-D. Schneider, *High-energy spectroscopy of lanthanide materials – An overview* 1
63. M. Campagna and F.U. Hillebrecht, *f-electron hybridization and dynamical screening of core holes in intermetallic compounds* 75
64. O. Gunnarsson and K. Schönhammer, *Many-body formulation of spectra of mixed valence systems* 103
65. A.J. Freeman, B.I. Min and M.R. Norman, *Local density supercell theory of photoemission and inverse photoemission spectra* 165
66. D.W. Lynch and J.H. Weaver, *Photoemission of Ce and its compounds* 231
67. S. Hüfner, *Photoemission in chalcogenides* 301
68. J.F. Herbst and J.W. Wilkins, *Calculation of 4f excitation energies in the metals and relevance to mixed valence systems* 321
69. B. Johansson and N. Mårtensson, *Thermodynamic aspects of 4f levels in metals and compounds* 361
70. F.U. Hillebrecht and M. Campagna, *Bremsstrahlung isochromat spectroscopy of alloys and mixed valent compounds* 425
71. J. Röhrler, *X-ray absorption and emission spectra* 453
72. F.P. Netzer and J.A.D. Matthew, *Inelastic electron scattering measurements* 547
Subject index 601

VOLUME 11: Two-hundred-year impact of rare earths on science

1988; ISBN 0-444-87080-6

H.J. Svec, *Prologue* 1

73. F. Szabadváry, *The history of the discovery and separation of the rare earths* 33
74. B.R. Judd, *Atomic theory and optical spectroscopy* 81
75. C.K. Jørgensen, *Influence of rare earths on chemical understanding and classification* 197
76. J.J. Rhyne, *Highlights from the exotic phenomena of lanthanide magnetism* 293
77. B. Bleaney, *Magnetic resonance spectroscopy and hyperfine interactions* 323
78. K.A. Gschneidner Jr and A.H. Daane, *Physical metallurgy* 409
79. S.R. Taylor and S.M. McLennan, *The significance of the rare earths in geochemistry and cosmochemistry* 485
Errata 579
Subject index 581

VOLUME 12

1989; ISBN 0-444-87105-5

80. J.S. Abell, *Preparation and crystal growth of rare earth elements and intermetallic compounds* 1
81. Z. Fisk and J.P. Remeika, *Growth of single crystals from molten metal fluxes* 53
82. E. Burzo and H.R. Kirchmayr, *Physical properties of $R_2Fe_{14}B$ -based alloys* 71
83. A. Szytuła and J. Leciejewicz, *Magnetic properties of ternary intermetallic compounds of the RT_2X_2 type* 133
84. H. Maletta and W. Zinn, *Spin glasses* 213
85. J. van Zytveld, *Liquid metals and alloys* 357
86. M.S. Chandrasekharaiah and K.A. Gingerich, *Thermodynamic properties of gaseous species* 409
87. W.M. Yen, *Laser spectroscopy* 433
Subject index 479

VOLUME 13

1990; ISBN 0-444-88547-1

88. E.I. Gladyshevsky, O.I. Bodak and V.K. Pecharsky, *Phase equilibria and crystal chemistry in ternary rare earth systems with metallic elements* 1
89. A.A. Eliseev and G.M. Kuzmichyeva, *Phase equilibrium and crystal chemistry in ternary rare earth systems with chalcogenide elements* 191
90. N. Kimizuka, E. Takayama-Muromachi and K. Siratori, *The systems R_2O_3 – M_2O_3 – $M'O$* 283
91. R.S. Houk, *Elemental analysis by atomic emission and mass spectrometry with inductively coupled plasmas* 385
92. P.H. Brown, A.H. Rathjen, R.D. Graham and D.E. Tribe, *Rare earth elements in biological systems* 423
Errata 453
Subject index 455

VOLUME 14

1991; ISBN 0-444-88743-1

93. R. Osborn, S.W. Lovesey, A.D. Taylor and E. Balcar, *Intermultiplet transitions using neutron spectroscopy* 1
94. E. Dormann, *NMR in intermetallic compounds* 63
95. E. Zirngiebl and G. Güntherodt, *Light scattering in intermetallic compounds* 163
96. P. Thalmeier and B. Lüthi, *The electron–phonon interaction in intermetallic compounds* 225
97. N. Grewe and F. Steglich, *Heavy fermions* 343
Subject index 475

VOLUME 15

1991; ISBN 0-444-88966-3

98. J.G. Sereni, *Low-temperature behaviour of cerium compounds* 1
 99. G.-y. Adachi, N. Imanaka and Zhang Fuzhong, *Rare earth carbides* 61
 100. A. Simon, H.J. Mattausch, G.J. Miller, W. Bauhofer and R.K. Kremer, *Metal-rich halides* 191
 101. R.M. Almeida, *Fluoride glasses* 287
 102. K.L. Nash and J.C. Sullivan, *Kinetics of complexation and redox reactions of the lanthanides in aqueous solutions* 347
 103. E.N. Rizkalla and G.R. Choppin, *Hydration and hydrolysis of lanthanides* 393
 104. L.M. Vallarino, *Macrocyclic complexes of the lanthanide(III), yttrium(III), and dioxouranium (VI) ions from metal-templated syntheses* 443
 Errata 513
 Subject index 515

CUMULATIVE INDEX, Vols. 1–15

1993; ISBN 0-444-89965-0

VOLUME 16

1993; ISBN 0-444-89782-8

105. M. Loewenhaupt and K.H. Fischer, *Valence-fluctuation and heavy-fermion 4f systems* 1
 106. I.A. Smirnov and V.S. Oskotski, *Thermal conductivity of rare earth compounds* 107
 107. M.A. Subramanian and A.W. Sleight, *Rare earth pyrochlores* 225
 108. R. Miyawaki and I. Nakai, *Crystal structures of rare earth minerals* 249
 109. D.R. Chopra, *Appearance potential spectroscopy of lanthanides and their intermetallics* 519
 Author index 547
 Subject index 579

VOLUME 17: Lanthanides/Actinides: Physics – I

1993; ISBN 0-444-81502-3

110. M.R. Norman and D.D. Koelling, *Electronic structure, Fermi surfaces, and superconductivity in f electron metals* 1
 111. S.H. Liu, *Phenomenological approach to heavy-fermion systems* 87
 112. B. Johansson and M.S.S. Brooks, *Theory of cohesion in rare earths and actinides* 149
 113. U. Benedict and W.B. Holzapfel, *High-pressure studies – Structural aspects* 245
 114. O. Vogt and K. Mattenberger, *Magnetic measurements on rare earth and actinide mononictides and monochalcogenides* 301
 115. J.M. Fournier and E. Gratz, *Transport properties of rare earth and actinide intermetallics* 409
 116. W. Potzel, G.M. Kalvius and J. Gal, *Mössbauer studies on electronic structure of intermetallic compounds* 539
 117. G.H. Lander, *Neutron elastic scattering from actinides and anomalous lanthanides* 635
 Author index 711
 Subject index 753

VOLUME 18: Lanthanides/Actinides: Chemistry

1994; ISBN 0-444-81724-7

118. G.T. Seaborg, *Origin of the actinide concept* 1
 119. K. Balasubramanian, *Relativistic effects and electronic structure of lanthanide and actinide molecules* 29
 120. J.V. Beitz, *Similarities and differences in trivalent lanthanide- and actinide-ion solution absorption spectra and luminescence studies* 159

121. K.L. Nash, *Separation chemistry for lanthanides and trivalent actinides* 197
 122. L.R. Morss, *Comparative thermochemical and oxidation – reduction properties of lanthanides and actinides* 239
 123. J.W. Ward and J.M. Haschke, *Comparison of 4f and 5f element hydride properties* 293
 124. H.A. Eick, *Lanthanide and actinide halides* 365
 125. R.G. Haire and L. Eyring, *Comparisons of the binary oxides* 413
 126. S.A. Kinkead, K.D. Abney and T.A. O'Donnell, *f-Element speciation in strongly acidic media: lanthanide and mid-actinide metals, oxides, fluorides and oxide fluorides in superacids* 507
 127. E.N. Rizkalla and G.R. Choppin, *Lanthanides and actinides hydration and hydrolysis* 529
 128. G.R. Choppin and E.N. Rizkalla, *Solution chemistry of actinides and lanthanides* 559
 129. J.R. Duffield, D.M. Taylor and D.R. Williams, *The biochemistry of the f-elements* 591
 Author index 623
 Subject index 659

VOLUME 19: Lanthanides/Actinides: Physics – II

1994; ISBN 0-444-82015-9

130. E. Holland-Moritz and G.H. Lander, *Neutron inelastic scattering from actinides and anomalous lanthanides* 1
 131. G. Aeppli and C. Broholm, *Magnetic correlations in heavy-fermion systems: neutron scattering from single crystals* 123
 132. P. Wachter, *Intermediate valence and heavy fermions* 177
 133. J.D. Thompson and J.M. Lawrence, *High pressure studies – Physical properties of anomalous Ce, Yb and U compounds* 383
 134. C. Colinet and A. Pasturel, *Thermodynamic properties of metallic systems* 479
 Author index 649
 Subject index 693

VOLUME 20

1995; ISBN 0-444-82014-0

135. Y. Ōnuki and A. Hasegawa, *Fermi surfaces of intermetallic compounds* 1
 136. M. Gasgnier, *The intricate world of rare earth thin films: metals, alloys, intermetallics, chemical compounds,...* 105
 137. P. Vajda, *Hydrogen in rare-earth metals, including RH_{2+x} phases* 207
 138. D. Gignoux and D. Schmitt, *Magnetic properties of intermetallic compounds* 293
 Author index 425
 Subject index 457

VOLUME 21

1995; ISBN 0-444-82178-3

139. R.G. Bautista, *Separation chemistry* 1
 140. B.W. Hinton, *Corrosion prevention and control* 29
 141. N.E. Ryan, *High-temperature corrosion protection* 93
 142. T. Sakai, M. Matsuoka and C. Iwakura, *Rare earth intermetallics for metal–hydrogen batteries* 133
 143. G.-y. Adachi and N. Imanaka, *Chemical sensors* 179
 144. D. Garcia and M. Faucher, *Crystal field in non-metallic (rare earth) compounds* 263
 145. J.-C.G. Bünzli and A. Milicic-Tang, *Solvation and anion interaction in organic solvents* 305
 146. V. Bhagavathy, T. Prasada Rao and A.D. Damodaran, *Trace determination of lanthanides in high-purity rare-earth oxides* 367
 Author index 385
 Subject index 411

VOLUME 22

1996; ISBN 0-444-82288-7

147. C.P. Flynn and M.B. Salamon, *Synthesis and properties of single-crystal nanostructures* 1
148. Z.S. Shan and D.J. Sellmyer, *Nanoscale rare earth–transition metal multilayers: magnetic structure and properties* 81
149. W. Suski, *The ThMn₁₂-type compounds of rare earths and actinides: structure, magnetic and related properties* 143
150. L.K. Aminov, B.Z. Malkin and M.A. Teplov, *Magnetic properties of nonmetallic lanthanide compounds* 295
151. F. Auzel, *Coherent emission in rare-earth materials* 507
152. M. Dolg and H. Stoll, *Electronic structure calculations for molecules containing lanthanide atoms* 607
Author index 731
Subject index 777

VOLUME 23

1996; ISBN 0-444-82507-X

153. J.H. Forsberg, *NMR studies of paramagnetic lanthanide complexes and shift reagents* 1
154. N. Sabbatini, M. Guardigli and I. Manet, *Antenna effect in encapsulation complexes of lanthanide ions* 69
155. C. Görlner-Walrand and K. Binnemans, *Rationalization of crystal-field parameterization* 121
156. Yu. Kuz'ma and S. Chykhrij, *Phosphides* 285
157. S. Boghosian and G.N. Papatheodorou, *Halide vapors and vapor complexes* 435
158. R.H. Byrne and E.R. Sholkovitz, *Marine chemistry and geochemistry of the lanthanides* 497
Author index 595
Subject index 631

VOLUME 24

1997; ISBN 0-444-82607-6

159. P.A. Dowben, D.N. McIlroy and Dongqi Li, *Surface magnetism of the lanthanides* 1
160. P.G. McCormick, *Mechanical alloying and mechanically induced chemical reactions* 47
161. A. Inoue, *Amorphous, quasicrystalline and nanocrystalline alloys in Al- and Mg-based systems* 83
162. B. Elschner and A. Loidl, *Electron-spin resonance on localized magnetic moments in metals* 221
163. N.H. Duc, *Intersublattice exchange coupling in the lanthanide-transition metal intermetallics* 339
164. R.V. Skolozdra, *Stannides of rare-earth and transition metals* 399
Author index 519
Subject index 559

VOLUME 25

1998; ISBN 0-444-82871-0

165. H. Nagai, *Rare earths in steels* 1
166. R. Marchand, *Ternary and higher order nitride materials* 51
167. C. Görlner-Walrand and K. Binnemans, *Spectral intensities of f–f transitions* 101
168. G. Bombieri and G. Paolucci, *Organometallic π complexes of the f-elements* 265
Author index 415
Subject index 459

VOLUME 26

1999; ISBN 0-444-50815-1

169. D.F. McMorrow, D. Gibbs and J. Bohr, *X-ray scattering studies of lanthanide magnetism* 1
 170. A.M. Tishin, Yu.I. Spichkin and J. Bohr, *Static and dynamic stresses* 87
 171. N.H. Duc and T. Goto, *Itinerant electron metamagnetism of Co sublattice in the lanthanide–cobalt intermetallics* 177
 172. A.J. Arko, P.S. Riseborough, A.B. Andrews, J.J. Joyce, A.N. Tahvildar-Zadeh and M. Jarrell, *Photo-electron spectroscopy in heavy fermion systems: Emphasis on single crystals* 265
 Author index 383
 Subject index 405

VOLUME 27

1999; ISBN 0-444-50342-0

173. P.S. Salamakha, O.L. Sologub and O.I. Bodak, *Ternary rare-earth-germanium systems* 1
 174. P.S. Salamakha, *Crystal structures and crystal chemistry of ternary rare-earth germanides* 225
 175. B. Ya. Kotur and E. Gratz, *Scandium alloy systems and intermetallics* 339
 Author index 535
 Subject index 553

VOLUME 28

2000; ISBN 0-444-50346-3

176. J.-P. Connerade and R.C. Karnatak, *Electronic excitation in atomic species* 1
 177. G. Meyer and M.S. Wickleder, *Simple and complex halides* 53
 178. R.V. Kumar and H. Iwahara, *Solid electrolytes* 131
 179. A. Halperin, *Activated thermoluminescence (TL) dosimeters and related radiation detectors* 187
 180. K.L. Nash and M.P. Jensen, *Analytical separations of the lanthanides: basic chemistry and methods* 311
 Author index 373
 Subject index 401

VOLUME 29: The role of rare earths in catalysis

2000; ISBN 0-444-50472-9

P. Maestro, *Foreword* 1

181. V. Paul-Boncour, L. Hilaire and A. Percheron-Guégan, *The metals and alloys in catalysis* 5
 182. H. Imamura, *The metals and alloys (prepared utilizing liquid ammonia solutions) in catalysis II* 45
 183. M.A. Ulla and E.A. Lombardo, *The mixed oxides* 75
 184. J. Kašpar, M. Graziani and P. Fornasiero, *Ceria-containing three-way catalysts* 159
 185. A. Corma and J.M. López Nieto, *The use of rare-earth-containing zeolite catalysts* 269
 186. S. Kobayashi, *Triflates* 315
 Author index 377
 Subject index 409

VOLUME 30: High-Temperature Superconductors – I

2000; ISBN 0-444-50528-8

187. M.B. Maple, *High-temperature superconductivity in layered cuprates: overview* 1
 188. B. Raveau, C. Michel and M. Hervieu, *Crystal chemistry of superconducting rare-earth cuprates* 31

189. Y. Shiohara and E.A. Goodilin, *Single-crystal growth for science and technology* 67
 190. P. Karen and A. Kjekshus, *Phase diagrams and thermodynamic properties* 229
 191. B. Elschner and A. Loidl, *Electron paramagnetic resonance in cuprate superconductors and in parent compounds* 375
 192. A.A. Manuel, *Positron annihilation in high-temperature superconductors* 417
 193. W.E. Pickett and I.I. Mazin, *RBa₂Cu₃O₇ compounds: electronic theory and physical properties* 453
 194. U. Staub and L. Soderholm, *Electronic 4f-state splittings in cuprates* 491
 Author index 547
 Subject index 621

VOLUME 31: High-Temperature Superconductors – II

2001; ISBN 0-444-50719-1

195. E. Kaldis, *Oxygen nonstoichiometry and lattice effects in YBa₂Cu₃O_x. Phase transitions, structural distortions and phase separation* 1
 196. H.W. Weber, *Flux pinning* 187
 197. C.C. Almasan and M.B. Maple, *Magnetoresistance and Hall effect* 251
 198. T.E. Mason, *Neutron scattering studies of spin fluctuations in high-temperature superconductors* 281
 199. J.W. Lynn and S. Skanthakumar, *Neutron scattering studies of lanthanide magnetic ordering* 315
 200. P.M. Allenspach and M.B. Maple, *Heat capacity* 351
 201. M. Schabel and Z.-X. Shen, *Angle-resolved photoemission studies of untwinned yttrium barium copper oxide* 391
 202. D.N. Basov and T. Timusk, *Infrared properties of high-T_c superconductors: an experimental overview* 437
 203. S.L. Cooper, *Electronic and magnetic Raman scattering studies of the high-T_c cuprates* 509
 204. H. Sugawara, T. Hasegawa and K. Kitazawa, *Characterization of cuprate superconductors using tunneling spectra and scanning tunneling microscopy* 563
 Author index 609
 Subject index 677

VOLUME 32

2001; ISBN 0-444-50762-0

205. N.H. Duc, *Giant magnetostriction in lanthanide-transition metal thin films* 1
 206. G.M. Kalvius, D.R. Noakes and O. Hartmann, *μSR studies of rare-earth and actinide magnetic materials* 55
 207. Rainer Pöttgen, Dirk Johrendt and Dirk Kußmann, *Structure–property relations of ternary equiatomic YbTX intermetallics* 453
 208. Kurima Kobayashi and Satoshi Hirose, *Permanent magnets* 515
 209. I.G. Vasilyeva, *Polysulfides* 567
 210. Dennis K.P. Ng, Jianzhuang Jiang, Kuninobu Kasuga and Kenichi Machida, *Half-sandwich tetrapyrrole complexes of rare earths and actinides* 611
 Author index 655
 Subject index 733

VOLUME 33

2003; ISBN 0-444-51323-X

211. Brian C. Sales, *Filled skutterudites* 1
 212. Oksana L. Sologub and Petro S. Salamakha, *Rare earth – antimony systems* 35
 213. R.J.M. Konings and A. Kovács, *Thermodynamic properties of the lanthanide (III) halides* 147

214. John B. Goodenough, *Rare earth – manganese perovskites* 249
 215. Claude Piguët and Carlos F.G.C. Geraldès, *Paramagnetic NMR lanthanide induced shifts for extracting solution structures* 353
 216. Isabelle Billard, *Lanthanide and actinide solution chemistry as studied by time-resolved emission spectroscopy* 465
 217. Thomas Tröster, *Optical studies of non-metallic compounds under pressure* 515
 Author index 591
 Subject index 637

VOLUME 34

2004; ISBN 0-444-51587-9

218. Yaroslav M. Kalychak, Vasyl' I. Zaremba, Rainer Pöttgen, Mar'yana Lukachuk and Rolf-Dieter Hoffman, *Rare earth–transition metal–indides* 1
 219. P. Thalmeier and G. Zwicknagl, *Unconventional superconductivity and magnetism in lanthanide and actinide intermetallic compounds* 135
 220. James P. Riehl and Gilles Muller, *Circularly polarized luminescence spectroscopy from lanthanide systems* 289
 221. Oliver Guillou and Carole Daiguebonne, *Lanthanide-containing coordination polymers* 359
 222. Makoto Komiyama, *Cutting DNA and RNA* 405
 Author index 455
 Subject index 493

VOLUME 35

2005; ISBN 0-444-52028-7

223. Natsuko Sakai, Katsuhiko Yamaji, Teruhisa Horita, Yue Ping Xiong and Harumi Yokokawa, *Rare-earth materials for solid oxide fuel cells (SOFC)* 1
 224. Mathias S. Wickleder, *Oxo-selenates of rare-earth elements* 45
 225. Koen Binnemans, *Rare-earth beta-diketonates* 107
 226. Satoshi Shinoda, Hiroyuki Miyake and Hiroshi Tsukube, *Molecular recognition and sensing via rare-earth complexes* 273
 Author index 337
 Subject index 377

VOLUME 36

2006; ISBN 0-444-52142-9

227. Arthur Mar, *Bismuthides* 1
 228. I. Aruna, L.K. Malhotra and B.R. Mehta, *Switchable metal hydride films* 83
 229. Koen Binnemans, *Applications of tetravalent cerium compounds* 281
 230. Robert A. Flowers II and Edamana Prasad, *Samarium (II) based reductants* 393
 Author index 475
 Subject index 511

VOLUME 37: Optical Spectroscopy

2007; ISBN 978-0-444-52144-6

231. Kazuyoshi Ogasawara, Shinta Watanabe, Hiroaki Toyoshima and Mikhail G. Brik, *First-principles calculations of $4f^n \rightarrow 4f^{n-1} 5d$ transition spectra* 1
 232. Gary W. Burdick and Michael F. Reid, *$4f^n - 4f^{n-1} 5d$ transitions* 61
 233. Guokui Liu and Xueyuan Chen, *Spectroscopic properties of lanthanides in nanomaterials* 99
 234. Takuya Nishioka, Kôichi Fukui and Kazuko Matsumoto, *Lanthanide chelates as luminescent labels in biomedical analyses* 171

235. Steve Comby and Jean-Claude G. Bünzli, *Lanthanide near-infrared luminescence in molecular probes and devices* 217
Author index 471
Subject index 503

VOLUME 38

2008; ISBN 978-0-444-52143-9

236. Z.C. Kang, *Lanthanide Higher Oxides: The Contributions of Leroy Eyring* 1
237. Rainer Pöttgen and Ute Ch. Rodewald, *Rare Earth–Transition Metal–Plumbides* 55
238. Takao Mori, *Higher Borides* 105
239. K.-H. Müller, M. Schneider, G. Fuchs and S.-L. Drechsler, *Rare-Earth Nickel Borocarbides* 175
240. Michael T. Pope, *Polyoxometalates* 337
Author index 383
Subject index 431

INDEX OF CONTENTS OF VOLUMES 1–39

- 4f excitation energies, calculations of **10**, ch. 68, p. 321
- 4f levels, thermodynamic aspects **10**, ch. 69, p. 361
- 4f state splittings in cuprates **30**, ch. 194, p. 491
- 4f states, character of **39**, ch. 241, p. 1
- 4fⁿ–4fⁿ⁻¹ 5d transitions **37**, ch. 231, p. 1; **37**, ch. 232, p. 61
- ab-initio calculation of energy levels **37**, ch. 231, p. 1
- absorption spectra of ions in solution **3**, ch. 24, p. 171; **18**, ch. 120, p. 150
- actinide concept, origin of **18**, ch. 118, p. 1
- activated phosphors **4**, ch. 34, p. 237
- activated thermoluminescence **28**, ch. 179, p. 187
- aluminates **39**, ch. 242, p. 113
- amorphous alloys **7**, ch. 52, p. 265
- Al- and Mg-based **24**, ch. 161, p. 83
- magnetic **2**, ch. 16, p. 259
- anion interaction in organic solvents **21**, ch. 145, p. 305
- antimony alloy systems **33**, ch. 212, p. 35
- atomic properties (free atom) **1**, ch. 1, p. 1
- atomic theory **11**, ch. 74, p. 81
- Belousov-Zhabotinsky reactions **36**, ch. 229, p. 281
- beta-diketonates **35**, ch. 225, p. 107
- biochemistry **18**, ch. 129, p. 591
- bioinorganic chemistry **4**, ch. 39, p. 515
- biological systems **13**, ch. 92, p. 423
- bismuth alloy systems **36**, ch. 227, p. 1
- borides **6**, ch. 48, p. 113; **6**, ch. 49, p. 335; **38**, ch. 238, p. 105; **38**, ch. 239, p. 175
- carbides **15**, ch. 99, p. 61; **38** ch. 239, p. 175
- Carnall, William T. **37**, dedication, p. xiii
- catalysis **29**, foreword, p. 1
- ceria-containing three-way **29**, ch. 184, p. 159
- metals and alloys **29**, ch. 181, p. 5
- metals and alloys in liquid ammonia solutions **29**, ch. 182, p. 45
- mixed oxides **29**, ch. 183, p. 75
- zeolites **29**, ch. 185, p. 269
- cerimetry **36**, ch. 229, p. 281
- cerium **1**, ch. 4, p. 337
- cerium compounds
- low-temperature behavior **15**, ch. 98, p. 1
- tetravalent **36**, ch. 229, p. 281
- cerium(IV)
- catalysts **36**, ch. 229, p. 281
- mediated reactions **36**, ch. 229, p. 281
- redox properties **36**, ch. 229, p. 281
- chalcogenides, magnetic measurements on mono- **17**, ch. 114, p. 301
- chemical analysis by
- atomic emission with inductively coupled plasmas **13**, ch. 91, p. 385
- mass spectrometry, see spectroscopy, mass
- neutron activation **4**, ch. 37F, p. 457
- optical absorption **4**, ch. 37D, p. 405
- optical atomic emission **4**, ch. 37D, p. 405
- polarography **4**, ch. 37A, p. 341; **8**, ch. 55, p. 163
- spectrophotometry **4**, ch. 37A, p. 341
- trace determination in high-purity oxides **21**, ch. 146, p. 367
- X-ray excited optical luminescence **4**, ch. 37E, p. 441
- chemical sensors **21**, ch. 143, p. 179
- chemical understanding and classification **11**, ch. 75, p. 197
- chirality sensing **35**, ch. 226, p. 273
- coherent emission **22**, ch. 151, p. 507
- cohesion, theory of **17**, ch. 112, p. 149
- complexes **3**, ch. 25, p. 209
- antenna effect **23**, ch. 154, p. 69
- beta-diketonates **35**, ch. 225, p. 107
- half-sandwich tetrapyrrole **32**, ch. 210, p. 611
- inorganic **8**, ch. 56, p. 203; **9**, ch. 59, p. 91
- macrocycles **15**, ch. 104, p. 443
- molecular recognition in **35**, ch. 226, p. 273
- organometallic π type **25**, ch. 168, p. 265
- polyoxometalates **38**, ch. 240, p. 337; **39**, ch. 243, p. 297
- sensing in **35**, ch. 226, p. 273

- with synthetic ionophores 9, ch. 60, p. 321
- coordination catalysis in stereospecific polymerization 9, ch. 61, p. 395
- coordination in organic solvents 21, ch. 145, p. 305
- coordination polymers 34, ch. 221, p. 359
- corrosion prevention and control 21, ch. 140, p. 29
- corrosion protection 21, ch. 141, p. 93
- cosmochemistry 11, ch. 79, p. 485
- crystal chemistry
 - of aluminates 39, ch. 242, p. 113
 - of gallates 39, ch. 242, p. 113
 - of higher borides 38, ch. 238, p. 105
 - of intermetallic compounds 2, ch. 13, p. 1
 - of ternary germanides 27, ch. 174, p. 225
 - of ternary systems with chalcogenides 13, ch. 89, p. 191
 - of ternary systems with metallic elements 13, ch. 88, p. 1
 - of ternary transition metal borides 6, ch. 48, p. 113
 - of ternary transition metal plumbides 38, ch. 237, p. 55
 - of ternary transition metal silicides 6, ch. 48, p. 113
 - of ThMn₁₂-type compounds 22, ch. 149, p. 143
- crystal field 2, ch. 17, p. 295
- in non-metallic compounds 21, ch. 144, p. 263
- parametrization, rationalization of 23, ch. 155, p. 121
- crystal structures, see crystal chemistry
- cuprates
 - 4f state splittings 30, ch. 194, p. 491
 - crystal chemistry 30, ch. 188, p. 31
 - electron paramagnetic resonance (EPR) 30, ch. 191, p. 375
 - electronic theory 30, ch. 193, p. 453
 - flux pinning 31, ch. 196, p. 187
 - Hall effect 31, ch. 197, p. 251
 - heat capacity 31, ch. 200, p. 351
 - infrared properties 31, ch. 202, p. 437
 - magnetoresistance 31, ch. 197, p. 251
 - neutron scattering
 - magnetic ordering 31, ch. 199, p. 315
 - spin fluctuations 31, ch. 198, p. 281
 - overview 30, ch. 187, p. 1
 - oxygen nonstoichiometry and lattice effect 31, ch. 195, p. 1
 - phase equilibria 30, ch. 190, p. 229
 - phase transitions, structural distortions and phase separation 31, ch. 195, p. 1
 - photoemission, angle-resolved studies 31, ch. 201, p. 391
 - physical properties 30, ch. 193, p. 453
 - positron annihilation 30, ch. 192, p. 417
 - Raman scattering 31, ch. 203, p. 509
 - scanning tunneling microscopy 31, ch. 204, p. 563
 - single crystals, growth of 30, ch. 189, p. 67
 - superconductivity 30; 31
 - thermochemical properties 30, ch. 190, p. 229
 - tunneling spectra 31, ch. 204, p. 563
- dedications
 - F.H. Spedding 11, p. 1
 - Friedrich Hund 14, p. ix
 - LeRoy Eyring 36, p. xi
 - William T. Carnall 37, p. xiii
- diffusion in metals 1, ch. 12, p. 847
- diketonates, see beta-diketonates
- divalent samarium in organic chemistry 6, ch. 50, p. 525; 36, ch. 230, p. 393
- divalent ytterbium derivatives in organic chemistry 6, ch. 50, p. 525
- DNA, cutting of 34, ch. 222, p. 405
- dynamical screening of core holes in intermetallic compounds 10, ch. 63, p. 75
- elastic and mechanical properties of metals 1, ch. 8, p. 591
- electron paramagnetic resonance (EPR) 2, ch. 18, p. 387; 24, ch. 162, p. 221
 - in cuprate superconductors 30, ch. 191, p. 375
- electronic excitation in atomic species 28, ch. 176, p. 1
- electronic structure
 - calculations for molecules 22, ch. 152, p. 607
 - of chalcogenides 39, ch. 241, p. 1
 - of metals 1, ch. 3, p. 233; 17, ch. 110, p. 1; 39, ch. 241, p. 1
 - of oxides 39, ch. 241, p. 1
 - of pnictides 39, ch. 241, p. 1
- electronic theory of cuprates 30, ch. 193, p. 453
- electron-phonon interaction in intermetallic compounds 14, ch. 96, p. 225
- electron-spin resonance, see electron paramagnetic resonance
- emission spectra 10, ch. 71, p. 453
- europium chalcogenides 2, ch. 19, p. 507
- exchange coupling in transition metal intermetallics 24, ch. 163, p. 339
- excited state phenomena in vitreous materials 9, ch. 58, p. 1
- Eyring, L.
 - dedication 36, p. xi
 - contributions of, higher oxides 38, ch. 236, p. 1
- f-electron hybridization 39, ch. 241, p. 1
 - in intermetallic compounds 10, ch. 63, p. 75

- f-element speciation in strongly acidic media (superacids) **18**, ch. 126, p. 507
- f-f transitions, spectral intensities **25**, ch. 167, p. 101
- f-states: dual, localized, band-like character **39**, ch. 241, p. 1
- Fermi surfaces
- of intermetallic compounds **20**, ch. 135, p. 1
 - of metals **17**, ch. 110, p. 1
- fluorescence spectra of ions in solution **3**, ch. 24, p. 171
- fluoride glasses **15**, ch. 101, p. 287
- fluorides **5**, ch. 45, p. 387
- flux pinning in cuprates **31**, ch. 196, p. 187
- gallates **39**, ch. 242, p. 113
- garnets **3**, ch. 29, p. 525
- geochemistry **3**, ch. 21, p. 1; **11**, ch. 79, p. 485; **23**, ch. 158, p. 497
- germanium, ternary systems **27**, ch. 173, p. 1
- halides **4**, ch. 32, p. 89; **18**, ch. 124, p. 365
- metal-rich **15**, ch. 100, p. 191
 - simple and complex **28**, ch. 177, p. 53
 - thermodynamic properties **33**, ch. 213, p. 147
 - vapors and vapor complexes **23**, ch. 157, p. 435
- Hall effect in cuprates **31**, ch. 197, p. 251
- heat capacity
- of cuprates **31**, ch. 200, p. 351
 - of metals **1**, ch. 5, p. 379
- heavy fermions **14**, ch. 97, p. 343; **16**, ch. 105, p. 1; **19**, ch. 132, p. 177
- phenomenological approach **17**, ch. 111, p. 87
 - photoelectron spectroscopy **26**, ch. 172, p. 265
- high pressure studies **1**, ch. 9, p. 707
- anomalous Ce, Yb and U compounds **19**, ch. 133, p. 383
 - optical studies of non-metallic compounds **33**, ch. 217, p. 515
 - structural aspects **17**, ch. 113, p. 245
- high temperature superconductors **30**; **31**
- history of the discovery and separation **11**, ch. 73, p. 33
- Hund, F. **14**, dedication, p. ix
- hydration **15**, ch. 103, p. 393; **18**, ch. 127, p. 529
- hydrides **3**, ch. 26, p. 299; **18**, ch. 123, p. 293
- switchable films **36**, ch. 228, p. 83
- hydrogen absorption in intermetallic compounds **6**, ch. 47, p. 1
- hydrogen in metals, including $\text{RH}_2 + x$ phases **20**, ch. 137, p. 207
- hydrolysis **15**, ch. 103, p. 393; **18**, ch. 127, p. 529
- hyperfine interactions **11**, ch. 77, p. 323
- inelastic electron scattering **10**, ch. 72, p. 547
- infrared properties of cuprates **31**, ch. 202, p. 437
- inorganic complex compounds **8**, ch. 56, p. 203; **9**, ch. 59, p. 91
- intermediate valence **19**, ch. 132, p. 177
- itinerant electron metamagnetism in cobalt intermetallics **26**, ch. 171, p. 177
- kinetics of complexation in aqueous solutions **15**, ch. 102, p. 347
- Kondo effect **1**, ch. 11, p. 797
- lanthanide-induced shifts **4**, ch. 38, p. 483; **23**, ch. 153, p. 1; **33**, ch. 215, p. 353
- lanthanide chelates
- for sensitizing NIR luminescence **37**, ch. 234, p. 171
 - in biomedical analyses **37**, ch. 235, p. 217
- laser spectroscopy **12**, ch. 87, p. 433
- lasers **4**, ch. 35, p. 275
- light scattering in intermetallic compounds **14**, ch. 95, p. 163
- liquid metals and alloys **12**, ch. 85, p. 357
- LIS, see lanthanide-induced shifts
- luminescence
- in biomedical analyses **37**, ch. 234, p. 171
 - in NIR molecular probes and devices **37**, ch. 235, p. 217
 - polyoxometalates **39**, ch. 243, p. 297
 - studies of ions **18**, ch. 120, p. 159
 - spectra of ions in solution **3**, ch. 24, p. 171
- μSR studies of magnetic materials, **32**, ch. 206, p. 55
- magnetic and transport properties of metals **1**, ch. 6, p. 411
- magnetic correlations in heavy-fermion systems **19**, ch. 131, p. 123
- magnetic properties (also see physical properties)
- of borides **38**, ch. 238, p. 105
 - of intermetallic compounds **2**, ch. 14, p. 55; **20**, ch. 138, p. 293
 - of nickel borocarbides **38**, ch. 239, p. 175
 - of nonmetallic compounds **22**, ch. 150, p. 295
 - of ternary RT_2X_2 type intermetallic compounds **12**, ch. 83, p. 133
 - of ThMn_{12} -type compounds **22**, ch. 149, p. 143
- magnetic structures **1**, ch. 7, p. 489
- magnetism **34**, ch. 219, p. 135
- exotic phenomena **11**, ch. 76, p. 293
 - surface **24**, ch. 159, p. 1
- magnetoresistance in cuprates **31**, ch. 197, p. 251

- magnetostriction
 – RFe₂ 2, ch. 15, p. 231
 – transition metal thin films 32, ch. 205, p. 1
 marine chemistry 23, ch. 158, p. 497
 mechanical alloying 24, ch. 160, p. 47
 mechanically induced chemical reactions 24,
 ch. 160, p. 47
 metal–hydrogen batteries 21, ch. 142, p. 133
 mineralogy 3, ch. 21, p. 1
 minerals, crystal structures 16, ch. 108, p. 249
 mixed valence systems
 – bremsstrahlung isochromat spectroscopy 10,
 ch. 70, p. 425
 – calculation of 4f excitation energies 10, ch. 68,
 p. 321
 – many-body formulation of spectra 10, ch. 64,
 p. 103
 molecular recognition 35, ch. 226, p. 273
 molybdates (VI) 3, ch. 30, p. 609
 Mössbauer effect 2, ch. 18, p. 387
 – of intermetallic compounds 17, ch. 116, p. 539
- nanostructures and nanomaterials
 – Al- and Mg-based systems 24, ch. 161, p. 83
 – photochemical nano-ring formation 39,
 ch. 243, p. 297
 – properties 22, ch. 147, p. 1
 – spectroscopic properties 37, ch. 233, p. 99
 – synthesis 22, ch. 147, p. 1
 – transition metal multilayers 22, ch. 148, p. 81
 neutron scattering
 – elastic 17, ch. 117, p. 635
 – in heavy-fermion systems 19, ch. 131, p. 123
 – inelastic 1, ch. 7, p. 489
 – inelastic of anomalous lanthanides 19, ch. 130,
 p. 1
 – intermultiple transitions 14, ch. 93, p. 1
 – of magnetic ordering in cuprates 31, ch. 199,
 p. 315
 – of spin fluctuations in cuprates 31, ch. 198,
 p. 281
 near-infrared luminescence in molecular probes
 and devices 37, ch. 235, p. 217
 nitride materials, ternary and higher order 24,
 ch. 166, p. 51
 NMR 2, ch. 18, p. 387
 – in intermetallic compounds 14, ch. 94, p. 63
 – lanthanide induced shifts for extracting
 solution structures 33, ch. 215, p. 353
 – of complexes 23, ch. 153, p. 1
 – of paramagnetic complexes 4, ch. 38, p. 483
 – solution structure by paramagnetic NMR
 analysis 33, ch. 215, p. 353
 nonradiative processes in crystals 4, ch. 36,
 p. 317
- nuclear magnetic resonance, see NMR
- organic synthesis 8, ch. 57, p. 335
 organometallic compounds 7, ch. 53, p. 446
 oxidation-reduction properties 18, ch. 122,
 p. 239
 oxides
 – aluminates 39, ch. 242, p. 113
 – binary 3, ch. 27, p. 337; 18, ch. 125, p. 413
 – gallates 39, ch. 242, p. 113
 – higher 38, ch. 236, p. 1
 – mixed 3, ch. 28, p. 401
 – sesqui, defects in 5, ch. 44, p. 321
 – sesqui, phase transformation in 5, ch. 44,
 p. 321
 – ternary systems, R₂O₃–M₂O₃–M'O 13, ch. 90,
 p. 283
 oxo-selenates 35, ch. 224, p. 45
 oxygen nonstoichiometry and lattice effect in
 YBa₂Cu₃O_x 31, ch. 195, p. 1
- permanent magnets 32, ch. 208, p. 515
 perovskites 3, ch. 29, p. 525
 – aluminates 39, ch. 242, p. 113
 – gallates 39, ch. 242, p. 113
 – manganese 33, ch. 214, p. 249
 phase equilibria
 – in cuprates 30, ch. 190, p. 229
 – in ternary systems with boron 6, ch. 49, p. 335;
 38, ch. 238, p. 105
 – in ternary systems with chalcogenides 13,
 ch. 89, p. 191
 – in ternary systems with metallic elements 13,
 ch. 88, p. 1
 – in ternary systems with lead 38, ch. 237, p. 55
 – in ternary systems with silicon 7, ch. 51, p. 1
 – intra rare earth binary alloys 8, ch. 54, p. 1
 phase transitions, structural distortions and
 phase separation in YBa₂Cu₃O_x 31,
 ch. 195, p. 1
 phosphides 23, ch. 156, p. 285
 photochemical nano-ring formation in
 polyoxometalates 39, ch. 243, p. 297
 photoemission
 – angle-resolved studies of untwinned
 YBa₂Cu₃O_x 31, ch. 201, p. 391
 – in chalcogenides 10, ch. 67, p. 301
 – inverse spectra, local density supercell
 theory 10, ch. 65, p. 165
 – of Ce and its compounds 10, ch. 66, p. 231
 – spectra, local density supercell theory 10,
 ch. 65, p. 165
 – theory of 39, ch. 241, p. 1
 physical metallurgy 11, ch. 78, p. 409
 physical properties (also see magnetic properties)

- of cuprates 30, ch. 193, p. 453
- of metals 1, ch. 2, p. 173
- of $R_2Fe_{14}B$ -based alloys 12, ch. 82, p. 71
- pnictides 4, ch. 33, p. 153
- magnetic measurements on mono- 17, ch. 114, p. 301
- polyoxometalates 38, ch. 240, p. 337
- luminescence of 39, ch. 243, p. 297
- positron annihilation in high-temperature superconductors 30, ch. 192, p. 417
- preparation and purification of metals 1, ch. 2, p. 173
- pyrochlores 16, ch. 107, p. 225

- quasicrystalline, Al- and Mg-based systems 24, ch. 161, p. 83

- Raman scattering of cuprates 31, ch. 203, p. 509
- redox reactions
 - in aqueous solutions 15, ch. 102, p. 347
 - Ce(IV)/Ce(III) 36, ch. 229, p. 347
- relativistic effects and electronic structure 18, ch. 119, p. 29
- RNA, cutting of 34, ch. 222, p. 405; 36, ch. 229, p. 392

- samarium(II) reductants 36, ch. 230, p. 393
- scandium alloy systems and intermetallics 27, ch. 175, p. 339
- scanning tunneling microscopy of cuprates 31, ch. 204, p. 563
- selenates 35, ch. 224, p. 45
- selenides 4, ch. 31, p. 1
- selenites 35, ch. 224, p. 45
- separation chemistry 3, ch. 22, p. 81; 18, ch. 121, p. 197; 21, ch. 139, p. 1
- analytical, basic chemistry and methods 28, ch. 180, p. 311
- shift reagents 4, ch. 38, p. 483; 23, ch. 153, p. 1; 33, ch. 215, p. 353; 35, ch. 225, p. 107
- single crystals
 - growth from molten metal fluxes 12, ch. 81, p. 53
 - growth of cuprates 30, ch. 189, p. 67
 - growth of metals and intermetallic compounds 12, ch. 80, p. 1
- skutterudites, filled 33, ch. 211, p. 1
- solid electrolytes 28, ch. 178, p. 131; 35, ch. 223, p. 1
- solid oxide fuel cells (SOFC) 35, ch. 223, p. 1
- solution chemistry 15, ch. 103, p. 393; 18, ch. 127, p. 529; 18, ch. 128, p. 559; 21, ch. 145, p. 305
- solvation in organic solvents 21, ch. 145, p. 305

- spectroscopic properties in transparent crystals 5, ch. 46, p. 461
- nanomaterials 37, ch. 233, p. 99
- spectroscopy
 - appearance potential 16, ch. 109, p. 519
 - bremsstrahlung isochromat 10, ch. 70, p. 425
 - circularly polarized luminescence 34, ch. 220, p. 289
 - high-energy 10, ch. 62, p. 1
 - magnetic resonance 11, ch. 77, p. 323
 - mass
 - – spark source matrices 4, ch. 37C, p. 377
 - – spark source trace element analysis 4, ch. 37B, p. 359
 - – stable-isotope dilution analysis 4, ch. 37G, p. 471
 - – with inductively coupled plasmas analysis 13, ch. 91, p. 385
 - optical 11, ch. 74, p. 81; 37, ch. 233, p. 99; ch. 234, p. 171; 37, ch. 235, p. 217
 - photoelectron in heavy fermion systems 26, ch. 172, p. 265
 - time-resolved emission in solution chemistry 33, ch. 216, p. 465
- Spedding, F.H., 11, prologue, p. 1
- spin glasses 12, ch. 84, p. 213
- stannides, transition metal ternary systems 24, ch. 164, p. 399
- steels 25, ch. 165, p. 1
- stresses, static and dynamic 26, ch. 170, p. 87
- sulfides 4, ch. 31, p. 1
 - poly 32, ch. 209, 567
- superconductivity 1, ch. 10, p. 749; 34, ch. 219, p. 135
 - crystal chemistry of cuprates 30, ch. 188, p. 31
 - in metals 17, ch. 110, p. 1
 - high-temperature layered cuprates:
 - overview 30, ch. 187, p. 1
 - nickel borocarbides 38, ch. 239, p. 175
 - unconventional and magnetism 34, ch. 219, p. 135
- surfaces
 - adsorption on 5, ch. 43, p. 217
 - catalysis on 5, ch. 43, p. 217
- switchable metal hydride films 36, ch. 228, p. 83
- systematics, intra rare earth binary alloys 8, ch. 54, p. 1

- tellurides 4, ch. 31, p. 1
- ternary equiatomic YbTX intermetallics 32, ch. 207, p. 453
- tetravalent cerium compounds 36, ch. 229, p. 281
- theoretical chemistry 3, ch. 23, p. 111

- thermal conductivity of compounds 16, ch. 106,
p. 107
- thermochemical properties 18, ch. 122, p. 239
 - of cuprates 30, ch. 190, p. 229
 - of gaseous species 12, ch. 86, p. 409
 - of metallic systems 19, ch. 134, p. 479
- thin films 5, ch. 41, p. 1; 20, ch. 136, p. 105
 - switchable metal hydrides 36, ch. 228, p. 83
- toxicity 4, ch. 40, p. 553
- transition metal-indides 34, ch. 218, p. 1
- transport properties of intermetallics 5, ch. 42,
p. 117; 17, ch. 115, p. 409
- triflates 29, ch. 186, p. 315
- tunneling spectra of cuprates 31, ch. 204, p. 563
- valence fluctuations 2, ch. 20, p. 575; 16,
ch. 105, p. 1; 39, ch. 241, p. 1
- X-ray absorption spectra 10, ch. 71, p. 453
- X-ray scattering 26, ch. 169, p. 1

The Dual, Localized or Band-Like, Character of the 4f-States

W.M. Temmerman*, **L. Petit[†]**, **A. Svane[†]**, **Z. Szotek***,
M. Lüders*, **P. Strange[‡]**, **J.B. Staunton[§]**, **I.D. Hughes[§]**, and
B.L. Gyorffy[¶]

Contents	List of Symbols and Acronyms	2
	1. Introduction	4
	2. Salient Physical Properties	6
	2.1 Lattice parameters	6
	2.2 Magnetic properties and magnetic order	8
	2.3 Fermi surfaces	12
	3. Band Structure Methods	15
	3.1 Local spin density approximation	15
	3.2 'f Core' approach	18
	3.3 OP scheme	18
	3.4 Local density approximation + Hubbard U	19
	3.5 Self-interaction-corrected local spin density approximation	20
	3.6 Local self-interaction-corrected local spin density approximation	24
	3.7 The GW method	26
	3.8 Dynamical mean field theory	28
	4. Valence and Valence Transitions	29
	4.1 Determining valence	29
	4.2 Valence of elemental lanthanides	30
	4.3 Valence of pnictides and chalcogenides	32
	4.4 Valence of ytterbium compounds	41
	4.5 Valence transitions	43
	4.6 Valence of lanthanide oxides	49

* Daresbury Laboratory, Daresbury, Warrington WA4 4AD, United Kingdom

[†] Department of Physics and Astronomy, University of Aarhus, DK-8000 Aarhus C, Denmark

[‡] School of Physical Sciences, University of Kent, Canterbury, Kent, CT2 7NH, United Kingdom

[§] Department of Physics, University of Warwick, Gibbet Hill Road, Coventry, CV4 7AL, United Kingdom

[¶] H.H. Wills Physics Laboratory, University of Bristol, Bristol BS8 1TL, United Kingdom

5.	Local Spin and Orbital Magnetic Moments	56
5.1	Hund's rules	57
5.2	The heavy lanthanides	57
5.3	The light lanthanides	62
6.	Spectroscopy	63
6.1	Hubbard-I approach to lanthanide photoemission spectra	64
6.2	Relativistic theory of resonant X-ray scattering	70
7.	Finite Temperature Phase Diagrams	75
7.1	Thermal fluctuations	75
7.2	Spin fluctuations: DLM picture	77
7.3	Valence fluctuations	97
8.	Dynamical Fluctuations: The 'Alloy Analogy' and the Landau Theory of Phase Transitions	102
9.	Conclusions	105
	References	105

List of Symbols and Acronyms

a	lattice parameter
a_0	Bohr radius
$A_{nk}(\omega), A_B(\mathbf{k}, E)$	Bloch spectral function, n is band index and \mathbf{k} is the wave vector
B	magnetic field
e	electron charge
E	(total) energy
g_J	Landé g-factor
$f_{\mathbf{q}^{\lambda}, \mathbf{q}^{\lambda'}}(\omega)$	scattering amplitude
F^I	Slater integrals
G	Green's function
GW	approximation for the self-energy based on the product of the Green's function (G) and the screened Coulomb interaction (W)
\hbar	Planck's constant
k_B	Boltzmann constant
\hat{L}	angular momentum operator
l	angular momentum quantum number
m	electron mass
$n, n(\mathbf{r})$	electron density
p	pressure
R	rare earth
\hat{S}	spin operator
S	Wigner Seitz (atomic sphere) radius
S_x	entropy, where x denotes the specific entropy contribution
$S^{(2)}$	direct correlation function of local moments
T	temperature
U	(Hubbard U), on-site Coulomb interaction
$U[n]$	Hartree (classical electrostatic) energy functional

V	volume
$V(\mathbf{r})$	potential
xc	exchange and correlation
Z	atomic number
β	inverse temperature $1/(k_B T)$
$\chi(\mathbf{q})$	magnetic susceptibility
μ_B	Bohr magneton
λ	Spin-orbit coupling parameter
Ω	(generalised) grand potential
$\Psi(\mathbf{r}_1, \mathbf{r}_2, \dots)$	electronic many body wave function
$\Psi(\mathbf{r})$	Electronic single particle wave function
Σ	self-energy
ω	frequency
ASA	atomic sphere approximation
BSF	Bloch spectral function
BZ	Brillouin zone
CPA	coherent potential approximation
DCA	dynamical cluster approximation
dhcp	double hexagonal closed packed
DFT	density functional theory
DLM	disordered local moment
DMFT	dynamical mean-field theory
DOS	density of states
ESRF	European Synchrotron Radiation Facility
fcc	face centered cubic
GGA	generalized gradient approximation
hcp	hexagonal closed packed
KKR	Korringa, Kohn, and Rostoker
LDA	local density approximation
LMTO	linear muffin-tin orbitals
LSDA	local spin density approximation
LS	spin-orbit
LSD	local spin density
LSIC	local self-interaction correction
MXRS	magnetic X-Ray Scattering
OP	orbital polarization
PAW	Projector augmented wave
RKKY	Ruderman-Kittel-Kasuya-Yoshida
SCF	self-consistent field
SI	self-interaction
SIC	self-interaction correction
SIC-LSD	self-interaction-corrected local spin density
SIC-LSDA	self-interaction-corrected local spin density approximation
WS	Wigner Seitz
XMaS	X-ray magnetic scattering

1. INTRODUCTION

Ab initio calculations for lanthanide solids were performed from the early days of band theory (Dimmock and Freeman, 1964). These pioneering calculations established that physical properties of the lanthanides could be described with the *f*-states being inert and treated as core states. For example, the crystal structures of the early lanthanides could be determined without consideration of the 4*f*-states (Duthie and Pettifor, 1977). Also the magnetic structures of the late lanthanides could be evaluated that way (Nordström and Mavromaras, 2000). Of course, one needed to postulate the number of *s*, *p*, and *d* valence electrons that is three in the case of a trivalent lanthanide solid or two in the case of a divalent lanthanide solid. Even this valence could be calculated in a semi-phenomenological way without taking the 4*f*-electrons explicitly into account (Delin *et al.*, 1997).

However, in some lanthanides, in particular the Ce compounds, and CeB₆ (Langford *et al.*, 1990) is an example, the 4*f*-level could either be part of the valence states or be inert and form part of the core. Fermiology measurements could determine how many electrons participated in the Fermi surface and hence could deduce the nature of the 4*f*-state as either part of the core or part of the valence states. These measurements were complemented by band structure calculations of the type '4*f*-core' or '4*f*-band', respectively treating the 4*f*-states as part of the core or as valence states.

Treating the 4*f*-electrons in Gd as valence states, in the '4*f*-band' approach, allowed for an accurate description of the Fermi surface (Temmerman and Sterne, 1990) but failed in obtaining the correct magnetic structure (Heinemann and Temmerman, 1994). What these and numerous other calculations demonstrated was that some properties of the lanthanides could be explained by a '4*f*-band' framework and some by a '4*f*-core' framework. This obviously implied a dual character of the 4*f* electron in lanthanides: some of the 4*f*-electrons are inert and are part of the core, some of the 4*f*-electrons are part of the valence and contribute to the Fermi surface.

The correct treatment of the 4*f* electrons in lanthanides is a great challenge of any modern theory. On the one hand, when considering the spatial extent of their atomic orbitals, the 4*f* electrons are confined to the region close to the nuclei, that is, they are very core-like. On the other hand, with respect to their position in energy, which is often in the vicinity of the Fermi level, they should rather be classified as valence electrons. Some of the most widely used theoretical methods for the description of lanthanide systems are based on DFT (Hohenberg and Kohn, 1964). Its basic concept is the energy functional of the total charge density of the electrons in the solid that, when minimized for given nuclear positions, provides the energy as well as the charge density of the ground state. However, for solids, the exact DFT energy functional is not known, and one is forced to use approximations, of which the most successful is the LSDA, where electron correlations are treated at the level of the homogeneous electron gas, and the *f* electrons are described by extended Bloch states, as all the other, *s*, *p*, and *d*, electrons are. But even in this approach, one can try to differentiate between the *f* and other electrons, by including them into the core ('*f*-core' approach). One step beyond

the local approximation, there are various flavours of the so-called GGAs, which, in addition to the dependence on a homogeneous charge distribution, include also some gradient corrections. Unfortunately, neither LDA nor GGA have proved very successful for systems where f electrons have a truly localized nature. Here, the SIC-LSD approaches have shown to be most useful, in particular as far as the cohesive properties are concerned.

The SIC-LSDA (Perdew and Zunger, 1981) provides an *ab initio* computational scheme that allows the differentiation between band-like and core-like f-electron (Temmerman et al., 1998). This is a consequence of the SIC being only substantial for localized states, which the 4f-states are. From this, one would expect to apply the SIC to all 4f-states since the delocalized s, p, and d electrons are not experiencing any self-interaction. But we do not know how many localized 4f-states there are. For a divalent lanthanide, there is one more localized 4f electron than for a trivalent lanthanide. To determine how many localized 4f electrons there are in a particular 4f-solid, we can be guided by minimizing the SIC-LSD total energy over all possible configurations of localized (SIC) and itinerant 4f-states. This chapter elaborates on the consequences of this, naturally leading to the dual character of the 4f electron: either localized after applying the SIC or LSD band-like and contributing to the Fermi surface. The SIC-LSD method forms the basis of most of the work reviewed in this chapter, and its focus will be on the total energy aspect and, as we will show, provides a quite accurate description of the cohesive properties throughout the lanthanide series.

Other known methods that have been used in the study of lanthanides include the OP scheme, the LDA + U approach, where U is the on-site Hubbard repulsion, and the DMFT, being the most recent and also the most advanced development. In particular, when combined with LDA + U , the so-called LDA + DMFT scheme, it has been rather successful for many complex systems. We note here that both DMFT and LDA + U focus mostly on spectroscopies and excited states (quasi-particles), expressed via the spectral DOS. In a recent review article (Held, 2007), the application of the LDA + DMFT to volume collapse in Ce was discussed. Finally, the GW approximation and method, based on an electron self-energy obtained by calculating the lowest order diagram in the dynamically screened Coulomb interaction, aims mainly at an improved description of excitations, and its most successful applications have been for weakly correlated systems. However, recently, there have been applications of the quasi-particle self-consistent GW method to localized 4f systems (Chantis et al., 2007).

The outline of the present chapter is as follows. Section 2 deals with the relevant physical, electronic, and magnetic properties of the lanthanides. Section 3 reviews briefly the above-mentioned theoretical methods, with the focus on the SIC-LSDA method, and, in particular, the full implementation of SIC, involving repeated transformations between Bloch and Wannier representations (Temmerman et al., 1998). This is then compared with the local-SIC, implemented in the multiple scattering theory (Lüders et al., 2005). Section 4 deals with the valence (Strange et al., 1999) and valence transitions of the lanthanides. Section 5 discusses the local magnetic moments of the lanthanides. Section 6 discusses two spectroscopies applied to lanthanides and some of their compounds. Section 7 outlines a methodology of calculating the finite temperature (T) properties of the lanthanides and their

compounds, and illustrates it on the study of finite T magnetism of the heavy lanthanides and the finite T diagram of the Ce α - γ phase transition. The *ab initio* theory of the finite T magnetism is based on the calculations of the paramagnetic susceptibility within the DLM picture (Gyorffy *et al.*, 1985). This combined DLM and SIC approach (Hughes *et al.*, 2007) for localized states provides an *ab initio* description of the magnetic properties of ionic systems, without the need of mapping onto the Heisenberg Hamiltonian. Finally, Section 8 addresses some remaining issues such as how to include dynamical fluctuations, and Section 9 concludes this chapter.

2. SALIENT PHYSICAL PROPERTIES

The physical properties of the lanthanides are rather unique among all metals. This is the consequence of the interaction of delocalized conduction electrons with the localized f-states. The physical properties are characterized by the continuously decreasing lattice parameter upon traversing the lanthanide series, the so-called lanthanide contraction. Their physical properties can be described very efficiently, and also catalogued, by the valence of the lanthanide. Most of the lanthanides and their compounds are trivalent, but towards the middle and the end of the lanthanide series, divalence (Sm, Eu, Tm, Yb) can occur. At the very beginning of the lanthanide series, in Ce and Pr and their compounds, also tetravalence is sometimes observed. For tetravalent Ce and Pr and their compounds, strong quasi-particle renormalization occurs and some Ce compounds exhibit heavy fermion behaviour. For lanthanides with higher atomic number than Pr, trivalence establishes itself, however, switching to divalence in Eu and some of the Sm and Eu compounds. For Gd, the f-shell is half-filled and the valence starts again, as in the beginning of the lanthanide series, as strongly trivalent and gradually reducing to divalence as seen in Yb and Tm compounds. Fingerprints of the valencies can be seen in the value of the spin and orbital magnetic moments and of the lattice parameter: divalent lattice parameters can be 10% larger than trivalent ones. Also the nature of the multiplet structure tells us about the valence, as do Fermiology measurements, by providing information on the number of f-states contributing to the Fermi surface. Finally, MXRS has the potential to determine the valence as well as to provide information on the symmetry of the localized states (Arola *et al.*, 2004).

2.1 Lattice parameters

The experimental lattice parameters as a function of lanthanide atomic number show the famous lanthanide contraction, the decrease of the lattice parameter across the lanthanide series, with the exception of the two anomalies for Eu and Yb, as seen in Figure 1 (top panel). What is plotted there is actually the atomic sphere radius S (in atomic units) as a function of the lanthanide element. A similar behaviour is also observed, for example, for lanthanide monochalcogenides and monopnictides, whose lattice parameters are also shown in Figure 1 (middle and bottom panels).

This lanthanide contraction is associated with the filling of the 4f shell across the lanthanide series. The effect is mainly due to an incomplete shielding of the nuclear charge by the 4f electrons and yields a contraction of the radii of outer electron shells.

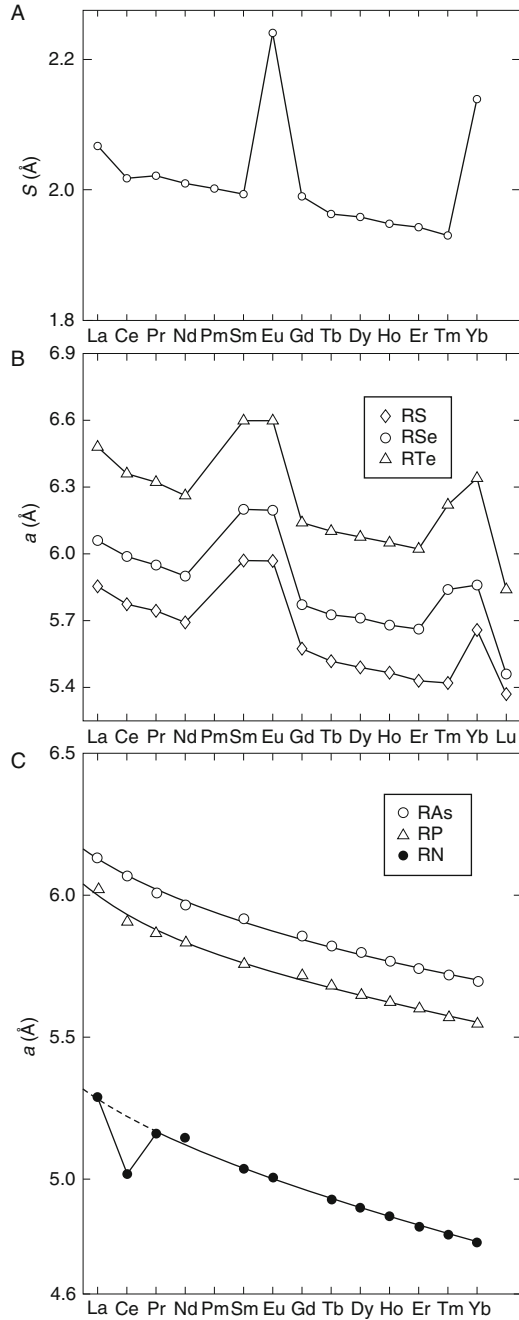


FIGURE 1 Lattice constants of the elemental lanthanides (top), their chalcogenides (middle) (after Jayaraman, 1979), and pnictides (bottom). For the elemental lanthanides, it is the atomic sphere radius, S , that is shown instead of the lattice parameter, where S is defined as $V = 4/3\pi S^3$ with V the unit cell volume.

The jumps in the lattice constants in [Figure 1](#), seen for the elemental Eu and Yb, as well as at the chalcogenides of Sm, Eu, Tm, and Yb, are due to the change in valence from trivalent to divalent. If a transition to the trivalent state were to occur, the lattice constant would also follow the monotonous behaviour of the other lanthanides, as seen in [Figure 2](#), where the ionic radii of trivalent lanthanide ions are displayed. For the pnictides, only CeN shows an anomaly, indicating a tetravalent state, whereas all the other compounds show a smooth, decreasing behaviour as a function of the lanthanide atomic number.

Pressure studies have been able to unravel a lot of the physics of the rare earths. Not only have pressure experiments seen changes of valence from divalent to trivalent, but also changes in the structural properties. In the case of Ce and Ce compounds, the valence changes under pressure from trivalent to tetravalent or from one localized f-state to a delocalized state have been observed. This will be discussed in greater detail in [Section 4](#) of this chapter.

2.2 Magnetic properties and magnetic order

The lanthanides are characterized by local magnetic moments coming from their highly localized 4f electron states. These moments polarize the conduction electrons which then mediate the long range magnetic interaction among them. The RKKY interaction is the simplest example of this mechanism. These long range magnetic interactions in lanthanide solids lead to the formation of a wide variety of magnetic structures, the periodicities of which are often incommensurate with the underlying crystal lattice. These are helical structures that have been studied in detail with neutron scattering ([Sinha, 1978](#); [Jensen and Mackintosh, 1991](#)). In the later sections of this chapter, we shall elaborate on our *ab initio* study of the finite temperature magnetism of the heavy lanthanides and elucidate the role of the conduction electrons in establishing the complex helical structures in these systems. This *ab initio* theory and calculations go beyond the 'standard model' of lanthanide magnetism ([Jensen and Mackintosh, 1991](#)).

The standard approach to describing the magnetism of lanthanides, and in particular their magnetic moments, is to assume the picture of electrons in an

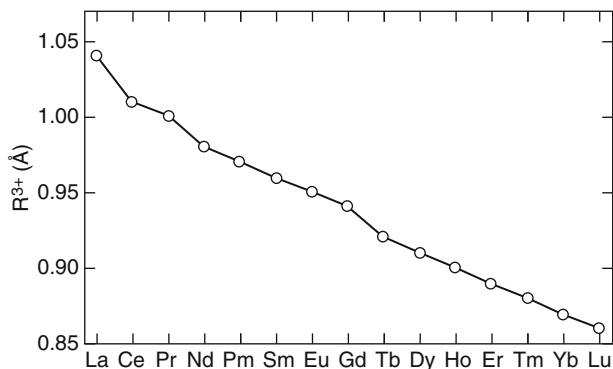


FIGURE 2 Ionic radii of trivalent lanthanides.

isolated atom. In the absence of spin-orbit coupling, the angular momenta of the electrons in an atom combine according to Russel-Saunders coupling to give a total orbital angular momentum \hat{L} and a total spin angular momentum \hat{S} , with the respective eigenvalues of $L(L+1)\hbar^2$ and $S(S+1)\hbar^2$ (Gasiorowicz, 1974). In the lanthanides, however, spin-orbit coupling $\lambda \hat{L} \cdot \hat{S}$ cannot be ignored (Strange, 1998) and therefore one has to introduce the total angular momentum $\hat{J} = \hat{L} + \hat{S}$. The wavefunctions describing the electrons then obey the eigenvalue relations:

$$\begin{aligned}\hat{J}^2\psi_{J,m_j,L,S} &= J(J+1)\hbar^2\psi_{J,m_j,L,S} \\ \hat{J}_z\psi_{J,m_j,L,S} &= m_j\hbar\psi_{J,m_j,L,S} \\ \hat{L}^2\psi_{J,m_j,L,S} &= L(L+1)\hbar^2\psi_{J,m_j,L,S} \\ \hat{S}^2\psi_{J,m_j,L,S} &= S(S+1)\hbar^2\psi_{J,m_j,L,S},\end{aligned}\quad (1)$$

where $\psi_{J,m_j,L,S}$ are normalized atomic wavefunctions, which are assumed to be located on a single atom nucleus.

The energy associated with a magnetic field in the lanthanide is small in comparison to electronic energies and it is usual to treat it applying perturbation theory. The perturbing potential is simply the scalar product of the magnetic moment, $\hat{\mu}$, and the magnetic field, \mathbf{B} , experienced by the atom:

$$\delta V = -\hat{\mu} \cdot \mathbf{B}, \quad (2)$$

where $\hat{\mu}$ is given as

$$\hat{\mu} = -\mu_B g_J \hat{J}. \quad (3)$$

Here, g_J is the Landé g-factor:

$$g_J = 1 + \frac{J(J+1) - L(L+1) + S(S+1)}{2J(J+1)}. \quad (4)$$

If this model is correct, then it is only necessary to know the values of the quantum numbers J , L , and S to calculate the magnetic moment of the lanthanides. These are determined by Hund's rules:

- (1) S will be a maximum subject to the Pauli exclusion principle
- (2) L will be a maximum subject to rule 1 and to the Pauli exclusion principle
- (3) If the shell is less than half-full, then the spin-orbit coupling coefficient λ is positive and $J = |L-S|$ is the ground state. For a shell that is greater than or equal to half-full λ is negative and $J = L + S$ is the ground state.

In Table 1, we show the quantum numbers for the trivalent lanthanide ions, the Landé g-factor, and the high-temperature paramagnetic moment given as:

$$\mu_t = \sqrt{\langle \hat{\mu}^2 \rangle} = \mu_B g_J \sqrt{J(J+1)}, \quad (5)$$

assuming that only the f-electrons contribute to the magnetic moment. If we know the energy levels of the lanthanide ions in a magnetic field, we can use standard statistical mechanics to calculate the susceptibility of the ions. For most of the ions,

TABLE 1 Quantum numbers and total f-electron magnetic moments of the trivalent lanthanide ions. μ_t is the magnetic moment calculated from Eq. (5). μ_e is the measured magnetic moment. All magnetic moments are expressed in Bohr magnetons

	S	L	J	Ground state	g_j	μ_t	μ_e^a
La	0.00	0.00	0.00	1S_0			
Ce	0.50	3.00	2.50	$^2F_{5/2}$	6/7	2.54	2.4
Pr	1.00	5.00	4.00	3H_4	4/5	3.58	3.5
Nd	1.50	6.00	4.50	$^4I_{9/2}$	8/11	3.62	3.5
Pm	2.00	6.00	4.00	5I_4	3/5	2.68	
Sm	2.50	5.00	2.50	$^6H_{5/2}$	2/7	0.85	1.5 ^b
Eu	3.00	3.00	0.00	7F_0		0.0	3.4 ^{b,c}
Gd	3.50	0.00	3.50	$^8S_{7/2}$	2	7.94	7.95
Tb	3.00	3.00	6.00	7F_6	3/2	9.72	9.5
Dy	2.50	5.00	7.50	$^6H_{15/2}$	4/3	10.65	10.6
Ho	2.00	6.00	8.00	5I_8	5/4	10.61	10.4
Er	1.50	6.00	7.50	$^4I_{15/2}$	6/5	9.58	9.5
Tm	1.00	5.00	6.00	3H_6	7/6	7.56	7.3
Yb	0.50	3.00	3.50	$^2F_{7/2}$	8/7	4.54	4.5
Lu	0.00	0.00	0.00	1S_0			

^a All experimental values taken from Kittel (1986).

^b See text.

^c Eu usually exists in the divalent form.

the difference in energy between the first excited state and the ground state is much greater than $k_B T$ at room temperature, where k_B is the Boltzmann constant, and essentially only the ground state is populated. This enables us to derive the Curie formula

$$\chi = \frac{N \langle \hat{\mu}^2 \rangle}{3k_B T} \quad (6)$$

for the susceptibility of a system of N non-interacting ions. More realistically, this formula should be replaced by the Curie-Weiss law, where the T in the denominator in Eq. (6) is replaced by $T - T_c$ where T_c is the magnetic ordering temperature. The Curie-Weiss formula was employed to determine the experimental magnetic moments, μ_e , in Table 1. For Sm^{3+} and Eu^{2+} , the first excited level is within $k_B T$ of the ground state and so is appreciably populated. To describe these two ions with numerical accuracy, it is necessary to sum over the allowed values of J and recall that each J contains $2J + 1$ states. The susceptibility then becomes considerably more complicated but does give a good description of Sm^{3+} and Eu^{2+} .

The theoretical magnetic moments in Table 1 are for single trivalent ions assuming no inter-ionic interactions. However, the experiments are performed on metallic elements where each individual ion is embedded in a crystal and feels

the crystalline electric field, which arises from charges on neighbouring ions. The excellent agreement between the magnetic moment measured experimentally and that obtained from Eq. (5) implies that the 4f-electrons are so well shielded that the effect of the crystalline environment can be neglected and the agreement with Eq. (6) supports this view. With the agreement between theory and experiment displayed in Table 1, it might reasonably be assumed that the magnetic moments of the lanthanide metals are well understood. While this is probably true qualitatively, it is certainly not true quantitatively. Questions about this model that may be raised are:

- (1) In the solid state, the interaction with the sea of conduction electrons distorts the pure atomic picture, and multiplets other than the Hund's rule ground state mix into the full wave function. In view of the success of the atomic approximation, it is likely that this mixing of different J quantum numbers is at the few percent level, nonetheless this is an assumption that should be tested.
- (2) The eigenfunctions $\Psi_{J,m,J,S}$ in Eq. (1) are generally quantum mechanically entangled, given as sums of Slater determinants constructed from atomic single-electron orbitals. The description of entangled quantum states in a solid state environment is extremely difficult. With the recent introduction of the DMFT (Section 3.8), one might have developed a scheme for this, however, more investigations are needed. Usually, one resorts to the independent particle approximation thus ignoring the 'many-body' nature of the wavefunction and the localized f-manifold is represented by a single 'best choice' Slater determinant. This is the approach taken in the various DFT schemes, including the SIC-LSD theory to be described in Section 3.5. How could such a picture arise from a more sophisticated and realistic description of the electronic structure of the lanthanides?
- (3) The picture of lanthanide magnetism described above is for independent trivalent lanthanide ions. Thus, it does not explain cooperative magnetism, that is ordered magnetic structures which are the most common low-temperature ground states of lanthanide solids. Our view of a lanthanide crystal is of a regular array of such ions in a sea of conduction electrons to which each ion has donated three electrons. For cooperative magnetism to exist, those ions must communicate with one another somehow. It is generally accepted that this occurs through indirect exchange in the lanthanide metals, the simplest example of this being the RKKY interaction (Ruderman and Kittel, 1954; Kasuya, 1956; Yosida, 1957). However, for this to occur, the conduction sd-electrons themselves must be polarized. This conduction electron polarization has been calculated using DFT many times and is found to be substantial. There have been many successes in descriptions of magnetic structures, some of which will be discussed in Section 7.2. However, in terms of the size of magnetic moments, the agreement between theory and experiment shown in Table 1 is considerably worsened (see discussion in Section 5). Why is this?

- (4) If the atomic model were rigorously correct, a lanthanide element would have the same magnetic moment in every material and crystalline environment. Of course, this is not the case, and more advanced methods have to be employed to determine the effect of the crystalline and chemical environment on magnetic moments with numerical precision. Examples of materials where the theory described above fails to give an accurate value for the lanthanide ion magnetic moment are ubiquitous. They include NdCo_5 (Alameda *et al.*, 1982), fullerene encapsulated lanthanide ions (Mirone, 2005), and lanthanide pyrochlores (Hassan *et al.*, 2003).

In conclusion, it is clear that the standard model makes an excellent first approximation to the magnetic properties of lanthanide materials, but to understand lanthanide materials on a detailed individual basis, a more sophisticated approach is required.

2.3 Fermi surfaces

The simple view of the lanthanide electronic structure as discussed previously is shown in Figure 3. The f-electrons are very localized, core-like, and responsible for magnetism, as described above, whereas the sd-electrons are responsible for other electronic properties, such as cohesive energy, transport properties, Fermi surfaces. This model, we call the standard model, is a good first approximation and a number of lanthanide properties can be explained in terms of it. The traditional DFT approach to the lanthanide electronic structure has involved a self-consistent calculation of the s, p, and d-bands with the filled f-states being treated as part of the core and the empty f-states essentially ignored. Again this approach works well and gives good agreement with experiment for structural and crystalline properties as well as de Haas van Alphen experiments and some spectroscopies. It has been used by a number of authors (Jackson, 1969; Skriver, 1983a, 1983b; Eriksson *et al.*, 1990a) and yields band structures that look remarkable similar to hexagonal transition metals such as yttrium and scandium. A major advantage of this approach is the stability of the calculation due to the absence of the localized

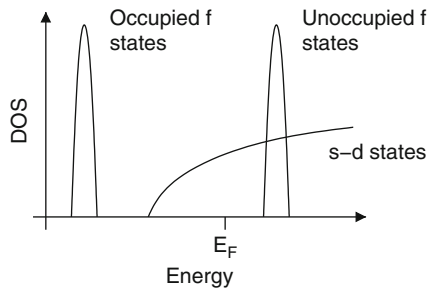


FIGURE 3 Model DOS for a lanthanide metal. The low-energy narrow peak represents the occupied f-band, the high-energy narrow peak just above the Fermi energy is the unoccupied f-states. These are superimposed on the sd-band which is free-electron like to a first approximation.

4fs. Both Skriver (1983b) and Eriksson et al. (1990a) have performed a successful calculation of the cohesive properties and the work of Skriver reproduces well the crystal structures which are sensitively dependent on the details of the valence band. For example, the partial 5d occupation numbers decrease across the series with a corresponding increase in the 6s occupation. The increase in 5d occupation is what causes the structural sequence hcp \rightarrow Sm structure \rightarrow dhcp \rightarrow fcc as the atomic number decreases or the pressure increases (Duthie and Pettifor, 1977). A detailed analysis of Jackson's work (Jackson, 1969) on Tb yields a Fermi surface that shows features with wave vector separations corresponding to the characteristic wave vector describing the spiral phase of Tb.

One of the successes of this approach is the comparison of calculated electronic structures with de Haas van Alphen measurements. The investigations of the Fermi surface of Gd using this technique among others were pioneered by Young and co-workers (Young et al., 1973; Mattocks and Young, 1977) and extended by Schirber and co-workers (Schirber et al., 1976). These studies found four frequencies along the *c*-direction and three in the basal plane and later work found a number of small frequencies (Sondhelm and Young, 1977). All these frequencies could be accounted for on the basis of the band structure calculations of the time. Sondhelm and Young also measured cyclotron masses and mass enhancements in Gd and found values in the region of 1.2–2.1 which were in agreement with the band structure calculations, but were rather smaller than those derived from low-temperature heat capacity measurements. More recently, angle-resolved photoemission have been used for Fermi surface studies of Tb (Döbrich et al., 2007) and also Dy and Ho metals were studied (Schüßler-Langeheine et al., 2000). Fermi surfaces of Gd-Y alloys were studied with positron annihilation (Fretwell et al., 1999; Crowe et al., 2004). In particular, the changes to the Fermi surface topology upon the transition from ferromagnetism to helical anti-ferromagnetism could be followed. Concerning the light lanthanides, the Fermi surface areas and cyclotron masses in Pr were measured (Wulff et al., 1988) with the de Haas van Alphen technique. Large mass enhancements, especially for an elemental metal, were measured and the understanding of the Fermi surface needed an approach well beyond the standard model (Temmerman et al., 1993).

This standard model does have several major drawbacks:

- (1) It can never get the magnetic properties correct.
- (2) It cannot describe systems with large mass enhancements.
- (3) There is one overarching shortcoming of the standard model, which is slightly more philosophical. It treats the *f*-electrons as localized and the *sd*-electrons as itinerant, that is, it treats electrons within the same material on a completely different basis. This is aesthetically unsatisfactory and furthermore makes it impossible to define a reference energy. In principle, one has to know, *a priori*, which electrons to treat as band electrons and which to treat as core electrons. It would be infinitely better if the theory itself contained the possibility of both localized and itinerant behaviour and it chose for itself how to describe the electrons.

For two elements, it is possible to perform LDA calculations including the *f*-electrons in the self-consistency cycle. The first is cerium where the *f*-electrons are not necessarily localized. Cerium and its compounds are right on the border between localized and itinerant behaviour of the 4*f* electrons. There has been much controversy over the nature of the *f*-state in materials containing cerium. The key issue is the γ - α phase transition where the localized magnetic moment associated with a 4*f*¹ configuration disappears with an associated volume collapse of around 14–17%, but no change in crystal symmetry. The *f* electron count is thought to be around one in both phases of Ce. What appears to be happening here is a transition from a localized to a delocalized *f*-state (Pickett *et al.*, 1981; Fujimori, 1983). Both Pickett *et al.* (1981) and Fujimori (1983) highlight the limitations of the band theory picture for cerium. In particular, Fujimori discusses the calculation of photoemission spectra and the reasons why band theory does not describe such spectroscopies well. The α -phase can be described satisfactorily using the standard band theory, while there is more difficulty in describing the γ -phase and the energy difference between the two phases (which is very small on the electronic scale) is not calculated correctly. The second lanthanide element where band theory may hope to shed some light on its properties is gadolinium. Here the *f*-levels are spilt into seven filled majority spin and seven unfilled minority spin bands, neither of which are close to the Fermi energy. It is feasible to perform a DFT calculation and converge to a reasonable result. This has been done by a number of authors (Jackson, 1969; Ahuja *et al.*, 1994; Temmerman and Sterne, 1990) with mixed results. Temmerman and Sterne were among the first to indicate that the semi-band nature of the 5*p* levels could significantly influence predicted properties. Sandratskii and Kübler (1993) took this work a bit further by investigating the stability of the conduction band moment with respect to disorder in the localized 4*f*-moment.

The experimentally determined Fermi surface of Gd (Schirber *et al.*, 1976; Mattocks and Young, 1977) has been used by several band structure calculations to determine whether the *f*-states have to be treated as core-like or band-like. Gd metal is the most thoroughly studied of all the lanthanides and one of the few lanthanides that have been studied by the de Haas van Alphen technique (Schirber *et al.*, 1976; Mattocks and Young, 1977). Being trivalent, it has, through the exchange splitting, a half-filled *f*-shell. The Gd *f*-states are well separated from the Fermi level, and therefore *f*-states are not contributing to the Fermi surface. This was seen in the Fermiology measurements (Schirber *et al.*, 1976; Mattocks and Young, 1977). Both *f*-core (Richter and Eschrig, 1989; Ahuja *et al.*, 1994) and *f*-band (Sticht and Kübler, 1985; Krutzen and Springelkamp, 1989; Temmerman and Sterne, 1990; Singh, 1991) calculations claim to be able to describe this Fermi surface.

While these methods provide some useful insight into Gd and Ce, they yield unrealistic results for any other lanthanide material as the *f*-bands bunch at the Fermi level leading to unphysically large densities of states at the Fermi energy and disagreement with the de Haas van Alphen measurements. It is clear that a satisfactory theory of lanthanide electronic structures requires a method that treats all electrons on an equal footing and from which both localized and itinerant behaviour of electrons may be derived. SIC to the LSDA provide one such theory.

This method is based on DFT and the free electron liquid, but corrects it for electrons where self-interactions are significant and takes the theory towards a more localized description.

3. BAND STRUCTURE METHODS

As described in [Section 1](#), there exist many theoretical approaches to calculating electronic structure of solids, and most of them have also been applied to lanthanides. In this section, we shall briefly overview some of the most widely used, focusing however on the SIC-LSD, in both full and local implementations, as this is the method of choice for most of the calculations reported in this chapter. The simplest approach to deal with the f electrons is to treat them like any other electron, that is, as itinerant band states. Hence, we start our review of modern methods with a brief account of the standard LDA and its spin-polarized version, namely the LSD approximation. We also comment on the use of LSD in the cases, where one restricts the variational space by fixing the assumed number of f electrons to be in the (chemically inert) core ('f-core' approach). Following this, we then briefly overview the basics of other, more advanced, electronic structure methods mentioned in [Section 1](#), as opposed to a more elaborate description of the SIC-LSD method.

3.1 Local spin density approximation

DFT relies on the proof ([Hohenberg and Kohn, 1964](#); [Kohn and Sham, 1965](#); [Dreizler and Gross, 1990](#); [Martin, 2004](#)) that for any non-degenerate many-electron system, there exists an energy functional $E[n]$, where $n(\mathbf{r})$ is the electron charge density in space-point \mathbf{r} , which when minimized (with respect to $n(\mathbf{r})$) provides the correct ground state energy as well as ground state electron charge density. Hence, the charge density $n(\mathbf{r})$, rather than the full many-electron wavefunction $\Psi(\mathbf{r}_1, \mathbf{r}_2, \dots, \mathbf{r}_N)$, becomes the basic variable, which constitutes a simplification from a complex-valued function depending on N sets of space coordinates to a non-negative function of only one set of space coordinates. The price paid is that the exact functional form of $E[n]$ is unknown, and presumably of such complexity that it will never be known. However, approximations of high accuracy for a diversity of applications exist and allow predictive investigations of many novel functional materials in condensed matter physics and materials science. The great advance in the field was facilitated by the observation ([Kohn and Sham, 1965](#)) that if one separates out from the total energy functional, $E[n]$, the kinetic energy, $T_0[n]$, of a non-interacting electron gas with charge density $n(\mathbf{r})$ (which does not coincide with the true kinetic energy of the system), and the classical electrostatic energy terms, then simple, yet accurate, functionals may be found to approximate the remainder, called the exchange-correlation (xc) energy functional $E_{xc}[n]$. Thus, the total energy functional can be written as

$$E[n] = T_0[n] + U[n] + V_{\text{ext}}[n] + E_{xc}[n], \quad (7)$$

where the electron–electron interaction (Hartree term) is given by

$$U[n] = \iint \frac{n(\mathbf{r})n(\mathbf{r}')}{|\mathbf{r} - \mathbf{r}'|} d^3r d^3r', \quad (8)$$

and the external potential energy, $V_{\text{ext}}[n]$, due to electron–ion and ion–ion interactions, respectively, is

$$V_{\text{ext}}[n] = \int n(\mathbf{r})V_{\text{ion}}(\mathbf{r})d^3r + E_{\text{ion,ion}}. \quad (9)$$

Here $V_{\text{ion}}(\mathbf{r})$ is the potential from the ions, and the atomic Rydberg units ($e^2/2 = 2m = \hbar = 1$) have been used in all the formulas. Since Eqs. (8) and (9) are explicitly defined in terms of the electron charge density, all approximations are applied to the last term in Eq. (7), the exchange and correlation energy.

In the LDA, it is assumed that each point in space contributes additively to E_{xc} :

$$E_{\text{xc}}^{\text{LDA}}[n] = \int n(\mathbf{r})\varepsilon_{\text{hom}}(n(\mathbf{r}))d^3r, \quad (10)$$

where $\varepsilon_{\text{hom}}(n)$ is the exchange and correlation energy of a homogeneous electron gas with charge density n . In the simplest case, when only exchange is considered, one has (Hohenberg and Kohn, 1964)

$$\varepsilon_{\text{hom}}(n) = -Cn^{1/3} \text{ with } C = \frac{3}{2} \left(\frac{3}{\pi}\right)^{1/3}. \quad (11)$$

Modern functionals include more elaborate expressions for $\varepsilon_{\text{hom}}(n)$ (Vosko *et al.*, 1980; Perdew and Zunger, 1981) relying on accurate Quantum Monte Carlo data for the homogeneous electron gas (Ceperley and Alder, 1980). Generalizing to magnetic solids, which is highly relevant for lanthanide materials, is straightforward as one merely has to consider two densities, one for spin-up and one for spin-down electrons, which corresponds to the LSD functional (von Barth and Hedin, 1972), E^{LSD} . Even more accurate calculations may be obtained by including corrections for the spatial variation of the electron charge density, which is accomplished by letting ε_{hom} also be dependent on gradients of the charge density, which constitutes the GGA (Perdew and Wang, 1992). Yet more accurate functionals may be composed by mixing some non-local exchange interaction into the E_{xc} (Becke, 1993), often named hybrid functionals.

The minimization of $E[n]$, with these approximate functionals, is accomplished by solving a one-particle Schrödinger equation for an effective potential, which includes an exchange–correlation part given by the functional derivative of $E_{\text{xc}}[n]$ with respect to $n(\mathbf{r})$. The non-interacting electron gas system with the charge density $n(\mathbf{r})$ is generated by populating the appropriate number of lowest energy solutions (the aufbau principle). Self-consistency must be reached between the charge density put into the effective potential and the charge density composed from the occupied eigenstates. This is usually accomplished by iterating the procedure until this condition is fulfilled.

Spin-orbit interaction is only included in the density functional framework if the proper fully relativistic formalism is invoked (Strange, 1998). Often an approximate treatment of relativistic effects is implemented, by solving for the kinetic energy in the scalar-relativistic approximation (Skriver, 1983a), and adding to the total energy functional the spin-orbit term as a perturbation of the form

$$E_{\text{so}} = \sum_{\alpha}^{\text{occ.}} \langle \psi_{\alpha} | \xi(\vec{r}) \vec{l} \cdot \vec{s} | \psi_{\alpha} \rangle, \quad (12)$$

where the sum extends over all occupied states $|\psi_{\alpha}\rangle$ and ξ is the spin-orbit parameter. Here \vec{l} and \vec{s} denote the one-particle operators for angular and spin moments. The method presupposes, which usually does not pose problems, that an appropriate region around each atom may be defined inside which the angular momentum operator acts.

The LDA and LSD, as well as their gradient corrected improvements, have been extremely successful in providing accurate, material specific, electronic, magnetic, and structural properties of a variety of weakly to moderately correlated solids, in terms of their ground state charge density (Jones and Gunnarsson, 1989; Kübler, 2000). However, these approaches often fail for systems containing both itinerant and localized electrons, and in particular d- and f-electron materials. For all lanthanides, and similarly the actinide elements beyond neptunium, the electron correlations are not adequately represented by LDA. In d-electron materials, for example, transition metal oxides, this inadequate description of localized electrons leads commonly to the prediction of wrong magnetic ground states and/or too small or non-existent band gaps and magnetic moments.

When applied to lanthanide systems, LSD (and GGA as well) leads to the formation of narrow bands which tend to fix and straddle the Fermi level. Due to their spatially confined nature, the f-orbitals hybridize only weakly and barely feel the crystal fields. Furthermore, on occupying the f-band states, the repulsive potential on the lanthanide increases due to the strong f-f Coulomb repulsion, so the f-bands fill up to the point where the total effective potential pins the f-states at the Fermi level. Generally, the band scenario leads to distinct overbinding (when compared to experimental data), since the occupation of the most advantageous f-band states favours crystal contraction (leading to increase in hybridization). Hence, the partially filled f-bands provide a negative pressure, which in most cases is unphysical. The same effect is well known to cause the characteristic parabolic behaviour of the specific volumes of the transition metals, and would lead to a similar parabolic behaviour for the specific volumes of the lanthanides, which is in variance with the observation seen in Figure 1 in Section 2.1. This will be discussed further in Section 4.2. Even if narrow, the f-bands in the vicinity of the Fermi level alone cannot describe the heavy fermion behaviour seen in many cerium and ytterbium compounds. Zwicky (1992) and co-workers applied a renormalization scheme to LDA band structures to describe the heavy fermion properties with successful application in particular to the understanding of Fermi surfaces.

3.2 ‘f Core’ approach

To remedy the failure of LSD, it was early realized that one could remove the spurious bonding due to f-bands by simply projecting out the f-degrees of freedom from variational space and instead include the appropriate number of f electrons in the core. This approach was used to study the crystal structures of the lanthanide elements (Duthie and Pettifor, 1977; Delin *et al.*, 1998), which are determined by the number of occupied d-states. In this approach, the lanthanide contraction neatly follows as an effect of the incomplete screening of the increasing nuclear charge by added f electrons, as one moves through the lanthanide series (Johansson and Rosengren, 1975). In a recent application, the ‘f core’ approach proved useful in the study of complex magnetic structures (Nordström and Mavromaras, 2000).

Johansson and co-workers have extended the ‘f core’ approach to compute energies of lanthanide solids, with different valencies assumed for the lanthanide ion, by combining the calculated LSD total energy for the corresponding ‘f core’ configurations with experimental spectroscopic data for the free atom (Delin *et al.*, 1997). This scheme correctly describes the trends in cohesive energies of the lanthanide metals, including the valence jumps at Eu and Yb, as well as the intricate valencies of Sm and Tm compounds.

3.3 OP scheme

The OP scheme was introduced by Eriksson *et al.* (1990b) to reduce the bonding of f-electrons without totally removing them from the active variational space. The idea copies the way spin polarization leads to reduced bonding if the exchange parameter is large enough (Kübler and Eyert, 1993). An extra term is added to the LSD functional (7):

$$E^{\text{OP}}[n] = E^{\text{LSD}}[n] - \sum_i E_i^3 L_{zi}^2, \quad (13)$$

where i numbers the atomic sites, L_{zi} is the total z-component of the orbital moment, and E_i^3 is a parameter (the Racah parameter), which can be calculated from an appropriate combination of Slater integrals (Eriksson *et al.*, 1990b). The added term favours the formation of an orbital moment and adds a potential shift $-E_i^3 L_{zi} m_l$ to each f orbital, where m_l is the azimuthal quantum number of the f electron considered. The effect is to partially split the f-band into 14 distinct bands (if the E^3 parameter exceeds hybridization and crystal fields). Since compression enhances the latter two effects, the OP scheme could successfully describe the γ - α transition of cerium as a transition from large to low orbital moment (Eriksson *et al.*, 1990b). This is then to be interpreted as a Mott-type transition in the f-manifold from a localized to a band-like behaviour. The OP scheme has also been applied to the pressure-induced volume collapse in Pr (Svane *et al.*, 1997). Generally, the OP term is too small in magnitude to fully describe the inertness of the f electrons in the lanthanide series beyond Pr. The OP scheme has been most successful in describing the orbital moment contribution to

itinerant systems, for example 3d-transition metal and actinide compounds (Eriksson et al., 1991; Trygg et al., 1995). The LSD (with spin-orbit interaction included) grossly underestimates orbital moments since there is no energy term describing the energetics of the Hund's second rule. The OP term in Eq. (13) remedies this as it largely describes the extra energy gain of an f-manifold by attaining its ground state configuration (compared to the average, 'grand bary centre' energy of the f-manifold). Eschrig et al. (2005), by analysing the formal relativistic DFT framework, showed that the functional form chosen by Eriksson et al. (1990b) is in fact quite accurate.

3.4 Local density approximation + Hubbard U

Similarly to the OP scheme, the LDA + U method (Anisimov et al., 1991) adds a quadratic term to the LSD Hamiltonian to improve the description of the correlated f-manifold, namely

$$E^{\text{LDA}+U}[n] = E^{\text{LSD}}[n] + \sum_i E^{\text{corr}}(\underline{N}_i), \quad (14)$$

where for each site i , the correlation energy term depends on the orbital occupation numbers $\underline{N} = \{N_k\}$. These are obtained by projecting the occupied eigenstates $|\psi_\alpha\rangle$ onto the f orbitals, $|f_k\rangle$, as

$$N_k = \sum_{\alpha}^{\text{occ.}} |\langle \psi_\alpha | f_k \rangle|^2. \quad (15)$$

In its simplest form (Anisimov et al., 1991), the correlation energy term includes a Hubbard repulsion term (Hubbard, 1963) and the so-called double-counting term E_{dc}

$$E^{\text{corr}}(\underline{N}) = \frac{1}{2}U \sum_{k \neq l} N_k N_l + E_{\text{dc}}. \quad (16)$$

Here, indices k and l run over the 14 f orbitals on the site considered, and U is the f-f Coulomb interaction. The double-counting term E_{dc} is needed to correct for the fact that $E^{\text{LSD}}[n]$ already includes some Coulomb correlation contribution. A major deficiency of the LDA + U method is that E_{dc} is not easily estimated, and therefore several forms of this correction have been introduced (Anisimov et al., 1991, 1993; Lichtenstein et al., 1995), each leading to some differences in results (Mohn et al., 2001; Petukhov et al., 2003). The appropriate value to use for U is somewhat uncertain, since it necessarily must include screening from the conduction electrons, which reduces the Coulomb interaction by a factor of 3–4 compared to the bare f-f Coulomb interaction energy. Its value may be deduced from constrained LDA calculations (Anisimov and Gunnarsson, 1991), by which the energy change due to an enforced increase of f occupancy is calculated, including effects of screening. However, this is an approximate procedure due to the intractable correlation effects inherent in the LDA.

The physical idea behind the LDA + U correction is like for the OP scheme (section 3.3) to facilitate an orbital imbalance within the f-manifold with ensuing loss in f contribution to bonding. However, the U parameter is significantly larger, usually in the range of 6–10 eV for lanthanides, compared to the E^3 parameter used in Eq. (13), which is of the order 0.1 eV in lanthanides. Therefore, LDA + U strongly favours OP and for lanthanides, generally pushes the f-bands either far below or far above the Fermi level (lower and upper Hubbard bands), that is the occupation numbers N_k attain values of either ~ 1 or ~ 0 . For this reason, the LDA + U scheme has not been applied to describe valence transitions. Improved descriptions include an exchange interaction parameter in the f-manifold with spin-polarization of the conduction electrons (LSD + U), and/or a rotationally invariant formulation (Lichtenstein *et al.*, 1995), by which the dependence on representation (e.g., spherical versus cubic harmonics) is avoided. In full implementation, this latter scheme introduces band shifts reminiscent of multiplet splittings (Gotsis and Mazin, 2003; Duan *et al.*, 2007).

The LDA + U has been extensively used in studies of lanthanides, but a comprehensive review will not be given here. Some significant applications and reviews are reported in Antonov *et al.* (1998), Gotsis and Mazin (2003), Duan *et al.* (2007), Larson *et al.* (2007), and Torumba *et al.* (2006). The method is almost as fast as a conventional band structure method, and when comparisons to experimental photoemission experiments are made, the LDA + U method provides a much improved energy position of localized bands over the LDA/LSD. In addition, often, the precise position of occupied f-states is not essential to describe bonding properties, rather the crucial effect is that the f-states are moved away from the Fermi level.

3.5 Self-interaction-corrected local spin density approximation

In solids containing localized electrons, the failure of LDA, LSD, as well as their gradient improvements can to a large extent be traced to the self-interaction error inherent in these approaches. The self-interaction problem of effective one-electron theories of solids has been realized for a long time (Cowan, 1967; Lindgren, 1971). The favoured formulation within the DFT framework is due to Perdew and Zunger (Zunger *et al.*, 1980; Perdew and Zunger, 1981).

Consider first a system of a single electron moving in an arbitrary external potential $V_{\text{ext}}(\mathbf{r})$. The wavefunction, Ψ_1 , is the solution to the Schrödinger equation

$$(-\nabla^2 + V_{\text{ext}})\psi_1 = \varepsilon_1\psi_1. \quad (17)$$

From this, the energy may easily be calculated as:

$$\varepsilon_1 = \langle \psi_1 | -\nabla^2 + V_{\text{ext}} | \psi_1 \rangle = T_0[n_1] + V_{\text{ext}}[n_1], \quad (18)$$

where the density is simply $n_1(r) = |\psi_1(r)|^2$, and T_0 is the kinetic energy and V_{ext} given by Eq. (9). When the same system is treated within DFT, the energy is written as in Eq. (7), that is, the two additional terms must cancel:

$$U[n_1] + E_{\text{xc}}[n_1] = 0. \quad (19)$$

This is a fundamental property of the true exchange-correlation functional, E_{xc} , valid for any one-electron density. In the LSD, E_{xc} is approximated, and the self-Coulomb and self-exchange do not cancel anymore. One speaks of spurious self-interactions that are introduced by the approximations in the local functionals (Dreizler and Gross, 1990).

Next we consider a many-electron system. When the electron density is decomposed into one-electron orbital densities, $n = \sum_{\alpha} n_{\alpha}$, it is straightforward to see that the Hartree term, Eq. (8), contains a contribution, $U[n_{\alpha}]$, that describes the electrostatic energy of orbital α interacting with itself. In the exact DFT, this self-interaction term is cancelled exactly by the self-exchange contribution to E_{xc} in the sense of Eq. (19) for orbital α , but not when approximate functionals are used for E_{xc} . The remedy to the self-interaction problem proposed by Perdew and Zunger (1981) was simply to subtract the spurious self-interactions from the LSD functional for each occupied orbital. Their SIC-LSD functional has the form

$$\begin{aligned} E^{\text{SIC-LSD}} &= E^{\text{LSD}} - \sum_{\alpha}^{\text{occ.}} \delta_{\alpha}^{\text{SIC}} \\ &= \sum_{\alpha}^{\text{occ.}} \langle \psi_{\alpha} | -\nabla^2 | \psi_{\alpha} \rangle + V_{\text{ext}}[n] + U[n] + E_{xc}^{\text{LSD}}[n_{\uparrow}, n_{\downarrow}] - \sum_{\alpha}^{\text{occ.}} \delta_{\alpha}^{\text{SIC}}. \end{aligned} \quad (20)$$

Here the sums run over all the occupied orbitals ψ_{α} , with the SIC given by

$$\delta_{\alpha}^{\text{SIC}} = U[n_{\alpha}] + E_{xc}^{\text{LSD}}[n_{\alpha}], \quad (21)$$

where

$$n_{\alpha} = |\psi_{\alpha}|^2 \quad (22)$$

and α is a combined index comprising all the relevant quantum numbers of the electrons. The spurious self-interactions are negligible for extended orbitals, but are substantial for spatially localized orbitals.

When applied to atoms, the most extreme case where all electrons occupy localized orbitals, the SIC-LSD functional drastically improves the description of the electronic structure (Perdew and Zunger, 1981). In solids, where not all electrons occupy localized orbitals, one has to deal with an *orbital-dependent* SIC-LSD functional [Eq. (20)]. In addition, since the LSD exchange-correlation functional depends non-linearly on the density, the SIC [Eq. (21)] and hence the SIC-LSD functional [Eq. (20)] are *not* invariant under unitary transformations of the occupied states, and therefore one is faced with a daunting functional minimization problem (Temmerman et al., 1998).

The minimization condition for the SIC-LSD functional in Eq. (20) gives rise to a generalized eigenvalue problem with an orbital dependent potential as

$$H_{\alpha} \psi_{\alpha}(\mathbf{r}) \equiv [-\nabla^2 + V^{\text{LSD}}(\mathbf{r}) + V_{\alpha}^{\text{SIC}}(\mathbf{r})] \psi_{\alpha}(\mathbf{r}) = \sum_{\alpha'}^{\text{occ.}} \epsilon_{\alpha\alpha'} \psi_{\alpha'}(\mathbf{r}), \quad (23)$$

with the Lagrange multipliers matrix, $\varepsilon_{\alpha\alpha'}$, ensuring the orthonormality of the orbitals. Since the SIC is only non-zero for localized electrons (Perdew and Zunger, 1981), the localized and delocalized electrons experience different potentials. The latter move in the LSD potentials, defined by the ground state charge density of all the occupied states (including the localized, SIC, states), whereas the former experience a potential from which the self-interaction term has been subtracted. Hence, in this formulation, one distinguishes between localized and itinerant states but treats them on equal footing. The decision whether a state is to be treated as localized or extended is based on a delicate energy balance between band formation and localization. As a result, one has to explore a variety of configurations consisting of different distributions of localized and itinerant states. The minimization of the SIC-LSD total energy functional with respect to those configurations defines the global energy minimum and thus the ground state energy and configuration. In addition, to ensure that the localized orbitals are indeed the most optimally localized ones, delivering the absolute energy minimum, a localization criterion (Pederson *et al.*, 1984, 1985)

$$\langle \psi_{\alpha} | V_{\alpha}^{\text{SIC}} - V_{\alpha'}^{\text{SIC}} | \psi_{\alpha'} \rangle = 0 \quad (24)$$

is checked at every iteration of the charge self-consistency process. The fulfilment of the above criterion is equivalent to ensuring that the Lagrange multiplier matrix in Eq. (23) is Hermitian, and the energy functional is minimal with respect to the unitary rotations among the occupied orbitals. The resulting SIC-LSD method is a first-principles theory for the ground state with no adjustable parameters. It is important to realize that the SIC-LSD functional subsumes the LSD functional, as in this case all electrons (besides the core electrons) are itinerant, which corresponds to the configuration where SIC is not applied to any orbitals, and thus the solution of the SIC-LSD functional is identical to that of the LSD.

The SIC constitutes a negative energy contribution gained by an f-electron when localizing, which competes with the band formation energy gained by the f-electron if allowed to delocalize and hybridize with the available conduction states. The volume dependence of δ_z is much weaker than the volume dependence of the band formation energy of lanthanide's 4f (or actinide's 5f) electrons, hence the overbinding of the LSD approximation for narrow f-band states is reduced when localization is realized.

One major advantage of the SIC-LSD energy functional is that it allows one to determine valencies of the constituent elements in the solid. This is accomplished by realizing different valence scenarios, consisting of atomic configurations with different total numbers of localized and itinerant states. The nominal valence is defined as the integer number of electrons available for band formation, namely

$$N_{\text{val}} = Z - N_{\text{core}} - N_{\text{SIC}}, \quad (25)$$

where Z is the atomic number, N_{core} is the total number of core (and semi-core) electrons, and N_{SIC} is the number of localized, SIC, states. The self-consistent minimization of the total energy with different configurations gives rise to

different local minima of the same functional, $E^{\text{SIC-LSD}}$ in Eq. (20), and hence their total energies may be compared. The configuration with the lowest energy defines the ground state configuration and the ensuing valence, according to Eq. (25). As already mentioned, if no localized states are realized, $E^{\text{SIC-LSD}}$ coincides with the conventional LSD functional, that is, the Kohn-Sham minimum of the E^{LSD} functional is also a local minimum of $E^{\text{SIC-LSD}}$. A second advantage of the SIC-LSD scheme is that one may consider localized f-states of different symmetry. In particular, the various crystal field eigenstates, either magnetic or paramagnetic may be investigated.

The SIC-LSD still considers the electronic structure of the solid to be built from individual one-electron states, but offers an alternative description to the Bloch picture, namely in terms of periodic arrays of localized atom-centred states (i.e., the Heitler-London picture in terms of the exponentially decaying Wannier orbitals). Nevertheless, there still exist states that will never benefit from the SIC. These states retain their itinerant character of the Bloch form and move in the effective LSD potential. This is the case for the non-f conduction electron states in the lanthanides. In the SIC-LSD method, the eigenvalue problem, Eq. (23), is solved in the space of Bloch states, but a transformation to the Wannier representation is made at every step of the self-consistency process to calculate the localized orbitals and the corresponding charges that give rise to the SIC potentials of the states that are truly localized. These repeated transformations between Bloch and Wannier representations constitute the major difference between the LSD and SIC-LSD methods.

It is easy to show that although the SIC-LSD energy functional in Eq. (20) appears to be a functional of all the one-electron orbitals, it can in fact be rewritten as a functional of the total (spin) density alone, as discussed by Svane (1995). The difference with respect to the LSD energy functional lies solely in the exchange-correlation functional, which is now defined to be self-interaction free. Since, however, it is rather impractical to evaluate this SIC exchange-correlation functional, one has to resort to the orbital-dependent minimization of Eq. (20).

Since the main effect of the SIC is to reduce the hybridization of localized electrons with the valence band, the technical difficulties of minimizing the SIC-LSD functional in solids can often be circumvented by introducing an empirical Coulomb interaction parameter U on the orbitals that are meant to be localized, which leads to the LDA + U approach, discussed in Section 3.4. The original derivation of the LDA + U approach (Anisimov et al., 1991) was based on the conjecture that LDA can be viewed as a homogeneous solution of the Hartree-Fock equations with equal, averaged, occupations of localized d- and/or f-orbitals in a solid. Therefore, as such, it can be modified to take into account the on-site Coulomb interaction, U , for those orbitals to provide a better description of their localization. The on-site Hubbard U is usually treated as an adjustable parameter, chosen to optimize agreement with spectroscopy experiments, and thus the method loses some of its predictive power. In contrast, SIC-LSD has no adjustable parameters and is not designed to agree with spectroscopy experiments. The LDA-based band structure is often compared to photoemission experiments. This is because the effective Kohn-Sham potentials can be viewed

as an energy-independent self-energy and hence the Kohn-Sham energy bands correspond to the mean field approximation for the spectral function. In the SIC-LSD, this argument only applies to the itinerant states that are not SI-corrected. The localized states that have been SI-corrected respond to a different potential, and the solution of the generalized SIC-LSD eigenvalue problem, which is different from the solution to the Kohn-Sham equations in the LDA, no longer corresponds to a mean field approximation of the spectral function. Nevertheless, one can make contact with spectroscopies by performing the so-called Δ_{SCF} calculations (Freeman *et al.*, 1987), or utilize the transition state concept of Slater (1951). The most advanced procedure, however, would be to combine the SIC-LSD with the GW approach (see Section 3.7) to obtain both the real and imaginary part of an energy-dependent self-energy and the excitation spectrum for both localized and itinerant states.

Finally, given the above SIC-LSD total energy functional, the computational procedure is similar to the LSD case, that is minimization is accomplished by iteration until self-consistency. In the present work, the electron wavefunctions are expanded in LMTO basis functions (Andersen, 1975; Andersen *et al.*, 1989), and the energy minimization problem becomes a non-linear optimization problem in the expansion coefficients, which is only slightly more complicated for the SIC-LSD functional than for the LDA/LSD functionals. Further technical details of the present numerical implementation can be found in Temmerman *et al.* (1998).

3.6 Local self-interaction-corrected local spin density approximation

A local formulation of the self-interaction-corrected (LSIC) energy functionals has been proposed and tested by Lüders *et al.* (2005). This local formulation has increased the functionality of the SIC methodology as presented in Section 3.5. The LSIC method relies on the observation that a localized state may be recognized by the phase shift, η_ℓ , defined by the logarithmic derivative:

$$D_\ell = \frac{S\phi'_\ell(S)}{\phi_\ell(S)}, \quad (26)$$

passing through a resonance. Here, S denotes the atomic radius, and $\phi_\ell(S)$ and $\phi'_\ell(S)$ are, respectively, the partial wave and its derivative at radius S with angular character ℓ . Specifically, the phase shift is given as

$$\tan(\eta_\ell(E)) = \frac{D_\ell - D_{0\ell}^-}{D_\ell - D_{0\ell}^+}. \quad (27)$$

$D_{0\ell}^-$ and $D_{0\ell}^+$ denote the corresponding logarithmic derivatives for the regular and irregular radial waves in zero potential, respectively (Martin, 2004). For a quasi-localized (resonant) state, the phase shift increases rapidly around the energy of that state and goes through a resonance, that is jumps from 0 to π passing rapidly through $\pi/2$. The energy derivative of the phase shift is related to the Wigner

delay-time (Taylor, 1972). If this is large, which is the case for a resonance, the electron spends a long time in the corresponding atomic orbital. Such ‘slow’ electron will be much more affected by the relaxations of other electrons in response to its presence, and therefore should see a SIC potential.

The phase shift carries all necessary information about the local potential and is the fundamental quantity in the multiple scattering formalism of the electronic structure problem (Martin, 2004). In this approach, the solid state Green’s function is formulated in terms of the scattering matrix (t -matrix), which is calculated from the phase shifts for constituent atoms at different angular momentum quantum numbers and a purely geometrical part expressed by the so-called structure constants. For the LSIC formulation, one merely replaces the scattering potential at a given resonant channel with the SIC potential. The local aspect of the approach is due to the SI-corrected potential being confined to the atomic sphere of the correlated atom.

Because of the multiple scattering aspect of the LSIC approach, we can easily calculate the Green’s functions and various observables from them for making contact with experiments, most notably the total energy given by Eq. (21) and, as for the full SIC of Section 3.5, also valencies. The great potential of the Green’s function formulation of the SIC-LSD method is that it can be easily generalized to study different types of disorder such as chemical, charge, and spin disorder. This is accomplished by combining LSIC with the CPA (Soven, 1967; Gyorffy and Stocks, 1978; Stocks et al., 1978; Faulkner and Stocks, 1981; Stocks and Winter, 1984). The CPA is the best possible single-site mean field theory of random disorder. In conjunction with the DLM formalism for spin fluctuations (Gyorffy et al., 1985; Staunton et al., 1986), the method allows also for different orientations of the local moments of the constituents involved, which will be demonstrated in Section 7.2 on the study of the finite temperature magnetism of the heavy lanthanide elements. The CPA used with the LSIC allows to study chemical disorder by investigating alloys of lanthanides, and to treat valence fluctuations by implementing an alloy analogy for a variety of phases, whose constituents are composed of, for example, two different configurations of a system, say f^n and f^{n+1} of a given lanthanide ion. In the latter application, thermal fluctuations are mapped onto a disordered system. If the total energies of these configurations are sufficiently close, one can envisage dynamical effects playing an important role as a consequence of tunnelling between these states. Such quantum fluctuations become important at low temperatures. In Section 7.3, we explore the thermal fluctuations for the study of the Ce $\alpha \rightarrow \gamma$ phase transition at finite temperatures, and in Section 8, we outline how to evaluate the quantum fluctuations. To fully take into account the finite temperature effects, one has to calculate the free energy of a system (pseudo-alloy), as a function of temperature, T ; volume, V ; and concentration, c , namely

$$F(T, c, V) = E_{\text{tot}}(T, c, V) - T(S_{\text{el}}(T, c, V) + S_{\text{mix}}(c) + S_{\text{mag}}(c) + S_{\text{vib}}(c)). \quad (28)$$

Here S_{el} is the electronic (particle-hole) entropy, S_{mix} the mixing entropy of the alloy, S_{mag} the magnetic entropy, and S_{vib} the entropy originating from the lattice vibrations. The discussion of cerium in [Section 7.3](#) includes finite temperature effects along these lines.

3.7 The GW method

The GW method ([Hedin, 1965](#); [Aryasetiawan and Gunnarsson, 1998](#)) is aimed at a precise determination of the excitations of the solid state system, which is fundamentally different from the focus on ground state properties of the density functional methods outlined in the preceding sections. In GW, the central object is the Green's function ([Mahan, 1990](#)). The excitation (quasi-particle) energies ω_α including correlations are expressed through the following equation

$$\left(\omega_\alpha - \hat{H}_0\right)\psi_\alpha(\mathbf{r}) - \int \Sigma(\omega_\alpha, \mathbf{r}, \mathbf{r}')\psi_\alpha(\mathbf{r}')d^3r' = 0. \quad (29)$$

Here, \hat{H}_0 denotes the Hamiltonian for the uncorrelated (reference) system, whereas ψ_α denote the quasi-particle wavefunctions and Σ is the self-energy. The physical meaning of this equation is that Σ , through the integration in the last term, causes a shift of the eigenenergy from ε_α in the non-interacting case (assuming $\hat{H}_0\psi_\alpha \sim \varepsilon_\alpha\psi_\alpha$) to ω_α with interactions turned on. Obviously, Σ is the crucial quantity to determine. The Green's function G of the interacting system is in fact given by

$$G(\omega) = (\omega - \varepsilon_\alpha - \Sigma)^{-1}, \quad (30)$$

so that [Eq. \(29\)](#) may be seen as a search for poles in G .

The GW method takes its name from the approximation invoked to calculate Σ , namely $\Sigma = G_0W$, or explicitly

$$\Sigma(\omega, \mathbf{r}, \mathbf{r}') = \frac{i}{2\pi} \int G_0(\omega + \omega', \mathbf{r}, \mathbf{r}')W(\omega', \mathbf{r}, \mathbf{r}')d\omega'. \quad (31)$$

In this equation, G_0 is the Green's function of the uncorrelated reference system, whereas W denotes the screened Coulomb interaction. Commonly, G_0 is constructed from an LDA or LDA + U band structure, in which case, the reference system strictly speaking is not uncorrelated, but the potential due to correlation is the exchange-correlation potential, V_{xc} , which is explicitly known and can be subtracted from Σ , namely $\Sigma = \Sigma - V_{\text{xc}}\delta(\mathbf{r} - \mathbf{r}')$.

In terms of the wavefunctions, $\psi_\alpha^0(\mathbf{r})$, of the reference system and the corresponding eigenenergies, ε_α , the reference Green's function reads

$$G_0(\omega, \mathbf{r}, \mathbf{r}') = \sum_\alpha \frac{\psi_\alpha^0(\mathbf{r})\psi_\alpha^{0*}(\mathbf{r}')}{\omega - \varepsilon_\alpha \pm i\delta}, \quad (32)$$

where the sum is over the eigenstates of the reference system. The $\pm i\delta$ in the denominator in [Eq. \(32\)](#) is introduced as a mathematical trick to distinguish between occupied and unoccupied states.

The bare interaction between an electron in the position \mathbf{r} and another electron in the position \mathbf{r}' is

$$V(\mathbf{r} - \mathbf{r}') = \frac{1}{|\mathbf{r} - \mathbf{r}'|} \quad (33)$$

that becomes screened by the presence of the other electrons in the solid. This screening is expressed through the dielectric function, $\varepsilon(\omega, \mathbf{r}, \mathbf{r}')$, so that the effective interaction is

$$W(\omega, \mathbf{r}, \mathbf{r}') = \int \varepsilon(\omega, \mathbf{r}, \mathbf{r}') V(\mathbf{r}' - \mathbf{r}) d^3 r', \quad (34)$$

which defines the second ingredient of the GW method, Eq. (31). Note that the pure exchange, Hartree-Fock, approximation can also be expressed as a GV method.

The difficult part of this method is the evaluation of the dielectric function. In the simplest meaningful approximation, this is accomplished in the random phase approximation, in which ε is given explicitly in terms of the $\psi_{\alpha}^0(\mathbf{r})$ and ε_{α} of the reference system [see, e.g., Hybertsen and Louie (1986), Godby et al. (1988), Mahan (1990), and Aryasetiawan and Gunnarsson (1994, 1998) for technical details]. In the random phase approximation, the screening is mediated through the excitations of electron-hole pairs. The screening is dynamic leading to the ω -dependence of ε and hence Σ . This then leads to the very non-linear dependence on ω_{α} in Eq. (29). Further complications arise because ε is a complex valued function, the imaginary part contributing to finite lifetimes of quasi-particles.

A final issue to consider is which reference system is best suited. By far, most applications have used LDA as starting point, but for optimum consistency, the initial band structure should reflect as closely as possible the final result, for example for a semi-conductor, the screening properties are quite dependent on the fundamental gap, which however is consistently underestimated in the LDA and GGA band structures. This is in particular a problem when the LDA band structure is metallic, as happens for Ge (van Schilfgaarde et al., 2006a) and InN (Rinke et al., 2006). Likewise, for lanthanides, because of the localized nature of the f electrons, LDA and GGA are inadequate reference band structures for GW, whereas SIC-LSD or LDA + U might be better suited. Unfortunately, no GW calculations of this sort have been reported for lanthanide systems. Recently, van Schilfgaarde et al. (2006b) in their quasi-particle self-consistent GW approximation suggested to iterate the input band structure to the point that it comes as close as possible to the GW output band structure, which is the most consistent choice, but evidently requires more computing effort. They applied their approach to the lanthanide elements Gd and Er, as well as to the compounds GdAs and ErAs, and GdN, ErN, and YbN (Chantis et al., 2007). The calculations show the occupied f-bands shifted away from the Fermi level, with some multiplet-like splittings, showing good agreement with experimental photoemission spectra. The unoccupied f-bands appear 1–3 eV above their experimental positions. All in all, as far as the f-manifold is concerned, the GW band structure is quite LDA + U like, as

indeed suggested by [Anisimov et al. \(1997\)](#). However, the authors do not find a straightforward mapping from GW to the appropriate parameters for LDA + U .

The greatest success of the GW method has hitherto been in the semi-conducting solids, where the underestimate of the fundamental gap within LDA/GGA is greatly improved ([Hybertsen and Louie, 1986](#); [van Schilfgaarde et al., 2006b](#)).

3.8 Dynamical mean field theory

The DMFT ([Georges et al., 1996](#); [Kotliar et al., 2006](#); [Held, 2007](#)) is a general framework for incorporating the self-energy of a correlated atom into the solid state environment. The basic assumption is that the correlation effects are local in nature, so that as a first step, the self-energy for a single atom may be computed in an otherwise uncorrelated environment, the conduction electron bath, which is described by the Green's function G_{bath} , that is:

$$\Sigma = \Sigma(G_{\text{bath}}). \quad (35)$$

This constitutes the DMFT impurity problem. Subsequently, the Green's function for the solid is constructed from

$$G^{-1} = G_0^{-1} - \Sigma(G_{\text{bath}}), \quad (36)$$

where G_0 is the Green's function of the uncorrelated solid, [Eq. \(32\)](#). From G , the solid state excitations can be obtained, for example the spectral function (generalized DOS) $A_{nk}(\omega)$ is given as:

$$A_{nk}(\omega) = \left| \frac{1}{\pi} \text{Im} G_{nk}(\omega) \right|, \quad (37)$$

for the quasi-particle labelled by band and k-vector index nk .

An intriguing aspect of DMFT is that the effective bath to be used in the impurity problem, [Eq. \(35\)](#), may be determined by averaging the solid state Green's function in [Eq. \(36\)](#) and subtracting the correlation term ($-\Sigma$), namely

$$[G_{\text{bath}}(\omega)]^{-1} = \left(\frac{1}{N_k} \sum_{\mathbf{k}}^{\text{BZ}} G_{\mathbf{k}}(\omega) \right)^{-1} + \Sigma(\omega). \quad (38)$$

Here, we explicitly write the averaging as a sum over the BZ. Hence, the imposed self-consistency condition is that the G_{bath} put into [Eq. \(35\)](#) should equal the G_{bath} extracted from [Eq. \(38\)](#) with [Eq. \(36\)](#). This is usually obtained via an iteration process (the DMFT self-consistency cycle).

Crucial to all DMFT calculations is how $\Sigma(G_{\text{bath}})$ is evaluated. There are many possibilities and the quality of the calculation depends on this. Two aspects need to be specified, namely the model adopted to describe the correlation effects of the impurity atom and the method/approximation used to solve the impurity problem (the impurity solver), once the model has been chosen. The choice of the model requires physical insight. The Hubbard model ([Hubbard, 1963](#)) is the

favoured choice in most approaches. Usually, it is necessary to reduce the number of degrees of freedom involved in the correlation problem to a minimum for computational reasons. Generally, the uncertainty of the double-counting term, haunting the LDA + U method (Section 3.4), also prevails in the DMFT treatment. The method of solving the impurity problem can be either numerical, as in the Quantum Monte Carlo and exact diagonalization methods, or rely on approximate methods (which again require physical insight), for example perturbation theory. For details, we refer the reader to the recent reviews of DMFT (Kotliar et al., 2006; Held, 2007). In Section 6.1, we describe results of a particularly simple DMFT implementation that is well applicable to lanthanide compounds, in which the full multiplet structure of the lanthanide ion is computed; however, it ignores the coupling to the conduction sea.

Many DMFT calculations have been reported in recent years, the majority discussing 3d systems, but also several dealing with actinides. Less attention has been paid to the lanthanides, most probably because the atomic limit, as outlined Section 6.1, is sufficient for an accurate description in most cases. An important exception is the γ - α transition in cerium, which has been the subject of several studies (Held et al., 2001; Zölf et al., 2001; McMahan et al., 2003; Haule et al., 2005; Amadon et al., 2006), all using the Hubbard model, but with various impurity solvers. Ce compounds have also been studied based on the Hubbard model (Lægsgaard and Svane, 1998; Sakai et al., 2005; Sakai and Shimuzi, 2007).

4. VALENCE AND VALENCE TRANSITIONS

4.1 Determining valence

Valence is a chemical concept but can be very useful in describing the lanthanides in the solid state, as it is strongly linked to their physical properties. In particular, valence changes can lead to anomalies of lattice parameters across the elemental lanthanides and their mononictides and monochalcogenides (Jayaraman, 1978). Most of the lanthanide atoms in solids are trivalent, although in the atomic state, most are divalent (Gschneidner, 1971). However, there are exceptions to this rule, Eu, Yb metals are divalent, and in some compounds Eu, Sm, Tm, and Yb, can be either divalent or trivalent (Gschneidner, 1969). On the other hand, Ce, and its phases and compounds, can be either trivalent or tetravalent. Of course, not all the lanthanides and their compounds can be associated with an integer valence, and some of them are classified as intermediate- or mixed-valent systems, as it is the case for the heavy fermion materials.

In the ionic picture, divalent, trivalent, or tetravalent valence means that two, three, or four electrons, respectively, are chemically active. In the solid state context, lanthanide valence means that two, three, or four valence bands are occupied by two, three, or four electrons. In addition, unlike in the ionic picture, these valence band electrons can have s, p, d, and even f character, as it is often the case for the lanthanide materials.

The effect of SIC is different between atoms and solids. In the case of atoms, the levels are being populated in steps of one electron and the self-interaction is always large. In the solid state, the occupancy of a particular orbital can vary between zero and one, and whether to apply the SIC is determined by a competition between the band formation energy (no SIC) and the localization energy (application of SIC) of each of the bands. This leads to a definition of valence because the SI-corrected, localized, states are well separated from the valence states and are no longer available for bonding and band formation. In the SIC-LSD method, one calculates valence from first-principles, by comparing local energy minima corresponding to different valence scenarios composed of different numbers of localized and itinerant electrons. As mentioned earlier, this comparison establishes the nominal valence to be given by

$$N_{\text{val}} = Z - N_{\text{core}} - N_{\text{SIC}},$$

with Z being the atomic number, N_{core} the total number of core (and semi-core) electrons, and N_{SIC} the number of localized, SI-corrected, states. Thus, in the SIC-LSD approach, these are the localized, SI-corrected, electrons that define the valence, and we shall come back to this point later.

It was postulated by [Gschneidner \(1971\)](#), more than 30 years ago, that there exist two types of f electrons in lanthanide materials, of which an integer number are atomic-like and a small, fractional number are band-like. Our *ab initio* approach confirms this dual character of f electrons, with the localized ones determining valence, and the itinerant ones, appearing at the Fermi level and hybridizing with the other, s, p, and d conduction electrons, being responsible for valence transitions, observed in many of the lanthanides systems. As, we shall discuss in the following, there exists a critical fractional number of these itinerant f electrons, above which, the solid will want to reduce its valence by localizing an additional electron. Such valence, and indeed also structural and magnetic, transitions can happen due to pressure or temperature.

4.2 Valence of elemental lanthanides

As already mentioned, in the SIC-LSD approach, one deals with the split f-manifold. The localized f electrons are responsible for establishing the ground state valence of the elements, based on the total energy considerations involving different valence configurations. In [Figure 4](#), we show the total energy differences between the divalent and trivalent scenarios for all the lanthanide elemental solids, and their sulphides (which will be discussed in [Section 4.3](#)), as calculated within the SIC-LSD approach. As we are only interested in trends in valence across the lanthanide series, for simplicity, all calculations have been performed in the fcc structure, assuming in addition the ferromagnetic ordering of spins. The energy differences seen in [Figure 4](#) are large and positive at the beginning of the lanthanide series, indicating preference for the trivalent state, but towards the middle of the series, they fall sharply, eventually becoming negative for Eu. This marks the change of valence to divalent state. From Eu to Gd, one observes a discontinuous jump due to the switch to a trivalent state at Gd, from where the

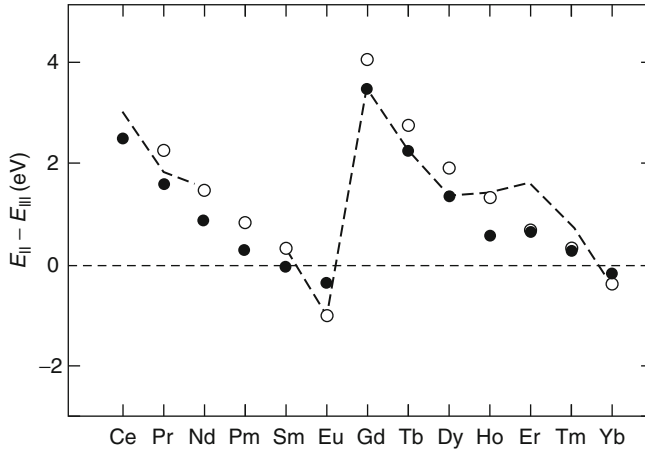


FIGURE 4 Total energy differences between divalent and trivalent elemental lanthanide metals (open circles) and their sulphides (solid circles). The dashed line shows the experimental values for the lanthanide metals. The calculated energy differences have been uniformly shifted upwards by 43 mRy to reproduce the valence transition pressure of 6 kbar in SmS. This rigid shift is sufficient to reproduce the correct valence states of the whole lanthanide metal series and their compounds.

behaviour of the energy differences repeats the one at the beginning of the series, until the arrival at Yb where a switch to divalence occurs.

To understand these anomalous changes in energies, in [Figure 5](#), we show the corresponding energy differences as a function of the change in the number of itinerant f electrons across the lanthanide series, and also for the sulphides. One sees clearly the change from positive to negative values occurring when the number of itinerant electrons in the trivalent solid reaches the value of about 0.7, at which point, it is more favourable for the system to switch its valence to divalent. As observed above, these changes of valence happen for Eu and Yb, and these are precisely the elements for which one observes the dramatic jumps of lattice parameters now displayed in comparison with experiment in [Figure 6](#). The agreement is very good and the anomalies are well reproduced. What we have learned from these *ab initio* SIC-LSDA calculations is that the dual character of the f electrons, postulated many years ago by [Gschneidner \(1971\)](#), can be understood from first principles and that both types of electrons play a different role in these systems. The localized electrons determine the valence and the magnetic and optical properties, whereas the valence transitions are driven by the itinerant f electrons. The latter are the conduction f electrons that hybridize strongly with the s, p, and d valence electrons, contributing to the DOS at the Fermi energy and establishing the Fermi surface. These itinerant f electrons exist only in the trivalent solids and, unlike the localized fs, they participate to bonding ([Gschneidner, 1993](#)).

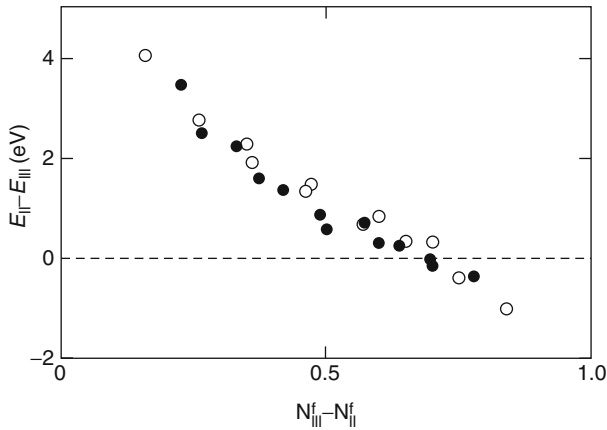


FIGURE 5 The energy differences between the divalent and trivalent valence states of the elemental lanthanides (open circles) and their sulphides (solid circles) versus the difference between the fractional numbers of itinerant f electrons in the two valence states.

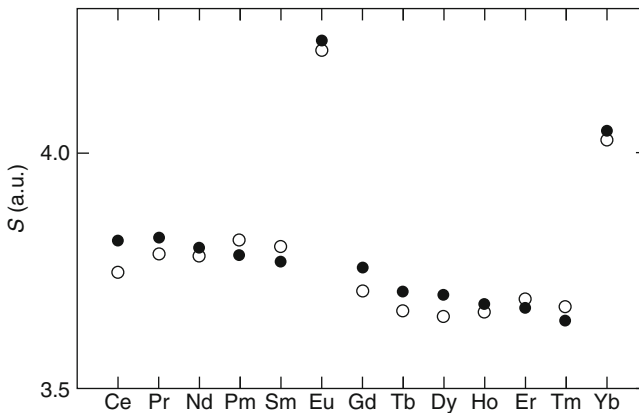


FIGURE 6 The calculated equilibrium atomic sphere radii, S , (open circles) and their experimental counterparts (solid circles) for all the lanthanide elements. The atomic sphere radius is defined in the caption of [Figure 1](#).

4.3 Valence of pnictides and chalcogenides

At ambient conditions, the lanthanide monopnictides RX ($X = N, P, As, Sb, Bi$) and monochalcogenides RX ($X = O, S, Se, Te, Po$) crystallize in the NaCl structure. Given the combination of an electropositive R-ion with an electronegative pnictide or chalcogenide, one might assume that an ionic picture can be applied here. But based on the observed properties, [Rhyne and McGuire \(1972\)](#) proposed a classification distinguishing between the so-called valence balanced compounds Pnictide³⁻R³⁺, Chalcogenide²⁻R²⁺, and valence unbalanced compounds such as

Chalcogenide²⁻R³⁺. The former being mostly ionic insulators, although there are exceptions, and the latter being mostly conductors.

The overall electronic properties of the lanthanide pnictides and chalcogenides are mainly determined by the f–f and f–d overlap between the corresponding orbitals on neighbouring lanthanide sites, and the f–p overlap between the lanthanide-sites and the pnictogen/chalcogen ion. While the f–f overlap in principle leads to narrow band formation, the corresponding small gain in energy has to compete with the strong intra-atomic correlations among the f-electrons that tend to localize them. As we will show, the difference between the valence balanced and valence unbalanced compounds is related to the competing trends of f-electron localization and f-band formation. In all our calculations, we assume the rock salt structure and ferromagnetic arrangement of spins. The reason is that the true magnetic structures of the lanthanide compounds are not always known.

4.3.1 The pnictides

The lanthanide pnictides have been studied extensively, given their potential applications. An overview of their electronic and magnetic properties has recently been written by [Duan et al. \(2007\)](#). An earlier review of the lanthanide pnictides can be found in [Hulliger \(1979\)](#). In this section, we shall mainly concentrate on the valencies of the lanthanide-ions, and the resulting electronic structure, as obtained within the SIC-LSD approach. In a simple ionic picture, one expects the pnictides to be trivalent insulators. The reason being that the pnictide ion, when alloyed with the lanthanide element, can accommodate additional three electrons through charge transfer and hybridization. The resulting trivalent lanthanide-ion configuration is confirmed by experiment and the present calculations. Many of these compounds, however, turn out not to be insulators.

Among the nitrides, only NdN, GdN, TbN, and DyN definitely order ferromagnetically, SmN is anti-ferromagnetic, and most of the remaining nitrides have not been investigated in sufficient detail for their magnetic structure to be unambiguously defined. The SIC-LSD study of the lanthanide–nitrides in the ferromagnetically ordered state finds all the compounds, from Pr onwards, to be trivalent in the ground state ([Aerts et al., 2004](#)). CeN is found to prefer, energetically, the tetravalent configuration. The calculated energy difference, $E_{\text{II}} - E_{\text{III}}$, between the divalent and trivalent configurations, is shown in [Figure 7](#). As expected, the trend is towards a strongly trivalent state at the beginning of the series, and a decreasing energy difference as a function of filling up the f-shell up to Eu. Trivalent Gd is again very energetically favourable, given the half-filled f-shell, after which the energy trend repeats itself. The divalent configuration, however, does not become favourable for any of the nitrides. The calculated lattice parameters ([Aerts et al., 2004](#)) are compared to the experimental values ([Wyckoff, 1968](#)) in [Figure 8](#). The jump between Ce and Pr is due to the valence change from tetravalent to trivalent. The overall agreement is very good, even though for some of the lighter lanthanides, the unexplained irregularities in the experimental data seem to reflect the relatively limited quality of the samples available at the time.

In [Table 2](#), we show the spin-resolved band gaps and densities of states of each material at the Fermi energy. It is clear from the table that our SIC-LSD

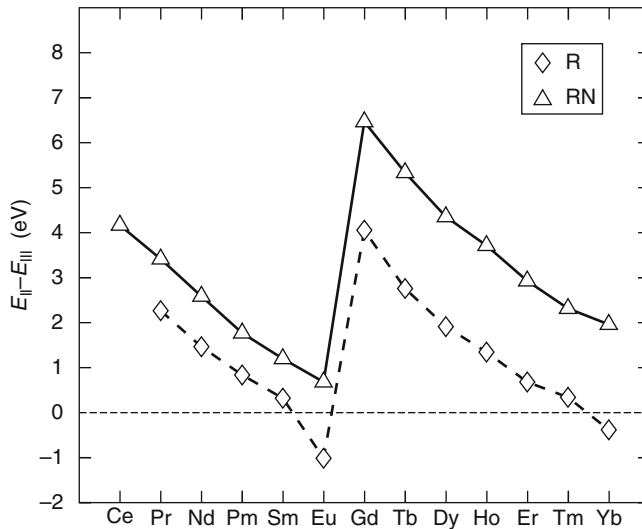


FIGURE 7 Total energy differences (in eV) between divalent and trivalent scenarios for lanthanide nitrides (triangles). The results for elemental lanthanides (diamonds) are repeated for an easy comparison (including 43 mRy correction, but not for the nitrides).

calculations find most of the light lanthanide nitrides to be half-metallic. Only CeN is metallic because it exists in the tetravalent state (in fact the trivalent state is also just metallic). TbN, DyN, and HoN are found to be narrow band gap insulators, and ErN, TmN, and YbN are metallic in both spin-channels, with the Fermi energy lying at the bottom of the spin-down 4f-states, leading to a rather large spin-down DOS at the Fermi energy. The insulating (semi-conducting), half-metallic, and full metallic behaviours that we have predicted for lanthanide nitrides is a consequence of the nitrogen p and the band-like lanthanide f-states occurring in the same energy window, in the vicinity of the Fermi level, which leads to strong hybridization of these states. Our results seem to suggest that lanthanide nitrides and their alloys may enable us to fabricate materials with a wide and continuous range of useful properties, particularly with regard to spin filtering applications where they may provide alternatives to the lanthanide chalcogenides already in use for this purpose (Moodera *et al.*, 1993; Worledge and Geballe, 2000; Filip *et al.*, 2002; LeClair *et al.*, 2002).

The total and species-decomposed spin magnetic moments are displayed in Table 3. There we also present the lanthanide orbital moments. With the exceptions of ErN, TmN, and YbN, the spin magnetic moments of these materials take on an integer value. This indicates that these systems are either insulating (Tb-, Dy-, and Ho-nitrides) or half-metallic (Pr- to Gd-nitrides), since one needs at least one full band in one of the spin channels to obtain an integer value for the spin magnetic moment. CeN is a non-magnetic metal, and the last three compounds of the series are metallic in both spin-channels. These results are as one would expect; the spin magnetic moment is dominated by the rare earth f-electrons, with some hybridization yielding small contributions from the rare

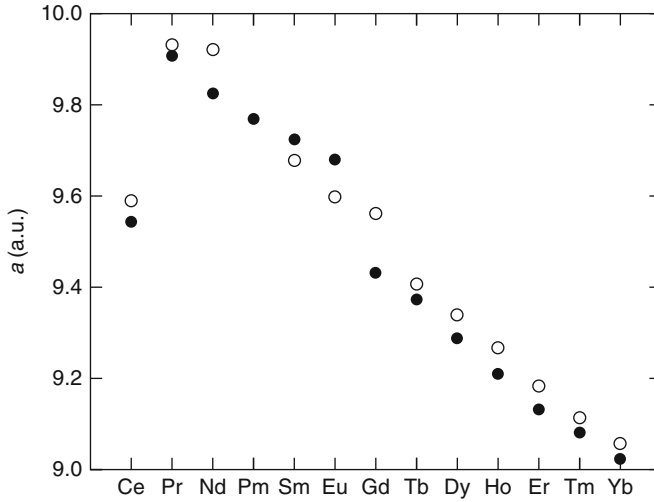


FIGURE 8 Lattice parameters of the lanthanide nitrides. The open circles are the experimental values, whereas the solid circles are the calculated lattice parameters.

TABLE 2 Spin-resolved band gaps (in Ry) and densities of states (in states/Rydberg/formula unit) at the Fermi energy for the lanthanide nitrides

Material	Band gap		DOS	
	Spin up	Spin down	Spin up	Spin down
CeN	0	0	15.37	15.37
PrN	0	0.039	0.0001	0
NdN	0	0.065	0.068	0
PmN	0	0.076	31.77	0
SmN	0	0.095	154.56	0
EuN	0	0.107	69.85	0
GdN	0	0.082	0.065	0
TbN	0.008	0.052	0	0
DyN	0.018	0.058	0	0
HoN	0.031	0.004	0	0
ErN	0	0	0.682	69.57
TmN	0	0	1.52	220.78
YbN	0	0	1.72	93.18

TABLE 3 Total and species-decomposed spin magnetic moments (M_S) of the rare earth nitrides. All values are in Bohr magnetons (μ_B). The contribution of the empty spheres to the total spin magnetic moments is not shown. Because of these empty spheres that were introduced in the unit cell to increase the accuracy of the calculation, the sum of the R and N spin magnetic contributions does not give the total spin magnetic moment. The lanthanide orbital moment (M_L) assumes that the lanthanide ions obey Hund's rules

Material	M_S			M_L
	R	N	Total	R
CeN	0.0	0.0	0.0	0.0
PrN	2.07	-0.08	2.00	-5.0
NdN	3.10	-0.11	3.00	-6.0
PmN	4.13	-0.14	4.00	-6.0
SmN	5.22	-0.24	5.00	-5.0
EuN	6.30	-0.30	6.00	-3.0
GdN	7.01	-0.04	7.00	-0.0
TbN	5.97	0.01	6.00	3.0
DyN	4.93	0.05	5.00	5.0
HoN	3.91	0.08	4.00	6.0
ErN	2.90	0.09	2.99	6.0
TmN	1.83	0.12	1.96	5.0
YbN	0.79	0.14	0.94	3.0

earth s-d electrons and the nitrogen p-states. This indicates that the nitrogen p-states occur in the same energy range as the valence rare earth states, allowing hybridization to occur. It is interesting to note that the contribution from the nitrogen atom to the spin moment changes sign half way through the series and becomes parallel to the lanthanide's spin moment. It appears that the nitrogen moment wants to point anti-parallel to the partially occupied majority f-spin channel.

With respect to the trends in the RX series as a function of pnictide X ($X = N, P, As, Sb, Bi$), a number of SIC-LSD investigations have been published, respectively for CeX (Svane *et al.*, 1996, 1998), PrX (Vaitheeswaran *et al.*, 2004), SmX (Svane *et al.*, 2005), EuX (Horne *et al.*, 2004), and YbX (Temmerman *et al.*, 1999). Generally, it has been found that the tendency towards trivalence decreases with increasing anion size, that is from N to Bi. The larger pnictide ions push the lanthanide-ions further apart, thus decreasing the mutual f-f and f-d overlaps. As a consequence, band formation becomes less favourable as the lanthanide size increases, resulting in less gain of band formation energy, and the gain in SIC-localization energy becoming relatively more important. Eventually, as is the case with the late Eupnictides and Yb-pnictides, the SIC-energy becomes the more important energy scale, localizing an additional electron in the divalent ground state configuration.

In Figure 9A, the band structure for PrSb is shown. Here Pr is assumed to be in its trivalent ground state configuration. The lowest lying bands, around -0.6 Ry

relative to the Fermi level, are mainly due to the Sb s-state, which is well separated from the remaining valence bands. Just below the Fermi level, we find the Sb p-band that is highly hybridized with Pr s- and d-states. The cluster of bands situated at 0.02–0.2 Ry above the Fermi level is due to the itinerant f-states of Pr. The two localized Pr f-states are not shown in the figure. PrSb remains metallic as hole pockets in the vicinity of the Γ -point compensate electron pockets around the X points. The major contribution to the DOS at the Fermi level comes from the d-states of Pr and the p-states of Sb. As can be seen from Figure 9B, the resulting DOS at the Fermi level is rather low, which makes PrSb a semi-metal, in agreement with results from an LDA + U calculation (Ghosh et al., 2003). With respect to the f-bands, we notice some hybridization with the spd-band, but the main part is bundled in the two large, exchange split peaks above the Fermi level.

For a given pnictogen, as we move through the lanthanide series, the lanthanide contraction results in increased localization of the f-electrons that, as we have seen for the RN compounds in Figure 7, results in a decreasing $E_{II}-E_{III}$. The

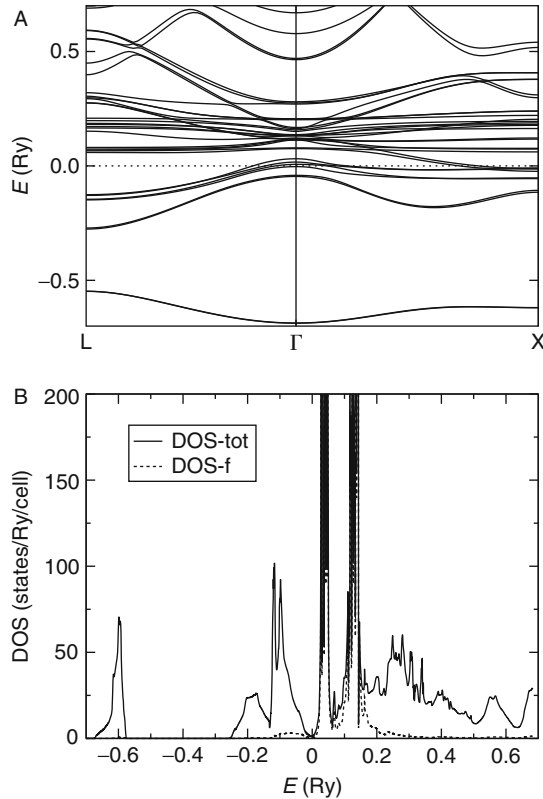


FIGURE 9 Band structure (A) and DOS (B) of trivalent PrSb. In (A), the dotted line marks the Fermi level. In (B), the energy (in Ry relative to the Fermi level) is plotted along the x-axis and the DOS (in units of states Ry⁻¹ per formula unit) along the y-axis. The full curve is the total DOS whereas the dotted curve gives the itinerant Pr f partial DOS. The SIC localized states are not shown.

increasing trend towards localization also means that the corresponding f-state energy levels move towards lower energies, that is they move closer to the pnictogen p-band. This can be observed, for example, in the previously described PrSb DOS depicted in Figure 9B, as compared with the DOS of SmAs shown in Figure 10. In the latter, we find two narrow Sm f resonances situated just above the Fermi level. With increasing localization of the lanthanide ion f-electrons, the itinerant f-peak gets pinned to the Fermi level, and as they move to lower energies, they start filling up with valence electrons. It was shown earlier that the degree of populating the delocalized narrow f-peak is correlated with $E_{II}-E_{III}$, in the sense that the SIC energy is related to the occupied f-states and becomes increasingly important as the f-peak is being occupied, eventually preferring to localize. Thus, the increased occupancy of the f-peak explains the observed trend in valence as a function of lanthanide ion.

Parallel to the observed trend towards filling up the f-peak as a function of the lanthanide ion, one also observes increased occupancy for a given lanthanide as one moves through the pnictide series from N to Bi. Again this can be correlated to the corresponding $E_{II}-E_{III}$. In the Sm pnictides, for example, the preference for a trivalent ground state configuration is reduced from 135 mRy per formula unit in SmN to only 6 mRy per formula unit in SmBi (Svane *et al.*, 2005). This trend is explained by the fact that with decreasing electronegativity, the p-bands move up in energy, which results in the Fermi energy moving progressively into the f-peak when going from N to Bi. As this happens, the pnictide p-bands are intersected at the top by the narrow f-band which pins the Fermi level.

The two trends of f-peak moving towards lower energies with increasing f-electron localization, and of the p-band moving towards higher energies with decreasing electronegativity, culminate for the Eu pnictides and Yb pnictides, and the resulting large degree of occupancy of the f-peak means that the gain in

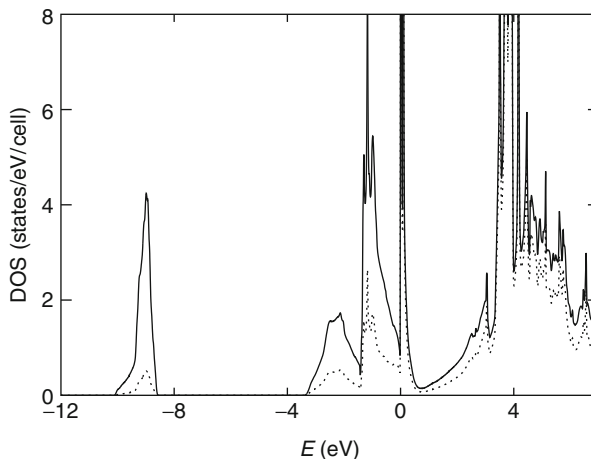


FIGURE 10 DOS with respect to the Fermi energy of trivalent SmAs. The full line shows the total DOS and the dotted line shows the Sm contribution. The SIC localized states are not shown.

SIC-energy becomes large enough to overcome the loss in band formation energy. Thus, from the calculated $E_{\text{II}}-E_{\text{III}}$, we observe that this energy difference eventually turns marginally positive or even negative for the later Eu pnictides, EuAs, EuSb, and EuBi, and YbBi. These findings are in good agreement with experiment, where it turns out that neither of the latter compounds exists in the NaCl structure (Iandelli and Franceschi, 1973), and one might speculate that this is due to the fact that the trivalent configuration is no longer stable in these compounds. Thus, EuAs adopts the hexagonal Na_2O_2 crystal structure (Ono et al., 1971; Wang et al., 1977), that is a distortion of the NiAs structure due to the formation of anion-anion pairs. In conclusion, although the large majority of the lanthanide pnictides prefer the trivalent ground state configuration, the trend towards trivalence decreases with cation size from Ce to Eu, and again from Gd to Yb, as well as with anion size from N to Bi. In the Eu series, the N and P are still sufficiently electronegative to support the charge transfer of three electrons resulting in Eu^{3+} ions, but starting with EuAs, seven f-electrons remain localized at the Eu site, and an eventual NaCl structure, with divalent Eu ions, is unstable to structural transition towards the Na_2O_2 crystal structure.

4.3.2 The chalcogenides

In many respects, the chalcogenides are similar to the pnictides, crystallizing in the same NaCl structure and with the s-, p-, and d-states situated at the same energy ranges as their corresponding neighbours to the left in the Periodic Table. Nevertheless, with respect to the electronic structure, they differ dramatically from each other, which can be traced to the fact that with one additional p-electron, there is only space for accommodating two additional electrons in the valence band, through charge transfer and hybridization. As a consequence, an eventual trivalent ground state is forced to accommodate the third electron in the narrow f-peak, which results in many more compounds being situated at the boundary of the trivalent-divalent phase transition. A divalent ground state configuration is in agreement with the ionic picture for chalcogenides.

Calculations with the SIC-LSD method of the lanthanide-sulphides (Strange et al., 1999) have shown that divalence already sets in here, although only with respect to the lanthanide ions Sm, Eu, and Yb, as can be seen from Figure 11. At the beginning of the lanthanide series, the empty f-levels are held well above the Fermi level, and the third electron is accommodated in the states at the bottom of the broad sd-band. As the atomic number increases, the f-levels move closer to the Fermi level and start picking up electrons. As we reach SmS, the state immediately above the Fermi level is almost entirely of f character, and the electrons now filling up the narrow peak prefer to localize, resulting in a divalent ground state. This behaviour occurs in the light lanthanide from CeS to EuS, and is repeated in the heavy lanthanide from GdS to YbS.

For the lanthanide chalcogenides, it was demonstrated experimentally that Sm, Eu, and Yb are divalent in their sulphide, selenide, and telluride compounds, while Tm becomes divalent for the telluride phase only (Jayaraman, 1978, 1979). The SIC-LSD calculations find all the Eu chalcogenides, including EuO, to be insulators in the ferromagnetic state, and to have a divalent configuration

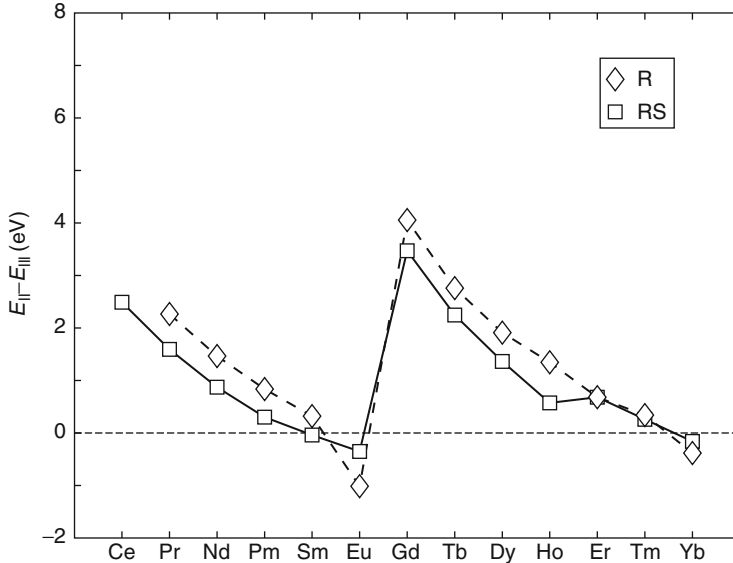


FIGURE 11 Total energy differences (in eV) between divalent and trivalent scenarios for lanthanide sulphides (squares). The results for elemental lanthanides (diamonds) are repeated for an easy comparison (including 43 mRy correction also applied to sulphides).

(Horne *et al.*, 2004). For the Yb chalcogenides, the divalent state is seen to be favoured in all cases by 35–70 mRy (Svane *et al.*, 2000). Both of these results are thus in good agreement with experiment. With respect to the Sm chalcogenides already in Sm monoxide, the divalent f^6 configuration is found to be energetically most favourable, by 6 mRy, and in SmS by 15 mRy (Svane *et al.*, 2005). Hence, the SIC-LSD predicts a Sm valence transition between the pnictides and chalcogenides, as shown in Figure 12. This is not in complete agreement with the experimental picture, according to which the divalent and trivalent ground states in SmS are almost degenerate, while Sm in SmO is trivalent and metallic (Krill *et al.*, 1980; Leger *et al.*, 1980). Thus, it appears that the SIC-LSD functional overestimates the tendency for divalence by approximately 15 mRy in SmS. Assuming this error to be similar for all SmX compounds, this would imply that the calculated energy balance curve in Figure 12 lies too high by approximately 15 mRy. In Figure 12, we therefore include a calibrated energy curve (dashed line) when 15 mRy correction is subtracted from the calculated trivalent-divalent energy difference. In the paper by Strange *et al.* (1999), a similar uniform calibration of 43 mRy (this uniform energy shift is already included in Figure 11) was applied to the trivalent-divalent energy difference of the lanthanide sulphides in order to account for the experimentally observed valence of SmS. The different size of the calibrating energy shift can to a large extent be traced to the neglect of spin-orbit coupling in the former work of Strange *et al.* (1999).

In the Tm chalcogenides, the calculated energy differences between divalent f^{13} and trivalent f^{12} are found to be -1.2 , -13.5 , -24.3 , and -37.3 mRy for TmS,

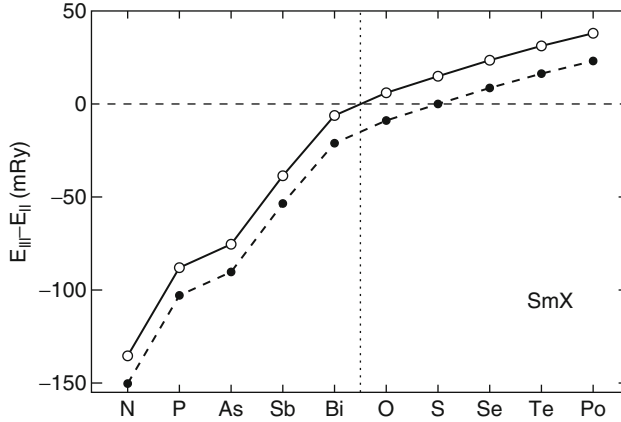


FIGURE 12 Total energy differences (in mRy) between divalent and trivalent scenarios for SmX (full line). A negative sign implies that the trivalent state is favoured. The dashed line marks a 15 mRy corrected energy curve: this is the amount by which the SIC-LSD (with spin-orbit included) overestimates the tendency to form the divalent configuration.

TmSe, TmTe, and TmPo, respectively, reflecting the trend towards greater localization with the larger ligand. Also here, it turns out that at ambient pressure, the trend towards localization is overestimated by some 15 mRy, as it is found experimentally that TmS is a trivalent metal and TmSe is in a mixed valent state.

4.4 Valence of ytterbium compounds

Ytterbium compounds show a wealth of anomalous physical phenomena caused by the intricate electronic structure related to its f-electrons (Cho et al., 1993; Wachter, 1993; Joyce et al., 1996). In the atomic ground state, Yb is divalent with a filled f^{14} shell, but in the solid state, the f-electrons may play an active role in the bonding giving rise to intermediate valent, heavy-fermion, or Kondo behaviour as well as complex magnetic structures. In Temmerman et al. (1999) and Svane et al. (2000), a number of Yb compounds were investigated with the SIC-LSD approach and the energetics of the valence of Yb ions was calculated. The divalent configuration is realized by applying SIC to all 14 f-electrons, while the nominally trivalent configuration is realized by applying SIC to 13 of 14 f-electrons. In this latter case, the last f-electron is allowed to hybridize with the normal sd conduction electrons and form band states. The effective Yb valence, which is given as the number of non-f valence electrons, is then determined by the degree of occupancy of these f-band states, and the resulting electronic structure may be viewed as a realization of an intermediate valence state. The highest effective valence found in this study is 2.88 (for YbN), that is, in no case is the ideal trivalent state reached. The results are summarized in Figure 13 that shows the energy difference between the two localization scenarios correlated with the degree of filling of the f-band in the nominally trivalent scenario.

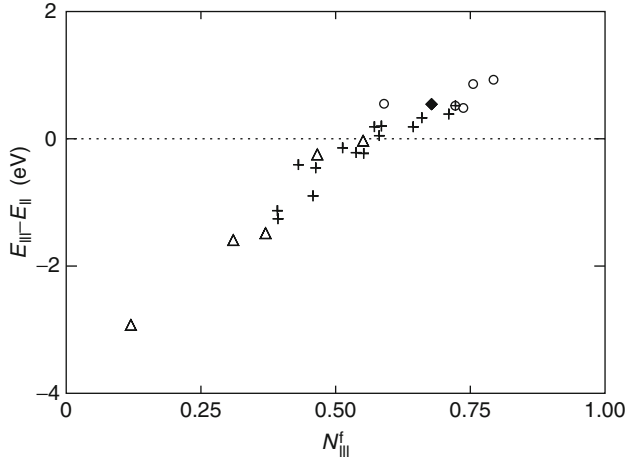


FIGURE 13 Energy difference between the configurations with 13 and 14 localized f-electrons, $\Delta E = E(f^{13}) - E(f^{14})$, correlated with the degree of filling of the 14th Yb f-band in the f^{13} configuration, N_f , for a sequence of Yb compounds. Triangles correspond to the mononitrides, in order of increasing N_f : YbN, YbP, YbAs, YbSb, and YbBi. Circles correspond to the monochalcogenides, in order of increasing N_f : YbO, YbS, YbSe, YbTe, and YbPo. Crosses correspond to the ytterbium intermetallics, in order of increasing N_f : YbAl₃, YbRu, YbIr, YbPd₃, YbRh, YbPd, YbAl₂, YbBiPt, YbZn, YbAu, YbAg, YbCd, Yb₃Pd, YbPb₃, and YbIn. Finally, the diamond denotes elemental fcc Yb.

The Yb compounds considered may be divided into three groups, according to the size and sign of the energy difference between the f^{14} and f^{13} localization scenarios. The group of strongly trivalent compounds comprises the mononitrides YbN, YbP, YbAs, and the intermetallics YbRu, YbRh, YbIr, YbAl₃, and YbPd₃. For this group, the f^{13} configuration is favourable over the f^{14} configuration by more than 0.25 eV per Yb atom. The effective valence ranges from 2.88 in YbN to 2.54 in YbRh and YbPd₃.

The second group consists of the strongly divalent Yb compounds, encompassing all the monochalcogenides YbO, YbS, YbSe, YbTe, and YbPo, as well as elemental Yb, Yb₃Pd, YbPb₃, and YbIn. Here the divalent Yb configuration is favoured over the nominally trivalent configuration by more than 0.25 eV. The effective valence is 2 for these compounds.

The remaining compounds are characterized by having the calculated energies of the f^{13} and f^{14} Yb configurations equal within 0.25 eV. Therefore, effects of valence fluctuations may start to be important. It has been found, however, that the weakly divalent compounds, the intermetallics YbCd, YbZn, YbAg, and YbAu, are in fact well described by the f^{14} localized configuration, as evidenced by the agreement between the calculated and experimental volumes (Svane *et al.*, 2000). Hence, for these compounds, there seems to be no need for additional cohesive contribution originating from valence fluctuations. Interesting behaviour may be expected when pressure is applied to these materials since the effects of valence fluctuations will then become more pronounced. Unfortunately, no

pressure experiments have been reported on any of the Yb compounds in this group. Finally, the compounds YbSb, YbBi, YbBiPt, YbPd, and YbAl₂ are weakly trivalent, that is according to the calculations, the f^{13} localization scenario is favoured by less than 0.25 eV. Among these, YbBiPt and YbAl₂ are known to be heavy-fermion compounds (Havinga et al., 1973; Robinson et al., 1994), and YbPd is believed to be a mixed valent system, with approximately equal proportions of Yb²⁺ and Yb³⁺ ions (Iandelli et al., 1980; Bonville et al., 1986). YbBi has never been synthesized, while YbSb in most respects resembles the other predominantly trivalent Yb pnictides, however, with somewhat unusual low-temperature magnetic behaviour (Kasuya, 1994; Oyamada et al., 1994; Li et al., 1995). Hence, for the compounds in this group, the valence fluctuation phenomena seem to be significant. The calculated effective valencies range from 2.53 in YbSb to 2.45 in YbBi and YbBiPt, that is, the band states of the 14th f-electron are approximately half-filled. The heavy-fermion character of YbBiPt is also confirmed by LDA + U calculations (Oppeneer et al., 1997).

In conclusion, the valence classification of Yb compounds, based on the SIC-LSD total energies, maps very well onto the physical properties observed experimentally. In particular, this allows to identify the third group of compounds as the heavy-fermion and mixed-valent systems on the trivalent side, and, on the divalent side, those systems that are likely to undergo pressure-induced valence transitions.

At ambient conditions, the Yb monopnictides and monochalcogenides crystallize in the B1 structure. As outlined, the Yb pnictides are all found to be well described by the nominally trivalent scenario, where the effective valence varies from 2.88 in YbN to 2.69, 2.63, and 2.53 in YbP, YbAs, and YbSb, respectively. Experimentally, the position of the f^{14} band is found ~ 0.2 eV above the Fermi level in YbN, YbP, and YbAs (Degiorgi et al., 1990, 1993). Other experiments have revealed heavy-electron behaviour in Yb pnictides (Ott et al., 1985; Sakon et al., 1992; Takeda et al., 1993), but this can be a reflection of sample non-stoichiometry (Degiorgi et al., 1990, 1993). The discrepancy between the present electronic structure and the picture provided by Degiorgi et al. (1990, 1993) can be due to the LSD approximation, since the position of the narrow f^{14} band in the theory is solely determined by the LSD potential (no correlation correction). LDA + U calculations on YbN (Larson et al., 2007) include a positive correlation shift of the unoccupied f-states that leads to an ideal trivalent Yb ion in accordance with Degiorgi et al. (1990, 1993).

In contrast to the pnictides, the equilibrium volumes of the Yb chalcogenides are accurately described assuming the divalent f^{14} configuration for Yb. As pressure is applied to the Yb chalcogenides, the f^{13} configuration becomes more and more favourable, and eventually a transition to an intermediate valence state occurs. Valence transitions in lanthanide systems will be discussed in the next section.

4.5 Valence transitions

When pressure is applied to lanthanide systems, the interaction of the electrons generally increases and at some point, it becomes advantageous for the f-electrons to contribute more actively to the bonding, that is the effective valence increases.

In the SIC-LSD formalism, this happens when localization scenarios of different f^n configurations become close in energy. In the present $T = 0$ K theory, only discontinuous pressure-induced transitions can be described, while experiments often, but not always, observe continuous transitions, signalled by anomalous softening of the pV -curve.

Tables 4 and 5 summarize results for valence transitions in the cerium and praseodymium pnictides (Svane *et al.*, 1996, 1998; Vaitheeswaran *et al.*, 2004) and selected rare earth chalcogenides (Svane *et al.*, 1998, 1999, 2001, 2004; Vaitheeswaran *et al.*, 2004; Lebegue *et al.*, 2005; Svane *et al.*, 2005). In Figure 14 is shown the total energy of CeP as calculated with SIC-LSD considering both the B1 (rocksalt) and B2 (caesium chloride) crystal structures as well as both the itinerant, f^0 , and the localized, f^1 , scenario for the Ce ions (Svane *et al.*, 1996). The lowest energy is found in the B1 phase with localized f-electrons and with a specific volume of 348 \AA^3 per formula unit, which coincides with the experimental equilibrium volume. The B1 phase with delocalized f-electrons has its minimum at a considerably lower volume, due to the significant f-electron band formation energy providing a large negative component to the pressure. From the common tangent, a phase transition is predicted at a pressure of 7.1 GPa with a volume collapse of $\Delta V/V_0 = 8\%$ (change in volume relative to the zero pressure equilibrium volume), which is in excellent agreement with the transition observed at 5.5 GPa (Mori *et al.*, 1993). The B2 structure is not as favourable for the CeP compound since the calculated energy is substantially higher than that of the B1 structure. This holds for both localized and delocalized f-electrons. From Figure 14, we conclude that the B2 structure with localized f-electrons is never reached in CeP, while at high pressure, a second phase transition to the B2 structure with delocalized f-electrons is found. The transition pressure is calculated to be 11.3 GPa and the volume collapse 12%, while experimentally, the B1 \rightarrow B2 phase transition is seen at 15 ± 4 GPa (Vedel *et al.*, 1987). The experimental volume collapse is 11%.

The results reported in Table 4 show that all of the observed pressure transitions in the cerium pnictides and chalcogenides are indeed reproduced (Svane *et al.*, 1998). In all cases except CeN is the localized f^1 configuration favoured in the ground state. The total energy curves look rather similar to those of CeP in Figure 14, but minor changes in the relative positions occur when the ligand is varied. The localized phases are generally more favoured when the ligand ion becomes heavier, and as a consequence, in CeAs, no isostructural delocalization transition occurs in the B1 structure. Instead, a transition directly from the B1 structure with localized f-electrons to the B2 structure with delocalized f-electrons occurs, in agreement with experiment. In CeSb and CeBi, the first high-pressure transition to occur is from B1 to B2, with localized f-electrons in both cases, and only at higher pressures is a delocalization transition predicted to take place. The calculated transition pressures for these delocalization processes are only slightly above the ranges studied experimentally. In this work, only the B2 structure was considered for the second transition, but in reality, the valence transition which eventually must take place in CeSb and CeBi may involve another unknown high pressure phase.

TABLE 4 Calculated transition pressures for the electronic and structural phase transitions in the Ce pnictides and chalcogenides. Also quoted are the volume discontinuities (relatively to the zero pressure equilibrium volume) at the transition. The notation (f^n) refers to SIC-LSD calculations with n localized f-electrons. For the cerium pnictides, B2* denotes the distorted B2 structure. Experimentally, the transitions of the Ce pnictides are discontinuous, while those of the cerium chalcogenides (at room temperature) are continuous

Compound	Transition	P_t (GPa)		Volume collapse (%)	
		Theoretical	Experimental	Theoretical	Experimental
CeN	B1(f^0) \rightarrow B2(f^0)	62.0	–	3.6	–
CeP	B1(f^1) \rightarrow B1(f^0)	7.1	9.0 ^a , 5.5 ^b	8.0	4 ^a
CeP	B1(f^0) \rightarrow B2(f^0)	11.3	15(4) ^a , 25.0 ^j	12.1	11 ^a
CeAs	B1(f^1) \rightarrow B2(f^0)	11.4	14(2) ^c , 21.0 ^j	18.0	11 ^c
CeSb	B1(f^1) \rightarrow B2*(f^1)	7.0	8.5(2.5) ^d , 15 ^j	10.9	10 ^d
CeSb	B2*(f^1) \rightarrow B2*(f^0)	25.2	–	3.7	–
CeBi	B1(f^1) \rightarrow B2*(f^1)	8.8	9(4) ^e	10.8	9 ^e
CeBi	B2*(f^1) \rightarrow B2*(f^0)	37.0	–	2.8	–
CeS	B1(f^1) \rightarrow B1(f^0)	10.1	– ^f , 12.5(1.5) ^g	6.3	5 ^g
CeS	B1(f^0) \rightarrow B2(f^1)	24.3	–	4.6	–
CeS	B2(f^1) \rightarrow B2(f^0)	29.5	–	3.6	–
CeSe	B1(f^1) \rightarrow B2(f^1)	12.4	17(3) ^h	11.1	9 ^h
CeSe	B2(f^1) \rightarrow B2(f^0)	37.7	–	3.1	–
CeTe	B1(f^1) \rightarrow B2(f^1)	74.0	5.5(2.5) ⁱ	11.7	9 ⁱ
CeTe	B2(f^1) \rightarrow B2(f^0)	43.5	–	2.4	–

^a Vedel et al. (1987); ^b Mori et al. (1993); ^c Werner et al. (1983); ^d Léger et al. (1984); ^e Léger et al. (1985); ^f Léger (1993); ^g Croft and Jayaraman (1980); ^h Léger and Redon (1989); ⁱ Léger et al. (1983).

In CeS, the first transition occurs to the B1 phase with delocalized f-electrons (Svane et al., 1999), that is, the theory predicts an isostructural phase transition in CeS similar to CeP. The calculated transition pressure is 10.1 GPa with a volume collapse of 6%. These findings are in excellent agreement with the experiment of Croft and Jayaraman (1980), but at variance with the results of Vedel et al. (1986), who observe a soft anomaly in the pV -curve but no discontinuity. These results may indicate the proximity of a critical point. At higher pressures, CeS transforms into the B2 phase. According to the present calculations, this occurs in two steps. First, at a pressure of 24.3 GPa, CeS goes into the trivalent B2 phase with a 4.6% volume change. In the second step, at a pressure of 29.5 GPa, the tetravalent B2 phase is reached with a 3.6% volume collapse (Svane et al., 1999). Unfortunately, no experiments have been performed beyond 25 GPa (Léger, 1993).

In both CeSe and CeTe, the only pressure transition observed is that from B1 to B2 with localized f-electrons in both phases. These are also first to occur according to the calculations, whereas valence transitions are predicted in the range of 40 GPa. Thus, the situation here is quite similar to that in CeSb and CeBi, apart from the tetragonal distortion in these compounds that was not found for CeSe and

TABLE 5 Calculated transition pressures for the electronic and structural phase transitions in the Pr pnictides and chalcogenides of Pr, Sm, Eu, Tm, and Yb. Also quoted are the volume discontinuities (relatively to the zero pressure equilibrium volume) at the transition. The notation (f^n) refers to SIC-LSD calculations with n localized f -electrons. Experimentally, the transitions of SmS are discontinuous, while those of SmSe, SmTe, EuO, EuS, and the Tm and Yb chalcogenides (at room temperature) are continuous. The volume changes for SmSe and SmTe as well as TmTe are obtained by extrapolation over the transition range. For Yb compounds, we quote the relative volumes at which the delocalization starts

Compound	Transition	P_t (GPa)		Volume collapse (%)	
		Theoretical	Experimental	Theoretical	Experimental
PrP	B1(f^2)→B2(f^2)	16.0	26 ^a	11.4	–
PrAs	B1(f^2)→B2(f^2)	12.0	27 ^a	12.4	18.4 ^a
PrSb	B1(f^2)→B2(f^2)	8.0	13 ^a	11.7	10.0 ^a
PrBi	B1(f^2)→B2(f^2)	8.0	14 ^a	10.9	9.0 ^a
PrS	B1(f^2)→B2(f^2)	22.0	–	8.0	–
PrSe	B1(f^2)→B2(f^2)	12.0	–	9.3	–
PrTe	B1(f^2)→B2(f^2)	5.0	9	11.7	–
SmS	B1(f^6)→B1(f^5)	0.1	0.65 ^b 1.24 ^c	11.1	13.5 ^b , 13.8 ^c
SmSe	B1(f^6)→B1(f^5)	3.3	~4 ^b , 3.4 ^c , 3–9 ^d , 2.6–4 ^e	9.8	8 ^b , 11 ^d , 7 ^e
SmTe	B1(f^6)→B1(f^5)	6.2	2–8 ^b , 5.2 ^c , 6–8 ^d , 4.6–7.5 ^e	8.4	9 ^d , 7 ^e
EuO	B1(f^7)→B1(f^6)	19.3	30 ^f , 13–30 ^g	6.3	5 ^f
EuS	B1(f^7)→B1(f^6)	11.6	16 ^h	5.7	0 ^h
TmSe	B1(f^{13})→B1(f^{13})	0	0–5 ^k	14	8 ^k
TmTe	B1(f^{13})→B1(f^{13})	3.0	2–5 ^k	15	14 ^k
TmPo	B1(f^{13})→B1(f^{13})	8.0	–	–	–
YbO	B1(f^{14})→B1(f^{13})	18.0	8 ⁱ	0.87	0.95 ⁱ
YbS	B1(f^{14})→B1(f^{13})	7.5	10 ^j	0.93	0.88 ^j
YbSe	B1(f^{14})→B1(f^{13})	16.0	15 ^f	0.79	0.75 ^f
YbTe	B1(f^{14})→B1(f^{13})	24.0	15 ^f	0.78	0.65 ^f

^a Shirovani *et al.* (2003); ^b Benedict and Holzapfel (1993); ^c Insulator-metal transition of Sidorov *et al.* (1989); ^d Present author's estimates from figures of Bihan *et al.* (1995) and ^e Tsiok *et al.* (1991); ^f Jayaraman *et al.* (1974); ^g Zimmer *et al.* (1984); ^h Insulator-metal transition, Syassen (1986). ⁱ Werner *et al.* (1981); ^j Syassen (1986). ^k Debray *et al.* (1982).

CeTe. The B1 → B2 transition in cerium chalcogenides has also been investigated within the GGA approach (Bouhemadou *et al.*, 2005), in which case, the f electrons are treated as itinerant.

The SIC-LSD studies on the Pr chalcogenides and pnictides show that the ground state favours the B1 structure over the B2 structure throughout the entire series. With applied pressure, all these compounds undergo a transition to the B2 CsCl structure (or a distorted version of it). For the Pr pnictides, the calculated transition pressures agree quite well with experiment, although they are

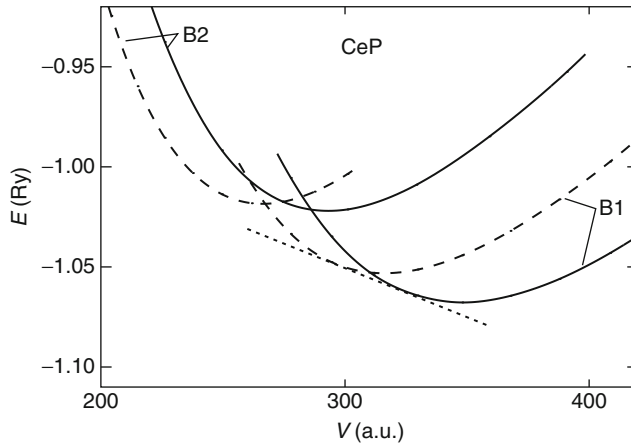


FIGURE 14 Cohesive energy of CeP (in Ry/formula unit) as a function of specific volume (in a_0^3 /formula unit). Two crystal structures, the B1 and B2, are considered, and each with two different treatments of the Ce f-electrons. The full drawn curves correspond to calculations with one localized f-electron per Ce atom, whereas the dashed curves correspond to itinerant f-electrons. The dotted line marks the common tangent at the isostructural phase transition in the B1 structure.

systematically lower, as can be seen from Table 5. The agreement with experiment is equally good for PrTe, while the values for PrS and PrSe have not yet been measured experimentally. Unlike in the case for the Ce pnictides and chalcogenides, the trivalent Pr configuration remains stable under pressure up to 50 GPa.

At ambient pressure, the Sm ions in samarium chalcogenides are divalent, f^6 , but the trivalent phase becomes relevant at high pressure. In this phase, the localized f^5 Sm ions coexist with a partly occupied narrow f-band, effectively describing an intermediate valent phase (Svane et al., 2005). The calculated and measured transition pressures are listed in Table 4. The good agreement both for transition pressures and for volume collapses shows that the bonding of the high-pressure phase is well described in the SIC-LSD approximation, even if the true many-body wavefunction of the intermediate valence phase is much more complicated than the corresponding SIC-LSD wavefunction. This is in line with the general philosophy of the density functional approach in obtaining good total energy estimates from simple reference systems (non-interacting electrons). The present theory cannot describe the continuous nature of the transition observed for SmSe and SmTe. The experiments were all conducted at room temperature and it would be interesting to investigate whether the continuous transition would exist at low temperature as well.

The calculated valence transition pressures for EuO and EuS in the B1 structure are compared with experiment in Table 5. Experimentally, the transition of EuO (at room temperature) is continuous, as in SmSe and SmTe. For EuS, the experiments show no anomalous compression curve (Jayaraman et al., 1974), but the band gap closes at 16 GPa, just before the structural transition to the B2 structure occurs (at 20 GPa) (Syassen, 1986). Due to the ASA in the LMTO-ASA band structure method,

significant uncertainty exists in the comparison of the total energy between different crystal structures. Also the spin-orbit interaction can significantly alter the results: we found that without spin-orbit, the structural transition occurs at 13.7 GPa (Svane *et al.*, 2001), however, without an isostructural transition occurring first.

For TmSe and TmTe, one observes continuous isostructural (B1 \rightarrow B1) valence transitions over a wide volume range, for TmSe already starting at ambient conditions. The calculated discontinuous volume changes are in good agreement with the experimental volumes.

For Yb chalcogenides, the application of pressure leads to a pronounced softening of the pV -curve (Jayaraman *et al.*, 1974; Werner *et al.*, 1981; Syassen, 1986). This softening is found to be correlated with the closure of the $f \rightarrow d$ energy band gap, that is, it starts as the f^{14} shell becomes unstable. In Figure 15, the experimental pV -curve (Syassen, 1986) of YbS is compared with the theoretical curves, obtained with SIC-LSD for the two valence scenarios f^{13} and f^{14} (Temmerman *et al.*, 1999). At pressures below 10 GPa, the experimental and theoretical (14 localized f -electrons) curves coincide. Above 10 GPa, the experimental curve is clearly anomalous, indicating valence instability (Syassen, 1986). The theoretical transition pressure is found to be $P_t \sim 7.5$ GPa, in good agreement with the observed onset of anomalous behaviour around ~ 10 GPa.

In Table 5, the calculated and available experimental data are collected for the isostructural pressure transitions in Yb chalcogenides. The general trends are reproduced by the calculations. Only for the case of YbO, the calculated transition pressure seems to be significantly too high. In the intermetallic YbAl₃ compound, pressure induces a continuous increase of valence (Kumar *et al.*, 2008), which is in good agreement with the calculated rate of depletion of the 14th f -band in the SIC-LSD calculations.

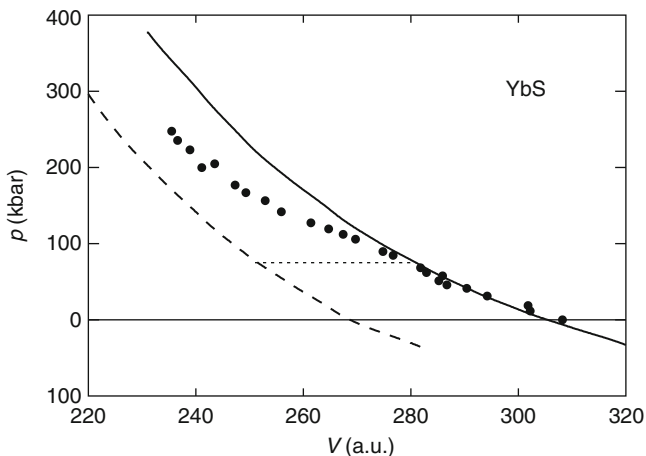


FIGURE 15 Equation of state for YbS as calculated by the SIC-LSD method. The two theoretical curves correspond to divalent Yb f^{14} ions (solid line) and trivalent Yb f^{13} ions (dashed line), respectively. The filled circles are the experimental data of Syassen *et al.* (1986). The dotted line marks the theoretical transition at $P_t = 7.5$ GPa.

4.6 Valence of lanthanide oxides

The lanthanide oxides find important applications in the catalysis, lighting, and electronics industries. In particular, the design of advanced devices based upon the integration of lanthanide oxides with silicon and other semiconductors calls for a detailed understanding of the bonding, electronic, and dielectric properties of these materials (Scarel et al., 2007). Here, we use the SIC-LSD to address the issue of the lanthanide valence in the dioxides RO_2 and sesquioxides R_2O_3 , for $\text{R} = \text{Ce}, \text{Pr}, \text{Nd}, \text{Pm}, \text{Sm}, \text{Eu}, \text{Gd}, \text{Tb}, \text{Dy}, \text{and Ho}$.

Even though all the lanthanide elements readily oxidize, they do so with varying strength (Holland-Moritz, 1992). Ce metal oxidizes completely to CeO_2 in the presence of air, whereas the stoichiometric fluorite structured PrO_2 and TbO_2 exist under positive oxygen pressure. With the exception of Tb, the R-oxides from Nd onwards all occur naturally as sesquioxides R_2O_3 . Under suitable conditions, all the lanthanide elements form as sesquioxides (Eyring, 1978), and there is general agreement, that in the corresponding ground states, the lanthanide atoms are in the trivalent R^{3+} configuration (Tanaka et al., 1995; Moewes et al., 1999). The debate is, however, still ongoing as to the tetravalent (Kern et al., 1984; Wuilloud et al., 1984; Hanyu et al., 1985; Karnatak et al., 1987; Marabelli and Wachter, 1987; Boothroyd et al., 2001) or intermediate-valent (Bianconi et al., 1988; Ogasawara et al., 1991; Butorin et al., 1997) configuration of the R-ions in CeO_2 , PrO_2 , and TbO_2 . In the SIC-LSD approach, by studying the divalent, trivalent, and tetravalent configurations of the lanthanide ions in the respective oxides, we determined the valencies from first-principles and established the corresponding ground state electronic structure.

The calculated energy differences between respectively the tetravalent and trivalent R-ion configurations for the corresponding dioxides and sesquioxides are shown in Figure 16. For CeO_2 , we find a clearly preferred tetravalent ground state configuration, as indicated by a large negative energy difference of 2.4 eV. With all the f-electrons delocalized, CeO_2 is thus best described in the LSD approximation, in line with results from earlier band structure calculations (Koelling et al., 1983; Skorodumova et al., 2001). The tetravalent state is also energetically most favourable for PrO_2 , indicating a $\text{Pr}(f^1)$ ground state configuration. The corresponding DOS is shown in Figure 17B, where it is compared with the LSD configuration with $\text{Pr}(f^0)$ in Figure 17A and the trivalent configuration with $\text{Pr}(f^2)$ in Figure 17C. In Figure 17A, with all the f-electrons treated as delocalized, the Fermi level is situated in the f-peak, in accordance with the LSD calculations by Koelling et al. (1983), but in disagreement with the experimentally observed insulating nature of PrO_2 . Localizing a single f-electron gives an insulator, with the Fermi level situated between the occupied O p-states and the empty Pr f-states, as shown in Figure 17B. In the trivalent scenario of Figure 17C, a further f-electron becomes localized to form $\text{Pr}(f^2)$, which results in some of the O p-states becoming depopulated (Wulff et al., 1988) with an associated cost in band formation energy that outweighs the gain in localization energy by 1.4 eV as can be seen from Figure 16.

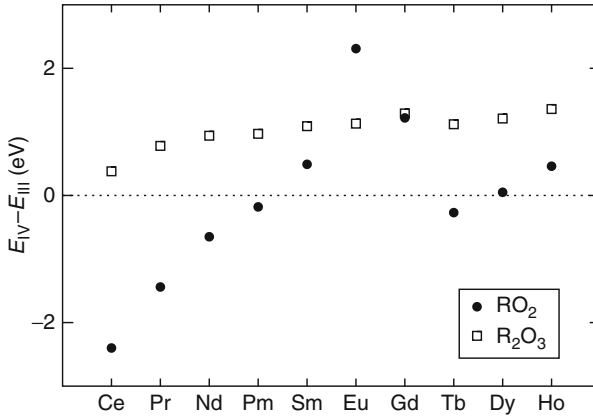


FIGURE 16 Energy difference $E_{IV}-E_{III}$ (in eV per lanthanide ion) between the tetravalent and trivalent lanthanide configurations in dioxides (solid circles) and A-type (hexagonal) sesquioxides (open squares).

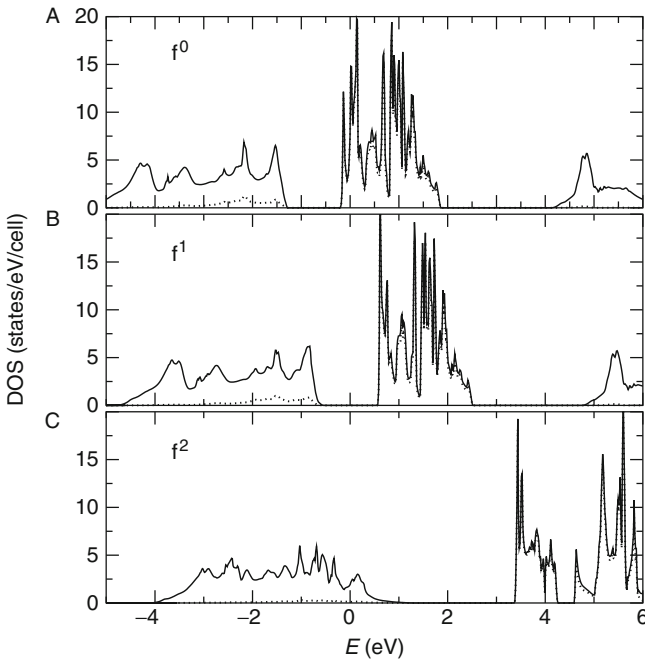


FIGURE 17 Total DOS (solid line) and f -projected DOS (dotted line) for PrO_2 , with Pr in (A) the pentavalent (f^0) configuration, (B) the tetravalent (f^1) configuration, and (C) the trivalent (f^2) configuration. The SIC localized states are not shown. The energy is in units of eV, with zero marking the Fermi level.

The tetravalent ground state in the SIC-LSD translates into a gain of band formation energy from delocalizing an additional f-electron compared with the corresponding trivalent lanthanide metal. In the light lanthanides, the f-electrons are less tightly bound, resulting in compounds that display a larger oxygen coordination number, as the lanthanide atom donates electrons to each of the strongly electronegative O ions. In TbO_2 , the tetravalent ground state configuration is also found to be energetically the most favourable, although the energy difference $E_{\text{IV}} - E_{\text{III}}$ is now reduced to 0.27 eV as can be seen from Figure 16. In Tb, the extra f-electron on top of the half-filled band is again less tightly bound that results in a valence larger than $3+$. The calculated equilibrium volumes in the tetravalent ground state are in good agreement with the experimental values, respectively for CeO_2 , 39.61 \AA^3 ($V_{\text{exp}} = 39.6 \text{ \AA}^3$); for PrO_2 , 39.22 \AA^3 ($V_{\text{exp}} = 39.4 \text{ \AA}^3$); and for TbO_2 , 36.50 \AA^3 ($V_{\text{exp}} = 35.6 \text{ \AA}^3$). We similarly find a tetravalent ground state for NdO_2 and PmO_2 , but it turns out that these dioxides do not form in nature, that is it is found that these compounds are unstable with respect to the reduction to their respective sesquioxide, as is the case for all lanthanides, except for CeO_2 , PrO_2 , and TbO_2 .

Calculations based on the LSD approximation tend to give a reliable picture of the electronic structure of CeO_2 (Koelling et al., 1983), resulting in the tetravalent ground state configuration, with no localized f-electrons. We find an energy gap between the valence band and the unoccupied conduction band (situated above the empty f-peak) to be around 5.1 eV (Gerward et al., 2005), as compared with the experimental value of 6 eV (Wuilloud et al., 1984). Not surprisingly, the LSD somewhat underestimates the band gap. Recent calculations with respectively the hybrid functional method (Silva et al., 2007), and the LDA + U approach (Loschen et al., 2007), find good agreement with experimental data when applied to CeO_2 . For PrO_2 , we find an energy gap of approximately 1.1 eV in the ground state f^1 configuration, considerably larger than the 0.262 eV derived from conductivity measurements by Gardiner et al. (2004), but smaller than the 6 eV obtained in LDA + U calculations treating the localized 4f-states with the open core approach (Diviš and Ruzs, 2005).

Our calculations do not confirm an intermediate valent ground state for either dioxide, which has, however, been proposed as a possible interpretation of core-level spectroscopy data (Bianconi et al., 1988; Ogasawara et al., 1991; Butorin et al., 1997). Koelling et al. (1983) have instead argued that the intermediate valence scenario is related to the ionic description of the lanthanide-oxides, which cannot account for the covalent f-p bonding. In the ionic picture, valence is defined as the number of valence electrons that have transferred from the R atoms to the O atoms, that is f-electrons do not participate in the bonding, and only exist as localized states at the lanthanide sites. Thus, a given integer valent configuration has an integral number of f-electrons, and consequently, a non-integral number of f-electrons can only result from an intermediate valence scenario. In the SIC picture, both localized and delocalized f-states coexist. The delocalized f-states are allowed to participate in the band formation, and they occur as part of the tails of the O p-states. The overall number of f-electrons is non-integral, in analogy to

the intermediate valent picture, however not as a consequence of intermediate valence but rather as a result of the p–f mixing.

At temperatures below 2000 °C, the lanthanide sesquioxides adopt three different structure types (Eyring, 1978). The light lanthanides crystallize in the hexagonal La_2O_3 structure (A-type, space group $P3m1$, no. 164), and the heavy lanthanides assume the cubic Mn_2O_3 structure (C-type, $Ia3$, no. 206), also known as the bixbyite structure (Villars and Calvert, 1991). The middle lanthanides can be found either in the C-type structure or a monoclinic distortion hereof (B-type structure). Transitions between the different structure types are induced under specific temperature and pressure conditions (Hoekstra and Gingerich, 1964). We investigated the electronic structure of both A-type and C-type sesquioxides (Petit *et al.*, 2005). The valence energy difference $E_{\text{IV}} - E_{\text{III}}$ for the sesquioxides in the A-type structure is displayed in Figure 16, where it can be seen that the trivalent configuration is the ground state in all cases. The overall trend is that of an increasing energy difference from Ce_2O_3 to Gd_2O_3 and again from Tb_2O_3 to Ho_2O_3 . Apart from the extraordinary stability of the half-filled shell, which results in a slightly increased influence of the tetravalent configuration in Tb_2O_3 relative to Gd_2O_3 , the general tendency towards trivalence is clearly related to the increasing localization of the f-electrons with increasing atomic number.

A similar total energy behaviour is observed for the simulated C-type structure sesquioxides. The highly directional f-orbitals are only partially able to screen each other from the attractive force of the nucleus, which results in a steadily increasing effective nuclear charge with an increasing number of f-electrons. The increase in localization leads to the well-known lanthanide contraction, that is the decrease in ionic radius across the lanthanide series, which is also reflected in the volumes of the lanthanide sesquioxide series, as illustrated in Figure 18. We notice that the agreement between theory and experiment is considerably better for the C-type structure than for the A-type one, which might be related to the fact that the ASA used in the calculations is likely less reliable when applied to the hexagonal A-type structure than when applied to the higher symmetry cubic C-type structure. Overall, for the C-type structure, the calculated values are in better agreement with the experimental values for the early lanthanide sesquioxides. This behaviour is compared in Figure 18 to the results obtained with the projector augmented PAW (Hirosaki *et al.*, 2003). Here the localized partly filled f-shell is treated as part of the core, which results in better agreement with experiment for the later lanthanides with localized f-states, but which may be too restrictive an approximation for the early lanthanide sesquioxides.

The DOS and band structures for all the sesquioxides are quite similar and differ mostly with respect to the unoccupied f-electron states (Petit *et al.*, 2007). In Figure 19, we show three representative examples, namely, Eu_2O_3 , Gd_2O_3 , and Tb_2O_3 . The energy zero has been placed at the top of the valence bands. The valence band, originating from the O p-states, is of equal width (of the order of 3.5 eV) in all the compounds, and is completely filled as a result of hybridization and charge transfer. In the DOS of Eu_2O_3 , depicted in the top panel of Figure 19, an empty f-band is situated in the gap between the valence band and the (non-f) conduction band. The low position of the f-band is caused by the exchange

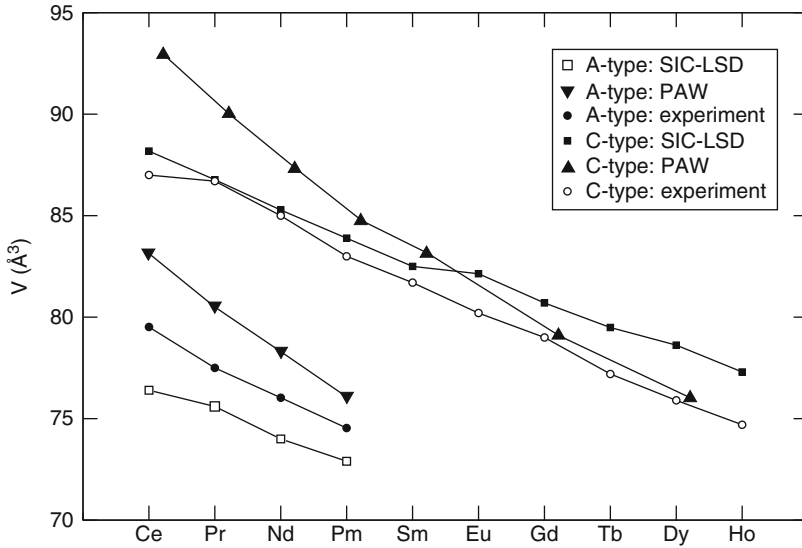


FIGURE 18 Calculated equilibrium volumes (in Å³) of the lanthanide sesquioxides, crystallizing in the hexagonal A-type structure and the cubic C-type structure. The triangles, squares, and circles refer to PAW (Hirosaki et al., 2003), SIC-LSD (present), and experimental results (Eyring, 1978), respectively.

interaction with the localized f^6 shell of Eu. In Gd_2O_3 and Tb_2O_3 , there are only unoccupied minority spin f -states, and their position is significantly higher. All the sesquioxides, with the exception of C-type Eu_2O_3 are found to be insulators.

In Figure 20A, we show the evolution across the sesquioxide series of the unoccupied f -band (hatched area indicating f -band width) and the non- f conduction band edge with respect to the top of the O p -bands (at zero energy). With respect to experimental data, in Figure 20B, one notices a considerable discrepancy between optical (Prokofiev et al., 1996) and conductivity (Lal and Gaur, 1988) measurements of the energy gaps. The direct comparison between theory and experiment (Petit et al., 2005) is further complicated by the fact that in the SIC-LSD, the bare f -bands always appear at too high binding energies due to the neglect of screening and relaxation effects (Temmerman et al., 1993). The position of the occupied and empty f -states with respect to the band edges is crucial, and the interpretation of the optical data is that the empty f -levels are situated above the conduction band minimum, while the gap energies obtained from conductivity measurements indicate that, for some compounds, the transitions are from valence $\rightarrow f$, that is that the empty levels can be situated in the gap between valence band maximum and conduction band minimum.

From experiment, we know that whereas all the lanthanide sesquioxides can be found in nature, the only lanthanide dioxides that occur naturally are CeO_2 , PrO_2 , and TbO_2 . On the other hand, SIC-LSD theory concludes that all the lanthanide sesquioxides prefer the trivalent ground state configuration, whereas the dioxides can be separated into tetravalent light lanthanide dioxides, including

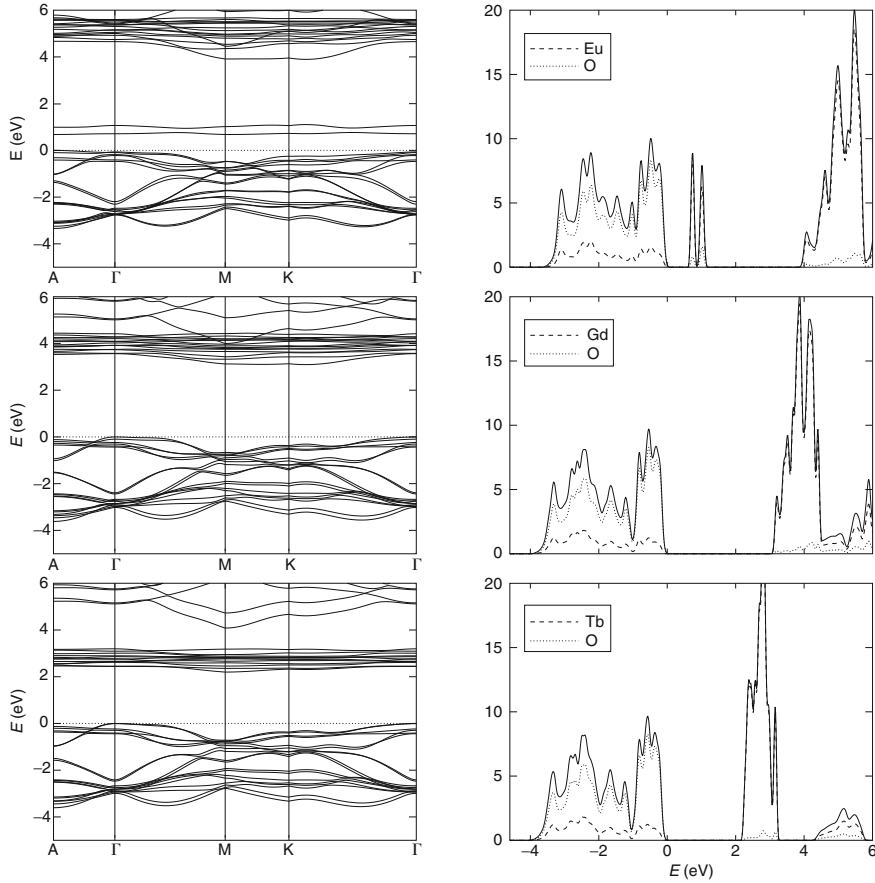


FIGURE 19 Band structure and DOS (in states per formula unit and eV) for Eu_2O_3 (top), Gd_2O_3 (middle), and Tb_2O_3 (bottom) in the trivalent configuration, in the A-type structure, and at the calculated equilibrium volume. The energy zero has been put at the top of the valence bands. The horizontal axis in the band structure diagram refers to the wave vector \mathbf{k} along the symmetry directions denoted by the high symmetry points of A, Γ , M, K, Γ , in the BZ of the A-type lattice. The total DOS in the DOS plots is indicated by a continuous line, whereas the R and O partial DOS are shown with dashed and dotted lines, respectively. The SIC localized states are not shown.

CeO_2 and PrO_2 , and trivalent heavy lanthanide dioxides, with the exception of TbO_2 , which again prefers the tetravalent ground state configuration. This leads us to conclude that with respect to the naturally occurring lanthanide oxides, the oxidation process from sesquioxide to dioxide goes hand in hand with the delocalization of an extra electron. The question then is why the heavy lanthanide dioxides do not form in nature. To shed some light on this issue, we have investigated the oxidation process



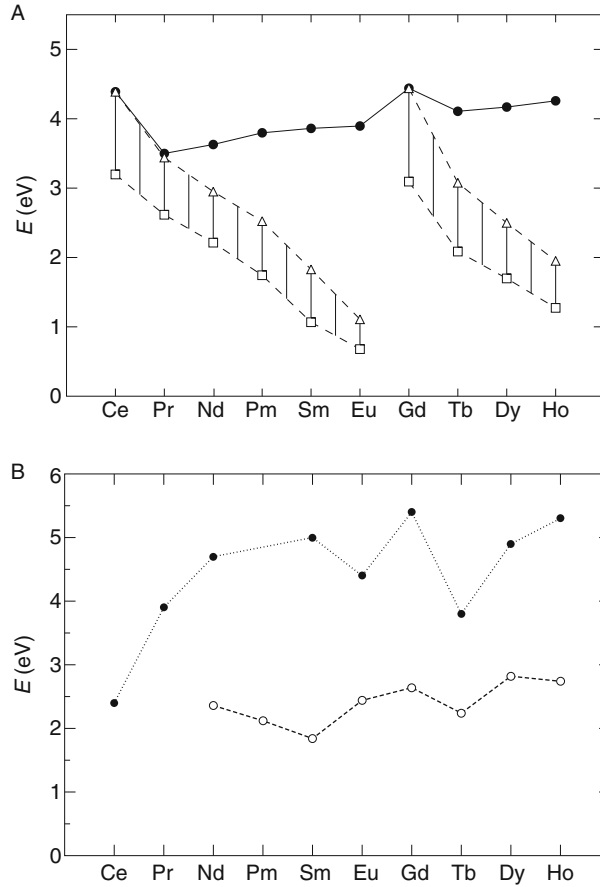


FIGURE 20 Band gaps of the lanthanide sesquioxides. Energy is in units of eV, and the valence band maximum is situated at zero energy. (A) Evolution of the SIC-LSD gap structure through the lanthanide sesquioxide series (A-type). The unoccupied f-band (of majority spin character only from Ce to Eu) is positioned between squares and triangles (hatched area). The non-f conduction band edge is marked with solid circles. (B) Experimental values for the optical gaps (Prokofiev et al., 1996) are shown as solid circles connected by a dotted line, while the energy gap E_g values, deduced from high-temperature conductivity experiments (Lal and Gaur, 1988) are shown as open circles connected by a dashed line.

The balance of this reaction in general will depend on the Gibbs free energy of the reactants at the given temperature and pressure. The *ab initio* calculations of these quantities are beyond the capability of the present theory. However, we can still to some extent analyse the reaction (39) by looking at the zero temperature and zero pressure limit (Petit et al., 2005). In that case, the free energy difference between the reactants reduces to the corresponding total energy difference, as obtained by the SIC calculations, namely

$$E_{\text{ox}} \equiv 2E^{\text{SIC}}(\text{RO}_2) - E^{\text{SIC}}(\text{R}_2\text{O}_3) - \mu_{\text{O}}, \quad (40)$$

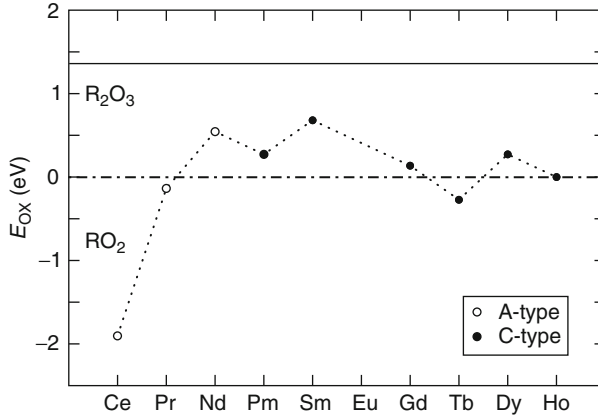


FIGURE 21 Oxidation energies, E_{ox} in Eq. (40), for the lanthanides Ce to Ho. The filled circle is for the cubic C-type sesquioxide and the open circle for the A-type hexagonal structure of the sesquioxide. Negative values indicate that the dioxide is stable. The chemical potential of free O is taken as $\mu_O = -6.12$ eV. The solid line just below 1.5 eV indicates the dioxide/sesquioxide borderline in the case when the FP-LMTO calculated value $\mu_O = -4.76$ eV is used.

where μ_O is the chemical potential of O. The result of this study is shown in Figure 21. Here a negative (positive) energy means that the formation of the dioxide (sesquioxide) is preferred energetically. Furthermore, the oxidation energies [Eq. (40)] with respect to both the A- and C-type sesquioxides were calculated, and the energetically most favourable of these two structures is compared to the corresponding dioxide in Figure 21. The conclusion is that for Ce, Pr, and Tb, the dioxide is energetically preferred. With respect to the corresponding sesquioxides, the A-type is closest in energy for Ce and Pr, while the C-type is closest in energy to the dioxide for Tb. All other compounds prefer reduction to the sesquioxide, which crystallizes in the A-type structure for Nd and the C-type structure for the remainder. This overall picture is in relatively good agreement with the degree of oxidation observed in the naturally occurring compounds.

5. LOCAL SPIN AND ORBITAL MAGNETIC MOMENTS

The SIC-LSD method provides an approach for the *ab initio* determination of the magnetic moment of materials. *Ab initio* theory has the advantage that it can be used to calculate quantities that are inaccessible to experiment. Here we exploit this advantage to explore the magnetic moments of the lanthanide elements. The electrons in the lanthanides generate an exchange field that is modelled as half of the difference in potential felt by spin-up and spin-down electrons. The exchange field defines a direction in the crystal and this is arbitrarily chosen as the z -direction. All magnetic moments are defined as parallel or anti-parallel to the exchange field. Within the electronic structure calculation, we define lattice vectors that also determine the z -direction and so a direction of the moment within

the crystal can be defined. The results discussed in this section are all the result of fully self-consistent relativistic calculations unless otherwise stated. This is absolutely necessary for a quantitative evaluation of the orbital moments. We discuss the light lanthanides and the heavy lanthanides separately.

5.1 Hund's rules

In the description of the standard model, [Section 2.2](#), it is assumed that the electrons distribute themselves among the available f-states according to Hund's rules. However, Hund's rules are essentially based on experiment. A good first-principles theory of electronic structure is one where Hund's rules drop out of the theory rather than having to be included empirically.

As already said, to apply the SIC to the f-states, it is first necessary to decide which (and how many) states it should be applied to based on total energy considerations. Of course, it needs to be applied to the occupied states, but not to the unoccupied ones. If we take trivalent praseodymium as our example, there are nominally two occupied f-states out of a possible 14, and in principle we can choose to occupy any 2. Let us start by occupying two states of opposite spin and a variety of possible m_l quantum numbers. During iteration to self-consistency, the SIC-states adjust but largely keep their initial characteristics, that is the scheme possesses many different solutions, which can be accessed by different starting conditions. In the end, it is the total energy that selects the proper ground state. For each arbitrarily chosen pair of initially occupied m_l values, a fully self-consistent SIC-LSD calculation is performed and we plot the energy and the total orbital moment. This process is repeated choosing two states with parallel spins. The results of this are shown in [Figure 22](#). It is clear that the data points separate into two clusters. Those above -2.28 Ry are those where the two spins are anti-parallel (solid circles) and those below -2.28 Ry are those with parallel spins (open circles). Evidently lining up the spins parallel to each other of the individual states is energetically preferable to having them anti-parallel, and so Hund's first rule is satisfied. Examining this figure further, we see that for the states with parallel spin, there is a rough linearity between the total energy and the orbital moment with the minimum total energy being when the orbital moment has maximum magnitude anti-parallel to the spin moment. Clearly, then Pr obeys all three of Hund's rules. In all honesty, Pr is the best example, but the trends displayed here are also observed in all the light lanthanides. In the heavy lanthanides, similar behaviour is displayed but the lowest total energy is when the orbital moment is a maximum and parallel to the spin moment, also completely consistent with Hund's rules.

5.2 The heavy lanthanides

Although the relativistic SIC-LSD ([Beiden et al., 1997](#)) calculations have been carried out for all the lanthanide metals, we start discussing results from the heavy lanthanides. Thus, in [Figures 23 and 24](#), we display the densities of states for Tb and Ho as illustrative examples. [Figure 23A](#) shows the majority spin d and f

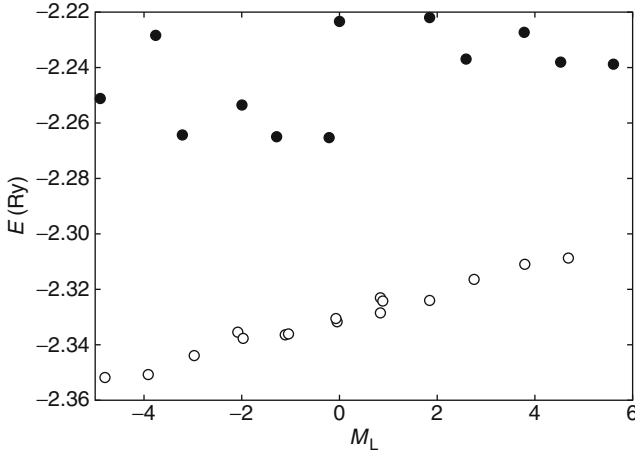


FIGURE 22 The total energy of praseodymium calculated as a function of orbital and spin magnetic moments. The SIC was applied to two f -states and the calculations were performed for a variety of m_s and m_l quantum numbers. All the total energies above -2.28 Ry (solid circles) are calculated with the spin of the localized electrons anti-parallel, while the points below -2.28 Ry (open circles) had parallel spins. This shows that the parallel arrangement is preferred and is consistent with Hund's first rule. The rough proportionality between total energy and orbital moment displayed by the parallel spin states, together with the fact that the most negative orbital moment has the lowest energy, is consistent with Hund's second rule.

densities of states for Tb. [Figure 23B](#) shows the equivalent minority spin curves. The details are described in the figure caption. In [Figure 24A and B](#), we display the equivalent curves for Ho. There are several key points to note about these curves. First, the amount of minority (majority) spin f -character hybridized into the majority (minority) spin bands is small on the scale of the f DOS, but appreciable on the scale of the d DOS. Second, the amount of hybridization between different f -spin states increases from Tb to Ho and generally increases in the heavy lanthanides as atomic number increases. It is straightforward to understand why this occurs. At the Gd end of the series, the exchange field dominates the spin-orbit coupling and so states are split according to their spin. At the Yb end of the series, the f -states are more or less completely filled and there is no exchange field, the dominant splitting in the f -states is spin-orbit coupling where each individual state has mixed spin-up and spin-down character. The change from exchange splitting to spin-orbit splitting is not abrupt, but occurs gradually as we proceed across the $4f$ -series. Comparison of the d -bands in [Figures 23 and 24](#) shows that they are all broadly similar. However, the effect of changing f -hybridization and small changes in the lattice such as a slightly different lattice constant and c/a ratio means that the details of the d densities of states vary from element to element. In turn, this affects the calculated lattice and magnetic properties.

Now we go on to discuss the results of the calculation of the heavy lanthanide magnetic moments. These calculations were performed on a hexagonal close packed lattice at the experimental lattice constant, so these numbers should be

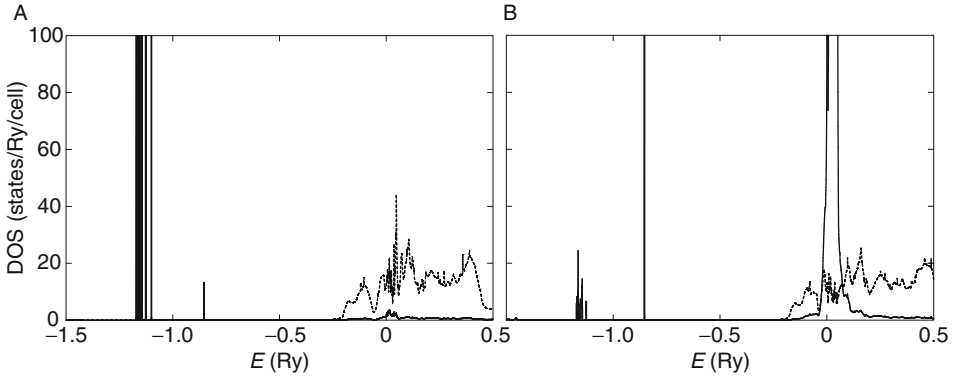


FIGURE 23 The d (dashed lines) and f (full lines) densities of states for Tb with respect to the Fermi energy. (A) Majority spin: the very tall and narrow peaks at around -1.15Ry are the majority spin f-states. The small peak at -0.85 is majority spin f hybridized into the minority spin states through spin-orbit coupling. From -0.25 to 0.5Ry , the d-bands dominate the DOS, but the lower curve indicates a very small majority spin f-contribution in this region. (B) Minority spin: there is considerable minority spin character hybridized into the occupied spin-up f-states. The single occupied predominantly minority spin f-state is at -0.85Ry . The minority spin f-states are close to the Fermi energy and these overlap and hybridize with the d-bands.

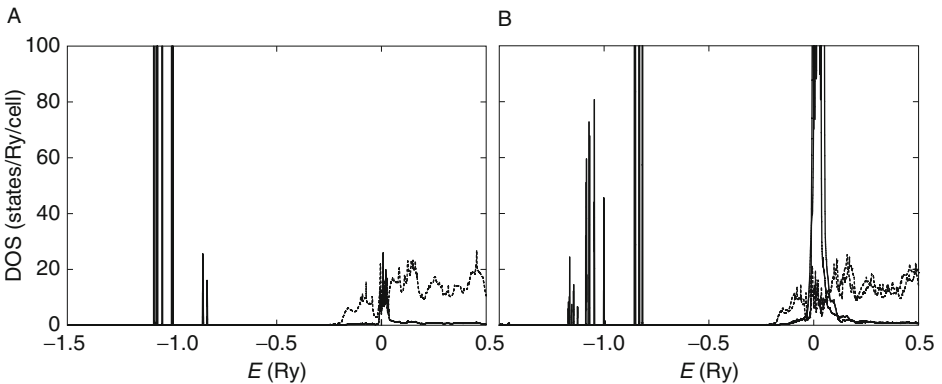


FIGURE 24 The d (dashed lines) and f (full lines) densities of states for Ho with respect to the Fermi energy. (A) Majority spin: The very tall and narrow peaks at around -1.1Ry are the majority spin f-states. The small peaks at -0.85 are majority spin f hybridized into the minority spin states through spin-orbit coupling. From -0.25 to 0.5Ry , the d-bands dominate the DOS, but the lower curve indicates a very small majority spin f-contribution in this region. There is considerable majority spin DOS hybridized into the d-bands around the Fermi energy. (B) Minority spin: There is considerable minority spin character hybridized into the occupied spin-up f-states. The three occupied predominantly minority spin f-states are at -0.85Ry . The minority spin f-states are close to the Fermi energy and these overlap and hybridize with the d-bands.

TABLE 6 The magnetic properties of the heavy lanthanides. The magnetic moments are all written in units of Bohr magnetons per atom. The first column is the spin magnetic moment of the valence states. The second column is the orbital moment associated with the valence electrons. The third column gives the spin moment for the SIC f-states, the fourth column is their orbital moment. The fifth column is the sum of all the previous contributions. The final column is the experimental saturated magnetic moment ([Jensen and Mackintosh, 1991](#)). For Gd through Tm, the calculations were done in the trivalent state. For Yb, the divalent state was the only state to which the calculation could be reliably converged and the moments are all close to zero and so are not shown. From Gd through Tm, the calculations were performed in the Hund's rule ground state

	Valence moments		f(SIC) moments		Total moment	
	Spin	Orbital	Spin	Orbital	Theoretical	Experimental
Gd	-0.05	0.53	6.94	0.013	7.43	7.63
Tb	-0.29	0.40	5.90	3.03	9.04	9.34
Dy	-0.45	0.12	4.88	5.04	9.59	10.33
Ho	-0.56	-0.34	3.84	6.06	9.00	10.34
Er	-0.65	-1.02	2.86	6.06	7.25	9.1
Tm	-0.83	-1.96	1.88	5.05	4.14	7.14

directly comparable with experiment. In [Table 6](#), we lay out all the magnetic quantities calculated within an SIC-LSD calculation. These are the expectation values of $2S_z$ and $L_{z,l}$, that is assuming an ordered magnetic state with a local intrinsic exchange field directed along the z -axis. The quantities obtained are those for the Hund's rule arrangement of initial states within the f -manifold. In principle, we could show systematically that this is the ground state by performing calculations for every possible configuration of electrons and finding that the Hund's rule state is the one with minimum energy. We have done this for some elements such as Pr above, and found the Hund's rule result, but a full systematic study has not been carried out. However, we assume that this could have been done and the Hund's rule configuration is assumed henceforth. The normal procedure to calculate the total magnetic moment for these elements would be to add all the different, valence and localized, contributions together. However, if we do this, it does not work well when compared with the experimental saturated magnetic moment as can be seen from the last two columns of [Table 6](#). There are only two systems, Gd and Tb, for which our calculations show a reasonable agreement with the experimental values of the saturated magnetic moment. These results of the calculations do not compare as well as the values obtained from the standard model (see [Table 1](#)), which contain only the localized f contributions. In particular, for Tm and Er, the valence orbital magnetic moments are large and anti-parallel to the orbital magnetic moments from the localized f -states. The valence orbital moment for Gd is positive, decreases for Tb and Dy, changes sign in Ho. The valence spin magnetic moment changes continuously from -0.05 in Gd to -0.83 in Tm. Thus, the present theory seems to overestimate these valence contributions to the ordered moment of the lanthanides. The

TABLE 7 The magnetic properties of the heavy lanthanides. The magnetic moments are all written in units of Bohr magnetons per atom. The first three columns are the S , L , and J quantum numbers and g_j is the effective Landé g -factor, all of which can be compared with the equivalent results in [Table 1](#). The remaining columns are, respectively, the effective moments calculated according to [Eq. \(5\)](#) and the experimental moment deduced from the Curie-Weiss behaviour of the magnetic susceptibilities in the paramagnetic phases ([Jensen and Mackintosh, 1991](#)). The Hund's rule ground state was chosen throughout

	S	L	J	g_j	μ_t	μ_e
Gd	3.47	0.013	3.48	1.997	7.88	7.95
Tb	2.95	3.03	5.98	1.493	9.65	9.5
Dy	2.44	5.04	7.48	1.326	10.56	10.6
Ho	1.92	6.06	7.98	1.240	10.50	10.4
Er	1.43	6.06	7.49	1.191	9.50	9.5
Tm	0.94	5.05	5.99	1.157	7.49	7.3

SIC-LSD method has a slight tendency to overlocalize states and as a result brings a small amount of unphysical valence f-states below the Fermi energy. This means that the lanthanides become divalent slightly too early as we proceed across the Periodic Table ([Strange et al., 1999](#)). The extra unphysical valence f-states replace d-states. However, they play a similar role in bonding to the d-states, so do not affect the prediction of crystal structural properties, but can distort the prediction of the magnetic moment.

A better agreement with experiment is obtained if the valence moments are ignored, as in the following procedure. The SIC states are highly localized on a particular lattice site. This can be seen from [Table 6](#) where the values of L_z and S_z of the SIC states of f-character are essentially the atomic values presented in [Table 1](#). Thus, we may interpret these as projections onto the z -axis corresponding to effective S , L , and ensuing J quantum numbers, which can be used in [Eqs. \(4\) and \(5\)](#) to determine the total magnetic moment due to the SIC states. In this estimate, the moment of the occupied valence states is ignored. In [Table 7](#), we show the results of this procedure and compare them directly with the experimental values. Surprisingly with the omission of the spin and orbital moments of the valence states, we obtain excellent agreement between theory and experiment. This can indicate that the experiment provides only the contribution of the localized states to the spin and orbital magnetic moments. This is plausible since these experimental magnetic moments are deduced from the linear dependence of the inverse magnetic susceptibilities on temperature in the high-temperature paramagnetic phases, [Eq. \(6\)](#). At these elevated temperatures, the magnetic behaviour is best described by the DLM model (see the next section), according to which the local f magnetic moments are not aligned but rather point randomly in all directions. As a consequence, one does not expect much of a valence electron polarization to develop and could even be negligible, which we assumed in our analysis presented in [Table 7](#). The success of this reasoning might also be construed as an illustration on how well the SIC describes the localized part of the f-states.

5.3 The light lanthanides

In this section, we discuss some calculations of the magnetic moments of the light lanthanides using SIC-LSD in a variety of situations. We have calculated the magnetic moments of all the light lanthanides on an fcc lattice with an identical volume per atom for each element. This has enabled us to untangle the effect of small lattice constant changes on the moment from the effect of the extra f-electron as we proceed across the Periodic Table. The results of these calculations are shown in [Tables 8 and 9](#), where we have explicitly shown all contributions to the moment. In [Table 8](#) are shown the ordered moments, whereas in [Table 9](#) are shown the paramagnetic moments, extracted as outlined for the heavy lanthanides in [subsection 5.2](#).

TABLE 8 The magnetic properties of the light lanthanides. The magnetic moments are all written in units of the Bohr magneton. The first column is the spin magnetic moment of the valence states. The second column is the orbital moment associated with the valence electrons. Column three is the spin moment for the SIC f-states, the next column is their orbital moment. The fifth column is the total moment and the last column is the experimental saturated magnetic moment ([Jensen and Mackintosh, 1991](#)). For Ce through Sm, the calculations were done in the trivalent state, whereas for Eu, the calculation was done in the divalent state. From Ce through Sm, the state chosen was the Hund's rule ground state and this turned out to be the lowest energy state

	Valence moments		f(SIC) moments		Total moment	
	Spin	Orbital	Spin	Orbital	Theoretical	Experimental
Ce	0.32	0.03	0.96	2.96	1.71	0.6
Pr	0.44	0.16	1.98	4.96	2.7	2.7
Nd	0.34	0.51	2.94	5.93	3.16	2.2
Pm	0.32	1.74	3.94	5.95	3.43	–
Sm	0.55	1.69	4.94	4.94	1.14	0.13
Eu	0.42	0.001	6.96	0.01	7.37	5.1

TABLE 9 The magnetic properties of the light lanthanides. The magnetic moments are all written in units of Bohr magnetons per atom. The first three columns are the S , L , and J quantum numbers and g_J is the effective Landé g -factor, all of which can be compared with the equivalent results in [Table 1](#). The remaining columns are the calculated effective moment calculated according to [Eq. \(5\)](#) and the experimental moment ([Jensen and Mackintosh, 1991](#)). The Hund's rule ground state was chosen throughout

	S	L	J	g_J	μ_t	μ_e
Ce	0.48	2.96	2.48	0.93	2.73	2.4
Pr	0.99	4.96	3.97	0.80	3.55	3.5
Nd	1.47	5.93	4.46	0.73	3.60	3.5
Pm	1.97	5.95	3.98	0.60	2.67	
Sm	2.47	4.94	2.47	0.29	0.84	1.5
Eu	3.48	0.01	3.47	1.96	7.72	3.4

TABLE 10 The magnetic properties of neodymium on a variety of crystal lattices (fcc, bcc, simple cubic, and hexagonal lattices) calculated as described in the text. The magnetic moments are all written in units of the Bohr magneton. The second column is the spin magnetic moment of the valence s, p, d, and f-states. The third column is the orbital moment associated with the valence electrons. The final two columns are the spin and orbital magnetic moments of the SI-corrected f-states

	Valence moments		f(SIC) moments	
	Spin	Orbital	Spin	Orbital
fcc	0.34	0.51	2.94	5.93
bcc	0.75	0.51	2.95	5.95
sic	0.90	0.88	2.93	5.89
hcp	0.74	0.34	2.94	5.96

It is notable that the spin and orbital contributions of the localized states are nearly the same as for the ionic case. This shows that in the light lanthanides, the f-states are as localized as for the heavy lanthanides. For the paramagnetic moments, the agreement between theory and experiment is very satisfactory (Table 9) and much better than using a band description of adding the contributions of the localized and delocalized states (Table 8). Sm and Eu are less well described by this procedure and it could be that the assumption of pure trivalent Sm and pure divalent Eu are not fully applicable and some divalent Sm and some trivalent Eu might be mixed into the ground state.

Now let us consider the effect of crystal environment on the magnetic moment of the lanthanides. In Table 10, we show the results of calculations of the magnetic moment of neodymium on several common crystal lattices. A trivalent Nd ion yields a spin moment of $3\mu_B$ and an orbital moment of $6\mu_B$. In the final two columns of Table 10, we see that the SIC-LSD theory yields values slightly less than, but very close to, these numbers. This is independent of the crystal structure. The valence electron polarization varies markedly between different crystal structures from $0.34\mu_B$ on the fcc structure to $0.90\mu_B$ on the simple cubic structure. It is not at all surprising that the valence electron moments can differ so strongly between different crystal structures. The importance of symmetry in electronic structure calculations cannot be overestimated. For example, the hcp lattice does not have a centre of inversion symmetry and this allows states with different parity to hybridize, so direct f–d hybridization is allowed. However, symmetry considerations forbid f–d hybridization in the cubic structures. Such differences in the way the valence electrons interact with the f-states will undoubtedly lead to strong variations in the valence band moments.

6. SPECTROSCOPY

In this section, we highlight two spectroscopies that can reveal information on the valence of the lanthanide ion. First, we will discuss high-energy photoemission spectroscopy that shows the multiplet nature of the lanthanide ion. Second, we

discuss resonant MXRS that allows us to study directly the spin and orbital magnetic properties of the late lanthanides. This experimental probe also has the potential to determine the number and symmetry of the localized f-states. In the first spectroscopy, the starting band structure is that of the LDA, while in the second one, the SIC-LSD is used.

6.1 Hubbard-I approach to lanthanide photoemission spectra

Photoemission is a powerful spectroscopy of lanthanide systems (Campagna *et al.*, 1979). This is due to the distinct atomic multiplet features, which serve as a fingerprint of the configuration adopted by the lanthanide ion in the solid environment.

In photoemission, a photon γ of energy $\hbar\omega$ impinges on a solid, which is an N -electron system in its ground state $|N; 0\rangle$. The photon is absorbed and its energy is transferred to an electron, which is emitted, leaving behind a solid with only $N-1$ electrons and in some excited state. Schematically,

$$\gamma + |N; 0\rangle \rightarrow |N-1; i\rangle + e. \quad (41)$$

The energy of the electron, E_e , is measured and contains information about the excitation energies in the $N-1$ electron system:

$$E_e = \hbar\omega + E(N; 0) - E(N-1; i). \quad (42)$$

In principle, all possible excitations contribute to the photoelectron spectrum and the proper quantum mechanical amplitude must be calculated. For the lanthanides, the atomic limit corresponds to the assumption that the photoelectron spectrum is dominated by those processes, where the photon hits a particular ion and causes an excitation on that ion without disturbing the remainder of the crystal. In the standard model, the lanthanide ion would initially be in its trivalent f^n configuration with the Hund's rule ground state multiplet (Table 1 in Section 2.2), and would be transferred into some multiplet $^{2S+1}L_J$ within configuration f^{n-1} when the photon has been absorbed. The photoelectron energy would thus be

$$E_e \approx \hbar\omega + E_{\text{ion}}(f^n; 0) - E_{\text{ion}}(f^{n-1}; ^{2S+1}L_J), \quad (43)$$

where E_{ion} is the atomic energy. The amplitude for this to happen is proportional to the product of two matrix elements:

$$A \propto \langle \psi_e | e^{i\mathbf{k}\cdot\mathbf{r}} | \phi_f \rangle \cdot \langle f^{n-1}; ^{2S+1}L_J | \hat{f} | f^n; 0 \rangle, \quad (44)$$

where the first factor is the matrix element of the photon field between the wavefunction of the outgoing electron ψ_e and the f electron wavefunction ϕ_f , whereas the second factor is the matrix element of the f destruction operator \hat{f} between the final and initial f multiplets.

In view of the strength of the Coulomb interaction, the atomic limit is certainly a quite idealized assumption. For example, in the real world, the kicked out electron still has some distance to travel through the solid before leaving at the surface and

might scatter off other atoms or electrons on its way (secondary processes). Furthermore, the sea of conduction electrons might react to the presence of a hole in the f-shell of the targeted ion, with some partial transfer of relaxation energy to the photoelectron (screening). Finally, the photon might induce some further excitations of the conduction electrons (shake up effects), for example by exciting plasmon oscillations. For a complete understanding of photoemission, all such processes must be considered, which is a formidable task. It so happens that the atomic limit is a good first approximation for many lanthanide systems, so we will describe in the following text its implementation within the DMFT framework (Lichtenstein and Katsnelson, 1998) and compare with experimental spectra.

The atomic multiplet DMFT method is a generalization of the Hubbard-I approximation (Hubbard, 1963, 1964a, 1964b) to a full f-manifold of 14 orbitals. The model adopted for the isolated atom considers only these 14 degrees of freedom, and their interaction through the Coulomb force in the atomic Hamiltonian

$$H^{\text{at}} = \frac{1}{2} \sum_{\{m_j\}} U_{m_1 m_2 m_3 m_4} \hat{f}_{m_1}^\dagger \hat{f}_{m_2}^\dagger \hat{f}_{m_3} \hat{f}_{m_4} + \xi \sum_i \vec{l}_i \cdot \vec{s}_i - \mu \sum_m \hat{f}_m^\dagger \hat{f}_m. \quad (45)$$

Here, index m_j labels the f orbitals, and \hat{f}_m^\dagger and \hat{f}_m are creation and annihilation operators. The first term in Eq. (45) is the electron–electron interaction, with the matrix element

$$\begin{aligned} U_{m_1 m_2 m_3 m_4} &= \iint \frac{\phi_{m_1}^*(\mathbf{r}) \phi_{m_2}^*(\mathbf{r}') \phi_{m_3}(\mathbf{r}') \phi_{m_4}(\mathbf{r})}{|\mathbf{r} - \mathbf{r}'|} d^3 r d^3 r' \\ &= \sum_\ell a_\ell(m_1 m_2 m_3 m_4) F_\ell, \end{aligned} \quad (46)$$

where $\varphi_m(\mathbf{r})$ are the f-orbitals. The Coulomb integrals may be expressed in terms of vector coupling coefficients, a_ℓ , and Slater integrals, F_ℓ , with $\ell = 0, 2, 4, 6$ (Lichtenstein and Katsnelson, 1998). The second and third terms in Eq. (45) are the spin-orbit interaction, and a chemical potential term used to align with the Fermi level of the solid [see, e.g., Lebegue et al. (2006a)].

The Hamiltonian, H^{at} , is solved by exact diagonalization in the space of all possible Slater determinants for each of the f^n configurations needed in the calculation (typically for the ground state configuration with n electrons and for the $n \pm 1$ configurations corresponding to excited states). The eigenvalues and eigenvectors, denoted respectively by E_v and $|v\rangle$, are obtained and the atomic Green's function $G_{mm'}^{\text{at}}$ calculated as:

$$G_{mm'}^{\text{at}}(\omega) = \sum_{\lambda v} g_{\lambda v} \frac{\langle \lambda | c_m | v \rangle \langle v | c_{m'}^\dagger | \lambda \rangle}{\omega + E_\lambda - E_v}, \quad (47)$$

where the weight factor $g_{\lambda v} = \delta_{\lambda,0} + \delta_{v,0}$ specifies that one of the states in the sum must be a ground state ($T = 0$). More generally, in a thermal environment, $g_{\lambda v}$ is given by the appropriate Boltzmann weights (Lichtenstein and Katsnelson, 1998).

From G^{at} the atomic self-energy, $\Sigma_{mm'}^{\text{at}}$, is finally extracted

$$\Sigma_{mm'}^{\text{at}}(\omega) = \omega \delta_{mm'} - (G^{\text{at}})^{-1}_{mm'}(\omega), \quad (48)$$

to be inserted in the DMFT Eq. (36) for the solid. We have used the LDA as reference system to obtain G^0 . The procedure outlined above describes the multiplets of the 4f atom and combines in a unified framework the strong intra-shell correlation effects related to the 4f electrons and the weaker interaction between s, p, and d electrons. Adding Σ^{at} to the LDA Hamiltonian on the right-hand side of Eq. (36) shifts the f-weight from the narrow LDA bands into the energy positions corresponding to multiplet excitation energies. The matrix elements in the numerator of Eq. (47) ensure that the proper transition amplitudes, according to atomic selection rules, enter the spectral function in Eq. (37). Not included in the description based upon Eq. (37) are the matrix elements between the outgoing photoelectron and the orbital of the left-behind hole. These matrix elements will depend on the angular character of the photo-hole. However, in the applications to be discussed in the following, we will focus on the f-part of the spectral function only, and compare to photoemission spectra using photon energies chosen so as to enhance the f-contribution. Viewed as a DMFT implementation, the above procedure is particularly simple since the impurity is uncoupled from the bath [G_{bath} does not enter in the model Eq. (45)].

In Figures 25 and 26, we show the calculated spectral functions, respectively, for SmAs and SmS using the above theory (Svane *et al.*, 2005). The chemical potential of the reference ion is chosen such that the ground state is $f^5(^6H)$ for trivalent Sm in SmAs and $f^6(^7F)$ for divalent Sm in SmS with an energy separation to the lowest $n-1$ excited levels [$f^4(^5I)$ of 4.0 eV for SmAs and $f^5(^6H)$ of 0.8 eV for SmS, respectively], to coincide with the experimental values for these energies. The Slater integrals entering into the Coulomb matrix in Eq. (46) are almost

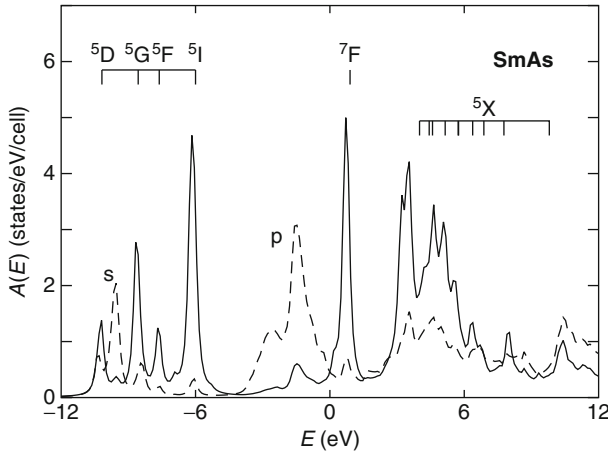


FIGURE 25 The calculated spectral function of trivalent Sm in SmAs at equilibrium volume, with $a = 5.91$ Å. The full curve shows the f-contribution and the dashed curve the non-f contribution. The energy is given relative to the Fermi level. The main lines are characterized by their final state characteristics, either As s, p-bands, or as Sm $f^{n\pm 1}$ multiplet term.

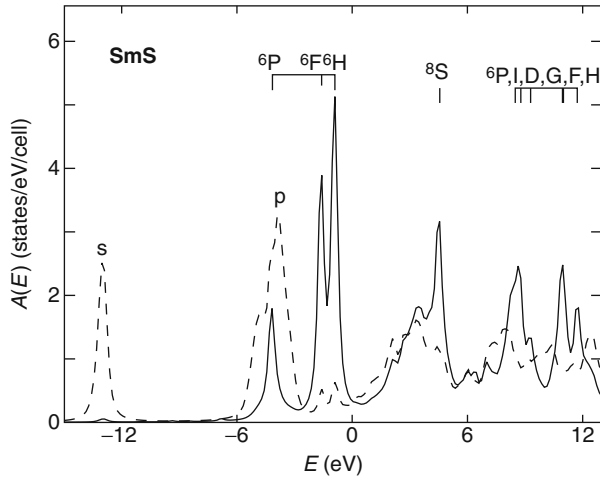


FIGURE 26 The calculated spectral function of divalent Sm in SmS (black phase, $a = 5.95 \text{ \AA}$). The full curve shows the f-contribution and the dashed curve the non-f contribution. The energy is given relative to the Fermi level. The main lines are characterized by their final state characteristics, either as Sulphur s, p-bands or as Sm $f^{n\pm 1}$ multiplet term.

equal for the two compounds, $F^\ell = 23.9, 10.6, 6.5,$ and 4.6 eV , respectively, for $\ell = 0, 2, 4, 6$ (evaluated with the f-radial wave at an energy given by the centre of gravity of the occupied f-partial DOS). However, for the direct Coulomb parameter, $F^0 \equiv U$, a screened value of $F^0 = 7.1 \text{ eV}$ was used instead of the unscreened value quoted above.

The SmAs spectral function in Figure 25 shows four distinct peaks between -5 and -12 eV corresponding to the $f^4(^5L)$, $L = D, G, F, I$, final states in the photoemission process. These states agree well with the three-peak structure observed by Pollak et al. (1974) at binding energies of approximately -10.0 eV , -8.2 eV , and -6.0 eV (presuming that the 5F emission is too weak to lead to a resolvable peak). In the positive frequency range, one observes the 7F peak just above the Fermi level whereas the f^6 final states of $S = 2$ are situated further up in energy, however, now with a considerable spread due to the many allowed multiplets. The position of the corresponding levels in the reference atomic calculation are marked in the figure.

The SmS spectral function is shown in Figure 26. The spectrum is now characterized by the low binding energy three-peak structure, which is also observed in several experiments (Campagna et al., 1974b; Pollak et al., 1974; Chainani et al., 2002; Ito et al., 2002), at binding energies -0.8 eV , -1.5 eV , and -4.0 eV , and which is attributed to the 6H , 6F , and 6P final states (Campagna et al., 1974b). The latter state coincides with the sulphur p-band, as also found in the calculations. The results in Figure 26 agree well with those obtained by Lehner et al. (1998) by a similar theoretical procedure.

The two spectra of SmAs and SmS demonstrate the distinctly different signatures of trivalent and divalent Sm ions in photoemission. Recent experiments (Chainani et al., 2002; Ito et al., 2002) show traces of Sm f^5 emission in SmS

photoemission experiments, possibly also present in older works (Pollak *et al.*, 1974). It is unclear whether this is due to small impurity concentrations or implies a more complicated ground state for SmS than the ideal divalent state, which is normally assumed and indeed also was found by the SIC-LSD calculations discussed in Section 4.3.1. It is well known that doping of SmS can lead to the intermediate valence phase, characterized by photoemission spectra of both the high and low binding energy type (Campagna *et al.*, 1974b; Pollak *et al.*, 1974). The unoccupied states of SmS have been monitored with bremsstrahlung inverse spectroscopy (Oh and Allen, 1984). The spectra reveal two broad structures, approximately 4.5 and 9 eV above the Fermi level, which are in good agreement with the positions in Figure 26 of the 8S and $^6P, I, D, G, F, H$ features, respectively.

As an example of application of the atomic multiplet theory to the elemental metals (Lebegue *et al.*, 2006a, 2006b), we show in Figure 27 a comparison of the calculated and measured spectra for terbium. The removal part of the spectrum at negative energies, corresponding to $f^8 \rightarrow f^7$ transitions, reveals the exchange splitting between the 8S and 6L ($L = G, H, I$) peaks, which in band language translates into the minority and majority spin bands. At positive energy, the spectrum is dominated by the strong peak at 3 eV with a shoulder towards higher energy. There is a one to one correspondence between the observed and calculated peaks, although their relative intensities differ, which could be a matrix element effect. For the high-energy shoulder, there is a 1.5 eV discrepancy in position, which could be due to the neglect of the non- f electrons in the theory. Similarly, the smaller hump-like spectral intensity observed in experiment, in the region just below the Fermi level, could be a reflection of the normal valence electrons,

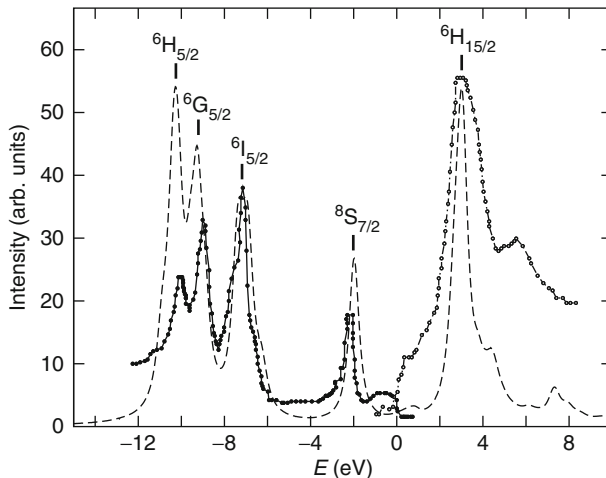


FIGURE 27 The calculated f -contribution to the spectral function of Tb in the hcp structure at the equilibrium volume computed within the Hubbard-I method (dashed line) compared with experiments (circles). Experimental data are X-ray photoemission and bremsstrahlung isochromat spectroscopy from Lang *et al.* (1981). The Fermi level is at zero energy and the dominating atomic final states are marked.

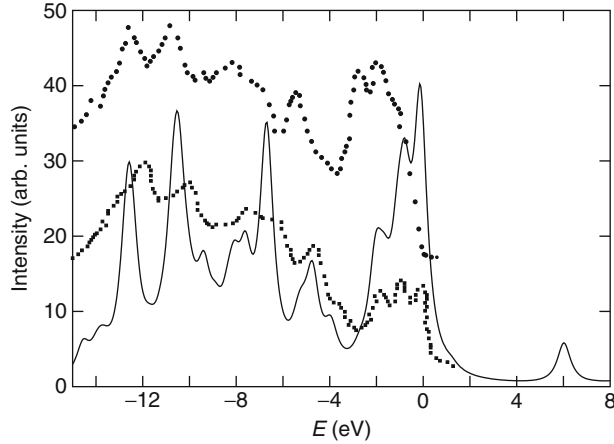


FIGURE 28 The calculated f-contribution to the spectral function of TmSe at equilibrium volume computed within the Hubbard-I method (full line) compared with photoemission spectrum of Campagna et al. (1974b) (solid squares) and of Ufuktepe et al. (1998) (solid circles) (vertically displayed for clarity). The Fermi level is at zero energy.

possibly with some small interaction effects with the f-manifold, which are not treated by the present theory.

As a final example we show in Figure 28 a mixed valence spectrum of TmSe (Lebegue et al., 2005). TmSe is situated between the predominantly trivalent TmS and the divalent TmTe in the thulium monochalcogenides series. The figure shows data from two different experiments (Campagna et al., 1974a; Ufuktepe et al., 1998) with similar results, possibly with a relative shift in the Fermi level position. The recorded photoemission spectra exhibit both low lying excitations (between the Fermi level and 3 eV below) due to $f^{13} \rightarrow f^{12}$ transitions and higher excitations (between 5 and ~ 13 eV below the Fermi level) due to $f^{12} \rightarrow f^{11}$ transitions, each of these with their distinct multiplet structure. TmTe shows only the former and TmS only the latter kinds of excitations (Lebegue et al., 2005). Again, there is good agreement between the positions of peaks in theory and experiment. The two experiments differ somewhat in the relative intensities of the divalent and trivalent parts. This could be an effect of different sample quality that influences the relative balance of the f^{13} and f^{12} configurations in the mixed valent ground state. A second possibility is a different surface sensitivity in the two experiments, combined with surface influence on the mixed valent ground state.

The theory presented here is not fully *ab initio* since it involves the adjustment of the chemical potential as well as the F^0 (or Hubbard U) parameter. The U parameter only enters in cases where three or more occupation numbers n of f^n configurations are involved, as is the case in the examples presented here. The size of multiplet splittings within a given configuration is solely determined by the F^ℓ ($\ell > 0$) parameters, which are calculated from the self consistent f partial wave, as the examples show with quite accurate results. Hence, screening effects do not enter as severely into the higher F^ℓ Slater integrals as they do for the Coulomb U parameter.

6.2 Relativistic theory of resonant X-ray scattering

MXRS is a well-developed technique for probing the magnetic and electronic structures of materials. The foundations of the theory of MXRS were laid down by [Blume \(1985\)](#). He showed that this spectroscopy is intrinsically relativistic. Later on [Blume and Gibbs \(1988\)](#) developed the theory further to show that the orbital and spin contributions to the magnetic moment can be measured separately using MXRS with a judicious choice of experimental geometry and polarization of the X-rays. This makes it a potentially very powerful spectroscopy. Integration of the SIC into the MXRS theory enables us to describe lanthanide and actinide materials on an equal footing with transition and simple materials. We then go further and make the connection between this theory and the standard theories of resonant X-ray scattering ([Hill and McMorro, 1996](#); [Lovesey and Collins, 1996](#)) and illustrate it with a calculation for the heavy lanthanides. In the relativistic SIC-LSD approach ([Beiden et al., 1997](#)), we adopt the same strategy as in the non-relativistic theory, but instead of [Eq. \(23\)](#), we have to solve the Dirac equation of the form

$$\left(\frac{c\hbar}{i} \boldsymbol{\alpha} \cdot \nabla + mc^2(\beta - I_4) + V^{\text{eff}}(\mathbf{r}) + \mu_B \beta \boldsymbol{\sigma} \cdot \mathbf{B}^{\text{eff}}(\mathbf{r}) + V_\gamma^{\text{SIC}}(\mathbf{r}) \right) \psi_\gamma(\mathbf{r}) = \sum_{\gamma'} \lambda_{\gamma, \gamma'} \psi_{\gamma'}(\mathbf{r}), \quad (49)$$

where $\boldsymbol{\alpha}$ and β are Dirac matrices, \mathbf{B}^{eff} is an effective magnetic field, σ_4 and I_4 are 4×4 spin operator and unit matrices, respectively, and $\lambda_{\gamma, \gamma'}$ is the Lagrange multipliers matrix. The SIC potential is given by

$$V_\gamma^{\text{SIC}}(\mathbf{r}) = - \left(\frac{e^2}{4\pi\epsilon_0} \int \frac{n_\gamma(\mathbf{r}')}{|\mathbf{r} - \mathbf{r}'|} d^3r' + \frac{\delta E_{\text{xc}}^{\text{LSD}}[\bar{n}_\gamma(\mathbf{r})]}{\delta n_\gamma(\mathbf{r})} - \mu_B \beta \boldsymbol{\sigma}_4 \cdot \frac{\delta E_{\text{xc}}^{\text{LSD}}[\bar{n}_\gamma(\mathbf{r})]}{\delta \mathbf{m}_\gamma(\mathbf{r})} \right), \quad (50)$$

with γ denoting orbitals and

$$\mathbf{m}_\gamma(\mathbf{r}) \equiv -\mu_B \psi_\gamma^\dagger(\mathbf{r}) \beta \boldsymbol{\sigma}_4 \psi_\gamma(\mathbf{r}).$$

The task of finding the single particle-like wavefunctions is now in principle equivalent to that within non-relativistic SIC-LSD theory. The four-component nature of the wavefunctions and the fact that neither spin nor orbital angular momentum are conserved separately presents some added technical difficulty, but this can be overcome using well-known techniques ([Strange et al., 1984](#)). The formal first-principles theory of MXRS, for materials with translational periodicity, is based on the fully relativistic spin-polarized SIC-LSD method in conjunction with second-order time-dependent perturbation theory ([Arola et al., 2004](#)).

6.2.1 Basic theory of X-ray scattering

The theory of X-ray scattering is based on the second-order golden rule for the transition probability per unit time:

$$w_{\text{if}} = \frac{2\pi}{\hbar} \left| \langle f | \hat{H}'_{\text{int}} | i \rangle + \sum_I \frac{\langle f | \hat{H}'_{\text{int}} | I \rangle \langle I | \hat{H}'_{\text{int}} | i \rangle}{E_i - E_I} \right|^2 \delta(E_f - E_i), \quad (51)$$

where $|i\rangle$, $|I\rangle$, and $|f\rangle$ are the initial, intermediate, and final states of the electron–photon system. E_i , E_I , and E_f are the corresponding energies. \hat{H}'_{int} is the time-independent part of the photon–electron interaction Hamiltonian

$$\hat{H}'_{\text{int}}(t) = -e \int_{\infty} \hat{\psi}^{\dagger}(\mathbf{r}, t) \boldsymbol{\alpha} \hat{\psi}(\mathbf{r}, t) \cdot \hat{A}(\mathbf{r}, t) d^3r \quad (52)$$

where $\hat{A}(\mathbf{r}, t)$ is the quantized radiation field operator, and $\hat{\psi}(\mathbf{r}, t)$ and $\hat{\psi}^{\dagger}(\mathbf{r}, t)$ are the quantized Dirac field operators. The formalism to reduce Eq. (51) to single-electron-like form has been published previously (Arola et al., 1997). Therefore, we will not repeat the details here, but only the equations that are key to an understanding of the theory.

In relativistic quantum theory, it is the second term in Eq. (51) that is entirely responsible for scattering as it is second order in the vector potential. It is convenient to divide this term into four components, and the X-ray scattering amplitude in the case of elastic scattering may be written as (Arola et al., 1997; Arola and Strange, 2001)

$$\begin{aligned} f_{\mathbf{q}\lambda;\mathbf{q}'\lambda'}(\omega) &= \sum_{I, \varepsilon_{\Lambda} > 0} \frac{\langle f | \hat{H}'_{\text{int}} | I \rangle \langle I | \hat{H}'_{\text{int}} | i \rangle}{E_i - E_I} - \sum_{I, \varepsilon_{\Lambda} < 0} \frac{\langle f | \hat{H}'_{\text{int}} | I \rangle \langle I | \hat{H}'_{\text{int}} | i \rangle}{E_i - E_I} \\ &= f_{\mathbf{q}\lambda;\mathbf{q}'\lambda'}^{+(\text{pos})}(\omega) + f_{\mathbf{q}\lambda;\mathbf{q}'\lambda'}^{-(\text{pos})}(\omega) + f_{\mathbf{q}\lambda;\mathbf{q}'\lambda'}^{+(\text{neg})}(\omega) + f_{\mathbf{q}\lambda;\mathbf{q}'\lambda'}^{-(\text{neg})}(\omega), \end{aligned} \quad (53)$$

where \mathbf{q} , λ (\mathbf{q}' , λ') represent the wave vector and polarization of the incident (outgoing) photon. Two different terms arise, as the distinction in energy is made between $\varepsilon_{\Lambda} > 0$ and $\varepsilon_{\Lambda} < 0$ according to whether the intermediate states contain excitations from the ‘negative-energy sea of electrons’, that is the creation of electron–positron pairs. For both positive and negative energies, there are two separate types of intermediate states, $|I\rangle$, that is those containing no photons and those containing two photons, which altogether results in the four separate scattering amplitudes. In the energy range of interest, $\hbar\omega \ll 2mc^2$, three of these components (the latter three) have no resonance, and so will only make a contribution to the cross section that is slowly varying. In the following, we shall only be interested in scattering around resonance, and the corresponding expression for the scattering amplitude reduces to the component that is large and rapidly varying around resonance, namely

$$f_{\mathbf{q}\lambda;\mathbf{q}'\lambda'}^{+(\text{pos})}(\omega) = f_{\mathbf{q}\lambda;\mathbf{q}'\lambda'}^{+(\text{pos})}(\omega) = - \sum_{\Lambda\Lambda'} \frac{\int d^3r u_{\Lambda}^{\dagger}(\mathbf{r}) X_{\mathbf{q}'\lambda'}^{\dagger}(\mathbf{r}) u_{\Lambda'}(\mathbf{r}) \int d^3r' u_{\Lambda'}^{\dagger}(\mathbf{r}') X_{\mathbf{q}\lambda}(\mathbf{r}') u_{\Lambda}(\mathbf{r}')}{\varepsilon_{\Lambda} - \varepsilon_{\Lambda'} + \hbar\omega} \quad (54)$$

where $u_{\Lambda}(\mathbf{r})$ and $v_{\Lambda}(\mathbf{r})$ are positive and negative energy electron eigenstates with quantum numbers Λ of the Dirac Hamiltonian for the crystal and form a complete orthonormal set of four-component basis functions in the Dirac space. The one-electron states are subject to the constraint that $\varepsilon_{\Lambda} \leq \varepsilon_F$ and $\varepsilon_{\Lambda'} > \varepsilon_F$, where ε_F is the Fermi energy. The relativistic photon–electron interaction vertex is

$$X_{\mathbf{q}\lambda}(\mathbf{r}) = -e \left(\frac{\hbar c^2}{2V\varepsilon_0\omega} \right)^{1/2} \boldsymbol{\alpha} \cdot \hat{\varepsilon}^{(\lambda)}(\mathbf{q}) e^{i\mathbf{q}\cdot\mathbf{r}}, \quad (55)$$

where $e = -|e|$, and $\hat{\varepsilon}^{(\lambda)}(\mathbf{q})$ is the polarization vector for the X-ray propagating in the direction of \mathbf{q} .

Equation (54) represents scattering with no photons and positive energy electrons only in the intermediate state. The corresponding theory is only applicable around resonance that makes it complementary to the work of Blume (1985), which is only valid well away from resonance.

The final expression for the resonant part of the scattering amplitude in Bragg diffraction is

$$f_{\mathbf{q}\lambda;\mathbf{q}'\lambda'}^{+(\text{pos})}(\omega) = f_{0;\mathbf{q}\lambda;\mathbf{q}'\lambda'}^{+(\text{pos})}(\omega) N_{\text{cells}} \delta_{\mathbf{Q}\mathbf{K}}, \quad (56A)$$

where N_{cells} stands for the number of unit cells, \mathbf{K} is a reciprocal lattice vector, $\mathbf{Q} \equiv \mathbf{q}' - \mathbf{q}$, and the 0th unit cell contribution to the scattering amplitude is

$$f_{0;\mathbf{q}\lambda;\mathbf{q}'\lambda'}^{+(\text{pos})}(\omega) = \sum_j \frac{V}{(2\pi)^3} \int_{\mathbf{k} \in 1.\text{BZ}} d^3k \sum_{t=1}^{N_{\text{type}}} \sum_{i=1}^{N_t} \sum_{\Lambda_t} e^{-i\mathbf{Q} \cdot \boldsymbol{\tau}_i^{(t)}} \times \frac{m_{\Lambda_t}^{(ti) + j\mathbf{k}}(\mathbf{q}'\lambda') m_{\Lambda_t}^{(ti) + j\mathbf{k}^*}(\mathbf{q}\lambda)}{\varepsilon_{\Lambda_t}^{(t)} - \varepsilon^{j\mathbf{k}} + \hbar\omega + \Gamma_{\Lambda_t}^{(t)}/2} \theta(\varepsilon^{j\mathbf{k}} - \varepsilon_F). \quad (56B)$$

Here j is the band index, N_{type} represents the number of different atom types and N_t is the number of atoms of each type. The matrix elements $m_{\Lambda_t}^{(ti) + j\mathbf{k}}(\mathbf{q}\lambda)$ are given by

$$m_{\Lambda_n}^{(n) + j\mathbf{k}}(\mathbf{q}\lambda) \equiv \int_{S_n} d^3r_n u_{\Lambda_n}^{(n)\dagger}(\mathbf{r}_n) X_{\mathbf{q}\lambda}^\dagger(\mathbf{r}_n) \psi^{j\mathbf{k}}(\mathbf{R}_n^{(0)} + \mathbf{r}_n), \quad (56C)$$

where S^n refers to the n th atomic sphere within the unit cell. The added phenomenological parameter $\Gamma_{\Lambda_t}^{(t)}$ represents the natural width of the intermediate states created by the core hole state $|\Lambda_t\rangle$ at the t type basis atom.

Within the electric dipole approximation [$e^{i\mathbf{q} \cdot \mathbf{r}} \approx 1$ in Eq. (55)], the polarization can be taken outside the matrix elements and the scattering amplitude of Eq. (56B) can be written as

$$f_{0;\mathbf{q}\lambda;\mathbf{q}'\lambda'}^{+(\text{pos})}(\omega) = \sum_j \frac{V}{(2\pi)^3} \int_{\mathbf{k} \in 1.\text{BZ}} d^3k \sum_{t=1}^{N_{\text{type}}} \sum_{i=1}^{N_t} \sum_{\Lambda_t} e^{-i\mathbf{Q} \cdot \boldsymbol{\tau}_i^{(t)}} \times \frac{\lambda' \cdot m_{\Lambda_t}^{(ti) + j\mathbf{k}}(\mathbf{q}') \lambda \cdot m_{\Lambda_t}^{(ti) + j\mathbf{k}^*}(\mathbf{q})}{\varepsilon_{\Lambda_t}^{(t)} - \varepsilon^{j\mathbf{k}} + \hbar\omega + \Gamma_{\Lambda_t}^{(t)}/2} \theta(\varepsilon^{j\mathbf{k}} - \varepsilon_F), \quad (57)$$

where the scalar product is between the photon polarization and the Pauli spin matrices that appear within the matrix elements in this formulation. This equation can be reduced to a rather appealing form. Using the notation

$$Q_{+1} = \frac{1}{\sqrt{2}}(Q_x + iQ_y) \quad Q_0 = Q_z \quad Q_{-1} = \frac{1}{\sqrt{2}}(Q_x - iQ_y) \quad (58)$$

the numerator in Eq. (57) can be written as

$$\begin{aligned}
(\lambda' \cdot m_{\Lambda_t}^{(ti) + j\mathbf{k}}) (\lambda \cdot m_{\Lambda_t}^{(ti) + j\mathbf{k}^*}) &= \sum_{v=0, \pm 1} \lambda'_v \lambda_v |m_{v\Lambda_t}^{(ti) + j\mathbf{k}}|^2 \\
&= \frac{1}{2} \left[(\lambda' \cdot \lambda) \left(|m_{+1\Lambda_t}^{(ti) + j\mathbf{k}}|^2 + |m_{-1\Lambda_t}^{(ti) + j\mathbf{k}}|^2 \right) \right. \\
&\quad + im_z \cdot (\lambda' \times \lambda) \left(|m_{-1\Lambda_t}^{(ti) + j\mathbf{k}}|^2 - |m_{+1\Lambda_t}^{(ti) + j\mathbf{k}}|^2 \right) \\
&\quad + (\lambda' \cdot m_z) (\lambda \cdot m_z) \left(2|m_{0\Lambda_t}^{(ti) + j\mathbf{k}}|^2 \right. \\
&\quad \left. \left. - |m_{+1\Lambda_t}^{(ti) + j\mathbf{k}}|^2 - |m_{-1\Lambda_t}^{(ti) + j\mathbf{k}}|^2 \right) \right], \tag{59}
\end{aligned}$$

where m_z is a unit vector in the direction of the magnetization. The advantage of a formulation of the scattering amplitude in these terms is that the geometry of the experiment is separated from the matrix elements and other atomic level information. It is possible to choose a geometry such that only one of the three terms in Eq. (59) is non-zero. For example, if we have π - π scattering with 90° between the incident and outgoing beam, the first term is zero. If the magnetization points at 90° to both the incident and outgoing polarizations, then the third term is zero and only the second term remains. This cancellation was exploited in [Brown et al. \(2007\)](#) in the investigation of magnetism in lanthanide elements (see below). Furthermore, if a spherical approximation is made for the electronic structure, the matrix elements can be calculated as a function of energy just once and all the angular dependence of the scattering is in the polarization and m_z dependence.

In the LMTO implementation, the resonant matrix element $m_{\Lambda_t}^{(ti) + j\mathbf{k}}(\mathbf{q}\lambda)$ can be written as

$$m_{\Lambda_t}^{(ti) + j\mathbf{k}}(\mathbf{q}\lambda) = \sum_{\Lambda} \left[A_{ti\Lambda}^{j\mathbf{k}} \left(u_{\Lambda_t}^{(t)} |X_{\mathbf{q}\lambda}^\dagger | \phi_{vt\Lambda} \right) + B_{ti\Lambda}^{j\mathbf{k}} \left(u_{\Lambda_t}^{(t)} |X_{\mathbf{q}\lambda}^\dagger | \dot{\phi}_{vt\Lambda} \right) \right], \tag{60A}$$

where A and B are the wavefunction coefficients of the LMTO-ASA wavefunction ([Skriver, 1983a](#)) and $(f|X_{\mathbf{q}\lambda}^\dagger|g)$ is defined as

$$(f|X_{\mathbf{q}\lambda}^\dagger|g) \equiv \int_{S^t} d^3r f^\dagger(\mathbf{r}) X_{\mathbf{q}\lambda}^\dagger(\mathbf{r}) g(\mathbf{r}), \tag{60B}$$

with $f \equiv u_{\Lambda_t}^{(t)}$ and $g \equiv \phi_{vt\Lambda}$ or $\dot{\phi}_{vt\Lambda}$

While the cross section is the fundamental measurable quantity in scattering theory, it is frequently more convenient in X-ray scattering from magnetic materials to measure the asymmetry ratio (dichroism). This is defined as the difference divided by the sum of the cross section for the moment in one direction and the moment in the opposite direction.

$$A(\mathbf{q}; \mathbf{q}'\lambda; \omega) \equiv \frac{\omega_{d\Omega}(\mathbf{q}+; \mathbf{q}'\lambda'; \omega) - \omega_{d\Omega}(\mathbf{q}-; \mathbf{q}'\lambda'; \omega)}{\omega_{d\Omega}(\mathbf{q}+; \mathbf{q}'\lambda'; \omega) + \omega_{d\Omega}(\mathbf{q}-; \mathbf{q}'\lambda'; \omega)} \tag{61}$$

where the scattering rate $\omega_{d\Omega}$ into a solid space angle $d\Omega$ can be written in terms of the scattering amplitude $f_{\mathbf{q}\lambda; \mathbf{q}'\lambda'}(\omega)$ as

$$\omega_{d\Omega} = \frac{2\pi}{\hbar} |f_{\mathbf{q}\lambda; \mathbf{q}'\lambda'}(\omega)|^2 \frac{V}{(2\pi)^3} \frac{\omega^2}{\hbar c^3} d\Omega \tag{62}$$

As shown by [Lovesey and Collins \(1996\)](#), the asymmetry ratio directly reflects the scattering amplitude rather than the cross section and emphasizes the interference between magnetic scattering and charge scattering.

6.2.2 Application to lanthanides

As discussed previously, the SIC-LSD method has been used successfully to describe properties of lanthanide materials that cannot be described within the bare LDA ([Strange *et al.*, 1999](#)). Here we look at how SIC-LSD describes resonant X-ray scattering. An important point made in the paper of [Arola *et al.* \(2004\)](#) is that the spectra are dependent on the number and symmetry of the localized states and intermediate states. Therefore, this spectroscopy could become quite important for the unravelling of the nature of the localized states.

Calculations of the asymmetry ratio for the heavy lanthanide metals have been carried out by [Brown *et al.* \(2007\)](#). They have shown that the asymmetry ratio consists of two features. There is a major peak in the asymmetry ratio that is predominantly due to dipolar scattering from the magnetic moment of the 5d states, and a smaller feature (below the elemental absorption edge) which in their experiment is also dipolar but in general is due to a mixture of dipolar and quadrupolar scattering. These features are labelled *A* and *B*, respectively, in [Figure 29](#). Feature *B* remains more or less in the same place relative to the absorption edge as we proceed along the lanthanide series whereas feature *A* gradually moves higher above the absorption edge. This means that these features separate and feature *B* changes from being a shoulder on the side of feature *A* to a separate peak. Note also the inversion of feature *A* in Tm. This is related to the fact that the d-electrons couple anti-ferromagnetically to the f-electrons in Tm, but ferromagnetically in the other heavy lanthanides. Obviously the data in [Figure 29](#) are providing information about the details of the electronic structure of the lanthanides. In [Figure 30](#), we present the 5d electron spin moment (left panel) and orbital moment (right panel) of the heavy lanthanides as a function of energy. As expected in the left panel, a lower energy peak is representing the majority spin states and a higher peak is representing the minority spin states. Features *A* and *B* from [Figure 29](#) are also shown. It is clear that feature *A* in the scattering corresponds to the peak in the 5d minority spin states. Feature *B* does not correspond exactly to anything in the spin moment although it is fairly close in energy to the maximum in the majority spin moment as a function of energy. If we look at the right panel, the magnitude of the 5d orbital moment is generally small, although for Er and Tm, it does become comparable to the spin moments. Clearly feature *A* has no correspondence with the orbital moment whereas feature *B* is close to a peak in the orbital moment. It is clear then that feature *A* arises from scattering from the empty spin states anti-parallel to the f spin moments whereas feature *B* represents scattering from both the orbital and spin moments parallel to the f spin moment. The correlation of peaks *A* and *B* in [Figure 29](#), with the structure in [Figure 30](#), demonstrates that the dipolar asymmetry ratios at the L_{III} edges reflect the progression from spin-dominated Gd to orbital-dominated Er and Tm electronic structure.

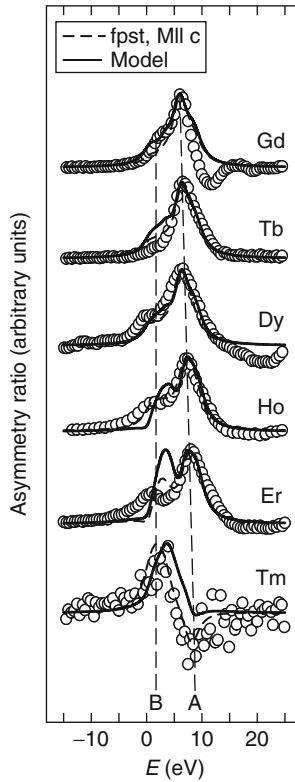


FIGURE 29 The asymmetry ratio of the lanthanides Gd through to Tm after [Brown et al. \(2007\)](#). The circles represent the experimental results measured on the XMaS beamline at the ESRF. The dashed line represents the full first-principles theory outlined in this section and yields at least good qualitative agreement with experiment. The full line is a simple model calculation that neglects all matrix elements and bases the asymmetry ratio on the DOS calculated using SIC-LSD theory. Note the features A and B that are discussed in the text.

7. FINITE TEMPERATURE PHASE DIAGRAMS

7.1 Thermal fluctuations

Up to now, we have concentrated on the physics at zero kelvin. In this section, we extend the studies to finite temperatures and discuss finite temperature phase diagrams. The physics at finite temperatures is dominated by thermal fluctuations between low lying excited states of the system. These fluctuations can include spin fluctuations, fluctuations between different valence states, or fluctuations between different orbitally ordered states, if present. Such fluctuations can be addressed through a so-called ‘alloy analogy’. If there is a timescale that is slow compared to the motion of the valence electrons, and on which the configurations persist between the system fluctuations, one can replace the temporal average over all fluctuations by an ensemble average over all possible (spatially

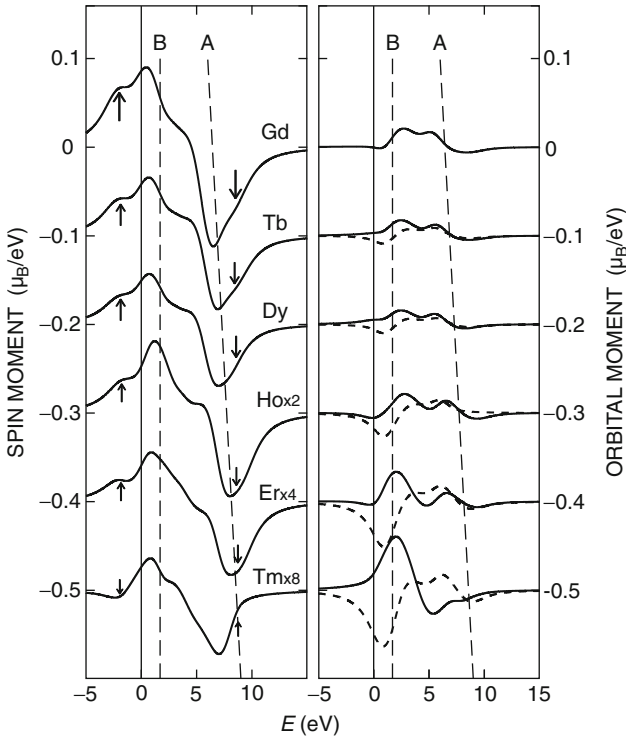


FIGURE 30 The spin and orbital moments associated with the 5d states in the heavy lanthanide metals after [Brown et al. \(2007\)](#). (A) The spin moment. The arrows on the left-hand side represent the coupling to the empty f-states above E_F . The zero of energy on this scale is the Fermi energy. Also shown are features A and B from [Figure 29](#). (B) The orbital moment of the 5d states. As expected, this quantity is generally small, although it becomes comparable with the spin moment in Er and Tm. The dashed line represents the case when the f-states are filled according to Hund's rules and the full line when they are filled directly opposite to Hund's rules.

disordered) configurations of the system. In the following text, we will explain this procedure in detail for the treatment of spin fluctuations, which leads to the well-known DLM theory of finite temperature magnetism. After that, the same methodology is applied to different valence configurations and demonstrated on the example of the finite temperature phase diagram of Ce.

This static alloy analogy picture should be a good description as long as there is a separation of timescales. If this breaks down, dynamical fluctuations—or quantum fluctuations—which are beyond this static picture, become important. These quantum fluctuations are the main emphasis of DMFT ([Georges et al., 1996](#)), which maps the system onto an effective Anderson impurity model, describing a dynamically fluctuating impurity in a self-consistently determined effective host. So far, DMFT has been formulated for model Hamiltonians, such as the Hubbard model, and material-specific results have been achieved by constructing these model Hamiltonians from realistic band structure calculations. In

the context of model Hamiltonians, it has been shown (Kakehashi, 2002) that DMFT is equivalent to a dynamical CPA. Hence, the static CPA approach, presented here, corresponds to the static limit of a, still to be developed, fully *ab initio* version of DMFT. A discussion on how such a theory could be constructed is given in Section 8.

7.2 Spin fluctuations: DLM picture

For low temperatures, calculations of the characteristics of the free energy (ground state energy) of a magnetic material are all based on an electronic band structure for a given configuration, such as a fixed spin-polarization, for example a uniform spin-polarization for a ferromagnet and fixed sublattice spin polarizations for an anti-ferromagnet, a given valence state, or, if present, a given orbital order. With increasing temperature, fluctuations between those configurations are induced that eventually destroy the long-range order. These collective electron modes interact as the temperature is raised and are dependent upon and affect the underlying electronic structure. In this and the following sections, we concentrate on magnetic order and magnetic excitations through spin fluctuations. For many materials, the magnetic excitations can be modelled by associating local spin-polarization axes with all lattice sites and the orientations vary very slowly on the timescale of the electronic motions (Moriya, 1981). These ‘local moment’ degrees of freedom produce local magnetic fields on the lattice sites that affect the electronic motions and are self-consistently maintained by them. By taking appropriate ensemble averages over the orientational configurations, the system’s magnetic properties can be determined. The DLM DFT-based theory has been developed and used in this context to describe the onset and type of magnetic order *ab initio* in many magnetic systems (Gyorffy et al., 1985; Staunton et al., 1985; Staunton and Gyorffy, 1992). Moreover, the recent inclusion of relativistic effects into DLM theory produces an *ab initio* description of the temperature dependence of magnetic anisotropy of metallic ferromagnets, which agrees well with experimental results and deviates qualitatively from simple, widely used models (Staunton et al., 2004, 2006). It is the incorporation of the LSIC method for describing strongly correlated electrons into the DLM theory that we focus on in this section and its application to the magnetic structure of Gd and other heavy lanthanide systems. The standard model of lanthanide electronic structure gives a good qualitative description of the formation and magnitude of the magnetic moments. It has long been understood that these local moments, formed predominantly by the localized f-electrons, interact with each other by spin-polarizing the sea of conduction electrons in which they sit. The RKKY interaction is the simplest example of this effect. As we will show, our DLM-LSIC theory gives a quantitative *ab initio* description of this physics.

In principle, the extension of electronic DFT to finite temperatures was carried out by Mermin (1965) soon after the pioneering papers of Hohenberg, Kohn, and Sham (Hohenberg and Kohn, 1964; Kohn and Sham, 1965). The single-particle entropy is included and the effective one-electron fields involve Ω_{xc} , the exchange-correlation part of the Gibbs free energy functional of particle and magnetization

densities. Formally, this can be expressed in terms of spin-dependent pair correlation functions $g_\lambda(\sigma, \sigma'; \mathbf{r}, \mathbf{r}')$, that is

$$\Omega_{\text{xc}}[n, \mathbf{m}] = \frac{e^2}{2} \int_0^1 d\lambda \int d^3r \int d^3r' \sum_{\sigma, \sigma'} \frac{n_\sigma(\mathbf{r})n_{\sigma'}(\mathbf{r}')}{|\mathbf{r} - \mathbf{r}'|} g_\lambda(\sigma, \sigma'; \mathbf{r}, \mathbf{r}') \quad (63)$$

where $n_\sigma(\mathbf{r})$ is the spin resolved charge density.

It would seem logical then simply to make the finite temperature extension of the LDA (or GGA) that is successfully exploited in applications on the ground state of magnetic materials in conjunction with, say, the SIC, to deal with localized states where appropriate. So, for example, $\Omega_{\text{xc}}[n, \mathbf{m}]$ is replaced by $\int d^3r n(\mathbf{r}) \Omega_{\text{xc}}^0(n(\mathbf{r}))$ where Ω_{xc}^0 is the exchange-correlation part of the Gibbs free energy of a homogeneous electron gas. This assumption allows the thermally averaged magnetization, $\bar{\mathbf{M}}$, along with the spin splitting of the electronic structure to decrease only by the excitation of particle-hole, ‘Stoner’ excitations across the Fermi surface. However, it severely underestimates the effects of the thermally induced spin-wave excitations. For lanthanide materials, these orientational magnetic fluctuations are entirely neglected, whereas in transition metal ferromagnets, the reliance on Stoner particle-hole excitations causes the calculated Curie temperatures to be typically an order of magnitude too high with no obvious mechanism for the Curie-Weiss behaviour of the uniform static paramagnetic susceptibility found for many metallic systems.

Evidently, part of the pair correlation function $g_\lambda(\sigma, \sigma'; \mathbf{r}, \mathbf{r}')$ should be related by the fluctuation dissipation theorem to the magnetic susceptibilities harbouring information about spin waves. These spin fluctuations interact as temperature is increased and so $\Omega_{\text{xc}}[n, \mathbf{m}]$ should deviate significantly from the local approximation with a consequent impact upon the form of the effective single electron states. Indeed, accounts of modern electronic structure theory for magnetic systems (Staunton, 1994; Kübler, 2000) have large sections devoted to work that is concerned with the modelling of spin fluctuation effects while maintaining the spin-polarized single electron basis.

Most of this work is based on a rather simple, pervasive picture of fluctuating ‘local moments’ that stems from the belief of a timescale separation of the electronic degrees of freedom. A conduction electron (in a lanthanide material) travels from site to site on a much faster timescale than that of the collective spin wave motion. So the dominant thermal fluctuation of the magnetization that the straightforward finite temperature extension of spin-polarized band theory misses can be pictured quite simply as orientational fluctuations of ‘local moments’. These entities are the magnetizations within each unit cell of the underlying crystal lattice that are largely determined by the localized *f*-electrons in the lanthanides, while in itinerant electron transition metal magnets, they are set up by the collective behaviour of all the electrons. Their orientations persist on timescales long compared to electronic ‘hopping’ times. At low temperatures, their long wavelength, slow spin wave dynamics can be directly extracted from the transverse part of the magnetic susceptibility. At higher temperatures, the more complex behaviour can be described with a classical treatment. The energy

is considered of the many interacting electron system constrained to have a set inhomogeneous magnetization profile. From atomic site to atomic site, the local magnetic moments are oriented along prescribed directions, that is producing a ‘local moment’ configuration. Averages over such orientational configurations are subsequently taken to determine the equilibrium properties of the system. $\bar{\mathbf{M}}$ can now vanish as the disorder of the ‘local moments’ grows. There remains, however, the issue as to which fluctuations are the most important.

Formally DFT (Gyorffy et al., 1985) is used to specify the ‘generalized’ grand potential, $\Omega^{(\hat{n})}(\{\hat{e}\})$, of an interacting electron system which is constrained in such a way that the site by site spin polarization axes are configured according to $\{\hat{e}\} = \{\hat{e}_1, \hat{e}_2, \dots, \hat{e}_N\}$, where N is the number of sites (moments) in the system. The $\{\hat{e}\}$, classical unit vectors, are thus the degrees of freedom describing the local moment orientations and $\Omega^{(\hat{n})}(\{\hat{e}\})$ is the ‘local moment’ Hamiltonian. (With relativistic effects such as spin-orbit coupling included, the temperature dependence of magnetic anisotropy can be described. This means that orientations of the local moments with respect to a specified direction \hat{n} within the material are relevant.)

One way forward from this point is to carry out calculations of $\Omega^{(\hat{n})}(\{\hat{e}\})$ for a selection of configurations (‘spin’ spirals, two impurities in a ferromagnet, magnetically ordered supercells, etc.) by making some assumptions about the most dominant fluctuations. One then fits the set of $\Omega^{(\hat{n})}(\{\hat{e}\})$ ’s to a simple functional form. Typically a classical Heisenberg model, $\Omega^{(\hat{n})}(\{\hat{e}\}) = -1/2 \sum_{ij} J_{ij} \hat{e}_i \cdot \hat{e}_j$ is set up and various statistical mechanics methods (e.g., Monte Carlo) are used to produce the desired thermodynamic averages. Many useful studies have been carried out in this way but there is a risk that a bias is produced so that some of the physics is missed. The spin-polarized electronic structures of the restricted set of constrained systems are not guaranteed to generate magnetic correlations that are consistent with the chosen sampling of the orientational configurations. In other words, the electronic and magnetic structures are not necessarily mutually consistent. In the following, we summarize the main points of our DLM theory which avoids these problems. Full details can be found in references Gyorffy et al. (1985), Staunton et al. (1985), and Staunton and Gyorffy (1992) and relativistic extension in references Staunton et al. (2004, 2006).

The DLM picture is implemented within a multiple-scattering formalism (KKR) (Korringa, 1947; Kohn and Rostoker, 1954; Stocks et al., 1978; Stocks and Winter, 1982; Johnson et al., 1986). Some applications include the description of the experimentally observed local exchange splitting and magnetic short-range order in both ultrathin Fe films (Razee et al., 2002) and bulk Fe (Gyorffy et al., 1985; Staunton et al., 1985), the damped RKKY-like magnetic interactions in the compositionally disordered CuMn ‘spin-glass’ alloys (Ling et al., 1994), and the onset of magnetic order in a range of alloys (Staunton et al., 1997; Crisan et al., 2002). By combining it with the LSIC (Lüders et al., 2005) for strong electron correlation effects, we have recently used it to account quantitatively for the magnetic ordering in the heavy lanthanides (Hughes et al., 2007). This gives an *ab initio* account of the well-known picture of f-electron magnetic moments interacting via the conduction electrons.

We consider a collinear magnetic system magnetized with reference to a single direction \hat{n} at a temperature T . (A non-collinear generalization can be made by making the notation more complicated.) The orientational probability distribution is denoted by $P^{(\hat{n})}(\{\hat{\epsilon}\})$, and its average for a lattice site i ,

$$\langle \hat{\epsilon}_i \rangle = \int \dots \int \hat{\epsilon}_i P^{(\hat{n})}(\{\hat{\epsilon}\}) d\hat{\epsilon}_1 \dots d\hat{\epsilon}_N = m\hat{n}, \quad (64)$$

is aligned with the magnetization direction \hat{n} . The canonical partition function and the probability function are defined as $Z^{(\hat{n})} = \int \dots \int e^{-\beta\Omega^{(\hat{n})}(\{\hat{\epsilon}\})} d\hat{\epsilon}_1 \dots d\hat{\epsilon}_N$ and $P^{(\hat{n})}(\{\hat{\epsilon}\}) = e^{-\beta\Omega^{(\hat{n})}(\{\hat{\epsilon}\})}/Z^{(\hat{n})}$, respectively. The thermodynamic free energy that includes the entropy associated with the orientational fluctuations as well as creation of electron-hole pairs is given by $F^{(\hat{n})} = -1/\beta(\ln Z^{(\hat{n})})$. By choosing a trial Hamiltonian function, $\Omega_0^{(\hat{n})}(\{\hat{\epsilon}\})$ with

$$Z_0^{(\hat{n})} = \int \dots \int e^{-\beta\Omega_0^{(\hat{n})}(\{\hat{\epsilon}\})} d\hat{\epsilon}_1 \dots d\hat{\epsilon}_N, \quad (65)$$

$$P_0^{(\hat{n})}(\{\hat{\epsilon}\}) = \frac{e^{-\beta\Omega_0^{(\hat{n})}(\{\hat{\epsilon}\})}}{Z_0^{(\hat{n})}}, \quad (66)$$

and $F_0^{(\hat{n})} = -1/\beta(\ln Z_0^{(\hat{n})})$, the *Feynman-Peierls Inequality* (Feynman, 1955) implies an upper bound for the free energy, that is,

$$F^{(\hat{n})} \leq F_0^{(\hat{n})} + \langle \Omega^{(\hat{n})} - \Omega_0^{(\hat{n})} \rangle^0, \quad (67)$$

where the average refers to the probability $P_0^{(\hat{n})}(\{\hat{\epsilon}\})$. By expanding $\Omega_0^{(\hat{n})}(\{\hat{\epsilon}\})$ as

$$\Omega_0^{(\hat{n})}(\{\hat{\epsilon}\}) = \sum_i \omega_i^{1(\hat{n})}(\hat{\epsilon}_i) + \frac{1}{2} \sum_{i \neq j} \omega_{i,j}^{2(\hat{n})}(\hat{\epsilon}_i, \hat{\epsilon}_j) + \dots, \quad (68)$$

the ‘best’ trial system is found to satisfy (Gyorffy *et al.*, 1985; Staunton and Gyorffy, 1992)

$$\langle \Omega^{(\hat{n})} \rangle_{\hat{\epsilon}_i}^0 - \langle \Omega^{(\hat{n})} \rangle^0 = \langle \Omega_0^{(\hat{n})} \rangle_{\hat{\epsilon}_i}^0 - \langle \Omega_0^{(\hat{n})} \rangle^0, \quad (69)$$

$$\langle \Omega^{(\hat{n})} \rangle_{\hat{\epsilon}_i, \hat{\epsilon}_j}^0 - \langle \Omega^{(\hat{n})} \rangle^0 = \langle \Omega_0^{(\hat{n})} \rangle_{\hat{\epsilon}_i, \hat{\epsilon}_j}^0 - \langle \Omega_0^{(\hat{n})} \rangle^0, \quad (70)$$

and so on, where $\langle \rangle_{\hat{\epsilon}_i}$ or $\langle \rangle_{\hat{\epsilon}_i, \hat{\epsilon}_j}$ denote restricted statistical averages with $\hat{\epsilon}_i$ or both $\hat{\epsilon}_i$ and $\hat{\epsilon}_j$ kept fixed, respectively. (In the following, we shall omit the superscript 0 from the averages.)

If we set $\Omega_0^{(\hat{n})}(\{\hat{\epsilon}\})$ as a sum of mean field Weiss terms, namely

$$\Omega_0^{(\hat{n})}(\{\hat{\epsilon}\}) = \sum_i \vec{h}_i^{(\hat{n})} \cdot \hat{\epsilon}_i, \quad (71)$$

where $\vec{h}_i^{(\hat{n})} = h_i^{(\hat{n})} \hat{n}$ with

$$h_i^{(\hat{n})} = \int \frac{3}{4\pi} (\hat{\epsilon}_i \cdot \hat{n}) \langle \Omega^{(\hat{n})} \rangle_{\hat{\epsilon}_i} d\hat{\epsilon}_i, \quad (72)$$

the probability distribution factorizes as

$$P_0^{(\hat{n})}(\{\hat{e}_i\}) = \prod_i P_i^{(\hat{n})}(\hat{e}_i) \quad (73)$$

with

$$P_i^{(\hat{n})}(\hat{e}_i) = \frac{\exp\left(-\beta \vec{h}_i^{(\hat{n})} \cdot \hat{e}_i\right)}{Z_i^{(\hat{n})}} = \frac{\beta h_i^{(\hat{n})}}{4\pi \sinh \beta h_i^{(\hat{n})}} \exp\left(-\beta \vec{h}_i^{(\hat{n})} \cdot \hat{e}_i\right). \quad (74)$$

The average alignment of the local moments, proportional to the magnetization, is

$$\vec{m}_i^{(\hat{n})} = \int \hat{e}_i P_i^{(\hat{n})}(\hat{e}_i) d\hat{e}_i = m_i^{(\hat{n})} \hat{n} \quad (75)$$

and

$$m_i^{(\hat{n})} = -\frac{d \ln Z_i^{(\hat{n})}}{d(\beta h_i^{(\hat{n})})} = \frac{1}{\beta h_i^{(\hat{n})}} - \coth \beta h_i^{(\hat{n})} = L\left(-\beta h_i^{(\hat{n})}\right) \quad (76)$$

follows, where $L(x)$ is the Langevin function. Moreover, the free energy of the system is

$$F^{(\hat{n})} = \langle \Omega^{(\hat{n})} \rangle + \frac{1}{\beta} \sum_i \int P_i^{(\hat{n})}(\hat{e}_i) \ln P_i^{(\hat{n})}(\hat{e}_i) d\hat{e}_i. \quad (77)$$

Another way of writing the Weiss field is (Gyorffy et al., 1985)

$$h_i^{(\hat{n})} = S_i^{1,(\hat{n})} = \frac{\partial \langle \Omega^{(\hat{n})} \rangle}{\partial m_i^{(\hat{n})}}. \quad (78)$$

Using Eqs. (74) and (76), this is shown to be equivalent to solving the equation of state

$$\frac{\partial F^{(\hat{n})}}{\partial m_i^{(\hat{n})}} = 0. \quad (79)$$

7.2.1 The role of the CPA

The averaging over local moment configurations is conveniently carried out using CPA technology (Soven, 1967; Stocks et al., 1978; Stocks and Winter, 1982; Johnson et al., 1986). The electronic charge density and also the magnetization density, which sets the magnitudes, $\{\mu\}$, of the local moments, are determined from an SCF-KKR-CPA (Stocks and Winter, 1982; Johnson et al., 1986) calculation. For a given set of (self-consistent) potentials, electronic charge and local moment magnitudes, the orientations of the local moments are accounted for by the similarity transformation of the single-site t-matrices (Messiah, 1965),

$$\underline{t}_i(\hat{e}_i) = \underline{R}(\hat{e}_i) \underline{t}_i(\hat{z}) \underline{R}(\hat{e}_i)^+, \quad (80)$$

where for a given energy (not labelled explicitly), $t_i(\hat{z})$ stands for the t -matrix with effective field pointing along the local z -axis (Strange *et al.*, 1984) and $R(\hat{e}_i)$ is a unitary representation of the $O(3)$ transformation that rotates the z axis along \hat{e}_i .

The CPA determines an effective medium through which the motion of an electron mimics the motion of an electron *on the average*. In a system magnetized with reference to a direction \hat{n} , the medium is specified by t -matrices, $t_{i,c}^{(\hat{n})}$, which satisfy the condition (Stocks *et al.*, 1978),

$$\langle \underline{\tau}_{ii}^{(\hat{n})}(\{\hat{e}\}) \rangle = \int \langle \underline{\tau}_{ii}^{(\hat{n})} \rangle_{\hat{e}_i} P_i^{(\hat{n})}(\hat{e}_i) d\hat{e}_i = \underline{\tau}_{ii,c}^{(\hat{n})}, \quad (81)$$

where the site-diagonal matrices of the multiple scattering path operator (Gyorffy and Stott, 1973) are defined as,

$$\langle \underline{\tau}_{ii}^{(\hat{n})} \rangle_{\hat{e}_i} = \underline{\tau}_{ii,c}^{(\hat{n})} \underline{D}_i^{(\hat{n})}(\hat{e}_i), \quad (82)$$

with the CPA projector

$$\underline{D}_i^{(\hat{n})}(\hat{e}_i) = \left(\underline{1} + \left[(t_i(\hat{e}_i))^{-1} - (t_{i,c}^{(\hat{n})})^{-1} \right] \underline{\tau}_{ii,c}^{(\hat{n})} \right)^{-1}, \quad (83)$$

and

$$\underline{\tau}_c^{(\hat{n})} = ((\underline{t}_c^{(\hat{n})})^{-1} - \underline{G}_0)^{-1}. \quad (84)$$

Equation (81) can be rewritten in terms of the excess scattering matrices,

$$\underline{X}_i^{(\hat{n})}(\hat{e}_i) = \left(\left[(t_{i,c}^{(\hat{n})})^{-1} - (t_i(\hat{e}_i))^{-1} \right]^{-1} - \underline{\tau}_{ii,c}^{(\hat{n})} \right)^{-1}, \quad (85)$$

in the form

$$\int \underline{X}_i^{(\hat{n})}(\hat{e}_i) P_i^{(\hat{n})}(\hat{e}_i) d\hat{e}_i = \underline{0}. \quad (86)$$

Thus, for a given set of Weiss fields, $h_i^{(\hat{n})}$, and corresponding probabilities, $P_i^{(\hat{n})}(\hat{e}_i)$, Eq.(86) can be solved by iterating together with Eqs. (85) and (84) to obtain the matrices, $t_{i,c}^{(\hat{n})}$ (Staunton *et al.*, 2006).

Using the magnetic force theorem, the single-particle energy part of the DFT grand potential gives

$$\Omega^{(\hat{n})}(\{\hat{e}\}) \simeq - \int d\varepsilon f_\beta(\varepsilon; v^{(\hat{n})}) N^{(\hat{n})}(\varepsilon; \{\hat{e}\}), \quad (87)$$

as an effective 'local moment' Hamiltonian, where $v^{(\hat{n})}$ is the chemical potential, $f_\beta(\varepsilon; v^{(\hat{n})})$ is the Fermi-Dirac distribution, and $N^{(\hat{n})}(\varepsilon; \{\hat{e}\})$ denotes the integrated DOS for the orientational configuration, $\{\hat{e}\}$. From the Lloyd formula (Lloyd and Best, 1975),

$$N^{(\hat{n})}(\varepsilon; \{\hat{e}\}) = N_o(\varepsilon) - \frac{1}{\pi} \text{Im} \ln \det \left(\underline{\underline{t}}^{(\hat{n})}(\varepsilon; \{\hat{e}\})^{-1} - \underline{\underline{G}}_0(\varepsilon) \right), \quad (88)$$

$[N_0(\varepsilon)$ being the integrated DOS of the free particles] and properties of the CPA effective medium, the partially averaged electronic Grand Potential is given by

$$\begin{aligned} \langle \Omega^{(\hat{n})} \rangle_{\hat{e}_i} = & - \int d\varepsilon f_\beta(\varepsilon; v^{(\hat{n})}) N_c^{(\hat{n})}(\varepsilon) \\ & + \frac{1}{\pi} \int d\varepsilon f_\beta(\varepsilon; v^{(\hat{n})}) \text{Im} \ln \det \underline{M}_i^{(\hat{n})}(\varepsilon; \hat{e}_i) \\ & + \sum_{j \neq i} \frac{1}{\pi} \int d\varepsilon f_\beta(\varepsilon; v^{(\hat{n})}) \text{Im} \langle \ln \det \underline{M}_j^{(\hat{n})}(\varepsilon; \hat{e}_j) \rangle, \end{aligned} \quad (89)$$

and the Weiss field, $h_i^{(\hat{n})}$, can be expressed, using Eq. (72), as

$$h_i^{(\hat{n})} = \frac{3}{4\pi} \int (\hat{e}_i \cdot \hat{n}) \left[\int d\varepsilon f_\beta(\varepsilon; v^{(\hat{n})}) \frac{1}{\pi} \text{Im} \ln \det \underline{M}_i^{(\hat{n})}(\varepsilon; \hat{e}_i) \right] d\hat{e}_i, \quad (90)$$

where

$$\begin{aligned} \underline{M}_i^{(\hat{n})}(\varepsilon; \hat{e}_i) &= \left(\underline{1} + \left[(\underline{t}_i(\hat{e}_i))^{-1} - (\underline{t}_{i,c}^{(\hat{n})})^{-1} \right] \underline{t}_{ii,c}^{(\hat{n})} \right) \text{ and} \\ N_c^{(\hat{n})}(\varepsilon) &= -\frac{1}{\pi} \text{Im} \ln \det \left(\underline{t}_{\underline{c}}^{(\hat{n})}(\varepsilon)^{-1} - \underline{\underline{G}}_0(\varepsilon) \right). \end{aligned}$$

The solution of Eqs. (90) and (76) produces the variation of the magnetization $m_i^{(\hat{n})}$ with temperature T with $m_i^{(\hat{n})}$ going to zero at $T = T_c^{(\hat{n})}$.

7.2.2 The paramagnetic DLM state

The paramagnetic state is given by the Weiss fields being zero so that the probabilities, $P_i^{(\hat{n})} = 1/4\pi$, and on any site, a moment has an equal chance of pointing in any direction. This means the magnetizations, $m_i^{(\hat{n})}$, vanish. The magnetic transition temperature, onset, and type of magnetic order can be extracted by studying the effects of a small inhomogeneous magnetic field on this high T paramagnetic state (Gyorffy et al., 1985; Staunton et al., 1985; Staunton and Gyorffy, 1992).

When relativistic spin-orbit coupling effects are omitted, the single-site matrix $\tilde{t}(\hat{e}_i)$ describing the scattering from a site with local moment orientated in the direction \hat{e}_i becomes

$$\tilde{t}_i = \frac{1}{2}(t_+ + t_-)\tilde{1} + \frac{1}{2}(t_+ - t_-)\tilde{\sigma} \cdot \hat{e}_i, \quad (91)$$

where $\tilde{\sigma}_x, \tilde{\sigma}_y$, and $\tilde{\sigma}_z$ are the three Pauli spin matrices defined according to the global z-axis. In the local reference frame, where the z-axis is aligned with \hat{e}_i , we evaluate the matrices t_+/t_- , representing the scattering of an electron with spin parallel/anti-parallel to the local moment direction \hat{e}_i . These matrices are calculated according to

$$t_{+(-)L}(\varepsilon) = -\frac{1}{\sqrt{\varepsilon}} \sin \delta_{+(-)L}(\varepsilon) e^{i\delta_{+(-)L}(\varepsilon)} \quad (92)$$

where the phase shifts $\delta_L(\varepsilon)$ are computed using effective DFT potentials. These effective potentials, v_+ and v_- , differ on account of the ‘local exchange splitting’, which is the cause of the local moment formation. Unlike the conventional LSDA implementation, the potentials v_+/v_- are orbital dependent when the DLM theory is combined with the SIC-LSD approach. This dependency comes about by our SI-correcting certain L channels as discussed earlier. Importantly, the SI-corrected channels of v_+ and v_- may differ. Indeed, as described in [Section 3.6](#), the channels to which we apply the SIC are those with a resonant phase shift ([Lüders et al., 2005](#)). Such resonant behaviour is characteristic of well-localized electron states, which will establish quasi-atomic like moments. Through the influence they exert on the electron motions, these moments will be reinforced by the spins of more itinerant-like electrons. It thus follows that resonant states will tend to define the local moment orientation and, as such, we expect to SI-correct a greater number of channels of v_+ than we do for v_- . For example, for Gd, all 7 v_+ f-channels are SI-corrected while no correction is applied to any of the v_- f-channels.

In the paramagnetic regime, we find

$$\tilde{D}_i^0 = \frac{1}{2}(D_+^0 + D_-^0)\tilde{\mathbf{1}} + \frac{1}{2}(D_+^0 - D_-^0)\tilde{\sigma} \cdot \hat{e}_i \quad (93)$$

where

$$D_{+(-)}^0 = \left[1 + \left[t_{+(-)}^{-1} - (t^c)^{-1} \right] \tau^{c,00} \right]^{-1}. \quad (94)$$

The superscript 0 signifies that the CPA projector is evaluated in the paramagnetic state. Substituting $P_i(\hat{e}_i) = P^0 = 1/4\pi$ into [Eq. \(81\)](#), we obtain

$$\frac{1}{4\pi} \int d\hat{e}_i \tilde{D}_i^0(\hat{e}_i) = \tilde{\mathbf{1}}, \quad (95)$$

which becomes, on carrying out the integration,

$$\frac{1}{2}D_+^0 + \frac{1}{2}D_-^0 = 1. \quad (96)$$

[Equation \(96\)](#) is evidently just the CPA equation for a system with 50% of moments pointing ‘up’ and 50% pointing ‘down’, that is an Ising-like system. The electronic structure problem is thus reduced to that of an equiatomic binary alloy, where the two ‘alloy’ components have anti-parallel local moments. Treating this ‘alloy’ problem with the KKR-CPA, in conjunction with the LSIC charge self-consistency procedure, outlined in [Section 3.6](#) and by [Lüders et al. \(2005\)](#), we arrive at a fully self-consistent LSIC-CPA description of the DLM paramagnetic state.

It should be noted that the equivalence of the DLM electronic structure problem to that of an Ising-like system is purely a consequence of the symmetry of the paramagnetic state, and is not the result of our imposing any restriction on the moment directions. Indeed, in the formalism for the paramagnetic spin susceptibility, which we outline now, we maintain and consider the full 3D orientational freedom of the moments.

Within the DLM method, the magnetization at a site i , \mathbf{M}_i , is given by $\int d\hat{e}_i \mu P_i(\hat{e}_i)\hat{e}_i$, where μ is the local moment magnitude, determined self-consistently. In the paramagnetic regime, where P_i is independent of \hat{e}_i and $\mathbf{M}_i = \mathbf{0}$, we can study the onset of magnetic order by considering the response to the application of an external, site-dependent magnetic field. Focusing on the dominant response of the system to line up the moments with the applied field, from the equation of state, we obtain the following expression for the static spin susceptibility:

$$\chi_{ij} = \frac{\beta}{3} \sum_k S_{ik}^{(2)} \chi_{kj} + \frac{\beta}{3} \delta_{ij}, \quad (97)$$

where $S^{(2)}$ is the direct correlation function for the local moments, defined by

$$S_{ik}^{(2)} = -\frac{\partial^2 \langle \Omega \rangle}{\partial m_i \partial m_k}, \quad (98)$$

and depends only on the vector difference between the positions of sites i and k . A lattice Fourier transform can hence be taken of Eq. (97), giving

$$\chi(\mathbf{q}) = \frac{1}{3} \beta \mu^2 \left(1 - \frac{1}{3} \beta S^{(2)}(\mathbf{q}) \right)^{-1}. \quad (99)$$

By investigating the wave vector dependence of the susceptibility, we gain information about the wave vector (\mathbf{q}) dependence of the spin fluctuations that characterize the paramagnetic state and the type of magnetic order that might occur as the temperature is lowered through a phase transition. For example in a ferromagnetic material, such as gadolinium, the paramagnetic state is characterized by ferromagnetic spin fluctuations, which have long wavelengths, $\mathbf{q} \sim (0, 0, 0)$, becoming unstable to them at the Curie temperature, T_C . For a system that orders into an incommensurate anti-ferromagnetic structure, the paramagnetic state is dominated by ‘anti-ferromagnetic’ spin fluctuations, specified by a finite, incommensurate, wave vector $\mathbf{q} = \mathbf{Q}_0$ which also characterizes the static magnetization or spin density wave state formed below the Néel temperature, T_N . For example, the magnetic structures of the heavy lanthanides terbium (Tb) to thulium (Tm) are described by wave vectors of the form $\mathbf{Q}_0 = (0, 0, q_{\text{inc}})$, where individual hexagonal layers are uniformly magnetized in a direction that changes from layer to layer according to the modulation vector q_{inc} .

An expression for $S^{(2)}(\mathbf{q})$, involving scattering quantities obtained from the electronic structure of the paramagnetic state, can be found in [Staunton et al. \(1986\)](#). In brief:

$$S^{(2)}(\mathbf{q}) = \int d\varepsilon f_\beta(\varepsilon; v^{(n)}) \frac{1}{\pi} \text{Im} \text{Tr} \underline{\Lambda}^0 \underline{\chi}_0(\mathbf{q}) \underline{\Lambda}(\mathbf{q}), \quad (100)$$

where

$$\underline{\chi}_0(\mathbf{q}) = \int_{\text{BZ}} d^3k \underline{\tau}^c(\mathbf{k}) \underline{\tau}^c(\mathbf{k} + \mathbf{q}) - \underline{\tau}^{c,00} \underline{\tau}^{c,00}, \quad (101)$$

which is the lattice Fourier transform of the ‘non-interacting’ susceptibility for the system, and $\underline{\Lambda}(\mathbf{q})$ satisfies the following Dyson-like equation:

$$\underline{\Lambda}(\mathbf{q}) = \underline{\Lambda}^0 + \underline{\Lambda}^0 \underline{\chi}_0(\mathbf{q}) \underline{\Lambda}(\mathbf{q}), \quad (102)$$

with $\underline{\Lambda}^0 = \underline{D}_+^0 (t_+^{-1} - t_-^{-1}) \underline{D}_-^0$.

7.2.3 Magnetic order in gadolinium: The prototype

A summary of this work is provided by [Hughes et al., \(2007\)](#). Gadolinium’s hcp crystal structure is parametrized by two variables, the c/a ratio of the lattice parameters and the atomic unit cell volume, expressed in terms of the WS radius. Experimentally, these two parameters are 1.597 and 3.762 a.u., respectively ([Banister et al., 1954](#)). A LSDA calculation of the DOS of gadolinium in its paramagnetic (DLM) state at these lattice parameters reveals the minority 4f-states making a significant contribution at the Fermi energy. This has important implications for the magnetic ordering in the system ([Heinemann and Temmerman, 1994](#)). A SIC-LSDA calculation, however, where all seven majority 4f-states are corrected, opens up a Hubbard gap between the occupied and unoccupied f-states. The majority f-states are pushed down to approximately 16 eV below the Fermi energy and the minority f-states are moved away from the conduction bands, reducing the f contribution to the DOS at the Fermi energy. The SIC-LSDA electronic structure thus describes the experimental picture well, with the f-states playing little role in conduction.

[Figure 31](#) shows paramagnetic spin susceptibilities for gadolinium, corresponding to these electronic structures. For the LDA calculation (a), the susceptibility attains its maximum at $\mathbf{q} = (0,0,1)$, indicating that the system should order with a commensurate type 1 anti-ferromagnetic (AF1) structure, where magnetic moments are oppositely aligned in alternate planes along the c -axis. This is consistent with ground state energy ($T = 0$ K) calculations from other LDA studies of gadolinium ([Heinemann and Temmerman, 1994](#)), where an anti-ferromagnetic structure was found to be energetically favourable over the experimentally observed ferromagnetic structure. The origin of this AF1 coupling derives from the proximity of 4f minority states to the Fermi energy ([Kurz et al., 2002](#)). Previous investigations have shown that by pushing the 4f-states away from the Fermi energy, either by treating them as part of the core ([Eriksson et al., 1995](#)) or including a Coulomb parameter U for the f-states (LDA + U) ([Harmon et al., 1995](#)), a ferromagnetic ground state can be obtained. Since the SIC succeeds in pushing the f-states away from the Fermi energy, the paramagnetic DLM state should show an instability to ferromagnetic order when the LSIC is included. This feature is evident in [Figure 31B](#), which shows the susceptibility attaining its maximum value at $\mathbf{q} = \mathbf{0}$. Note, however, the presence of a shoulder in the susceptibility along the [001] direction, around $q = 0.2$. This feature is significant as we shall show.

Having demonstrated that the LSIC gives an appropriate treatment of the 4f-states, leading to a ferromagnetic ground state, we proceed further with the investigation of gadolinium. We determined the theoretical lattice parameters of

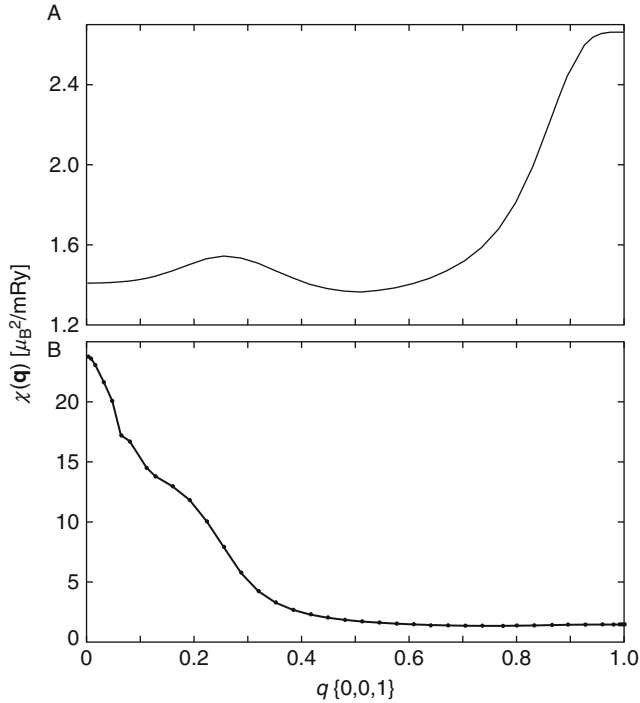


FIGURE 31 Paramagnetic spin susceptibilities for gadolinium at wave vectors along the $[0,0,1]$ direction, obtained from (A) LSDA calculation and (B) LSIC-LSDA calculation.

the paramagnetic state from calculations of the total energy. The energy is minimized at a WS radius which is almost invariant of the c/a values. The overall minimum occurs at a c/a ratio of 1.63 and a WS radius of 3.654 a.u. We find the paramagnetic spin susceptibility for these lattice parameters to attain its maximum at $\mathbf{q} = \mathbf{0}$ also and hence to infer ferromagnetic ordering.

Figure 32 shows the temperature dependence of the $\mathbf{q} = \mathbf{0}$ (ferromagnetic) susceptibility of gadolinium. A Curie-Weiss type behaviour is observed, with $T_C = 280$ K/324 K for the theoretical/experimental lattice parameters in fair agreement with that measured experimentally, $T_C = 293$ K (Jensen and Mackintosh, 1991). The effective magnetic moment was $7.34\mu_B/7.36\mu_B$ for the theoretical/experimental lattice parameters, also in reasonable agreement with the experimental value of $7.63\mu_B$ and also the results from calculations where the 4f-states were treated as part of the core [$7.44\mu_B$ (Turek et al., 2003)] or the LDA + U was used [$7.41\mu_B$ (Kurz et al., 2002)]. Examining the l -decomposed spin densities obtained from the LSIC DOS shows the magnetic moment to originate mainly from the f-states ($\sim 6.95\mu_B$), with the remainder coming from a polarization of the d-states ($\sim 0.34\mu_B$) and a small contribution from the s- and p-states ($\sim 0.07\mu_B$).

In our computations, we find the magnetic ordering tendencies of gadolinium to change as the lattice parameters are altered away from their equilibrium values. On changing the c/a ratio over the range 1.54–1.66, with the WS-radius fixed at the

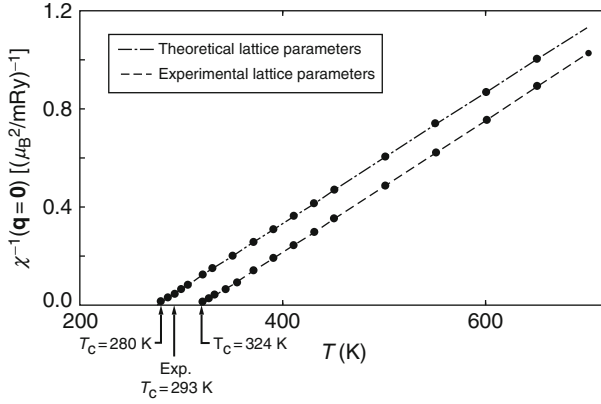


FIGURE 32 Inverse spin susceptibilities for Gd as a function of temperature, calculated for the theoretical and experimental lattice parameters.

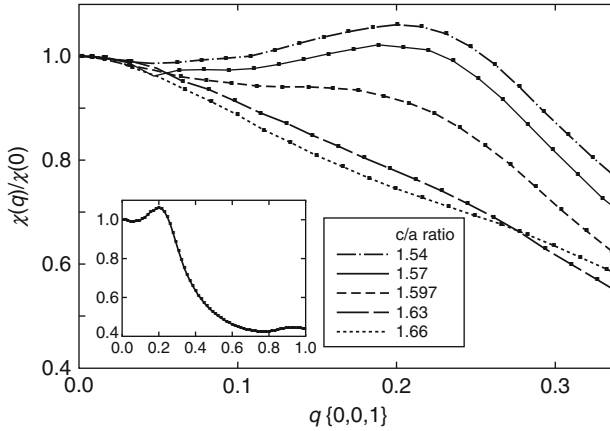


FIGURE 33 Normalized paramagnetic spin susceptibilities for Gd, obtained using the theoretical unit cell volume. The inset shows the susceptibility up to the zone boundary for c/a ratio 1.54.

theoretical value (3.654 a.u.), our calculated paramagnetic spin susceptibility, shown in Figure 33, starts to develop a shoulder near $\mathbf{q} = (0,0,0.2)$, similar to that observed in Figure 31B. Moreover, at the lowest c/a ratios, this shoulder grows into a peak and the susceptibility no longer attains its maximum value at $\mathbf{q} = \mathbf{0}$. The maximum occurs instead at some incommensurate wave vector, q_{inc} , meaning that the system now has a tendency to order into an incommensurate magnetic structure at low temperatures. This could be helical, where the helix turn angle, that is the angle between magnetic moments in adjacent layers, would be given by πq_{inc} .

Such incommensurate ordering is characteristic of the heavy lanthanide elements, terbium to thulium, and is associated with a ‘webbing’ feature of their

Fermi surfaces. This webbing structure contains large parallel sheets of Fermi surface, which can nest together when translated by some vector in \mathbf{k} -space. This can cause an enhancement of the magnetic susceptibility at the nesting vector, and indeed it has been shown, both theoretically (Keeton and Loucks, 1968) and experimentally (Dugdale et al., 1997), that the size of the nesting vector in the heavy lanthanides is correlated with their magnetic ordering vectors. The shape of the Fermi surface in heavy lanthanide metals depends critically on the c/a ratio of the lattice parameters (Cracknell and Wong, 1973), implying that the magnetic structures of these elements are sensitive to the c/a ratio. This is corroborated by experimental studies by Andrianov and others, which have shown that it is possible to alter the magnetic state of lanthanide metals and alloys by changing the lattice parameters through application of external pressure or tension (Andrianov and Chistiakov, 1997; Andrianov et al., 2000) and by alloying with yttrium (Andrianov, 1995). Such behaviour is possibly interpreted in terms of an electronic topological transition (Lifshitz, 1960; Blanter et al., 1994) at some critical c/a ratio, where the webbing structure of the Fermi surface ruptures.

To analyse our susceptibility results shown in Figures 31B and 33, we investigate the Fermi surface of paramagnetic (DLM) gadolinium at various c/a ratios. For a given configuration of local moments, this Fermi surface can be defined in the usual way. However, when considering the whole ensemble of moment orientations, the 'Fermi surface' is a smeared out average of itself over all moment configurations. A useful tool for defining this surface is the BSF (Faulkner, 1982) that is periodic in reciprocal wave vector \mathbf{k} space and is given by

$$\bar{A}_B(\mathbf{k}, E) = -\frac{1}{\pi} \text{Im} \sum_{nm} \exp[i\mathbf{k} \cdot (\mathbf{R}_n - \mathbf{R}_m)] \int d^3r \langle G(\mathbf{r} + \mathbf{R}_n, \mathbf{r} + \mathbf{R}_m, E) \rangle, \quad (103)$$

in terms of an ensemble average, $\langle \rangle$, of the electronic real space Green's function and where the integral over \mathbf{r} is within the unit cell at the origin. In this case, the ensemble average is taken over local moment configurations (Szotek et al., 1984). For ordered systems, $\bar{A}_B(\mathbf{k}, E)$ consists of a set of δ -function peaks:

$$\bar{A}_B(\mathbf{k}, E) = \sum_n \delta(E - E_n(\mathbf{k})), \quad (104)$$

where $E_n(\mathbf{k})$ is the Bloch energy eigenvalue for the wave vector \mathbf{k} and band index n . With disorder (here the local moment spin fluctuation disorder), these peaks broaden but their positions can be regarded as an effective band structure, with their width in energy interpreted as an inverse lifetime (Szotek et al., 1984). The Fermi surface of a disordered system is defined as the locus of these peaks at the constant energy $E = E_F$.

Figure 34 shows the BSF of paramagnetic Gd at the Fermi energy, E_F , calculated for the sets of lattice parameters used in Figure 33. For c/a ratios of 1.597 or smaller, a webbing feature is displayed and the corresponding nesting vector is indicated by an arrow in panel (a). At a c/a ratio of 1.63 (Figure 33D), the webbing feature has started to rupture, and at a c/a ratio of 1.66 (Figure 33E), the rupturing is complete and the Fermi surface no longer has any significant regions of nesting.

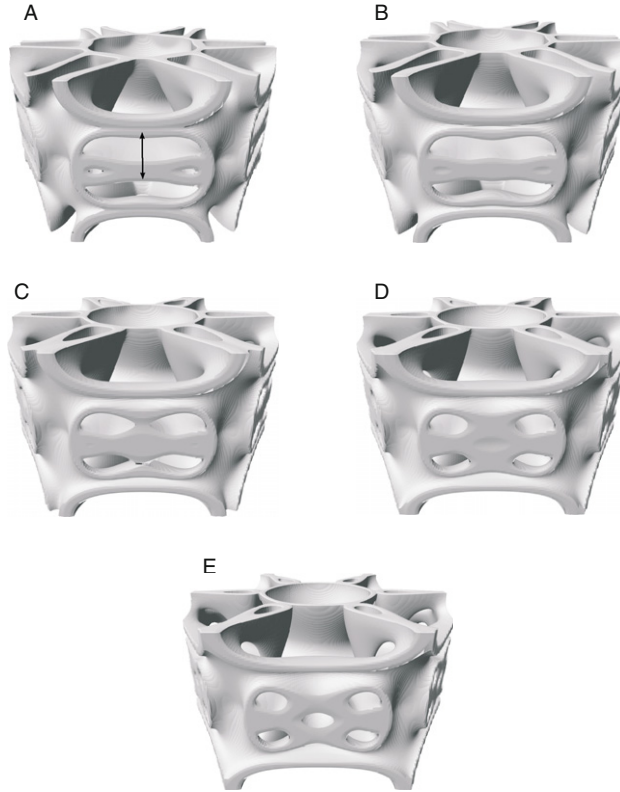


FIGURE 34 Bloch spectral function of Gd in the hexagonal BZ, calculated at the Fermi energy. Panels (A), (B), (C), (D), and (E) are for c/a ratios 1.54, 1.57, 1.597, 1.63, and 1.66, respectively, with theoretical unit cell volumes used but not for high c/a ratios.

This concurs with the results shown in [Figure 33](#), where the susceptibility is enhanced at some incommensurate \mathbf{q} vector for low c/a ratios, [Figure 35A](#) shows a cross section through the webbing structure for c/a ratio 1.54. The nesting structure is created by two bands which just cross the Fermi energy along the L–M direction. The broadening of the spectral function peaks, caused by the local moment disorder, means that the bands are smeared, which results in their merging together at the L point. The magnitude of the nesting vector, \mathbf{Q}_0 , is ~ 0.2 (in units of $2\pi/c$) and coincides with the size of the magnetic ordering wave vector, q_{inc} , observed in [Figure 33A](#). [Figure 35B and C](#) show the same cross section of the BZ, with the BSF evaluated using c/a ratios 1.57 and 1.66, respectively. In panel (b), the Fermi surface has a distinctive ‘dog-bone’ shape, with two extremal vectors, one centred and the other non-centred, connecting the sheets of Fermi surface. [Figure 35A and B](#) show the length of the centred nesting vector to decrease as the c/a ratio increases. This is in keeping with the experimental results of Andrianov, where the length of the magnetic ordering vector decreases continuously as the c/a ratio is increased. This does not, however, interpret the

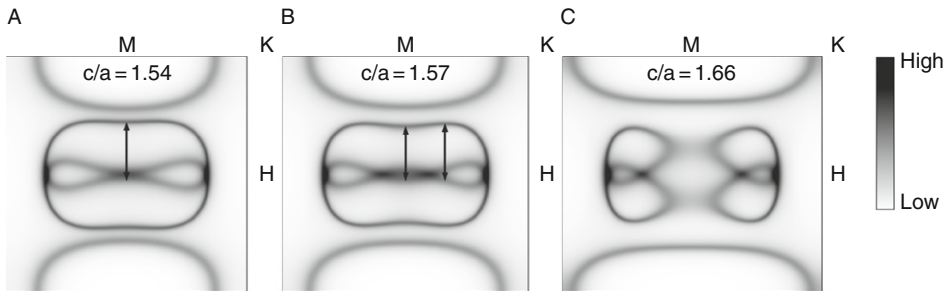


FIGURE 35 Bloch spectral function of Gd on the HLMK plane of the hexagonal BZ. Panels (A), (B), and (C) are for c/a ratios 1.54, 1.57, and 1.66, respectively, with theoretical unit cell volumes used. The centre of the plane is the L point. Nesting vectors are indicated by arrows. The colour plot can be found in [Hughes et al. \(2007\)](#).

susceptibility results shown in [Figure 33](#) correctly, where the position of the incommensurate ordering peak is almost invariant to the c/a ratio used. If, instead, we look at the length of the non-centred vector, we see that it stays fairly constant as the c/a ratio is altered. It thus appears that it is the non-centred nesting vector which is responsible for the incommensurate ordering observed in our calculations. This is in agreement with recent theoretical work by [Nordström and Mavromaras \(2000\)](#) who found that the non-centred vector was the appropriate nesting vector.

Turning now to the magnetic ordering behaviour as a function of unit cell volume, from our susceptibility calculations, we find two distinct cases differentiated according to the c/a ratio of the lattice parameters. For high c/a ratios, corresponding to systems with no webbing feature, ferromagnetic ordering is predicted for all volumes. For low c/a ratios, corresponding to systems with webbing, a more complicated picture emerges as shown in [Figure 36](#). The webbing produces an enhancement of the susceptibility at the nesting vector for all volumes. However, as the volume increases, the height of the incommensurate peak relative to the $\mathbf{q} = \mathbf{0}$ (ferromagnetic) peak decreases, and at a WS radius of 3.710 a.u., there is a near degeneracy between the two ordering types. For the highest WS-radii, the susceptibility obtains its maximum value at $\mathbf{q} = \mathbf{0}$ and so we predict the system to be ferromagnetic. Thus, in order for the nesting enhancement to be strong enough so that incommensurate ordering wins out over ferromagnetic ordering, the unit cell volume needs to be below a certain critical value.

The behaviour of the paramagnetic spin susceptibility, χ , is determined by the direct correlation function, $S^{(2)}$ [[Eq. \(100\)](#)]. This function can be fit in terms of real-space parameters:

$$S^{(2)}(\mathbf{q}) = \sum_n \sum_{i \in n} S_n^{(2)} \exp(i\mathbf{q} \cdot \mathbf{R}_i), \quad (105)$$

where $S_n^{(2)}$ is the direct pair interaction between an atom at the origin and another in the n th neighbour shell, with position vector \mathbf{R}_i . For the magnetic structures

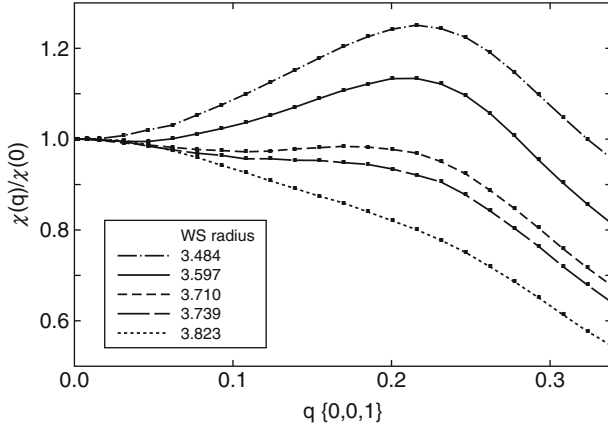


FIGURE 36 Normalized paramagnetic spin susceptibilities for Gd for various WS radii, obtained using a c/a ratio of 1.54.

considered in this section, $\mathbf{q} = (0, 0, q)$ and hence $\exp(i\mathbf{q} \cdot \mathbf{R}_i) = \exp(iqR_z)$, where R_z is the z -component of \mathbf{R}_i . Since the heavy lanthanides adopt hcp structures, with two atoms per unit cell, they can be considered in terms of two interpenetrating sublattices. Consequently, two distinct sets of pair correlations can be considered, one where both sites are on the same sublattice ('intra sublattice') and one where the sites are on different sublattices ('inter-sublattice'). For intra- (inter-) sublattice pairs, $R_z = l * c$ ($R_z = (l-1/2) * c$) where $l \in \mathbb{Z}$ and c is the ' c ' lattice parameter. The 'layer' indices, l , can be used to reparametrize the real space fit of Eq. (105):

$$S^{(2)\text{-intra}}(\mathbf{q}) = S_0^{(2)\text{-intra}} + \sum_{l \in \mathbb{N}}^{l_{\text{top}}} S_l^{(2)\text{-intra}} \cos(qlc) \quad (106)$$

$$S^{(2)\text{-inter}}(\mathbf{q}) = \sum_{l \in \mathbb{N}}^{l_{\text{top}}} S_l^{(2)\text{-inter}} \cos[q(l - (1/2))c],$$

where $S_l^{(2)}$ is the sum of all pairwise interactions between sites in the l th layer and the site at the origin. The $S_0^{(2)}$ component corresponds to the sum of pair interactions between the atom at the origin and atoms in the layer containing the origin. For the fitting of the direct correlation function to be computationally tractable, the sum over layers, l , in Eq. (106) is truncated at some finite value, l_{top} . We find that $l_{\text{top}} = 8$ gives a good fit of $S^{(2)\text{-intra}}$ and $S^{(2)\text{-inter}}$. Figure 37 shows layer-resolved component of $S^{(2)}$ where integer (half-integer) values of R_z/c correspond to intra- (inter-) sublattice components. The biggest contribution to $S_l^{(2)}$ comes from the layers at $R_z = \pm c/2$. This is to be expected since, in hcp structures that have a c/a ratio less than the ideal value $\sqrt{8/3} \approx 1.63$, the nearest neighbours to any given atom are contained within the layers adjacent to the atom, not the layer in which the atom actually lays. The components of $S^{(2)}$ are seen to oscillate as a function of R_z , in the manner of an RKKY-type interaction.

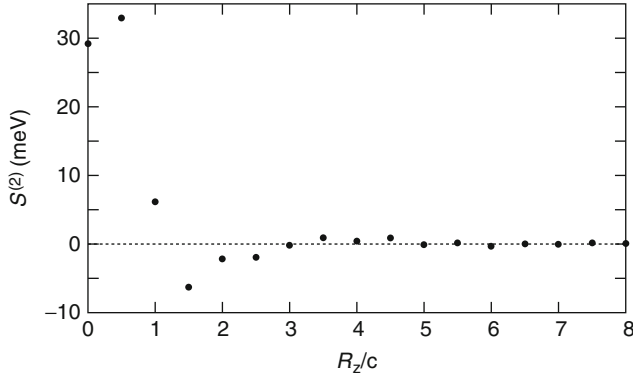


FIGURE 37 Layer-resolved components of the effective exchange interaction, $S^{(2)}$.

7.2.4 Magnetic phase diagram for the heavy lanthanide metals

The two types of magnetic ordering that we encountered during our investigation of gadolinium (ferromagnetic ordering and incommensurate ordering, modulated along the c -axis) correspond to the two types of ordering that are observed experimentally across the heavy lanthanide series. To investigate the competition between these two ordering types, we define a ‘magnetic ordering parameter’, α , which gives a measure of the relative strengths of the ‘incommensurate spin fluctuations’ and ferromagnetic spin fluctuations that characterize the paramagnetic state. To do this, we examine the wave vector-dependent critical temperature, $T_c(\mathbf{q})$, obtained from our susceptibility and direct correlation function calculations, that is from $\det[\mathbf{I}_n - 1/3\beta\mathbf{S}^{(2)}(\mathbf{q})] = 0$ with the 2×2 $\mathbf{S}^{(2)}$ matrix specified by

$$\begin{pmatrix} S^{(2)\text{-intra}}(\mathbf{q}) & S^{(2)\text{-inter}}(\mathbf{q}) \\ S^{(2)\text{-inter}}(\mathbf{q}) & S^{(2)\text{-intra}}(\mathbf{q}) \end{pmatrix},$$

where $S^{(2)\text{-intra}}(\mathbf{q})$ and $S^{(2)\text{-inter}}(\mathbf{q})$ correspond to the fit functions in Eq. (106). By using these fit functions, we mitigate the effects of computational noise, which may be important when analysing the delicate competition between the two ordering types.

If the critical temperature function $T_c(\mathbf{q})$ has only one peak, at $\mathbf{q} = \mathbf{0}$, we set $\alpha = 0$. If $T_c(\mathbf{q})$ has only one peak, but at some incommensurate \mathbf{q} -vector, q_{inc} , we set $\alpha = 1$. Clearly, $\alpha = 0$ corresponds to the paramagnetic state being dominated by ferromagnetic spin fluctuations and $\alpha = 1$ corresponds to its domination by spin fluctuations with some finite, incommensurate wave vector. When $T_c(\mathbf{q})$ has a two peak structure, corresponding to a competition between the two ordering types, we examine the values of $T_c(\mathbf{q})$ at its turning points. We define $T_0 = T_c(\mathbf{q} = \mathbf{0})$, $T_{\text{inc}} = T_c(\mathbf{q} = (0, 0, q_{\text{inc}}))$ and $T_{\text{min}} = T_c(\mathbf{q} = \mathbf{q}_{\text{min}})$, where \mathbf{q}_{min} is the position of the minimum that occurs between the $\mathbf{q} = \mathbf{0}$ and $\mathbf{q} = (0, 0, q_{\text{inc}})$ maxima. If $T_0 > T_{\text{inc}}$ we set

$$\alpha = \frac{T_{\text{inc}} - T_{\text{min}}}{2(T_0 - T_{\text{min}})} \quad (107)$$

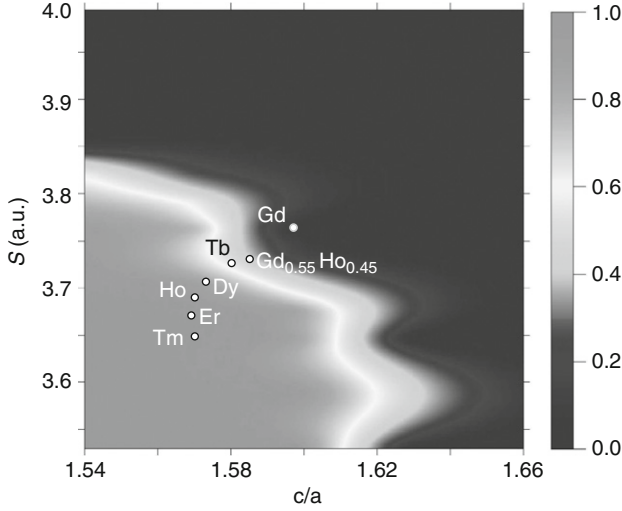


FIGURE 38 Ordering parameter, α , for gadolinium as a function of c/a ratio and WS radius. The black region corresponds to ferromagnetic and the grey region to incommensurate anti-ferromagnetic spin fluctuations. The experimental lattice parameters of all the heavy lanthanide elements are indicated by circles; a grey (black) circle indicates that experimentally the high-temperature ordered state of the element is ferromagnetic (incommensurate anti-ferromagnetic). The circle for $\text{Gd}_{0.55}\text{Ho}_{0.45}$ indicates the experimental lattice parameters of a Gd–Ho alloy at the critical concentration of Ho at which an incommensurate anti-ferromagnetic phase first appears. The colour plot can be found in [Hughes et al. \(2007\)](#).

and if $T_0 < T_{\text{inc}}$, we set

$$\alpha = 1 - \frac{T_0 - T_{\text{min}}}{2(T_{\text{inc}} - T_{\text{min}})}. \quad (108)$$

Clearly, α is defined such that $\alpha > 0.5$ indicates a stronger tendency towards incommensurate ordering and $\alpha < 0.5$ indicates a stronger tendency towards ferromagnetic ordering.

In [Figure 38](#), we show α for gadolinium as a function of c/a ratio and unit cell volume. To account for the difference between the theoretical and experimental volumes, the WS-radii in the figure are scaled, such that data shown at the experimental WS radius of gadolinium corresponds to data calculated at the theoretical WS-radius. On this phase diagram, we also indicate where the experimental lattice parameters of all the heavy lanthanide elements lie, as well as those of a Gd–Ho alloy. Since the heavy lanthanide elements differ only in how many 4f electrons they have, and it is the sd conduction electrons that are responsible for mediating the interaction between magnetic moments, gadolinium can be considered a magnetic ‘prototype’ for the post-Gd heavy lanthanide elements. Thus, we propose that the behaviour of gadolinium as a function of lattice parameters is a model of all the other heavy lanthanide elements. By considering the phase diagram, [Figure 38](#), as being universal to all heavy lanthanide systems, we predict

that when going left to right in the heavy lanthanide series, there will be a trend away from ferromagnetism and towards incommensurate ordering. This is exactly what is observed experimentally, with the magnetic modulation vector starting out at zero for gadolinium (ferromagnetic ordering) and then progressively increasing through the series to give rise to various incommensurate anti-ferromagnetic structures. From the phase diagram, we predict that the transition between ferromagnetism and incommensurate ordering occurs very rapidly as a function of c/a ratio, particularly for the higher unit cell volumes. This is consistent with recent experimental work on terbium under uniaxial tension. Terbium exhibits helical ordering and has a WS-radius of 3.724 a.u., with a c/a ratio of 1.580. It has been shown (Andrianov et al., 2000) that by increasing the c/a ratio by as little as 0.002 the helical ordering could be completely suppressed. In the phase diagram, the elements dysprosium and terbium are positioned close to, or within, the transition region between ferromagnetic and incommensurate ordering. This is consistent with the experimental behaviour of these two systems, which exhibit incommensurate ordering at high temperatures and ferromagnetic ordering at low temperatures.

Because of their structural similarities, Gd alloys easily with all the other heavy lanthanide elements, R' . These alloys transform from ferromagnets to incommensurate magnetically structured materials once the concentration of R' exceeds a certain critical concentration x_c . We can use the phase diagram to predict these critical alloy concentrations. These are listed in Table 11 and are in good agreement with experimental values where known.

We can also compute estimates of the magnetic ordering vectors of all the heavy lanthanides from our susceptibility calculations for gadolinium at the appropriate lattice parameters. The results are shown in Figure 39. For example, when we performed a calculation for Gd at the experimental lattice parameters of terbium (Tb), specified by a c/a ratio of 1.580 and a WS-radius of 3.724 a.u., the susceptibility peaked at a wave vector $\mathbf{q} = (0, 0, 0.13)$, which is in good agreement with the experimental ordering vector of Tb, $(0, 0, 0.11)$. Overall, we predict a gradual increase in the ordering vector across the heavy lanthanide series, in agreement with experiment. We also find that the magnetic ordering vectors of

TABLE 11 Critical alloy concentrations of $Gd_{1-x}R_x$ systems

System	Critical concentration, x_c	
	Theoretical	Experimental
$Gd_{1-x}Tb_x$	0.78	
$Gd_{1-x}Dy_x$	0.56	0.50 ^a
$Gd_{1-x}Ho_x$	0.49	0.45 ^b
$Gd_{1-x}Er_x$	0.45	
$Gd_{1-x}Tm_x$	0.42	

^a Milstein and Robinson (1967).

^b Taken from Andrianov and Chistiakov (1997).

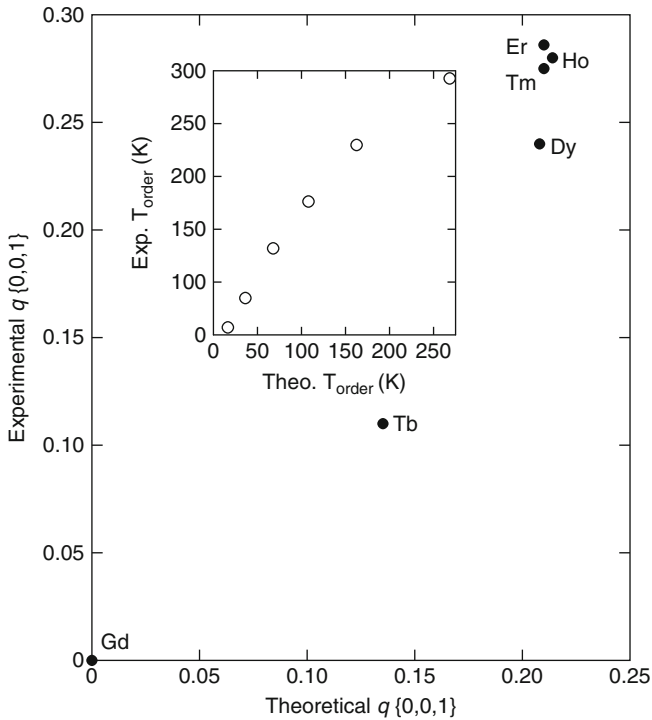


FIGURE 39 Experimental magnetic ordering vectors of the heavy lanthanides versus those predicted from *ab initio* calculations for gadolinium. The inset shows the corresponding ordering temperatures. Experimentally Gd has the highest ordering temperature, which decreases monotonically through the heavy lanthanide series.

the last three members of the series (Ho, Er and Tm) all lie close together, again in agreement with experiment.

Making Gd the prototype for magnetic order in the heavy lanthanides is justified since the Gd ion has orbital angular momentum $L = 0$ and so spin-orbit coupling effects do not need to be incorporated into our calculations. However, if we want to infer magnetic transition temperatures for the other heavy lanthanides from our Gd calculations, LS coupling has to be considered. This can be accomplished by scaling our magnetic transition temperature estimates with the de Gennes factor $(g_J - 1)^2 J(J + 1)$ (Blundell, 2001). As shown in the inset of Figure 39, the transition temperatures obtained from this approach reproduce the experimental trend, although the magnitudes of the temperatures are systematically underestimated. It is worth noting that when we computed the estimates of the magnetic ordering vectors, spin-orbit coupling was not important. This is because, as argued earlier, the type of magnetic order exhibited by the heavy lanthanides is determined by the *sd* conduction electrons, which are little affected by spin-orbit coupling and which all the heavy lanthanides have in common.

Overall, the physical picture that emerges from the magnetic ordering phase diagram, Figure 38, links unequivocally the lattice parameters of the heavy

lanthanides with their magnetic properties. Our results have verified the critical role that the c/a ratio plays in determining the magnetic ordering types of the heavy lanthanides and how this is linked to the Fermi surface of the paramagnetic phase. However, our discovery that the atomic unit cell volume, associated with the lattice parameters, is just as important in determining the magnetic properties has enabled us to develop a much more complete understanding of heavy lanthanide magnetism. In particular, we have shown that even when the c/a ratio of a heavy lanthanide system is below the critical value needed for a webbing structure, incommensurate anti-ferromagnetic ordering is not necessarily favoured over ferromagnetic ordering; for incommensurate ordering to win out over ferromagnetic ordering, the unit cell volume needs to be below a certain value. Experimentally, the unit cell volumes of the heavy lanthanides decrease with increasing atomic number, in accord with the well-known ‘lanthanide contraction’ (Taylor and Darby, 1972). This contraction occurs because as the number of electrons in the poorly shielding 4f orbitals is increased, there is an increase in the effective nuclear charge and, correspondingly, a decrease in ionic radii. Our findings evidently suggest that this contraction helps promote the incommensurate ordering in the post-Gd heavy lanthanides. The roles that the different types of valence electrons play in determining the magnetic structures of the heavy lanthanides are thus clear; the itinerant sd electrons, common to all the heavy lanthanides, mediate the interaction between magnetic moments and it is the nesting of their Fermi surfaces that can lead to instabilities in the paramagnetic phase with respect to the formation of incommensurate spin density waves. The f electrons, on the other hand, are responsible for setting up the magnetic moments and, as their number increases across the heavy lanthanide series, they play an indirect role in promoting the incommensurate ordering by means of the lanthanide contraction.

7.3 Valence fluctuations

As mentioned in Section 7.1, the alloy analogy is a versatile approach that can be applied to different types of thermal fluctuations. In particular, we will now also include valence fluctuations. The theoretical framework remains largely as outlined in the previous section, but the possible configurations at a given site now include the valence state in addition to the direction of the local moment. In the following, this approach will be applied to the finite temperature phase diagram of Ce, focusing on the isostructural α - γ transition (Lüders et al., 2005). At absolute zero, the two phases can be identified as the tetravalent α -phase at low volumes, and the trivalent γ -phase at high volumes. Thus, these phases correspond to a delocalized or localized f -state, respectively. Figure 40 shows the ground state energies for different valence configurations, namely the tetravalent f^0 configuration, corresponding to an LDA calculation, and SIC-LSD calculations for trivalent f^1 configurations, where f -states with different symmetries are treated as localized, as seen in Table 12. These zero temperature calculations assume a ferromagnetic alignment of the local moments in the γ -phase. However, when discussing the finite temperature phase diagram of Ce, we will account for the

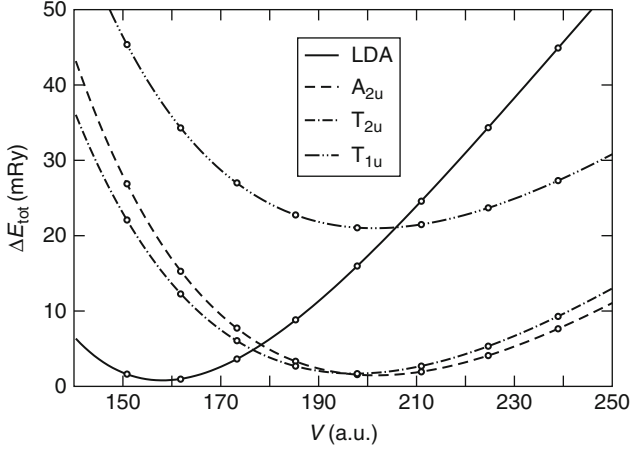


FIGURE 40 The calculated total energies for Ce from LDA and SIC-LSD, with different f-states localized, as functions of volume, given in atomic units $[(a_0)^3]$.

TABLE 12 The total energy differences as obtained from the LDA and SIC-LSD calculations, with respect to the ground state energy solution (LDA), for Ce in different f-configurations. The corresponding volumes and bulk moduli (evaluated at the theoretical lattice constants) are also given

		ΔE (mRy)	V (a_0^3)	B (kbar)
LDA		0.0	158	701
SIC	A_{2u}	0.8	202	355
	T_{1u}	20.3	201	352
	T_{2u}	1.5	197	351

paramagnetic state with its disorder of the local moments using the DLM framework of Section 7.2. The splittings of the states, shown in Table 12, are due to the crystal field since in this calculation, the spin-orbit coupling has been neglected. We will later account for spin-orbit coupling through the magnetic entropy terms. Table 12 shows that the state with the A_{2u} symmetry provides the lowest energy solution for the γ -phase. Only 0.8 mRy separate the minima of the α - and γ -phases, giving rise to the transition pressure at the absolute zero of about -2.3 kbar. This is in good agreement with the experimental value of -7 kbar, when extrapolated to zero temperature, and with other theoretical values. The bulk moduli, given in Table 12, are calculated at the theoretical equilibrium volumes. When evaluated at the experimental volumes, their values are substantially reduced to 239 kbar for the α -phase and 203 kbar for the γ -phase, which is in considerably better agreement with the experimental data. The volume collapse is obtained at 22%, which also compares well with the experimental values of 14–17%. We note that the underestimate of the volumes of both the α - and γ -phases is mainly due to the KKR l -convergence problem. Although it seems that this l -convergence problem should affect the LSD and SIC-LSD calculations in a similar manner, we observe a

significantly larger error for the α -phase. This larger error for the α -phase, which is also found in the LMTO-ASA calculations, is most likely because LDA is not adequate for describing the correlated nature of the α -phase, as observed in experiments. In fact, the LDA calculations correspond to the high-pressure α' -phase, which is purely tetravalent and has a smaller lattice constant than the observed α -phase.

We now return to the description of Ce at finite temperatures. The alloy analogy for describing the thermal valence and spin fluctuations gives rise to a ternary alloy, consisting of Ce atoms with localized f-electrons, described by SIC-LSD, with a concentration of $c/2$ for each spin direction (spin up and spin down), and Ce atoms with delocalized f-electrons, described by the LDA, with the concentration $(1-c)$. The free energy of the system is obtained by adding the relevant entropy contributions to the total energy [see Eq. (28)]. The electronic particle-hole entropy, $S_{\text{el}} = -k_B \int d\varepsilon n(\varepsilon)[f_\beta(\varepsilon) \ln f_\beta(\varepsilon) + (1-f_\beta(\varepsilon)) \ln (1-f_\beta(\varepsilon))]$, is obtained from the underlying band structure calculations (Nicholson et al., 1994). Here $n(\varepsilon)$ is the DOS and $f_\beta(\varepsilon)$ denotes the Fermi distribution. The magnetic entropy $S_{\text{mag}}(c) = k_B c \ln 6$, which corresponds to a spin-orbit coupled state with $J = 5/2$, accounting for the magnetic disorder, while the mixing entropy, $S_{\text{mix}}(c) = -k_B(c \ln c + (1-c) \ln (1-c))$, stems from the disorder among the localized and delocalized Ce atoms. The vibrational entropy, S_{vib} , is assumed to be the same in both phases and therefore is neglected here. In order to determine the full p - T phase diagram, it is necessary to calculate the Gibbs free energy:

$$G(T, c, p) = F(T, c, V(T, c, p)) + p(T, c, p). \quad (109)$$

From this, at each given pressure and temperature, we can determine the concentration of the trivalent Ce, by minimizing the Gibbs free energy with respect to c .

Our calculations go beyond all the earlier work because SIC-LSDA treats all the f-states on equal footing and the KKR-CPA allows for a consistent description of spin and valence disorder. Johansson et al. (1995) used a binary pseudo-alloy concept, but needed one adjustable parameter to put on a common energy scale both the γ -phase, described by LSDA with one f-state included into the core, and the α -phase, described by the standard LSD approximation, with all the f-states treated as valence bands. Svane (1996) performed SIC-LSD calculations using a supercell geometry which limited him to the study of a few concentrations only.

We can obtain the free energy of the physical system at a given volume by evaluating the concentration-dependent free energy at the minimizing concentration c_{min} :

$$F(T, V) = F(T, c_{\text{min}}, V). \quad (110)$$

This free energy, as a function of volume and temperature, is displayed in Figure 41, clearly showing a double-well behaviour for low temperatures, which gets gradually smoothed out into a single minimum as the temperature is increased. In addition, it is found that at elevated temperatures the free energy is lowered mainly at large lattice volumes, which is due to the greater entropy of the γ -phase.

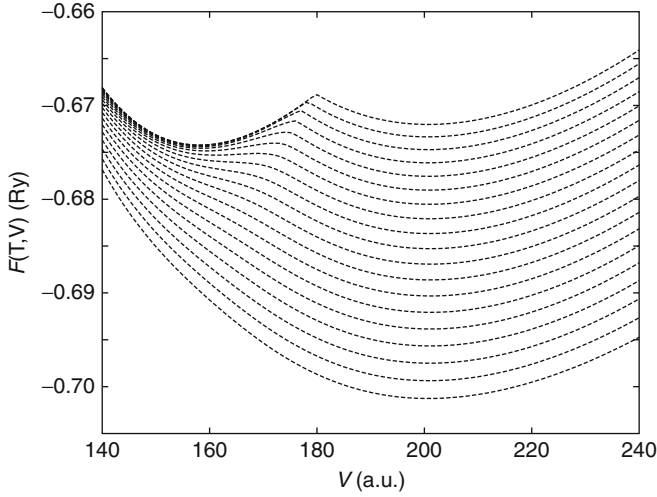


FIGURE 41 The free energies as function of the volume for the temperatures 0 (highest curve) and 1800 K (lowest curve) in steps of 100 K.

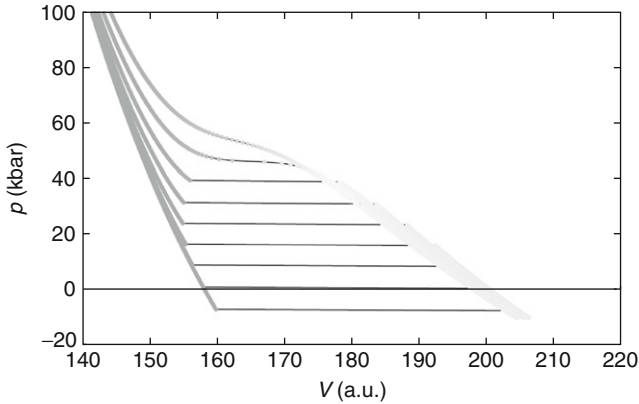


FIGURE 42 Calculated equation of state of Ce for the temperatures $T = 0$ (lowest curve), 200, 400, 600, 800, 1000, 1200, 1400, and 1600 K (highest curve). The shading indicates the fraction of localized electrons: light is all localized (γ -phase) and dark is all delocalized (α -phase).

Inserting the minimizing concentration c_{\min} into the pressure–volume relation

$$p(T, V) = p(T, c_{\min}, V) = -\frac{\partial}{\partial V} F(T, c_{\min}, V) \quad (111)$$

allows one to calculate the isothermal pV-relations of Ce, which are displayed in [Figure 42](#), where it can be seen that the average valence, close to the coexistence line, gradually changes with increasing temperature. Above the critical temperature, the valence changes continuously with increasing pressure from trivalent to tetravalent.

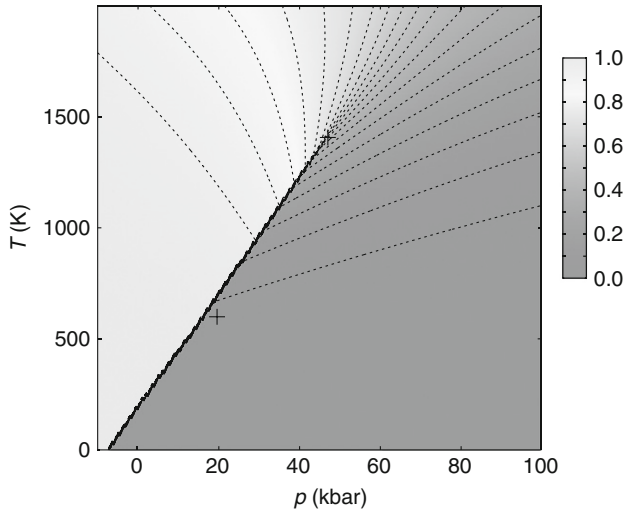


FIGURE 43 Phase diagram obtained for the pseudo-alloy, composed of α -Ce (light grey area) and γ -Ce (dark grey area). The grey shades display the fraction of localized electrons. The crosses indicate the calculated (upper cross) and experimental (lower cross) critical points.

In [Figure 43](#), we present the phase diagram, obtained from the free energies of the α - γ pseudo-alloy, with the γ -phase described by the DLM state. Here, it can be easily followed how the transition becomes continuous above the critical point. The calculated critical temperature overestimates the experimental value by about a factor of 2. It is still reasonable considering that the critical temperature is very sensitive to various small details of the calculations and in particular the theoretical lattice parameters of both the α - and γ -Ce phases. Also, the calculated slope of the phase separation line is slightly too steep, compared to the experimental phase diagram. The likely reason being the overestimate of the volume collapse that enters the definition of the slope, given by the ratio $(V_\gamma - V_\alpha)/(S_\gamma - S_\alpha)$, where $S_{\alpha(\gamma)}$ and $V_{\alpha(\gamma)}$ are, respectively, values of the entropy and volume of the $\alpha(\gamma)$ -phase at $T = 0$ K.

Examining in more detail the discontinuity across the phase separation line displayed in [Figure 44](#), we find the magnitude of the discontinuities for the various contributions to the Gibbs free energy. As expected, all contributions vanish at the critical temperature, above which there is a continuous cross-over between the α - and the γ -phase. It can be seen that it is the entropy discontinuity which is by far the largest contribution. The phase transition is therefore driven by entropy, rather than by energetics. The entropy discontinuity itself is mainly determined by the magnetic entropy.

Summarising this section, we have demonstrated that the alloy analogy of fluctuations can be very useful, giving rise to a simple picture of the underlying physics, relating the magnetic phase diagram of the late lanthanides to the lanthanide contraction, and identifying the entropy as the driving force behind the α - γ phase transition in Ce. In [Section 8](#), we will outline how this approach can be

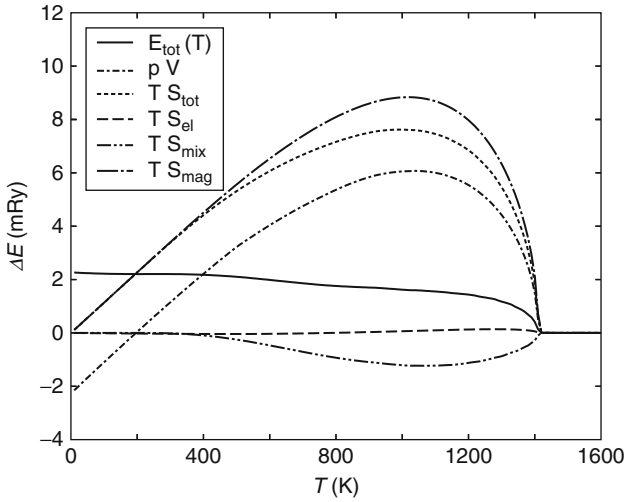


FIGURE 44 Discontinuities of the total energy, the total entropy TS , and the pV term over the phase separation line as function of the temperature. The entropy term is further decomposed into the electronic, the mixing, and the magnetic contribution.

generalized to describe also dynamical, namely quantum, fluctuations, which up to now have been ignored.

8. DYNAMICAL FLUCTUATIONS: THE ‘ALLOY ANALOGY’ AND THE LANDAU THEORY OF PHASE TRANSITIONS

Having made use of the ‘alloy analogy’ approach to describe fluctuations in density functional theories, a number of comments concerning its status in the general theory of condensed-matter are in order. First, it should be stressed that while in the context of phase transitions, such methodology yields an accurate description of the high temperature, homogeneous disordered state, and a reliable account of its instability at some critical transition temperature T_c , it is seriously incomplete for $T < T_c$ as the ground state is approached. Second, one should not fail to mention that there is now a fairly well-developed conceptual framework, a dynamical version of the ‘alloy analogy’, in terms of which the shortcomings of the above static version near $T \rightarrow 0$ can be understood, and even remedied.

As is well known, there are two ways of approaching the problem of phase transitions. One of these starts with a study of the ground state and seeks to determine the critical temperature T_c at which thermal fluctuations destroy the equilibrium state smoothly connected to it. Usually, at this point either some symmetry breaking order of the ground state is lost, as in a continuous phase transitions, or the system becomes an inhomogeneous mixture of coexisting phases as in the cases of the Ce α - γ , liquid-gas or other first-order transitions. The alternative to this approach is to start with the high temperature, $T > T_c$ high

symmetry, disordered phase, and investigate its stability as the temperature is lowered. This is the strategy adopted in a phenomenological Landau Theory (Landau and Lifschitz, 1980). From the point of view of first-principles calculations, the former seems easier as it involves ground state calculations. However, the ‘alloy analogy’ calculations highlighted in this review correspond to the latter. Evidently, in these the role of the CPA is to describe thermal fluctuations of various local electronic configurations and hence the KKR-CPA procedure is an appropriate tool for the study of the high-temperature, high-symmetry equilibrium states. In fact, when suitably generalized, it can be used for calculating the coefficients in the Landau expansion of the free energy (Gyorffy et al., 1989) and thereby turning the phenomenological theory into a material specific, quantitative first-principles theory.

Examining the accuracy and reliability of the calculations reviewed in Sections 7.2 and 7.3 in the light of the above remarks prompts the following observation: the electronic structure relevant to these calculations is a smeared out version of that at $T = 0$. Namely, any coherent fluctuation lasting longer than $\hbar/k_B T$ can be assumed to have been averaged to zero and hence such calculations are more forgiving than those near $T = 0$ where timescales much longer than $\hbar/k_B T_c$ need to be accounted for. Thus, the first-principles Landau Theory alluded to above can be considered a robust and efficient theory of the phase diagrams. By contrast for $T < T_c$, as T tends to 0, longer and longer timescales make their presence felt and a more accurate description of the many-electron problem becomes necessary.

A particular general shortcoming of the ‘alloy analogy’ approximation is that it cannot describe quantum fluctuations such as the zero point fluctuations of spin waves. Evidently, these can be important at and near $T = 0$. Moreover, an ensemble average of static fluctuations depicted by the ‘alloy’ configurations will, within the CPA, inevitably lead to quasi-particles with finite lifetime even at $T = 0$. Namely, the ground state is generically not that of a Fermi liquid as it mostly should be. In what follows we shall summarize briefly the current state of conceptual framework that needs to be invoked to deal with these issues.

In condensed matter at a site, an electron scatters from both the atomic nuclei and the other electrons in its vicinity. Such ‘target’ is not, in general, a static, spin-dependent electrostatic, c-number potential but a time-dependent quantum mechanical object which recoils during the scattering process. Clearly, the full complexity of scattering events produced by such ‘targets’ are not described by the static mean field theory language of the ‘alloy analogy’. However, it turns out that their essence is adequately captured by a dynamical generalization of this well tried methodology, namely the DMFT (Georges et al., 1996). Like the ‘alloy analogy’, this elegant procedure focuses on the single site nature of the many-electron problem in solids and it can be viewed as a time-dependent CPA in which the potential seen by an electron at a site changes with time during the scattering process and the averaging over configurations becomes average over all histories of such variations (Takehashi, 2002).

A remarkable consequence of introducing time-dependent one-electron potentials into the calculation is that the well-known instability of a degenerate Fermi system to sudden local perturbations (Anderson, 1967) comes into play. This

effect, which is well understood in the context of the X-ray edge-singularity (Nozieres and DeDominicis, 1969) and the Kondo (Anderson *et al.*, 1970) problems, leads to qualitatively new features in the one-electron spectra predicted by the DMFT compared with the consequences of the static CPA-based theories. The most spectacular of these is the central peak, arising from the Kondo resonance at the Fermi energy, between the upper and lower Hubbard bands, which are already evident in the static alloy analogy calculations. As physical consequences of this peak, one might mention its role in the explanation of the metal-insulator Mott transition (Georges *et al.*, 1996) and the spin-polarization Kondo cloud that screens magnetic impurities in dilute alloys (Anderson *et al.*, 1970). Indeed, it may very well be relevant to the Ce α - γ transition discussed in Section 7.3 (Held *et al.*, 2001).

Since their invention in the early 1990s, the DMFT technique (Georges *et al.*, 1996) and its cluster generalization DCA (Hettler *et al.*, 1998) have been studied intensively and have been successfully applied to many different problems in metal physics. But, while its virtues and limitations are well documented for simple tight binding model Hamiltonians, its implementation within the context of a fully first-principles theory remains an aspiration only. What has been done, repeatedly and with considerable success, is what may be called the LDA + U + DMFT method (Georges *et al.*, 1996). In these calculations, the LDA + U part is a method for generating an effective, usually a multi-band Hubbard, Hamiltonian which serves as input into a DMFT procedure, but there is rarely an effort to recalculate the LDA bands (site energies and hopping integrals) or the electron-electron interaction parameter U with the view of iterating to self-consistency. Strangely, although technically the problem appears to be difficult conceptually, thanks to the numerous analytical and numerical results mentioned above, it is relatively simple. The fluctuations to be captured by the putative theoretical framework are tunnelling between atomic-like local electronic configurations, and of these, there are only few that are degenerate in energy and hence can be the source of a Kondo-like resonance. In other words, at an atomic centre, an electron scatters from a quantum mechanical two or few level systems instead of a classical effective electrostatic potential. Scaling arguments suggest that the occurrences of such resonances are general consequences of degenerate Fermi systems being perturbed by sudden, local, quantum perturbations and their width is a new, emergent, low-energy scale $k_B T_K$ where T_K is usually referred as the ‘Kondo’ temperature (Cox and Zawadowski, 1999). From the point of view of our present concern, the importance of these results are twofold. First, this low-energy scale, which governs the behaviour of low-temperature fluctuations, has no counterpart in the static mean field theory. Second, $k_B T_K$ varies dramatically from material to material from 1 to 1000 K. Thus, there is need for a sophisticated first-principles theory which can make quantitative material specific predictions of $k_B T_K$. Clearly, if $T_K \ll T_c$ for some particular order, the high-temperature phase is well described by the ensemble of static fluctuations depicted in the ‘alloy analogy’ calculation. On the other hand, if $T_K \gg T_c$, the static calculations miss out important aspects of the physics. To highlight the burden of this remark, we note that the Curie temperatures of ferromagnets and the critical temperatures of the conventional

superconductors can be calculated fairly reliably for the majority of materials. Evidently, the challenge here is to do the same for $k_B T_K$.

9. CONCLUSIONS

This chapter has given an *ab initio* justification for the dual, localized and band-like, character of the 4f-states in the lanthanides. The SIC-LSD provided the first-principles band theory scheme allowing for this differentiation between band-like, where the gain in band formation energy dominates, and localized 4f electrons, where the gain in localization energy dominates. From this, the notion of nominal valence was developed defining the number of remaining band-like states as the valence of the lanthanide ion. These band-like states determine the bonding properties. This definition of valence turned out to be extremely useful and in Section 4, we gave numerous examples how this notion of valence contributed to a better understanding of the physical properties of the lanthanides and their compounds. In particular, the bonding properties of the lanthanides, such as the lattice constants, and their pressure behaviour could be studied without using adjustable parameters. Local magnetic moments and spectroscopic investigations provided a study of some of the properties of the localized f-states. Specifically, we found the degree of 4f localization to be similar in the light and heavy lanthanides. The one-electron SIC-LSD is shown to be an *ab initio* computational scheme consistent with all three Hund's rules.

A finite temperature generalization based on the LSIC-LSD method led to the first-principles study of the phase diagrams of the lanthanides. The study of a magnetic phase diagram for the heavy lanthanides led to the discovery of the role played by the lanthanide contraction in determining the magnetic structure of heavy lanthanides. Also, the importance of the Fermi surface webbing features in driving the magnetic order was explained. Calculating the phase diagram of the α - γ phase transition in elemental Ce allowed us to identify the entropy as the driving force in this transition. These finite temperature studies incorporated thermal fluctuations only. Finally, an outline was given on how to include dynamical, quantum, fluctuations in the present methodology.

REFERENCES

- Aerts, C.M., Strange, P., Horne, M., Temmerman, W.M., Szotek, Z., Svane, A. Phys. Rev. B 2004, **69**, 045115.
- Ahuja, R., Auluck, S., Johansson, B., Brooks, M.S.S. Phys. Rev. B 1994, **50**(8), 5147–5154.
- Alameda, J.M., Givord, D., Lemaire, R., Lu, Q., Palmer, S.B., Tasset, F. J. Phys. 1982, **43**, 133.
- Amadon, B., Biermann, S., Georges, A., Aryasetiawan, F. Phys. Rev. Lett. 2006, **96**, 066402.
- Anderson, P.W. Phys. Rev. Lett. 1967, **18**, 1049.
- Andersen, O.K. Phys. Rev. B 1975, **12**, 3060.
- Andersen, O.K., Jepsen, O., Glötzel, D. in: Bassani, F., Fumi, F., Tosi, M.P., editors. Highlights of Condensed Matter Theory, International School of Physics Enrico Fermi, Course 89, Amsterdam: North Holland; 1989, p. 59.
- Anderson, P.W., Yuval, G., Haman, D.R. Phys. Rev. B 1970, **1**, 4464.

- Andrianov, A.V. J. Magn. Magn. Mater. 1995, **140–144**, 749.
- Andrianov, A.V., Chistiakov, O.D. Phys. Rev. B 1997, **55**, 14107.
- Andrianov, A.V., Kosarev, D.I., Beskrovnyi, A.I. Phys. Rev. B 2000, **62**, 13844.
- Anisimov, V.I., Gunnarsson, O. Phys. Rev. B 1991, **43**, 7570.
- Anisimov, V.I., Aryasetiawan, F., Lichtenstein, A.I. J. Phys.: Condens. Matter 1997, **9**, 767.
- Anisimov, V.I., Zaanen, J., Andersen, O.K. Phys. Rev. B 1991, **44**, 943.
- Anisimov, V.I., Solov'yev, I.V., Korotin, M.A., Czyzyk, M.T., Sawatzky, G.A. Phys. Rev. B 1993, **48**, 16929.
- Antonov, V.N., Yaresko, A.N., Perlov, A.Y., Thalmeier, A., Fulde, P., Oppeneer, P.M., Eschrig, H. Phys. Rev. B 1998, **58**, 9752–9762.
- Arola, E., Strange, P. Appl. Phys. A 2001, **73**, 667.
- Arola, E., Strange, P., Gyroffly, B.L. Phys. Rev. B 1997, **55**, 472.
- Arola, E., Horne, M., Strange, P., Winter, H., Szotek, Z., Temmerman, W.M. Phys. Rev. B 2004, **70**, 235127.
- Aryasetiawan, F., Gunnarsson, O. Phys. Rev. B 1994, **49**, 16214.
- Aryasetiawan, F., Gunnarsson, O. Rep. Prog. Phys. 1998, **61**, 237.
- Banister, J.R., Legvold, S., Spedding, F.H. Phys. Rev. 1954, **94**, 1140.
- Becke, A.D. J. Chem. Phys. 1993, **98**, 5648.
- Beiden, S.V., Temmerman, W.M., Szotek, Z., Gehring, G.A. Phys. Rev. Lett. 1997, **79**, 3970.
- Benedict, U., Holzapfel, W.B. in: Gschneidner, K.A., Eyring, L., Lander, G.H., Choppin, G.R., editors. Handbook on the Physics and Chemistry of Rare Earths. vol. 17, Amsterdam: North-Holland; 1993, chap. 113.
- Bianconi, A., Kotani, A., Okada, K., Giorgi, R., Gargano, A., Marcelli, A., Miyahara, K. Phys. Rev. B 1988, **38**, 3433.
- Bihan, T.L., Darracq, S., Heathman, S., Benedict, U., Mattenberger, K., Vogt, O. J. Alloys Compd. 1995, **226**, 143.
- Blanter, Y.M., Kaganov, M.I., Pantsulaya, A.V., Varlamov, A.A. Phys. Rep. 1994, **245**, 159.
- Blume, M. J. Appl. Phys. 1985, **57**, 3615.
- Blume, M., Gibbs, D. Phys. Rev. B 1988, **37**, 1779.
- Blundell, S. 2001. Magnetism in Condensed Matter, Oxford: Oxford University Press.
- Bonville, P., Hammann, J., Hodges, J.A., Imbert, P., Jéhanno, G.J. Phys. Rev. Lett. 1986, **57**, 2733.
- Boothroyd, A.T., Gardiner, C.H., Lister, S.J.S., Santini, P., Noailles, B.D.R.L.D., Currie, D.B., Eccleston, R.S., Bewleya, R.I. Phys. Rev. Lett. 2001, **86**, 2082.
- Bouhemadou, A., Khenata, R., Sahnoun, M., Baltache, H., Kharoubi, M. Physica B 2005, **363**, 255.
- Brown, S.D., Strange, P., Bouchenoire, L., Zarychta, B., Thompson, P., Mannix, D., Stockton, S., Horne, M., Arola, E., Ebert, H., Szotek, Z., Temmerman, W.M., Fort, D. Phys. Rev. Lett 2007, **99**, 247401.
- Butorin, S.M., Duda, L.-C., Guo, J.-H., Wassdahl, N., Nordgren, J., Nakazawa, M., Kotani, A. J. Phys.: Condens. Matter. 1997, **9**, 8155.
- Campagna, M., Bucher, E., Wertheim, G.K., Buchanan, D.N.E., Longinotti, L.D. Phys. Rev. Lett. 1974a, **32**, 885.
- Campagna, M., Bucher, E., Wertheim, G.K., Longinotti, L.D. Phys. Rev. Lett. 1974b, **33**, 165.
- Campagna, M., Wertheim, G.K., Baer, Y. in: Ley, L., Cardona, M., editors. Photoemission in Solids. vol. II. Berlin: Springer; 1979, chap. 4.
- Ceperley, D.M., Alder, B.J. Phys. Rev. Lett. 1980, **45**, 566–569.
- Chainani, A., Kumigashira, H., Ito, T., Sato, T., Takahashi, T., Yokoya, T., Higuchi, T., Takeuchi, T., Shin, S., Sato, N.K. Phys. Rev. B 2002, **65**, 155201.
- Chantis, A.N., van Schilfgaarde, M., Kotani, T. Phys. Rev. B 2007, **76**, 165126.
- Cho, E.-J., Chung, J.-S., Oh, S.-J., Suga, S., Taniguchi, M., Kakizaki, A., Fujimori, A., Kato, H., Miyahara, T., Suzuki, T., Kasuya, T. Phys. Rev. B 1993, **47**, 3933.
- Cowan, R.D. Phys. Rev. 1967, **163**, 54.
- Cox, D.I., Zawadowski, A. Exotic Kondo Effects in Metals, London: Taylor and Francis; 1999.
- Cracknell, A.P., Wong, K.C. The Fermi Surface, Oxford: Clarendon; 1973.
- Crisan, V., Entel, P., Ebert, H., Akai, H., Johnson, D.D., Staunton, J.B. Phys. Rev. B 2002, **66**(1), 014416.
- Croft, M., Jayaraman, A. Solid State Commun. 1980, **35**, 203.

- Crowe, S.J., Dugdale, S.B., Major, Z., Alam, M.A., Duffy, J.A., Palmer, S.B. *Europhys. Lett.* 2004, **65**, 235.
- Debray, D., Werner, A., Decker, D.L., Loewenhaupt, M., Holland-Moritz, E. *Phys. Rev. B* 1982, **25**, 3841.
- Degiorgi, L., Bacsá, W., Wachter, P. *Phys. Rev. B* 1990, **42**, 530.
- Degiorgi, L., Teraoka, S., Compagnini, G., Wachter, P. *Phys. Rev. B* 1993, **47**, 5715.
- Delin, A., Fast, L., Johansson, B., Wills, J.M., Eriksson, O. *Phys. Rev. Lett.* 1997, **79**(23), 4637–4640.
- Delin, A., Fast, L., Johansson, B., Eriksson, O., Wills, J.M. *Phys. Rev. B* 1998, **58**, 4345–4351.
- Dimmock, J.O., Freeman, A.J. *Phys. Rev. Lett.* 1964, **13**(25), 750–752.
- Diviš, M., Ruzs, J. *J. Magn. Magn. Mater.* 2005, **290–291**, 1015.
- Döbrich, K.M., Bihlmayer, G., Starke, K., Prieto, J.E., Rossnagel, K., Koh, H., Rotenberg, E., Blügel, S., Kaindl, G. *Phys. Rev. B* 2007, **76**, 035123.
- Dreizler, R.M., Gross, E.K.U. *Density Functional Theory*, Berlin: Springer-Verlag; 1990.
- Duan, C.-G., Sabirianov, R.F., Mei, W.N., Dowben, P.A., Jaswal, S.S., Tsymbal, E.Y. *J. Phys.: Condens. Matter* 2007, **19**, 315220.
- Dugdale, S.B., Fretwell, H.M., Alam, M.A., Kontrym-Sznajd, G., West, R.N., Badrzadeh, S. *Phys. Rev. Lett.* 1997, **79**(5), 941–944.
- Duthie, J.C., Pettifor, D.G. *Phys. Rev. Lett.* 1977, **38**(10), 564–567.
- Eriksson, O., Brooks, M.S.S., Johansson, B. *J. Less Common. Met.* 1990a, **158**, 207.
- Eriksson, O., Brooks, M.S.S., Johansson, B. *Phys. Rev. B* 1990b, **41**, 7311–7314.
- Eriksson, O., Brooks, M.S.S., Johansson, B., Albers, R.C., Boring, A.M. *J. Appl. Phys.* 1991, **69**, 5897–5902.
- Eriksson, O., Ahuja, R., Ormeci, A., Trygg, J., Hjortstam, O., Söderlind, P., Johansson, B., Wills, J.M. *Phys. Rev. B* 1995, **52**, 4420.
- Eschrig, H., Sargolzaei, M., Koepernik, K., Richter, M. *Europhys. Lett.* 2005, **72**, 611–617.
- Eyring, L. in: Gschneidner Jr., K.A., Eyring, L., editors. *Handbook on the Physics and Chemistry of Rare Earths*. vol. 3. Amsterdam: North-Holland; 1978, chap. 9.
- Faulkner, J.S. *Prog. Mater. Sci* 1982, **27**, 1.
- Faulkner, J.S., Stocks, G.M. *Phys. Rev. B* 1981, **23**, R5628.
- Feynman, R.P. *Phys. Rev.* 1955, **97**, 660.
- Filip, A.T., LeClair, P., Smitts, C.J.P., Kohlhepp, J.T., Swagten, J.M., Koopmans, B., de Jonge, W.J.M. *Appl. Phys. Lett.* 2002, **81**, 1815.
- Freeman, A.J., Min, B.L., Norman, M.R. in: Eyring Jr., K.A.L., Hüfner, S., editors. *Handbook on the Physics and Chemistry of Rare Earths*. vol. 10, pp. 165–229. Amsterdam Elsevier; 1987.
- Fretwell, H.M., Dugdale, S.B., Alam, M.A., Hedley, D.C.R., Rodriguez-Gonzalez, A., Palmer, S.B. *Phys. Rev. Lett.* 1999, **82**(19), 3867–3870.
- Fujimori, A. *Phys. Rev. B* 1983, **28**, 4489.
- Gardiner, C.H., Boothroyd, A.T., Pattison, P., McKelvy, M.J., McIntyre, G.J., Lister, S.J.S. *Phys. Rev. B* 2004, **70**, 024415.
- Gasiorowicz, S. *Quantum Physics*, New York: John Wiley and Sons; 1974.
- Georges, A., Kotliar, G., Krauth, W., Rozenberg, M.J. *Rev. Mod. Phys.* 1996, **68**, 13.
- Gerward, L., Olsen, J.S., Petit, L., Vaitheeswaran, G., Kanchana, V., Svane, A. *J. Alloys Compd.* 2005, **400**, 56.
- Ghosh, D.B., De, M., De, S.K. *Phys. Rev. B* 2003, **67**, 035118.
- Godby, R.W., Schlüter, M., Sham, L.J. *Phys. Rev. B* 1988, **37**, 10159.
- Gotsis, H.J., Mazin, I.I. *Phys. Rev. B* 2003, **68**, 224427.
- Gschneidner Jr., K.A. *J. Less-Common Met.* 1969, **17**, 13.
- Gschneidner Jr., K.A. *J. Less-Common. Met.* 1971, **25**, 405.
- Gschneidner Jr., K.A. *J. Alloys Compds.* 1993, **192**, 1.
- Gyorffy, B.L., Stott, M.J. in: Fabian, D.J., Watson, L.M., editors. *Band Structure Spectroscopy of Metals and Alloys*, New York: Academic Press; 1973.
- Gyorffy, B.L., Stocks, G.M. in: Phariseau, P., Gyorffy, B.L., Scheire, L., editors. *Electrons in Disordered Metals and at Metallic Surfaces*, vol. 42 of NATO 'ASI Series Physics B', New York: Plenum Press; 1978.
- Gyorffy, B.L., Pindor, A.J., Staunton, J., Stocks, G.M., Winter, H. *J. Phys. F-Met. Phys.* 1985, **15**(6), 1337–1386.
- Gyorffy, B.L., Johnson, D.D., Pinski, F.J., Nicholson, D.M., Stocks, G.M. in: Stocks, G.M., Gonis, A., editors. *Alloy Phase Stability*, pp. 421–468. Dordrecht, Kluwer Academic Publisher; 1989.

- Hanyu, T., Ishii, H., Yanagihara, M., Kamada, T., Miyahara, T., Kato, H., Naito, K., Suzuki, S., Ishii, T. *Solid State Commun.* 1985, **56**, 381.
- Harmon, B.N., Antropov, V.P., Lichtenstein, A.I., Solovyev, I.V., Anisimov, V.I. *J. Phys. Chem. Solids* 1995, **56**, 1521–1524.
- Hassan, A.K., Levy, L.P., Darie, C., Strobel, P. *Phys. Rev. B* 2003, **67**, 214432.
- Haule, K., Oudovenko, V., Savrasov, S.Y., Kotliar, G. *Phys. Rev. Lett.* 2005, **94**, 036401.
- Havinga, E.E., Buschow, K.H.J., van Daal, H.J. *Solid State Commun.* 1973, **13**, 621.
- Hedin, L. *Phys. Rev. A* 1965, **139**, 796.
- Heinemann, M., Temmerman, W.M. *Phys. Rev. B* 1994, **49**(6), 4348–4351.
- Held, K. *Adv. Phys.* 2007, **56**, 829.
- Held, K., McMahan, A.K., Scalettar, R.T. *Phys. Rev. Lett.* 2001, **87**, 276404.
- Hettler, M.H., Tahvildar-Zadeh, A.N., Jarrell, M., Pruschke, T., Krishnamurthy, H.R. *Phys. Rev. B* 1998, **58**, 7475.
- Hill, J.P., McMorro, D.F. *Acta Crystallogr. A* 1996, **52**, 236.
- Hirosaki, N., Ogata, S., Kocer, C. *J. Alloys Compd.* 2003, **351**, 31.
- Hoekstra, H.R., Gingerich, K.A. *Science* 1964, **146**, 1163.
- Hohenberg, P., Kohn, W. *Phys. Rev.* 1964, **136**, B864–B871.
- Holland-Moritz, N. *Z. Phys. B: Condens. Matter* 1992, **89**, 285.
- Horne, M., Strange, P., Temmerman, W.M., Szotek, Z., Svane, A., Winter, H. *J. Phys.: Condens. Matter* 2004, **16**, 5061.
- Hubbard, J. *Proc. R. Soc. London, Ser. A* 1963, **276**, 238.
- Hubbard, J. *Proc. R. Soc. London, Ser. A* 1964a, **277**, 237.
- Hubbard, J. *Proc. R. Soc. London, Ser. A* 1964b, **281**, 401.
- Hughes, I.D., Däne, M., Ernst, A., Hergert, W., Lüders, M., Poulter, J., Staunton, J.B., Svane, A., Szotek, Z., Temmerman, W.M. *Nature* 2007, **446**(7136), 650–653.
- Hulliger, F. in: Gschneidner Jr., K.A., Eyring, L., editors. *Handbook on the Physics and Chemistry of Rare Earths*. vol. 4. Amsterdam: North-Holland; 1979, chap. 33.
- Hybertsen, M.S., Louie, S.G. *Phys. Rev. B* 1986, **34**, 5390.
- Iandelli, A., Franceschi, E. *J. Less-Common. Met.* 1973, **30**, 211.
- Iandelli, A., Olcese, G.L., Palenzona, A. *J. Less-Common. Met.* 1980, **76**, 317.
- Ito, T., Chainani, A., Takahashi, H.K.T., Sato, N.K. *Phys. Rev. B* 2002, **65**, 155202.
- Jackson, C. *Phys. Rev.* 1969, **178**, 949.
- Jayaraman, A. in: Gschneidner Jr., K.A., Eyring, L., editors. *Handbook on the Physics and Chemistry of Rare Earths*. vol. 1. Amsterdam: North-Holland; 1978, chap. 9.
- Jayaraman, A., Singh, A.K., Chatterjee, A., Devi, S.U. *Phys. Rev. B* 1974, **9**, 2513.
- Jayaraman, A. in: Gschneidner Jr., K.A., Eyring, L., editors. *Handbook on the Physics and Chemistry of Rare Earths*. vol. 2. Amsterdam: North-Holland; 1979, chap. 20.
- Jensen, J., Mackintosh, A.K. *Rare Earth Magnetism*, Oxford: Clarendon; 1991.
- Johansson, B., Rosengren, A. *Phys. Rev. B* 1975, **11**, 2836–2857.
- Johnson, D.D., Nicholson, D.M., Pinski, F.J., Gyorffy, B.L., Stocks, G.M. *Phys. Rev. Lett.* 1986, **56**(19), 2088–2091.
- Johansson, B., Abrikosov, I.A., Aldén, M., Ruban, A.V., Skriver, H.L. *Phys. Rev. Lett.* 1995, **74**, 2335.
- Jones, R.O., Gunnarsson, O. *Rev. Mod. Phys.* 1989, **61**, 689.
- Joyce, J.J., Andrews, A.B., Arko, A.J., Bartlett, R.J., Blythe, R.I.R., Olson, C.G., Benning, P.J., Canfield, P. C., Poirier, D.M. *Phys. Rev. B* 1996, **54**, 17515.
- Kakehashi, Y. *Phys. Rev. B* 2002, **66**, 104428.
- Karnatak, R.C., Esteva, J.-M., Dexpert, H., Gasgnier, M., Caro, P.E., Albert, L. *Phys. Rev. B* 1987, **36**, 1745.
- Kasuya, T. *Prog. Theor. Phys.* 1956, **16**.
- Kasuya, T. *J. Phys. Soc. Japan* 1994, **63**, 843.
- Keeton, S.C., Loucks, T.L. *Phys. Rev.* 1968, **168**, 672.
- Kern, S., Loong, C.-K., Faber Jr, J.Jr, Lander, G.H. *Solid State Commun.* 1984, **49**, 295.
- Kittel, C. *Introduction to Solid State Physics* 6th edition New York: John Wiley and Sons; 1986.
- Koelling, D.D., Boring, A.M., Wood, J.H. *Solid State Commun.* 1983, **47**, 227.
- Kohn, W., Rostoker, N. *Phys. Rev.* 1954, **94**, 1111.

- Kohn, W., Sham, L.J. *Phys. Rev.* 1965, **140**, A1133–A1138.
- Korringa, J. *Physica* 1947, **13**, 392.
- Kotliar, G., Savrasov, S.Y., Haule, K., Oudovenko, V.S., Parcollet, O., Marianetti, C.A. *Rev. Mod. Phys.* 2006, **78**, 865.
- Krill, G., Ravet, M.F., Kappler, J.P., Abadli, L., Leger, J.M., Yacoubi, N., Loriers, C. *Solid State Commun.* 1980, **33**, 351.
- Krutzen, B.C.H., Springelkamp, F. *J. Phys.: Condens. Matter* 1989, **1**, 8369.
- Kübler, J. *International Series of Monographs on Physics*, vol. 106 Oxford University Press; 2000.
- Kübler, J., Eyert, V. in: Cahn, R.W., Haasen, P., Kramer, E.J., editors. *Materials Science and Technology*. vol. 3a, p. 1. New York: Weinheim; 1993.
- Kumar, R.S., Cornelius, A.L., Svane, A., Vaitheeswaran, G., Kanchana, V., Bauer, E.D., Hu, M., Nicol, F. *Phys. Rev. B* 2008, **78**, 075117.
- Kurz, P., Bihlmayer, G., Blügel, S. *J. Phys. Condens. Matter* 2002, **14**, 6353.
- Lægsgaard, J., Svane, A. *Phys. Rev. B* 1998, **58**, 12817.
- Lal, H.B., Gaur, K. *J. Mater. Sci.* 1988, **23**, 919.
- Landau, L.D., Lifschitz, E.M. *Course of Theoretical Physics*, vol. 5, 3rd edition. Oxford: Pergamon; 1980.
- Lang, J.K., Baer, Y., Cox, P.A. *J. Phys. F* 1981, **11**, 121.
- Langford, H.D., Temmerman, W.M., Gehring, G.A. *J. Phys.: Condens. Matter* 1990, **2**, 559.
- Larson, P., Lambrecht, W.R.L., Chantis, A.N., van Schilfgaarde, M. *Phys. Rev. B* 2007, **75**, 045114.
- Lebegue, S., Santi, G., Svane, A., Bengone, O., Katsnelson, M.I., Lichtenstein, A.I., Eriksson, O. *Phys. Rev. B* 2005, **72**, 245102.
- Lebegue, S., Svane, A., Katsnelson, M.I., Lichtenstein, A.I., Eriksson, O. *Phys. Rev. B* 2006a, **74**, 045114.
- Lebegue, S., Svane, A., Katsnelson, M.I., Lichtenstein, A.I., Eriksson, O. *J. Phys.: Condens. Matter* 2006b, **18**, 6329.
- LeClair, P., Ha, J.K., Swagten, H.J.M., van de Vin, C.H., Kohlhepp, J.T., de Jonge, W.J.M. *J. Appl. Phys.* 2002, **80**, 625.
- Léger, J.M. *Physica B* 1993, **190**, 84.
- Leger, J.M., Aimonino, P., Loriers, J., Dordor, P., Coqblin, B. *Phys. Lett.* 1980, **80A**, 325.
- Léger, J.M., Epain, R., Loriers, J., Ravot, D., Rossat-Mignod, J. *Phys. Rev. B* 1983, **28**, 7125.
- Léger, J.M., Ravot, D., Rossat-Mignod, J. *J. Phys. C* 1984, **17**, 4935.
- Léger, J.M., Oki, K., Rossat-Mignod, J., Vogt, O. *J. Phys.* 1985, **46**, 889.
- Léger, J.M., Redon, A.M. *J. Less-Common. Met.* 1989, **156**, 137.
- Lehner, C., Richter, M., Eschrig, H. *Phys. Rev. B* 1998, **58**, 6807.
- Li, D.X., Oyamada, A., Hashi, K., Haga, Y., Matsumara, T., Shida, H., Suzuki, T., Kasuya, T., Dönni, A., Hulliger, F. *J. Magn. Mater.* 1995, **140–144**, 1169.
- Lichtenstein, A.I., Anisimov, V.I., Zaanen, J. *Phys. Rev. B* 1995, **52**, R5467–5470.
- Lichtenstein, A.I., Katsnelson, M.I. *Phys. Rev. B* 1998, **57**, 6884.
- Lifshitz, I.M. *Sov. Phys. JETP* 1960, **11**, 1130.
- Lindgren, I. *Int. J. Quantum Chem.* 1971, **5**, 411.
- Ling, M.F., Staunton, J.B., Johnson, D.D. *Europhys. Lett.* 1994, **25(8)**, 631–636.
- Lloyd, P., Best, P.R. *J. Phys. C-Solid State Phys.* 1975, **8**, 3752.
- Loschen, C., Carrasco, J., Neyman, K.M., Illas, F. *Phys. Rev. B* 2007, **75**, 035115.
- Lovesey, S.W., Collins, S.P. *X-ray Scattering and Absorption by Magnetic Materials*, Oxford: Clarendon; 1996.
- Lüders, M., Ernst, A., Däne, M., Szotek, Z., Svane, A., Ködderitzsch, D., Hergert, W., Györffy, B.L., Temmerman, W. *Phys. Rev. B* 2005, **71(20)**, 205109.
- Mahan, G.D. *Many-Particle Physics*, New York: Plenum Press; 1990.
- Marabelli, F., Wachter, P. *Phys. Rev. B* 1987, **36**, 1238.
- Martin, R.M. *Electronic Structure: Basic Theory and Practical Methods*, Cambridge: Cambridge University Press 2004.
- Mattocks, P.G., Young, R.C. *J. Phys. F* 1977, **7**, 1219.
- McMahan, A.K., Held, K., Scalettar, R.T. *Phys. Rev. B* 2003, **67**, 075108.
- Mermin, N.D. *Phys. Rev.* 1965, **137**, A1441.
- Messiah, A. *Quantum Mechanics*, Amsterdam North Holland; 1965.
- Milstein, F., Robinson, L.B. *Phys. Rev.* 1967, **159**, 466.

- Mirone, A. *Eur. J. Phys. B: Condens. Matter Complex Syst.* 2005, **47**, 509.
- Moewes, A., Ederer, D.L., Grush, M.M., Callcott, T.A. *Phys. Rev. B* 1999, **59**, 5452.
- Mohn, P., Persson, C., Blaha, P., Schwarz, K., Novak, P., Eschrig, H. *Phys. Rev. Lett.* 2001, **87**, 196401.
- Mooder, J.S., Meservey, R., Hao, X. *Phys. Rev. Lett.* 1993, **70**, 853.
- Mori, N., Okayama, Y., Takahashi, H., Haga, Y., Suzuki, T. *Physica B* 1993, **186–188**, 444.
- Moriya, T. *Solid State Sciences*, vol. 29, Springer Series Berlin and New York: Springer; 1981.
- Nicholson, D.M.C., Stocks, G.M., Wang, Y., Szotek, Z., Temmerman, W.M. *Phys. Rev. B* 1994, **50**, 14686.
- Nordström, L., Mavromaras, A. *Europhys. Lett.* 2000, **49**, 775.
- Nozieres, P., DeDominicis, C. *Phys. Rev.* 1969, **178**, 1097.
- Ogasawara, H., Kotani, A., Okada, K., Thole, B.T. *Phys. Rev. B* 1991, **43**, 854.
- Oh, S.-J., Allen, J.W. *Phys. Rev. B* 1984, **29**, 589.
- Ono, S., Hui, F.L., Despault, J.G., Calvert, L.D., Taylor, J.B. *J. Less-Common. Met.* 1971, **25**, 287.
- Oppeneer, P.M., Antonov, V.N., Yaresko, A.N., Perlov, A.Y., Eschrig, H. *Phys. Rev. Lett.* 1997, **78**, 4079.
- Ott, H.R., Rudigier, H., Hulliger, F. *Solid State Commun.* 1985, **55**, 113.
- Oyamada, A., Hashi, K., Maegawa, S., Goto, T., Li, D.X., Suzuki, T., Dönni, A., Hulliger, F. *Physica B* 1994, **199 & 200**, 42.
- Pederson, M.R., Heaton, R.A., Lin, C.C. *J. Chem. Phys.* 1984, **80**, 1972.
- Pederson, M.R., Heaton, R.A., Lin, C.C. *J. Chem. Phys.* 1985, **82**, 2688.
- Perdew, J.P., Zunger, A. *Phys. Rev. B* 1981, **23**, 5048.
- Perdew, J.P., Wang, Y. *Phys. Rev. B* 1992, **45**, 13244–13249.
- Petit, L., Svane, A., Szotek, Z., Temmerman, W.M. *Phys. Rev. B* 2005, **72**, 205118.
- Petit, L., Svane, A., Szotek, Z., Temmerman, W.M. in: Fanciulli, M., Scarel, G., editors. *Topics in Applied Physics*, vol. 106, p. 331. Berlin Heidelberg: Springer-Verlag; 2007.
- Petukhov, A.G., Mazin, I.I., Chioncel, L., Lichtenstein, A.I. *Phys. Rev. B* 2003, **67**, 153106.
- Pickett, W.E., Koelling, D.D., Freeman, A.J. *Phys. Rev. B* 1981, **23**, 1266.
- Pollak, R.A., Holtzberg, F., Freeouf, J.L., Eastman, D.E. *Phys. Rev. Lett.* 1974, **33**, 820.
- Prokofiev, A.V., Shelyakh, A.I., Melekh, B.T. *J. Alloys Compd.* 1996, **242**, 41.
- Razee, S.S.A., Staunton, J.B., Szunyogh, L., Gyorffy, B.L. *Phys. Rev. Lett.* 2002, **88**(14), 147201.
- Rhyne, J.J., McGuire, T. *IEEE Trans. Magn.* 1972, **MAG-8**, 105.
- Richter, M., Eschrig, H. *Solid State Commun.* 1989, **72**, 263.
- Rinke, P., Scheffler, M., Qteish, A., Winkelkemper, M., Bimberg, D., Neugebauer, J. *Appl. Phys. Lett.* 2006, **89**, 161919.
- Robinson, R.A., Purwanto, A., Kohgi, M., Canfield, P.C., Kamiyami, T., Ishigaki, T., Lynn, J.W., Erwin, R., Peterson, E., Movshovich, R. *Phys. Rev. B* 1994, **50**, 9595.
- Ruderman, M.A., Kittel, C. *Phys. Rev.* 1954, **96**, 99.
- Sakai, O., Shimuzi, Y., Kaneta, Y. *J. Phys. Soc. Jpn.* 2005, **74**, 2517.
- Sakai, O., Shimuzi, Y. *J. Phys. Soc. Jpn.* 2007, **76**, 044707.
- Sakon, T., Sato, N., Oyamada, A., Takeda, N., Suzuki, T., Komatsubara, T. *J. Phys. Soc. Jpn.* 1992, **61**, 2209.
- Sandratsakii, L.M., Kübler, J. *Europhys. Lett* 1993, **23**, 661.
- Scarel, G., Svane, A., Fanciulli, M. in: Fanciulli, M., Scarel, G., editors. *Topics in Applied Physics*, vol. 106, p. 1. Berlin Heidelberg: Springer-Verlag; 2007.
- Schirber, J.E., Schmidt, F.A., Harmon, B.N., Koelling, D.D. *Phys. Rev. Lett.* 1976, **36**(8), 448–450.
- Schüßler-Langeheine, C., Weschke, E., Mazumdar, C., Meier, R., Grigoriev, A.Y., Kaindl, G., Sutter, C., Abernathy, D., Grübel, G., Richter, M. *Phys. Rev. Lett.* 2000, **84**(24), 5624–5627.
- Shirotani, I., Hayashi, J., Yamanashi, K., Hirano, K., Adachi, T., Ishimatsu, N., Shimomura, O., Kikegawa, T. *Physica B* 2003, **334**, 167.
- Sidorov, V.A., Stepanov, N.N., Khvostantsev, L.G., Tsiok, O.B., Golubkov, A.V., Oskotski, V.S., Smirnov, I.A. *Semicond. Sci. Technol.* 1989, **4**, 286.
- Silva, J.L.F.D., Ganduglia-Pirovano, M.V., Sauer, J., Bayer, V., Kresse, G. *Phys. Rev. B* 2007, **75**, 045121.
- Singh, D.J. *Phys. Rev. B* 1991, **44**(14), 7451–7454.
- Sinha, S.K. in: Gschneidner Jr., K.A., Eyring, L., editors. *Handbook on the Physics and Chemistry of Rare Earths*. vol. 1. Amsterdam, New York, Oxford: North-Holland; 1978, chap. 7.
- Skorodumova, N.V., Ahuja, R., Simak, S.I., Abrikosov, I.A., Johansson, B., Lundqvist, B.I. *Phys. Rev. B* 2001, **64**, 115108.

- Skriver, H.L. *Solid-State Sciences*, vol. 41, Springer Series Berlin: Springer; 1983a.
- Skriver, H.L. in: Sinha, S.P., editor. *Systematics and Properties of the Lanthanides*, p. 213. Dordrecht: Reidel; 1983b.
- Slater, J.C. *Phys. Rev.* 1951, **81**, 385.
- Sondhelm, S.A., Young, R.C. *J. Phys. F* 1977, **15**, L261.
- Soven, P. *Phys. Rev.* 1967, **156**, 809.
- Staunton, J.B. *Rep. Prog. Phys.* 1994, **57**, 1289.
- Staunton, J.B., Gyorffy, B.L. *Phys. Rev. Lett.* 1992, **69**, 371.
- Staunton, J., Gyorffy, B.L., Pindor, A.J., Stocks, G.M., Winter, H. *J. Phys. F-Met. Phys.* 1985, **15**(6), 1387–1404.
- Staunton, J., Gyorffy, B.L., Stocks, G.M., Wadsworth, J. *J. Phys. F-Met. Phys.* 1986, **16**(11), 1761–1788.
- Staunton, J.B., Ling, M.F., Johnson, D.D. *J. Phys.-Condens. Matter* 1997, **9**(6), 1281–1300.
- Staunton, J.B., Ostanin, S., Razee, S.S.A., Gyorffy, B.L., Szunyogh, L., Ginatempo, B., Bruno, E. *Phys. Rev. Lett.* 2004, **93**(25), 257204.
- Staunton, J.B., Szunyogh, L., Buruzs, A., Gyorffy, B.L., Ostanin, S., Udvardi, L. *Phys. Rev. B* 2006, **74**(14), 144411.
- Sticht, J., Kübler, J. *Solid State Commun.* 1985, **53**, 529.
- Stocks, G.M., Winter, H. *Zeitschrift für Physik B-Condens. Matter* 1982, **46**(2), 95–98.
- Stocks, G.M., Winter, H. in: Phariseau, P., Temmerman, W.M., editors. *The Electronic Structure of Complex Systems*. Vol. NATO ASI Series Physics B113, New York: Plenum Press; 1984.
- Stocks, G.M., Temmerman, W.M., Gyorffy, B.L. *Phys. Rev. Lett.* 1978, **41**(5), 339–343.
- Strange, P. *Relativistic Quantum Physics*, Cambridge: Cambridge University Press; 1998.
- Strange, P., Staunton, J., Gyorffy, B.L. *J. Phys. C-Solid State Phys.* 1984, **17**(19), 3355–3371.
- Strange, P., Svane, A., Temmerman, W.M., Szotek, Z., Winter, H. *Nature* 1999, **399**, 756–758.
- Svane, A. *Phys. Rev. B* 1995, **51**(12), 7924–7926.
- Svane, A. *Phys. Rev. B* 1996, **53**, 4275.
- Svane, A., Szotek, Z., Temmerman, W.M., Winter, H. *Solid State Commun.* 1996, **102**, 473.
- Svane, A., Trygg, J., Johansson, B., Eriksson, O. *Phys. Rev. B* 1997, **56**, 7143–7148.
- Svane, A., Szotek, Z., Temmerman, W.M., Lægsgaard, J., Winter, H. *J. Phys.: Condens. Matter* 1998, **10**, 5309.
- Svane, A., Temmerman, W.M., Szotek, Z. *Phys. Rev. B* 1999, **59**, 7888.
- Svane, A., Temmerman, W.M., Szotek, Z., Petit, L., Strange, P., Winter, H. *Phys. Rev. B* 2000, **62**, 13394.
- Svane, A., Strange, P., Temmerman, W.M., Szotek, Z., Winter, H., Petit, L. *Phys. Stat. Sol. (b)* 2001, **223**, 105.
- Svane, A., Santi, G., Szotek, Z., Temmerman, W.M., Strange, P., Horne, M., Vaitheeswaran, G., Kanchana, V., Petit, L. *Phys. Stat. Sol. (b)* 2004, **241**, 3185.
- Svane, A., Kanchana, V., Vaitheeswaran, G., Santi, G., Temmerman, W.M., Szotek, Z., Strange, P., Petit, L. *Phys. Rev. B* 2005, **71**, 045119.
- Syassen, K. *Physica B* 1986, **139**, 277.
- Szotek, Z., Gyorffy, B.L., Stocks, G.M., Temmerman, W.M. *J. Phys. F-Met. Phys.* 1984, **14**(11), 2571–2599.
- Takeda, N., Tanaka, K., Kagawa, M., Oyamada, A., Sato, N., Sakatsumi, S., Aoki, H., Suzuki, T., Komatsubara, T. *J. Phys. Soc. Jpn.* 1993, **62**, 2098.
- Tanaka, S., Ogasawara, H., Okada, K., Kotani, A. *J. Phys. Soc. Jpn.* 1995, **64**, 2225.
- Taylor, J. *Scattering Theory*, New York: Wiley; 1972.
- Taylor, K.N.R., Darby, M.I. *Physics of Rare Earth Solids*, London: Chapman and Hall; 1972.
- Temmerman, W.M., Sterne, P.A. *J. Phys.: Condens. Matter* 1990, **2**, 5529.
- Temmerman, W.M., Szotek, Z., Winter, H. *Phys. Rev. B* 1993, **47**, 1184–1189.
- Temmerman, W.M., Svane, A., Szotek, Z., Winter, H. in: Dobson, J.F., Vignale, G., Das, M.P., editors. *Electronic Density Functional Theory: Recent Progress and New Directions*, p. 327. New York: Plenum; 1998.
- Temmerman, W.M., Szotek, Z., Svane, A., Strange, P., Winter, H., Delin, A., Johansson, B., Eriksson, O., Fast, L., Wills, J.M. *Phys. Rev. Lett.* 1999, **83**, 3900.
- Torumba, D., Vanhoof, V., Rots, M., Cottenier, S. *Phys. Rev. B* 2006, **74**, 014409.
- Trygg, J., Johansson, B., Eriksson, O., Wills, J.M. *Phys. Rev. Lett.* 1995, **75**, 2871–2874.

- Tsiok, O.B., Sidorov, V.A., Bredikhin, V.V., Khvostantsev, L.G., Golubkov, A.V., Smirnov, I.A. *Solid State Commun.* 1991, **79**, 227.
- Turek, I., Kudrnovský, J., Bihlmayer, G., Blügel, S. *J. Phys. Condens. Matter* 2003, **15**, 2771.
- Ufuktepe, Y., Kimura, S., Kinoshita, T., Nath, K.G., Kumigashira, H., Takahashi, T., Matsumura, T., Suzuki, T., Ogasawara, H., Kotani, A. *J. Phys. Soc. Jpn.* 1998, **67**(6), 2018–2026.
- Vaitheeswaran, G., Petit, L., Svane, A., Kanchana, V., Rajagopalan, M. *J. Phys.: Condens. Matter* 2004, **16**, 4429.
- van Schilfhaarde, M., Kotani, T., Faleev, S. *Phys. Rev. B* 2006a, **74**, 245125.
- van Schilfhaarde, M., Kotani, T., Faleev, S. *Phys. Rev. Lett.* 2006b, **96**, 226402.
- Vedel, I., Redon, A.M., Rossat-Mignod, J., Vogt, O., Léger, J.M. *J. Phys. C* 1986, **19**, 6297.
- Vedel, I., Redon, A.M., Rossat-Mignod, J., Vogt, O., Léger, J.M. *J. Phys. C* 1987, **20**, 3439.
- Villars, P., Calvert, L.D. in: *Pearson's Handbook of Crystallographic Data for Intermetallic Phases* 2nd edition. Ohio: ASM International; 1991.
- von Barth, U., Hedin, L. *J. Phys. C: Sol. State Phys.* 1972, **5**, 1629–1642.
- Vosko, S.H., Wilk, L., Nusair, M. *Can. J. Phys.* 1980, **58**, 1200–1211.
- Wachter, P. in: Gschneidner Jr., K.A., Eyring, L., editors. *Handbook on the Physics and Chemistry of Rare Earths*. vol. 19. Amsterdam, New York, Oxford: North-Holland; 1993, chap. 132.
- Wang, B.Y., Gabe, E.J., Calvert, L.D., Taylor, J.B. *Acta Crystallogr. B* 1977, **33**, 131.
- Werner, A., Hochheimer, H.D., Jayaraman, A. *Solid State Commun.* 1981, **38**, 325.
- Werner, A., Hochheimer, H.D., Meng, R.L., Bucher, E. *Phys. Lett.* 1983, **97A**, 207.
- Worledge, D.C., Geballe, T.H. *J. Appl. Phys.* 2000, **88**, 5277.
- Wuilloud, E., Delley, B., Schneider, W.-D., Baer, Y. *Phys. Rev. Lett.* 1984, **53**, 202.
- Wulff, M., Lonzarich, G.G., Fort, D., Skriver, H.L. *Europhys. Lett.* 1988, **7**, 629.
- Wyckoff, R.W.G. *Crystal Structures* 1968, vol. 1. New York: Interscience; 1968.
- Yosida, K. *Phys. Rev.* 1957, **106**, 893.
- Young, R.C., Jordan, R.G., Jones, D.W. *Phys. Rev. Lett.* 1973, **31**, 1473.
- Zimmer, H.G., Takemura, K., Syassen, K., Fischer, K. *Phys. Rev. B* 1984, **29**, 2350.
- Zölfl, M.B., Nekrasov, I.A., Pruschke, T., Anisimov, V.I., Keller, J. *Phys. Rev. Lett.* 2001, **87**, 276403.
- Zunger, A., Perdew, J.P., Oliver, G.L. *Sol. State Commun.* 1980, **34**, 933.
- Zwicky, G. *Adv. Phys.* 1992, **41**, 203–302.

Perovskite-Type Aluminates and Gallates

L. Vasylechko*, A. Senyshyn*[†], and U. Bismayer[‡]

In memory of Professor Andrii O. Matkovskii

Contents	List of Symbols and Abbreviations	114
	1. Introduction	114
	2. Aluminates	116
	2.1 Formation and preparation	116
	2.2 Crystal structure	125
	2.3 Solid solutions based on RAIO_3 perovskite-type compounds	161
	2.4 Comparative analysis of RAIO_3 structures	191
	2.5 Phase transitions and thermal expansion of RAIO_3 perovskites	207
	2.6 Dielectric properties of rare earth aluminates	216
	3. Gallates	224
	3.1 Formation and preparation	224
	3.2 Crystal structure of RGaO_3	228
	3.3 Solid solutions based on RGaO_3 compounds	248
	3.4 Room temperature crystal structures of RGaO_3 and stoichiometric solid solutions: Patterns of consistence	268
	3.5 Stability of the perovskite structure in rare earth gallates	271
	3.6 Phase transitions and thermal expansion	275
	3.7 Dielectric properties of rare earth gallates	280
	Acknowledgements	284
	References	284

* Semiconductor Electronics Department, Lviv Polytechnic National University, 79013 Lviv, Ukraine

[†] Institute of Material Science, Darmstadt University of Technology, D-64297, Darmstadt, Germany

[‡] Institute of Mineralogy and Petrography, Hamburg University, Grindelallee 48, 20146 Hamburg, Germany

List of Symbols and Abbreviations

CMR	colossal magnetoresistance
CN	coordination number
CVD	chemical vapour deposition
DTA/DSC	differential thermal analysis/differential scanning calorimetry
FZ	floating zone
HP	high pressure
HRPD	high-resolution powder diffraction
HT	high temperature
HTSC	HT superconductor
LT	low temperature
OBI	image plate detector 'Ortsfest auslesbarer Bildplattendetektor' installed at powder diffractometer (beamline B2, HASYLAB/DESY)
RT	room temperature
SC	single crystal
S.G.	space group
SR	synchrotron radiation
TEC	thermal expansion coefficient
$a, b, c, \alpha, \beta, \gamma$	unit cell dimensions (a, b, c in Å) and angles (α, β, γ in degrees)
x, y, z	fractional coordinates of atoms in the unit cell
B_{iso}	isotropic displacement parameters of atoms, $B_{\text{iso}} = 8\pi^2 u^2_{\text{iso}}$
B_{11}, \dots, B_{23}	components of harmonic tensor representing anisotropic displacement parameters of atoms
a_p, b_p, c_p, V_p	lattice parameters and cell volume, normalized to the perovskite-like cell. Depending on the structure, these are defined as follows:
rhombohedral $R\bar{3}c$ structure:	$a_p = a_r/\sqrt{2}, c_p = c_r/\sqrt{12}, V_p = V_r/6$
orthorhombic $Pbnm$ structure:	$a_p = a_0/\sqrt{2}, b_p = b_0/\sqrt{2}, c_p = c_0/2, V_p = V_0/4;$
orthorhombic $Imma$ structure:	$a_p = a_0/\sqrt{2}, b_p = b_0/2, c_p = c_0/\sqrt{2}, V_p = V_0/4;$
monoclinic $I2/m$ structure:	$a_p = a_m/\sqrt{2}, b_p = b_m/2, c_p = c_m/\sqrt{2}, V_p = V_m/4;$
tetragonal $I4/mcm$ structure:	$a_p = a_t/\sqrt{2}, c_p = c_t/2, V_p = V_t/4.$

1. INTRODUCTION

The perovskite family is one of the most important representative among a large variety of inorganic compounds. The majority of chemical elements from the periodic table can form ABX_3 compounds with the perovskite structure (Goodenough and Longo, 1970; Goodenough, 1971; Fesenko, 1972; Reller, 1993; Woodward,

1997a,b; Lufaso and Woodward, 2001; Pena and Fierro, 2001). Complex oxides and halides are typical representatives of perovskite compounds, although the perovskite-type structure can also be formed by various classes of inorganic compounds, namely sulphides, hydrides, cyanides, oxyfluorides, oxynitrides, intermetallic, and metalorganic compounds. The diversity of chemical elements, which form perovskite structures, their ability to create cation- or anion-deficient structures, and a rich variety of distorted perovskite structures lead to an extremely broad range of physical properties. Because of this, the perovskite structure is often called the 'inorganic chameleon' (Islam, 2002). Ferro- and piezoelectricity, high electronic and ionic conductivity, diverse magnetism, and colossal magnetoresistive effects, paraelectricity and superconductivity—all of these phenomena are known to occur in perovskite-type compounds.

Rare earth aluminates and gallates with perovskite structure are widely used as substrate materials for the epitaxy of HTSC and CMR materials, and GaN films (Koren et al., 1989; Giess et al., 1990; Sasaura et al., 1990a; Scheel et al., 1991; Grishin et al., 1993; Young and Strother, 1993; Kebin et al., 1997; Okazaki et al., 1997; Liu et al., 2002), as materials for solid oxide fuel cells (Minh, 1993; Feng and Goodenough, 1994; Ishihara et al., 1994; Slater et al., 1998a,b; Lybye et al., 2000), as active and passive laser media (Kaminskii, 1995; Abu Safia, 1997; Sekita et al., 1998; Henke et al., 2000; Noginov et al., 2002), as scintillators (Moses et al., 1995; Mares et al., 2002), and as microwave dielectric materials (Cho et al., 1999a,b; Huang and Chen, 2002a). For the epitaxy of thin films of HTSC, magnetoresistive materials, and GaN films, single crystalline substrates of NdGaO_3 , LaGaO_3 , PrGaO_3 , LaAlO_3 , and YAlO_3 are commonly used. Jourdan et al. (2004) reported on the epitaxial growth of the heavy fermion superconductor UNi_2Al_3 on (112)-oriented YAlO_3 substrates. Single crystals of YAlO_3 , doped with Nd, Tm, and Er, are well known as laser media (Kaminskii, 1995). As prospective laser materials, also $\text{LuAlO}_3\text{:Nd}$ and TbAlO_3 are considered (Abu Safia, 1997; Sekita et al., 1998). YAlO_3 doped with Yb^{2+} or V^{4+} was proposed as material for tunable solid-state lasers (Henke et al., 2000; Noginov et al., 2002), whereas optical properties of $\text{YAlO}_3\text{:Mn}$ crystals are suitable for holographic and optical storage devices (Loutts et al., 1998). Most of the rare earth aluminates achieve dielectric permittivity with 'high-quality factor' suitable for applications in dielectric resonators and substrates for microwave components (Cho et al., 1999a,b; Huang and Chen, 2002a). Cerium-containing oxides (including perovskites) are of great interest in the chemistry of modern materials for efficient lighting as well as in the technology of weapons-grade Pu in mixed-oxide fuel, that is, to make it acceptable for nuclear plants. Ceria in this case is used as a substitute (surrogate) for plutonia due to similarity of their chemical and physical properties (Putnam et al., 2000). Rare earth aluminates, such as DyAlO_3 , ErAlO_3 , and HoAlO_3 , are paramagnetic down to very low temperatures (typically a few Kelvin) and on ordering, they arrange anti-ferromagnetically. This fact together with large values of magnetic moments typical for rare earth elements makes them suitable for working bodies in magnetic refrigerators for the production of liquid helium (Kuz'min and Tishin, 1991; Kimura et al., 1995).

To better understand the physical nature of the rare earth perovskite materials availability of detailed information about their crystal structures is the key. The above-mentioned physical and chemical properties of rare earth aluminates

are closely linked to their crystallography. The crystal structure itself (or the tilt system) can be highly affected either by iso/aliovalent substitutions in both anion and cation sites or by varying the environmental conditions. Bearing in mind the high stability of perovskites, the knowledge of the crystal structure and the resulting physical properties opens up pathways for tailoring of perovskite properties by manipulating their structures. Thus, by modifying the crystal structure (or tilt system) of perovskites, their physical and physico-chemical properties can be tuned until material with the desired properties is engineering, for example a microwave dielectric material, where near-zero temperature coefficient of resonant frequency has been achieved by modifying perovskite-type rare earth aluminates with alkaline-earth titanates.

As the reader may have already guessed, present chapter deals with rare earth (R) aluminates and gallates, which adopt the perovskite-type structure. Experimental data on crystal structures, their thermal evolution and transformations of over hundred of RAlO_3 and RGaO_3 compounds, and their solid solutions are reviewed. Crystal chemistry has been applied to study and analyse perovskite structures and distortions, which take place in R aluminates and gallates over a wide temperature range. Crystal structures of RAlO_3 and RGaO_3 compounds and their solid solutions have been analysed in terms of structure deformation parameters, for example bond-length distortion, tilting angles between octahedra, polyhedral volume ratio, tolerance factors in different coordinations, and individual and average cation–cation distances. Experimental results have been supplemented by bond-valence calculations. The influence of isovalent substitution in the rare earth sublattice on the average structure, its thermal behaviour, and phase transformations has been established for R aluminates and gallates. Based on our own experimental results and available reference data, phase diagrams of RAlO_3 – $\text{R}'\text{AlO}_3$ and RGaO_3 – $\text{R}'\text{GaO}_3$ systems versus average radii of R-cations are proposed. Common features of the thermal expansion of rare earth aluminates and gallates, as well as the observed anomalies, including the negative thermal expansion observed in RGaO_3 containing praseodymium, are analysed and discussed. Reference data on dielectric properties of R aluminates and gallates with perovskite structure are reviewed.

2. ALUMINATES

2.1 Formation and preparation

2.1.1 Phase formation and stability

Studies of the phase behaviour in the R_2O_3 – Al_2O_3 pseudo-binary systems have been pioneered at the turn of the 1950th and are still in progress. During these decades, phase diagrams were studied for almost all R_2O_3 – Al_2O_3 systems, with the exception of Tb, Tm, and Pm (Table 1). Great attention was paid to the Y_2O_3 – Al_2O_3 system owing to technological importance of the YAlO_3 (YAP) and $\text{Y}_3\text{Al}_5\text{O}_{12}$ (YAG) compounds. Available information about the phase diagrams and formation of compounds in the R_2O_3 – Al_2O_3 systems along with the corresponding references is summarized in Table 1. Besides experimental results, the data obtained from thermodynamic calculations are also included. Particularly

TABLE 1 Formation of compounds in the $R_2O_3-Al_2O_3$ systems

System	Phase diagram	Compounds, formation, temperature (K)				Reference
		2:1	1:1	3:5	1:11	
$La_2O_3-Al_2O_3$	PD	–	C, 2373	–	P, 2203	Bondar and Vinogradova (1964)
	PD	–	C	–	P, 2128	Rolin and Thanh (1965)
	PD	–	C, 2383	–	P, 2121	Mizuno et al. (1974)
	PD ^c	–	C, 2383	–	P ³ , 2201	Wu and Pelton (1992)
$Ce_2O_3-Al_2O_3$	PD	–	C, 2303	–	P, 2223	Leonov et al. (1966)
	PD	–	C, 2348	–	P, 2163	Mizuno et al. (1975)
	PD ^c	–	C, 2303	–	P ³ , 2192	Wu and Pelton (1992)
	–	–	C	–	P	Tas and Akinc (1994)
$Pr_2O_3-Al_2O_3$	–	–	+	–	+	Godina and Kohler (1966)
	PD	–	C,	–	P ³	Mizuno et al. (1977a)
	PD ^c	P ³ , 2088	C, 2183	–	P ³ , 2122	Wu and Pelton (1992)
$Nd_2O_3-Al_2O_3$	PD	–	C, 2343	–	–	Toropov and Kiseleva (1961)
	PD	–	C, 2438	–	P, 2068	Mizuno et al. (1977b)
	PD	P, 2178	C, 2363	–	P, 2173	Coutures (1985)
	PD ^c	P, 2178	C, 2373	–	P ³ , 2070	Wu and Pelton (1992)
	PD ^c	P ³ , 2124	C, 2350	–	P, 2160	Li et al. (1997)
	PD ^c	C, 2222	C, 2373	P, 1150	–	Wu and Pelton (1992)
$Sm_2O_3-Al_2O_3$	PD	P, 2193	C, 2333	–	–	Budnikov et al. (1965)
	PD	–	C, 2373	–	P, 2073 ²	Bondar and Toropov (1966)
	PD	C, 2250	C, 2377	–	–	Mizuno et al. (1977c)
	PD ^c	C, 2223	C, 2373	P, 1440	–	Wu and Pelton (1992)
	PD ^c	–	C, 2340	–	P, 2190	Li et al. (1997)
$Eu_2O_3-Al_2O_3$	–	–	C	–	P ²	Bondar and Toropov (1966)
	PD	–	C, 2213	–	P, 2073	Timofeeva et al. (1969)

(continued)

TABLE 1 (continued)

System	Phase diagram	Compounds, formation, temperature (K)				Reference
		2:1	1:1	3:5	1:11	
Gd ₂ O ₃ -Al ₂ O ₃	PD	C, 2223	C, 2320	–	–	Mizuno et al. (1977d)
	PD ^c	C, 2223	C ³ , 2320	P, 2040	–	Wu and Pelton (1992)
	PD	P, 2223	C, 2323	–	–	Budnikov et al. (1965)
	PD	C, 2224	C, 2342	–	–	Mizuno et al. (1977d)
	PD ^c	C, 2220	C, 2334	–	–	Li et al. (1999)
	PD ^c	C, 2224	C ³ , 2342	P, 2080	–	Wu and Pelton (1992)
Tb ₂ O ₃ -Al ₂ O ₃	PD ^c	P, 2213	C, 2318	–	–	Lakiza et al. (2006)
	–	+	+ ²	+	–	Bondar and Toropov (1966)
Dy ₂ O ₃ -Al ₂ O ₃	PD ^c	C, 2224	C ³ , 2313	P, 2151	–	Wu and Pelton (1992)
	PD	C	C	P	–	Gilissen et al. (1974)
Ho ₂ O ₃ -Al ₂ O ₃	PD	C, 2227	C, 2273	C, 2193	–	Mizuno et al. (1978)
	PD ^c	C, 2225	C ³ , 2265	C, 2189	–	Wu and Pelton (1992)
	PD	C, 2248	C, 2253	C, 2223	–	Mizuno (1979)
Er ₂ O ₃ -Al ₂ O ₃	PD ^c	C, 2239	C ³ , 2253	C, 2223	–	Wu and Pelton (1992)
	PD	C, 2263	C, 2236	C, 2233	–	Mizuno (1979)
Tm ₂ O ₃ -Al ₂ O ₃	PD ^c	C, 2249	C ³ , 2236	C, 2233	–	Wu and Pelton (1992)
	PD ^c	C, 2259	C ³ , 2193	C, 2253	–	Wu and Pelton (1992)
Yb ₂ O ₃ -Al ₂ O ₃	PD	P ³ , 2123	–	C, 2173	–	Bondar and Toropov (1966)
	PD	P, 2275	–	C, 2273	–	Mizuno and Noguchi (1980)
	PD ^c	C, 2273	P ³ , 2151	C, 2283	–	Wu and Pelton (1992)

Lu ₂ O ₃ -Al ₂ O ₃	PD	P, 2273	C ²	C, 2333	–	Shirvinskaya and Popova (1977)
	PD ^c	C, 2313	P ³ , 2180	C, 2316	–	Wu and Pelton (1992)
Y ₂ O ₃ -Al ₂ O ₃	PD	P ³ , 2273	P ³ , 2203	C, 2333	–	Petrosyan et al. (2006)
	PD	C, 2303	+ ²	C, 2243	–	Warshaw and Roy (1959)
	PD	C, 2293	P ³ , 2143	C, 2203	–	Toropov et al. (1964)
	PD	C, 2293	C ³ , 2148	C, 2203	–	Mizuno and Noguchi (1967)
	PD	C, 2203	C, 2148	C, 2243	–	Abell et al. (1974)
	PD ^c	C, 2250	P ³ , 2150	C, 2170	–	Kaufman et al. (1981)
	PD	C, 2293	C ³ , 2213	C, 2223	–	Bondar et al. (1984)
	PD	C ³ , 2203	C, 2143	C, 2243	–	Cockayne (1985)
	PD	C, 2250	C, 2190	C, 2215	–	Adylov et al. (1988)
	PD ^c	C, 2294	P, 2196	C, 2208	–	Lysenko and Voronin (1990)
	PD ¹	C, 2293	P, 2148	C, 2213	–	Maier and Savinova (1996)
	PD ^c	C, 2299	C, 2184	C, 2213	–	Gröbner et al. (1996)
	–	–	C, 2184	C, 2210	–	Stankus and Tyagel'sky (1996)
	PD ¹	C	C, 2183	C, 2223	–	Lakiza and Lopato (1997)
Sc ₂ O ₃ -Al ₂ O ₃	PD	–	C ³ , 2143	–	Toropov and Vasilieva (1963)	

C, congruently melting; P, peritectic (incongruently melting); PD, phase diagram; Superscript c, calculated/optimized diagram.

¹ Partial diagram.

² Metastable phase.

³ Limited thermal stability range.

valuable is the paper published by [Wu and Pelton \(1992\)](#), in which a comprehensive critical assessment of the available data for the R_2O_3 – Al_2O_3 systems ($R = La$ – Lu) has been carried out through the technique of coupled thermodynamic-phase diagram analysis, pioneered in large part by the Computer Coupling of Phase Diagrams and Thermochemistry (CALPHAD) group. Thermodynamic properties of the compounds and liquid oxide solutions have been deduced and then used to calculate optimized phase diagrams for 15 lanthanide oxide–alumina systems, including those, for which no experimental phase diagrams have been reported (Pm, Tb, and Tm). Besides the references collected in [Table 1](#), the readers are also referred to several handbooks, in which phase diagrams of R_2O_3 – Al_2O_3 systems are summarized and reviewed ([Arsenev et al., 1983](#); [Udalov, 1985](#); [Table 1](#)).

Aluminates, $RAIO_3$, of the perovskite-type are known for all rare earth elements, with the exception of promethium. The occurrence of $PmAlO_3$ in the Pm_2O_3 – Al_2O_3 system has been predicted by [Wu and Pelton \(1992\)](#). Besides perovskite phases, compounds with compositions $R_4Al_2O_9$ ($R = La, Pr$ – Lu , and Y), $R_3Al_5O_{12}$ ($R = Gd$ – Lu and Y), and $RAI_{11}O_{18}$ ($R = La$ – Eu) are known to form in R_2O_3 – Al_2O_3 systems ([Table 1](#)). Some authors reported also the formation of metastable phases with orthorhombic structures in the La_2O_3 – Al_2O_3 and Ce_2O_3 – Al_2O_3 systems at 82.5 and 78.7 mol% of R_2O_3 , respectively ([Mizuno et al., 1974, 1975](#)). Another metastable compound in the lanthanum system, $La_{10}Al_4O_{21}$ ($5La_2O_3 \times 2Al_2O_3$), has been assigned by [Yamaguchi et al. \(1985\)](#). Two additional metastable states were recently observed in the alumina-rich parts of La_2O_3 – Al_2O_3 and Nd_2O_3 – Al_2O_3 systems ([Key and Crist, 2005](#)).

The thermodynamic properties of $RAIO_3$ compounds were studied by several authors ([Kaufman et al., 1981](#); [Lysenko and Voronin, 1990](#); [Gröbner et al., 1996](#); [Putnam et al., 2000](#)). [Wu and Pelton \(1992\)](#) published the equations for the Gibbs free energy of formation of all compounds formed in the R_2O_3 – Al_2O_3 systems ($R = La$ – Lu). [Kanke and Navrotsky \(1998\)](#) showed that standard molar enthalpies of formation of $RAIO_3$ perovskites vary regularly as a function of the inverse R-cation radii and they become more negative in the series $R = La, Nd, Sm, Eu, Gd, Dy$, and Y . Thermodynamic data reported in these publications, together with the values of the melting points shown in [Table 1](#), clearly indicate that $RAIO_3$ compounds become less thermodynamically stable when the radius of the R-cation decreases. Aluminates with $R = La$ – Tm, Y , and Sc melt congruently, whereas $YbAlO_3$ and $LuAlO_3$ are formed via peritectic reactions and are metastable ([Wu and Pelton, 1992](#); [Petrosyan et al., 2006](#)). Some members of the $RAIO_3$ series ($R = La$ – Eu) are stable over a wide temperature range and melt congruently at temperatures from 2263 to 2438 K ([Table 1](#)). An exception is $CeAlO_3$ that is stable in reducing atmosphere up to the melting point (2030 K), but it decomposes on heating in air into Ce_2O_3 and Al_2O_3 ; the decomposition starts at 1070 K. Thermodynamic calculations performed by [Wu and Pelton \(1992\)](#) predict lower (eutectoid) decomposition temperatures for aluminates with $R = Eu$ to Tm , which increase as the compounds become less stable from ca. 470 K for $EuAlO_3$ to 1670 K for $TmAlO_3$. Earlier, such a limited range of stability was reported for $RAIO_3$ compounds with Gd, Tb, Dy , and Ho ([Arsenev et al., 1983](#)). According to [Arsenev](#)

et al. (1983), thulium, ytterbium, lutetium, and scandium monoaluminates are metastable and could be obtained at non-equilibrium conditions from super-cooled melts. Wu and Pelton (1992) estimated the ranges of stability of YbAlO_3 and LuAlO_3 perovskites as being quite small between 1923 (1973) K and 2140 (2180) K, respectively. Petrosyan et al. (2006) showed that LuAlO_3 is stable only in a narrow region of 2023–2203 K. The limited stability range between 2003 and 2143 K was also reported for ScAlO_3 by Toropov and Vasilieva (1963). There are controversial data in numerous publications about the formation of perovskite-type phases in the $\text{Y}_2\text{O}_3\text{--Al}_2\text{O}_3$ system (Table 1), nevertheless, the majority of authors agree that YAlO_3 melts congruently.

2.1.2 Preparation

The majority of RAlO_3 compounds can be obtained by solid state reactions from their constituent oxides or oxide precursors, such as carbonates and oxalates at temperatures 1770–1970 K (Keith and Roy, 1954; Schneider et al., 1961; Arsenev et al., 1983; Udalov, 1985; Kanke and Navrotsky, 1998; Cho et al., 1999a). High synthesis temperature, chemical inhomogeneity, low sintering ability, and large particle size are major drawbacks of solid state reaction methods. Preparation of rare earth aluminates by thermal decomposition and calcination of coprecipitated mixtures of hydroxides, cyanides, and nitrates of rare earth elements, solid as well as aluminium, allows one to reduce the sintering temperature (Udalov, 1985; Vidyasagaret al., 1985). One of the lowest temperatures to synthesize RAlO_3 compounds was reported by Krylov et al. (1973). It was claimed that pure crystalline LaAlO_3 may evolve when amorphous gel-like mixed hydroxides of rare earth elements and aluminium were heated only to temperatures 918–943 K. Other RAlO_3 compounds ($\text{R} = \text{Pr}, \text{Nd}, \text{Sm}, \text{Eu}, \text{Gd}, \text{and Dy}$) were obtained at 1078–1203 K.

Sintering temperature of RAlO_3 perovskites can also be reduced by adding sintering aids. For instance, the addition of $\text{CuO} + \text{ZnO}$ and V_2O_5 as liquid phase sintering aids reduces the synthesis temperature of SmAlO_3 and NdAlO_3 from 1923 to 1703 K and to 1663–1683 K, respectively (Huang and Chen, 2002a, 2003). Cruciani et al. (2005) prepared chromium-doped $\text{RAl}_{0.965}\text{Cr}_{0.035}\text{O}_3$ compounds with $\text{R} = \text{Y}, \text{Nd}, \text{Pr}, \text{Sm}, \text{Eu}, \text{Gd}, \text{Dy}, \text{Ho}, \text{Er}, \text{and Yb}$ from raw materials containing the corresponding oxides mixed with 1 wt% of alkaline-earth fluorides and carbonates, added as mineralizers. Mixtures were ground in a porcelain jar-mill and then dried and fired at 1773 K with a firing cycle of 15 h and a soaking time of 1 h. In such a way, almost single-phase specimens with the amount of perovskite phase ranging from 86 wt.% for the Yb and 98.8 wt.% for the Eu systems were obtained.

Diverse modifications of the flux method have been proposed for the preparation of RAlO_3 perovskites. Garton and Wanklyn (1967) reported the synthesis of optically clear single crystals of RAlO_3 ($\text{R} = \text{Nd--Dy}$ and Y) from a PbO/PbF_2 flux at 1533–1613 K. For the Tm and Yb systems, a mixture of perovskite and garnet phases were obtained, and LuAlO_3 could not be synthesized under these conditions. Transparent crystals of RAlO_3 ($\text{R} = \text{Eu--Er}$) up to 20 mm³ in volume have been grown upon slow cooling from a PbO/PbF_2 flux containing B_2O_3 and MoO_3

as additives (Wanklyn *et al.*, 1975). Using the same technique, Razdan *et al.* (2000) have obtained crystals of RAIO_3 perovskites with $R = \text{La, Gd, Tb, Dy, Ho, and Er}$. Shishido *et al.* (1993, 1995a) reported the preparation of RAIO_3 single crystals ($R = \text{La–Lu}$) up to 30–60 μm in size (300–600 μm for NdAlO_3) at 1280 K and atmospheric pressure using a KF flux. To prevent oxidation, CeAlO_3 , PrAlO_3 , and TbAlO_3 were grown in helium atmosphere, whereas all other crystals were grown in air. Ceramics of cerium monoaluminate were obtained at 1623–1773 K in reducing atmosphere with H_3BO_3 as flux (Wang *et al.*, 2005). Besides the pure RAIO_3 crystals, the flux-growth technique could also be used for the preparation of doped and mixed perovskites, for instance, $\text{La}_{1-x}\text{Pr}_x\text{AlO}_3$ crystals with $x = 0.25$ and 0.75 (Kotru *et al.*, 1989).

Preparation of RAIO_3 compounds containing small R^{3+} ions, such as Tm, Yb, Lu, and Sc, requires a high pressure synthesis technique. Dernier and Maines (1971) reported the synthesis of rare earth aluminates RAIO_3 with $R = \text{Dy–Lu}$ using equimolar mixtures of constituent oxides from an NaOH flux at 1470 K and 3.25 GPa. Single crystals of ScAlO_3 perovskite ranging from 10 to 200 μm in size have been synthesized at 3.5 GPa pressure and 1523 K using lithium fluoride as a high-temperature solvent (Sinclair *et al.*, 1979). Polycrystalline specimens of ScAlO_3 were obtained in a 1000-ton multi-anvil press at 10 GPa and 1470 K (Kung *et al.*, 2000). High-pressure techniques can also be applied for the synthesis of those RAIO_3 polymorphs, which are not stable at ambient conditions. For instance, cubic single-crystals of LaAlO_3 perovskite had been obtained at 4.5 GPa and 1273 K in the presence of an NaCl/KCl flux (Nakatsuka *et al.*, 2005).

For preparation of RAIO_3 compounds, synthesis from the melt is often used, which is a higher temperature method than solid-state reaction techniques. The arc melting technique has been applied by Shishido *et al.* (1995b, 1997a,b) for the synthesis of RAIO_3 compounds with $R = \text{La–Tm}$. Single phases were obtained for all compounds, with the exception of CeAlO_3 , for which a small amount of CeO_2 and Al_2O_3 was found to be precipitated at the grain boundaries. In the case of the $\text{Yb}_2\text{O}_3\text{–Al}_2\text{O}_3$ and the $\text{Lu}_2\text{O}_3\text{–Al}_2\text{O}_3$, a mixture of $\text{R}_3\text{Al}_5\text{O}_{12}$ and R_2O_3 phases were found. The formation range of perovskite-type phases using this synthetic method is limited to the Goldschmidt tolerance factor $t = 0.95$, both for RAIO_3 and RGO_3 compounds (Shishido *et al.*, 1997a). A similar method was used for the synthesis of RAIO_3 compounds ($R = \text{La–Tm}$) (Vasylechko *et al.*, 2002a, 2003a, 2004a; Vasylechko and Matkovskii, 2004), as well as for the preparation of $\text{Ce}_{1-x}\text{R}_x\text{AlO}_3$ ($R = \text{La, Pr, and Nd}$) solid solutions (Vasylechko *et al.*, 2003b, c, 2004a, 2007b). CeAlO_3 -based samples were obtained by combining the solid state reaction in a dynamic vacuum at 1730 K with subsequent arc melting in Ar atmosphere. Ishigaki *et al.* (2006) showed that various perovskite compounds such as LaAlO_3 , GdScO_3 , ATiO_3 ($A = \text{Ba, Sr, and Ca}$), and their solid solutions can be obtained in a single step from mixed oxide powders by the rapid synthesis via melt-solidification methods using an arc-imaging furnace.

In the last decade, a polymer complex method, corresponding to the sol-gel method, had been widely applied for the preparation of various mixed oxide compositions, including rare earth aluminates (Rao, 1996; Lo and Tseng, 1998). By using this technique, RAIO_3 compounds of La–Ho except for Ce and Pm can be

prepared as single phases at an annealing temperature of 1423 K (Takata et al., 2006). For the Er, Tm, Yb, and Lu systems, mixtures of RAIO_3 , $\text{R}_3\text{Al}_5\text{O}_{12}$, and R_2O_3 phases were obtained. Kakihana and Okubo (1998) reported the low-temperature synthesis of LaAlO_3 powder using the polymer complex technique based on *in situ* polyesterification between citric acid and ethyleneglycol. The formation of pure perovskite occurred when the precursor was head-treated at 973 K for 8 h or at 1023 K for 2h. Sinha et al. (2006) proposed citrate gel process for the synthesis of GdAlO_3 and calcium-doped $\text{Gd}_{1-x}\text{Ca}_x\text{AlO}_{3-\delta}$ ($x = 0-0.3$) samples at 1273 K.

For the low-temperature synthesis of LaAlO_3 , Taspinar and Tas (1997) proposed a self-propagating combustion synthesis from aqueous solution containing urea and the respective nitrate salts. A pure perovskite phase was obtained at 1023 K, which is one of the lowest temperatures reported for the powder synthesis of LaAlO_3 so far. Han et al. (2006) used a combustion method for the synthesis of Eu^{3+} -activated YAlO_3 and GdAlO_3 by redox reactions between the respective metal nitrates and glycine in a preheated furnace at 773 K.

Mechanical solid-state reaction in a high-energy ball mill (mechanical alloying) is an alternative way for the low-temperature synthesis of RAIO_3 compounds. Guo and Sakurai (2000a) and Sakurai and Guo (2001) reported the formation of a fine powder of pure and cerium-doped YAlO_3 using the mechanical solid-state reaction. It has been shown (Sakurai and Guo, 2001) that mixing Y_2O_3 , CeO_2 , and aluminium hydroxide as starting materials in a planetary ball mill and subsequent heating to 1423 K allows for a transition to crystalline phase and the substitution of cerium at the yttrium site, thus forming $\text{Y}_{0.995}\text{Ce}_{0.005}\text{AlO}_3$. Guo and Sakurai (2000b) reported that a similar approach may provide crystallization of YAlO_3 perovskite near room temperature. Room-temperature mechanochemical synthesis of other aluminates has been proposed by Zhang and Saito (2000). Grinding of lanthanum oxide with alumina for 120 min in a planetary ball mill led to a single-phase LaAlO_3 . The formation of the perovskite phase was observed only when so-called 'transition' alumina prepared by thermal decomposition of $\text{Al}(\text{OH})_3$ at temperatures 673–1073 K was used. Similar to LaAlO_3 , single-phase NdAlO_3 , SmAlO_3 , and DyAlO_3 materials were obtained. The formation of CeAlO_3 and PrAlO_3 was also confirmed; however, the CeO_2 and Pr_6O_{11} starting oxides were still present in the mixtures. Mechanical alloying has also been used for the preparation of aluminium-yttrium powder mixtures, in order to form composites with a dominant matrix phase, including YAlO_3 in $\text{Y}_3\text{Al}_5\text{O}_{12}$ or YAlO_3 in $\text{Y}_4\text{Al}_2\text{O}_9$ (Alkebro et al., 2000, 2002).

The spray pyrolysis technique was applied by Lux et al. (1993) for the preparation of spherical lanthanum aluminate powders approximately 1 μm in diameter. Intermediate products converted completely to lanthanum aluminate after annealing in air for 1 h at 1373 K. Putnam et al. (2000) reported the synthesis of CeAlO_3 by spray drying stoichiometric nitrate solution. The voluminous precursors were decomposed in air at 873 K and then reacted at 1373 K in hydrogen atmosphere for 8 h.

Nanosized powders of single and binary oxides can be produced by decomposition of the respective metal nitrates and polyvinyl alcohol (PVA) or a mixture of PVA and polyacrylic acids (Pramanik, 1996). Using this technique,

nanoparticles of LaAlO_3 and NdGaO_3 were obtained among other mixed oxides. For the fabrication of nanocomposites containing a homogeneous dispersion of NdAlO_3 nanocrystals in an Al_2O_3 matrix, CVD of the mixed-metal precursor (Veith *et al.*, 2000) and the sol-gel technique (Mathur *et al.*, 2002) have been applied. Shmurak *et al.* (2005) described the synthesis of nanocrystalline rare earth aluminates and gallates with perovskite and garnet structures by dissolving the initial oxides or nitrates in ammonium nitrate melt at about 473 K and subsequent annealing at temperatures ranging from 773 to about 1273 K. Hreniak *et al.* (2006) prepared nanocrystalline powders of LaAlO_3 doped with Eu^{3+} using a sol-gel derived Pechini's method. The average size of LaAlO_3 grains was 30–45 nm, depending on the annealing temperature, which varied from 1073 to 1373 K. Kuznetsova *et al.* (2006) reported the synthesis of mesoporous precursors of nanocrystalline YAlO_3 with perovskite structure by the coprecipitation of Y^{3+} and Al^{3+} cations from deionized yttrium-aluminium nanosols with ammonium hydroxide. The average size of perovskite-type crystallites that resulted from the templated precipitation of the precursor was no larger than 300 nm. Kagawa *et al.* (1993) proposed a gas-phase synthesis for the preparation of ultrafine particles and thin films of yttrium aluminates. Powders and thin films of Y–Al–O were synthesized by introducing atomized solutions of Y and Al chlorides or nitrates into an argon inductively coupled plasma at temperatures above 5000 K (the spray-ICP technique). The powders consisted of fine spherical particles of 10–50 nm diameter and were mixtures of amorphous and crystalline material whose phase composition varied from $\text{Y}_4\text{Al}_2\text{O}_9$ to hexagonal YAlO_3 depending on the Y:Al ratio in the precursor solution.

RAlO_3 compounds can also be obtained in a glassy state. Zhang *et al.* (2003) and Zhang and Navrotsky (2004) reported on the fabrication of a series of glasses of RAlO_3 composition (R = La, Pr, Nd, Sm, and Gd) using containerless processing techniques in oxygen (argon for Pr) atmosphere. It was found that the enthalpies of vitrification for RAlO_3 increase slightly with increasing ionic radius.

Several other experimental techniques can be applied for the preparation of some RAlO_3 compounds. Selvam and Rao (2000) developed a novel microwave method for synthesis and consolidation of GdAlO_3 perovskite. Using this method, gadolinium and aluminium oxides react completely under microwave irradiation at 2.45 GHz with a maximum power of 900 W. By using this approach, single-phase GdAlO_3 has been obtained at 1473 K after 1 min. An *et al.* (2006) have studied the irradiation effect of a pulsed microsecond laser on the synthesis of terbium aluminate. It was reported that crystalline TbAlO_3 with orthorhombic perovskite structure is formed on the irradiated surface of the target made of $\text{Tb}_4\text{O}_7 + 2\text{Al}_2\text{O}_3$ mixture directly under atmospheric conditions.

Thin films of rare earth aluminates are usually obtained by sol-gel (Beach *et al.*, 1998) and CVD methods (Veith *et al.*, 2001). Shoup *et al.* (1998) prepared thin films of LaAlO_3 and NdAlO_3 deposited on biaxially textured (100) nickel substrates using a solution deposition technique (sol-gel method). Epitaxial films were obtained after heating the compounds to 1423 K in Ar-4% H_2 for 1 h. Yamaguchi *et al.* (2002a, b) used a coating-pyrolysis process for the fabrication of buffer layers of EuAlO_3 and NdAlO_3 thin films on $\alpha\text{-Al}_2\text{O}_3$ substrates. Kosola

et al. (2005) applied the atomic layer deposition method for the preparation of NdAlO_3 thin films on Si(100) substrate at 473–723 K. An amorphous NdAlO_3 film deposited at 573 K has been crystallized during annealing in nitrogen or oxygen at 1123–1173 K.

For technical applications, highly perfect large single crystals of RAIO_3 perovskites are often required. In most cases, such crystals are obtained by the Czochralski technique. For instance, the Czochralsky method was applied for pulling pure and doped LaAlO_3 (Fay and Brandle, 1967), NdAlO_3 (Miyazawa et al., 1993a), PrAlO_3 (Pawlak et al., 2005), GdAlO_3 (Mazelsky et al., 1968; Mares et al., 1993), TbAlO_3 (Sekita et al., 1994), HoAlO_3 , ErAlO_3 , DyAlO_3 (Okano et al., 1993; Kimura et al., 1995), YbAlO_3 , LuAlO_3 (Ananieva et al., 1978; Mares et al., 1995), and YAlO_3 (Neuroth and Wallrafen, 1999; Savytskii et al., 2000a; Matkovskii et al., 2002). This method is also used for the growth of solid solution single crystals such as $\text{Tb}_{1-x}\text{Gd}_x\text{AlO}_3$ (Morita et al., 1996), $\text{Lu}_{1-x}\text{R}_x\text{AlO}_3$ ($\text{R} = \text{Y}$ and Gd) (Mares et al., 2002), and $\text{Yb}_{1-x}\text{Y}_x\text{AlO}_3$ (Nikl et al., 2004). For the fabrication of large crystals of CeAlO_3 , the so-called cold-crucible technique has been used (Shelych and Melekh, 2003). The Bridgman melt technique is also suitable for producing large RAIO_3 crystals. Petrosyan et al. (1999, 2002) used this method to grow large single crystals (up 100 mm long and 15 mm in diameter) of LuAlO_3 , YAlO_3 , and $\text{Lu}_{1-x}\text{Y}_x\text{AlO}_3$ solid solutions. Fahey et al. (1993) fabricated crystals of LaAlO_3 and DyAlO_3 up to 3 cm in diameter and NdAlO_3 up to 5 cm by the vertical gradient-freeze technique in sealed tungsten crucibles. The FZ method was applied for the growth of $\text{Nd}_{1-x}\text{Y}_x\text{AlO}_3$ (Tanaka et al., 1993a) and $\text{La}_{1-x}\text{Ca}_x\text{AlO}_3$ single crystals (Mizusaki et al., 1993). Yb-doped fibre crystals of $(\text{Lu},\text{Y})\text{AlO}_3$ were obtained using the micro-pulling-down method (Shim et al., 2004).

2.2 Crystal structure

Systematic structural investigations of the RAIO_3 compounds have been pioneered in the second half of the 1950th by Geller et al. (Geller and Bala, 1956; Geller and Wood, 1956). It was shown that at room temperature, members of the RAIO_3 series— LaAlO_3 , PrAlO_3 , and NdAlO_3 —exhibit a rhombohedral deformation of the perovskite lattice, whereas other RAIO_3 compounds ($\text{R} = \text{Sm}$ – Lu and Y) adopt orthorhombic symmetry and GdFeO_3 structure type. Besides, Bertaut and Mareschal (1963) reported possible formation of HT phases of RAIO_3 ($\text{R} = \text{Y}$, Eu , Gd , Tb , Dy , Ho , and Er) with hexagonal symmetry (S.G. $P6_3/mmc$).

2.2.1 Lanthanum aluminate LaAlO_3

Originally, the crystal structure of LaAlO_3 has been determined and refined at RT in space group $R3m$ (Geller and Bala, 1956; Fedulov et al., 1962). Subsequent investigations showed that the space group is $R\bar{3}c$ with double the lattice parameter of the original non-centrosymmetric rhombohedral cell (Derighetti et al., 1965; De Rango et al., 1966; Yu et al., 1993; Taspinar and Tas, 1997). Yang et al. (1991) revealed the presence of a fourfold axis in the LaAlO_3 structure by means of electron diffraction technique. As a result, they proposed the cubic symmetry

(S.G. $Fm\bar{3}c$) and doubling of the lattice parameter of the ideal perovskite cell for the LaAlO_3 structure at RT. But recent re-examinations of the crystal structure performed by coherent-beam electron diffraction patterns tilted away from the major zone axis (Jones, 2007) reconfirm the rhombohedral $R\bar{3}c$ structure of LaAlO_3 . The rhombohedral structure of LaAlO_3 has also been proved in numerous investigations performed using synchrotron X-ray and neutron diffraction techniques (Chakoumakos *et al.*, 1998; Howard *et al.*, 2000; Lehnert *et al.*, 2000a,b; Hayward *et al.*, 2005). LaAlO_3 exhibits a continuous phase transition from the rhombohedral to the ideal cubic perovskite structure (S.G. $Pm\bar{3}m$) at 813 K (Geller and Bala, 1956; Müller *et al.*, 1968; Scott, 1969; Geller and Raccah, 1970; Chakoumakos *et al.*, 1998; Howard *et al.*, 2000; Lehnert *et al.*, 2000b; Hayward *et al.*, 2002). Nakatsuka *et al.* (2005) report the ideal $Pm\bar{3}m$ cubic perovskite structure at RT for LaAlO_3 crystals synthesized at 4.5 GPa and 1273 K in the presence of an NaCl + KCl flux.

Temperature dependencies on the lattice parameters of LaAlO_3 are presented in Figure 1. Crystallographic data for different modifications of the LaAlO_3 structure are shown in Table 2.

Hayward *et al.* (2005) performed a comprehensive investigation of LaAlO_3 in the temperature range of 10–750 K and determined the crystal structure, dielectric relaxation, specific heat, birefringence, and the frequencies of the two soft modes via Raman spectroscopy. While all these experiments show that the behaviour at the critical point around $T_C = 813$ K is consistent with a second-order transition, some evidence for an additional anomalous behaviour below 730 K have been shown. This anomaly was explained by a biquadratic coupling between the primary order parameter of the transition and the hopping of intrinsic oxygen vacancies.

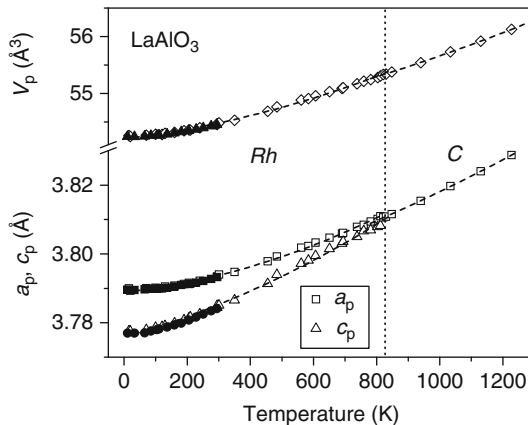


FIGURE 1 Thermal behaviour of the normalized lattice parameters and cell volume of rhombohedral (Rh) and cubic (C) phases of LaAlO_3 according to Howard *et al.* (2000) (open symbols) and Vasylechko (2005) (solid symbols). The dashed lines are polynomial fits: $a_p(T) = 3.78958(8) [1 + 1.37(3) \times 10^{-8}T^2 - 6.6(4) \times 10^{-11}T^3]$; $c_p(T) = 3.77766(9) [1 + 2.58(4) \times 10^{-8}T^2 - 1.67(5) \times 10^{-11}T^3]$ for the temperature range 15–812 K and $a_p(T) = 3.7922(6) [1 + 8.8(5) \times 10^{-9}T^2 - 1.9(3) \times 10^{-12}T^3]$ for the temperature range 821–1227 K.

TABLE 2 Structural parameters of the rhombohedral (S.G. $R\bar{3}c$) and cubic (S.G. $Pm\bar{3}m$) modifications of LaAlO_3 at different temperatures

Parameters	Chakoumakos et al. (1998) ¹	Chakoumakos et al. (1998) ¹	Howard et al. (2000) ¹	Howard et al. (2000) ¹	Howard et al. (2000) ¹	Lehnert et al. (2000b) ¹	Lehnert et al. (2000b) ¹	Lehnert et al. (2000b) ¹	Zhao et al. (2004a) ²	Vasylechko et al. (2005) ³	Nakatsuka et al. (2005) ²	
	$R\bar{3}c$ (296 K)	$Pm\bar{3}m$ (1223 K)	$R\bar{3}c$ (15 K)	$R\bar{3}c$ (295 K)	$R\bar{3}c$ (812 K)	$R\bar{3}c$ (300 K)	$R\bar{3}c$ (800 K)	$Pm\bar{3}m$ (973 K)	$R\bar{3}c$ (RT)	$R\bar{3}c$ (12 K)	$Pm\bar{3}m$ (RT)	
a (Å)	5.36462(4)	3.82842(6)	5.3598(1)	5.3647(1)	5.3895(1)	5.36382(4)	5.3862(3)	3.81593(3)	5.3660(2)	5.3594(1)	3.7913(2)	
Atom: sites	c (Å)	13.1096(1)	—	13.0859(1)	13.1114(3)	13.1919(8)	13.1091(1)	13.1923(8)	—	13.1090(6)	13.0840(3)	—
La: 6c in	x	0	1/2	0	0	0	0	0	1/2	0	0	1/2
$R\bar{3}c$; 1b	y	0	1/2	0	0	0	0	0	1/2	0	0	1/2
in	z	1/4	1/2	1/4	1/4	1/4	1/4	1/4	1/2	1/4	1/4	1/2
$Pm\bar{3}m$	B_{iso} (Å ²)	0.36(2)*	1.11(2)*	—	—	—	0.23(4)	0.83(4)	1.14(5)	0.60(3)	0.21(4)	0.247(2)*
Al: 6b in	x	0	0	0	0	0	0	0	0	0	0	0
$R\bar{3}c$; 1a	y	0	0	0	0	0	0	0	0	0	0	0
in	z	0	0	0	0	0	0	0	0	0	0	0
$Pm\bar{3}m$	B_{iso} (Å ²)	0.166(8)*	1.02(5)*	—	—	—	0.21(7)	0.62(7)	0.70(9)	0.66(14)	0.4(2)	0.218(6)*
O: 18e in	x	0.47505(8)	1/2	0.5281(1)	0.5251(2)	0.5047(6)	0.4749(2)	0.4909(4)	1/2	0.5265(5)	0.527(2)	1/2
$R\bar{3}c$; 3d	y	0	0	0	0	0	0	0	0	0	0	0
in	z	1/4	0	1/4	1/4	1/4	1/4	1/4	0	1/4	1/4	0
$Pm\bar{3}m$	B_{iso} (Å ²)	0.411(8)*	1.71(2)*	—	—	—	—	—	—	0.91(10)	0.53(15)	0.81(2)*

In this table, the numbers in parentheses give statistical errors (least squares standard deviations) expressed in the last significant digit.

¹ Neutron powder diffraction data.

² X-ray single crystal diffraction data.

³ Synchrotron powder diffraction data.

* Calculated from the U_{iso} or U_{ij} values given in the references.

Studies of pressure-dependent structural properties of LaAlO_3 have been performed by [Bouvier and Kreisel \(2002\)](#). High-pressure examination of the LaAlO_3 structure at RT using Raman spectroscopy and synchrotron radiation revealed a structural instability under pressure due to soft-mode-driven rhombohedral-to-cubic phase transition in the vicinity of 14 GPa. [Zhao et al. \(2004a\)](#) studied the evolution of the atomic-scale structure of LaAlO_3 at RT under pressure up to 8.6 GPa. It was shown that the LaO_{12} polyhedra are less compressible than the AlO_6 ones that results in a decrease of the tilting of the AlO_6 octahedra with pressure and ultimately the pressure-induced second-order phase transition from the rhombohedral to the cubic structure. The authors showed that similarly to orthorhombic GdFeO_3 -type perovskites, the response of a rhombohedral perovskite to pressure can be ascribed to the relative compression of the AO_{12} and BO_6 polyhedra. Crystallographic data obtained at ambient pressure in conjunction with bond-valence parameters can therefore be used to predict compressibility and phase transitions of all rhombohedral perovskites.

2.2.2 Cerium aluminate CeAlO_3

For the first time, the crystal structure of cerium aluminate was reported by [Zachariassen \(1949\)](#) as being tetragonal, with a weak elongation in one of the cubic perovskite axes. Later, a variety of hexagonal ([Keith and Roy, 1954](#)), trigonal ([Roth, 1957](#); [Kim, 1968](#); [Mizuno et al., 1975](#)), and cubic ([Leonov, 1963](#)) structures of CeAlO_3 have been reported. However, the data reported by [Kaufherr et al. \(1985\)](#) and single crystal diffraction investigations performed by [Tanaka et al. \(1993b\)](#) revealed a simple tetragonal structure for CeAlO_3 (S.G. $P4/mmm$, $a = 3.7669 \text{ \AA}$, $c = 3.7967 \text{ \AA}$), as it was initially proposed by Zachariassen. This structure was commonly confirmed for the cerium aluminate throughout the last decade ([Shelykh et al., 1994](#); [Tas and Akinc, 1994](#); [Shishido et al., 1995a, 1997b](#); [Shelykh and Melekh, 2003](#); [Okada et al., 2004](#)). Only once ([Tozawa et al., 2003](#)) the growth of orthorhombic CeAlO_3 single crystal with lattice constants $a_1 = 5.316 \text{ \AA}$, $a_2 = 5.314 \text{ \AA}$, and $c = 7.576 \text{ \AA}$, close to a cubic system, was reported.

First information on the phase transformations in CeAlO_3 had been reported in the 1960th. [Leonov et al. \(1966\)](#) and [Leonov \(1970\)](#) observed two phase transitions in CeAlO_3 using optical methods: one was from the tetragonal to a rhombohedral phase at 363 K and another from the rhombohedral to a cubic one at 1253 K. [Geller and Raccah \(1970\)](#) have predicted the rhombohedral-to-cubic transition in CeAlO_3 at 1230 K from the extrapolation of the corresponding transition temperatures in the related RAlO_3 ($R = \text{La, Pr, and Nd}$) compounds. [Egorov et al. \(1998\)](#) have described two phase transformations in CeAlO_3 at ca. 310 K and ca. 450 K using DTA. Electrical and optical properties of CeAlO_3 single crystals have been studied by [Shelykh and Melekh \(2003\)](#). These authors confirmed phase transformations at 310 and 440 K as well as the high-temperature transition to the optically isotropic cubic phase, which starts at 1170 K and is completed at about 1400 K. A thermal hysteresis of about 100 K has been observed. However, the aforementioned publications give no information about structural peculiarities of different modifications of CeAlO_3 or about their thermal behaviour.

First results of structural investigations of CeAlO_3 over a wide temperature range of 12–1230 K were published in 2002 (Vasylechko et al., 2002a; Vasylechko and Matkovskii, 2004). RT examination of the crystal structure using high-resolution powder diffraction techniques with very high signal-to-noise ratio revealed the presence of several weak superstructure reflections, which could not be indexed using a simple tetragonal perovskite-type cell. Accordingly, the CeAlO_3 structure at RT has been refined in space group $I4/mcm$ with a $\sqrt{2}a_p \times \sqrt{2}a_p \times 2a_p$ lattice. Hence, the tetragonal $I4/mcm$ phase observed at RT in CeAlO_3 is lone exception among all $A^{3+}M^{3+}O_3$ perovskites. In agreement with the Inorganic Crystal Structure Database (ICSD, 2005), this structure type only occurs among $A^{2+}M^{4+}O_3$ perovskites, namely BaTbO_3 at RT; SrTiO_3 at LT; SrRuO_3 , SrZrO_3 , SrHfO_3 , and BaPbO_3 at HT.

Based on *in situ* synchrotron powder diffraction examinations and DTA/DSC studies (Vasylechko et al., 2002a; 2007b; Vasylechko and Matkovskii, 2004), it was shown that CeAlO_3 undergoes a sequence of structural phase transformations: $I4/mcm$ – $Imma$ at 314 K, $Imma$ – $R\bar{3}c$ at 430 K, and $R\bar{3}c$ – $Pm\bar{3}m$ at 1250 K. The same RT structure of CeAlO_3 was confirmed by Fu and Ijdo (2004), and a similar sequence of phase transformations was observed independently using *in situ* time-of-flight neutron powder diffraction (Fu and Ijdo, 2006). Temperature dependencies of the lattice parameters of CeAlO_3 are shown in Figure 2, and crystallographic data of different structural polymorphs are summarized in Tables 3 and 4.

From the temperature behaviour of the lattice parameters and the cell volumes across the HT transition in CeAlO_3 , as well as due to the absence of thermal effects

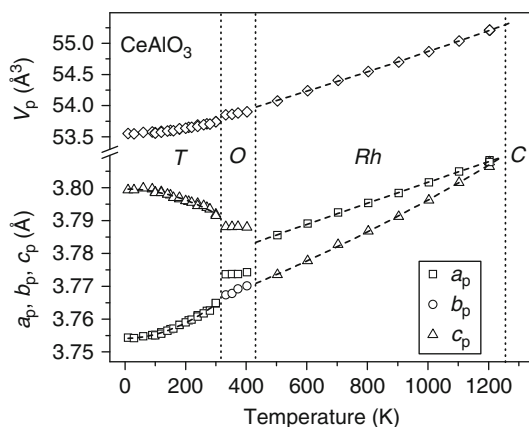


FIGURE 2 Temperature dependencies of the normalized lattice parameters and cell volume of tetragonal (T), orthorhombic (O), and rhombohedral (Rh) phases of CeAlO_3 according to Vasylechko et al. (2007b). The dashed lines are polynomial fits: $a_p(T) = 3.7541(1) [1 + 3.3(3) \times 10^{-8}T^2 - 6.5(6) \times 10^{-11}T^3]$; $c_p(T) = 3.7996(2) [1 - 2.2(5) \times 10^{-8}T^2 - 1.4(4) \times 10^{-13}T^3]$ for the temperature range 12–300 K; $a_p(T) = 3.771(1) + 9(3) \times 10^{-6}T$; $b_p(T) = 3.753(2) + 4.0(6) \times 10^{-6}T$; $c_p(T) = 3.7888(6) - 1.8(6) \times 10^{-6}T$ for the temperature range 333–403 K; and $a_p(T) = 3.7781(7) [1 + 1.02(7) \times 10^{-8}T^2 - 3.92(5) \times 10^{-12}T^3]$; $c_p(T) = 3.764(1) [1 + 1.2(1) \times 10^{-8}T^2 - 3.5(9) \times 10^{-12}T^3]$ for the temperature range 503–1203 K.

TABLE 3 Structural parameters of tetragonal (S.G. *I4/mcm*) and orthorhombic (S.G. *Imma* and *Ibmm*) modifications of CeAlO₃

Parameters	Tanaka et al. (1993b) ¹	Vasylechko (2005), Vasylechko et al. (2007b) ²	Vasylechko and Matkovskii (2004) ²	Vasylechko et al. (2002a, 2007b) ²	Vasylechko (2005), Vasylechko et al. (2007b) ²	Fu and Ijdo (2004) ³	Fu and Ijdo (2006) ⁴	Fu and Ijdo (2006) ⁴	Fu and Ijdo (2006) ⁴	
	<i>P4/mmm</i> (298 K)	<i>I4/mcm</i> (12 K)	<i>I4/mcm</i> (100 K)	<i>I4/mcm</i> (298 K)	<i>Imma</i> (373 K)	<i>I4/mcm</i> (RT)	<i>I4/mcm</i> (4.2 K)	<i>I4/mcm</i> (300 K)	<i>Ibmm</i> (373 K)	
<i>a</i> (Å)	3.7669(9)	5.30945(5)	5.31483(4)	5.32970(7)	5.33725(9)	5.32489(6)	5.31001(1)	5.32358(1)	5.35834(3)	
<i>b</i> (Å)	–	–	–	–	7.5370(1)	–	–	–	5.33759(2)	
Atom: sites	<i>c</i> (Å)	3.7967(7)	7.59866(9)	7.60328(1)	7.5868(1)	7.58976(10)	7.59984(3)	7.58849(4)	7.53647(3)	
Ce: 1 <i>d</i> in <i>P4/mmm</i> ; 4 <i>b</i> in <i>I4/mcm</i> ; 4 <i>e</i> in <i>Imma</i> , <i>Ibmm</i>	<i>x</i>	1/2	0	0	0	1/2	0	0	0.4996(3)	
	<i>y</i>	1/2	1/2	1/2	1/2	1/4	0	1/2	1/2	0
	<i>z</i>	1/2	1/4	1/4	1/4	0.4968(7)	1/4	1/4	1/4	1/4
	<i>B</i> _{iso} (Å ²)	0.298(4)	0.16(3)	0.48(2)	1.03(2)	0.69(1)	0.54(2)	0.82(2)*	0.74(2)*	0.88(2)*
Al: 1 <i>a</i> in <i>P4/mmm</i> ; 4 <i>b</i> in <i>I4/mcm</i> ; 4 <i>c</i> in <i>Imma</i> , <i>Ibmm</i>	<i>x</i>	0	0	0	0	0	0	0	0	
	<i>y</i>	0	0	0	0	0	0	0	0	
	<i>z</i>	0	0	0	0	0	0	0	0	
	<i>B</i> _{iso} (Å ²)	0.24(2)	0.19(11)	0.48(2)	1.26(10)	0.7(15)	0.49(6)	1.06(3)*	0.76(2)*	0.84(2)*
O1: 2 <i>f</i> in <i>P4/mmm</i> ; 4 <i>a</i> in <i>I4/mcm</i> ; 4 <i>e</i> in <i>Imma</i> , <i>Ibmm</i>	<i>x</i>	1/2	0	0	0	0	0	0	0.0429(2)	
	<i>y</i>	0	0	0	0	1/4	0	0	0	
	<i>z</i>	0	1/4	1/4	1/4	–0.039(9)	1/4	1/4	1/4	1/4
	<i>B</i> _{iso} (Å ²)	2.1(2)	0.9(3)	1.0(2)	0.8(2)	1.2(3)	1.1(2)	0.95(2)*	1.12(2)*	0.95(3)*
O2: 2 <i>f</i> in <i>P4/mmm</i> ; 8 <i>h</i> in <i>I4/mcm</i> ; 8 <i>g</i> in <i>Imma</i> , <i>Ibmm</i>	<i>x</i>	0	0.2146(11)	0.2160(8)	0.2202(11)	1/4	0.2777(8)	0.28531(7)	0.28119(7)	1/4
	<i>y</i>	1/2	<i>x</i> + 1/2	<i>x</i> + 1/2	<i>x</i> + 1/2	–0.008(5)	<i>x</i> + 1/2	<i>x</i> + 1/2	<i>x</i> + 1/2	1/4
	<i>z</i>	0	0	0	0	1/4	0	0	0	–0.02158(9)
	<i>B</i> _{iso} (Å ²)	2.3(1)	0.7(2)	0.9(2)	0.9(2)	0.8(15)	0.4(1)	0.96(2)*	0.83(2)*	1.00(2)*
O3: 1 <i>b</i> in <i>P4/mmm</i>	<i>x</i>	0	–	–	–	–	–	–	–	
	<i>y</i>	0	–	–	–	–	–	–	–	
	<i>z</i>	1/2	–	–	–	–	–	–	–	
	<i>B</i> _{iso} (Å ²)	0.77(5)	–	–	–	–	–	–	–	

¹ X-ray single crystal diffraction data. Split model, in which Ce and oxygen atoms are shifted from their ideal positions, is also proposed in the paper.² Synchrotron powder diffraction data.³ X-ray powder diffraction data.⁴ Neutron powder diffraction data.* Calculated from the *U*_{iso} values given in the reference.

TABLE 4 Structural parameters of rhombohedral (S.G. $R\bar{3}c$, hexagonal and rhombohedral settings) and cubic (S.G. $Pm\bar{3}m$) modifications of $CeAlO_3$

Parameters	Vasylechko (2005), Vasylechko et al. (2007b) ¹	Vasylechko (2005), Vasylechko et al. (2007b) ¹	Vasylechko (2005), Vasylechko et al. (2007b) ¹	Fu and Ijdo (2006) ²	Fu and Ijdo (2006) ²	Fu and Ijdo (2006) ²	Fu and Ijdo (2006) ²	
	$R\bar{3}c$ (603 K)	$R\bar{3}c$ (1203 K)	$Pm\bar{3}m$ (1203 K)	$R\bar{3}c$ (<i>Rh</i>) (473 K)	$R\bar{3}c$ (<i>Rh</i>) (1323 K)	$Pm\bar{3}m$ (1373 K)	$Pm\bar{3}m$ (1423 K)	
a (Å)	5.35866(7)	5.3859(2)	3.80786(3)	5.33946(2)	5.39614(21)	3.817880(7)	3.820115(7)	
c (Å)	13.0868(3)	13.1859(9)	–	–	–	–	–	
Atom: sites	α (°)	–	–	–	60.134(1)	60.004(4)	–	
Ce: $6c$ in $R\bar{3}c$; $2a$ in $R\bar{3}c$, <i>Rh</i> ; $1b$ in $Pm\bar{3}m$	x	0	0	1/2	1/4	1/4	1/2	
	y	0	0	1/2	1/4	1/4	1/2	
	z	1/4	1/4	1/2	1/4	1/4	1/2	
	B_{iso} (Å ²)	0.75(3)	1.22(14)	1.29(1)	0.96(2)*	2.11(5)*	2.19(3)*	2.31(3)*
Al: $6b$ in $R\bar{3}c$; $2b$ in $R\bar{3}c$, <i>Rh</i> ; $1a$ in $Pm\bar{3}m$	x	0	0	0	0	0	0	
	y	0	0	0	0	0	0	
	z	0	0	0	0	0	0	
	B_{iso} (Å ²)	0.64(14)	0.7(8)	0.91(5)	0.84(2)*	1.43(3)*	1.50(3)*	1.56(3)*
O: $18e$ in $R\bar{3}c$; $6e$ in $R\bar{3}c$, <i>Rh</i> ; $3d$ in $Pm\bar{3}m$	x	0.528(2)	0.519(3)	1/2	0.78375(8)	0.76202(17)	1/2	1/2
	y	0	0	0	1/2– x	1/2– x	0	0
	z	1/4	1/4	0	1/4	1/4	0	0
	B_{iso} (Å ²)	1.9(4)	2.5(18)	2.8(2)	0.95(3)*	2.56(2)*	2.75(2)*	2.82(2)*

¹ Synchrotron powder diffraction data.² Neutron powder diffraction data.* Calculated from the U_{iso} values given in the reference.

in the DTA/DSC curves, a continuous character of the $R\bar{3}c-Pm\bar{3}m$ transformation was concluded (Vasylechko *et al.*, 2007b). The analysis of the temperature variation of the AlO_6 octahedra tilt angle $\varphi(T)$ (Vasylechko and Matkovskii, 2004) showed that the $R\bar{3}c-Pm\bar{3}m$ transition in $CeAlO_3$ is between second-order and tri-critical. Similar fitting of $\varphi(T)$ obtained from neutron diffraction data by Fu and Ijdo (2006) also suggests that the character of this transition in $CeAlO_3$ is between second-order and tri-critical. Both LT phase transitions in $CeAlO_3$ ($R\bar{3}c-Imma$ and $Imma-I4/mcm$) are accompanied by the step-like changes in the cell volumes and small endothermic effects in the DSC that give evidence for the discontinuous character of these transformations. Besides, in both cases, the coexistence of LT and HT phases over the temperature range ± 30 K in the vicinity of the phase transitions has been detected. This together with the observation of a temperature hysteresis in the magnetic susceptibility indicates the first-order character of both transitions (Vasylechko *et al.*, 2007b).

It is important to note that the observed sequence of phase transitions in $CeAlO_3$ is unique among all other AMO_3 compounds with perovskite structures. Similar complicated phase behaviour was observed only for praseodymium aluminate, described in Section 2.2.3.

2.2.3 Praseodymium aluminate $PrAlO_3$

Praseodymium aluminate, $PrAlO_3$, is one of the most extensively studied compounds among all $RAIO_3$ perovskites, mainly because of its unusual structural behaviour below RT. Nevertheless, the discussions concerning these transitions and the crystal structures of the LT phases are not settled even today. Initially, Geller and Bala (1956) proposed S.G. $R\bar{3}m$ for the rhombohedral structure of $PrAlO_3$ at RT. Later, Derighetti *et al.* (1965) showed that similar to $LaAlO_3$, the correct space group for $PrAlO_3$ is in fact $R\bar{3}c$. The rhombohedral structure of $PrAlO_3$ transforms into the cubic perovskite structure on heating. The temperature of this transition has been predicted by Scott (1969) at 1320 K from the extrapolation of some Raman modes. However, based on *in situ* HT powder diffraction and DTA data, Geller and Raccah (1970) reported that the rhombohedral-to-cubic phase transition in $PrAlO_3$ occurs at a considerably higher temperature (1643 K). Recent precise structural investigations of $PrAlO_3$ performed by Howard *et al.* (2000) showed that the continuous transition from the rhombohedral to cubic structure of $PrAlO_3$ occurs as high as 1770 K (Figure 3). In this respect, the praseodymium aluminate is similar to the isostructural $LaAlO_3$ and $NdAlO_3$ perovskites.

But in contrast to these two compounds, $PrAlO_3$ undergoes additional phase transformations below RT: the first-order transition from the rhombohedral to an orthorhombic structure at 205 K and the second-order transformation from the orthorhombic to a monoclinic structure at 151 K (Cohen *et al.*, 1969; Harley *et al.*, 1973; Birgeneau *et al.*, 1974; Lyons *et al.*, 1975; Young, 1975). These transitions are considered to be caused by the electronic effects involving Pr^{3+} ions, such as the coupling between Pr^{3+} electronic states and phonons, as well as cooperative Jahn-Teller effects. According to the qualitative X-ray diffraction study performed by Burbank (1970) using a multi-domain $PrAlO_3$ single crystal, the most likely space

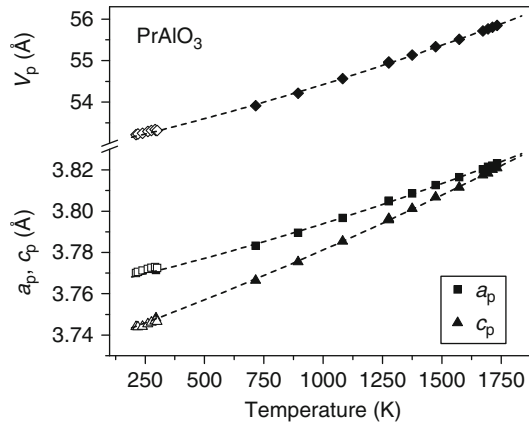


FIGURE 3 Temperature dependencies of the normalized lattice parameters and cell volumes of the rhombohedral phase of PrAlO_3 . Solid symbols indicate the HT data of Howard et al. (2000), open symbols indicate the LT data reported by Vasylechko (unpublished data). The dashed lines are polynomial fits: $a_p(T) = 3.7356(9) + 3.5(4) \times 10^{-5}T + 1.3(5) \times 10^{-8}T^2 - 3(1) \times 10^{-12}T^3$, $c_p(T) = 3.7683(8) + 7(4) \times 10^{-6}T + 2.4(5) \times 10^{-8}T^2 - 5(1) \times 10^{-12}T^3$ for the temperature range 212–1733 K.

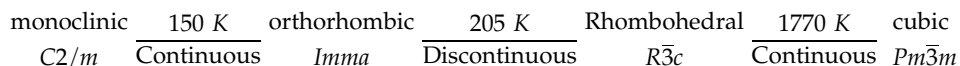
groups for the corresponding polymorphs are $\bar{F}32$ at 293 K, $I2/m$ at 172 K, and $I\bar{1}$ at 135 K. In addition to these transformations, several authors reported an additional transition to a tetragonal structure around 118 K, which was considered to be due to the coupling between acoustic phonons and temperature-dependent optical modes (Harley et al., 1973; Fleury et al., 1974; Sturge et al., 1975; Benard and Walker, 1976; Harley, 1977; D'Iorio et al., 1984). Structural modulations of PrAlO_3 in the vicinity of the structural phase transitions around 120, 150, and 210 K have been studied using X-ray diffraction combining energy-dispersive methods and using a modified Weissenberg camera (Fujii et al., 1999). The authors concluded that the phase transition at 120 K is second-order and proposed the following transition sequence in PrAlO_3 :

			120 K		150 K		205 K		1320 K	
Phase	V	→	IV	→	III	→	II	→	I	
Symmetry	Tetragonal		Monoclinic		Orthorhombic		Trigonal		Cubic	

This sequence was confirmed by a recent investigation performed by Watanabe et al. (2006) using neutron diffraction. According to their study, the PrAlO_3 structure successively transforms from the rhombohedral $R\bar{3}c$ (phase II) to the orthorhombic $Imma$ (phase III), orthorhombic $Imma$ (phase IV), and tetragonal $I4/mcm$ (phase V) at 215, 153, and 122 K, respectively. Note that the phases III and IV are described as having the same orthorhombic $Imma$ structure, but with a different scheme of AlO_6 octahedra tilting angles: $\psi_a = \psi_c$, $\psi_b = 0$ in phase III and $\psi_a \neq \psi_c$, $\psi_b = 0$ in phase IV. Phase IV is characterized by an intermediate state in which the ψ_a tilts are continuously reduced by Jahn-Teller distortion of the $\text{Pr}^{3+} 4f$

orbital in PrO_{12} polyhedra, which disappear just above the 122 K transition. Unfortunately, the authors did not provide any structural information on the different modifications of PrAlO_3 in their work.

Another interpretation of the LT structural behaviour of PrAlO_3 was given by [Moussa et al. \(2001\)](#) and [Carpenter et al. \(2005\)](#). Based on a combination of high-resolution neutron and synchrotron powder diffraction data, [Moussa et al. \(2001\)](#) showed that the RT rhombohedral structure of PrAlO_3 transforms into an orthorhombic $Imma$ structure on cooling to about 205 K than to a monoclinic $C2/m$ structure near 150 K. The structure tends towards tetragonal symmetry as the sample is further cooled; however, the symmetry remains monoclinic down to 10 K. The authors proposed the following transition scheme in PrAlO_3 :



The described subsequent phase transitions have been interpreted in terms of strain/order parameter coupling using a simple Landau free-energy expansion for the $Pm\bar{3}m$ structure for two instabilities ([Carpenter et al., 2005](#)). According to this comprehensive study, the $R\bar{3}c$ – $Imma$ transition can be understood as occurring because of the coupling between tilting and electronic order-parameter components via a common tetragonal strain. The strain for the $Imma$ – $I2/m$ transition agrees closely with the Landau solution for a proper ferroelastic transition of second-order and a low-temperature saturation. This transition could effectively be driven by the electronic instability alone. Due to the authors, the acoustic and optical anomalies reported in the literature around 118 K appear to be associated with a metrically tetragonal structure that develops as accidental strain degeneracy between 110 and 120 K. Crystallographic data for LT modifications of PrAlO_3 evaluated from neutron powder diffraction data and temperature dependencies of the lattice parameters and some interatomic distances in the temperature range 4.2–300 K are given in the paper ([Carpenter et al., 2005](#)). *In situ* examination of the structure in the temperature range 12–298 K performed by using high-resolution powder diffraction techniques and synchrotron radiation (Vasylechko, unpublished data) confirms the earlier reported phase behaviour of PrAlO_3 . The temperature dependencies of the lattice parameters obtained on cooling and heating ([Figure 4](#)) clearly reflect all three anomalies (110, 150, and 205 K) described in the literature. They are in an excellent agreement with the data derived from neutron diffraction by [Carpenter et al. \(2005\)](#).

The structures of the phases below 150 and 120 K were refined based on three possible symmetries—orthorhombic, monoclinic, and tetragonal. The structure of the LT-V phase below 110 K may successfully be refined both in the tetragonal and monoclinic lattices with practically the same residuals (see [Table 5](#)). In spite of more adjustable parameters in the monoclinic model, no improvement of the residuals was achieved. For the Pr and O3 atoms in the monoclinic model, no deviation from the tetragonal symmetry was found within the uncertainties. Besides, physically meaningless values of atomic displacement parameters (adp)

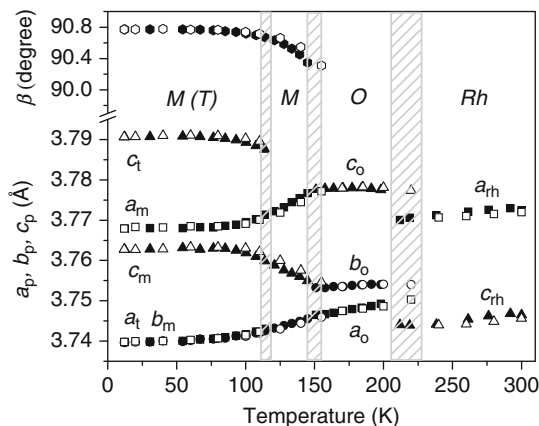


FIGURE 4 Low-temperature dependencies of the lattice parameters of (pseudo)-tetragonal (T), monoclinic (M), orthorhombic (O), and rhombohedral (Rh) PrAlO_3 phases, obtained on cooling and heating (solid and open symbols, respectively). The lines are guides for the eye. For the LT-V phase below 110 K, both monoclinic and tetragonal lattice parameters are shown (Vasylechko, unpublished data).

were observed for the oxygen atoms using the monoclinic model. All of this indicates that the tetragonal structure for the LT-V phase of PrAlO_3 is a better approximation than the monoclinic variant. Nevertheless, considering all arguments of different research groups that were given in favour of either one or the other structural model for the LT-V phase of PrAlO_3 , we decided to list structural information for both the tetragonal and monoclinic settings of PrAlO_3 below 110 K in Table 5.

It was also observed that the structure of the LT-IV phase could not satisfactorily be refined in the orthorhombic $Imma$ lattice, as proposed by Watanabe et al. (2006), whereas the refinement in the monoclinic space group $I2/m$ showed a good agreement between the observed and calculated profiles, leading to the final structural parameters given in Table 6. These results match well with the data recently published by Carpenter et al. (2005).

The behaviour of PrAlO_3 at high pressures has been studied by Kennedy et al. (2002a) at RT. The authors showed that the compound undergoes a phase transition from the rhombohedral to the orthorhombic $Imma$ structure upon pressuring to 9.1 GPa. It was also shown that the structure initially evolves towards a high-symmetry configuration as the pressure is increased before ultimately undergoing a phase transition to a lower-symmetry orthorhombic structure. This is in contrast with the parent LaAlO_3 compound that undergoes a transition from rhombohedral to the ideal cubic structure in the vicinity of 14 GPa at room temperature (Bouvier and Kreisel, 2002; Zhao et al., 2004a). Kennedy et al. (2002a) showed that the pressure induced phase transition in PrAlO_3 is associated with measurable changes of the volume of the AlO_6 octahedra. The authors concluded that ‘high pressure induces the same crystallographic phase transition in PrAlO_3 as does cooling’.

TABLE 5 Structural parameters of PrAlO₃ at 12 K, refined in tetragonal and monoclinic lattices

Lattice parameters (Å)	Atoms, sites	<i>x</i>	<i>y</i>	<i>z</i>	<i>B</i> _{iso} (Å ²)	<i>B</i> ₁₁	<i>B</i> ₂₂	<i>B</i> ₃₃	<i>B</i> ₁₂	<i>B</i> ₁₃	<i>B</i> ₂₃
S.G. <i>I4/mcm</i> [#] , <i>R</i> _I = 0.0503; <i>R</i> _P = 0.0841											
<i>a</i> = 5.28882(6),	Pr, 4 <i>b</i>	0	1/2	1/4	0.41(1)	0.39(1)	<i>B</i> ₁₁	0.46(2)	0	0	0
<i>c</i> = 7.5812(1)	Al, 4 <i>c</i>	0	0	0	0.44(4)	0.52(5)	<i>B</i> ₁₁	0.30(9)	0	0	0
	O1, 4 <i>a</i>	0	0	1/4	0.83(12)	0.9(2)	<i>B</i> ₁₁	0.8(2)	0	0	0
	O2, 8 <i>h</i>	0.2111(6)	<i>x</i> + 1/2	0	0.70(10)	0.4(2)	<i>B</i> ₁₁	1.3(2)	-0.1(2)	0	0
S.G. <i>I2/m</i> , <i>R</i> _I = 0.0528, <i>R</i> _P = 0.0825											
<i>a</i> = 5.3214(2),	Pr, 4 <i>i</i>	0.2504(13)	0	0.7493(12)	0.43(5)	0.56(8)	0.35(10)	0.39(6)	0	0.03(6)	0
<i>b</i> = 7.4784(3),	Al, 4 <i>e</i>	1/4	1/4	1/4	0.5(2)	0.9(4)	0.2(5)	0.4(3)	0.2(13)	0.3(3)	-0.3(13)
<i>c</i> = 5.3292(2),	O1, 4 <i>i</i>	0.196(6)	0	0.196(5)	-0.4(4)	-0.7(8)	0.4(6)	-0.9(7)	0	-0.2(5)	0
<i>β</i> = 90.765(3)	O2, 4 <i>g</i>	0	0.273(4)	0	0.9(6)	1.4(12)	-0.7(10)	1.9(10)	0	-1.3(5)	0
	O3, 4 <i>h</i>	1/2	0.249(18)	0	1.7(7)	-0.5(6)	5.8(19)	-0.2(5)	0	-1.1(3)	0

[#] ©JCPDS—International Centre for Diffraction data, to be published.

TABLE 6 Structural parameters of monoclinic (S.G. $I2/m$) and orthorhombic (S.G. $Imma$) modifications of PrAlO_3

Parameters	Carpenter et al. (2005) ¹	Carpenter et al. (2005) ¹	Carpenter et al. (2005) ¹	Carpenter et al. (2005) ¹	Basyuk and Vasylechko (2007) ²	Basyuk and Vasylechko (2007) ²	
	$I2/m$ (4.2 K)	$I2/m$ (100 K)	$I2/m$ (140 K)	$Imma$ (185 K)	$I2/m$ (120 K) [#]	$Imma$ (170 K) [#]	
a (Å)	5.3189(1)	5.3183(1)	5.3109(1)	5.3092(1)	5.3353(3)	5.3089(1)	
b (Å)	7.4797(2)	7.4835(2)	7.4907(1)	7.4969(1)	7.4862(6)	7.4947(1)	
c (Å)	5.3299(1)	5.3313(1)	5.3394(1)	5.3423(1)	5.3160(4)	5.34350(9)	
Atom: sites	β (°)	90.753(1)	90.703(1)	90.413(1)	—	90.637(7)	—
Pr: 4i in $I2/m$; 4e in $Imma$	x	0.2524(14)	0.2525(14)	0.2498(8)	0	0.2510(8)	0
	y	0	0	0	1/4	0	1/4
	z	0.7517(12)	0.7507(12)	0.7483(6)	0.5018(4)	0.7494(7)	0.5013(4)
	B_{iso} (Å ²)	0.33(3)*	0.31(3)*	0.35(3)*	0.43(3)*	0.799(7)	0.716(8)
Al: 4e in $I2/m$; 4b in $Imma$	x	1/4	1/4	1/4	0	1/4	0
	y	1/4	1/4	1/4	0	1/4	0
	z	1/4	1/4	1/4	0	1/4	0
	B_{iso} (Å ²)	0.45(4)*	0.40(5)*	0.42(5)*	0.45(4)*	0.78(3)	0.76(3)
O1: 4i in $I2/m$; 4e in $Imma$	x	0.2177(8)	0.2206(9)	0.2351(5)	0	0.204(3)	0
	y	0	0	0	1/4	0	1/4
	z	0.2067(8)	0.2049(8)	0.1979(4)	0.0527(3)	0.248(3)	0.0558(15)
	B_{so} (Å ²)	0.30(9)*	0.40(9)*	0.43(5)*	0.45(3)*	1.0(3)	0.7(2)
O2: 4g in $I2/m$; 8g in $Imma$	x	0	0	0	1/4	0	1/4
	y	0.2904(8)	0.2897(8)	0.2849(3)	−0.0277(1)	0.294(2)	−0.0227(10)
	z	0	0	0	1/4	0	1/4
	B_{iso} (Å ²)	0.77(10)*	0.65(10)*	0.58(5)*	0.66(2)*	0.4(2)	0.80(11)
O3: 4h in $I2/m$	x	1/2	1/2	1/2	—	1/2	—
	y	0.2588(7)	0.2605(7)	0.2696(4)	—	0.239(3)	—
	z	0	0	0	—	0	—
	B_{iso} (Å ²)	0.56(3)*	0.53(4)*	0.54(5)*	—	0.89(10)	—

¹ Neutron powder diffraction data.² Synchrotron powder diffraction data.* Calculated from the U_{iso} values given in the reference.[#] © JCPDS—International Centre for Diffraction data, to be published.

Crystallographic data for all structural modifications of PrAlO_3 reported by different research groups are summarized in [Tables 6 and 7](#).

2.2.4 Neodymium aluminate NdAlO_3

The crystal structure of NdAlO_3 has been studied using X-ray powder diffraction ([Geller and Bala, 1956](#)), single crystal diffraction ([Marezio *et al.*, 1972](#)), and neutron powder diffraction techniques ([Roult *et al.*, 1983](#)). It was shown that at RT, NdAlO_3 possesses a rhombohedral structure, S.G. $R\bar{3}c$, which then transforms into the cubic perovskite structure at elevated temperatures. The temperatures for this transition reported by different research groups vary considerably: 1640 ± 30 K ([Scott, 1969](#)), 1373 K ([Mizuno *et al.*, 1977b](#)), 1823 K ([Coutures and Coutures, 1984](#)), 2020 K ([Geller and Raccah, 1970](#)), and 2180 K ([Howard *et al.*, 2000](#)). These discrepancies may be explained by difficulties in the detection of the temperature for a continuous phase transition by using low-resolution thermal analysis or laboratory X-ray diffraction methods. From the analysis of numerous data on similar phase transitions in related RAlO_3 compounds ($R = \text{La, Ce, and Pr}$) and corresponding solid solutions (see [Section 2.5](#)), it is evident that the rhombohedral-to-cubic transition in NdAlO_3 occurs near 2100 K.

Another type of phase transition in NdAlO_3 , namely the LT transformation from the rhombohedral to orthorhombic structure, has been predicted at 16 K from the extrapolation of transition temperatures in the $\text{Nd}_{1-x}\text{Sm}_x\text{AlO}_3$ solid solution ([Yoshikawa *et al.*, 1998](#)). This transition, however, was not confirmed using synchrotron powder diffraction data collected *in situ* at temperatures down to 12 K ([Vasylechko *et al.*, 2007b](#)) and neutron diffraction measurements at 0.5 and 1 K ([Palacios *et al.*, 2003](#)). [Figure 5](#) displays the temperature evolution of the lattice parameters and cell volume of NdAlO_3 . Structural parameters of the rhombohedral phase of NdAlO_3 over a broad temperature range are given in [Table 8](#).

2.2.5 Samarium aluminate SmAlO_3

Samarium aluminate is the first member in the series of RAlO_3 compounds exhibiting an orthorhombic structure at RT. The GdFeO_3 type of structure of SmAlO_3 has been reported for the first time by [Geller and Bala \(1956\)](#). Later it was confirmed by [Dernier and Maines \(1971\)](#). A full structural investigation of SmAlO_3 was performed by [Marezio *et al.* \(1972\)](#), who refined atomic coordinates and anisotropic displacement parameters of the atoms using X-ray single crystal diffraction data. SmAlO_3 undergoes a discontinuous phase transition from an orthorhombic to a rhombohedral structure around 1023–1058 K, according to the data reported by several authors ([Arsenev *et al.*, 1983](#); [Coutures and Coutures, 1984](#); [Yoshikawa *et al.*, 1998](#); [O'Bryan *et al.*, 1990](#); [Vasylechko *et al.*, 2004a](#)). Based on *in situ* X-ray diffraction studies, [Coutures and Coutures \(1984\)](#) found another reversible phase transitions in SmAlO_3 —from rhombohedral to cubic structure at 2223 K. However, this transition was not confirmed by other researchers. From the temperature behaviour of the rhombohedral-to-cubic phase transitions in the $\text{R}_{1-x}\text{R}'_x\text{AlO}_3$ solid solutions (see [Section 2.5](#)), a similar transition

TABLE 7 Structural parameters of the rhombohedral modification of PrAlO₃ (S.G. $R\bar{3}c$) at different temperatures

	Parameters	Howard et al.	Howard et al.	Howard et al.	Howard et al.	Carpenter	This	This
		(2000) ¹	(2000) ¹	(2000) ¹	(2000) ¹	et al. (2005) ¹	work ²	work ²
		295 K	716 K	1277 K	1733 K	300 K	219 K	300 K
Atom: sites	a (Å)	5.3337(2)	5.3504(2)	5.3807(2)	5.4067(3)	5.33375(2)	5.33246(8)	5.33509(8)
	c (Å)	12.9842(4)	13.0474(5)	13.1486(5)	13.2360(15)	12.9773(1)	12.9693(2)	12.9783(2)
Pr, 6c	x	0	0	0	0	0	0	0
	y	0	0	0	0	0	0	0
	z	1/4	1/4	1/4	1/4	1/4	1/4	1/4
	B_{iso} (Å ²)	—	—	—	—	0.55(3)*	0.830(8)	0.89(1)
Al, 6b	x	0	0	0	0	0	0	0
	y	0	0	0	0	0	0	0
	z	0	0	0	0	0	0	0
	B_{iso} (Å ²)	—	—	—	—	0.55(3)*	0.89(3)	0.95(4)
O, 18e	x	0.5421(2)	0.5387(2)	0.5318(3)	0.5151(5)	0.5428(1)	0.5408(9)	0.5420(7)
	y	0	0	0	0	0	0	0
	z	1/4	1/4	1/4	1/4	1/4	1/4	1/4
	B_{iso} (Å ²)	—	—	—	—	0.72(2)*	0.92(7)	0.93(7)

¹ Neutron powder diffraction data.² Synchrotron powder diffraction data.* Calculated from the U_{iso} values given in the reference.

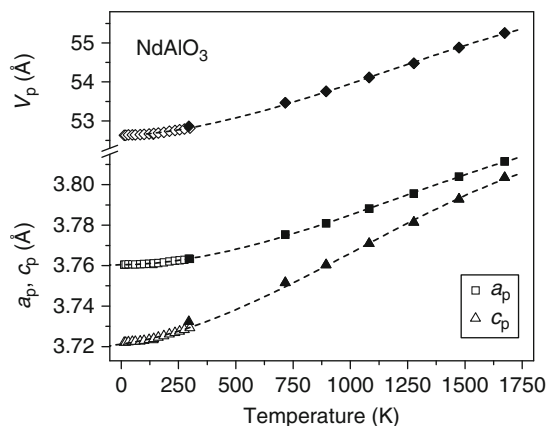


FIGURE 5 Thermal evolution of the normalized lattice parameters of NdAlO₃. Lattice parameters are taken from Howard *et al.* (2000) (HT data, solid symbols) and Vasylechko (2005) (LT data, open symbols). The dashed lines are polynomial fits: $a_p(T) = 3.7603(1) + 1.9(9) \times 10^{-6}T + 3.1(2) \times 10^{-8}T^2 - 8.4(6) \times 10^{-12}T^3$, $c_p(T) = 3.7211(3) + 1.6(3) \times 10^{-5}T + 4.2(4) \times 10^{-8}T^2 - 1.4(2) \times 10^{-11}T^3$ for the temperature range 13–1673 K.

in SmAlO₃ could be predicted about 2500 K, which is above the melting temperature of the compound. Low-temperature examinations of SmAlO₃ performed *in situ* by means of synchrotron powder diffraction revealed that the structure remains orthorhombic down to 12 K (Vasylechko *et al.*, 2004a; Vasylechko, 2005). The thermal evolution of normalized lattice parameters of SmAlO₃ in the temperature range 12–1223 K is shown in Figure 6. Table 9 summarizes the refined structural parameters of SmAlO₃ for different temperatures.

Both the orthorhombic and rhombohedral phases of SmAlO₃ show anisotropic and non-linear thermal expansion in different directions. Peculiarly, the orthorhombic phase with different cell parameter ratio a_p , b_p , and c_p within the same GdFeO₃ type of structure is observed in different temperature ranges (Figure 6). First, $b_p > a_p > c_p$ at temperatures below 200 K, followed by $a_p > b_p > c_p$ in the temperature range 200–700 K, and finally, $a_p > c_p > b_p$ at the temperatures 700–1050 K, just before the transition to the rhombohedral phase. As was shown (Vasylechko *et al.*, 2005), the following cell parameter ratio $a_p > b_p > c_p$ ($a_p > c_p \approx b_p$) observed in GdFeO₃-type perovskites can serve as an indicator of the forthcoming phase transition from the orthorhombic to the rhombohedral structure.

2.2.6 Europium aluminate EuAlO₃

Another compound in the RAlO₃ series, which adopts the orthorhombic GdFeO₃-type structure at RT, is europium aluminate EuAlO₃ (Geller and Bala, 1956). Nevertheless, the first reports of the refined structural parameters of EuAlO₃ appeared only 50 years later, when the structural parameters of EuAlO₃ were obtained from synchrotron powder diffraction data over the

TABLE 8 Structural parameters of NdAlO₃ (S.G. R $\bar{3}c$) at different temperatures

	Parameters	Marezio et al.	Roult et al.	Howard et al.	Howard et al.	Vasylechko	Vasylechko
		(1972) ¹	(1983) ²	(2000) ²	(2000) ²	(2005) ³	(2005) ³
		RT	296 K	295 K	1673 K	12 K	298 K
Atom: sites	a (Å)	5.322(2)	5.3200(1)	5.3223(2)	5.3902(2)	5.31804(4)	5.32221(4)
	c (Å)	12.916(5)	12.9125(6)	12.9292(5)	13.1756(5)	12.8937(1)	12.9185(1)
Nd, 6c	x	0	0	0	0	0	0
	y	0	0	0	0	0	0
	z	1/4	1/4	1/4	1/4	1/4	1/4
	B_{iso} (Å ²)	0.34	0.49	—	—	0.46(1)	0.80(1)
Al, 6b	x	0	0	0	0	0	0
	y	0	0	0	0	0	0
	z	0	0	0	0	0	0
	B_{iso} (Å ²)	0.22	0.48	—	—	0.27(5)	0.59(6)
O, 18e	x	0.5516(9)	0.5477(2)	0.5470(2)	0.5330(4)	0.5483(8)	0.5480(8)
	y	0	0	0	0	0	0
	z	1/4	1/4	1/4	1/4	1/4	1/4
	B_{iso} (Å ²)	0.48	0.69	—	—	0.74(14)	0.9(2)

¹ X-ray powder diffraction data.² Neutron powder diffraction data.³ Synchrotron powder diffraction data.

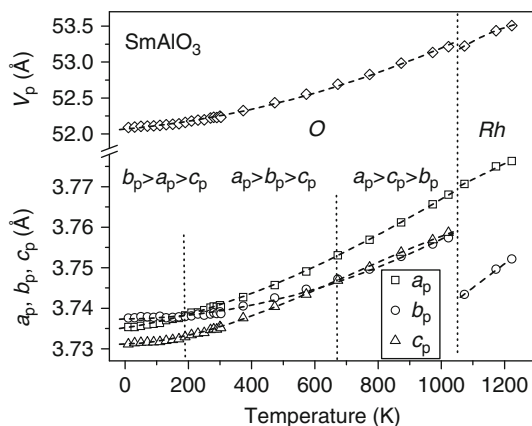


FIGURE 6 Temperature dependencies of the normalized lattice parameters and cell volume of orthorhombic (O) and rhombohedral (Rh) SmAlO_3 phases (Vasylechko, 2005). The dashed lines are polynomial fits: $a_p(T) = 3.7357(1) [1 + 2.03(9) \times 10^{-8}T^2 - 2.1(2) \times 10^{-11}T^3 + 9(1) \times 10^{-15}T^4]$; $b_p(T) = 3.7375(1) [1 + 3(1) \times 10^{-9}T^2 + 7(2) \times 10^{-11}T^3 - 5(1) \times 10^{-15}T^4]$; $c_p(T) = 3.73115(6) [1 + 1.54(6) \times 10^{-8}T^2 - 1.1(1) \times 10^{-11}T^3 + 2.6(8) \times 10^{-15}T^4]$ for the temperature range 12–1023 K and $a_p(T) = 3.729(5) + 3.9(5) \times 10^{-5}T$; $c_p(T) = 3.680(3) + 5.9(3) \times 10^{-5}T$ for the temperature range 1073–1223 K.

temperature range 298–1173 K (Vasylechko *et al.*, 2003a; Vasylechko and Matkovskii, 2004; Vasylechko, 2005). It was shown that the structure is orthorhombic over the whole investigated temperature range. Recent low-temperature examination of EuAlO_3 (Vasylechko *et al.*, 2007a) revealed that the structure remains orthorhombic at least down to 14 K. No obvious anomalies were observed, although the LT expansivity in the b -direction is lower than expected from a simple Debye–Grüneisen approximation (Figure 7A). Because of the anisotropic character of the thermal expansion, the values of the normalized lattice parameters a_p , b_p , and c_p merge near 1200 K (Figure 7B). The analysis of selected interatomic distances and angles, as well as the perovskite structure deformation parameters, such as bond-length distortion and observed tolerance factors (Vasylechko, 2005), however, clearly indicate that the symmetry of EuAlO_3 remains orthorhombic and only the lattice shape becomes dimensionally cubic around 1200 K. Extrapolation of the temperature dependencies of the lattice parameters towards high temperatures shows that above 1280 K, the following ratio of lattice parameters $a_p > c_p > b_p$ will be observed, which indicates a forthcoming phase transition to the rhombohedral structure. According to Coutures and Coutures (1984), such a phase transition in EuAlO_3 occurs at 1603 K. A lower temperature of the phase transition was reported by Alain and Piriou (1975). Based on their analysis of polarized Raman spectra at various temperatures from 77 to 1500 K, the authors concluded that a first-order phase transition in EuAlO_3 occurs at 1420 K. The temperature evolution of the lattice parameters of EuAlO_3 is presented in Figure 7. Refined structural parameters of EuAlO_3 at 14 K, RT, and 1173 K are given in Table 10.

TABLE 9 Structural parameters of orthorhombic (S.G. $Pbnm$) and rhombohedral (S.G. $R\bar{3}c$) modifications of SmAlO_3

Parameters		Marezio et al. (1972) ¹	Vasylechko (2005) ²	Vasylechko (2005) ²	Vasylechko (2005) ²	Vasylechko (2005) ²	Vasylechko (2005) ²
		$Pbnm$ (RT)	$Pbnm$ (12 K)	$Pbnm$ (298 K)	$Pbnm$ (1023 K)	$R\bar{3}c$ (1073 K)	$R\bar{3}c$ (1223 K)
a (Å)		5.2912(2)	5.2826(1)	5.2903(1)	5.32881(7)	5.33252(4)	5.34055(4)
b (Å)		5.2904(2)	5.28595(9)	5.2880(1)	5.31373(7)	—	—
Atom: sites	c (Å)	7.4740(2)	7.4624(1)	7.4709(2)	7.5173(1)	12.9675(2)	12.9978(2)
Sm: 4c in $Pbnm$; 6c in $R\bar{3}c$	x	−0.00501(4)	−0.0056(2)	−0.0061(2)	−0.0065(4)	0	0
	y	0.02402(7)	0.02720(9)	0.0249(1)	0.0165(2)	0	0
	z	1/4	1/4	1/4	1/4	1/4	1/4
	B_{iso} (Å ²)	0.517(16)*	0.428(7)	0.663(8)	1.41(1)	1.55(2)	1.59(2)
Al: 4b in $Pbnm$; 6b in $R\bar{3}c$	x	1/2	1/2	1/2	1/2	0	0
	y	0	0	0	0	0	0
	z	0	0	0	0	0	0
	B_{iso} (Å ²)	0.44(6)*	0.38(3)	0.57(3)	1.04(5)	1.13(8)	1.15(8)
O1: 4c in $Pbnm$; 18e in $R\bar{3}c$	x	0.0644(8)	0.076(2)	0.079(2)	0.083(3)	0.5476(14)	0.5481(15)
	y	0.4903(11)	0.500(2)	0.503(2)	0.503(3)	0	0
	z	1/4	1/4	1/4	1/4	1/4	1/4
	B_{iso} (Å ²)	0.76(13)*	0.7(2)	1.2(3)	1.8(4)	1.7(2)	1.8(2)
O2: 8d in $Pbnm$	x	−0.2766(6)	−0.279(3)	−0.275(3)	−0.285(3)	—	—
	y	0.2770(6)	0.283(3)	0.270(3)	0.292(3)	—	—
	z	0.0335(6)	0.0275(14)	0.0278(14)	0.011(3)	—	—
	B_{iso} (Å ²)	0.70(8)*	0.50(11)	0.69(10)	1.3(2)	—	—

¹ X-ray single crystal diffraction data.² Synchrotron powder diffraction data.* Calculated from β_{ij} values given in the reference.

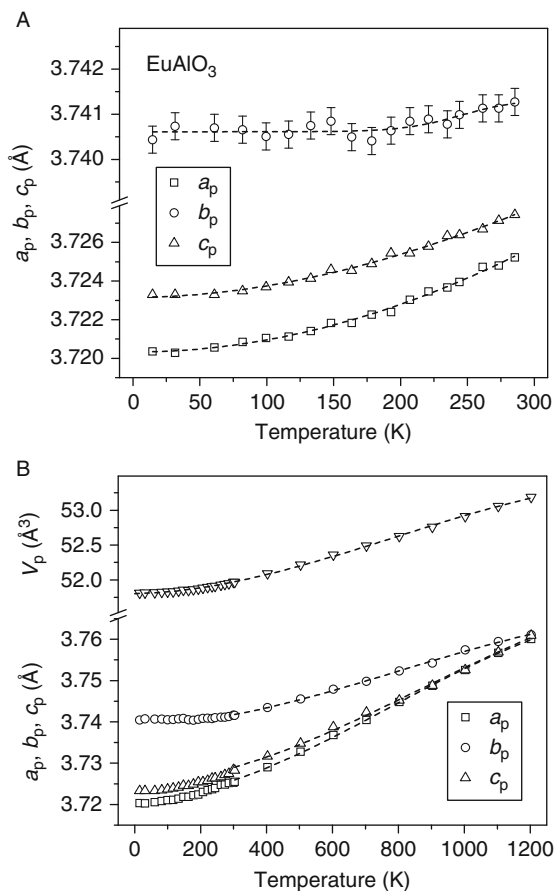


FIGURE 7 Thermal behaviour of the normalized lattice parameters of EuAlO₃ in the temperature ranges of 14–298 K (A) and 14–1200 K (B). The dashed lines are polynomial fits: $a_p(T) = 3.72033(7) [1 + 1.7(2) \times 10^{-8}T^2 - 2.2(4) \times 10^{-12}T^3]$; $b_p(T) = 3.7406(1) - 7.3(3) \times 10^{-4} / [1 + \exp\{(T - 2.4(4) \times 10^2) / 22(9)\}]$; $c_p(T) = 3.72316(6) [1 + 1.7(2) \times 10^{-8}T^2 - 9.3(6) \times 10^{-12}T^3]$ for the temperature range 15–300 K and $a_p(T) = 3.7215(3) [1 + 1.84(5) \times 10^{-8}T^2 - 6.4(4) \times 10^{-12}T^3]$; $b_p(T) = 3.7394(3) [1 + 8.1(4) \times 10^{-9}T^2 - 3.4(3) \times 10^{-12}T^3]$; $c_p(T) = 3.7254(6) [1 + 1.21(9) \times 10^{-8}T^2 - 4.6(7) \times 10^{-12}T^3]$ for the temperature range 303–1203 K.

2.2.7 Gadolinium aluminate GdAlO₃

Geller and Bala (1956) have shown that similar to SmAlO₃ and EuAlO₃, gadolinium aluminate belongs to the GdFeO₃ type structure. According to HT X-ray diffraction and DTA investigations performed by Coutures and Coutures (1984), GdAlO₃ undergoes a first-order phase transition from an orthorhombic to rhombohedral structure at 1973 K. Besides this, from extrapolation of the c/a parameter ratio of the rhombohedral phase, a continuous transition to the cubic phase was predicted near 2580 K, which is above the melting point (2273 K). Earlier data on the possible HT phase transition in GdAlO₃ have been also reported in

TABLE 10 Structural parameters of EuAlO_3 (S.G. $Pbnm$) at different temperatures, refined from synchrotron powder diffraction data

	Parameters	Vasylechko et al. (2003a)	This work	This work
		298 K	14 K	1203 K
	a (Å)	5.26830(4)	5.2634(1)	5.3190(3)
	b (Å)	5.29149(4)	5.29183(9)	5.3195(3)
Atom: sites	c (Å)	7.45684(6)	7.4495(2)	7.5190(4)
Eu, 4c	x	-0.0064(2)	-0.0069(2)	-0.0063(7)
	y	0.0326(1)	0.0335(1)	0.0217(3)
	z	1/4	1/4	1/4
	B_{iso} (Å ²)	0.99(3)	0.508(8)	1.51(2)
Al, 4b	x	1/2	1/2	1/2
	y	0	0	0
	z	0	0	0
	B_{iso} (Å ²)	0.77(11)	0.32(4)	0.82(8)
O1, 4c	x	0.0856(10)	0.069(3)	0.062(7)
	y	0.4769(9)	0.498(2)	0.517(6)
	z	1/4	1/4	1/4
	B_{iso} (Å ²)	1.09(13)	0.3(3)	2.4(8)
O ₂ , 8d	x	-0.2878(10)	-0.283(2)	-0.305(8)
	y	0.2904(9)	0.286(2)	0.275(7)
	z	0.0399(6)	0.035(2)	0.013(5)
	B_{iso} (Å ²)	1.59(9)	0.8(2)	1.1(6)

Mazelsky et al. (1968) and Portnoj and Timofeeva (1986). The crystal structure of GdAlO_3 at RT has been determined precisely using single-crystal synchrotron X-ray diffraction technique. For their studies, Vasylechko et al. (2003a) used a small crystal extracted from a crushed boule grown by the Czochralsky technique, whereas du Boulay et al. (2004) used a flux-grown single crystal obtained by dissolving Gd_2O_3 and Al_2O_3 in a PbO , PbF_2 , and B_2O_3 flux. Ross et al. (2004a,b) have studied the structure of GdAlO_3 perovskite at room temperature and pressure up to 7.95 GPa using single-crystal X-ray diffraction. It was shown that GdAlO_3 remains isostructural over the whole pressure range studied. The GdO_{12} polyhedron is less compressible than the AlO_6 one, resulting in an increase of both, Al–O1–Al and Al–O₂–Al angles on increasing pressure. Thus, the GdAlO_3 perovskite undergoes weaker distortions at elevated pressures. The analysis of the unit cell parameter data shows that the [100] direction is less compressible than the others. The pseudo-cubic unit cell parameter a_c and b_c are predicted to merge near 12 GPa, signifying, in the judgment of the authors, a possible transition from the orthorhombic to tetragonal symmetry. This may, however, be an accidental merging of the lattice parameters in a pseudo-tetragonal lattice.

The thermal behaviour of the GdAlO_3 structure has been studied *in situ* in the temperature range 14–1170 K using synchrotron powder diffraction (Vasylechko *et al.*, 2003a, 2007a). It was shown that the structure remains orthorhombic in the whole temperature range investigated. Similar to other rare earth aluminates, the lattice expansion displays anisotropic behaviour: the relative expansion in the b -direction is smaller compared with the a - and c -directions (Figure 8). A clear anomaly in the LT expansion along the b -direction is also observed (Figure 8A). Structural parameters of GdAlO_3 at different temperatures refined from powder and single crystal diffraction data are given in Table 11.

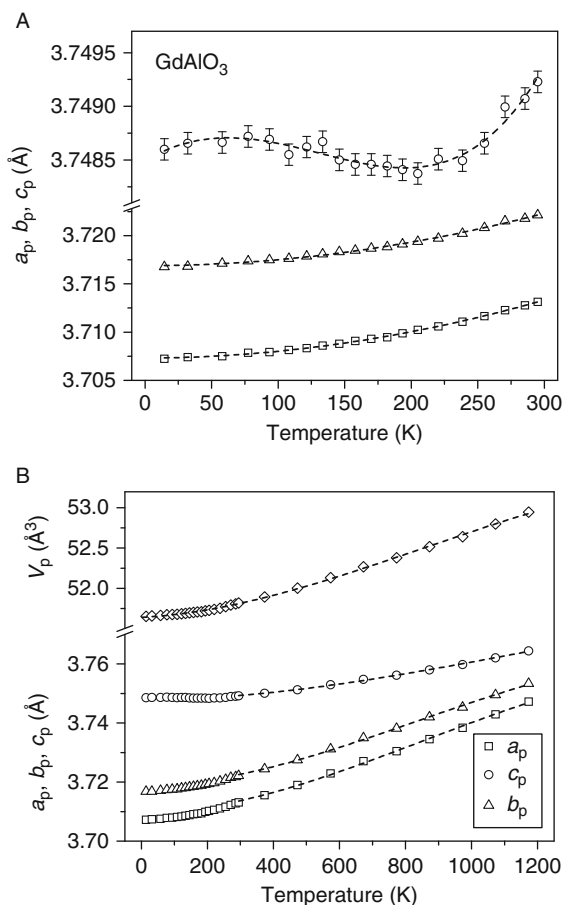


FIGURE 8 Variation of the normalized lattice parameters of GdAlO_3 in the temperature range of 14–298 K (A) and 14–1200 K (B). The dashed lines are polynomial fits: $a_p(T) = 3.70732(3) [1 + 1.91(9) \times 10^{-8}T^2 - 3.7(6) \times 10^{-12}T^3]$; $b_p(T) = 3.74845(7) [1 + 2.5(5) \times 10^{-6}T - 2.7(4) \times 10^{-8}T^2 + 7.1(7) \times 10^{-11}T^3]$; $c_p(T) = 3.71688(5) [1 + 1.7(1) \times 10^{-8}T^2 - 1.7(6) \times 10^{-12}T^3]$ for the temperature range 15–300 K and $a_p(T) = 3.7097(4) [1 + 1.35(7) \times 10^{-8}T^2 - 5.3(5) \times 10^{-12}T^3]$; $b_p(T) = 3.7479(2) [1 + 4.7(3) \times 10^{-9}T^2 - 1.3(3) \times 10^{-12}T^3]$; $c_p(T) = 3.7189(4) [1 + 1.26(6) \times 10^{-8}T^2 - 5.0(5) \times 10^{-12}T^3]$ for the temperature range 303–1203 K.

TABLE 11 Structural parameters of GdAlO₃ (S.G. *Pbnm* and *Pnma*) at different temperatures

	Parameters	Vasylechko	du Boulay	Ross et al.	Ross et al.	Vasylechko	This work ³	This work ³
		et al. (2003a) ¹	et al. (2004) ¹	(2004b) ²	(2004a) ²	(2005) ³		
		<i>Pbnm</i> (RT)	<i>Pnma</i> (295 K)	<i>Pbnm</i> (RT)	<i>Pbnm</i> (RT)	<i>Pbnm</i> (RT)	<i>Pbnm</i> (14 K)	<i>Pbnm</i> (1173 K)
	<i>a</i> (Å)	5.2491(1)	5.3049(7)	5.25368(11)	5.2537(1)	5.25108(6)	5.24281(9)	5.29967(7)
	<i>b</i> (Å)	5.3006(1)	7.4485(9)	5.30304(10)	5.3039(1)	5.30212(6)	5.30132(8)	5.32399(7)
Atom: sites	<i>c</i> (Å)	7.4420(2)	5.2537(6)	7.44346(24)	7.4435(2)	7.44417(9)	7.4336(1)	7.5071(1)
Gd, 4c	<i>x</i>	−0.00815(8)	0.462223(7)	−0.00793 (3)	−0.00822 (6)	−0.0075(4)	−0.0085(2)	−0.0095(3)
	<i>y</i>	0.0380(1)	1/4	0.03763(4)	0.03770(8)	0.0371(2)	0.0394(1)	0.0296(2)
	<i>z</i>	1/4	−0.008091 (7)	1/4	1/4	1/4	1/4	1/4
	<i>B</i> _{iso} (Å ²)	0.37(1)	0.578(3)*	0.380(9)*	0.43(1)	0.83(1)	0.578(9)	1.79(2)
Al: 4b in <i>Pbnm</i> ; 4a in <i>Pnma</i>	<i>x</i>	1/2	0	1/2	1/2	1/2	1/2	1/2
	<i>y</i>	0	0	0	0	0	0	0
	<i>z</i>	0	0	0	0	0	0	0
	<i>B</i> _{iso} (Å ²)	0.42(7)	0.467(12)*	0.28(4)*	0.36(4)	0.79(7)	0.48(5)	1.49(7)
O1, 4c	<i>x</i>	0.0719(12)	0.01389(12)	0.0724(6)	0.074(1)	0.055(3)	0.075(2)	0.060(3)
	<i>y</i>	0.487(2)	1/4	0.4863(6)	0.486(1)	0.484(2)	0.488(2)	0.484(3)
	<i>z</i>	1/4	0.07210(12)	1/4	1/4	1/4	1/4	1/4
	<i>B</i> _{iso} (Å ²)	0.39(14)	0.67(2)*	0.46(4)*	0.43(7)	0.6(3)	0.5(2)	3.0(4)
O2, 8d	<i>x</i>	−0.2848(7)	0.28504(8)	0.7147(4)	0.7149(6)	−0.295(2)	−0.280(2)	−0.292(3)
	<i>y</i>	0.2840(11)	−0.03823(6)	0.2855(3)	0.2847(7)	0.284(2)	0.293(2)	0.264(4)
	<i>z</i>	0.0398(7)	0.21534(8)	0.0387(3)	0.0397(4)	0.037(2)	0.0389(13)	0.019(3)
	<i>B</i> _{iso} (Å ²)	0.31(10)	0.73(2)*	0.44(6)*	0.41(5)	0.6(2)	0.8(2)	2.7(2)

¹ Single crystal synchrotron diffraction data.² X-ray single crystal diffraction data.³ Synchrotron powder diffraction data.* Calculated from U_{ij} and β_{ij} values given in the references.

2.2.8 Terbium aluminate TbAlO₃

First publications about the structure and lattice parameters of TbAlO₃ have appeared in 1960th (Garton and Wanklyn, 1967; Dernier and Maines, 1971). Based on Guinier X-ray diffraction data, it was shown that TbAlO₃ displays an orthorhombically distorted perovskite-type structure at RT. Atomic parameters of the TbAlO₃ structure at 12 K and RT have been reported by Brown *et al.* (1992) in a study devoted to the magnetic structure of a TbAlO₃ single crystal studied using zero-field neutron polarimetry and neutron-integrated intensity measurements. The latter authors reported refined positional and displacement parameters of the atoms at 12 and 300 K, but no lattice parameters are given in this paper. Bombik *et al.* (1997) studied the structure and magnetic behaviour of the TbFe_{1-x}Al_xO₃ solid solution. Structural parameters of TbAlO₃ at RT were refined in this work based on X-ray powder diffraction data. Vasylechko *et al.* (2003a) reported positional and displacement parameters of atoms in the TbAlO₃ structure obtained from synchrotron powder diffraction experiments. *In situ* neutron powder diffraction has been employed by Ranløv and Nielsen (1995) to study terbium aluminate, doped with Mg (TbAl_{0.95}Mg_{0.05}O_{3-x}) at temperatures 273, 573, 773, 1023, and 1223 K. It was shown that the structure remains orthorhombic over the whole investigated temperature range. Low- and high-temperature behaviour of the TbAlO₃ structure at temperatures ranging from 18 to 1173 K has been studied using *in situ* powder diffraction with synchrotron radiation (Vasylechko *et al.*, 2006, 2007a). A noticeable deviation from the 'normal' behaviour, especially along the *a*-direction, has been revealed at low temperatures (Figure 9A). As a consequence, a negative volumetric thermal expansion of the TbAlO₃ structure is observed in the temperature range from 18 to 60 K. No obvious anomalies were observed in the HT expansion (Figure 10). Structural parameters of TbAlO₃ reported in the literature together with the newly obtained LT and HT data are summarized in Table 12.

2.2.9 Dysprosium aluminate DyAlO₃

One of the first communications about the perovskite-type structure of DyAlO₃ was given by Dalziel and Welch (1960). Based on the analysis of Guinier photographs, these authors note that DyAlO₃ with lattice parameters $a = 5.215$, $b = 5.311$ and $c = 7.407$ is 'nearly isomorphous' with other orthorhombic perovskites. Positional parameters of atoms in the DyAlO₃ structure were determined by Bidaux and Meriel (1968) from a neutron powder diffraction study. The temperature behaviour of the DyAlO₃ structure in the range 298–1170 K was reported by Vasylechko *et al.* (2003a) and Vasylechko (2005). Similar to other RAlO₃ compounds, DyAlO₃ displays an anisotropic expansion along different directions. No anomalies of the HT expansion were observed at 298–1170 K. Recent low-temperature diffraction studies of the DyAlO₃ structure revealed an anomaly of the lattice expansion, especially pronounced in the *b*-direction (Figure 11B). Variation of the normalized lattice parameters of DyAlO₃ over a wide temperature range of 20–1170 K is shown in Figure 12, and the refined structural parameters at different temperatures are summarized in Table 13.

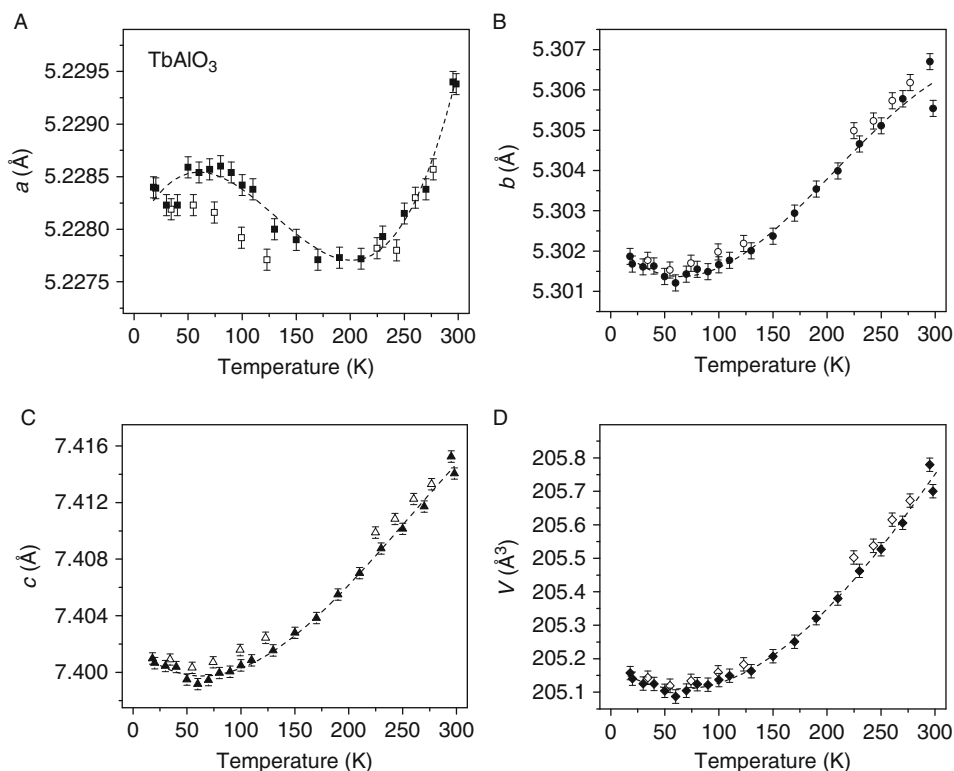


FIGURE 9 Evolution of the lattice parameters (A–C) and cell volume (D) of TbAlO_3 at low temperature, obtained at cooling and heating (solid and open symbols, respectively) (Vasylechko et al., 2006). The dashed lines are polynomial fits: $a_o(T) = 5.2280(1) [1 + 4.2(6) \times 10^{-6}T - 4.5(4) \times 10^{-8}T^2 + 1.14(9) \times 10^{-10}T^3]$; $b_o(T) = 5.3023(2) [1 - 6(1) \times 10^{-6}T + 5.3(9) \times 10^{-8}T^2 - 8(2) \times 10^{-11}T^3]$; $c_o(T) = 7.4018(4) [1 - 9(1) \times 10^{-6}T + 8(1) \times 10^{-8}T^2 - 1.1(2) \times 10^{-10}T^3]$ for the temperature range 15–300 K.

2.2.10 Holmium aluminate HoAlO_3

The lattice parameters of the orthorhombic HoAlO_3 structure were reported by Toropov et al., 1969; Dernier and Maines, 1971; and Shishido et al., 1995a. First communication of the atomic parameters in HoAlO_3 has been made by Hammann and Ocio (1977). Based on neutron diffraction data collected at 0.04 K, lattice constants, positional parameters, and displacement parameters of atoms were evaluated. It is interesting to note that the corresponding structural parameters for the RT structure were reported only 15 year after (Levin, 1992; Vorotilova et al., 1993). Low- and high-temperature behaviour of HoAlO_3 has been studied using high-resolution synchrotron powder diffraction technique over the temperature range of 14–1173 K (Vasylechko et al., 2004a, 2007a). No visible anomalies of thermal expansion have been observed neither in the LT nor in the HT expansion. Similar to other orthorhombic RAIO_3 perovskites, the thermal expansion of HoAlO_3 is strongly anisotropic: the relative expansion along the b -direction

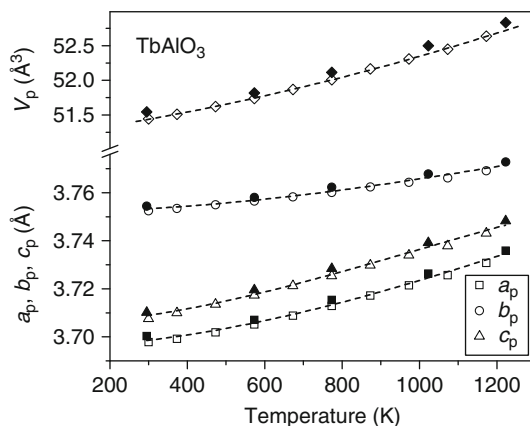


FIGURE 10 Temperature dependencies of the normalized lattice parameters of TbAlO₃ between 300 and 1200 K (open symbols) according to Vasylechko (unpublished data). Solid symbols represent the data for TbAl_{0.95}Mg_{0.05}O₃ (Ranløv and Nielsen, 1995). The dashed lines are polynomial fits: $a_p(T) = 3.696(1) [1 + 9(1) \times 10^{-9}T^2 - 2(1) \times 10^{-12}T^3]$; $b_p(T) = 3.7519(9) [1 + 4(1) \times 10^{-9}T^2 - 8(1) \times 10^{-12}T^3]$; $c_p(T) = 3.705(1) [1 + 1.3(2) \times 10^{-8}T^2 - 4(1) \times 10^{-12}T^3]$ for the temperature range 303–1203 K.

is ca. two times smaller as the corresponding values along the *a*- and *c*-axes. Temperature dependencies of the lattice parameters of HoAlO₃ are shown in Figure 13. Table 14 summarizes the structural parameters refined at different temperatures.

2.2.11 Erbium aluminate ErAlO₃

The lattice parameters of erbium orthoaluminate have been first mentioned by Toropov *et al.* (1969). Dernier and Maines (1971) reported the lattice parameters of ErAlO₃, together with data for other RAlO₃ compounds with orthorhombic structure. Coutures and Coutures (1984) studied the evolution of the lattice parameters in the temperature range 298–2173 K and showed that the structure remains orthorhombic. A full structural investigation of ErAlO₃ was performed only recently by Vasylechko *et al.* (2003a) and Vasylechko and Matkovskii (2004). The crystal structure of ErAlO₃ and its high-temperature behaviour have been studied using the high-resolution X-ray powder diffraction technique using synchrotron radiation in the temperature range 298–1173 K. Corresponding structural parameters are given in Table 15.

Bombik *et al.* (2005a) studied the LT changes of the lattice parameters of ErAlO₃ single crystal by means of X-ray single diffraction. It was shown that above 150 K, the experimental results correspond well with the phonon mechanism and can be effectively described by a simple Debye–Grüneisen approximation, whereas distinct anomalies were observed at low temperatures, especially in *a*-direction (Figure 14A). According to the authors, the observed anomalies of the thermal expansion are mainly caused by the crystal-field effects.

TABLE 12 Structural parameters of TbAlO₃ (S.G. *Pbnm*) at different temperatures

Parameters		Brown et al. (1992) ¹	Brown et al. (1992) ¹	Bombik et al. (1997) ²	Vasylechko and Matkovskii (2004) ²	This work ³	This work ³	This work ³
		12 K	300 K	RT	RT	18 K	298 K	1173 K
Atom: sites	<i>a</i> (Å)	–	–	5.2296(1)	5.22938(4)	5.22840(4)	5.22947(3)	5.27619(5)
	<i>b</i> (Å)	–	–	5.3058(2)	5.30554(3)	5.30187(4)	5.30683(3)	5.33044(4)
	<i>c</i> (Å)	–	–	7.4154(2)	7.41405(5)	7.40098(6)	7.41508(4)	7.48620(7)
Tb, 4c	<i>x</i>	–0.0086(11)	–0.0096(4)	0.9897(9)	–0.0082(2)	–0.0089(1)	–0.0083(1)	–0.0066(2)
	<i>y</i>	0.0444(10)	0.0429(3)	0.0426(3)	0.0419(1)	0.04290(9)	0.04258(7)	0.0358(1)
	<i>z</i>	1/4	1/4	1/4	1/4	1/4	1/4	1/4
	<i>B</i> _{iso} (Å ²)	0.01*	0.02(9)	–	0.63(2)	0.674(5)	0.901(7)	1.720(8)
Al, 4b	<i>x</i>	1/2	1/2	1/2	1/2	1/2	1/2	1/2
	<i>y</i>	0	0	0	0	0	0	0
	<i>z</i>	0	0	0	0	0	0	0
	<i>B</i> _{iso} (Å ²)	0.06*	0.11(13)	–	0.84(11)	0.782(8)	0.63(5)	1.22(4)
O1, 4c	<i>x</i>	0.0792(13)	0.0768(6)	0.103(4)	0.0831(14)	0.0668(15)	0.0703(11)	0.066(2)
	<i>y</i>	0.4829(14)	0.4832(4)	0.473(4)	0.4908(13)	0.4827(13)	0.4836(10)	0.4901(13)
	<i>z</i>	1/4	1/4	1/4	1/4	1/4	1/4	1/4
	<i>B</i> _{iso} (Å ²)	0.12*	0.23(9)	–	1.8(2)	0.998(8)	1.20(11)	2.1(2)
O2, 8d	<i>x</i>	–0.2891(9)	–0.2892(3)	0.720(4)	–0.2851(12)	–0.2854(12)	–0.2939(8)	–0.2888(14)
	<i>y</i>	0.2893(8)	0.2888(2)	0.291(4)	0.2907(11)	0.2906(12)	0.2897(8)	0.2876(14)
	<i>z</i>	0.0419(16)	0.0427*	0.034(3)	0.0353(8)	0.0402(8)	0.0345(6)	0.0320(11)
	<i>B</i> _{iso} (Å ²)	0.08*	0.16(9)	–	1.15(12)	0.610(8)	0.75(7)	1.95(14)

¹ Single crystal neutron diffraction data.² X-ray powder diffraction data.³ Synchrotron powder diffraction data.

* Corresponding parameters were fixed in the refinement.

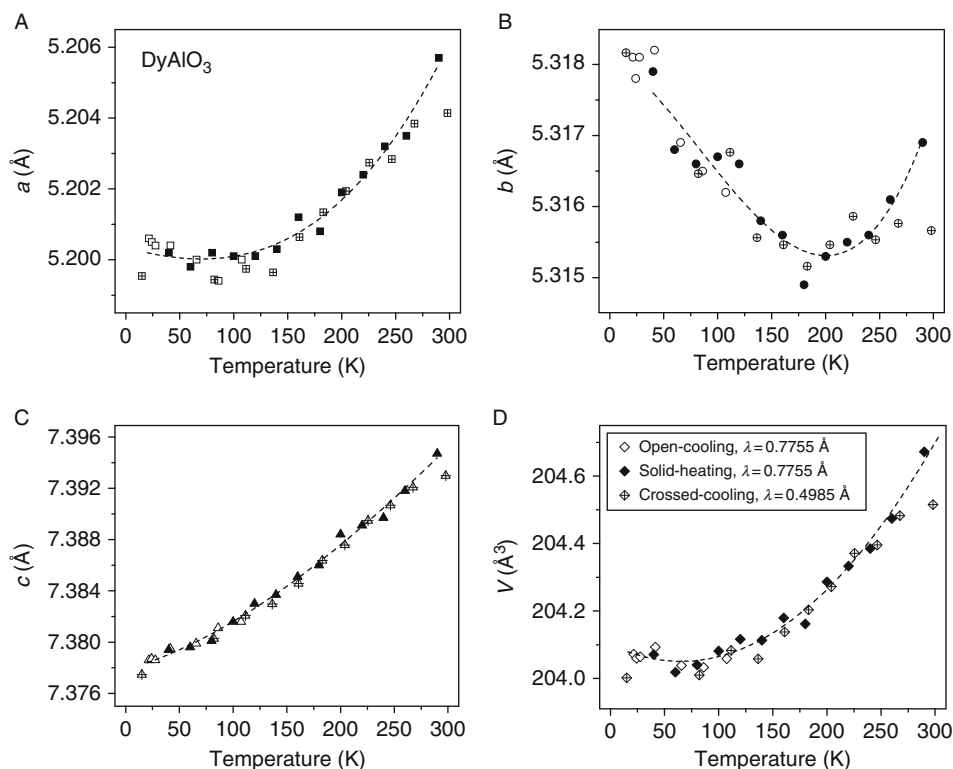


FIGURE 11 Lattice parameters (A–C) and cell volume (D) of DyAlO₃ measured low temperature at using $\lambda = 0.77855 \text{ \AA}$ on cooling (open symbols) and heating (solid symbols). Crossed symbols indicate the data obtained on cooling using $\lambda = 0.4955 \text{ \AA}$. The dashed lines are polynomial fits: $a_o(T) = 5.2003(7) [1 - 1.6(3) \times 10^{-6}T + 7.9(4) \times 10^{-8}T^2 + 3.2(5) \times 10^{-11}T^3]$; $b_o(T) = 5.3181(8) [1 - 1.8(3) \times 10^{-6}T - 2.2(4) \times 10^{-8}T^2 + 8.7(6) \times 10^{-11}T^3]$; $c_o(T) = 7.378(1) [1 + 3.3(4) \times 10^{-6}T + 1.9(5) \times 10^{-8}T^2 - 1.4(5) \times 10^{-11}T^3]$ for the temperature range 20–300K.

The HT expansion of the ErAlO₃ structure displays a rather ‘normal’ for all RAlO₃ compounds with the orthorhombic perovskite structure behaviour. Relative expansion along *a*- and *c*-directions is practically similar, whereas the corresponding expansion in *b*-direction is about two times smaller (Figure 15).

2.2.12 Thulium aluminate TmAlO₃

After the first communications of the lattice parameters of TmAlO₃ by Toropov *et al.* (1969) and Dernier and Maines (1971), no further structural investigations appeared until 2003, when Vasylechko *et al.* (2003a) have published refined values of atomic parameters at RT. Examination of the LT behaviour of the TmAlO₃ structure performed by Senyshyn *et al.* (2005a) revealed unusual ‘sigmoidal’ temperature dependencies of *a*- and *b*-parameters and cell volume (Figure 16A and B). High-temperature studies of the TmAlO₃ structure performed *in situ* in the temperature range 298–1170 K (Vasylechko *et al.*, 2004a; Vasylechko, 2005) showed no

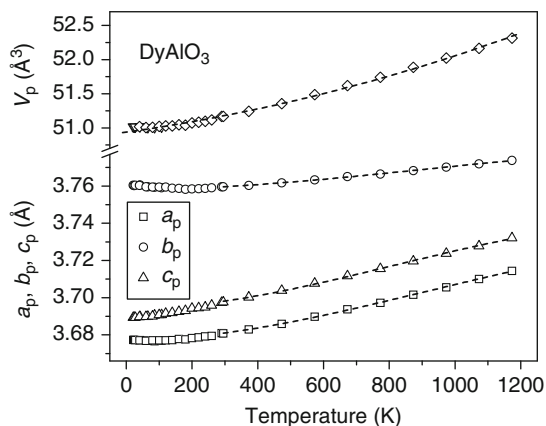


FIGURE 12 Temperature dependencies of normalized lattice parameters and cell volume of DyAlO_3 . The dashed lines are polynomial fits: $a_p(T) = 3.6773(3) [1 + 1.28(4) \times 10^{-8}T^2 - 4.7(3) \times 10^{-12}T^3]$; $b_p(T) = 3.7581(1) [1 + 5.3(2) \times 10^{-9}T^2 - 1.9(1) \times 10^{-12}T^3]$; $c_p(T) = 3.6940(4) [1 + 1.43(6) \times 10^{-8}T^2 - 5.9(5) \times 10^{-12}T^3]$ for the temperature range 303–1203 K.

deviation from the ‘normal’ Debye–Grüneisen behaviour. Similar to other orthorhombic aluminates, TmAlO_3 displays anisotropic expansion: the relative expansion in b -direction is two times lower compared with the a - and c -directions (Figure 17). Refined values of structural parameters of TmAlO_3 are listed in Table 16.

2.2.13 Ytterbium aluminate YbAlO_3

Original values of lattice parameters from X-ray powder diffraction patterns of YbAlO_3 were reported by Garton and Wanklyn (1967), Dernier and Maines (1971), and Ananieva et al. (1978). Radhakrishna et al. (1981) studied the anti-ferromagnetic ordering in YbAlO_3 and reported the atomic coordinates at 4.2 K refined from neutron powder diffraction data. Positional and displacement parameters of atoms at RT of the YbAlO_3 structure refined from single crystal synchrotron diffraction data were published by Vasylechko et al. (2003a). Besides this, temperature dependencies of lattice parameters over the temperature range 298–1173 K were reported in their communication. It was shown that the HT behaviour of the YbAlO_3 structure is similar to that of other RAlO_3 perovskites. A preliminary LT synchrotron powder diffraction study of the YbAlO_3 structure performed over the temperature range 20–298 K (Vasylechko et al., 2007a) did not reveal significant deviations from a conventional behaviour. The lattice parameters and the cell volume as functions of temperature are shown in Figure 18. Refined values of the structural parameters of YbAlO_3 are given in Table 17.

2.2.14 Lutetium aluminate LuAlO_3

Despite the fact that a number of publications is devoted to the synthesis, stability, and potential applications of LuAlO_3 , structural information about this compound was limited to relatively old papers by Dernier and Maines (1971) and

TABLE 13 Structural parameters of DyAlO₃ (S.G. *Pbnm*) at different temperatures

	Parameters	Bidaux and Meriel	Vasylechko et al.	Vasylechko	This work ³	This work ³	This work ³
		(1968) ¹	(2003a) ²	(2005) ³	22 K	180 K	1173 K
		RT	RT	RT			
	<i>a</i> (Å)	5.215	5.20502(9)	5.20541(4)	5.2007(2)	5.2008(2)	5.25327(4)
	<i>b</i> (Å)	5.311	5.31653(8)	5.31691(4)	5.3181(2)	5.3149(2)	5.33727(4)
Atom: sites	<i>c</i> (Å)	7.407	7.3941(1)	7.39516(6)	7.3786(2)	7.3861(3)	7.46475(6)
Dy, 4 <i>c</i>	<i>x</i>	−0.007(6)	−0.0113(4)	−0.0100(2)	−0.0094(7)	−0.0101(8)	−0.0086(3)
	<i>y</i>	0.050(2)	0.0485(2)	0.0473(1)	0.0497(4)	0.0507(4)	0.0408(1)
	<i>z</i>	1/4	1/4	1/4	1/4	1/4	1/4
	<i>B</i> _{iso} (Å ²)	–	0.77(3)	0.81(1)	0.62(4)	0.91(3)	1.51(1)
Al, 4 <i>b</i>	<i>x</i>	1/2	1/2	1/2	1/2	1/2	1/2
	<i>y</i>	0	0	0	0	0	0
	<i>z</i>	0	0	0	0	0	0
	<i>B</i> _{iso} (Å ²)	–	1.2(2)	0.55(10)	0.9(3)	0.9(2)	1.07(7)
O1, 4 <i>c</i>	<i>x</i>	0.052(10)	0.081(2)	0.082(2)	0.060(5)	0.067(7)	0.077(2)
	<i>y</i>	0.474(7)	0.480(2)	0.475(2)	0.477(5)	0.503(6)	0.489(2)
	<i>z</i>	1/4	1/4	1/4	1/4	1/4	1/4
	<i>B</i> _{iso} (Å ²)	–	1.0(3)	1.0(2)	0.2(5)	1.7(8)	1.0(2)
O2, 8 <i>d</i>	<i>x</i>	−0.302(6)	−0.286(2)	−0.2973(14)	−0.294(4)	−0.291(6)	−0.305(2)
	<i>y</i>	0.283(6)	0.294(2)	0.2922(15)	0.281(4)	0.308(6)	0.291(2)
	<i>z</i>	0.053(5)	0.0436(14)	0.0380(10)	0.057(3)	0.055(4)	0.0344(13)
	<i>B</i> _{iso} (Å ²)	–	0.7(2)	0.64(14)	0.4(4)	2.7(6)	2.0(2)

¹ Neutron powder diffraction data.² X-ray powder diffraction data.³ Synchrotron powder diffraction data.

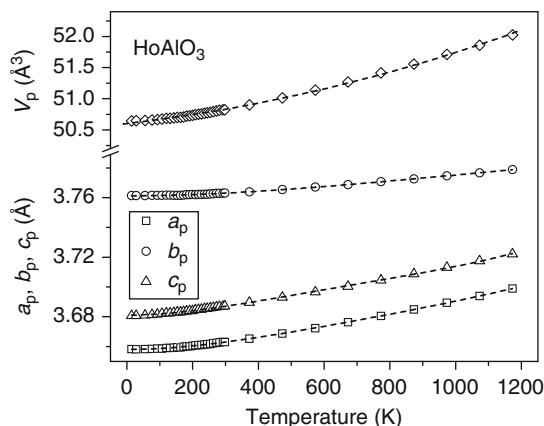


FIGURE 13 Temperature dependencies of the normalized lattice parameters and cell volume of HoAlO_3 . The dashed lines are polynomial fits: $a_p(T) = 3.65807(4) [1 + 1.92(3) \times 10^{-8}T^2 - 1.57(7) \times 10^{-11}T^3 + 5.3(4) \times 10^{-15}T^4]$; $b_p(T) = 3.76126(3) [1 + 6.3(3) \times 10^{-9}T^2 - 3.1(6) \times 10^{-12}T^3 + 5(1) \times 10^{-16}T^4]$; $c_p(T) = 3.68111(9) [1 + 2.49(8) \times 10^{-8}T^2 - 2.6(2) \times 10^{-11}T^3 + 1.01(8) \times 10^{-15}T^4]$ for the temperature range 15–1173 K.

Ananieva et al. (1978). Recently, new refined values of atomic coordinates at RT were reported (Vasylechko et al., 2003a; Vasylechko and Matkovskii, 2004). *In situ* examination of the LuAlO_3 structure over a broad temperature range of 18–1173 K (Vasylechko et al., 2003a, 2006) showed that the thermal dependence of the lattice parameters displays a rather typical behaviour. No anomalies were observed in the investigated temperature range (Figure 19). Table 18 summarizes the structural parameters of LuAlO_3 structure refined at different temperatures.

2.2.15 Yttrium aluminate YAlO_3

Yttrium orthoaluminate is one of the most extensively studied compounds not only among the rare earth aluminates but also among all other ABO_3 perovskites. As it was shown in the pioneering work of Geller and Wood (1956), YAlO_3 has orthorhombic perovskite structure, similar to GdFeO_3 described before. A full crystal structure investigation of YAlO_3 was performed by Diehl and Braundt (1975). Atomic coordinates and anisotropic displacement parameters of atoms were refined in this work based on X-ray single-crystal diffraction data. Ranløv and Nielsen (1995) studied the crystal structure of $\text{YAl}_{0.95}\text{Mg}_{0.05}\text{O}_{3-x}$ at temperatures ranging from 273 to 1223 K by using neutron powder diffraction data. Vasylechko et al. (1999a) refined the positional and displacement parameters of atoms in Nd-doped YAlO_3 crystal based on X-ray powder diffraction data. Precise single crystal diffraction experiments applying synchrotron radiation have been performed by Vasylechko et al. (2000a) in order to clarify the atomic structure of YAlO_3 doped with 0.05% Mn. The high-temperature behaviour of YAlO_3 has been studied over the temperature range 298–1173 K using synchrotron powder diffraction (Vasylechko et al., 2003a) and X-ray powder diffraction measurements at temperatures 298–923 K (Chaix-Pluchery et al., 2005).

TABLE 14 Structural parameters of HoAlO₃ (S.G. *Pbnm*) at different temperatures

Parameters		Hammann and Ocio (1977) ¹	Levin (1992) ²	Vasylychko (2005) ³	This work ³	This work ³
		0.04 K	RT	RT	14 K	1173 K
	<i>a</i> (Å)	5.182	5.180(2)	5.18026(5)	5.17357(8)	5.23057(7)
	<i>b</i> (Å)	5.324	5.322(1)	5.32182(5)	5.31949(8)	5.34359(7)
Atom: sites	<i>c</i> (Å)	7.37	7.374(1)	7.37416(7)	7.3614(1)	7.44372(9)
Ho, 4 <i>c</i>	<i>x</i>	−0.0007(7)	0.98811(4)	−0.0108(2)	−0.0108(2)	−0.0094(3)
	<i>y</i>	0.059(4)	0.05190(4)	0.0518(1)	0.0531(1)	0.0460(2)
	<i>z</i>	1/4	1/4	1/4	1/4	1/4
	<i>B</i> _{iso} (Å ²)	–	0.178(4)	1.07(1)	0.50(1)	1.85(2)
Al, 4 <i>b</i>	<i>x</i>	1/2	1/2	1/2	1/2	1/2
	<i>y</i>	0	0	0	0	0
	<i>z</i>	0	0	0	0	0
	<i>B</i> _{iso} (Å ²)	–	0.11(4)	0.81(6)	0.42(7)	1.83(9)
O1, 4 <i>c</i>	<i>x</i>	0.094(9)	0.0827(7)	0.078(2)	0.087(2)	0.093(2)
	<i>y</i>	0.493(6)	0.4793(8)	0.488(2)	0.478(2)	0.470(2)
	<i>z</i>	1/4	1/4	1/4	1/4	1/4
	<i>B</i> _{iso} (Å ²)	–	0.26(7)	0.9(2)	0.7(2)	1.6(3)
O2, 8 <i>d</i>	<i>x</i>	−0.297(5)	0.7057(5)	−0.287(2)	−0.294(2)	−0.288(2)
	<i>y</i>	0.290(5)	0.2935(5)	0.295(2)	0.289(2)	0.286(2)
	<i>z</i>	0.038(4)	0.0442(6)	0.0512(10)	0.0405(12)	0.0373(14)
	<i>B</i> _{iso} (Å ²)	–	0.18(5)	0.94(14)	0.7(2)	2.1(2)

¹ Neutron powder diffraction data.² X-ray single crystal diffraction data.³ Synchrotron powder diffraction data.

TABLE 15 Structural parameters of ErAlO₃ at RT and 1173 K (S.G. *Pbnm*)

	Parameters	Vasylechko et al. (2003a) ¹	This work ²	This work ²
		RT	RT	1173 K
	<i>a</i> (Å)	5.16103(5)	5.16151(4)	5.20979(5)
	<i>b</i> (Å)	5.32811(4)	5.32898(4)	5.35168(5)
Atom: sites	<i>c</i> (Å)	7.35570(7)	7.35730(6)	7.42428(7)
Er, 4c	<i>x</i>	−0.0141(2)	−0.0123(3)	−0.0099(4)
	<i>y</i>	0.0560(1)	0.0540(2)	0.0495(2)
	<i>z</i>	1/4	1/4	1/4
	<i>B</i> _{iso} (Å ²)	0.65(2)	1.03(1)	1.88(2)
Al, 4b	<i>x</i>	1/2	1/2	1/2
	<i>y</i>	0	0	0
	<i>z</i>	0	0	0
	<i>B</i> _{iso} (Å ²)	0.74(10)	1.07(9)	0.95(9)
O1, 4c	<i>x</i>	0.0876(14)	0.062(2)	0.067(2)
	<i>y</i>	0.4806(13)	0.475(2)	0.475(2)
	<i>z</i>	1/4	1/4	1/4
	<i>B</i> _{iso} (Å ²)	0.7(2)	0.7(2)	1.6(3)
O2, 8d	<i>x</i>	−0.2985(11)	−0.302(2)	−0.299(2)
	<i>y</i>	0.2936(11)	0.307(2)	0.291(2)
	<i>z</i>	0.0475(8)	0.0490(13)	0.0528(13)
	<i>B</i> _{iso} (Å ²)	1.02(13)	0.7(2)	1.5(2)

¹ X-ray powder diffraction data.² Synchrotron powder diffraction data.

Results are shown in Figure 20, together with the data of YAl_{0.95}Mg_{0.05}O_{3−δ} reported by Ranløv and Nielsen (1995).

Recent examinations of the LT behaviour of YAlO₃ crystals using neutron and synchrotron diffraction techniques revealed pronounced anomalies in the expansion along the *b*-direction (Figure 21B). It should be noted that for synchrotron powder diffraction experiment, an Mn-doped crystal was chosen, whereas for neutron diffraction experiment, a sample containing 1 at.% Nd was used. At LT, the anomaly occurs in both Mn- and Nd-doped crystals.

The influence of high pressure (up to 8.5 GPa) on the YAlO₃ structure at RT has been studied in a series of publications (Ross, 1996; Ross et al., 2004c; Zhao et al., 2004b). It was shown that the compression of Y–O bonds is strongly anisotropic. The four longest Y–O distances are more compressible than the eight shorter Y–O bond lengths. In contrast, the AlO₆ polyhedron nearly undergoes isotropic compression and is more compressible than the YO₁₂ polyhedra. The octahedra tilt angles show significant increase with pressure. These findings indicate that the structure of YAlO₃ perovskite becomes less distorted with increasing pressure (Ross et al., 2004c).

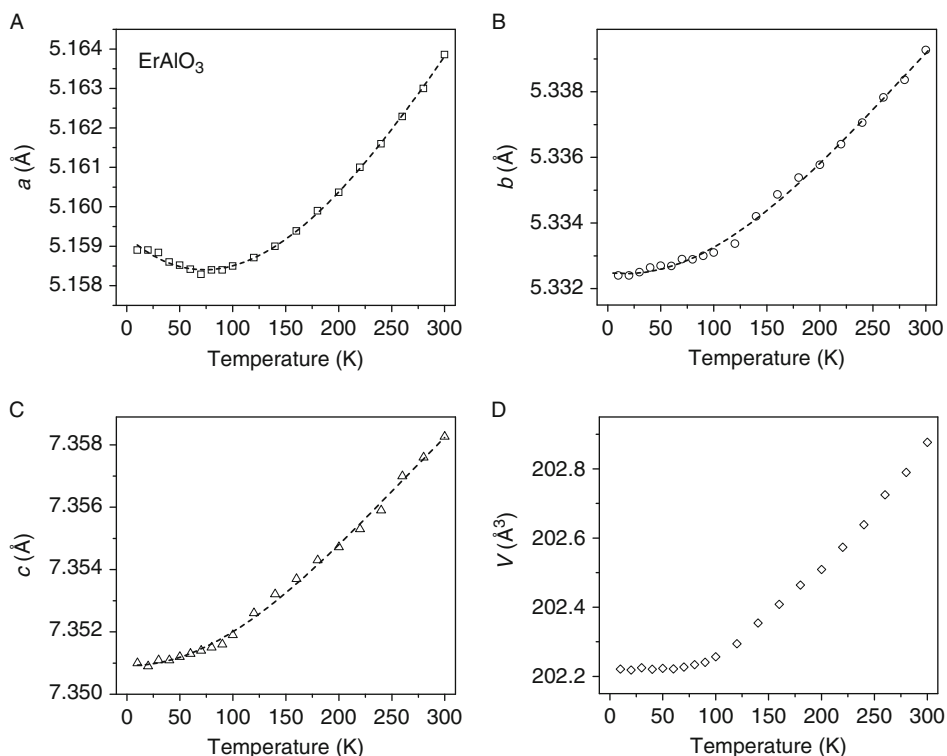


FIGURE 14 Temperature behaviour of lattice parameters (A–C) and cell volume (D) of ErAlO_3 in the temperature range of 12–298 K extracted from the [Bombik et al. \(2005a\)](#). Note, that the b -parameter of 5.33927 Å at RT originally given by [Bombik et al. \(2005a\)](#) is about 0.01 Å higher as the values of 5.326–5.329 Å reported by other authors (PDF 24–394; [Shishido et al., 1995a](#); [Dernier and Maines, 1971](#); [Coutures and Coutures, 1984](#); [Vasylechko et al., 2003a](#)). The dashed lines are polynomial fits: $a_o(T) = 5.15925(6) [1 - 4.7(3) \times 10^{-6}T + 3.6(3) \times 10^{-8}T^2 - 3.4(5) \times 10^{-11}T^3]$; $b_o(T) = 5.3325(1) [1 - 8.8(9) \times 10^{-7}T + 2.6(5) \times 10^{-8}T^2 - 3(1) \times 10^{-11}T^3]$; $c_o(T) = 7.3509(1) [1 - 2.04(5) \times 10^{-7}T + 1.91(4) \times 10^{-8}T^2 - 2.5(8) \times 10^{-11}T^3]$ for the temperature range 10–300 K.

Published structural parameters of YAlO_3 at RT together with the recently refined values of atomic parameters at LT and HT are collected in [Table 19](#).

2.2.16 Scandium aluminate ScAlO_3

The crystal structure of ScAlO_3 was refined for the first time by [Reid and Ringwood \(1975\)](#) using X-ray powder diffraction data. Single crystal diffraction experiment performed by [Sinclair et al. \(1979\)](#) confirmed the GdFeO_3 -type structure of ScAlO_3 . [Hill and Jackson \(1990\)](#) refined the structure of ScAlO_3 at temperatures up to 1373 K on the basis of X-ray powder diffraction data. The authors mentioned that the thermal expansion of ScAlO_3 could be adequately described by a Grüneisen–Debye model. The cell dimensions vary almost linearly with increasing temperature and a pronounced anisotropy is evident ([Figure 22](#)). Similar to other RAIO_3 compounds, the average linear expansivities parallel

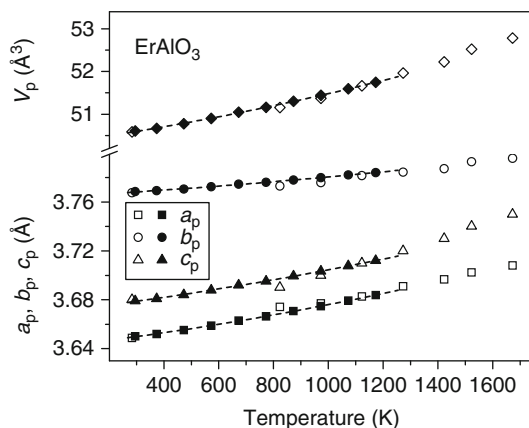


FIGURE 15 High-temperature evolution of the normalized lattice parameters and cell volume of ErAlO_3 according to [Coutures and Coutures \(1984\)](#) (open symbols) and [Vasylechko et al. \(2003a\)](#) (solid symbols). The dashed lines are polynomial fits: $a_p(T) = 3.64158(4) [1 + 6.8(1) \times 10^{-6}T + 2.6(1) \times 10^{-9}T^2]$; $b_p(T) = 3.76433(5) [1 + 3.17(8) \times 10^{-6}T + 1.1(2) \times 10^{-9}T^2]$; $c_p(T) = 3.67023(7) [1 + 7.12(4) \times 10^{-6}T + 2.21(4) \times 10^{-9}T^2]$ for the temperature range 300–1200 K.

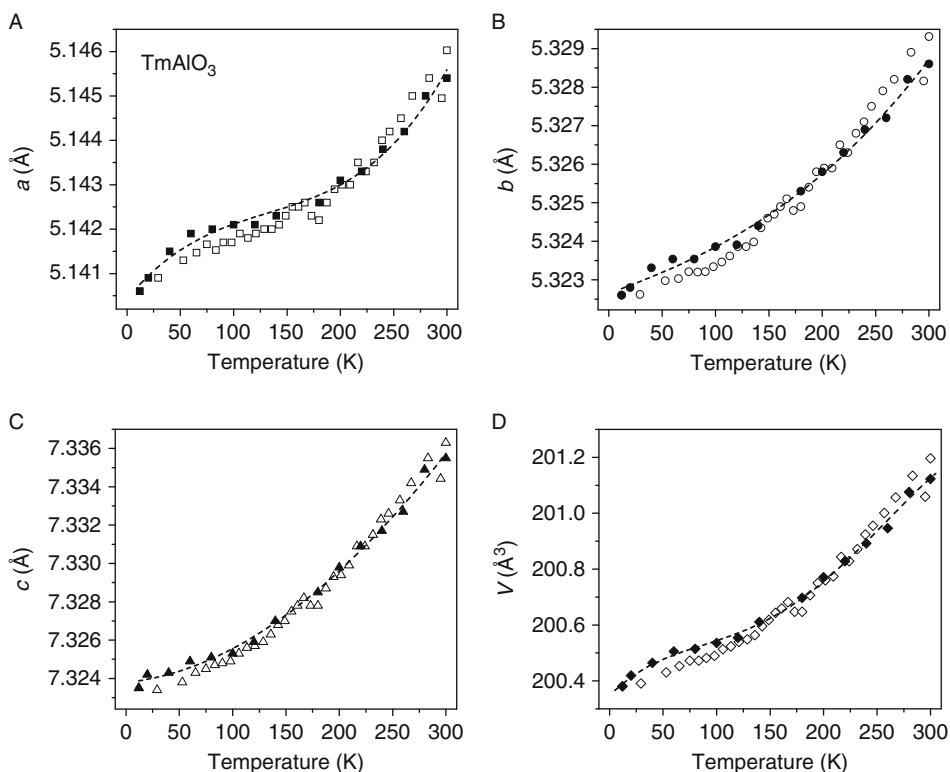


FIGURE 16 Lattice parameters (A–C) and cell volume (D) of TmAlO_3 obtained on cooling (open symbols) and heating (solid symbols) between 12 and 300 K. The dashed lines are polynomial fits: $a_o(T) = 5.1404(2) [1 + 5.7(9) \times 10^{-6}T - 3.2(7) \times 10^{-8}T^2 + 8(1) \times 10^{-11}T^3]$; $b_o(T) = 5.3227(2) [1 + 1.9(3) \times 10^{-7}T + 2.7(5) \times 10^{-9}T^2 + 1.2(4) \times 10^{-11}T^3]$; $c_o(T) = 7.3238(3) [1 + 7.6(6) \times 10^{-7}T + 1.7(3) \times 10^{-8}T^2 - 4.7(6) \times 10^{-12}T^3]$ for the temperature range 12–300 K.

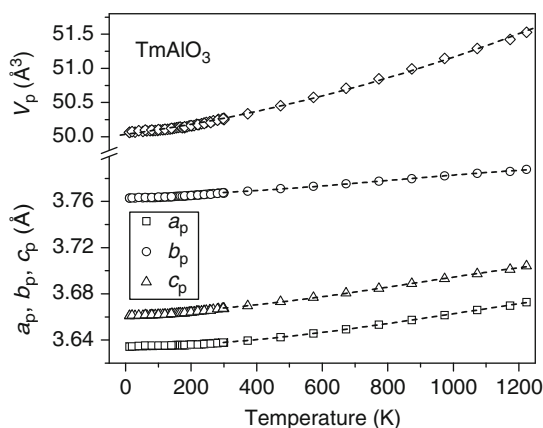


FIGURE 17 Normalized lattice parameters and cell volume of TmAlO_3 over the temperature range 12–1170 K. The dashed lines are polynomial fits: $a_p(T) = 3.6346(2) [1 + 1.13(3) \times 10^{-8}T^2 - 3.5(2) \times 10^{-11}T^3]$; $b_p(T) = 3.7654(3) [1 + 7.8(4) \times 10^{-8}T^2 - 3.2(3) \times 10^{-12}T^3]$; $c_p(T) = 3.6639(3) [1 + 1.33(5) \times 10^{-8}T^2 - 5.0(4) \times 10^{-11}T^3]$ for the temperature range 300–1223 K.

TABLE 16 Structural parameters of TmAlO_3 (S.G. $Pbnm$) at different temperatures

	Parameters	Vasylechko et al.	Senyshyn	Senyshyn	This work ²
		(2003a) ¹	et al. (2005) ²	et al. (2005) ²	
		RT	12 K	RT	1223 K
Atom: sites	a (Å)	5.14495(6)	5.13962(6)	5.14502(5)	5.19409(5)
	b (Å)	5.32816(5)	5.32137(6)	5.32817(5)	5.35683(5)
	c (Å)	7.33442(9)	7.32203(8)	7.33491(7)	7.40813(7)
Tm, 4c	x	−0.0142(2)	−0.0134(2)	−0.0129(2)	−0.0126(2)
	y	0.0579(1)	0.0577(1)	0.0577(1)	0.0530(2)
	z	1/4	1/4	1/4	1/4
	B_{iso} (Å ²)	0.91(2)	0.56(1)	0.81(1)	1.49(2)
Al, 4b	x	1/2	1/2	1/2	1/2
	y	0	0	0	0
	z	0	0	0	0
	B_{iso} (Å ²)	1.36(11)	0.62(10)	0.83(9)	1.03(9)
O1, 4c	x	0.087(2)	0.090(2)	0.090(2)	0.427(2)
	y	0.4813(14)	0.4835(15)	0.479(2)	−0.029(2)
	z	1/4	1/4	1/4	1/4
	B_{iso} (Å ²)	1.0(2)	0.1(2)	1.0(3)	2.2(3)
O2, 8d	x	−0.3014(12)	−0.3028(13)	−0.2985(14)	0.705(2)
	y	0.3059(12)	0.2990(13)	0.3017(14)	0.299(2)
	z	0.0340(10)	0.0463(10)	0.0464(10)	0.0464(13)
	B_{iso} (Å ²)	1.20(14)	0.57(13)	1.0(2)	1.7(2)

¹ X-ray powder diffraction data.

² Synchrotron powder diffraction data.

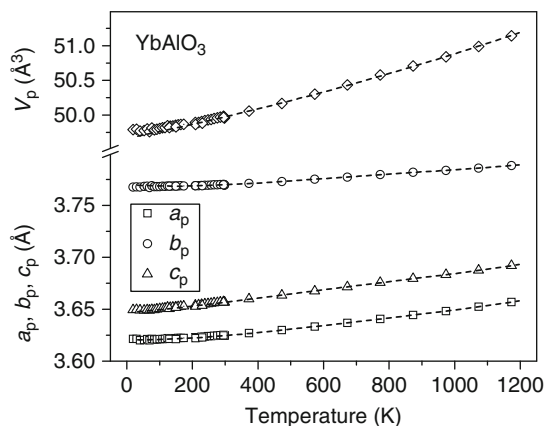


FIGURE 18 Temperature dependencies of normalized lattice parameters and cell volume of YbAlO_3 . The dashed lines are polynomial fits: $a_p(T) = 3.6219(2) [1 + 1.4(2) \times 10^{-8}T^2 - 8.0(5) \times 10^{-11}T^3 + 2.1(5) \times 10^{-14}T^4]$; $b_p(T) = 3.7691(2) [1 + 4.3(3) \times 10^{-9}T^2 + 1.9(4) \times 10^{-12}T^3 - 2.0(6) \times 10^{-15}T^4]$; $c_p(T) = 3.65054(2) [1 + 3.0(2) \times 10^{-8}T^2 - 3.5(4) \times 10^{-11}T^3 + 1.4(2) \times 10^{-14}T^4]$ for the temperature range 19–1173 K.

to the a - and c -axes are almost the same, whereas the expansion parallel to the b -axis is substantially smaller. From the analysis of structural information, it was concluded that the thermal volume expansion of 3% between 283 and 1373 K may be associated with the expansion of the AlO_6 octahedra.

Ross (1998) studied the crystal structure of ScAlO_3 under pressure up to 5 GPa at RT using single-crystal X-ray diffraction. It was shown that the compression of the structure is anisotropic. The interoctahedral angles do not vary significantly with pressure, therefore the compression of the structure is entirely attributable to the compression of the AlO_6 octahedra. It was found that the compressibility of constituent AlO_6 and ScO_{12} polyhedra are well matched; therefore, the distortion of the structure shows no significant change with increasing pressure. Structural parameters of ScAlO_3 are given in Table 20.

2.3 Solid solutions based on RAIO_3 perovskite-type compounds

It has been shown in literature that isostructural orthoaluminates form continuous solid solutions where the lattice parameters change monotonically with the chemical composition. Morphotropic phase transitions are observed when the RAIO_3 compounds belong to different structure types (Brusset et al., 1975; Arsenev et al., 1983). However, experimental data on the interaction in the RAIO_3 – $\text{R}'\text{AlO}_3$ pseudo-binary systems are rather limited. Systems with first members of the RAIO_3 series were studied extensively, whereas information on the interaction in the RAIO_3 – $\text{R}'\text{AlO}_3$ systems with Ho, Tm, and Sc is not available.

RAIO_3 compounds also form solid solution $\text{RA}_{1-x}\text{M}_x\text{O}_3$, in which cation substitution occurs in the octahedral sites. Brusset et al. (1975) discussed phase

TABLE 17 Structural parameters of YbAlO₃ (S.G. *Pbnm*) at different temperatures

Parameters		Radhakrishna et al. (1981) ¹	Vasylychko et al. (2003a) ²	This work ³	This work ³
		4.2 K	298 K	100 K	1173 K
Atom: sites	<i>a</i> (Å)	–	5.1261(1)	5.1210(2)	5.17167(6)
	<i>b</i> (Å)	–	5.3314(1)	5.3286(2)	5.35761(6)
	<i>c</i> (Å)	–	7.3132(2)	7.3010(3)	7.38376(8)
Yb, 4 <i>c</i>	<i>x</i>	–0.007(1)	–0.01362(6)	–0.0125(6)	–0.0132(3)
	<i>y</i>	0.050(2)	0.06007(5)	0.0609(4)	0.0559(2)
	<i>z</i>	1/4	1/4	1/4	1/4
	<i>B</i> _{iso} (Å ²)	–	0.40(1)	0.80(3)	1.50(2)
Al, 4 <i>b</i>	<i>x</i>	1/2	1/2	1/2	1/2
	<i>y</i>	0	0	0	0
	<i>z</i>	0	0	0	0
	<i>B</i> _{iso} (Å ²)	–	0.40(5)	0.5(2)	1.10(11)
O1, 4 <i>c</i>	<i>x</i>	–0.05(1)	0.0912(10)	0.091(5)	0.080(3)
	<i>y</i>	0.474(7)	0.4716(8)	0.463(5)	0.482(3)
	<i>z</i>	1/4	1/4	1/4	1/4
	<i>B</i> _{iso} (Å ²)	–	0.53(8)	0.6(5)	2.1(4)
O2, 8 <i>d</i>	<i>x</i>	–0.260(9)	–0.3004(7)	–0.303(4)	–0.299(2)
	<i>y</i>	0.290(1)	0.2991(5)	0.296(4)	0.299(2)
	<i>z</i>	–0.0070(4)	0.0475(5)	0.060(3)	0.044(2)
	<i>B</i> _{iso} (Å ²)	–	0.55(6)	0.9(4)	1.5(3)

¹ Neutron powder diffraction data.² Single crystal synchrotron diffraction data.³ Synchrotron powder diffraction data.

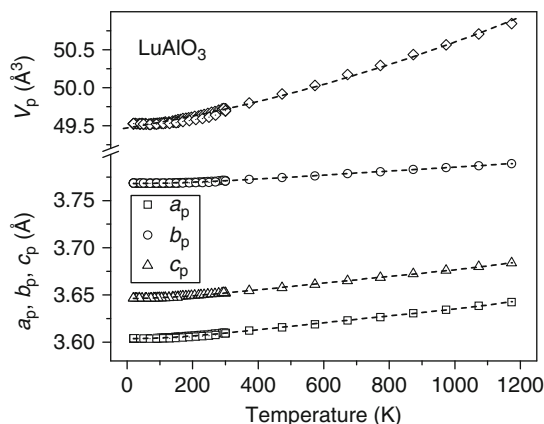


FIGURE 19 Temperature dependencies of the normalized lattice parameters and cell volume of LuAlO_3 over the temperature range of 18–1173 K. The dashed lines are polynomial fits: $a_p(T) = 3.60364(6) [1 + 2.54(7) \times 10^{-8}T^2 - 2.7(1) \times 10^{-11}T^3 + 1.00(8) \times 10^{-14}T^4]$; $b_p(T) = 3.76810(5) [1 + 1.16(5) \times 10^{-9}T^2 - 1.0(1) \times 10^{-12}T^3 + 3.4(6) \times 10^{-15}T^4]$; $c_p(T) = 3.64625(6) [1 + 2.44(6) \times 10^{-8}T^2 - 2.6(1) \times 10^{-11}T^3 + 9.7(7) \times 10^{-15}T^4]$ for the temperature range 19–1173 K.

relationships in $\text{RAlO}_3\text{--RGaO}_3$ ($\text{R} = \text{La}, \text{Pr}, \text{and Nd}$) systems. According to this study, two kinds of $\text{RAl}_{1-x}\text{Ga}_x\text{O}_3$ solid solutions with rhombohedral and pseudo-monoclinic (orthorhombic) structures exist in these systems. In the $\text{LaAlO}_3\text{--LaGaO}_3$ system, the boundary separating rhombohedral and orthorhombic (pseudo-monoclinic) structure is located at 95 mol.% LaGaO_3 . This observation was recently confirmed by [Matraszek et al. \(2003\)](#). The authors showed that solid solutions $\text{LaAl}_{1-x}\text{Ga}_x\text{O}_3$ with $x = 0.95$ display orthorhombic GdFeO_3 -type structures, whereas for compositions with $x \leq 0.9$, the rhombohedral $R\bar{3}c$ structure is typical. Reported variation of the lattice parameters confirms the existence of the solid solution with rhombohedral structure in the $\text{LaAlO}_3\text{--LaGaO}_3$ system. In the $\text{PrAlO}_3\text{--PrGaO}_3$ and $\text{NdAlO}_3\text{--NdGaO}_3$ systems, miscibility gaps were reported ([Brusset et al., 1975](#)).

The formation of solid solutions in $\text{RAlO}_3\text{--RFeO}_3$ ($\text{R} = \text{Tb and Er}$) has been studied by [Bombik et al. \(1997, 2005b\)](#). Refined values of structural parameters and concentration dependence of the lattice parameters clearly prove the existence of a continuous $\text{TbAl}_{1-x}\text{Fe}_x\text{O}_3$ solid solution with the orthorhombic $Pbnm$ structure in $\text{TbAlO}_3\text{--TbFeO}_3$. For $\text{ErAlO}_3\text{--ErFeO}_3$ system, single-phase specimens with the orthorhombic GdFeO_3 type of crystal structure were obtained for $\text{ErFe}_{1-x}\text{Al}_x\text{O}_3$ compositions with $0 \leq x \leq 0.4$.

The formation of mixed aluminates-chromites with perovskite structures in $\text{RAlO}_3\text{--RCrO}_3$ ($\text{R} = \text{Gd and Yb}$) has been studied by [Golub et al. \(1978\)](#). It was shown that a continuous solid solution $\text{GdAl}_{1-x}\text{Cr}_x\text{O}_3$ with an orthorhombic structure is formed in the $\text{GdAlO}_3\text{--GdCrO}_3$ system, whereas in the system with ytterbium, the stability range of the $\text{YbAl}_{1-x}\text{Cr}_x\text{O}_3$ solid solution is limited to $0.65 \leq x \leq 1$.

For RAlO_3 compounds, simultaneous substitution of R- and Al-cations, including compensative aliovalent substitution, is also typical. In particular, the solid

TABLE 18 Structural parameters of LuAlO₃ (S.G. *Pbnm*) at different temperatures

Atom: sites	Parameters	Vasylechko et al. (2003a) ¹	This work ²	This work ²	This work ²		
		298 K	19 K	RT	1173 K		
		<i>a</i> (Å)	<i>b</i> (Å)	<i>c</i> (Å)	<i>x</i>	<i>y</i>	<i>z</i>
Lu, 4 <i>c</i>	<i>a</i> (Å)	5.10501(4)	5.09669(4)	5.10496(5)	5.15137(5)		
	<i>b</i> (Å)	5.33343(4)	5.32937(4)	5.33332(5)	5.35907(4)		
	<i>c</i> (Å)	7.30444(5)	7.29308(5)	7.30448(7)	7.36788(6)		
	<i>x</i>	−0.0149(1)	−0.0157(2)	−0.0151(2)	−0.0147(2)		
Al, 4 <i>b</i>	<i>y</i>	0.06238(9)	0.0630(1)	0.0621(2)	0.0585(2)		
	<i>z</i>	1/4	1/4	1/4	1/4		
	<i>B</i> _{iso} (Å ²)	0.86(1)	0.630(8)	0.873(9)	1.40(2)		
	<i>x</i>	1/2	1/2	1/2	1/2		
O1, 4 <i>c</i>	<i>y</i>	0	0	0	0		
	<i>z</i>	0	0	0	0		
	<i>B</i> _{iso} (Å ²)	0.59(7)	0.62(6)	0.92(8)	0.80(9)		
	<i>x</i>	0.0961(11)	0.089(2)	0.089(2)	0.091(2)		
O2, 8 <i>d</i>	<i>y</i>	0.4694(10)	0.474(2)	0.476(2)	0.477(2)		
	<i>z</i>	1/4	1/4	1/4	1/4		
	<i>B</i> _{iso} (Å ²)	0.7(2)	0.3(2)	0.9(2)	1.8(3)		
	<i>x</i>	−0.3050(8)	−0.2969(14)	−0.3004(15)	−0.305(2)		
	<i>y</i>	0.2982(8)	0.303(2)	0.304(2)	0.296(2)		
	<i>z</i>	0.0485(6)	0.0503(10)	0.0499(11)	0.0420(13)		
	<i>B</i> _{iso} (Å ²)	0.87(13)	0.42(13)	0.40(13)	1.4(2)		

¹ X-ray powder diffraction data.² Synchrotron powder diffraction data.

solutions R_{1-x}Ca_xAl_{1-x}Ti_xO₃ (R = La, Nd, and Sm) are known to exist in the corresponding RAlO₃–CaTiO₃ systems (Jančar *et al.*, 2001; Grebenshchikov *et al.*, 2003; Jančar *et al.*, 2004).

In the present section, structural peculiarities of solid solutions in RAlO₃–R'AlO₃ pseudo-binary systems are considered and discussed.

2.3.1 LaAlO₃–RAlO₃

Among the LaAlO₃–RAlO₃ systems, the most extensively studied are the systems with R = cerium and praseodymium, for which a full or partial phase diagrams were reported. Since the phase behaviour in those systems is for the most part determined by peculiarities of the CeAlO₃ and PrAlO₃ structures, they will be analysed in the corresponding sections devoted to CeAlO₃- and PrAlO₃-based solid solutions.

In the LaAlO₃–NdAlO₃ pseudo-binary system, a continuous solid solution with rhombohedral structure exists at RT. Lattice parameters and cell volume of the

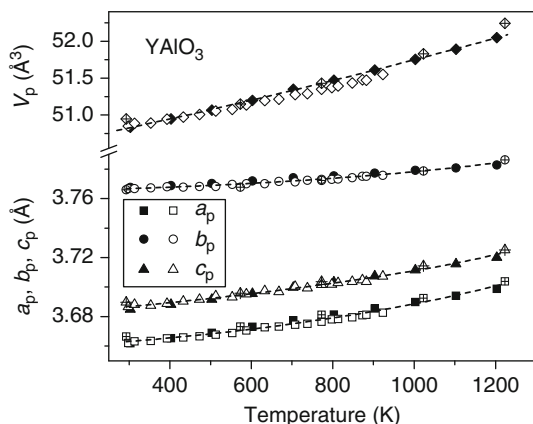


FIGURE 20 Temperature dependencies of normalized lattice parameters and cell volume of $YAlO_3$ according to Vasylechko et al. (2003a) (solid symbols) and Chaix-Pluchery et al. (2005) (open symbols). For comparison, the data for $YAl_{0.95}Mg_{0.05}O_{3-x}$ (Ranløv and Nielsen, 1995), crossed symbols, are also shown. The dashed lines are polynomial fits: $a_p(T) = 3.6608(8) [1 + 8.3(6) \times 10^{-9}T^2 - 7.0(9) \times 10^{-13}T^3]$; $b_p(T) = 3.7658(5) [1 + 3.1(7) \times 10^{-9}T^2 + 2.0(5) \times 10^{-13}T^3]$; $c_p(T) = 3.6845(7) [1 + 9.1(9) \times 10^{-9}T^2 - 1.8(8) \times 10^{-13}T^3]$; for the temperature range 300–1223 K.

corresponding $La_{1-x}Nd_xAlO_3$ samples decrease monotonically with increasing neodymium content (Figure 23).

Similar to the end members, the mixed lanthanide $La_{1-x}Nd_xAlO_3$ samples undergo a phase transition from the rhombohedral to cubic structure at elevated temperatures. Geller and Raccah (1970) observed such a transition in $La_{0.65}Nd_{0.35}AlO_3$ near 1230 K and Vasylechko et al. (2007b) reported transition temperatures of 1095, 1350, and 1780 K for $La_{1-x}Nd_xAlO_3$ samples with $x = 0.2$, 0.38, and 0.7, respectively. No LT transitions were found in the $La_{1-x}Nd_xAlO_3$ system down to 12 K. The temperature evolution of the lattice parameters of $La_{1-x}Nd_xAlO_3$ solid solution is illustrated for $La_{0.8}Nd_{0.2}AlO_3$ and $La_{0.68}Nd_{0.32}AlO_3$ in Figure 24. The refined values of structural parameters for various compositions in the $LaAlO_3$ – $NdAlO_3$ system are given in Table 21.

Based on the results reported in the literature, the following phase diagram of the $LaAlO_3$ – $NdAlO_3$ pseudo-binary system may be constructed (Figure 25).

Much different phase relationships are observed in $LaAlO_3$ – $RAlO_3$ with $RAlO_3$ compounds possessing an orthorhombic structure at RT. In such systems, two types of $La_{1-x}R_xAlO_3$ solid solutions with different perovskite-type structures occur. Originally, phase relationships in $LaAlO_3$ – $EuAlO_3$ and $LaAlO_3$ – $GdAlO_3$ at RT have been described by Brusset et al. (1975). It was reported that $La_{1-x}Eu_xAlO_3$ solid solutions with rhombohedral and pseudo-monoclinic (orthorhombic) structures are formed for $x < 0.5$ and $x > 0.64$, respectively. Immiscibility gap exists between these two perovskite-type phases. In the $LaAlO_3$ – $GdAlO_3$ system, the boundary between the rhombohedral and pseudo-monoclinic or pseudo-cubic phase is located near 0.4 molar fractions of $GdAlO_3$. The data were confirmed for the majority of structures in recent investigations performed

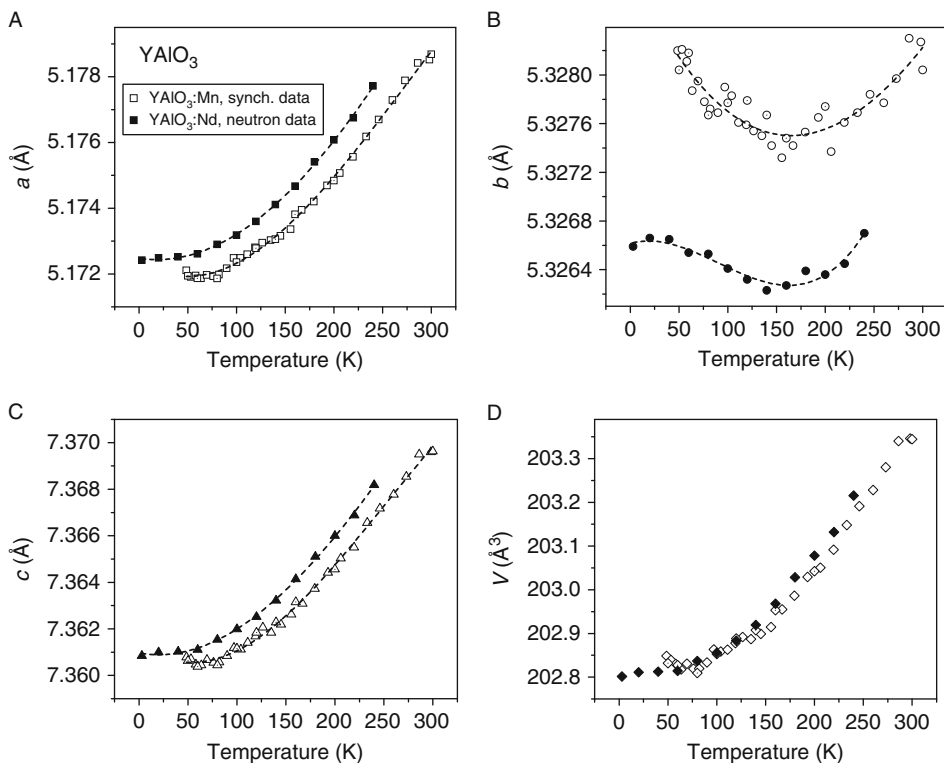


FIGURE 21 Dependencies of the lattice parameters (A–C) and cell volume (D) of the Mn- and Nd-doped YAlO_3 crystals at low temperature, obtained from synchrotron and neutron powder diffraction data. The dashed lines are polynomial fits: $a_o(T) = 5.1724(2) [1 - 3.7(9) \times 10^{-7}T + 4.0(6) \times 10^{-8}T^2 - 5(1) \times 10^{-11}T^3]$; $b_o(T) = 5.3289(2) [1 - 3.3(9) \times 10^{-6}T + 2.7(5) \times 10^{-8}T^2 - 7(1) \times 10^{-12}T^3]$; $c_o(T) = 7.3614(3) [1 - 4.4(9) \times 10^{-6}T + 4.5(6) \times 10^{-8}T^2 - 6.0(9) \times 10^{-11}T^3]$ for temperature range 50–300 K (synchrotron) and $a_o(T) = 5.17248(5) [1 - 8.7(4) \times 10^{-7}T + 2.4(3) \times 10^{-8}T^2 - 1.26(9) \times 10^{-11}T^3]$; $b_o(T) = 5.32662(4) [1 + 4.2(2) \times 10^{-7}T - 1.2(3) \times 10^{-8}T^2 + 4.6(8) \times 10^{-11}T^3]$; $c_o(T) = 7.36097(8) [1 - 1.0(4) \times 10^{-6}T + 2.7(4) \times 10^{-8}T^2 - 2.3(6) \times 10^{-11}T^3]$ for temperature range 3–240 K (neutrons).

by Basyuk *et al.* (2007a) (Figure 26B and C). In addition to the two systems mentioned above, the concentration-induced phase transition has also been observed in $\text{LaAlO}_3\text{--SmAlO}_3$, where both rhombohedral and orthorhombic phases co-exist around 0.6 molar fractions of SmAlO_3 (Figure 26A).

Increasing the difference between ionic radii of R-elements in the $\text{LaAlO}_3\text{--RAlO}_3$ systems results in the expansion of the immiscibility gap between rhombohedral and orthorhombic phases and its shift towards LaAlO_3 . For example, the two-phase region in the $\text{LaAlO}_3\text{--TbAlO}_3$ pseudo-binary system is observed between 0.18 and 0.42 molar fractions of TbAlO_3 (Figure 26D), and in the $\text{LaAlO}_3\text{--ErAlO}_3$ system, the existence of the rhombohedral phase only extends to 0.07 molar fractions of ErAlO_3 (Figure 26E). In $\text{LaAlO}_3\text{--YAlO}_3$, the pure rhombohedral structure was observed in $\text{La}_{0.9}\text{Y}_{0.1}\text{AlO}_3$ sample, whereas

TABLE 19 Structural parameters of YAlO_3 (S.G. $Pbnm$) at different temperatures

	Parameters	Diehl and Braundt (1975) ¹	Ross (1996) ²	Vasylechko et al. (1999a) ²	Vasylechko et al. (2000a) ³	Ross et al. (2004c) ⁴	This work ⁵	This work ⁵	This work ⁶	This work ⁶
		RT	RT	RT ⁷	RT ⁸	RT	3 K ⁷	160 K ⁷	50 K ⁸	1173 K ⁸
Atom: sites	a (Å)	5.180(2)	5.1671(6)	5.17901(7)	5.1791(1)	5.18027(38)	5.17242(9)	5.17467(10)	5.17194(6)	5.23087(4)
	b (Å)	5.330(2)	5.3148(8)	5.32663(7)	5.3266(1)	5.32951(16)	5.32659(9)	5.32627(10)	5.32804(6)	5.34975(4)
	c (Å)	7.375(2)	7.3538(9)	7.36971(9)	7.3697(2)	7.37059(12)	7.36085(13)	7.36414(15)	7.36063(9)	7.44006(6)
Y, 4c	x	−0.0104(2)	0.9882(3)	−0.0117(3)	−0.01177(4)	−0.01192(7)	0.01241(12)	0.01240(14)	−0.0122(2)	−0.0091(3)
	y	0.0526(2)	0.0527(3)	0.0528(2)	0.05299(3)	0.05305(7)	0.55406(9)	0.55354(10)	0.0542(2)	0.0470(2)
	z	1/4	1/4	1/4	1/4	1/4	1/4	1/4	1/4	1/4
	B_{iso} (Å ²)	0.75(6)*	0.71(4)	1.38(3)	0.383(7)	0.420(11)	0.12(1)*	0.172(11)*	0.63(2)	1.74(2)
Al, 4b	x	1/2	1/2	1/2	1/2	1/2	1/2	1/2	1/2	1/2
	y	0	0	0	0	0	0	0	0	0
	z	0	0	0	0	0	0	0	0	0
	B_{iso} (Å ²)	0.69(17)*	0.86(4)	0.90(7)	0.37(2)	0.342(20)	0.126(15)*	0.19(2)*	0.75(5)	1.55(8)
O1, 4c	x	0.086(2)	0.0832(17)	0.086(2)	0.0841(4)	0.0840(6)	−0.08385(15)	−0.08359(17)	0.0840(10)	0.0803(11)
	y	0.475(2)	0.4769(23)	0.472(2)	0.4784(3)	0.4775(5)	−0.02195(13)	−0.02194(15)	0.4833(9)	0.4876(10)
	z	1/4	1/4	1/4	1/4	1/4	1/4	1/4	1/4	1/4
	B_{iso} (Å ²)	0.8(4)*	0.92(17)	1.6(2)	0.42(3)	0.51(4)	0.056(13)*	0.108(14)*	0.75(12)	1.8(2)
O2, 8d	x	−0.297(2)	0.7072(9)	0.7079(12)	−0.2948(3)	0.7049(3)	0.20470(10)	0.20464(11)	−0.2956(8)	−0.3010(9)
	y	0.293(2)	0.2923(14)	0.2920(11)	0.2945(2)	0.2949(3)	0.29483(9)	0.29464(10)	0.2883(8)	0.2978(9)
	z	0.044(2)	0.0421(12)	0.0463(8)	0.0439(2)	0.0441(2)	0.04427(7)	0.04408(7)	0.0461(5)	0.0422(6)
	B_{iso} (Å ²)	1.0(3)*	0.61(11)	1.01(14)	0.43(2)	0.47(3)	0.14(1)*	0.182(13)*	1.00(9)	1.8(2)

¹ X-ray single crystal diffraction data.² X-ray powder diffraction data.³ Single crystal synchrotron diffraction data.⁴ Single crystal X-ray diffraction data.⁵ Neutron powder diffraction data.⁶ Synchrotron powder diffraction data.⁷ Nd doped.⁸ Mn doped.* Calculated from the U_{ij} values.

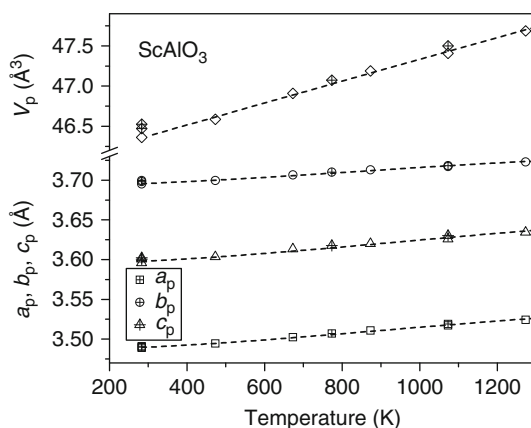


FIGURE 22 Temperature dependencies of the normalized lattice parameters and cell volume of ScAlO_3 according to Hill and Jackson (1990). Open symbols show data obtained from the continuous-scan powder diffraction measurements, symbols with dots show step-scan Rietveld powder refinement data. The dashed lines are polynomial fits: $a_p(T) = 3.4862(9) [1 + 1.3(1) \times 10^{-9}T^2 - 4.8(6) \times 10^{-13}T^3]$; $b_p(T) = 3.6931(9) [1 + 1.03(9) \times 10^{-9}T^2 - 4.11(6) \times 10^{-13}T^3]$; $c_p(T) = 3.595(2) [1 + 1.3(2) \times 10^{-9}T^2 - 4.6(1.4) \times 10^{-13}T^3]$ for the temperature range 300–1473 K.

$\text{La}_{0.3}\text{Y}_{0.7}\text{AlO}_3$, $\text{La}_{0.2}\text{Y}_{0.8}\text{AlO}_3$, and $\text{La}_{0.1}\text{Y}_{0.9}\text{AlO}_3$ compositions show orthorhombic symmetry. Two perovskite-type phases with rhombohedral and orthorhombic structures have been found in $\text{La}_{1-x}\text{Y}_x\text{AlO}_3$ samples with nominal compositions of $x = 0.2, 0.3, 0.5$, and 0.6 (Figure 26F). Somewhat different phase relationships in the LaAlO_3 – YAlO_3 system were reported by Kyomen and Itoh (2002). The authors claim that the $\text{La}_{1-x}\text{Y}_x\text{AlO}_3$ samples with $x = 0.1, 0.3$, and 0.9 have been obtained as single phases, whereas the $x = 0.5$ sample separates into two phases with perovskite-type structures, possibly lanthanum-rich and yttrium-rich ones. Based on X-ray powder diffraction patterns, rhombohedral symmetry was suggested for the sample with $x = 0.1$, whereas the yttrium-rich $\text{La}_{0.1}\text{Y}_{0.9}\text{AlO}_3$ sample was shown to be orthorhombic. Unexpectedly, the orthorhombic $Pnma$ structural model was also chosen for the Rietveld refinement of the lanthanum-rich $\text{La}_{0.7}\text{Y}_{0.3}\text{AlO}_3$ sample. The authors claimed that the statistical (crystallographic) reliability parameters were sufficiently good, therefore such an assumption for the space group was considered to be plausible. Unfortunately, neither refined values of the structural parameters nor lattice dimensions were reported in this paper. Figure 26 shows the compositional dependencies of the lattice dimensions of solid solutions in the LaAlO_3 – RAlO_3 systems ($R = \text{Sm, Eu, Gd, Tb, Er, and Y}$) at RT.

The HT behaviour of $\text{La}_{1-x}\text{R}_x\text{AlO}_3$ solid solutions with different perovskite structures was examined using the examples of $\text{La}_{1-x}\text{Sm}_x\text{AlO}_3$ ($x = 0.1$ and 0.9) and $\text{La}_{1-x}\text{Eu}_x\text{AlO}_3$ ($x = 0.1$ and 0.8) (Basyuk and Vasylechko, 2007, unpublished data). It was shown that depending on the composition, two kinds of phase transitions can be observed among $\text{La}_{1-x}\text{R}_x\text{AlO}_3$ solid solutions. A first-order transition from the orthorhombic to rhombohedral structure occurs in $\text{La}_{0.1}\text{Sm}_{0.9}\text{AlO}_3$ and $\text{La}_{0.2}\text{Eu}_{0.8}\text{AlO}_3$ at 823 and 1025 K, respectively (Figure 27A and C). A similar

TABLE 20 Structural parameters of ScAlO₃ (S.G. *Pbnm*)

Parameters		Reid and Ringwood (1975) ¹	Sinclair et al. (1979) ²	Ross (1998) ²	Hill and Jackson (1990) ¹	Hill and Jackson (1990) ¹
		RT	RT	RT	283 K	1373 K
Atom: sites	<i>a</i> (Å)	4.933(3)	4.9355(3)	4.9371(7)	4.9370(2)	4.9930(2)
	<i>b</i> (Å)	5.226(3)	5.2313(3)	5.2322(7)	5.2321(2)	5.2690(2)
	<i>c</i> (Å)	7.193(5)	7.2007(5)	7.2042(6)	7.2045(2)	7.2846(2)
Sc, 4 <i>c</i>	<i>x</i>	0.974(4)	0.9793(1)	0.9796(3)	0.9775(3)	0.9813(3)
	<i>y</i>	0.072(4)	0.0701(1)	0.0695(2)	0.0700(2)	0.0676(2)
	<i>z</i>	1/4	1/4	1/4	1/4	1/4
	<i>B</i> _{iso} (Å ²)	0.4	0.35	0.67(3)	0.46(5)	0.96(4)
Al, 4 <i>b</i>	<i>x</i>	1/2	1/2	1/2	1/2	1/2
	<i>y</i>	0	0	0	0	0
	<i>z</i>	0	0	0	0	0
	<i>B</i> _{iso} (Å ²)	0.4	0.29	0.63(4)	0.23(6)	0.49(5)
O1, 4 <i>c</i>	<i>x</i>	0.133(11)	0.1196(3)	0.1211(9)	0.1252(8)	0.1250(6)
	<i>y</i>	0.446(12)	0.4551(3)	0.4561(9)	0.4462(8)	0.4478(7)
	<i>z</i>	1/4	1/4	1/4	1/4	1/4
	<i>B</i> _{iso} (Å ²)	0.4	0.34	0.75(8)	−0.02(10)	0.08(8)
O2, 8 <i>d</i>	<i>x</i>	0.691(8)	0.6906(2)	0.6897(6)	0.6935(6)	0.6919(5)
	<i>y</i>	0.312(9)	0.3061(2)	0.3066(6)	0.3055(5)	0.3063(5)
	<i>z</i>	0.075(6)	0.0611(1)	0.0609(3)	0.0625(3)	0.0621(3)
	<i>B</i> _{iso} (Å ²)	0.4	0.37	0.61(6)	−0.61(7)	−0.10(7)

¹ X-ray powder diffraction data.² X-ray single crystal diffraction data.

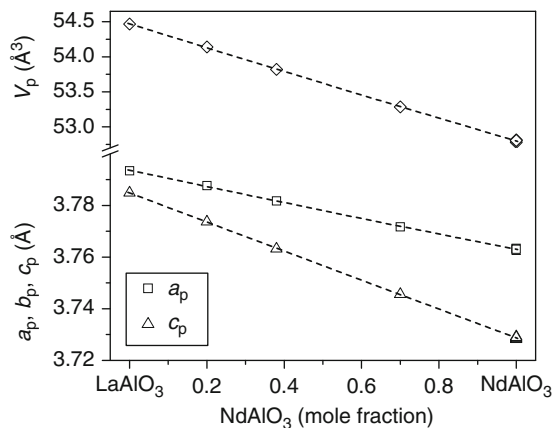


FIGURE 23 Concentration dependencies of the normalized lattice parameters and cell volume of $\text{La}_{1-x}\text{Nd}_x\text{AlO}_3$ solid solution at RT (Basyuk *et al.*, 2007a). Linear fit of lattice parameters: $a_p(x) = 3.7935(2) - 0.0305(3) \times x$; $c_p(x) = 3.7848(3) - 0.0561(4) \times x$.

transition was observed in $\text{La}_{0.32}\text{Gd}_{0.68}\text{AlO}_3$ at 850 K (Vasylechko, 2005). For the La-rich compositions $\text{La}_{0.9}\text{Sm}_{0.1}\text{AlO}_3$ and $\text{La}_{0.9}\text{Eu}_{0.1}\text{AlO}_3$, a continuous phase transition from rhombohedral to cubic structure takes place at 973 and 1120 K, respectively (Figure 27B and D). Refined structural parameters of different structural modifications of $\text{La}_{1-x}\text{R}_x\text{AlO}_3$ solid solutions (R = Sm, Eu, Gd, Tb, Er, and Y) are summarized in Tables 22 and 23.

2.3.2 CeAlO_3 – RAlO_3

First communication on the formation of solid solutions in CeAlO_3 -based systems appeared more than 40 years ago (Leonov, 1963). It was reported that continuous solid solutions with the (pseudo)-cubic perovskite structure are formed in CeAlO_3 – LaAlO_3 and CeAlO_3 – SmAlO_3 systems. A comprehensive study of the structural behaviour in CeAlO_3 – RAlO_3 (R = La and Nd) systems in the temperature range 12–1173 K has been performed by Vasylechko *et al.* (2007b). $\text{Ce}_{1-x}\text{R}_x\text{AlO}_3$ solid solutions with tetragonal, orthorhombic, rhombohedral, and cubic perovskite-type structures are formed in CeAlO_3 – LaAlO_3 , depending on the composition and temperature. The sequence of the phase transitions $I4/mcm$ – $Imma$ – $R\bar{3}c$ – $Pm\bar{3}m$ detected in $\text{Ce}_{1-x}\text{La}_x\text{AlO}_3$ samples is identical to that observed in CeAlO_3 . All transition temperatures decrease significantly with decreasing cerium concentration. The CeAlO_3 – NdAlO_3 system exhibits a more complex behaviour. In contrast to the CeAlO_3 – LaAlO_3 system, LT modifications of $\text{Ce}_{1-x}\text{Nd}_x\text{AlO}_3$ solid solutions show a monoclinic deformation of the perovskite structure, and the tetragonal LT structure is observed only for the Ce-rich $\text{Ce}_{0.9}\text{Nd}_{0.1}\text{AlO}_3$ sample. Thus, $\text{Ce}_{1-x}\text{Nd}_x\text{AlO}_3$ samples with $x = 0.3$ and 0.5 undergo a sequence of phase transformations $I2/m$ – $Imma$ – $R\bar{3}c$ – $Pm\bar{3}m$, similar to those observed in praseodymium aluminate PrAlO_3 . For $\text{Ce}_{0.9}\text{Nd}_{0.1}\text{AlO}_3$, three LT phase transitions were observed: $I4/mcm$ – $I2/m$ at 205 K, $I2/m$ – $Imma$ at 263 K,

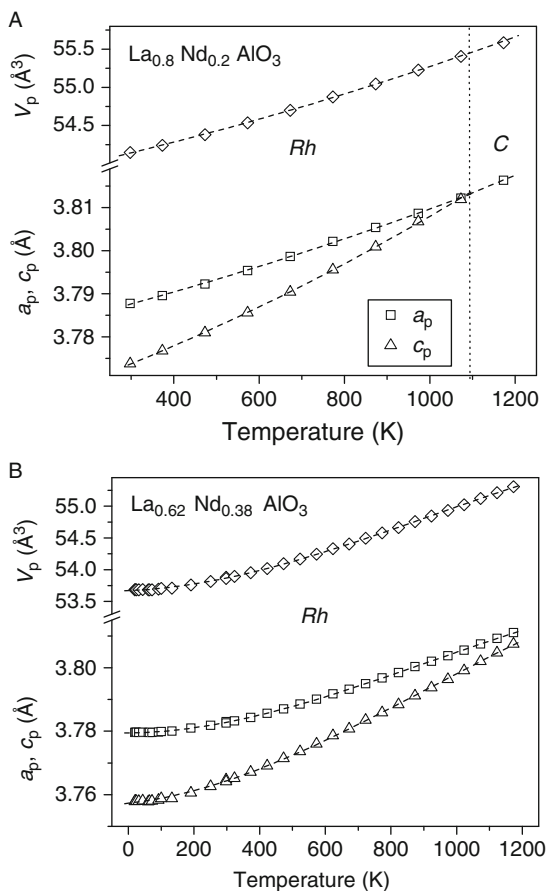


FIGURE 24 Temperature dependencies of the normalized lattice parameters and cell volume of $\text{La}_{0.8}\text{Nd}_{0.2}\text{AlO}_3$ and $\text{La}_{0.62}\text{Nd}_{0.38}\text{AlO}_3$ (Basyuk et al., 2007a). The dashed lines are polynomial fits: $a_p(T) = 3.7845(2) [1 + 1.14(3) \times 10^{-8}T^2 - 4.8(2) \times 10^{-12}T^3]$; $c_p(T) = 3.7691(3) [1 + 1.69(4) \times 10^{-8}T^2 - 6.6(4) \times 10^{-12}T^3]$ ($\text{La}_{0.8}\text{Nd}_{0.2}\text{AlO}_3$) and $a_p(T) = 3.77952(3) [1 + 1.069(8) \times 10^{-8}T^2 - 3.97(7) \times 10^{-12}T^3]$; $c_p(T) = 3.7582(2) [1 + 1.86(4) \times 10^{-8}T^2 - 7.9(3) \times 10^{-12}T^3]$ ($\text{La}_{0.62}\text{Nd}_{0.38}\text{AlO}_3$).

and $\text{Imma}-R\bar{3}c$ at 405 K. A fourth HT transition to the cubic structure was predicted to occur at 1360 K. The thermal behaviour of the lattice parameters in $\text{Ce}_{1-x}\text{R}_x\text{AlO}_3$ solid solutions of $\text{Ce}_{0.5}\text{La}_{0.5}\text{AlO}_3$ and $\text{Ce}_{0.5}\text{Nd}_{0.5}\text{AlO}_3$ samples is presented in Figure 28A and B.

Final results of the structural refinements of different $\text{Ce}_{1-x}\text{La}_x\text{AlO}_3$ and $\text{Ce}_{1-x}\text{Nd}_x\text{AlO}_3$ polymorphs are summarized in Tables 24 and 25. Based on the *in situ* powder diffraction and DTA/DSC studies, the phase diagrams of the CeAlO_3 - LaAlO_3 and CeAlO_3 - NdAlO_3 pseudo-binary systems have been constructed (Figure 29A and B).

The synthesis and *in situ* low- and high-temperature powder diffraction examinations of $\text{Ce}_{1-x}\text{Pr}_x\text{AlO}_3$ compositions with $x = 0.1, 0.3, 0.5, 0.7,$ and 0.9 within the

TABLE 21 Structural parameters of rhombohedral (S.G. $R\bar{3}c$) and cubic (S.G. $Pm\bar{3}m$) modifications of $\text{La}_{1-x}\text{Nd}_x\text{AlO}_3$ solid solutions refined from synchrotron powder diffraction data (Basyuk and Vasylechko, 2007)

Parameters		$\text{La}_{0.3}\text{Nd}_{0.7}$	$\text{La}_{0.3}\text{Nd}_{0.7}$	$\text{La}_{0.62}\text{Nd}_{0.38}$	$\text{La}_{0.62}\text{Nd}_{0.38}$	$\text{La}_{0.62}\text{Nd}_{0.38}$	$\text{La}_{0.8}\text{Nd}_{0.2}$	$\text{La}_{0.8}\text{Nd}_{0.2}$	$\text{La}_{0.8}\text{Nd}_{0.2}$
		$R\bar{3}c$ (298 K)	$R\bar{3}c$ (1173 K)	$R\bar{3}c$ (12 K)	$R\bar{3}c$ (298 K)	$R\bar{3}c$ (1173 K)	$R\bar{3}c$ (298 K) [#]	$R\bar{3}c$ (973 K)	$Pm\bar{3}m$ (1173 K) [#]
	a (Å)	5.33554(2)	5.37544(4)	5.34514(6)	5.34937(2)	5.3897(1)	5.35667(2)	5.3863(2)	3.81641(2)
Atom: sites	c (Å)	12.97835(8)	13.1286(2)	13.0176(1)	13.03927(9)	13.1896(5)	13.0727(1)	13.187(1)	—
La(Nd): $6c$ in $R\bar{3}c$; $1b$ in $Pm\bar{3}m$	x	0	0	0	0	0	0	0	1/2
	y	0	0	0	0	0	0	0	1/2
	z	1/4	1/4	1/4	1/4	1/4	1/4	1/4	1/2
	B_{iso} (Å ²)	0.684(5)	1.48(2)	0.171(4)	0.671(5)	1.46(3)	0.640(7)	1.27(5)	1.387(9)
Al: $6b$ in $R\bar{3}c$; $1a$ in $Pm\bar{3}m$	x	0	0	0	0	0	0	0	0
	y	0	0	0	0	0	0	0	0
	z	0	0	0	0	0	0	0	0
	B_{iso} (Å ²)	0.45(2)	1.20(8)	0.29(2)	0.64(2)	1.1(2)	0.60(4)	0.9(2)	0.87(3)
O: $18e$ in $R\bar{3}c$; $3d$ in $Pm\bar{3}m$	x	0.5382(7)	0.5367(13)	0.5355(8)	0.5375(6)	0.529(2)	0.5282(8)	0.514(3)	1/2
	y	0	0	0	0	0	0	0	0
	z	1/4	1/4	1/4	1/4	1/4	1/4	1/4	0
	B_{iso} (Å ²)	1.31(7)	1.4(2)	0.39(6)	0.53(5)	1.16(10)	0.61(5)	1.23(8)	1.57(11)

[#] © JCPDS—International Centre for Diffraction data, to be published.

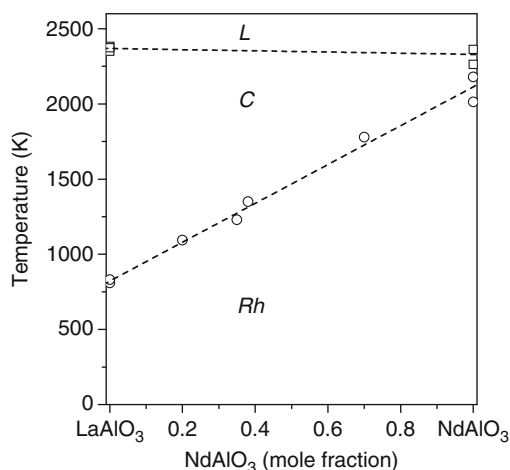


FIGURE 25 Phase diagram of the LaAlO_3 – NdAlO_3 pseudobinary system. The letters L, C and Rh designate liquid, cubic, and rhombohedral phase fields, respectively. Temperatures of the rhombohedral-to-cubic phase transition for $\text{La}_{0.62}\text{Nd}_{0.38}\text{AlO}_3$ and $\text{La}_{0.3}\text{Nd}_{0.7}\text{AlO}_3$ have been estimated from the extrapolation of the rhombohedral cell parameters ratio. Transition temperatures in the pure RAIO_3 compounds and their melting points are taken from [Fay and Brandle \(1967\)](#), [Howard et al. \(2000\)](#), [Geller and Raccach \(1970\)](#), and [Portnoj and Timofeeva \(1986\)](#). Linear fit of the critical temperatures in $\text{La}_{1-x}\text{Nd}_x\text{AlO}_3$: $T_{\text{C-Rh}}(x) = 826(26) + 1290(47) \times x$; $T_{\text{L}}(x) = 2369(25) - 56(39) \times x$.

CeAlO_3 – PrAlO_3 pseudo-binary system have been reported in [Vasylechko et al. \(2004b\)](#). According to this study, five $\text{Ce}_{1-x}\text{Pr}_x\text{AlO}_3$ phases with tetragonal, monoclinic, orthorhombic, rhombohedral, and cubic symmetry were found depending on composition and temperature. A tentative phase diagram of the CeAlO_3 – PrAlO_3 system has been proposed according to the results of *in situ* synchrotron powder diffraction and DTA/DSC investigations ([Figure 30](#)). Taking into account the observed sequence of phase transitions $I4/mcm$ – $I2/m$ – $Imma$ – $R\bar{3}c$ – $Pm\bar{3}m$ and only subtle differences between different kinds of perovskite-type structures, a comprehensive understanding of this system requires high-resolution neutron and synchrotron powder diffraction studies, especially at the phase boundaries between the tetragonal and monoclinic (pseudo-tetragonal) structures. Additional *in situ* single crystal diffraction experiments should also be beneficial. Unfortunately, such investigations are quite complicated due to poly-domain microstructure of these materials and associated difficulties in obtaining single-domain specimens suitable for data collection.

2.3.3 PrAlO_3 – AlO_3

PrAlO_3 forms continuous solid solutions with the isostructural lanthanum and neodymium aluminates in the whole range of concentrations. Rhombohedral lattice parameters and cell volumes of $\text{Pr}_{1-x}\text{La}_x\text{AlO}_3$ and $\text{Pr}_{1-x}\text{Nd}_x\text{AlO}_3$ samples

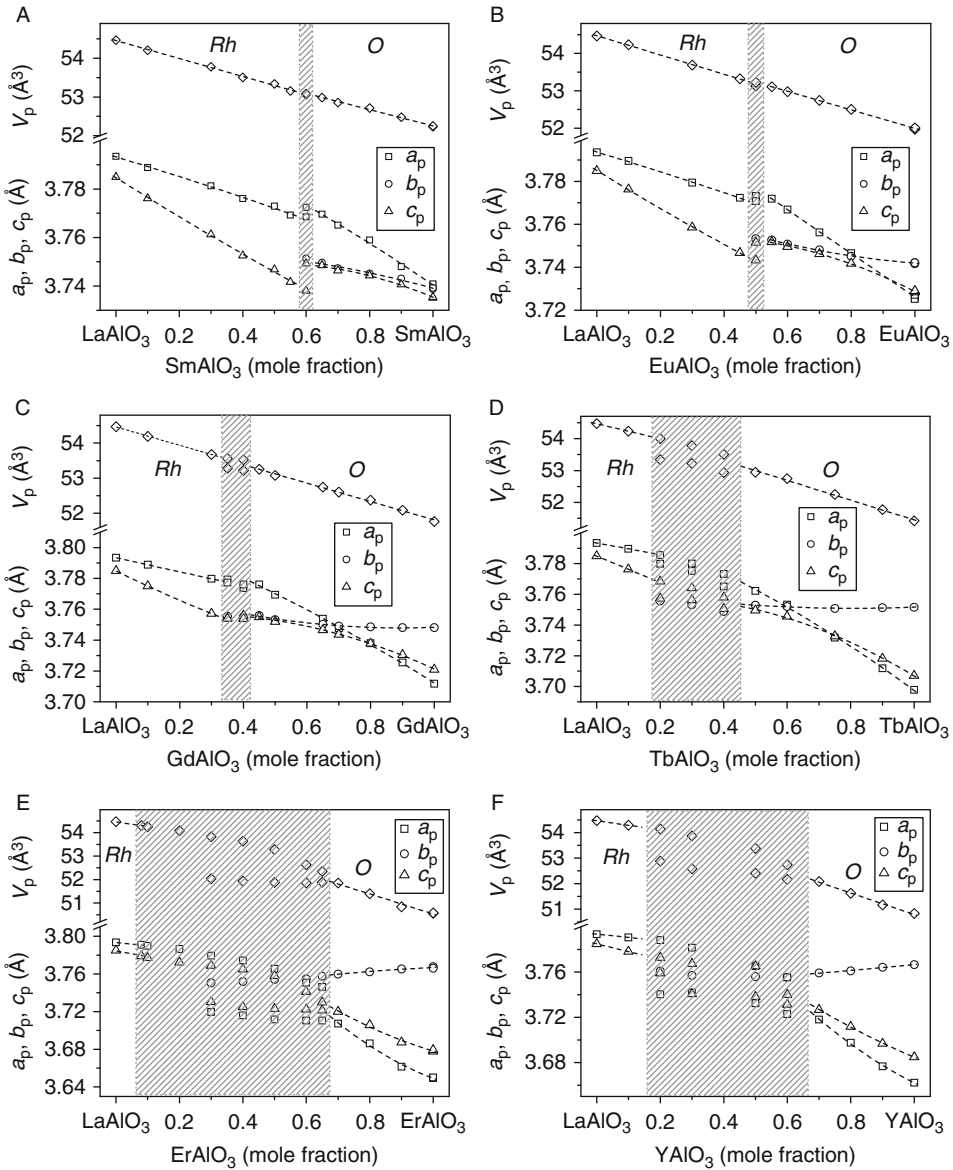


FIGURE 26 Concentration dependencies of the normalized lattice parameters and cell volumes of rhombohedral (Rh) and orthorhombic (O) solid solutions $\text{La}_{1-x}\text{R}_x\text{AlO}_3$ ($R = \text{Sm}, \text{Eu}, \text{Gd}, \text{Tb}, \text{Er}, \text{Y}$) at RT according to [Basyuk et al. \(2007a\)](#). The shaded areas correspond to two-phase regions.

change monotonically with compositions, in accordance with the variation of the ionic radii of the rare earth elements ([Figure 31A and B](#)).

Details about the formation of PrAlO_3 -based solid solutions are known since 1970, when [Geller and Raccach \(1970\)](#) examined HT phase transitions in selected

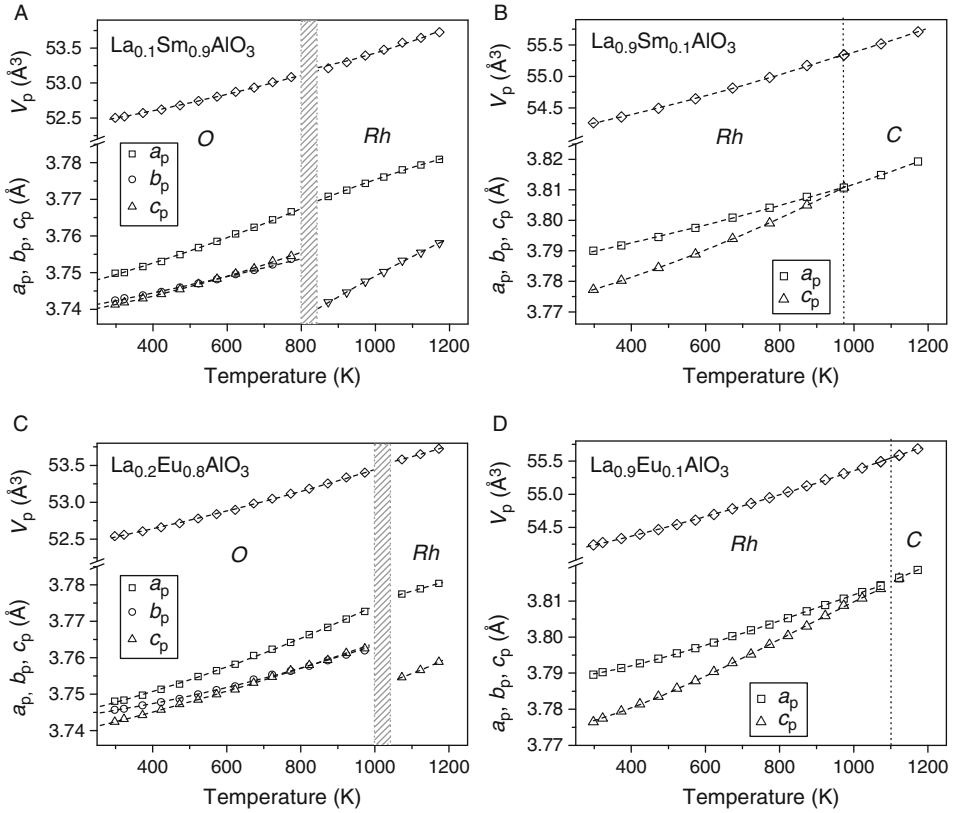


FIGURE 27 Temperature dependencies of the normalized lattice parameters and cell volumes of $\text{La}_{1-x}\text{Sm}_x\text{AlO}_3$, $x = 0.1$ and 0.9 (A, B) and $\text{La}_{1-x}\text{Eu}_x\text{AlO}_3$, $x = 0.1$ and 0.8 (C, D) (Basyuk and Vasylechko, 2007). The letters O, Rh, and C designate orthorhombic, rhombohedral, and cubic phases, respectively. The dashed lines are polynomial fits: $\text{La}_{0.1}\text{Sm}_{0.9}\text{AlO}_3$ $a_p(T) = 3.7455(3) [1 + 1.43(9) \times 10^{-8}T^2 - 6(1) \times 10^{-12}T^3]$; $b_p(T) = 3.7400(1) [1 + 8.60(4) \times 10^{-8}T^2 - 3.3(5) \times 10^{-12}T^3]$; $c_p(T) = 3.7383(2) [1 + 1.07(7) \times 10^{-8}T^2 - 4.3(9) \times 10^{-12}T^3]$; (orthorhombic) and $a_p(T) = 3.748(2) [1 + 1.3(2) \times 10^{-8}T^2 - 5.5(9) \times 10^{-12}T^3]$; $c_p(T) = 3.707(3) [1 + 1.9(2) \times 10^{-8}T^2 - 8(1) \times 10^{-12}T^3]$ (rhombohedral); $\text{La}_{0.9}\text{Sm}_{0.1}\text{AlO}_3$ $a_p(T) = 3.7865(1) [1 + 1.21(3) \times 10^{-8}T^2 - 5.5(3) \times 10^{-12}T^3]$; $c_p(T) = 3.7727(3) [1 + 1.65(6) \times 10^{-8}T^2 - 6.0(6) \times 10^{-12}T^3]$ (rhombohedral) and $a_p(T) = 3.7694(9) + 4.24(9) \times 10^{-5}T$ (cubic); $\text{La}_{0.2}\text{Eu}_{0.8}\text{AlO}_3$ $a_p(T) = 3.7441(2) [1 + 1.30(4) \times 10^{-8}T^2 - 5.1(4) \times 10^{-12}T^3]$; $b_p(T) = 3.7433(2) [1 + 0.79(4) \times 10^{-8}T^2 - 2.6(4) \times 10^{-12}T^3]$; $c_p(T) = 3.7392(2) [1 + 1.18(4) \times 10^{-8}T^2 - 5.4(4) \times 10^{-12}T^3]$; (orthorhombic) and $a_p(T) = 3.7464(1) + 2.89(1) \times 10^{-5}T$; $c_p(T) = 3.709(1) + 4.2(2) \times 10^{-5}T$; (rhombohedral); $\text{La}_{0.9}\text{Eu}_{0.1}\text{AlO}_3$ $a_p(T) = 3.78665(8) [1 + 1.05(1) \times 10^{-8}T^2 - 3.9(1) \times 10^{-12}T^3]$; $c_p(T) = 3.7718(2) [1 + 1.68(3) \times 10^{-8}T^2 - 6.8(3) \times 10^{-12}T^3]$ (rhombohedral) and $a_p(T) = 3.7679(9) + 4.32(9) \times 10^{-5}T$ (cubic).

samples in the PrAlO_3 – LaAlO_3 system. At the same time, Nordland and Van Uiter (1970) studied the LT variation of the dielectric constants of $\text{Pr}_{1-x}\text{Nd}_x\text{AlO}_3$ samples between 300 and 5 K and showed that the temperatures of both 205 K and 151 K phase transformations in PrAlO_3 are suppressed with the substitution of Nd for Pr. Five years later, Glynn et al. (1975) described the LT structural phase

TABLE 22 Structural parameters of orthorhombic modifications (S.G. *Pbnm*) of solid solutions $\text{La}_{1-x}\text{R}_x\text{AlO}_3$ with R = Sm, Eu, Gd, Tb, Er, and Y (Basyuk and Vasylechko, 2007)

	Parameters	$\text{La}_{0.1}\text{Sm}_{0.9}$	$\text{La}_{0.1}\text{Sm}_{0.9}$	$\text{La}_{0.2}\text{Eu}_{0.8}$	$\text{La}_{0.2}\text{Eu}_{0.8}$	$\text{La}_{0.5}\text{Gd}_{0.5}$	$\text{La}_{0.4}\text{Tb}_{0.6}$	$\text{La}_{0.2}\text{Er}_{0.8}$	$\text{La}_{0.1}\text{Y}_{0.9}$
		RT [#]	723 K ¹	RT [#]	923 K ¹	RT ²	RT ²	RT ²	RT ²
	a (Å)	5.30261(5)	5.32370(6)	5.30060(8)	5.33247(8)	5.33081(9)	5.3080(1)	5.21330(6)	5.19963(4)
	b (Å)	5.29287(5)	5.30644(8)	5.29726(6)	5.31865(9)	5.30800(9)	5.3058(1)	5.32054(6)	5.32351(4)
Atom: sites	c (Å)	7.48232(7)	7.5062(1)	7.48484(9)	7.5225(1)	7.5040(1)	7.4910(1)	7.4118(1)	7.39364(6)
La(R), 4c	x	−0.0049(2)	−0.0035(3)	−0.0051(2)	−0.0020(5)	−0.0036(4)	−0.0043(2)	−0.0099(2)	−0.0112(2)
	y	0.02159(7)	0.0158(1)	0.02261(7)	0.0144(1)	0.0106(2)	0.02192(7)	0.0437(1)	0.04680(9)
	z	1/4	1/4	1/4	1/4	1/4	1/4	1/4	1/4
	B_{iso} (Å ²)	0.618(5)	1.026(8)	0.771(5)	1.406(9)	0.86(2)	0.88(1)	0.75(2)	0.66(1)
Al, 4b	x	1/2	1/2	1/2	1/2	1/2	1/2	1/2	1/2
	y	0	0	0	0	0	0	0	0
	z	0	0	0	0	0	0	0	0
	B_{iso} (Å ²)	0.50(2)	0.65(3)	0.60(2)	1.01(4)	1.42(6)	0.64(3)	0.73(6)	1.09(4)
O1, 4c	x	0.061(2)	0.062(3)	0.072(2)	0.070(2)	0.086(2)	0.1185(12)	0.0789(13)	0.0841(8)
	y	0.4890(11)	0.488(2)	0.4887(13)	0.494(2)	0.489(3)	0.4842(12)	0.4880(12)	0.4794(7)
	z	1/4	1/4	1/4	1/4	1/4	1/4	1/4	1/4
	B_{iso} (Å ²)	0.7(2)	1.5(3)	1.6(2)	1.0(2)	2.9(4)	2.4(4)	1.4(2)	1.11(11)
O2, 8d	x	−0.269(2)	−0.261(3)	−0.2612(15)	−0.253(3)	−0.262(3)	−0.260(2)	−0.2907(11)	−0.2976(6)
	y	0.283(2)	0.268(3)	0.2812(14)	0.277(2)	0.256(4)	0.2644(15)	0.2927(11)	0.2817(6)
	z	0.0311(10)	0.0279(15)	0.0331(8)	0.0283(12)	0.0237(12)	0.0265(6)	0.0397(8)	0.0363(4)
	B_{iso} (Å ²)	0.81(11)	1.3(2)	0.16(8)	1.2(2)	0.20(13)	0.4(4)	1.38(13)	0.94(7)

¹ Synchrotron powder diffraction data.

² X-ray powder diffraction data.

[#] © JCPDS—International Centre for Diffraction data, to be published.

TABLE 23 Structural parameters of rhombohedral (S.G. $R\bar{3}c$) and cubic (S.G. $Pm\bar{3}m$) solid solutions $\text{La}_{1-x}\text{R}_x\text{AlO}_3$ with R = Sm, Eu, Gd, Tb, Er, and Y (Basyuk and Vasylechko, 2007)

Parameters		$\text{La}_{0.5}\text{Sm}_{0.5}$	$\text{La}_{0.1}\text{Sm}_{0.9}$	$\text{La}_{0.7}\text{Eu}_{0.3}$	$\text{La}_{0.2}\text{Eu}_{0.8}$	$\text{La}_{0.7}\text{Gd}_{0.3}$	$\text{La}_{0.9}\text{Tb}_{0.1}$	$\text{La}_{0.9}\text{Er}_{0.1}$	$\text{La}_{0.9}\text{Y}_{0.1}$	$\text{La}_{0.9}\text{Sm}_{0.1}$	$\text{La}_{0.9}\text{Eu}_{0.1}$
		$R\bar{3}c$ (RT) ¹	$R\bar{3}c$ (1123 K) ¹	$R\bar{3}c$ (RT) ¹	$R\bar{3}c$ (1123 K) ¹	$R\bar{3}c$ (RT) ²	$R\bar{3}c$ (RT) ²	$R\bar{3}c$ (RT) ²	$R\bar{3}c$ (RT) ²	$Pm\bar{3}m$ (1073 K) ¹	$Pm\bar{3}m$ (1123 K) ¹
a (Å)		5.33550(6)	5.34480(4)	5.34485(3)	5.34420(4)	5.34527(3)	5.35937(3)	5.3591(1)	5.36072(3)	3.81483(2)	3.81644(2)
c (Å)		12.9787(2)	13.0095(1)	13.0203(1)	13.0132(2)	13.0153(1)	13.0815(1)	13.0857(4)	13.0875(1)	–	–
La(R): 6c in $R\bar{3}c$; 1b in $Pm\bar{3}m$	x	0	0	0	0	0	0	0	0	1/2	1/2
	y	0	0	0	0	0	0	0	0	1/2	1/2
	z	1/4	1/4	1/4	1/4	1/4	1/4	1/4	1/4	1/2	1/2
	B_{iso} (Å ²)	0.67(3)	1.58(1)	0.80(1)	1.64(1)	0.64(1)	0.67(1)	0.54(4)	0.82(2)	1.34(1)	1.57(1)
Al: 6b in $R\bar{3}c$; 1a in $Pm\bar{3}m$	x	0	0	0	0	0	0	0	0	0	0
	y	0	0	0	0	0	0	0	0	0	0
	z	0	0	0	0	0	0	0	0	0	0
	B_{iso} (Å ²)	0.78(9)	1.09(4)	0.70(4)	1.07(5)	0.99(4)	1.03(7)	0.94(13)	1.03(7)	1.09(5)	1.04(5)
O: 18e in $R\bar{3}c$; 3d in $Pm\bar{3}m$	x	0.554(2)	0.5458(10)	0.5447(7)	0.5453(12)	0.5497(6)	0.5391(8)	0.536(3)	0.5345(9)	1/2	1/2
	y	0	0	0	0	0	0	0	0	0	0
	z	1/4	1/4	1/4	1/4	1/4	1/4	1/4	1/4	0	0
	B_{iso} (Å ²)	2.2(2)	1.77(11)	1.29(7)	2.14(13)	1.06(7)	0.99(7)	2.4(3)	1.56(8)	1.55(7)	2.37(9)

¹ Synchrotron powder diffraction data.

² X-ray powder diffraction data.

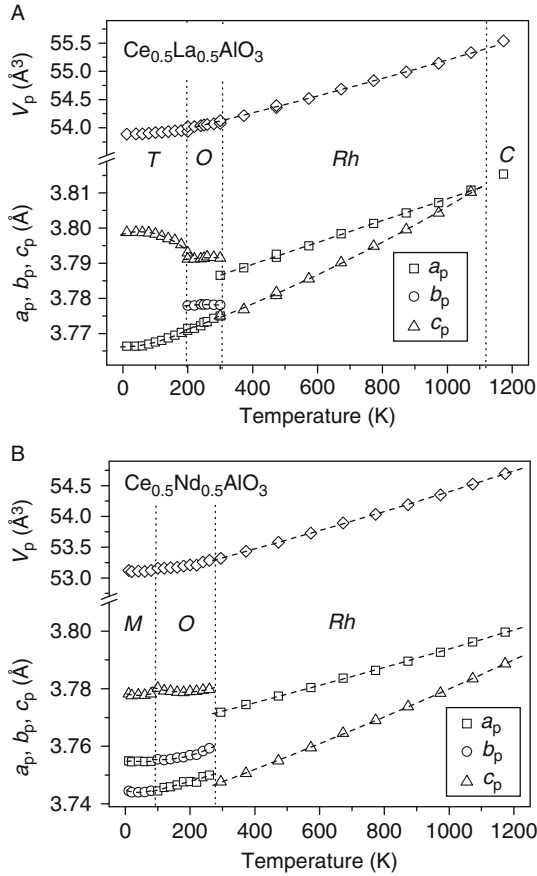


FIGURE 28 Temperature dependencies of the lattice parameters and cell volumes of $\text{Ce}_{0.5}\text{La}_{0.5}\text{AlO}_3$ (A) and $\text{Ce}_{0.5}\text{Nd}_{0.5}\text{AlO}_3$ (B) (Vasylechko, 2005). The letters T, M, O, Rh and C designate tetragonal, monoclinic, orthorhombic, rhombohedral, and cubic phases, respectively. The dashed lines are polynomial fits of lattice parameters: $\text{Ce}_{0.5}\text{La}_{0.5}\text{AlO}_3$ $a_p(T) = 3.7661 + 1.639 \times 10^{-6}T + 1.137 \times 10^{-7}T^2$; $c_p(T) = 3.7982 + 2.570 \times 10^{-5}T - 2.473 \times 10^{-7}T^2$ (tetragonal), $a_p(T) = 3.7713 - 2.709 \times 10^{-5}T + 1.330 \times 10^{-7}T^2$; $b_p(T) = 3.7724 + 4.518 \times 10^{-5}T - 8.814 \times 10^{-8}T^2$; $c_p(T) = 3.7867 + 3.356 \times 10^{-5}T - 5.744 \times 10^{-8}T^2$ (orthorhombic), $a_p(T) = 3.7771 + 3.147 \times 10^{-5}T - 2.901 \times 10^{-10}T^2$; $c_p(T) = 3.7645 + 3.002 \times 10^{-5}T + 1.151 \times 10^{-8}T^2$ (rhombohedral) and $a_p(T) = 3.7588(9) + 4.8(4) \times 10^{-5}T$ (cubic); $\text{Ce}_{0.5}\text{Nd}_{0.5}\text{AlO}_3$ $a_p(T) = 3.7548 - 5.680 \times 10^{-6}T + 4.562 \times 10^{-8}T^2$; $b_p(T) = 3.7447 - 3.6490 \times 10^{-5}T + 4.248 \times 10^{-8}T^2$; $c_p(T) = 3.7783 - 3.023 \times 10^{-5}T + 3.609 \times 10^{-7}T^2$ (monoclinic), $a_p(T) = 3.7421 + 2.459 \times 10^{-5}T - 1.893 \times 10^{-8}T^2$; $b_p(T) = 3.7573 - 3.582 \times 10^{-5}T + 1.654 \times 10^{-8}T^2$; $c_p(T) = 3.7847 - 6.559 \times 10^{-5}T + 1.804 \times 10^{-8}T^2$ (orthorhombic) and $a_p(T) = 3.7637 + 2.745 \times 10^{-5}T + 2.586 \times 10^{-9}T^2$; $c_p(T) = 3.7353 + 3.964 \times 10^{-5}T + 4.953 \times 10^{-9}T^2$ (rhombohedral).

transitions occurring in $\text{PrAlO}_3\text{--LaAlO}_3$. Based on Raman scattering and optical absorption measurements, it was shown that the temperatures of all LT phase transitions in the $\text{Pr}_{1-x}\text{La}_x\text{AlO}_3$ solid solution decrease with increasing La content. Low-temperature behaviour of the phase diagram (up to 250 K) of

TABLE 24 Structural parameters of tetragonal (S.G. $I4/mcm$), monoclinic (S.G. $I2/m$), and orthorhombic (S.G. $Imma$) modifications of solid solutions $Ce_{1-x}R_xAlO_3$ (R = La, Pr, Nd) refined from synchrotron powder diffraction data (Vasylechko et al., 2003c, 2007b; Vasylechko, 2005; Basyuk and Vasylechko, 2007)

Parameters	$Ce_{0.5}La_{0.5}$	$Ce_{0.1}Pr_{0.9}$	$Ce_{0.5}Nd_{0.5}$	$Ce_{0.1}Pr_{0.9}$	$Ce_{0.5}La_{0.5}$	$Ce_{0.1}Pr_{0.9}$	$Ce_{0.5}Pr_{0.5}$	$Ce_{0.7}Nd_{0.3}$
	$I4/mcm$ (12 K)	$I4/mcm$ (12 K) [#]	$I2/m$ (12 K)	$I2/m$ (127 K) [#]	$Imma$ (250 K)	$Imma$ (200 K) [#]	$Imma$ (298 K) [#]	$Imma$ (298 K)
a (Å)	5.32607(7)	5.29030(3)	5.3103(1)	5.31842(9)	5.3432(2)	5.3121(3)	5.32165(6)	5.3210(1)
b (Å)	—	—	7.4890(1)	7.4896(1)	7.5457(3)	7.4991(3)	7.51347(9)	7.5127(1)
c (Å)	7.5976(1)	7.58359(6)	5.3432(1)	5.33675(9)	5.3620(2)	5.3453(2)	5.34942(5)	5.3488(1)
Atom: sites	β , °	—	—	90.255(1)	90.606(1)	—	—	—
Ce(R): 4b in $I4/mcm$; 4i in $I2/m$; 4e in $Imma$	x	0	0	0.2485(11)	0.2526(8)	0	0	0
	y	1/2	1/2	0	0	1/4	1/4	1/4
	z	1/4	1/4	0.7519(9)	0.7513(10)	0.5001(11)	0.5012(6)	0.50014(4)
	B_{iso} (Å ²)	0.45(3)	0.430(6)	0.38(5)	0.618(9)	0.68(5)	0.625(9)	0.81(1)
Al: 4c in $I4/mcm$;	x	0	0	1/4	1/4	0	0	0
4e in $I2/m$;	y	0	0	1/4	1/4	0	0	0
4b in $Imma$	z	0	0	1/4	1/4	0	0	0
	B_{iso} (Å ²)	0.31(10)	0.30(3)	0.3(2)	0.31(3)	0.6(2)	0.38(3)	0.58(4)
O1: 4a in $I4/mcm$;	x	0	0	0.262(7)	0.270(3)	0	0	0
4i in $I2/m$;	y	0	0	0	0	1/4	1/4	1/4
4e in $Imma$	z	1/4	1/4	0.299(4)	0.302(2)	−0.032(4)	−0.049(2)	−0.047(2)
	B_{iso} (Å ²)	0.9(3)	0.69(9)	0.9(7)	1.1(2)	1.1(6)	1.4(2)	1.4(2)
O2: 8h in $I4/mcm$;	x	0.2211(14)	0.2110(5)	0	0	1/4	1/4	1/4
4g in $I2/m$;	y	$x + 1/2$	$x + 1/2$	0.205(2)	0.2134(13)	−0.018(2)	−0.0235(12)	−0.0193(12)
8g in $Imma$	z	0	0	0	0	1/4	1/4	1/4
	B_{iso} (Å ²)	0.9(2)	0.63(9)	0.8(8)	0.6(2)	1.0(4)	0.96(12)	1.02(9)
O3: 4h in $I2/m$	x	—	—	1/2	1/2	—	—	—
	y	—	—	0.237(5)	0.232(3)	—	—	—
	z	—	—	0	0	—	—	—
	B_{iso} (Å ²)	—	—	0.7(6)	0.7(2)	—	—	—

[#] © JCPDS—International Centre for Diffraction data, PDF ## 00-057-0846, 00-057-0847, 00-057-0848, and 00-057-0635.

TABLE 25 Structural parameters of rhombohedral (S.G. $R\bar{3}c$) and cubic (S.G. $Pm\bar{3}m$) modifications of solid solutions $Ce_{1-x}R_xAlO_3$ with R = La, Pr and Nd refined from synchrotron powder diffraction data (Vasylechko et al., 2003c, 2007b; Vasylechko, 2005; Basyuk and Vasylechko, 2007)

Parameters		$Ce_{0.3}La_{0.7}$	$Ce_{0.1}La_{0.9}$	$Ce_{0.1}Pr_{0.9}$	$Ce_{0.1}Nd_{0.9}$	$Ce_{0.1}Nd_{0.9}$	$Ce_{0.5}La_{0.5}$	$Ce_{0.7}Nd_{0.3}$	$Ce_{0.5}Pr_{0.5}$	$Ce_{0.1}La_{0.9}$	$Ce_{0.5}La_{0.5}$
		$R\bar{3}c$ (RT)	$R\bar{3}c$ (RT)	$R\bar{3}c$ (RT) [#]	$R\bar{3}c$ (12 K)	$R\bar{3}c$ (RT)	$R\bar{3}c$ (473 K)	$R\bar{3}c$ (473 K)	$R\bar{3}c$ (1223 K) [#]	$Pm\bar{3}m$ (1173 K)	$Pm\bar{3}m$ (1173 K) [#]
	a (Å)	5.35854(4)	5.3611(2)	5.33225(3)	5.31649(6)	5.32322(4)	5.36358(5)	5.34790(4)	5.38099(6)	3.8208(1)	3.81534(5)
Atom: sites	c (Å)	13.0858(2)	13.0978(6)	12.9736(1)	12.9077(2)	12.9270(1)	13.1004(2)	13.0310(1)	13.1543(3)	—	—
Ce(R): 6c in $R\bar{3}c$; 1b in $Pm\bar{3}m$	x	0	0	0	0	0	0	0	0	1/2	1/2
	y	0	0	0	0	0	0	0	0	1/2	1/2
	z	1/4	1/4	1/4	1/4	1/4	1/4	1/4	1/4	1/2	1/2
	B_{iso} (Å ²)	0.80(1)	0.74(2)	0.77(1)	0.34(1)	0.91(1)	1.06(2)	1.03(2)	1.25(3)	1.83(2)	1.70(3)
Al: 6b in $R\bar{3}c$; 1a in $Pm\bar{3}m$	x	0	0	0	0	0	0	0	0	0	0
	y	0	0	0	0	0	0	0	0	0	0
	z	0	0	0	0	0	0	0	0	0	0
	B_{iso} (Å ²)	0.60(7)	0.67(7)	0.63(5)	0.29(4)	0.88(7)	0.74(9)	0.54(7)	0.60(9)	1.23(7)	1.18(8)
O: 18e in $R\bar{3}c$; 3d in $Pm\bar{3}m$	x	0.5273(15)	0.529(3)	0.5409(10)	0.5491(12)	0.5423(10)	0.526(2)	0.5356(12)	0.525(2)	1/2	1/2
	y	0	0	0	0	0	0	0	0	0	0
	z	1/4	1/4	1/4	1/4	1/4	1/4	1/4	1/4	0	0
	B_{iso} (Å ²)	1.4(2)	0.5(2)	1.00(9)	0.84(12)	0.9(2)	1.2(3)	1.3(2)	1.7(2)	1.9(2)	1.7(4)

[#] © JCPDS—International Centre for Diffraction data, PDF ## 00-057-0640 and 00-057-0636.

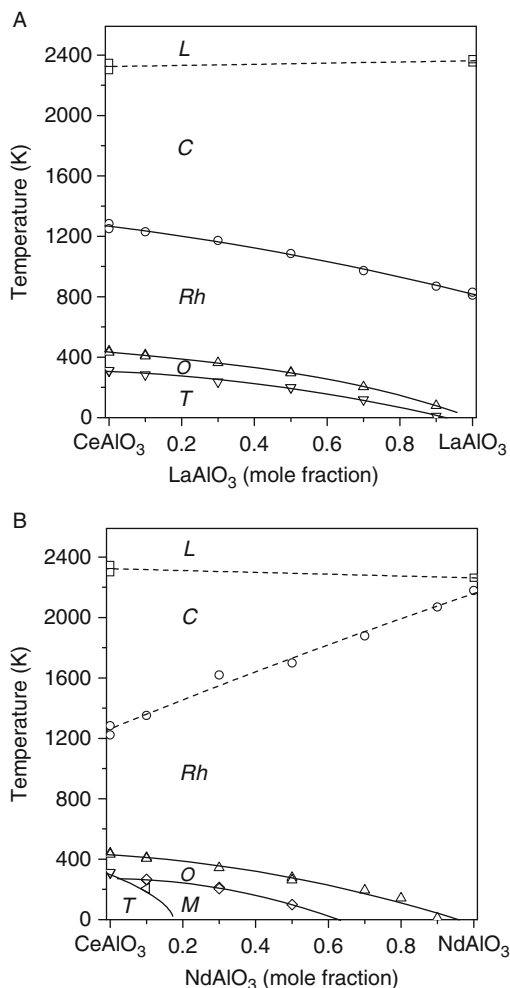


FIGURE 29 Phase diagrams of the CeAlO₃-LaAlO₃ (A) and CeAlO₃-NdAlO₃ (B) pseudobinary systems. The letters L, C, Rh, O, T, and M designate liquid, cubic, rhombohedral, orthorhombic, tetragonal, and monoclinic phases, respectively. Temperatures of the rhombohedral-to-cubic phase transitions for Ce_{1-x}Nd_xAlO₃ have been estimated from the extrapolation of the rhombohedral cell parameters ratio. Melting temperatures for pure RAlO₃ compounds are taken from [Wu and Pelton \(1992\)](#). Polynomial fits of observed critical temperatures are: Ce_{1-x}La_xAlO₃ $T_{T-O}(x) = 307(7) - 103(39) \times x - 243(45) \times x^2$; $T_{O-Rh}(x) = 432(3) - 130(21) \times x - 286(25) \times x^2$; $T_{Rh-C}(x) = 1282(10) - 454(16) \times x$; $T_L(x) = 2324(19) + 38(26) \times x$; Ce_{1-x}Nd_xAlO₃ $T_{M-O}(x) = 272(7) - 6(4) \times x - 680(100) \times x^2$; $T_{M-T}(x) = 312(1) - 1065(21) \times x$; $T_{O-Rh}(x) = 429(12) - 147(78) \times x - 313(89) \times x^2$; $T_{Rh-C}(x) = 1270(22) + 900(39) \times x$; $T_L(x) = 2324(24) - 61(42) \times x$.

PrAlO₃-LaAlO₃ has been proposed in this work. Investigation of the HT phase and the structural behaviour performed *in situ* using synchrotron powder diffraction revealed that the rhombohedral-to-cubic transition temperature in Pr_{1-x}La_xAlO₃ decreases monotonically with increasing x , whereas for PrAlO₃-NdAlO₃ system,

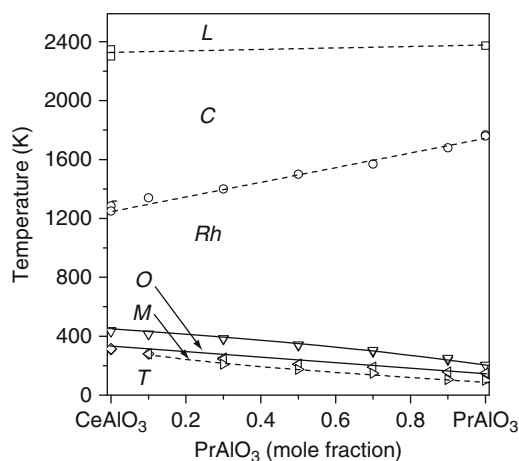


FIGURE 30 Phase diagram of the CeAlO_3 – PrAlO_3 pseudobinary system. The letters L, C, Rh, O, M, and T designate liquid, cubic, rhombohedral, orthorhombic, monoclinic, and (pseudo)-tetragonal phases, respectively. Temperatures of rhombohedral-to-cubic phase transitions for the $\text{Ce}_{1-x}\text{Pr}_x\text{AlO}_3$ samples have been estimated from extrapolation of the rhombohedral cell parameters ratio. Melting temperatures for pure AlO_3 are taken from [Wu and Pelton \(1992\)](#). Polynomial fits of measured critical temperatures in $\text{Ce}_{1-x}\text{Pr}_x\text{AlO}_3$ are: $T_{\text{M-O}}(x) = 300(5) - 196(21) \times x + 46(17) \times x^2$; $T_{\text{M-T}}(x) = 267(22) - 199(73) \times x + 32(6) \times x^2$; $T_{\text{T-O}}(x) = 304.8 - 432 T_{\text{O-Rh}}(x) = 433(4) - 139(18) \times x - 81(18) \times x^2$; $T_{\text{Rh-C}}(x) = 1268(12) + 476(19) \times x$; $T_{\text{L}}(x) = 2324(24) + 49(42) \times x$.

the increase of the transition temperature is observed when the Nd concentration increase ([Kennedy et al., 2002b](#); [Basyuk et al., 2007b](#)). This temperature decrease linearly with increasing average R-cation radius in $\text{Pr}_{1-x}\text{R}_x\text{AlO}_3$ solid solutions, similarly to the CeAlO_3 – AlO_3 systems described above. Temperatures of LT transformations in $\text{Pr}_{1-x}\text{La}_x\text{AlO}_3$ and $\text{Pr}_{1-x}\text{Nd}_x\text{AlO}_3$ systems do not depend on the average radius of R-cation and they decrease with decreasing Pr content. Similar to PrAlO_3 , LT modifications of $\text{Pr}_{1-x}\text{La}_x\text{AlO}_3$ solid solutions display orthorhombic $Imma$, monoclinic $I2/m$, and (pseudo)-tetragonal $I4/mcm$ structures. The same LT structures are typical for the Pr-rich compositions in PrAlO_3 – NdAlO_3 system ([Table 26](#)). Unexpectedly, a rare triclinic perovskite structure has been found in the $\text{Pr}_{0.44}\text{Nd}_{0.56}\text{AlO}_3$ sample below 70 K. Structural parameters of $\text{Pr}_{0.44}\text{Nd}_{0.56}\text{AlO}_3$ at 20K, refined in space group $I\bar{1}$, are presented in [Table 26](#). Atomic parameters in BaLaNiRuO_6 structure ([Battle et al., 1989](#)) were taken as a starting model for the refinement. To the best of our knowledge, it is the first representative of a triclinic structure among perovskites with a single B-cation. To date, similar structure was known only among $A_2BB'O_6$ and $AA'BB'O_6$ perovskites, namely, $\text{Ba}_2\text{LaRuO}_6$, BaLaNiRuO_6 , BaLaCoIrO_6 , and $\text{Sr}_2\text{FeIrO}_6$ ([ICSD, 2005](#)).

Structural parameters of different modifications of perovskite structure existing in the PrAlO_3 – LaAlO_3 and PrAlO_3 – NdAlO_3 systems are listed in [Table 26](#). Temperature dependencies of the lattice parameters of $\text{Pr}_{0.16}\text{La}_{0.84}\text{AlO}_3$ and $\text{Pr}_{0.65}\text{Nd}_{0.35}\text{AlO}_3$ are shown in [Figure 32A and B](#).

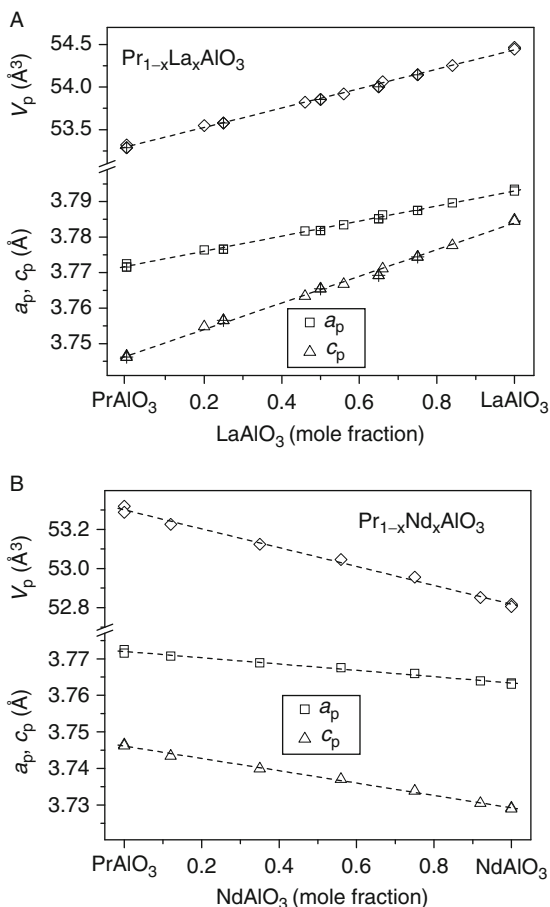


FIGURE 31 Concentration dependencies of the normalized lattice parameters and cell volumes of $\text{Pr}_{1-x}\text{La}_x\text{AlO}_3$ (A) and $\text{Pr}_{1-x}\text{Nd}_x\text{AlO}_3$ (B) solid solution at RT according to Basyuk et al. (2007a). Crossed symbols indicate data taken from Geller and Raccach (1970) and Kennedy et al. (2002b). The dashed lines are linear fits of lattice parameters: $\text{Pr}_{1-x}\text{La}_x\text{AlO}_3$ $a_p(x) = 3.7718(2) + 0.0212(4) \times x$; $c_p(x) = 3.7465(4) + 0.0375(6) \times x$; $\text{Pr}_{1-x}\text{Nd}_x\text{AlO}_3$ $a_p(x) = 3.7720(2) - 0.0086(3) \times x$; $c_p(x) = 3.7461(2) - 0.0169(3) \times x$.

Phase diagrams of PrAlO_3 – LaAlO_3 and PrAlO_3 – NdAlO_3 , constructed using data reported by Geller and Raccach (1970), Nordland and Van Uitert (1970), Glynn et al. (1975), Kennedy et al. (2002b), Basyuk et al. (2007b), and Vasylechko (unpublished data), are presented in Figure 33A and B.

Phase relations in the PrAlO_3 – EuAlO_3 system at RT have been studied by Brusset et al. (1975). The authors showed that similar to the LaAlO_3 – EuAlO_3 system, two kinds of $\text{Pr}_{1-x}\text{Eu}_x\text{AlO}_3$ solid solutions are formed. For EuAlO_3 concentration of less than 0.42 molar fractions, the solid solution adopts rhombohedral structure, whereas the orthorhombic (pseudo-monoclinic) structure is typical for samples with $x > 0.56$. An immiscibility gap exists between the two

TABLE 26 Structural parameters of different modifications of solid solutions $\text{Pr}_{1-x}\text{R}_x\text{AlO}_3$ (R = La, Nd) (Basyuk and Vasylechko, 2007)

Parameters	$\text{Pr}_{0.8}\text{La}_{0.2}$	$\text{Pr}_{0.8}\text{La}_{0.2}$	$\text{Pr}_{0.44}\text{La}_{0.56}$	$\text{Pr}_{0.44}\text{La}_{0.56}$	$\text{Pr}_{0.16}\text{La}_{0.84}$	$\text{Pr}_{0.65}\text{Nd}_{0.35}$	$\text{Pr}_{0.65}\text{Nd}_{0.35}$	$\text{Pr}_{0.65}\text{Nd}_{0.35}$	$\text{Pr}_{0.44}\text{Nd}_{0.56}$	$\text{Pr}_{0.44}\text{Nd}_{0.56}$	
	$I2/m$ (110 K) [#]	$Imma$ (170 K) [#]	$R\bar{3}c$ (RT)	$R\bar{3}c$ (1073 K)	$Pm\bar{3}m$ (1073 K)	$I2/m$ (60 K)	$Imma$ (115 K)	$R\bar{3}c$ (1173 K)	$I\bar{1}$ (20 K) [#]	$R\bar{3}c$ (RT)	
a (Å)	5.3426(3)	5.3180(2)	5.34951(3)	5.3841(1)	3.81525(2)	5.3377(2)	5.3013(1)	5.36972(8)	5.3304(2)	5.32805(4)	
b (Å)	7.5035(6)	7.5092(3)	—	—	—	7.4834(2)	7.4892(2)	—	5.2960(2)	—	
c (Å)	5.3232(3)	5.3483(2)	13.0458(1)	13.1755(6)	—	5.3036(2)	5.3386(1)	13.1064(2)	7.4882(3)	12.9454(1)	
α , °	90	90	90	90	90	90	90	90	90.382(4)	90	
β , °	90.479(6)	90	90	90	90	90.378(2)	90	90	89.952(4)	90	
Atom: sites	γ , °	90	90	120	120	90	90	90	120	90.291(4)	120
Pr(R): 4i in $I2/m$ and $I\bar{1}$; 4e in $Imma$; 6c in $R\bar{3}c$, 1b in $Pm\bar{3}m$	x	0.2524(6)	0	0	0	1/2	0.2514(10)	0	0	-0.0008(6)	0
	y	0	1/4	0	0	1/2	0	1/4	0	0.4998(7)	0
	z	0.7501(8)	0.5014(5)	1/4	1/4	1/2	0.7498(13)	0.4992(6)	1/4	0.2500(6)	1/4
	B_{iso} (Å ²)	0.48(1)	0.59(1)	0.882(6)	1.53(1)	1.55(1)	0.68(1)	0.71(1)	1.70(1)	0.632(6)	0.974(9)
Al1: 4e in $I2/m$, 4b in $Imma$; 6b in $R\bar{3}c$, 1a in $Pm\bar{3}m$, 2a in $I\bar{1}$	x	1/4	0	0	0	0	1/4	0	0	0	
	y	1/4	0	0	0	0	1/4	0	0	0	
	z	1/4	0	0	0	0	1/4	0	0	0	
	B_{iso} (Å ²)	0.60(4)	0.65(4)	0.81(3)	1.14(4)	0.97(5)	0.70(5)	0.55(4)	1.21(5)	0.66(5)	1.03(4)
Al2: 2b in $I\bar{1}$	x	—	—	—	—	—	—	—	0	—	
	y	—	—	—	—	—	—	—	0	—	
	z	—	—	—	—	—	—	—	1/2	—	
	B_{iso} (Å ²)	—	—	—	—	—	—	—	0.65(5)	—	

O1: 4i in $I2/m$ and $I\bar{1}$; 4e in $Imma$; 18e in $R\bar{3}c$, 3d in $Pm\bar{3}m$	x	0.213(3)	0	0.5341(8)	0.521(2)	1/2	0.199(4)	0	0.5365(14)	0.0564(12)	0.5456(9)
	y	0	1/4	0	0	0	0	1/4	0	-0.006(2)	0
	z	0.229(6)	0.043(2)	1/4	1/4	0	0.212(6)	0.048(2)	1/4	0.248(2)	1/4
	$B_{\text{iso}} (\text{Å}^2)$	1.0(3)	0.9(2)	0.91(6)	1.66(11)	1.69(7)	0.8(4)	0.2(3)	1.53(11)	0.36(14)	0.83(8)
O2: 4g in $I2/m$, 8g in $Imma$; 4i in $I\bar{1}$	x	0	1/4	—	—	—	0	1/4	—	0.234(4)	—
	y	0.281(3)	-0.0198(12)	—	—	—	0.274(5)	-0.0291(14)	—	0.731(4)	—
	z	0	1/4	—	—	—	0	1/4	—	-0.005(3)	—
	$B_{\text{iso}} (\text{Å}^2)$	0.4(3)	0.59(11)	—	—	—	1.2(5)	1.0(2)	—	0.9(2)	—
O3: 4h in $I2/m$; 4i in $I\bar{1}$	x	1/2	—	—	—	—	1/2	—	—	-0.255(3)	—
	y	0.233(3)	—	—	—	—	0.223(4)	—	—	0.756(2)	—
	z	0	—	—	—	—	0	—	—	0.4558(9)	—
	$B_{\text{iso}} (\text{Å}^2)$	0.5(2)	—	—	—	—	0.7(4)	—	—	0.3(2)	—

© JCPDS—International Centre for Diffraction data, to be published.

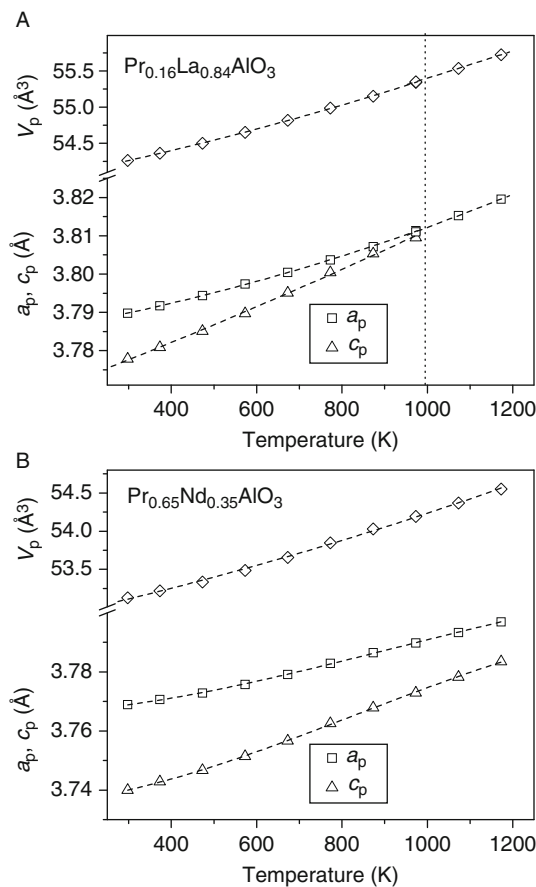


FIGURE 32 Temperature dependencies of the normalized lattice parameters and cell volumes of $\text{Pr}_{0.16}\text{La}_{0.84}\text{AlO}_3$ (A) and $\text{Pr}_{0.65}\text{Nd}_{0.35}\text{AlO}_3$ (B) samples (Basyuk and Vasylechko, 2007). The dashed lines are polynomial fits for: $\text{Pr}_{0.16}\text{La}_{0.84}\text{AlO}_3$ $a_p(T) = 3.7869(3) [1 + 1.03(6) \times 10^{-8}T^2 - 3.7(6) \times 10^{-12}T^3]$; $c_p(T) = 3.7721(3) [1 + 2.00(5) \times 10^{-8}T^2 - 9.8(5) \times 10^{-12}T^3]$; (rhombohedral) and $a_p(T) = 3.7694(3) + 4.28(3) \times 10^{-5}T$ (cubic); $\text{Pr}_{0.65}\text{Nd}_{0.35}\text{AlO}_3$ $a_p(T) = 3.7657(2) [1 + 1.05(3) \times 10^{-8}T^2 - 3.8(3) \times 10^{-12}T^3]$; $c_p(T) = 3.7348(2) [1 + 1.78(4) \times 10^{-8}T^2 - 7.1(3) \times 10^{-12}T^3]$ (rhombohedral).

perovskite-type phases. It was also reported that a solid solution with pseudo-cubic symmetry, which differs from the pseudo-monoclinic one by a larger movement of cations, has been found in the system.

2.3.4 $\text{NdAlO}_3\text{--RAlO}_3$

Phase behaviour in the $\text{NdAlO}_3\text{--SmAlO}_3$ system and structural changes caused by substitution of Nd for Sm atoms have been carefully investigated using high-resolution synchrotron radiation powder diffraction technique (Saitow *et al.*, 1998; Yoshikawa *et al.*, 1998). It was found that two kinds of $\text{Nd}_{1-x}\text{Sm}_x\text{AlO}_3$ solid solutions with rhombohedral $R\bar{3}c$ and orthorhombic $Pbnm$ structure are formed.

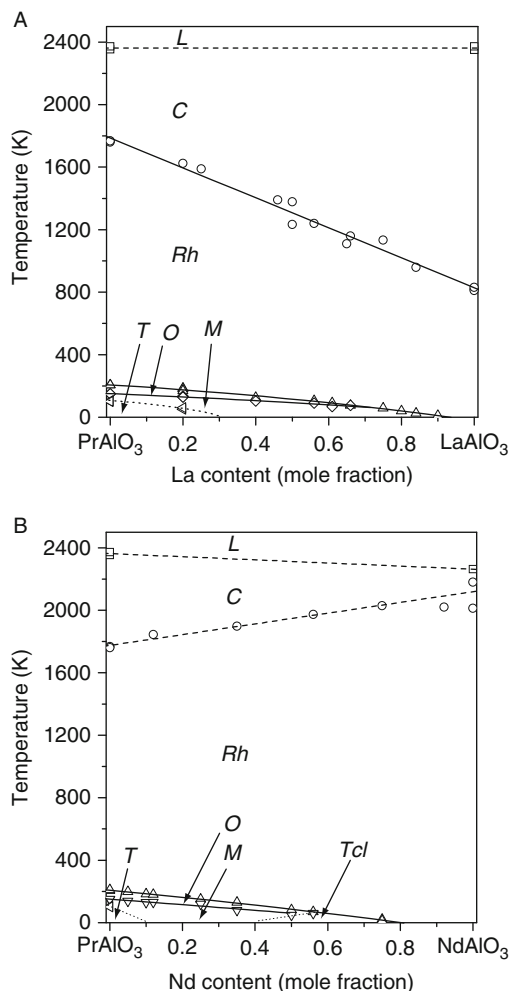


FIGURE 33 Phase diagrams of $\text{PrAlO}_3\text{-LaAlO}_3$ (A) and $\text{PrAlO}_3\text{-NdAlO}_3$ (B) pseudobinary systems. The letters L, C, Rh, O, M, T, and Tcl designate liquid, cubic, rhombohedral, orthorhombic, monoclinic, (pseudo)-tetragonal, and triclinic phase fields, respectively. Temperatures of the rhombohedral-to-cubic phase transition for $\text{Pr}_{1-x}\text{Nd}_x\text{AlO}_3$ have been estimated from the extrapolation of the rhombohedral cell parameters ratio. Polynomial fits of the observed critical temperatures: $\text{Pr}_{1-x}\text{La}_x\text{AlO}_3$ $T_{\text{M-O}}(x) = 150(3) - 94(25) \times x - 42(38) \times x^2$ for $x < 0.65$; $T_{\text{O-Rh}}(x) = 206(4) - 135(21) \times x - 91(23) \times x^2$ for $x < 0.9$; $T_{\text{Rh-C}}(x) = 1787(19) - 959(31) \times x$; $T_{\text{L}}(x) = 2363(11) - 1(15) \times x$; $\text{Pr}_{1-x}\text{Nd}_x\text{AlO}_3$ $T_{\text{M-O}}(x) = 150(4) - 173(53) \times x - 12(96) \times x^2$ for $x < 0.5$; $T_{\text{O-Rh}}(x) = 208(2) - 218(15) \times x - 50(20) \times x^2$ for $x < 0.8$; $T_{\text{Rh-C}}(x) = 1775(23) + 344(38) \times x$; $T_{\text{L}}(x) = 2363(1) - 100(17) \times x$.

At room temperature, the transition from orthorhombic to rhombohedral structure takes place around $x = 0.27$ (Figure 34).

Temperature-induced phase transition from orthorhombic to trigonal structure has been detected in $\text{Nd}_{1-x}\text{Sm}_x\text{AlO}_3$ samples with $x = 0.4$ and 0.6 at 463 and 643 K, respectively (Yoshikawa et al., 1998). It was shown that the transition is

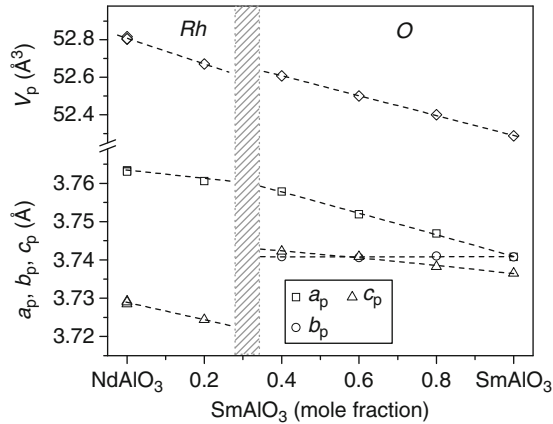


FIGURE 34 Variation of lattice parameters and cell volume of rhombohedral (Rh) and orthorhombic (O) $\text{Nd}_{1-x}\text{Sm}_x\text{AlO}_3$ solid solution according to Saitow *et al.* (1998). The shaded area corresponds to two-phase region. The dashed lines are polynomial fits of lattice parameters: $a_p(x) = 3.7686 - 0.0268 \times x - 0.0009 \times x^2$; $b_p(x) = 3.7409 - 0.0005 \times x + 0.0004 \times x^2$; $c_p(x) = 3.7454 - 0.0069 \times x - 0.0022 \times x^2$ (orthorhombic) and $a_p(x) = 3.7632 - 0.0131 \times x$; $c_p(x) = 3.7289 - 0.0226 \times x$ (rhombohedral).

reversible and first-order in character. Both orthorhombic and rhombohedral phases coexist near the transition temperatures over a range of about ± 5 K. Using the temperatures of the phase transition reported in the literature for NdAlO_3 , SmAlO_3 , and solid solutions between them, a tentative phase diagram of the NdAlO_3 – SmAlO_3 system can be constructed (Figure 35).

Phase relations in the pseudo-binary systems NdAlO_3 – RAlO_3 ($R = \text{Eu}, \text{Dy}, \text{and Er}$) at RT have been examined by Brusset *et al.* (1975). According to their study, two kinds of $\text{Nd}_{1-x}\text{Eu}_x\text{AlO}_3$ solid solutions with rhombohedral and pseudo-monoclinic structure exist in the NdAlO_3 – EuAlO_3 system at $x < 0.18$ and $x > 0.25$, respectively. It was also claimed that a solid solution with pseudo-cubic symmetry exists in the $\text{Nd}_{1-x}\text{Er}_x\text{AlO}_3$ system when $0.07 < x < 0.5$. Evidently, there is a two-phase region between two perovskite-type phases with rhombohedral and orthorhombic structures. In the NdAlO_3 – DyAlO_3 system, the boundary between rhombohedral and pseudo-cubic phases is located near 0.08 molar fractions of DyAlO_3 .

The formation of solid solution in the NdAlO_3 – YAlO_3 system was described by Tanaka *et al.* (1993a). The authors examined $\text{Nd}_{1-x}\text{Y}_x\text{AlO}_3$ crystals ($0 \leq x \leq 0.25$) grown by the FZ method and claimed that the transformation from the hexagonal (rhombohedral) lattice to the cubic perovskite structure occurs at $x = 0.2$. As-grown crystals with $x = 0.2$ and 0.25 were opaque and contained many cracks and subgrain boundaries, and the yttrium concentration in these crystal was not uniform. Nevertheless, the authors concluded that the rhombohedral form of pure NdAlO_3 can be changed to the cubic structure by substitution of at least 20 at.% Y for Nd. Apparently, this conclusion is erroneous because the substitution of smaller Y^{3+} cations for larger Nd^{3+} will result in the decrease of the Goldschmidt tolerance factor and, as a consequence, in an increased

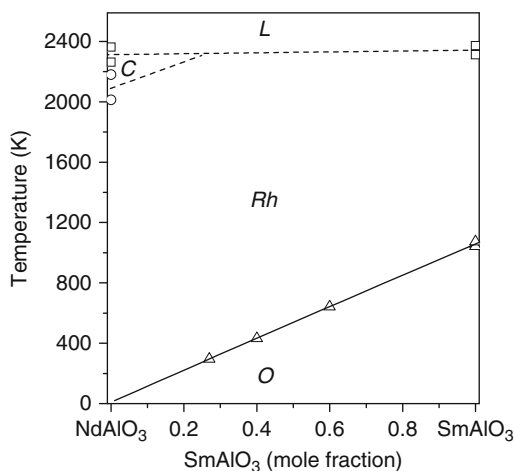


FIGURE 35 Tentative phase diagram of the NdAlO_3 – SmAlO_3 pseudobinary system. The letters L, C, Rh, and O designate liquid, cubic, rhombohedral, and orthorhombic phase fields, respectively. Transition temperatures in the $\text{Nd}_{1-x}\text{Sm}_x\text{AlO}_3$ solid solution were taken from Yoshikawa et al. (1998). Besides, the transition and melting temperatures in NdAlO_3 and SmAlO_3 reported by Howard et al. (2000), Portnoj and Timofeeva (1986), Wu and Pelton (1992), Coutures and Coutures (1984) were used. Linear fits of observed critical temperatures: $T_{\text{O-Rh}}(x) = 16(11) + 1043(14) \times x$; $T_{\text{L}}(x) = 2313(41) + 30(58) \times x$.

deformation of the rhombohedral perovskite structure. Therefore, it is reasonable to assume that similar to other NdAlO_3 – RAlO_3 systems, a mixture of two different perovskite-type phases—rhombohedral and orthorhombic ones—is formed in the $\text{Nd}_{1-x}\text{Y}_x\text{AlO}_3$ system when $x = 0.2$ and 0.25 .

2.3.5 GdAlO_3 – RAlO_3

$\text{Gd}_{1-x}\text{Tb}_x\text{AlO}_3$ single crystals with $x = 0.03, 0.1, 0.2, 0.3, 0.6, 0.8,$ and 0.9 were grown using the Czochralski method in order to study the substitution of Gd for Tb ions in the GdAlO_3 – TbAlO_3 pseudo-binary system (Morita et al., 1996). The authors reported that all obtained crystals adopt orthorhombic structure at RT. Only for the $\text{Gd}_{0.1}\text{Tb}_{0.9}\text{AlO}_3$ composition, the lattice parameters were given. From the composition dependence of the density of as-grown crystals presented in the paper, it may be concluded that a continuous solid solution exists in the GdAlO_3 – TbAlO_3 system at RT.

In the GdAlO_3 – LuAlO_3 system, mixed $\text{Gd}_{1-x}\text{Lu}_x\text{AlO}_3$ crystals doped with Ce were obtained using the Czochralski method (Chval et al., 2000; Mares et al., 2002). The best results were obtained for Lu concentration range of $0.6 \leq x \leq 0.7$. A full-structure refinement was performed for $\text{Gd}_{0.35}\text{Lu}_{0.65}\text{AlO}_3:\text{Ce}$ by Vasylechko (2005). The corresponding structural data are given in Table 27.

The growth of an Nd-doped crystal from the GdAlO_3 – YAlO_3 system with composition $\text{Y}_{0.6}\text{Gd}_{0.35}\text{Nd}_{0.05}\text{AlO}_3$ has been reported by Arsenev et al. (1975). However, no structural information is found in this paper.

TABLE 27 Structural parameters of orthorhombic (S.G. *Pbnm*) solid solutions $\text{Gd}_{0.35}\text{Lu}_{0.65}\text{AlO}_3$, $\text{Y}_{0.5}\text{Er}_{0.5}\text{AlO}_3$ and $\text{Y}_{1-x}\text{Lu}_x\text{AlO}_3$ at RT

	Parameters	Vasylechko (2005)	Vasylechko et al. (1996)	Vasylechko (2005)	Vasylechko (2005)	Vasylechko (2005)
		$\text{Gd}_{0.35}\text{Lu}_{0.65}$	$\text{Y}_{0.5}\text{Er}_{0.5}$	$\text{Y}_{0.9}\text{Lu}_{0.1}$	$\text{Y}_{0.8}\text{Lu}_{0.2}$	$\text{Y}_{0.7}\text{Lu}_{0.3}$
	a (Å)	5.17194(8)	5.16959(4)	5.17161(4)	5.16687(5)	5.15842(6)
	b (Å)	5.32512(7)	5.32817(4)	5.32868(4)	5.32947(4)	5.33073(5)
Atom: sites	c (Å)	7.3708(1)	7.36245(7)	7.36362(5)	7.35937(6)	7.35174(8)
R, 4c	x	−0.0129(2)	−0.0131(1)	−0.0128(2)	−0.0127(2)	−0.0130(2)
	y	0.0535(1)	0.0555(1)	0.0542(1)	0.0551(1)	0.0563(1)
	z	1/4	1/4	1/4	1/4	1/4
	B_{iso} (Å ²)	0.82(2)	0.54(2)	0.74(2)	0.85(1)	0.76(2)
Al, 4b	x	1/2	1/2	1/2	1/2	1/2
	y	0	0	0	0	0
	z	0	0	0	0	0
	B_{iso} (Å ²)	0.71(12)	0.79(7)	0.90(6)	0.81(6)	0.61(8)
O1, 4c	x	0.082(2)	0.0877(9)	0.0817(10)	0.0868(9)	0.0877(11)
	y	0.478(2)	0.4819(9)	0.4769(9)	0.4792(8)	0.4762(11)
	z	1/4	1/4	1/4	1/4	1/4
	B_{iso} (Å ²)	1.4(3)	0.9(2)	0.90(11)	0.72(10)	0.72(13)
O2, 8d	x	−0.297(2)	−0.2977(7)	−0.2995(8)	−0.2974(8)	−0.2995(10)
	y	0.2951(15)	0.2978(7)	0.2941(7)	0.2989(7)	0.2946(9)
	z	0.0481(10)	0.0444(5)	0.0447(5)	0.0443(5)	0.0450(6)
	B_{iso} (Å ²)	0.9(2)	0.88(14)	0.76(8)	0.98(8)	0.95(10)

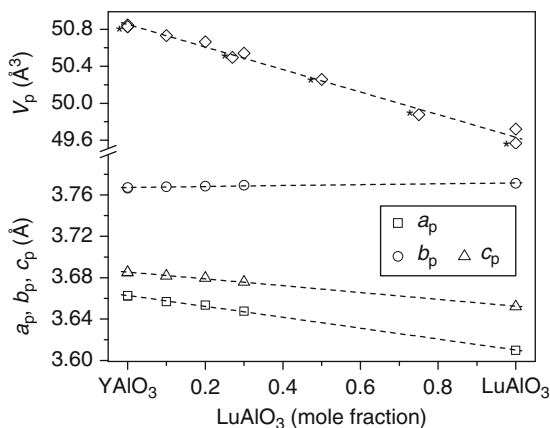


FIGURE 36 Concentration dependence of the normalized lattice parameters and cell volume in $Y_{1-x}Lu_xAlO_3$ solid solution according to Vasylechko (2005). The asterisks indicate data extracted from a figure in Petrosyan et al. (1999). The dashed lines are linear fits of lattice parameters: $a_p(x) = 3.6628(4) - 0.053(1) \times x$; $b_p(x) = 3.7673(3) + 0.0043(8) \times x$; $c_p(x) = 3.6854(3) - 0.0329(7) \times x$.

2.3.6 $YAlO_3$ – $RAIO_3$

In the $YAlO_3$ – $YbAlO_3$ system, the preparation of crystals at $Y_{1-x}Yb_xAlO_3$ ($x = 0.02$ – 0.45) stoichiometries has been reported (Nikl et al., 2004). No structural information was given in this work. Lattice parameters for a $Y_{0.8}Yb_{0.2}AlO_3$ crystal were reported by Zhao et al. (2004c).

Ce-doped single crystals of $Y_{1-x}Lu_xAlO_3$ solid solutions ($x = 0.2$ – 0.85) were grown using the vertical Bridgman process (Petrosyan et al., 1999). A linear decrease of the cell volume was observed with increasing Lu concentration. The variation of the unit cell volumes reported in the chapter proves that the $YAlO_3$ – $LuAlO_3$ system is a solid-solution system in the whole range of compositions. The preparation of single-phase compositions of $Y_{1-x}Lu_xAlO_3$ solid solution with orthorhombic structure has also been reported in Chval et al. (2000) and Kyomen and Itoh (2002). It was stated that the compositional dependence of the cell volume is linear at least in the range $0 \leq x \leq 0.5$. A full structure refinement was carried out for $Y_{1-x}Lu_xAlO_3$ ($x = 0.1, 0.2$, and 0.3) samples by Vasylechko (2005). The corresponding data are given in Table 27. The variation of lattice parameters and cell volume of the solid solution of $YAlO_3$ – $LuAlO_3$ is shown in Figure 36.

Besides the above-mentioned systems, the crystal structure parameters of $Y_{0.5}Er_{0.5}AlO_3$ from the $YAlO_3$ – $ErAlO_3$ system have been reported by Vasylechko et al. (1996). Refined structural parameters are listed in Table 27.

2.4 Comparative analysis of $RAIO_3$ structures

As mentioned in a previous section 2.2, the majority of $RAIO_3$ compounds at RT adopt either the rhombohedral $R\bar{3}c$ ($R = La, Pr$, and Nd) or the orthorhombic $Pbnm$ structure ($R = Sm$ – Lu and Y). The only exception is the RT tetragonal structure of

CeAlO₃, where the rhombohedral modification exists in the temperature range of 363–1253 K. It is worth noting that the orthorhombic GdFeO₃-type structure is the most widespread structure among all ABX₃ perovskites. According to Lufaso and Woodward (2001), over 50% of known perovskites with a single octahedral cation adopt this structure type. The rhombohedral LaAlO₃-type is characteristic for about 17% of the known perovskites.

In the present section, various structural parameters of RAlO₃ perovskites and their solid solutions, for example lattice parameters, selected interatomic distances and angles, parameters of structure deformation, are analysed as a function of the average ionic radii of R-cations. Shannon's ionic radii for ninefold coordinated R³⁺ cations have been chosen since 9 is highest CN tabulated for all rare earth atoms (Shannon, 1976). The mean ionic radii of R-cations in R_{1-x}R'_xAlO₃ solid solutions were calculated as simple arithmetic average, that is $r_{ave} = (x-1) \cdot r(R') + x \cdot r(R)$.

Lattice parameters and cell volumes in a series of rare earth aluminates with perovskite structure are shown in Figure 37. Besides RAlO₃ compounds, the corresponding values of various solid solutions La_{1-x}R_xAlO₃ (R = Ce–Tb, Er, and Y), Nd_{1-x}R_xAlO₃ (R = Ce, Pr, and Sm), and Y_{1-x}R_xAlO₃ (R = Sm–Gd and Dy–Lu) are displayed as well. In accordance with the increasing radius of R-cation, a nearly linear increase of cell volume is observed for both the orthorhombic and rhombohedral perovskites. The phase transition between the orthorhombic and rhombohedral structures is accompanied by an approximately 0.72% decrease of the normalized cell volume. Highly anisotropic character of the changes in the lattice parameters is observed in orthorhombic perovskites.

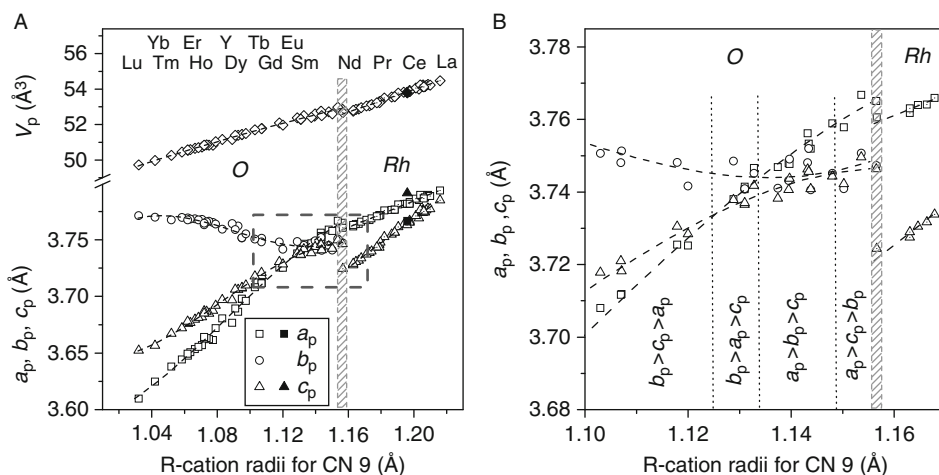


FIGURE 37 Normalized lattice parameters and cell volumes of rare earth aluminates versus ionic radius of R-cations. Panel (B) is an expanded view of the region highlighted by a rectangular box in panel (A). The dashed lines are guides for the eye. The letters O and Rh designate orthorhombic and rhombohedral phases, respectively. The shaded area corresponds to two-phase region. Solid symbols indicate the tetragonal lattice parameters of CeAlO₃. The vertical dotted lines separate regions with different ratios of the normalized lattice parameters.

An increase of the a - and c -parameters with increasing R-cation radius is accompanied by a noticeable reduction of the b -parameter. A change of the slope, especially pronounced for the b -parameter, is observed for r -values around 1.075 Å. Note that a similar behaviour of the lattice parameters is also observed among other RMO_3 compounds ($M = \text{Ni, Fe, Cr, Ti, Ga, Co, Mn, and V}$) and seems rather typical for all GdFeO_3 -type perovskites (Zhou and Goodenough, 2005).

The difference between the lattice parameters of RAIO_3 compounds decreases with increasing R-cation radius and it practically vanishes in SmAlO_3 —the end member of the series of aluminates with the orthorhombic structure. Further increase of the ionic radius of R-cations above 1.156 Å leads to the rearrangement of the perovskite structure resulting in the transition from the orthorhombic to the rhombohedral structure observed in NdAlO_3 , PrAlO_3 , and LaAlO_3 . The rhombohedral perovskite structure is also typical for all solid solutions $\text{R}_{1-x}\text{R}'_x\text{AlO}_3$ with average R-cation radius above 1.156 Å. The deformation of the rhombohedral perovskite lattice decreases with increasing R-cation radius and reaches a minimum in LaAlO_3 . The rhombohedral distortion of the LaAlO_3 structure is small, therefore its transformation to the cubic structure occurs at a relatively low temperature of 813 K.

The ideal cubic perovskite structure of LaAlO_3 and other RAIO_3 compounds can be viewed as a framework of corner-sharing AlO_6 octahedra containing cubo-octahedral holes occupied by R-cations (Figure 38). The coordination polyhedra in this structure are regularly shaped, that is there are 12 equal R–O and 6 Al–O distances (Table 28). The octahedral axes in the AlO_6 polyhedra are parallel to the fourfold $[001]_p$ axis of the cubic perovskite-type cell (Figure 38). According to Glazer's notation (Glazer, 1972, 1975; Woodward, 1997a), the structure belongs to the $a^0a^0a^0$ tilt system. This notation was developed to describe various distortions of ABO_3 perovskite structures caused by tilts of the ideal BO_6 octahedra. In this notation, the tilt system is described by specifying the rotations of the octahedra about each of the $[100]_p$, $[010]_p$, and $[001]_p$ axes of the aristotype cubic perovskite cell. In the abbreviation $a^+b^-c^0$, the letters indicate the relative magnitude of the

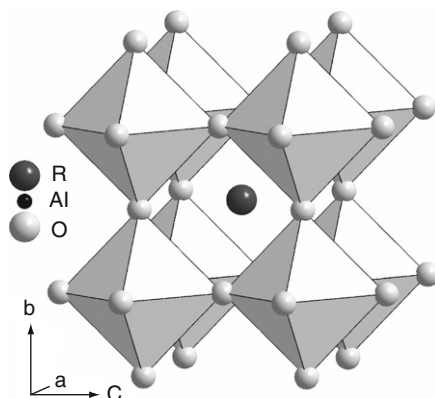


FIGURE 38 The ideal cubic perovskite structure.

TABLE 28 Selected interatomic distances and angles in different RAIO_3 structures

Atoms	Distances (Å)	Atoms	Distances (Å)	Atoms	Distances (Å)	Atoms	Angles (°)
S.G. $Pm\bar{3}m$ (LaAlO_3 at 1223 K)							
Al-6O	1.914	R-8Al	3.316	O-8O	2.707	O-Al-O	90
R-12O	2.707	R-6R	3.828			O-Al-O	180
		Al-6Al	3.828			Al-O-Al	180.0
S.G. $R\bar{3}c$ (LaAlO_3 at RT)							
Al-6O	1.900	R-2Al	3.277	O-4O	2.681	O-Al-O	179.98; 180.0
R-3O	2.548	R-6Al	3.284	O-4O	2.692	O-Al-O	89.77; 90.23
R-6O	2.681	R-6R	3.790				
R-3O	2.816	Al-6Al	3.790			Al-O-Al	171.9
S.G. $Pbnm$ (YbAlO_3 at RT)							
Al-2O1	1.893	R-2Al	2.975	O1-2O2	2.659	O1-Al-O2	91.23; 88.67
Al-2O2	1.908	R-2Al	3.108	O1-2O2	2.669	O1-Al-O2	91.33; 88.77
Al-2O2	1.926	R-2Al	3.221	O1-2O2	2.716	O2-Al-O2	90.18; 89.82
R-O1	2.216	R-2Al	3.502	O1-2O2	2.732	O1-Al-O1	180.0
R-2O2	2.244	R-2R	3.603	O2-2O2	2.707	O2-Al-O2	179.98; 180.0
R-O1	2.259	R-2R	3.715	O2-2O2	2.715		
R-2O2	2.445	R-2R	3.796	O2-O2	2.962	Al-O1-Al	149.9
R-2O2	2.548	Al-2Al	3.657	O2-O2	3.043	Al-O2-Al	149.4
R-O1	2.998	Al-4Al	3.698				
R-O1	3.183						
R-2O2	3.315						
S.G. $Imma$ (CeAlO_3 at 373 K)							
Al-2O1	1.891	R-4Al	3.267	Al-2Al	3.769	O1-Al-O2	83.7; 96.3
Al-4O2	1.896	R-2Al	3.261	Al-4Al	3.781	O2-Al-O2	89.73; 90.27
R-O1	2.487	R-2Al	3.289	O1-4O2	2.527	O1-Al-O1	179.98
R-4O2	2.636	R-2R	3.757	O1-4O2	2.821	O2-Al-O2	180

R-2O1	2.678	R-2R	3.769	O2-2O2	2.669		
R-4O2	2.704	R-2R	3.805			Al-O1-Al	167.37
R-O1	2.870					Al-O2-Al	176.35
S.G. $I4/mcm$ (CeAlO ₃ at RT)							
Al-4O2	1.898	R-8Al	3.271	O1-8O2	2.681	O1-Al-O1	180
Al-2O1	1.897	R-4R	3.769	O2-4O2	2.684	O1-Al-O2	90
R-4O2	2.520	R-2R	3.793			O2-Al-O2	90.0; 180.0
R-4O1	2.6654	Al-4Al	3.769				
R-4O2	2.836	Al-2Al	3.793			Al-O1-Al	180
						Al-O2-Al	166.4
S.G. $I2/m$ (PrAlO ₃ at 120 K)							
Al-2O1	1.888	R-2Al	3.248	Al-2Al	3.743	O1-Al-O3	87.3; 92.7
Al-2O3	1.895	R-2Al	3.253	Al-2Al	3.745	O1-Al-O2	85.5; 94.5
Al-2O2	1.901	R-2Al	3.254	Al-2Al	3.787	O3-Al-O2	90.6; 89.4
R-O1	2.427	R-2Al	3.263	O1-2O2	2.573	O1-Al-O1	180.0
R-2O2	2.437	R-R	3.741	O1-2O3	2.61	O2-Al-O2	180.0
R-2O3	2.59	R-2R	3.743	O1-2O3	2.74	O3-Al-O3	180.0
R-O1	2.67	R-R	3.748	O1-2O2	2.782		
R-O1	2.67	R-R	3.775	O2-2O3	2.670	Al-O1-Al	165.0
R-2O3	2.71	R-R	3.799	O2-2O3	2.699	Al-O2-Al	160.0
R-2O2	2.908					Al-O3-Al	175.2
R-O1	2.909						
S.G. $I\bar{1}$ (Pr _{0.44} Nd _{0.56} AlO ₃ at 20 K)							
Al1-2O1	1.88	R-Al1	3.232	O1-O2	2.53	O1-Al1-O2	96.1; 83.9
Al1-2O2	1.90	R-Al2	3.234	O1-O2	2.53	O1-Al1-O3	85.4; 94.6
Al1-2O3	1.908	R-Al2	3.252	O1-O3	2.57	O2-Al1-O3	94.7; 85.3
Al2-2O2	1.88	R-Al1	3.253	O1-O3	2.60	O1-Al1-O1	180.0

(continued)

TABLE 28 (continued)

Atoms	Distances (Å)	Atoms	Distances (Å)	Atoms	Distances (Å)	Atoms	Angles (°)
Al2–O3	1.899	R–Al1	3.254	O1–O3	2.78	O2–Al1–O2	180.0
Al2–O1	1.91	R–Al2	3.255	O1–O3	2.79	O3–Al1–O3	180.0
R–O1	2.369	R–Al2	3.259	O1–O2	2.81	O2–Al2–O3	95.8; 84.2
R–O3	2.404	R–Al1	3.261	O1–O2	2.82	O2–Al2–O1	83.8; 96.2
R–O3	2.460	R–R	3.741	O2–O3	2.53	O3–Al2–O1	86.1; 93.9
R–O2	2.53	R–2R	3.744	O2–O3	2.58	O1–Al2–O1	180.0
R–O2	2.59	R–R	3.755	O2–O3	2.80	O2–Al2–O2	180.0
R–O1	2.631	R–R	3.763	O2–O3	2.80	O3–Al2–O3	180.0
R–O1	2.700	R–R	3.771				
R–O2	2.72	Al1–2Al2	3.744			Al1–O1–Al2	161.6
R–O2	2.76	Al1–2Al2	3.748			Al2–O2–Al1	171.9
R–O3	2.864	Al1–2Al2	3.767			Al2–O3–Al1	159.8
R–O3	2.936						
R–O1	2.962						

rotation about a given axis (identical letters indicate equal tilts), and superscripts (+) and (−) denote the phase of the octahedral tilting in neighbouring layers (in-phase and out-of-phase, respectively). Zero as a superscript (0) signifies no tilting about that axis. For example, in the $a^-a^-a^-$ system, the rotation angle is the same about each of the three axes, and the rotations of octahedra in adjacent layers are in opposite directions (out-of-phase tilts). In the $a^+b^+c^+$ system, the rotation angles about the $[100]_p$, $[010]_p$, and $[001]_p$ axes are different, and the octahedra in adjacent layers rotate in the same direction (in-phase tilts). Magnitudes of the octahedral tilts are quantified as deviations of the interoctahedral Al–O–Al angles from 180° .

The rhombohedral $R\bar{3}c$ perovskite structure (Figure 39A) is formed via a minor cooperative displacement of the oxygen atoms from their ideal positions. As a

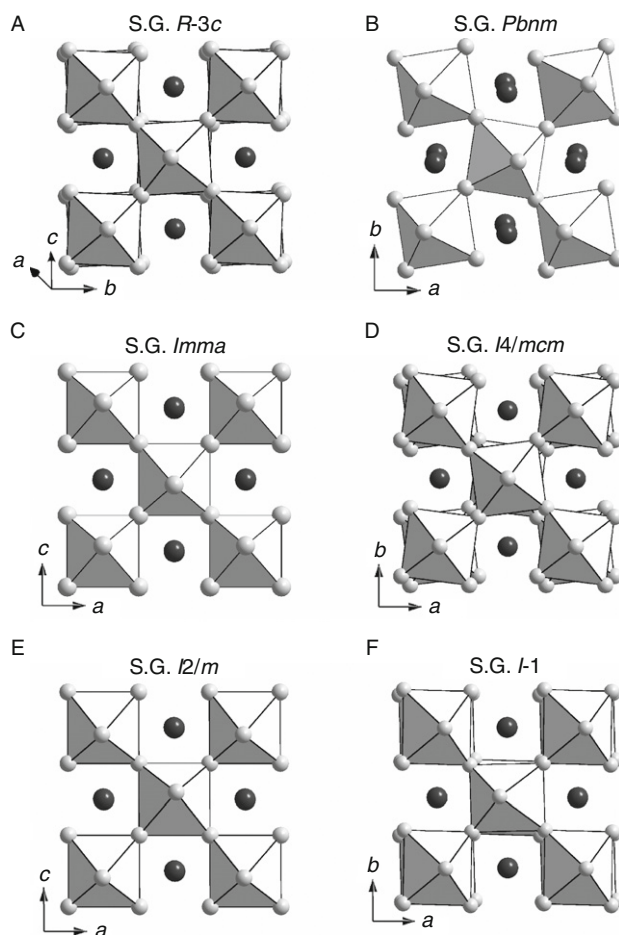


FIGURE 39 Structures of the rhombohedral (A), orthorhombic $Pbnm$ (B), orthorhombic $Imma$ (C), tetragonal (D), monoclinic (E), and triclinic (F) modifications of $RAlO_3$ perovskites. Frameworks of corner-sharing AlO_6 octahedra and R-cations are shown.

result, the ideal RO_{12} cubo-octahedron made of 12 equal R–O distances transforms into a polyhedron with 3 ‘short’, 6 ‘medium’, and 3 ‘long’ R–O bonds (Table 28). Even though all six Al–O distances remain equal, the octahedron itself undergoes a distortion due to the minor deviation of the O–Al–O angles from 90° . All R–R and Al–Al distances remain equal, whereas eight nearest R–Al distances split into two shorter and six longer ones (Table 28). The rhombohedral distortion of the perovskite lattice is also reflected by the tilting of the octahedra around the threefold $[111]_p$ axis, which is reflected by a deviation of Al–O–Al angles from 180° (Table 28). Using Glazer’s notations, the $R\bar{3}c$ structure is characterized by anti-phase tilting of the octahedra with the same magnitude along all fourfold axes, and therefore it belongs to the threefold tilting system $a^-a^-a^-$ (Figure 39A).

For the orthorhombic $Pbmm$ structure, mutual displacements of the rare earth and oxygen atoms from their ideal positions are observed. The maximum shift of R-cation is observed along the $[010]$ direction, whereas the displacement along $[100]$ is considerably smaller and does not exceed $0.07\text{--}0.08 \text{ \AA}$ (Figure 40). The magnitude of the R-cation displacement decreases with increasing cationic radius and approaches zero when the transition to rhombohedral perovskites occurs for $r(R^{3+}) > 1.155 \text{ \AA}$ (Figure 40).

Mutual displacements of rare earth and oxygen atoms in orthorhombic perovskite structures lead to further redistribution of R–O and Al–O distances. There is a set of eight R–O distances (typically grouped in 1-2-1-2-2-1-1-2) in the RO_{12} polyhedra (Table 28). The six Al–O bonds, which are equal in the cubic and rhombohedral structures, split into two shorter, two medium, and two longer distances in the $Pbmm$ structure. The deformation of the AlO_6 octahedra is also reflected by a deviation of the O–Al–O angles from 90° and 180° . Nevertheless, only a minor deformation of interoctahedral bonds and angles is observed. Mutual displacement of oxygen atoms results mainly in the considerable deviation of Al–O–Al angles from 180° (Table 28) and is reflected by cooperative tilts of the AlO_6 octahedra (Figure 39B). Using Glazer’s notation, the orthorhombic $Pbmm$ structure belongs to the three-tilt system $a^+b^-b^-$ (Nr. 10). Due to the deformation of the cation sublattice, a redistribution of R–R, R–Al, and Al–Al distances can be observed (Table 28).

Another type of deformation of the perovskite structure is known to occur among the LT modifications of cerium and praseodymium aluminates and solid solutions based on them. In the orthorhombic $Imma$ structures, 12 nearest distances in the RO_{12} polyhedra split into a set of five unique R–O distances, typically grouped as 1-4-2-4-1. The six Al–O bonds within the octahedra split into two shorter and four longer distances, but this deformation is very weak and octahedra are distorted mainly due to considerable deviations of the O–Al–O angles from 90° (see Table 28). Moreover, the octahedra tilt either about the twofold $[110]_p$ axis or about both $[010]_p$ and $[001]_p$ pseudo-axes of the perovskite cell, which corresponds to the tilt system $a^0b^-b^-$ (Figure 39C).

In the tetragonal $I4/mcm$ structure, in $CeAlO_3$ below 314 K, the RO_{12} polyhedra are based on four short, four medium, and four longer bonds, whereas the AlO_6 octahedra remain practically regular (Table 28). Deformation from the ideal perovskite structure is also reflected by cooperative anti-phase rotations of

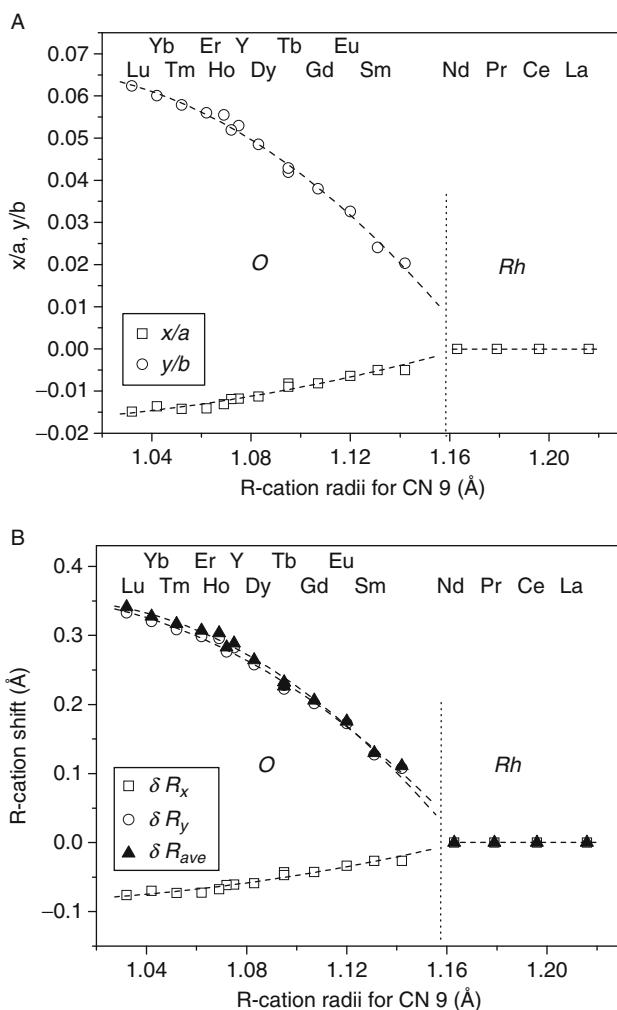


FIGURE 40 Relative (A) and absolute (B) displacements of R-cation from their ideal positions in the ideal cubic perovskite lattice in a series of RAlO₃ perovskites.

octahedra about the fourfold [001]_p axis. Using Glazer's notation, the tetragonal LT structure of CeAlO₃ and Ce_{1-x}La_xAlO₃ solid solutions belongs to the $a^0a^0c^-$ one-tilt system (Figure 39D).

Yet another type of distortion may be illustrated by an example of the monoclinic $I2/m$ structure, which is known for LT modifications of PrAlO₃ and solid solutions existing in the CeAlO₃-NdAlO₃ system. In the monoclinic $I2/m$ structure, eight distinct R-O and three Al-O bond lengths develop in sets of 1-2-1-2-2-1-2-1 and 2-2-2, respectively. Nevertheless, deformation of the Al-O bonds remains weak, whereas 12 R-O distances are distributed over a broad range of 2.43–2.91 Å (Table 28). The AlO₆ octahedra are tilted with respect to the *a* and *c* axes of

the monoclinic cell, or, in other words, the tilts rotate about the $[010]_p$ and $[001]_p$ axes of the ideal perovskite (tilt system $a^0b^-c^-$) (Figure 39E).

In the triclinic $I\bar{1}$ modification of the perovskite structure, discovered in $\text{Pr}_{0.44}\text{Nd}_{0.56}\text{AlO}_3$ below 70 K, 12 distinct R–O distances are distributed over the range of 2.37–2.96 Å (Table 28). The AlO_6 octahedra are quite distorted mainly due to considerable deviations of the intraoctahedral O–Al–O angles from 90° , which reach as much as 6° in the case of $\text{Pr}_{0.44}\text{Nd}_{0.56}\text{AlO}_3$ at 20 K (Table 28). In terms of Glaser notation, this structure belongs to the three-tilt system $a^-b^-c^-$ (Figure 39F).

It is worth noting that the tetragonal $I4/mcm$, monoclinic $I2/m$, and triclinic $I\bar{1}$ structures occur very rarely among perovskite-type oxides. As it was mentioned above, the tetragonal $I4/mcm$ structure, observed in CeAlO_3 and $\text{Ce}_{1-x}\text{La}_x\text{AlO}_3$ solid solutions, is the only exception among all $\text{A}^{3+}\text{M}^{3+}\text{O}_3$ perovskites and it is much more common among $\text{A}^{2+}\text{M}^{4+}\text{O}_3$ compounds. The monoclinic $I2/m$ structure has been reported for BaPbO_3 , $\text{BaPb}_{0.75}\text{Bi}_{0.25}\text{O}_3$, and $\text{BaCe}_{1-x}\text{Y}_x\text{O}_{3-z}$ solid solutions, in addition to PrAlO_3 and $\text{Ce}_{1-x}\text{Nd}_x\text{AlO}_3$ samples. And the triclinic $I\bar{1}$ structure was known to date only among some double perovskites, namely, $\text{Ba}_2\text{LaRuO}_6$, BaLaNiRuO_6 , BaLaCoIrO_6 , and $\text{Sr}_2\text{FeIrO}_6$ (ICSD, 2005).

The dependencies of selected interatomic distances in RAIO_3 structures on the average radius of R-cation are shown in Figure 41A–D. The increase of the R-cation radii results in an increase of six shortest R–Al distances and shortening of two longest distances (Figure 41A). The R–Al interatomic distances show a pronounced variation of the slope around $r = 1.07$ Å, similar to one observed in the dependencies of the b -parameter (see Figure 37). Slightly different behaviour is observed for the nearest distances between R-cations, where four short R–R distances increase but two long ones remain nearly constant (Figure 41B). In both cases, the difference between various R–Al or R–R distances decreases with increasing R-cation radius, which indicates that the degree of deformation of the perovskite structure is reduced. The change of the 12 nearest R–O distances also reflects the structural changes in the series of RAIO_3 compounds. In orthorhombic perovskites, eight shortest R–O bonds increase linearly with increasing $r(\text{R})$, whereas four long bonds become shorter (Figure 41C). For compounds with the rhombohedral structure, the increase of nine short R–O bonds is supplemented by the respective shortening of three long R–O distances. It is evident that the increase of the R-cation radius affects not only the tilting of the octahedra but also the strengths of the Al–O bonds. The difference between equatorial and apical distances in the AlO_6 octahedra decreases and it practically vanishes in the SmAlO_3 structure (Figure 41D). In the rhombohedral perovskites, all six Al–O distances are equal.

In parallel with the increasing R-cation radius in RAIO_3 compounds, the average cation–cation distances $(\text{RAI})_8$, $(\text{AlAl})_6$, and $(\text{RR})_6$ also increase (Figure 42A). A similar tendency has been observed for the average $(\text{RO})_{8-12}$ distances, which were calculated for various coordination numbers of R-cations (Figure 42B). The opposite behaviour is observed for the average $(\text{AlO})_6$ and $(\text{OO})_8$ distances, which decrease slightly with increasing R-cation radius (Figure 42B). Although in the LuAlO_3 – LaAlO_3 series, the radius of R-cation increases, approaching the radii of O^{2-} anions, a compaction (densification) of the structure is observed. This leads to a decrease of the octahedral voids and to reduced effective radius of oxygen ions and hence, to a close packed system.

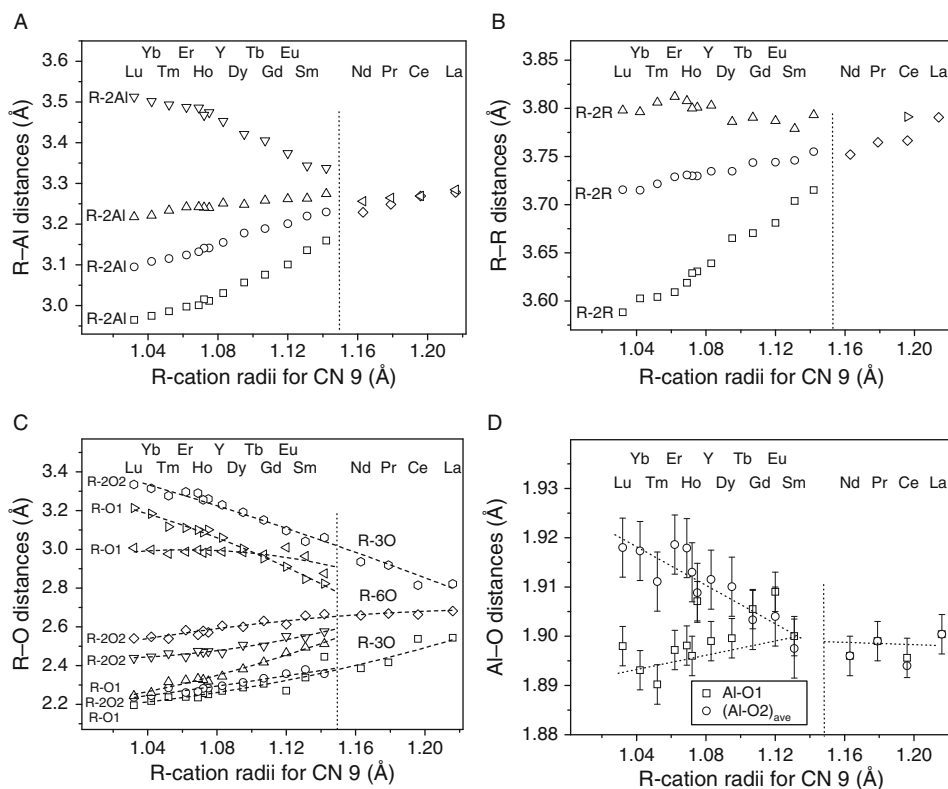


FIGURE 41 Interatomic distances R-Al (A), R-R (B), R-O (C), and Al-O (D) in $RAlO_3$ perovskites as function of R-cation radius.

The changes in the character of distribution of the interatomic distances in $RAlO_3$ structures reflect the decreasing deformation of the perovskite structure in the series of $LuAlO_3$ – $LaAlO_3$ and illustrate the transition from the orthorhombic to the rhombohedral symmetry when $r(R^{3+}) > 1.155 \text{ \AA}$.

The decrease of perovskite structure deformation with increasing radius of R-cations in $RAlO_3$ series is also reflected by a systematic decrease of the magnitude of rotations of AlO_6 octahedra. Figure 43 shows the dependencies of octahedra tilt angles in orthorhombic, rhombohedral, and tetragonal $RAlO_3$ perovskites, calculated from the experimental values of the Al–O–Al angles in the corresponding structures.

To estimate the deviation from an ideal cubic model of perovskites, the cell distortion factor, d , was proposed by Sasaki et al. (1983):

$$d = \frac{\{(a/\sqrt{2} - a_p)^2 + (b/\sqrt{2} - a_p)^2 + (c/2 - a_p)^2\}}{3a_p^2} \times 10^4 \quad (1)$$

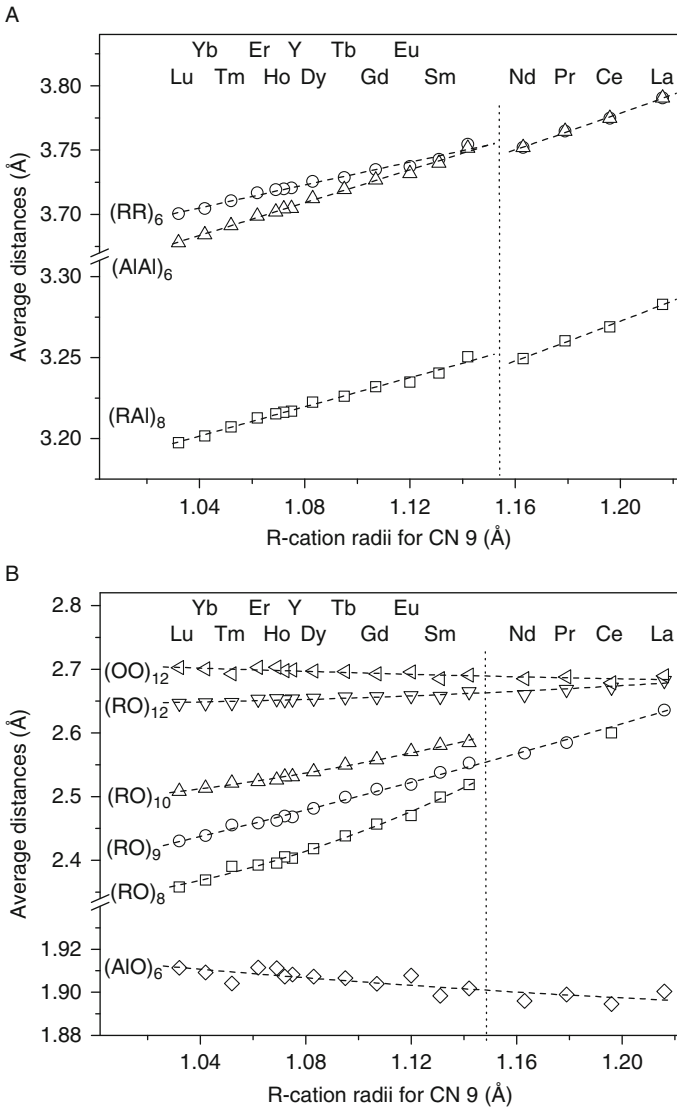


FIGURE 42 Average interatomic distances (RAI)₈, (AlAl)₆, (RR)₆ in panel (A) and (AlO)₆, (R-O)_{8–12}, (OO)₁₂ in panel (B) in the structures of RAlO₃ as functions of R-cation radius.

where

$$a_p = \frac{1}{3} \left(\frac{a}{\sqrt{2}} + \frac{b}{\sqrt{2}} + \frac{c}{2} \right)$$

Figure 44 represents the corresponding values calculated for RAlO₃ discussed in this chapter. The cell distortion factor in RAlO₃ falls sharply from LuAlO₃ to TbAlO₃, showing a rapid decrease of the distortion from the cubic cell. However,

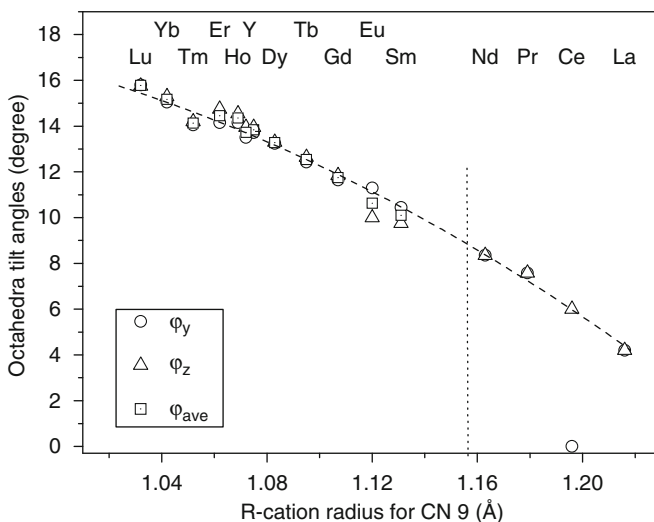


FIGURE 43 Octahedra tilt angles as functions of R-cation radius. $\phi_y = (180 - (\text{Al-O1-Al}))/2$, $\phi_z = (180 - (\text{Al-O}_2\text{-Al}))/2$ for orthorhombic and tetragonal structures; $\phi_y = \phi_z = (180 - (\text{Al-O-Al}))/2$ for rhombohedral structures. For orthorhombic structures, the average tilt angles are shown as well.

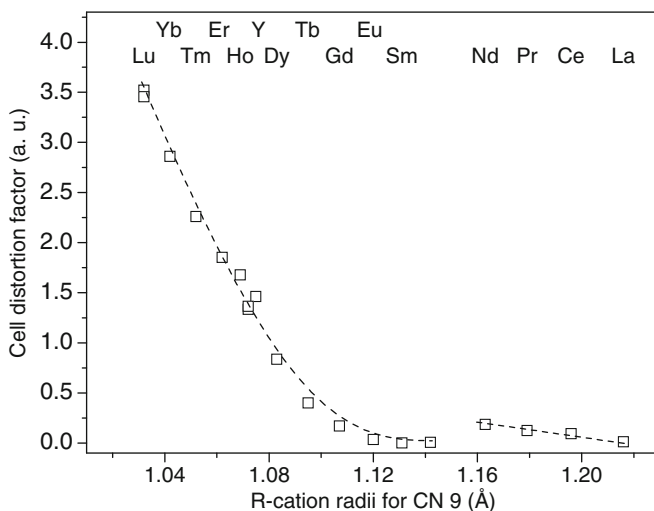


FIGURE 44 Cell distortion factor, d , in the series of RAlO_3 compounds.

this criterion works suitably only for strongly distorted perovskite lattices. In case of weakly distorted GdFeO_3 -type perovskites, the cell distortion factor does not properly reflect deviations from the perovskite lattice. This is especially important when changes in the cell parameters ratio occur. As can be seen in [Figure 44](#), the calculated cell distortion factors of orthorhombic EuAlO_3 and

SmAlO₃ are smaller than the corresponding values of NdAlO₃ and PrAlO₃, which have a rhombohedral structure. Therefore, this approach can not be applied to characterize the deviation from the perovskite structure in general since it does not reflect the peculiar features of individual deformations of the perovskite structure at the transition boundary, for example, between orthorhombic and rhombohedral structures.

Deviations from the ideal perovskite structure may better be described by the observed tolerance factors, t_0 , and the bond-length distortions of polyhedra, Δ . Such criteria were introduced by Sasaki *et al.* (1983) in order to describe structural deformations, arising from tilts and/or distortions of polyhedra in the perovskite-type structures. These parameters are defined as follows:

$$t_0 = \frac{l_{\text{CN}12}}{\sqrt{2}l_{\text{CN}6}}, \quad (2)$$

$$\Delta = \frac{1}{n} \sum \left(\frac{l_i - l_{\text{CN}}}{l_{\text{CN}}} \right)^2 \times 10^3, \quad (3)$$

where l_i and l_{CN} are the individual and average interatomic distances in polyhedra with corresponding coordination number, and n is the number of bonds.

Experimental values of the observed tolerance factor calculated for all relevant CN of R-cations in the RAlO₃ structures are presented in Figure 45A. They increase linearly with increasing R-cation radius that underlines a systematic decrease of the deformation of the perovskite structure in the series LuAlO₃–LaAlO₃. The analysis of the bond-length distortions calculated for the corresponding RO₈–RO₁₂ polyhedra also confirms the same tendency, that is that deformations decrease with increasing R-cation radius. It shows that CN values of 8–10 are preferable for the R atoms in RAlO₃ compounds with the orthorhombic structures. Figure 45B shows that RO₁₂ cubo-octahedra are strongly distorted in comparison with the RO₈, RO₉, and RO₁₀ polyhedra. Decreasing deformations of the perovskite structure in LuAlO₃–SmAlO₃ series and transition between orthorhombic and rhombohedral structures are illustrated by the corresponding dependencies of the Δ values, calculated for the nearest R–R and R–Al distances (Figure 45C and D).

The ratios of the cation–cation distances $(AB)_{\text{max}}/(AB)_{\text{min}}$ and the average distances $(AA)_6/(BB)_6$ could also serve to characterize the degree of deformation in ABO₃ perovskites (Vasylechko *et al.*, 1999a,b). In the ideal cubic perovskite structure, all individual A–B, A–A, and B–B distances are equal and hence it is trivial that the ratios of $(AB)_{\text{max}}/(AB)_{\text{min}}$ and $(AA)_6/(BB)_6$ distances must be equal to 1. The latter ratio also equals 1 in the rhombohedral perovskite structures. In the series of RAlO₃ compounds with orthorhombic structures, both ratios decrease with increasing R-cation radius (Figure 46). Since the transition between orthorhombic and rhombohedral structures is clearly reflected by such dependencies, these criteria could be used for the prediction of the $Pbnm$ – $R\bar{3}c$ transformation in corresponding perovskite structures (Vasylechko *et al.*, 2005).

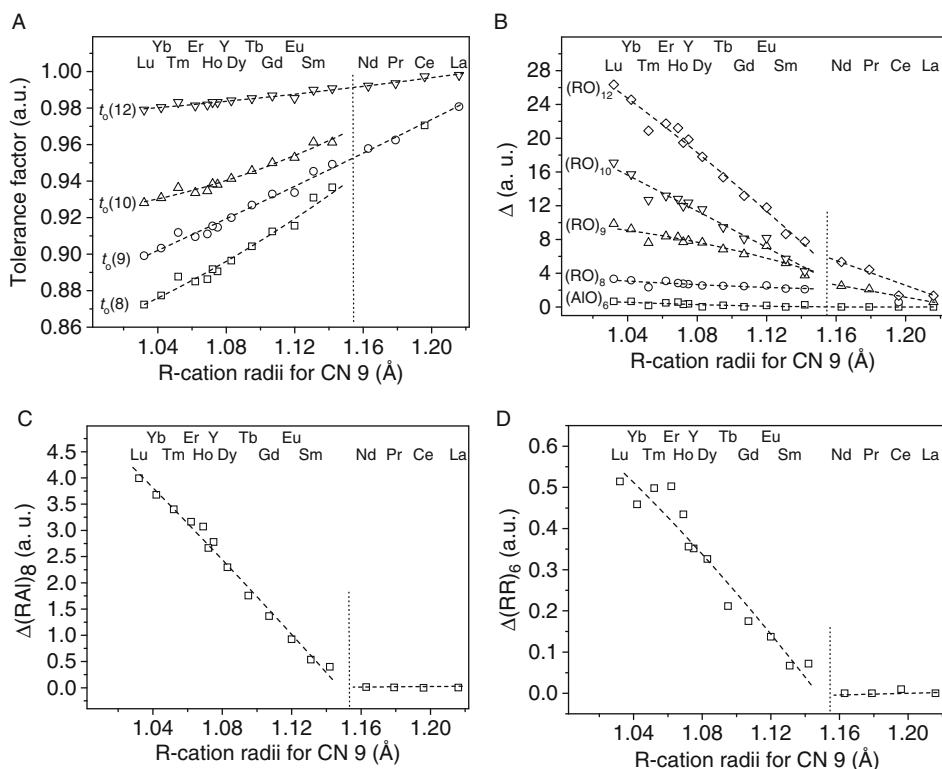


FIGURE 45 Observed tolerance factors (A) and bond-length distortions of polyhedra (B–D) in $RAlO_3$ structures as functions of the average R-cation radius.

Over the last decades, the concept of bond-valence calculations has been widely applied in solid state chemistry for prediction of bond lengths, as well as for determination of coordination numbers in corresponding compounds. Besides, this concept serves as a criterion to verify the reliability of structure determinations (Brown, 1978; Brown and Altermatt, 1985; Altermatt and Brown, 1987). According to their approach, the atomic valence of an atom, V_i , is defined as the sum of bond valences v_{ij}

$$V_i = \sum_j v_{ij}, \quad (4)$$

where

$$v_{ij} = \exp\left\{\frac{R_{ij} - l_{ij}}{B}\right\}. \quad (5)$$

Here, bond valence v_{ij} is associated with each cation–anion interaction, l_{ij} is the cation–anion distance, B is the so-called ‘universal’ constant equal to 0.37 Å (Brown and Altermatt, 1985), and R_{ij} is the bond-valence parameter.

Based on experimental values of interatomic distances R–O and Al–O and using the tabulated values of R_{ij} for the corresponding bonds (Brese and

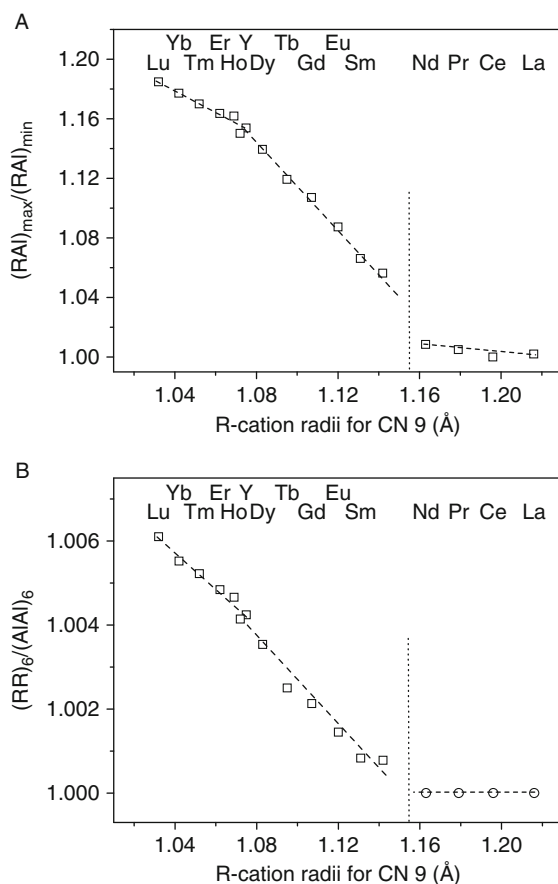


FIGURE 46 Distance ratios $(RAI)_{max}/(RAI)_{min}$ in (A) and $(RR)_6/(|Al|)_6$ in (B) as functions of R-cation radius.

O'Keefe, 1991), the valence V_i of cations in $RAIO_3$ compounds has been calculated by Vasylechko and Matkovskii (2004) (Figure 47). It can be seen that the calculated values for R-cations with CN 8–9 and Al atoms (CN 6) are located within the limits of 3 ± 0.1 , which corresponds to the formal valence of these cations. A minor increase of the V_i values of aluminium is observed with increasing of R-cation radius, whereas the corresponding values of rare earth cations decrease slightly (Figure 47). A comparison of V_i values calculated for differently coordinated R-cations shows that for 'small' cations (Lu^{3+} – Dy^{3+}) in orthorhombic $RAIO_3$ structures, a better agreement between the formal and calculated valences is observed for CN 8. For Tb, Gd, and Eu atoms, coordination number 9 is preferred, whereas for Sm atoms, CN 10 is rather typical. In the rhombohedral $NdAlO_3$ and $PrAlO_3$ structures, the same difference between formal and calculated valence is observed for CN 9 and 12, whereas in $LaAlO_3$, preferred coordination number of La is 12. The same coordination number (12) can be assigned to Ce ions in the tetragonal $CeAlO_3$ structure.

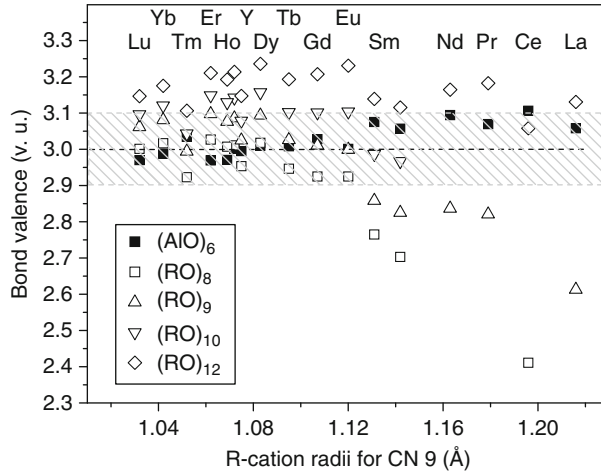


FIGURE 47 Calculated valence of cations in the series of RAlO_3 compounds.

For characterization of the overall structure stability of perovskites, the Global Instability Index (GII), has been proposed (Salinas-Sanchez et al., 1992; Lufaso and Woodward, 2001). GII is defined as:

$$GII = \sqrt{\frac{1}{N} \sum_{i=1}^N (V_{i(\text{ox})} - V_{i(\text{calc})})^2} \quad (6)$$

where $V_{i(\text{ox})}$ and $V_{i(\text{calc})}$ correspond to formal and calculated valence of the i th ion, respectively, and N is the number of atoms in the asymmetric unit.

It is assumed that for an unstrained structure, GII is typically smaller than 0.1 valence units, whereas for structures with lattice-induced strain $0.1 < \text{GII} < 0.2$. Crystal structures with $\text{GII} > 0.2$ are found to be unstable (Rao et al., 1998; Lufaso and Woodward, 2001). Vasylechko and Matkovskii (2004) calculated GII values for RAlO_3 compounds taking into account different possible CN of R-cations. It was shown that in terms of the GII concept, all RAlO_3 perovskites can be considered as unstrained structures. High GII values 0.21 and 0.14 valence units, observed in CeAlO_3 for CN 8 and LaAlO_3 for CN 9, indicate that the chosen coordination numbers are not suitable for those structures.

2.5 Phase transitions and thermal expansion of RAlO_3 perovskites

Seven types of phase transitions exist in RAlO_3 compounds and in their solid solutions. A continuous phase transition $Pm\bar{3}m-R\bar{3}c$ is typical for the early members of the RAlO_3 series ($R = \text{La}, \text{Ce}, \text{Pr}, \text{and Nd}$), whereas a first-order phase transformation $R\bar{3}c-Pbnm$ is observed for SmAlO_3 , GdAlO_3 , and EuAlO_3 . Similar phase transitions are also observed in solid solutions $\text{R}_{1-x}\text{R}'_x\text{AlO}_3$ with average radius of R-cation larger than 1.105 Å. Five other kinds of phase transitions,

namely $R\bar{3}c$ - $Imma$, $Imma$ - $I4/mcm$, $Imma$ - $I2/m$, $I2/m$ - $I4/mcm$, and $R\bar{3}c$ - $\bar{I}1$, occur at low temperatures and are observed only in $CeAlO_3$ and $PrAlO_3$ and in their solid solutions.

Based on a large number of literature data concerning the temperatures of phase transformations in rare earth aluminates combined with own results, a tentative generalized phase diagram of $RAIO_3$ compounds with perovskite structures was constructed by Vasylechko and Matkovskii (2004). In this diagram, the transition temperatures are presented as a function of average radius of R-cation. Such a diagram supplemented with recently obtained data for several compositions of $R_{1-x}R'_xAlO_3$ solid solutions is depicted in Figure 48.

According to literature, rare earth aluminates from $TmAlO_3$ to $LaAlO_3$ and $YAlO_3$ are formed from the melt. Crystallization temperatures of the $RAIO_3$ compounds increase slightly with increasing R-cation radius (Figure 48). Aluminates with R-cations radius above 1.16 Å (La, Ce, Pr, and Nd) and the corresponding solid solutions crystallize with cubic symmetry. Upon cooling, they undergo a continuous phase transformation to the rhombohedral structure, and the temperature of the transformation decreases with increasing the radius of the R-cation. As it was mentioned above, the discrepancies in transition temperatures reported in literature for $PrAlO_3$ and $NdAlO_3$ are ca. 500 K. The continuous character of this transformation makes it difficult to determine transition temperatures using classical methods of thermal analysis or laboratory X-ray diffraction. Therefore, for a

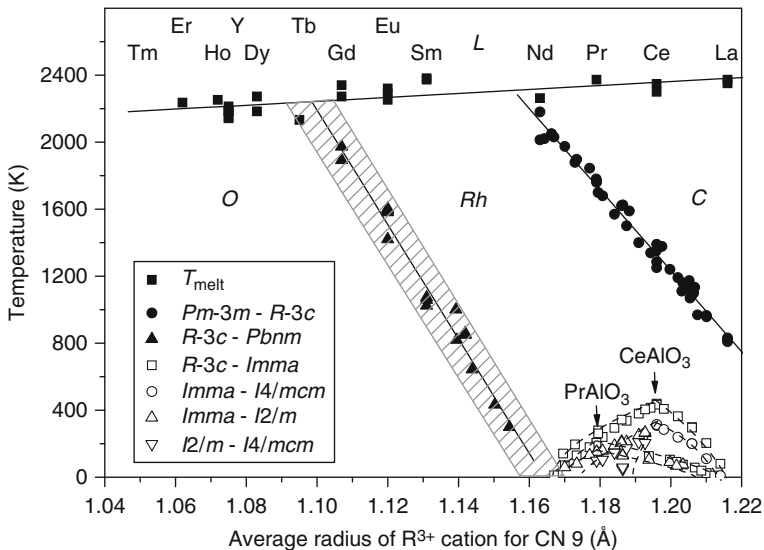


FIGURE 48 Generalized phase diagram of perovskite-type $RAIO_3$ systems. The letters L, O, Rh, and C designate liquid, orthorhombic, rhombohedral, and cubic phase fields, respectively. Open symbols indicate LT phase transitions observed in $CeAlO_3$, $PrAlO_3$, and the corresponding solid solutions. Linear fits of the observed critical temperatures: $T_{O-Rh}(r) = 40(2) \times 10^2 - 34(2) \times 10^3 \times r$; $T_{Rh-C}(r) = 30.2(5) \times 10^3 - 24.2(5) \times 10^3 \times r$; $T_L(r) = 0.9(3) \times 10^3 + 1.2(2) \times 10^3 \times r$.

precise determination of the change from the rhombohedral to cubic phases shown in Figure 48, recent data obtained by using modern high-resolution synchrotron and neutron radiation diffraction techniques were used.

Samarium, europium, and gadolinium aluminates, as well as those solid solutions $R_{1-x}R'_xAlO_3$ with an average radius of the R-cation in the range between 1.05 and 1.16 Å, crystallize with rhombohedral symmetry and undergo a transformation to orthorhombic symmetry on cooling. Finally, $RAIO_3$ compounds with R-cation radius smaller than 1.05 Å (Tb–Lu and Y) and the corresponding solid solutions are orthorhombic and do not undergo any phase transformation in the whole temperature range studied (at least down to 12 K).

A first-order rhombohedral-to-orthorhombic phase transition $R\bar{3}c-Pbnm$ occurs in $RAIO_3$ compounds and solid solutions with the average ionic radii of R-cation $1.05 < r < 1.16$. For such transitions, the existence of a two-phase region between the two different perovskite-type structures is typical. The coexistence of LT and HT phases is usually observed over a temperature range of 30–50 K, although in some cases, these coexistence ranges may reach even 150–200 K. For concentration-induced transformations that occur in $R_{1-x}R'_xAlO_3$ solid solutions, the width of the two-phase region depends strongly on the difference between the ionic radii of R-cations and it may vary from 1–3 at.% to 40–50 at.% (see Figure 26).

Both HT phase transformations occurring in $RAIO_3$ compounds— $Pm\bar{3}m-R\bar{3}c$ and $R\bar{3}c-Pbnm$ —are characterized by decreasing transition temperatures with increasing radius of R-cation (Figure 48). This behaviour can be explained by a decrease of the perovskite structural deformation as a consequence of the increasing Goldschmidt tolerance factors in the series $RAIO_3$. Taking into account that in both cases, the transition temperatures decrease almost linearly with increasing R-cation, it is evident that the geometrical factor has a considerable influence on these transformations.

Temperatures of the phase transformations $R\bar{3}c-Imma$, $Imma-I4/mcm$, $Imma-I2/m$, and $I2/m-I4/mcm$, which are observed only among the cerium- and praseodymium-containing rare earth aluminates, decrease with decreasing Ce or Pr concentration in the corresponding solid solutions $Ce_{1-x}R_xAlO_3$ or $Pr_{1-x}R_xAlO_3$, and do not depend on the average R-cation radius. In Figure 48, the temperatures of these transitions are shown as open symbols. It is evident that in contrast to the high-temperature $R\bar{3}c-Pm\bar{3}m$ and $R\bar{3}c-Pbnm$ transitions, the low-temperature transformations in the cerium- and praseodymium-based systems are not caused by geometrical factors, but rather by specific properties of the Ce^{3+} and Pr^{3+} ions, that is their electronic structure. The absence of similar transitions in the solid solutions of the $LaAlO_3-NdAlO_3$ system confirms this assumption. Particularly, the $La_{0.62}Nd_{0.38}AlO_3$ and $La_{0.3}Nd_{0.7}AlO_3$ samples with average R-cation radii 1.196 and 1.179 Å, that is close to the Ce^{3+} and Pr^{3+} ions, do not change their rhombohedral structures at least down to 12 K. At the same time, both samples undergo HT transitions to the cubic phase at 1350 and 1780 K, respectively, which practically coincides with the corresponding transition temperatures for $CeAlO_3$ and $PrAlO_3$.

The rhombohedral-to-orthorhombic transition $R\bar{3}c-Imma$ observed in cerium and praseodymium aluminates is discontinuous and hence, first-order in character. The same holds true for the orthorhombic-to-tetragonal $Imma-I4/mcm$ and

monoclinic-to-tetragonal $I2/m-I4/mcm$ transformations. The orthorhombic-to-monoclinic transition $Imma-I2/m(C2/m)$, which is typical for Pr-based aluminates and for some $Ce_{1-x}Nd_xAlO_3$ compositions, is restricted by symmetry to be continuous. It is not entirely clear whether the LT phase transitions in the $CeAlO_3$ -based systems follow the same mechanism as $PrAlO_3$. It is interesting to note that the sequence of phase transitions typical for $PrAlO_3$ has been observed for Ce-containing aluminates only among the samples of the $CeAlO_3$ - $NdAlO_3$ system, and the temperature variations of the lattice parameters of some $Ce_{1-x}Nd_xAlO_3$ compositions are very similar to those reported for $PrAlO_3$, including the existence of metrically tetragonal monoclinic lattice below 110–120 K (Vasylechko *et al.*, 2007b).

The temperature behaviour of the lattice parameters and cell volumes of the $RAIO_3$ compounds and their relative expansion in different crystallographic directions are shown in Figures 49–51. Besides the $RAIO_3$ compounds, the corresponding data for some $R_{1-x}R'_xAlO_3$ solid solutions are given as well. Relative volumetric expansion and relative expansion in different crystallographic directions were calculated as follows:

$$\eta_L = \frac{L(T) - L(T_0)}{L(T_0)} \times 100\%, \quad (7)$$

where $L(T)$ is the cell dimension or volume at the corresponding temperature T ; the RT value (298 K) was taken as T_0 .

Figure 49 shows that the relative high-temperature expansion in a - and c -directions is similar for all orthorhombic aluminates and it lies in the limits of 0.87–1% at 1200 K. At this temperature, a maximum expansion ($\sim 1\%$) is observed in $YAlO_3$ and $YbAlO_3$, whereas it is smallest in $YbAlO_3$ and $EuAlO_3$ ($\sim 0.9\%$). Thermal expansion at HT in the b -direction is about two times smaller compared with the a - and c -directions (Figure 49C and D), which is common to the $RAIO_3$ compounds of the $GdFeO_3$ -type. A maximum elongation in the b -direction at 1200 K is observed for $DyAlO_3$ (0.53%), whereas it is a minimum in $YAlO_3$ (0.40%).

A more complicated behaviour is observed for the low-temperature expansion of rare earth aluminates. As mentioned above, the majority of $RAIO_3$ compounds show remarkable anomalies, which is manifested by a significant deviation from the 'normal' expansion. In Gd, Tb, Dy, Er, Tm, and Y aluminates, such LT deviations are especially pronounced in the b -direction (Figure 49C and D). Besides, $TbAlO_3$ and $TmAlO_3$ display remarkable anomalies in the a -direction (Figure 49A and B). Some deviations from the normal behaviour are also observed along the c -axis, although they are less pronounced.

In contrast to orthorhombic aluminates, $RAIO_3$ compounds with rhombohedral structures display no anomalies both in the low- and high-temperature expansion (Figure 50). For rhombohedral perovskites, the thermal expansion in the a -direction is smaller compared with the c -direction (0.75% and 1% at 1200 K, respectively). The η_a and η_c values are practically identical for all rhombohedral rare earth aluminates (Figure 50B and D). The analysis of some representatives of $R_{1-x}R'_xAlO_3$ solid solutions shows that the character of their thermal expansion is

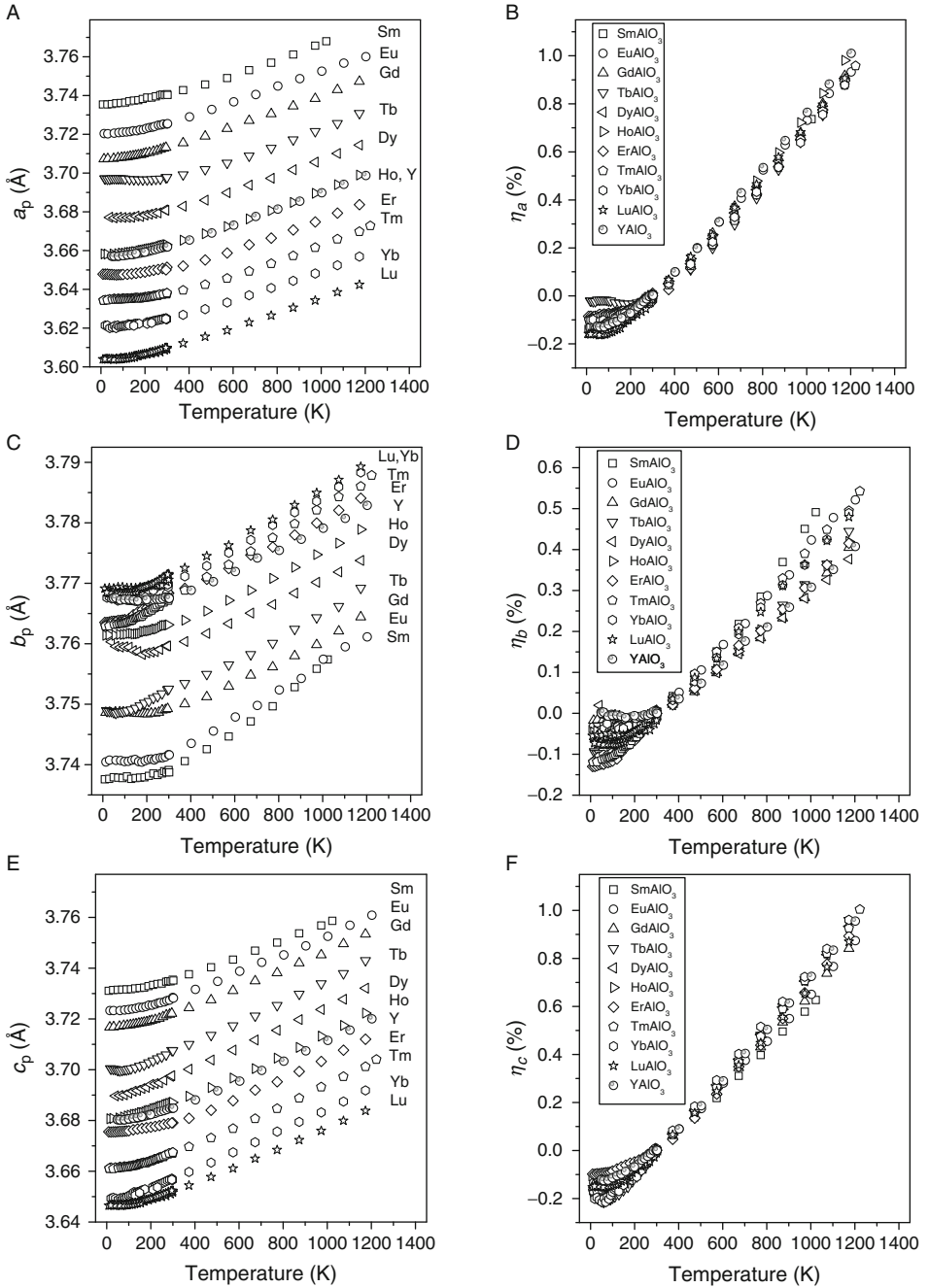


FIGURE 49 Temperature dependencies of lattice parameters (A, C, E) and their relative expansion (B, D, F) in $R\text{AlO}_3$ compounds with orthorhombic structures.

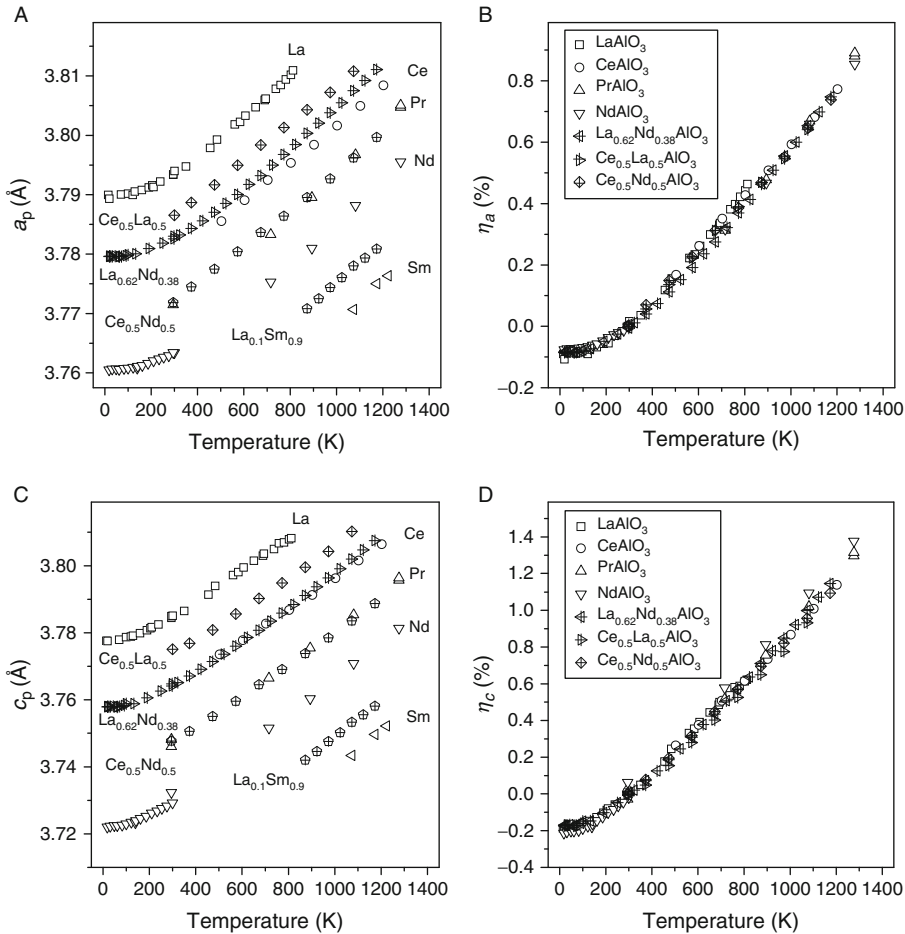


FIGURE 50 Temperature dependencies of lattice parameters (A, C) and their relative expansion (B, D) of RAlO₃ compounds with rhombohedral structures.

mainly determined by the behaviour of the constituent RAlO₃ compounds and the geometrical factor. This fact is illustrated by the thermal behaviour of the lattice parameters and the cell volumes of $La_{0.62}Nd_{0.38}AlO_3$, $Ce_{0.5}La_{0.5}AlO_3$ and $Ce_{0.5}Nd_{0.5}AlO_3$, whose lattice parameters are between the corresponding values for the boundary compositions $LaAlO_3$, $CeAlO_3$, or $NdAlO_3$ (Figure 50).

Analysis of the temperature behaviour of the cell volumes of all RAlO₃ compounds and their thermal expansion (Figure 51A and B) shows that rhombohedral aluminates have somewhat higher η_V values when compared with the orthorhombic compounds. When they belong to the same structural type, RAlO₃ expand in a very similar way and differences in the volumetric thermal expansion can not be distinguished.

The coefficient of the thermal expansion has been calculated from the thermal evolution of the lattice parameters and the cell volume as follows

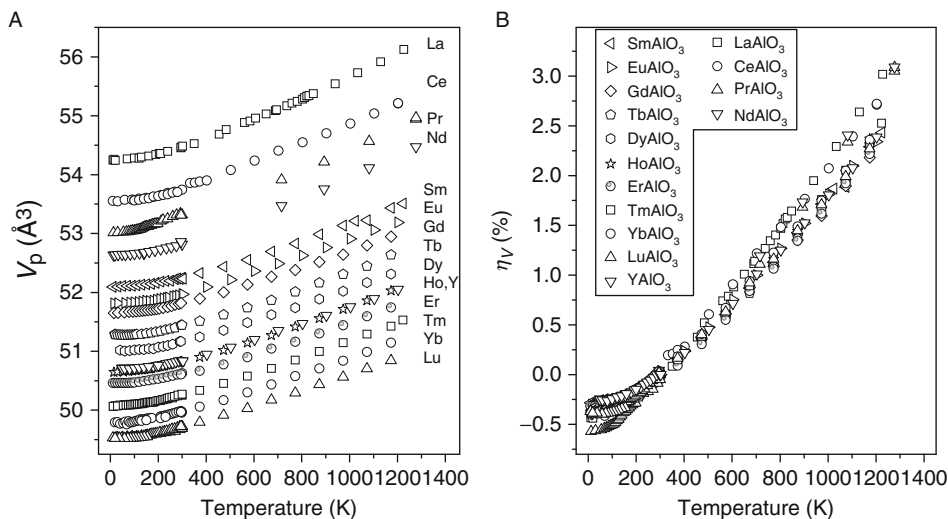


FIGURE 51 Temperature evolution of cell volumes (A) and the relative volumetric expansion of $RAlO_3$ compounds and some solid solutions (B).

$$\alpha_L = \frac{L(T_2) - L(T_1)}{L(T_2) \times (T_2 - T_1)} \quad (8)$$

where $L(T_2)$ and $L(T_1)$ are the cell dimension or volume at the corresponding temperatures.

For simplicity, the experimental values of the lattice parameters in a given temperature range were approximated by linear functions. Corresponding values of TEC are listed in Table 29 and depicted in Figure 52, where the linear and volumetric TEC of $RAlO_3$ perovskites are given as functions of the radius of the R-cation.

From Table 29 and Figure 52A, it is evident that the linear thermal expansion coefficients for orthorhombic rare earth aluminates in the temperature range of 300–1200 K lie within the limits $\alpha_a = (8.9\text{--}11.3) \times 10^{-6} \text{ K}^{-1}$, $\alpha_b = (3.8\text{--}7.5) \times 10^{-6} \text{ K}^{-1}$, and $\alpha_c = (7.6\text{--}10.9) \times 10^{-6} \text{ K}^{-1}$ and they show little dependence on the size of R-cation. For rhombohedral perovskites, the α_a and α_c values lie in the range of $(7.7\text{--}10.3) \times 10^{-6} \text{ K}^{-1}$ and $(11.7\text{--}15.8) \times 10^{-6} \text{ K}^{-1}$, respectively. The values of volumetric TEC, α_V for lanthanum, cerium, praseodymium, and neodymium aluminates with rhombohedral structures are higher than the corresponding values of the compounds with orthorhombic structures. This tendency holds also in the $La_{0.32}Gd_{0.68}AlO_3$, $La_{0.2}Eu_{0.8}AlO_3$, and $La_{0.1}Sm_{0.9}AlO_3$ samples, where the α_V values of HT rhombohedral phases are higher relatively to the orthorhombic ones (Table 29, Figure 52B). The highest values of the volumetric TEC are observed for the rhombohedral phase of $SmAlO_3$ and the cubic modifications of $LaAlO_3$ and $La_{1-x}R_xAlO_3$ ($R = Ce, Pr, Nd, Sm, \text{ and } Eu$) solid solutions.

Similar to the lattice parameters, the thermal behaviour of the average interatomic distances in the $RAlO_3$ structures has been analysed (Vasylychko, 2005).

TABLE 29 Experimental values of the thermal expansion coefficients of RAIO_3 compounds

Compound	S.G.	Temperature (K)	$\alpha(a) \times 10^6 \text{ (K}^{-1}\text{)}$	$\alpha(b) \times 10^6 \text{ (K}^{-1}\text{)}$	$\alpha(c) \times 10^6 \text{ (K}^{-1}\text{)}$	$\alpha(V) \times 10^6 \text{ (K}^{-1}\text{)}$
LaAlO_3 ¹	$R\bar{3}c$	298–800	8.83	–	12.29	29.93
LaAlO_3 ¹	$Pm\bar{3}m$	800–1200	11.76	–	–	35.91
CeAlO_3	$I4/mcm$	12–100	3.96	–	–0.90	7.01
CeAlO_3	$I4/mcm$	100–330	12.38	–	–8.62	16.15
CeAlO_3	$Imma$	330–450	2.33	11.24	–0.47	13.10
CeAlO_3	$R\bar{3}c$	450–1200	8.50	–	12.48	29.87
PrAlO_3 ¹	$R\bar{3}c$	298–1200	8.97	–	13.25	31.53
NdAlO_3 ¹	$R\bar{3}c$	298–1200	8.67	–	13.37	31.04
SmAlO_3	$Pbnm$	298–970	10.11	6.74	8.66	25.66
SmAlO_3	$R\bar{3}c$	970–1200	10.34	–	15.77	37.30
EuAlO_3	$Pbnm$	298–1200	10.48	5.97	9.63	26.17
GdAlO_3	$Pbnm$	298–1200	10.48	4.60	9.60	24.91
TbAlO_3	$Pbnm$	298–1200	10.38	5.03	10.95	26.54
DyAlO_3	$Pbnm$	298–1200	10.51	4.36	10.68	25.81
HoAlO_3	$Pbnm$	298–1200	11.25	4.84	10.88	27.18
ErAlO_3	$Pbnm$	298–1200	10.63	4.80	10.33	25.91
TmAlO_3	$Pbnm$	298–1200	10.25	5.77	10.70	26.88
YbAlO_3	$Pbnm$	298–1200	10.12	5.64	10.89	26.83
LuAlO_3	$Pbnm$	298–1200	10.37	5.48	9.91	25.96
YAlO_3	$Pbnm$	298–1200	11.22	4.55	10.67	26.57
YAlO_3 ²	$Pbnm$	298–920	8.9	3.8	8.5	–
YAlO_3 ³	$Pbnm$?	9.5	4.3	10.8	–
ScAlO_3	$Pbnm$	298–1200	10.46	7.52	10.90	29.22

La _{0.32} Gd _{0.68} AlO ₃	<i>Pbnm</i>	298–850	11.08	7.37	8.68	27.31
La _{0.32} Gd _{0.68} AlO ₃	<i>R$\bar{3}c$</i>	850–1200	8.49	–	12.94	30.41
La _{0.2} Eu _{0.8} AlO ₃	<i>Pbnm</i>	298–970	9.94	6.63	8.09	24.79
La _{0.2} Eu _{0.8} AlO ₃	<i>R$\bar{3}c$</i>	970–1200	7.66	–	11.23	25.63
La _{0.1} Sm _{0.9} AlO ₃	<i>Pbnm</i>	298–800	9.63	6.41	7.57	23.79
La _{0.1} Sm _{0.9} AlO ₃	<i>R$\bar{3}c$</i>	800–1200	9.03	–	14.50	32.71
La _{0.9} Eu _{0.1} AlO ₃	<i>R$\bar{3}c$</i>	298–1000	8.55	–	12.85	30.18
La _{0.9} Eu _{0.1} AlO ₃	<i>Pm$\bar{3}m$</i>	1000–1200	11.53	–	–	34.53
La _{0.9} Sm _{0.1} AlO ₃	<i>R$\bar{3}c$</i>	300–970	8.22	–	13.14	29.77
La _{0.9} Sm _{0.1} AlO ₃	<i>Pm$\bar{3}m$</i>	970–1200	11.13	–	–	33.42
La _{0.8} Nd _{0.2} AlO ₃	<i>R$\bar{3}c$</i>	300–1070	8.43	–	13.17	30.28
La _{0.8} Nd _{0.2} AlO ₃	<i>Pm$\bar{3}m$</i>	1070–1200	10.62	–	–	31.95
La _{0.8} Pr _{0.2} AlO ₃	<i>R$\bar{3}c$</i>	300–970	8.31	–	12.72	29.53
La _{0.8} Pr _{0.2} AlO ₃	<i>Pm$\bar{3}m$</i>	970–1200	11.21	–	–	33.79
Pr _{0.5} Nd _{0.5} AlO ₃	<i>R$\bar{3}c$</i>	298–1200	8.60	–	13.71	31.19
Ce _{0.3} La _{0.7} AlO ₃	<i>R$\bar{3}c$</i>	298–970	8.12	–	12.53	28.96
Ce _{0.3} La _{0.7} AlO ₃	<i>Pm$\bar{3}m$</i>	970–1200	11.61	–	–	35.55
Ce _{0.5} La _{0.5} AlO ₃	<i>R$\bar{3}c$</i>	298–1100	8.26	–	12.15	29.95
Ce _{0.5} La _{0.5} AlO ₃	<i>Pm$\bar{3}m$</i>	1100–1200	11.06	–	–	33.75
Ce _{0.7} La _{0.3} AlO ₃	<i>R$\bar{3}c$</i>	370–1170	8.19	–	12.42	29.11
Ce _{0.7} Nd _{0.3} AlO ₃	<i>R$\bar{3}c$</i>	350–1200	8.36	–	12.33	29.33
Ce _{0.5} Nd _{0.5} AlO ₃	<i>R$\bar{3}c$</i>	298–1200	8.28	–	12.51	29.26
Ce _{0.3} Nd _{0.7} AlO ₃	<i>R$\bar{3}c$</i>	298–1200	8.41	–	13.04	30.16
Ce _{0.1} Nd _{0.9} AlO ₃	<i>R$\bar{3}c$</i>	298–1200	8.25	–	13.15	29.89

¹ Calculated from the data Howard et al. (2000).

² Chaix-Pluchery et al. (2005).

³ Kaminskii (1995).

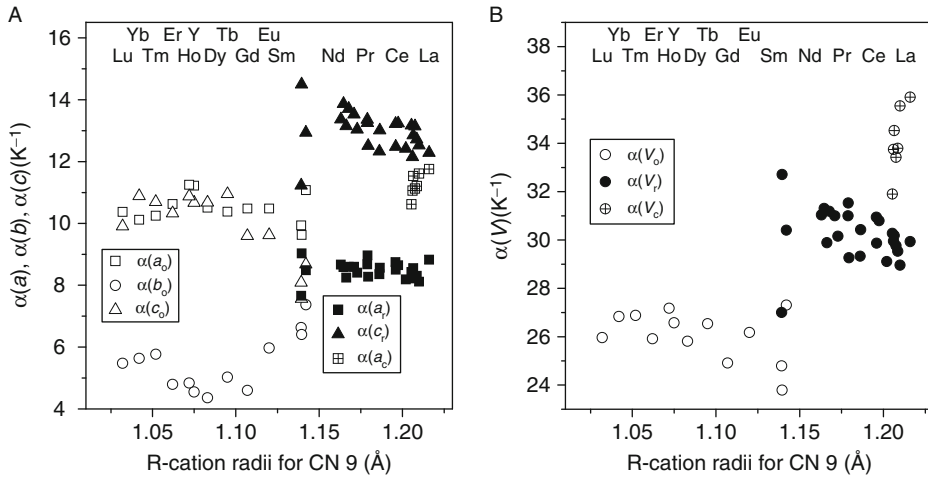


FIGURE 52 Linear (A) and volumetric (B) TEC of RAlO₃ perovskites as functions of the radius of R-cation.

Among all investigated structures, the highest thermal elongation (1.0–2.14% at 1200 K) is observed for average (RO)₉ distances. The minimal elongation (−0.2–0.88%) has been found for (AlO)₆, (OO)₈, and (RO)₁₂ distances. Such non-uniform character of the thermal expansion of R–O and Al–O distances is the reason for the effect described above, the decrease of the perovskite structural deformation of RAlO₃ compounds with increasing temperature. The relative elongations of the average distances (RR)₆, (RAl)₈, and (AlAl)₆ are practically the same for all RAlO₃ compounds and lie within 0.7–0.8% at 1200 K. Only in CeAlO₃, the corresponding values are somewhat higher.

2.6 Dielectric properties of rare earth aluminates

New microwave dielectric ceramics with excellent functionalities, a high-quality factor Q_f (Hughes *et al.*, 2001; Moussa *et al.*, 2003), and a high relative permittivity ϵ_r (Belous *et al.*, 2000) are required in microelectronics. This is especially important for wireless communication technologies, which were one of the most rapidly growing sectors of the electronics industry over the last 20 years. The sizes of the ceramic elements can be reduced with increasing ϵ_r . This makes the device more compact, whereas the signal quality can be improved by the minimization of dielectric losses (Robertson, 2006). Another key property required for microwave dielectric ceramics is a near-zero temperature coefficient of the resonance frequency (t_f), which determines the temperature stability of many parameters. Several approaches have been reported in literature that allow for tuning the t_f , either due to mixtures (Kim *et al.*, 2000; Ang *et al.*, 2003) or due to solid solutions (Jančar *et al.*, 2004; Kutty and Jayanthi, 2005; Wang *et al.*, 2006) between the two end members that have opposite signs of t_f .

Rare earth aluminates with perovskite structure possess negative t_f and high Q -values (Cho et al., 1999a), which makes them suitable to be used in conjunction with alkaline-earth titanates as temperature-stable high- Q microwave dielectrics. Solid solutions with promising microwave dielectric properties can be synthesized in the $\text{CaTiO}_3\text{-RAIO}_3$ ($R = \text{La, Nd, and Sm}$) pseudo-binary systems (Sun et al., 1998; Moon et al., 1999; Jančar et al., 2001, 2002, 2003). The highest Q -values among microwave ceramics based on alkaline-earth titanates were reported for $\text{SrTiO}_3\text{-LaAlO}_3$ ceramics. The system exhibits solid solubility across the entire compositional range with crystal structures changing from cubic to rhombohedral at $x = 0.2$. With increasing concentration of LaAlO_3 , the Q -value increases rapidly whereas t_f and ϵ_r decrease. It was shown that by changing the concentration of LaAlO_3 , the value of t_f can be tuned. Jančar et al. (2002, 2003) showed that the variation of dielectric properties with increasing x does not significantly depend on the nature of the rare earth element in RAIO_3 . The replacement of RAIO_3 by RGAO_3 slightly not only improves the permittivity of solid solutions but also affects the Q -value. Partial substitution of Ca^{2+} by Ba^{2+} leads to an increase of t_f and a decrease of the Q -value, whereas ϵ_r remains almost unchanged. Replacement of Ca^{2+} by Mg^{2+} or Sr^{2+} mostly results in a decrease of the high-quality factor.

Perovskite-type rare earth aluminates are also prospective materials for deposition of GaN and AlN layers and manufacturing of blue light semiconductor lasers, as well as epitaxial layers of HTSC materials. LaAlO_3 and LSAT ($\text{La}_{1-x}\text{Sr}_x\text{Al}_{1-y}\text{Ta}_y\text{O}_3$) are well known in this respect. The application of a material as a substrate requires the knowledge of its physical characteristics and their temperature evolution in addition to the standard condition, which is the minimum mismatch between the cell parameters of the deposited film and the substrate. For details refer to O'Bryan et al. (1990).

Another requirement is a low dielectric loss (δ). Some authors (Hollmann et al., 1994) defined special conditions for dielectric properties of substrates for the HTSC film deposition:

1. $\tan \delta < 10^{-4}$;
2. if $\epsilon \approx 10$, substrate utilization is permitted in HTSC microwave integrated circuits with operating frequency above 10 GHz;
3. if $\epsilon \leq 25$, substrate utilization is permitted in HTSC microwave integrated circuits with operating frequency below 10 GHz.

The improvement of the loss tangent is especially interesting because of the need for faster and faster switching times. A gate dielectric material for dynamic random access memory devices must have a loss tangent of less than 0.005 (Stoneham et al., 2005; Robertson, 2006) and $\text{Ca}(\text{Sr, Ba})\text{TiO}_3\text{-RAIO}_3$ ($R = \text{La, Nd, and Sm}$) solid solutions fulfil this requirement, they exhibit the corresponding low loss tangents (Jančar et al., 2002).

Dielectric data for microwave dielectric materials, namely, the relative dielectric permittivity (ϵ_r), the product of the quality factor Q and the frequency ($Q \times f$), the frequency of the measurement (f), and the temperature coefficient of the resonance frequency (τ_f) based on rare earth aluminates are listed in Table 30. Measurements carried out using low-frequency (MHz) impedance methods are

TABLE 30 Dielectric properties of microwave dielectric materials based on LaAlO_3

Composition	Sample, sintering conditions ¹	ϵ_r	$Q \times f$ (GHz)	f (GHz)	t_f (ppm/K)	Reference
LaAlO_3	single crystal	24.0	200 000	10	–	Mazierska et al. (2004)
LaAlO_3	single crystal	24.1	294 000	10	–	Shimada et al. (2005)
LaAlO_3	single crystal	24.0	509 000	10	–	
LaAlO_3	1680	19.6	24 500	10	–56	Sebastian et al. (2005)
LaAlO_3	1650/2	23.4	68 000	10	–44	Cho et al. (1999a)
$\text{LaAlO}_3 + 0.25\%$ (w/w) CuO	1460	20.7	48 000	–	–80	Hsu and Huang (2001)
$\text{LaAlO}_3 + 10\%$ (v/v) $\text{Sr}_2\text{Nb}_2\text{O}_7$	1575/3	22.8	18 610	7.63	46	Liu and Chen (2004)
$\text{LaAlO}_3 + 5\%$ (v/v) $\text{Sr}_2\text{Nb}_2\text{O}_7$	1600/1	23.1	20 550	10.89	4.5	
$\text{LaAlO}_3 + 5\%$ (v/v) $\text{Sr}_2\text{Nb}_2\text{O}_7$	1575/3	23.4	20 790	10.81	–25	
$(\text{LaAlO}_3)_{0.5}(\text{La}_{2/3}\text{TiO}_3)_{0.5}$	142	34.4	45 000	6.7	–23	Suvorov et al. (1998)
$(\text{LaAlO}_3)_{0.4}(\text{La}_{2/3}\text{TiO}_3)_{0.6}$	1400/33	39.6	42 200	6	–15	
$(\text{LaAlO}_3)_{0.4}(\text{La}_{2/3}\text{TiO}_3)_{0.6}$	1400/33 (oxygen)	40	50 800	6	–15	
$(\text{LaAlO}_3)_{0.3}(\text{La}_{2/3}\text{TiO}_3)_{0.7}$	1400/33	44.9	33 000	6	7	
$(\text{LaAlO}_3)_{0.2}(\text{La}_{2/3}\text{TiO}_3)_{0.8}$	1400	53.9	29 000	5.4	35	
$(\text{LaAlO}_3)_{0.15}(\text{La}_{2/3}\text{TiO}_3)_{0.85}$	1375	57.7	27 900	5.2	65	
$(\text{LaAlO}_3)_{0.1}(\text{La}_{2/3}\text{TiO}_3)_{0.9}$	1350	62.6	26 100	4.9	82	
$(\text{LaAlO}_3)_{0.08}(\text{La}_{2/3}\text{TiO}_3)_{0.92}$	1350	66.9	28 350	4.8	82	
$(\text{LaAlO}_3)_{0.65}(\text{CaTiO}_3)_{0.35}$	1600	37	47 000	–	–2	Moon et al. (1999)
$(\text{LaAlO}_3)_{0.35}(\text{CaTiO}_3)_{0.65}$	1450/12	41	33 000	–	–17	Suvorov et al. (2001)
$(\text{LaAlO}_3)_{0.3}(\text{CaTiO}_3)_{0.7}$	1450/12	44	30 000	–	–3	
$(\text{LaAlO}_3)_{0.25}(\text{CaTiO}_3)_{0.75}$	1450/12	47	36 000	13		
$(\text{La}_{0.5}\text{Nd}_{0.5}\text{AlO}_3)_{0.3}(\text{CaTiO}_3)_{0.7}$	–	41.5	37 000	8	4	Nenasheva et al. (2003)
$\text{La}_{0.5}\text{Nd}_{0.5}\text{AlO}_3\text{-CaTiO}_3\text{-}$ $\text{Ca}(\text{Zn}_{1/3}\text{Nb}_{2/3})\text{O}_3$	–	50	32 700	–	–0.3	Sebastian et al. (2005)
$(\text{LaAlO}_3)_{0.9}(\text{SrTiO}_3)_{0.1}$	1680	25.1	128 000	10	–51	
$(\text{LaAlO}_3)_{0.8}(\text{SrTiO}_3)_{0.2}$	1680	26.7	139 000	10	–50	

$(\text{LaAlO}_3)_{0.7}(\text{SrTiO}_3)_{0.3}$	1680	28.9	120 000	9.9	-44	
$(\text{LaAlO}_3)_{0.5}(\text{SrTiO}_3)_{0.5}$	1680	35.9	108 800	9.7	-21	
$(\text{LaAlO}_3)_{0.5}(\text{SrTiO}_3)_{0.5}$	-	35	27 000	-	-18	Cho et al. (1999b)
$(\text{LaAlO}_3)_{0.5}(\text{SrTiO}_3)_{0.5}+0.25\%$ (w/w) B_2O_3	1430/2	34.5	43 200	7	-10.7	Huang and Hsu (2001)
$(\text{LaAlO}_3)_{0.46}(\text{SrTiO}_3)_{0.53}+2\%$ (w/w) B_2O_3	1460	35	38 000	7	-1	Huang and Chiang (2002)
$(\text{LaAlO}_3)_{0.4}(\text{SrTiO}_3)_{0.6}$	1680	42.1	83 000	9.5	8.4	Sebastian et al. (2005)
$(\text{LaAlO}_3)_{0.3}(\text{SrTiO}_3)_{0.7}$	1680	52	50 800	9.3	56.4	
$\text{La}_{0.3}\text{Sr}_{0.7}\text{Al}_{0.65}\text{Ta}_{0.35}\text{O}_3$ (LSAT)	Single crystal	23.13	86 000	15.5	-	Jacob et al. (2004)
50% (w/w) $(\text{LaAlO}_3)+50\%$ (w/w) TiO_2	-	37	37 000	-	-1	Lim et al. (1999)
CeAlO_3	1500	20.7	40 117	9.5	-57	Feteira et al. (2007)
PrAlO_3	1650/2	23.2	51 000	10	-25	Cho et al. (1999a)
$\text{Pr}_{0.3}\text{Nd}_{0.7}\text{AlO}_3\text{-CaTiO}_3\text{-}$ $\text{Ca}(\text{Zn}_{1/3}\text{Nb}_{2/3})\text{O}_3$	-	49	33 400	-	0.4	Ishikawa et al. (2002)
NdAlO_3	1650/2	22.3	58 000	10	-33	Cho et al. (1999a)
$\text{NdAlO}_3 + 0.25\%$ (w/w) V_2O_5	1410	21.5	64 000	9	-30	Huang and Chen (2003)
$\text{NdAlO}_3 + 0.25\%$ (w/w) CuO	1420/2	22.4	63 000	10	-35	Huang and Chen (2002b)
$(\text{NdAlO}_3)_{0.3}(\text{CaTiO}_3)_{0.7}$	-	43	47 000	-	0	Hirahara et al. (1994)
$(\text{NdAlO}_3)_{0.3}(\text{CaTiO}_3)_{0.7}$	-	43.5	30 000	8	-2.1	Nenasheva et al. (2003)
$(\text{NdAlO}_3)_{0.4}(\text{CaTiO}_3)_{0.6}$	1450/10	37.18	40 750	-	114	Suvorov et al. (2001)
$(\text{NdAlO}_3)_{0.33}(\text{CaTiO}_3)_{0.77}$	1450/10	41.98	42 900	-	45	
$(\text{NdAlO}_3)_{0.3}(\text{CaTiO}_3)_{0.7}$	1450/10	43.73	34 800	-	14	
$(\text{NdAlO}_3)_{0.3}(\text{CaTiO}_3)_{0.7}$	1450/10	45	44 000	-	3	
$(\text{NdAlO}_3)_{0.27}(\text{CaTiO}_3)_{0.73}$	1450/10	44.99	31 000	-	15	
$(\text{NdAlO}_3)_{0.29}(\text{CaTiO}_3)_{0.71}$	1450/10	45.11	38 450	-	6	

(continued)

TABLE 30 (continued)

Composition	Sample, sintering conditions [†]	ϵ_r	$Q \times f$ (GHz)	f (GHz)	t_f (ppm/K)	Reference
(NdAlO ₃) _{0.3} (CaTiO ₃) _{0.7}	1450	45	45 000	—	0	Jančar et al. (2003)
Nd _{0.5} Y _{0.5} AlO ₃ -CaTiO ₃ - Ca(Zn _{1/3} Nb _{2/3})O ₃	—	45	32 500	—	-0.5	Badshaw et al. (2003)
SmAlO ₃	1650/2	20.4	65 000	10	-74	Cho et al. (1999a)
(SmAlO ₃) _{0.35} (CaTiO ₃) _{0.65}	1450/12	41	42 000	—	-18	Suvorov et al. (2001)
(SmAlO ₃) _{0.3} (CaTiO ₃) _{0.7}	1450/12	45	42 000	—	1	
(SmAlO ₃) _{0.25} (CaTiO ₃) _{0.75}	1450/12	51	31 000	—	31	
(SmAlO ₃) _{0.3} (Ca _{0.99} Sr _{0.01} TiO ₃) _{0.7}	1450/10	44	34 000	5	2	Jančar et al. (2002)
(SmAlO ₃) _{0.3} (Ca _{0.95} Sr _{0.05} TiO ₃) _{0.7}	1450/10	46	31 000	5	6	
(SmAlO ₃) _{0.3} (Ca _{0.9} Sr _{0.1} TiO ₃) _{0.7}	1450/10	46	33 000	5	12	
(SmAlO ₃) _{0.3} (Ca _{0.99} Ba _{0.01} TiO ₃) _{0.7}	1450/10	45	36 000	5	2	
(SmAlO ₃) _{0.3} (Ca _{0.95} Ba _{0.05} TiO ₃) _{0.7}	1450/10	43	16 000	5	16	
(SmAlO ₃) _{0.3} (Ca _{0.9} Ba _{0.1} TiO ₃) _{0.7}	1450/10	42	1700	5	—	
(SmAlO ₃) _{0.3} (Ca _{0.99} Mg _{0.01} TiO ₃) _{0.7}	1450/10	46	34 000	5	2	
(SmAlO ₃) _{0.3} (Ca _{0.95} Mg _{0.05} TiO ₃) _{0.7}	1450/10	45	31 000	5	6	
(SmAlO ₃) _{0.3} (Ca _{0.9} Mg _{0.1} TiO ₃) _{0.7}	1450/10	47	25 000	5	12	
GdAlO ₃	1650/2	18.4	11 000	10	-54	Cho et al. (1999a)
GdAlO ₃	Single crystal	25	39 000	—	—	Sharma et al. (1998)
DyAlO ₃	1650/2	17.6	38 000	10	-34	Cho et al. (1999a)
ErAlO ₃	1650/2	16.3	44 200	10	-40	
YAlO ₃	1650/2	15.7	68 000	10	-59	
YAlO ₃	1500	12.4	12 390	11	-66	Feteira et al. (2005)
(YAlO ₃) _{0.9} (CaTiO ₃) _{0.1}	1500	15.5	13 811	10.1	-63	
(YAlO ₃) _{0.9} (CaTiO ₃) _{0.1} +0.25% (w/w) ZnO	1500	16.2	10 021	11.3	-63	

(YAlO ₃) _{0.9} (CaTiO ₃) _{0.1} +1% (w/w) Nb ₂ O ₅	1500	16.6	7998	11.3	-63
(YAlO ₃) _{0.7} (CaTiO ₃) _{0.3}	1500	19.4	15 465	9.5	-63
(YAlO ₃) _{0.7} (CaTiO ₃) _{0.3} +0.25% (w/w) ZnO	1500	20.3	8452	9.7	-63
(YAlO ₃) _{0.7} (CaTiO ₃) _{0.3} +1% (w/w) Nb ₂ O ₅	1500	19.9	13 987	10.1	-63
(YAlO ₃) _{0.5} (CaTiO ₃) _{0.5}	1500	24.8	16 872	8.4	-35
(YAlO ₃) _{0.5} (CaTiO ₃) _{0.5} +0.25% (w/w) ZnO	1500	25.4	9823	8.5	-35
(YAlO ₃) _{0.5} (CaTiO ₃) _{0.5} +1% (w/w) Nb ₂ O ₅	1500	24.7	14 337	8.4	-35
(YAlO ₃) _{0.3} (CaTiO ₃) _{0.7}	1500	38.1	14 212	7.7	-14
(YAlO ₃) _{0.3} (CaTiO ₃) _{0.7} +0.25% (w/w) ZnO	1500	39.0	8552	6.5	-14
(YAlO ₃) _{0.3} (CaTiO ₃) _{0.7} +1% (w/w) Nb ₂ O ₅	1500	37.8	11 532	6.8	-14
(YAlO ₃) _{0.1} (CaTiO ₃) _{0.9}	1400	81.8	17 151	4.8	266
(YAlO ₃) _{0.1} (CaTiO ₃) _{0.9} +0.25% (w/w) ZnO	1400	81.7	12 954	4.4	266
(YAlO ₃) _{0.1} (CaTiO ₃) _{0.9} +1% (w/w) Nb ₂ O ₅	1400	80.5	16 090	4.8	266

¹ Sintering temperature (in K)/time (in hours).

excluded from our considerations as they are incapable for the study of materials with loss tangent below 10^{-3} . Also, basic properties of ceramics (i.e., porosity, grain size, purity of raw materials), measurement methods, and equipment used for measurements strongly affect observed dielectric properties. Therefore, exact comparison of dielectric properties for identical compositions that were manufactured in different ways and conditions is impossible. Similar trends can be observed, when the dielectric properties of single crystals are studied (see also Table 30).

Dielectric properties of LaAlO_3 are a matter of discussion for many years. Simon *et al.* (1988) have reported $\epsilon_r = 15.3$, whereas considerably higher values have been measured by other authors: 24.5–25 (Samara, 1990), 27 (Yang *et al.*, 1990), 24 (Konaka *et al.*, 1991), and 23.8 (Konopka and Wolff, 1992). Makeev *et al.* (2002) performed studies of the dielectric permittivity on two different LaAlO_3 single crystals obtained from the Institute for Single Crystals (Kharkiv, Ukraine) and from the Coating & Crystal Technology Company (Kittanning, Pennsylvania, US). As has been stated earlier (Makeev *et al.*, 2002), depending on the sample, the ϵ value was about 23.1–24.2, which means that the dielectric constant in the single crystal measurements was highly affected by the anisotropy of the crystal. The scattering follows from the presence of defects, especially twins and also from the growth conditions of the crystal (i.e., ϵ_r can vary even in samples cut from the same ingot). Anisotropy of dielectric properties has also been observed for LaAlO_3 single crystals: ϵ_r is 20.3 in the $[10\bar{1}0]$ direction and 24.7 in the $[21\bar{3}0]$ direction (Gorshunov *et al.*, 1991).

In another example, the dielectric properties of cerium aluminate are chosen, for example, Wang *et al.* (2005) reported dielectric properties of cerium aluminate ceramics sintered at 1400°C ($\epsilon_r = 610$, $Q \times f = 4000$ GHz at 10 MHz) and suggested that this material is a promising candidate for high-frequency electronic device applications. Studies of the dielectric properties of CeAlO_3 ceramics performed by Keith and Roy (1954) reveal an increase of ϵ_r with temperature and large ϵ_r values of 9, 209, and 1796 at temperatures of 93, 298, and 549 K, respectively. Other authors (Shelykh and Melekh, 2003) observed ϵ_r varying from 16 (below 170 K) to a few thousands (250–600 K). At temperatures above 600 K, a weak increase of ϵ_r was observed in CeAlO_3 with an activation energy close to that observed in conductivity measurements, $2.3(5) - 0.62 \times 10^{-3}T$ (eV) for the band gap energy. The latter is a rather common indicator for ionic conductivity. In a paper by Ioffe *et al.* (1962), an $\epsilon_r = 14$ –300 was determined depending on temperature conditions during the sample preparation.

Cerium aluminate possesses a centrosymmetric $I4/mcm$ crystal structure at RT. This feature together with an extremely high value of the relative dielectric permittivity observed by Keith and Roy (1954), Ioffe *et al.* (1962), Shelykh and Melekh (2003), and Wang *et al.* (2005) would immediately imply the ferroelectricity as a possible origin. Feteira *et al.* (2007) reinvestigated the structure of CeAlO_3 ceramics using X-ray/electron diffraction and TEM as well as dielectric properties and showed that CeAlO_3 exhibits a low value of $\epsilon_r = 20.7$ and higher microwave dielectric losses than LaAlO_3 and PrAlO_3 . The observed differences in ϵ_r were attributed to grain boundary effects.

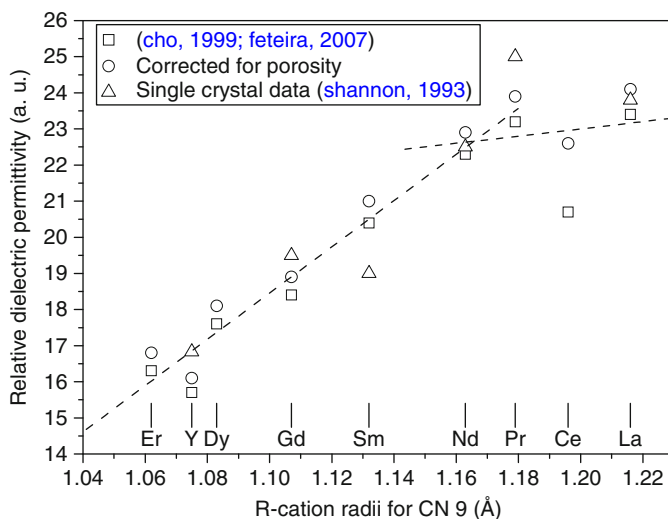


FIGURE 53 Relative dielectric permittivity versus rare earth ionic radius. The dashed lines are linear fits $\epsilon_r(r_R) = 11+10 r_R$ and $\epsilon_r(r_R) = -52+64 r_R$.

For consistence, the relative dielectric permittivities for rare earth aluminates are plotted in Figure 53, where the experimental data from (Cho et al., 1999a,b; Feteira et al., 2007) are given as squares. Feteira et al. (2007) applied a porosity (ratio of observed material density to 'ideal' material density) correction to ϵ_r and the resulting data are displayed in Figure 53 by circles. Relative permittivities for RAlO_3 single crystals (Shannon, 1993) are plotted as triangles.

Similar to RTiNbO_6 (Sebastian et al., 2001) and RTiTaO_6 (Surendran et al., 2002), the dielectric constants of RAlO_3 show a pronounced dependency on the ionic radius of the rare earth element. This can be roughly approximated by two lines intersecting near NdAlO_3 (Figure 53). Change of the slope separating RAlO_3 with $R = \text{La, Ce, Pr, and Nd}$ and with $R = \text{Sm, Gd, Dy, Er, and Y}$ is likely related to differences in the crystal structures of the rare earth aluminates. In the case of an isomorphous rare earth substitution, the dielectric permittivity should directly depend on the rare earth ionic radii.

Nordland and Van Uitert (1970) reported the low-frequency (1kHz) values of the dielectric constant of Pr(Nd)AlO_3 solid solutions single crystals in the temperature range 5–300 K. Two different anomalies were observed in pure PrAlO_3 at 205 and 151 K, respectively, and the measured dielectric constant ϵ changed by about 3%. The high-temperature anomaly (205 K) shows a stepwise decrease in ϵ and a temperature hysteresis loop of 3 K, while the low-temperature anomaly (at 151 K) shows smooth changes in the thermal dependence of the dielectric constant and no hysteresis, which is consistent with a second-order phase transformation. With increasing of neodymium content in the $\text{Pr}_{1-x}\text{Nd}_x\text{AlO}_3$ solid solution, the temperatures of the observed anomalies were shifted to the low-temperature region and in neodymium aluminate, no sign of anomalous behaviour has been observed. Anomalies in the thermal variation of the dielectric

constants observed by Nordland and Van Uitert (1970) correlate well with the structural phase transformations taking place in $\text{Ce}_{1-x}\text{R}_x\text{AlO}_3$ ($\text{R} = \text{La}$ and Nd) solid solutions (Vasylechko *et al.*, 2007b). Furthermore, the dielectric permittivity is strongly affected by the crystal structure, which may be the reason for the changes of the slope of ϵ_r (Figure 53). *In situ* studies of the dielectric permittivity may therefore be a sensitive tool to monitor any structural phase transformations occurring in the system.

Practical interest in rare earth aluminates as microwave dielectric materials remains high. Recently, Shevlin *et al.* (2005) reported that $\text{La}_x\text{Y}_{1-x}\text{AlO}_3$ solid solutions ($0.2 < x < 0.4$) possess unique physical attributes for possible application as gate dielectrics (which would offer an alternative to silicon dioxide in complementary metal-oxide semiconductor devices) when stabilized in the rhombohedral perovskite structure. The needed properties are lost in the orthorhombic modification. However, our previous consideration of the crystal structure (see Section 2.3.1) together with the results of Kyomen and Itoh (2002) reveal that this feature is difficult to realize in practice, that is the rhombohedral modification of $\text{La}_x\text{Y}_{1-x}\text{AlO}_3$ solid solution only exists in a narrow concentration range with $x > 0.85$, while in the range $0.2 < x < 0.4$, the crystal structure will remain orthorhombic.

The fact that dielectric and structural properties of rare earth aluminates fulfill the demands of microwave engineering, even though some other properties (primarily the formation of twins and chemical purity of precursors) are unfavourable, should continue to support a considerable interest in the attempts to tailor new varieties of aluminate crystals.

3. GALLATES

3.1 Formation and preparation

As mentioned above, rare earth gallates RGaO_3 with perovskite-type structure are known for all rare earth elements except promethium and scandium. In addition to phases with perovskite structure, other compounds such as $\text{R}_3\text{Ga}_5\text{O}_{12}$ ($\text{R} = \text{Pr}$, Nd – Lu , and Y), $\text{R}_4\text{Ga}_2\text{O}_9$ (La , Pr – Gd , and Y), and R_3GaO_6 ($\text{R} = \text{Nd}$ – Er) exist in R_2O_3 – Ga_2O_3 pseudo-binary systems (Schneider *et al.*, 1961; Carruthers *et al.*, 1973; Allibert *et al.*, 1974; DiGiuseppe *et al.*, 1980; Nicolas *et al.*, 1983, 1984; Coutures *et al.*, 1983; Mizuno and Yamada, 1985, 1988, 1989, 1992; Mizuno *et al.*, 1985; Bondar *et al.*, 1988; Yamane *et al.*, 1995; Liu *et al.*, 2004). Furthermore, Antic-Fidancev *et al.* (1997) reported the formation of LaGa_3O_6 and PrGa_3O_6 compounds in the corresponding systems. HT modifications of YGaO_3 , HoGaO_3 , and ErGaO_3 possessing non-perovskite hexagonal structure (S.G. $P6_3cm$) have been obtained by Geller *et al.* (1975) by quenching from the melt at 2220 K.

Among all R_2O_3 – Ga_2O_3 systems, the experimental phase diagrams are fully or partially studied for La , Nd , Sm , Eu , Gd , and Tb (Table 31). For several other R_2O_3 – Ga_2O_3 systems, only predicted subsolidus were reported by Schneider *et al.* (1961).

TABLE 31 Formation of compounds in the R_2O_3 - Ga_2O_3 systems

System	Phase diagram	Compounds, formation, temperature (K)				Reference
		3:1	2:1	1:1	3:5	
La_2O_3 - Ga_2O_3	PS	–	C, 1770	C, 1780	–	Schneider et al. (1961)
	PD	–	C, 1977	C, 1988	–	Mizuno et al. (1985)
	PD ^c	–	C, 1977	C, 1953	–	Zinkevich et al. (2004)
	PD ^c	–	C, 1986	C, 1971	–	Zinkevich et al. (2006)
Ce_2O_3 - Ga_2O_3	–	–	–	+	–	Leonov et al. (1966)
	–	–	–	+	–	Stan et al. (2002)
Pr_2O_3 - Ga_2O_3	–	–	C, 1976	C	–	Mizuno and Yamada (1985)
Nd_2O_3 - Ga_2O_3	PS	–	C, 1870	C, 1870	C, 1790	Schneider et al. (1961)
	PD	P, 1563	C, 1948	C, 1883	C, 1828	Nicolas et al. (1983)
	–	–	C, 1977	C, 1943	C, 1913	Mizuno and Yamada (1985)
	PD	P, 1773	C, 1977	C, 1943	C, 1913	Mizuno and Yamada (1989)
	–	–	+	+	+	Zinoviev et al. (1989)
Sm_2O_3 - Ga_2O_3	PS	C, 1770	C, 1790	–	C, 1810	Schneider et al. (1961)
	PD	P, 1988	C, 1983	P, 1838	C, 1928	Nicolas et al. (1984)
	–	P, 2028	C, 1881	–	C, 1953	Mizuno and Yamada (1985)
	PD	P, 2030	C, 1980	+	C, 1880	Mizuno and Yamada (1989)
Eu_2O_3 - Ga_2O_3	PS	C, 1870	C, 1890	–	C, 1780	Schneider et al. (1961)
	–	P, 2035	C, 1987	–	C, 1990	Mizuno and Yamada (1985)
	PD	P, 2035	C, 1987	–	C, 1990	Mizuno and Yamada (1992)
Gd_2O_3 - Ga_2O_3	PS	C, 1810	–	–	C, 1780	Schneider et al. (1961)
	PD ¹	–	–	C, 2080	C	Allibert et al. (1974)
	PD ¹	–	–	C, 2080	C, 2013	DiGiuseppe et al. (1980)
	PD	P, 2033	P, 1973	²	C, 2013	Nicolas et al. (1984)
	–	P, 2053	P, 1993	–	C, 2016	Mizuno and Yamada (1985)

(continued)

TABLE 31 (continued)

System	Phase diagram	Compounds, formation, temperature (K)				Reference
		3:1	2:1	1:1	3:5	
	PD	P, 2048	P, 1988	P, 1948 ³	C, 2023	Bondar et al. (1988)
	–	+	–	–	+	Zinoviev et al. (1989)
Tb ₂ O ₃ -Ga ₂ O ₃	PD	P, 2053	P, 1993	–	C, 2016	Mizuno and Yamada (1992)
	PD ¹	–	–	P ² , 2130	C, 2185	Udalov et al. (2003)
Dy ₂ O ₃ -Ga ₂ O ₃	PS	P, 1850	–	–	C, 1840	Schneider et al. (1961)
	–	P, 2073	–	–	C, 2061	Mizuno and Yamada (1985)
Ho ₂ O ₃ -Ga ₂ O ₃	PS	P, 1725	–	–	C, 1730	Schneider et al. (1961)
	–	P, 2078	–	–	C, 2081	Mizuno and Yamada (1985)
Er ₂ O ₃ -Ga ₂ O ₃	PS	P, 1870	–	–	C, 1870	Schneider et al. (1961)
	–	P, 2073	–	–	C, 2113	Mizuno and Yamada (1985)
Tm ₂ O ₃ -Ga ₂ O ₃	PS	–	–	–	C, 1770	Schneider et al. (1961)
Yb ₂ O ₃ -Ga ₂ O ₃	PS	–	–	–	C, 1770	Schneider et al. (1961)
	–	–	–	–	C, 2151	Mizuno and Yamada (1985)
Lu ₂ O ₃ -Ga ₂ O ₃	PS	–	–	–	C, 1770	Schneider et al. (1961)
	–	–	–	–	+	Zinoviev et al. (1989)
Y ₂ O ₃ -Ga ₂ O ₃	PS	P, 1910	–	–	C, 1800	Schneider et al. (1961)
	–	–	–	–	C, 2043	Bondar et al. (1984)

C, congruently melting; P, peritectic (incongruently melting); PD, phase diagram; PS, predicted subsolidus, formation temperatures are roughly estimated from the figures given in the reference; superscript c, calculated/optimized diagram.

¹ Partial diagram.

² Metastable phase.

³ Limited thermal stability range.

Thermodynamic properties of RGaO_3 compounds were studied by Kanke and Navrotsky (1998), Jacob et al. (2000), Kapala (2004), Cheng and Navrotsky (2004), Zinkevich et al. (2006), and Wu et al. (2007). It was shown that similar to AlO_3 perovskites, standard molar enthalpies of formation of RGaO_3 compounds become more negative with decreasing the radius of R-cations (Kanke and Navrotsky, 1998). The authors concluded that ΔH of the perovskite formation is mainly controlled by two factors, the strengthening of the ionic bond in R_2O_3 with decreasing R-cation radius and the weakening of the ionic bond between R and the four distant oxygen atoms in RGaO_3 structures. The stability of RGaO_3 perovskites against disproportionation to $\text{R}_3\text{Ga}_5\text{O}_{12}$ and R_2O_3 phases is controlled almost entirely by ΔH and $P\Delta V$ terms but not by $T\Delta S$ contribution (Kanke and Navrotsky, 1998).

First members of the RGaO_3 series—lanthanum, praseodymium, and neodymium gallates—can be obtained from the melt and they solidify congruently at 1998, 1873, and 1880 K, respectively (Nicolas et al., 1983; Mizuno et al., 1985; Mizuno and Yamada, 1985, 1988; Kapala, 2004). Samarium gallate, SmGaO_3 , melts incongruently and exists only in the narrow temperature region 20–30 K below the liquidus. Gadolinium gallate GdGaO_3 can be obtained only by fast melting and subsequent quenching (Nicolas et al., 1984). The latter authors reported that ‘short melting and overheating of the melt using the laser device yield pure SmGaO_3 and GdGaO_3 .’ According to Bondar et al. (1988), gadolinium orthogallate exists only in the narrow temperature range between 1923 and 1948 K. At 1948 K, GdGaO_3 decomposes into $\text{Gd}_4\text{Ga}_2\text{O}_9$ and liquid, whereas a solid-state decomposition into $\text{Gd}_4\text{Ga}_2\text{O}_9$ and garnet phases occurs at 1923 K. The gallium-rich part of the Tb_2O_3 – Ga_2O_3 system has been studied by Udalov et al. (2003). The authors report that TbGaO_3 exists only near the peritectic reaction temperature and it melts incongruently.

Among all RGaO_3 perovskites, only LaGaO_3 , PrGaO_3 , and NdGaO_3 can be synthesized by solid-phase synthesis (Geller et al., 1974; Nicolas et al., 1984; Mizuno et al., 1985). This method was also employed for the preparation of cerium gallate CeGaO_3 , but in this case, the synthesis had to be performed in an inert or reducing atmosphere (Stan et al., 2002; Vasylechko et al., 2002a; Vasylechko and Senyshyn, 2004). Leonov et al. (1966) obtained single-phase CeGaO_3 perovskite at 1573 K in evacuated and sealed quartz tube via the reaction $2\text{CeO}_2 + 2/3\text{Ga}_2\text{O}_3 + 2/3\text{Ga} = 2\text{CeGaO}_3$.

Pure and doped RGaO_3 compounds can also be obtained in different modifications using the sol–gel method. For example, Polini et al. (2004) described the preparation of $\text{La}_{1-x}\text{Sr}_x\text{Ga}_{1-y}\text{Mg}_y\text{O}_{3-z}$ (LSGM) powders containing different amounts of Sr^{2+} and Mg^{2+} ions using either the Pechini or the citrate sol–gel method. The glycine-nitrate combustion synthesis was applied by Fu et al. (2003) for the preparation of pure and Sr- and Mn-doped powders of LaGaO_3 .

The arc melting technique has been used for the synthesis of CeGaO_3 from a stoichiometric oxide mixture in argon atmosphere (Geller, 1957; Shishido et al., 1996, 1997b). A similar technique was applied for the preparation of several solid solutions of $\text{La}_{1-x}\text{R}_x\text{GaO}_3$ (R = Ce, Sm, Eu, and Gd) (Vasylechko et al., 1999b, 2000b, 2001a; Vasylechko, 2005). Dabkowska et al. (1993) obtained single crystals

of solid solutions of NdGaO_3 – PrGaO_3 with dimensions up to $4.5 \times 4 \times 2 \text{ mm}^3$ by using a PbO – PbF_2 – MoO_3 flux. Large single crystals of LaGaO_3 , NdGaO_3 , and PrGaO_3 with high structural quality have been produced by the Czochralski technique (Giess *et al.*, 1990; Sasaura *et al.*, 1990a; Sasaura and Miyazawa, 1992; Sasaura and Miyazawa, 1993). The same method is used for growing solid solution crystals such as $\text{La}_{1-x}\text{Nd}_x\text{GaO}_3$ and $\text{La}_{1-x}\text{Pr}_x\text{GaO}_3$ (Berkowski *et al.*, 2000, 2001). For the preparation of $\text{La}_{1-x}\text{Pr}_x\text{GaO}_3$ and $\text{Nd}_{1-x}\text{R}_x\text{GaO}_3$ ($\text{R} = \text{Pr}$ and Sm) single crystals, the FZ technique has been applied (Aleksiyko *et al.*, 2001).

It should be noted that single crystals of LaGaO_3 , PrGaO_3 , and NdGaO_3 as well as their solid solutions have a pronounced tendency of twinning (Ruse and Geller, 1975; Belt and Uhrin, 1989; Miyazawa, 1989; Wang *et al.*, 1991; Morozov *et al.*, 1992; Bdikin *et al.*, 1993; Miyazawa *et al.*, 1993b; Ubizskii *et al.*, 1994; Uecker *et al.*, 1994; Savvitskii *et al.*, 1996, 2000b, 2000c, 2003a; Kleptsyn *et al.*, 1997; Vasylechko *et al.*, 2002b). The presence of reconstructive phase transformations below the melting point is believed to be the main reason for the formation of twins in these materials (Sasaura and Miyazawa, 1992).

Rare earth gallates, which could not be synthesized by solid-state reactions, were obtained by decomposition of the corresponding garnet phases at high pressure in the presence of NaOH flux (Marezio *et al.*, 1966; Marezio *et al.*, 1968). Using this approach, single crystals of RGaO_3 ($\text{R} = \text{Sm}$ – Lu and Y) have been prepared at 1273 K and pressure of 45 kbar. Geller *et al.* (1974) obtained RGaO_3 perovskites ($\text{R} = \text{Sm}$ – Er) at ambient pressure by quenching molten equimolar mixtures of constituent R_2O_3 and Ga_2O_3 oxides. The melts were kept for about 10 min at 1923–2273 K, depending on the compositions, and then quenched. It was reported that single-phase products were obtained for all compositions except for ErGaO_3 and HoGaO_3 .

Many applications require materials as thin film. Morell *et al.* (1999) reported that epitaxial LaGaO_3 films can be obtained on a single crystal LaAlO_3 substrate by using the sol–gel process followed by annealing at 1123 K. Kagawa *et al.* (1999) obtained a stoichiometric LaGaO_3 film on a sapphire substrate at 1173 K by the spray-ICP method. Transparent LaGaO_3 films deposited by atomic layer epitaxy at 598–698 K at different substrates (Si, sapphire, MgO , SrTiO_3 , LaAlO_3) were reported by Nieminen *et al.* (2001). The metal organic chemical vapour deposition technique was proposed for the preparation of heteroepitaxial PrGaO_3 and NdGaO_3 films on LaAlO_3 substrates (Han *et al.*, 1992, 1993). Dense films of $\text{La}_{1-x}\text{Sr}_x\text{Ga}_{1-y}\text{Mg}_y\text{O}_{3-z}$, known as a superior oxide ion conductor, can be prepared using the pulsed laser deposition technique (Kanazawa *et al.*, 2003) or using electrophoretic deposition of ceramic powders on graphite substrates followed by sintering using a controlled heating profile (Matsuda *et al.*, 2003).

3.2 Crystal structure of RGaO_3

Perovskite-type rare earth gallates RGaO_3 attract the interest of scientists for a long time. First attempts to study the crystal structure of RGaO_3 compounds began in the pioneering works of the early 1950th (Moeller and King, 1953; Ruggiero and Ferro, 1954). Because of the relatively weak distortion of RGaO_3

from the cubic structure, the materials were considered as 'ideal' perovskites. Only several years later, Geller (1956) discovered a new structure type of an orthorhombically distorted perovskite in gadolinium ferrite and attributed it to the crystal structures of RGaO_3 ($\text{R} = \text{La}, \text{Pr}, \text{and Nd}$) (Geller, 1957). Marezio et al. (1968) showed that the GdFeO_3 structure is intrinsic to the entire series of rare earth orthogallates. The lattice parameters for all RGaO_3 perovskites, except for cerium, promethium, and yttrium, have been calculated and analysed as functions of the atomic number of the R-element. The authors reveal that the lattice parameters a and c decrease smoothly from La to Lu, whereas the b -parameter passes through a maximum located at Gd and Tb. It was suggested that the anomalous behaviour of the b -parameter can be explained by the variation of the coordination number of the R-cation. A similar behaviour of the lattice parameters in the series of RGaO_3 perovskites was observed by Geller et al. (1974).

Taking into account the difficulties in the preparation of RGaO_3 compounds described above, full crystallographic data are available only for the first four members of the RGaO_3 family ($\text{R} = \text{La}, \text{Ce}, \text{Pr}, \text{and Nd}$), and for GdGaO_3 . The latter structure, solved from single crystal diffraction data, was reported by Guitel et al. (1976). It is necessary to note that pronounced twinning usually observed in RGaO_3 crystals causes serious problems in single crystal diffraction studies of these materials. Therefore, the majority of structural studies of RGaO_3 perovskites are typically performed using powder diffraction techniques.

At RT, all RGaO_3 exhibit paramagnetism and they order magnetically at temperatures below 4 K. To the best of our knowledge, structural studies of the magnetic ordering were performed only for neodymium gallate below 1 K (Marti et al., 1995) and have been found to be rather typical for other magnetic structures compatible with the $Pbnm$ symmetry (Bertaut, 1968).

In the present section, structural data for RGaO_3 compounds available from the literature are presented together with our recent work to supplement the knowledge about the crystal structures for these materials.

3.2.1 Lanthanum gallate LaGaO_3

First results on the formation of LaGaO_3 perovskite and its cubic structure had been reported by Moeller and King (1953) and Ruggiero and Ferro (1954). Shortly after, Geller (1957) found the orthorhombic deformation of the LaGaO_3 structure, similar to the one observed in GdFeO_3 . The author also described the phase transformation from orthorhombic to rhombohedral symmetry at 1173 K. However, further studies on the thermal behaviour of LaGaO_3 revealed that this transition occurs at much lower temperatures, at ca. 420 K (Miyazawa, 1989; O'Bryan et al., 1990; Berkstresser et al., 1991; Kobayashi et al., 1991). O'Bryan et al. (1990) found a second-order phase transformation at 1450 K in LaGaO_3 , but this observation was not confirmed by other authors. Both the room- and high-temperature modifications of the LaGaO_3 structure have been refined by Wang et al. (1991) using X-ray powder data and Rietveld full-pattern method. The authors showed that at room temperature LaGaO_3 possesses a centrosymmetric space group $Pbnm$ and that its high-temperature modification belongs to the centrosymmetric space group $R\bar{3}c$. Based on X-ray diffraction studies of a single

crystalline plate of LaGaO₃, [Morozov et al. \(1993a, 1993b\)](#) concluded that its RT structure is not orthorhombic. However, the author's suggestion of a triclinic structure of LaGaO₃ was not confirmed. The concluded structure was based on the observation of twin lamellae with {100} and {010} composition planes, which have been found in an LaGaO₃ single crystals. According to group theoretical considerations performed by [Savytskii \(1997\)](#) and [Vasylechko et al. \(2002b\)](#), the anti-phase domains in the GdFeO₃-type crystals are possible just in the crystallographic planes (100) and (010). Similar anti-phase domains (merohedral twins) have also been found using X-ray methods in CaTiO₃ ([Arakcheeva et al., 1997](#)).

More recent structural investigations of LaGaO₃ performed by different research groups showed unambiguously that the RT LaGaO₃ structure belongs to the orthorhombic GdFeO₃ type ([Marti et al., 1994, 1996](#); [Sanjuán et al., 1998](#); [Slater et al., 1998a, 1998b](#); [Howard and Kennedy, 1999](#); [Vasylechko et al., 1999a, 1999b](#); [Lerch et al., 2001](#); [Kajitani et al., 2005](#)). It should be noted that different cell parameter ratios are reported in the literature for the orthorhombic modification of LaGaO₃. [Geller \(1957\)](#) in his early work mentioned the cell parameters: $a = 5.496 \text{ \AA}$, $b = 5.524 \text{ \AA}$, $c = 7.787 \text{ \AA}$ where $a < b$. This parameter ratio has been accepted for LaGaO₃ in numerous publications ([Mizuno et al., 1985](#); [Giess et al., 1990](#); [O'Bryan et al., 1990](#); [Kobayashi et al., 1991](#); [Wang et al., 1991](#); [Morozov et al., 1993b](#); [Utke et al., 1997](#)) and the PDF database (File 24-1102). Another set of orthorhombic lattice parameters of LaGaO₃, namely, $a = 5.526 \text{ \AA}$, $b = 5.473 \text{ \AA}$, $c = 7.767 \text{ \AA}$ where $a > b$ was reported by [Marezio et al. \(1968\)](#) and others ([Geller et al., 1974](#); [Marti et al., 1994, 1996](#)). In order to clarify the situation, [Vasylechko et al. \(1999a\)](#) carried out Rietveld refinements of the LaGaO₃ structure using the models, reported by [Wang et al. \(1991\)](#) and [Marti et al. \(1994\)](#). They differ mainly by the a and b cell parameter ratio, that is $a < b$ or $a > b$. It was shown that the structure refinement when using $a > b$ cell parameters gives a better fit of the observed profiles. The difference between both models can be distinguished mainly from the positions of weak $0kl$ reflections with odd l -indices. The observed 'ratio-sensitive' reflections are, however, very weak (less than 1% of the maximal intensity), which might be the reason for incorrect settings of the lattice parameters reported in the literature. Later examinations of the LaGaO₃ structure by using high-resolution synchrotron powder diffraction technique with a high signal-to-noise ratio unambiguously confirmed the $a > b$ parameter ratio ([Vasylechko et al., 2002b](#); [Savytskii et al., 2003b](#)). Note that the cell parameter ratio observed in LaGaO₃ is a rather rare case among the GdFeO₃-type perovskites, for the majority of which the $a < b$ parameter ratio is typical. Hence, the existence of solid solutions with metrically tetragonal and cubic structures is expected in the LaGaO₃-RGaO₃ pseudo-binary systems (see below).

There is no common opinion in the literature concerning the HT modification of LaGaO₃. Based on *in situ* X-ray diffraction and differential scanning calorimetry studies, [Kobayashi et al. \(1991\)](#) concluded that between 420 K and 1270 K, LaGaO₃ is monoclinic. The monoclinic distortion was reported to be small below 1020 K but described to be significant at higher temperatures. However, this observation was not confirmed by structural refinements of other authors. As mentioned above, [Wang et al. \(1991\)](#) reported that the HT modification of LaGaO₃ is rhombohedral, which was confirmed later by comprehensive investigations using

elastic neutron scattering and X-ray diffraction technique (Slater et al., 1998a; Howard and Kennedy, 1999; Lerch et al., 2001; Kajitani et al., 2005). Nevertheless, discrepancies about symmetry of the HT phase of lanthanum gallate remain unsolved to date. Marti et al. (1994) in their first publication refined the LaGaO_3 structure from neutron diffraction data at 573, 1353, and 1673 K in the non-centrosymmetric space group $R3c$. The same structure model has been applied by Slater et al. (1998a) for the HT structure. In contrast, the LaAlO_3 type of structure and S.G. $R\bar{3}c$ have been assigned to the HT phase of LaGaO_3 by Marti et al. 1996; Howard and Kennedy, and Lerch et al. (2001), as it was initially proposed by Wang et al. (1991). From the analysis of the available data for related rare earth aluminates (see previous chapter) as well as from structural data for other RGaO_3 compounds and their solid solutions (see below), it is evident that the LaAlO_3 structure type seems to be the correct structural model for HT modification of LaGaO_3 .

LT structural parameters of lanthanum gallate refined from the neutron diffraction data at 12 K were reported for the first time by Marti et al. (1994). It was shown that the structure remains orthorhombic at least down to 12 K. The low-temperature behaviour of LaGaO_3 in the temperature range 12–300 K has been studied in detail using the HRPD technique with synchrotron radiation (Vasylechko et al., 2002b; Savytskii et al., 2003b; Vasylechko, 2005). Low- and high-temperature behaviour of lattice parameters of LaGaO_3 are shown in Figure 54A and B. A good agreement has been found between the LT lattice parameters (Savytskii et al., 2003b) and HT values obtained using neutron powder diffraction at temperatures 400–1670 K (Slater et al., 1998a; Howard and Kennedy, 1999). All lattice parameters increase smoothly on heating and the lattice parameters and cell volume change weakly at the orthorhombic-to-rhombohedral transition temperature (−0.01%) (Figure 54B). The crystallographic data for all modifications of LaGaO_3 at different temperatures are given in Tables 32 and 33.

3.2.2 Cerium gallate CeGaO_3

The information about the crystal structure of CeGaO_3 is controversial. The crystal structure is known from first X-ray studies of Ruggiero and Ferro (1954) who attributed it to the cubic perovskite structure. Shishido et al. (1997b) reported tetragonal symmetry for cerium gallate (S.G. $P4/mmm$, $Z = 1$) with lattice constants $a = 3.873 \text{ \AA}$ and $c = 3.880 \text{ \AA}$. Schoonover et al. (2000) proposed cubic symmetry for CeGaO_3 from studies of mixed nuclear fuel oxide $\text{CeO}_2\text{--PuO}_2\text{--UO}_2\text{--Ga}$ using a combination of scanning electron microscopy, energy dispersive X-ray spectroscopy, and Raman spectroscopy. Stan et al. (2002) published an orthorhombic GdFeO_3 type of structure for cerium gallate, where estimated lattice parameters were obtained by interpolating the data of Geller et al. (1974) ($a = b = 5.490 \text{ \AA}$, $c = 7.749 \text{ \AA}$). Positional and displacement parameters of the atoms in the CeGaO_3 structure were refined from X-ray powder diffraction data at RT (Stan et al., 2002). According to this study, the unit cell of CeGaO_3 is at RT very close to tetragonal, but the symmetry of the structure remains orthorhombic. This observation was also confirmed by using the HRPD technique with synchrotron radiation (Vasylechko et al., 2002a). The thermal behaviour of the CeGaO_3 structure has been described in

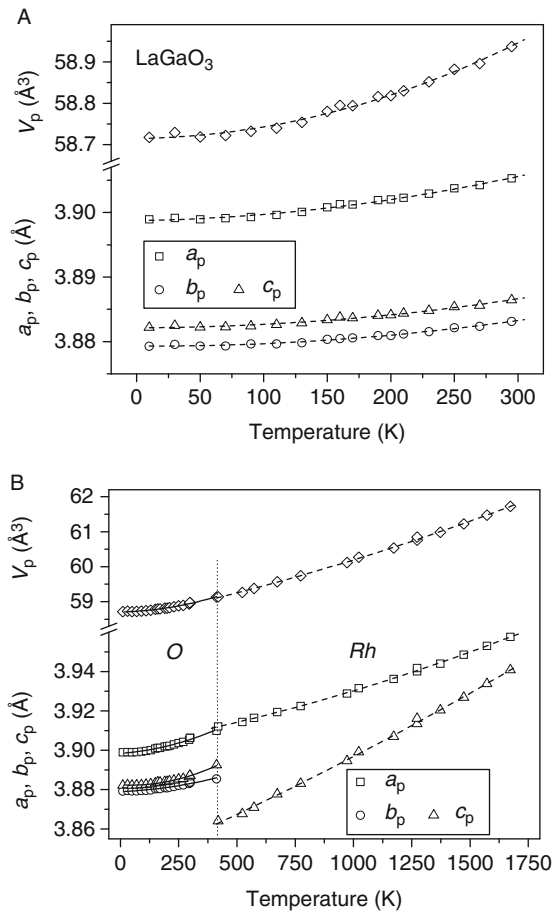


FIGURE 54 Normalized lattice parameters of orthorhombic (O) and rhombohedral (Rh) phases of LaGaO₃ in the temperature range 12–300 K (A) and 12–1673 K (B). LT lattice parameters were taken from Savytskii *et al.* (2003b) whereas the HT data from Slater *et al.* (1998a) and Howard and Kennedy (1999). The dashed lines are polynomial fits: $a_p(T) = 3.8987(1) [1 + 2.7(2) \times 10^{-8}T^2 - 2.5(5) \times 10^{-11}T^3]$; $b_p(T) = 3.8791(1) [1 + 1.6(2) \times 10^{-8}T^2 - 1.5(4) \times 10^{-11}T^3]$; $c_p(T) = 3.88222(9) [1 + 9(1) \times 10^{-9}T^2 + 1.6(3) \times 10^{-11}T^3]$ for the temperature range 12–410 K and $a_p(T) = 3.8557(9) [1 + 1.46(7) \times 10^{-8}T^2 - 4.1(4) \times 10^{-12}T^3]$; $c_p(T) = 3.9081(5) [1 + 7.3(4) \times 10^{-9}T^2 - 1.7(2) \times 10^{-12}T^3]$ for the temperature range 410–1673 K.

detail by Vasylechko and Senyshyn (2004). *In situ* HRPD measurements using synchrotron radiation have been performed in the temperature range 12–1230 K together with calorimetric studies. Both, DTA/TG and HT diffraction studies performed in air confirmed the previously reported (Shishido *et al.*, 1997b; Stan *et al.*, 2002) thermal instability of CeGaO₃ and its decomposition into CeO₂ and Ga₂O₃ due to oxidation above 840 K. Therefore, further HT investigations of the structural change of cerium gallate were carried out in a sample in a 0.3 mm quartz capillary, sealed in argon. It was shown that the GdFeO₃ structure type remains

TABLE 32 Structural parameters of orthorhombic modification of LaGaO₃ at different temperatures

Parameters		Marti et al. (1994) ¹	Savytskii et al. (2003b) ²	Wang et al. (1991) ³	Morozov et al. (1993a) ³	Marti et al. (1994) ¹	Slater et al. (1998a) ⁴	Sanjuán et al. (1998) ³	Vasylechko et al. (1999a) ³	Howard and Kennedy (1999) ¹	Jerch et al. (2001) ¹	Kajitani et al. (2005) ⁴
		<i>Pbnm</i> (12 K)	<i>Pbnm</i> (12 K)	<i>Pbnm</i> (298 K)	<i>Pbnm</i> (RT)	<i>Pbnm</i> (RT)	<i>Pbnm</i> (RT)	<i>Pbnm</i> (RT)	<i>Pbnm</i> (RT)	<i>Pbnm</i> (RT)	<i>Pbnm</i> (RT)	<i>Pnma</i> (298 K)
Atom: sites	<i>a</i> (Å)	5.5028(6)	5.51395(2)	5.496(1)	5.503	5.4332(2)	5.52432(2)	5.5217(1)	5.52298(8)	5.5245(1)	5.4908(1)	5.5272(2)
	<i>b</i> (Å)	5.4736(5)	5.48589(2)	5.527(1)	5.474	5.5034(2)	5.49246(2)	5.4893(1)	5.49139(9)	5.4922(1)	7.7725(1)	5.4943(1)
	<i>c</i> (Å)	7.7507(10)	7.76421(3)	7.781(2)	7.751	7.7155(3)	7.77448(4)	7.7701(1)	7.7725(1)	7.7740(2)	5.5227(1)	7.7781(3)
La, 4c	<i>x</i>	−0.0021(11)	−0.0050(3)	0.9964(15)	−0.01	0.0094(4)	−0.0047(2)	−0.0043(2)	−0.0036(9)	0.0041(3)	−0.0170(2)	−0.0045(4)
	<i>y</i>	−0.0216(6)	0.0200(2)	0.0163(7)	0.03	0.0421(2)	−0.0168(2)	−0.0171(1)	0.0170(3)	0.5168(3)	3/4	−0.0165(3)
	<i>z</i>	1/4	1/4	1/4	1/4	1/4	1/4	1/4	1/4	1/4	0.4955(2)	1/4
	<i>B</i> _{iso} (Å ²)	−0.02(4)	0.08(2)	−	−	−0.03(3)	0.39(2)	0.46(2)	0.37(5)	0.36(2)	0.36(4)*	0.37(2)
Ga, 4b	<i>x</i>	1/2	1/2	0	1/2	1/2	1/2	1/2	1/2	0	0	1/2
	<i>y</i>	0	0	1/2	0	0	0	0	0	0	0	0
	<i>z</i>	0	0	0	0	0	0	0	0	0	0	0
	<i>B</i> _{iso} (Å ²)	0.12(4)	0.20(3)	−	−	0.13(3)	0.29(2)	0.48(2)	0.23(5)	0.19(2)	0.16(5)*	0.37(2)
O1, 4c	<i>x</i>	0.0709(10)	0.071(2)	0.064(10)	0.01	0.9171(5)	0.0681(2)	0.0654(20)	0.057(4)	−0.0669(3)	−0.070(3)	0.0677(4)
	<i>y</i>	0.5056(12)	0.487(2)	0.500(5)	0.5	0.4820(4)	0.5078(3)	0.5039(16)	0.495(4)	−0.0058(4)	1/4	0.5066(6)
	<i>z</i>	1/4	1/4	1/4	1/4	1/4	1/4	1/4	1/4	1/4	0.0672(2)	1/4
	<i>B</i> _{iso} (Å ²)	0.25(4)	0.94	−	−	0.22(4)	0.41(2)	0.85(23)	0.7(5)	0.41(3)	0.49(5)*	0.55(8)
O2, 8d	<i>x</i>	−0.2276(8)	−0.281(2)	0.708(6)	0.74	0.2905(3)	0.2705(2)	0.7704(19)	−0.280(5)	0.2299(3)	0.2714(2)	−0.2307(3)
	<i>y</i>	0.2273(8)	0.277(2)	0.284(10)	0.26	0.2919(3)	0.2714(2)	0.2275(18)	0.285(5)	0.2704(3)	0.0354(1)	0.2304(3)
	<i>z</i>	0.0347(4)	0.0367(11)	0.033(6)	0.9	0.4569(2)	0.5365(1)	0.0378(10)	0.029(3)	0.0356(2)	0.7706(1)	0.0356(2)
	<i>B</i> _{iso} (Å ²)	0.25(4)	0.94	−	−	0.19(4)	0.53(2)	0.80(12)	1.1(5)	0.54(3)	0.52(3)*	0.63(8)

¹ Neutron powder diffraction data.² Synchrotron powder diffraction data.³ X-ray powder diffraction data.⁴ Time-of-flight neutron powder diffraction data.* Calculated from β_{ij} values given in the reference.

TABLE 33 Structural parameters of rhombohedral (S.G. $R\bar{3}c$ and $R3c$) modification of LaGaO_3 at different temperatures

Parameters	Wang et al. (1991) ¹	Wang et al. (1991) ¹	Marti et al. (1994) ²	Marti et al. (1994) ²	Slater et al. (1998a) ²	Slater et al. (1998a) ²	Marti et al. (1996) ²	Howard and Kennedy (1999) ²	Howard and Kennedy (1999) ²	Lerch et al. (2001) ²	Lerch et al. (2001) ²	
	$R\bar{3}c$ (423 K)	$R\bar{3}c$ (1173 K)	$R3c$ (573 K)	$R3c$ (1673 K)	$R3c$ (523 K)	$R3c$ (1273 K)	$R\bar{3}c$ (573 K)	$R\bar{3}c$ (637 K)	$R\bar{3}c$ (1373 K)	$R\bar{3}c$ (1073 K)	$R\bar{3}c$ (1273 K)	
a (Å)	5.5146(7)	5.5712(8)	5.5388(3)	5.6118(14)	5.5358(7)	5.5745(8)	5.5387(3)	5.5429(1)	5.5777(1)	5.5899(1)	5.5987(1)	
Atom sites	c (Å)	13.3436(16)	13.5501(22)	13.4090(9)	13.7472(45)	13.39797(6)	13.56587(7)	13.4090(9)	13.4328(1)	13.5806(3)	13.6279(3)	13.6611(3)
La: $6c$ in	x	0	0	0	0	0	0	0	0	0	0	0
$R\bar{3}c$; $6a$ in	y	0	0	0	0	0	0	0	0	0	0	0
$R3c$	z	1/4	1/4	0.2507(12)	0.2422(15)	0.2508(3)	0.2508(3)	1/4	1/4	1/4	1/4	1/4
	B_{iso} (Å ²)	—	—	0.63(7)	3.71(29)	0.66(2)	1.63(3)	0.66(5)	0.86(4)	1.87(6)	2.65(5)*	3.04(6)*
Ga: $6b$ in	x	0	0	0	0	0	0	0	0	0	0	0
$R\bar{3}c$; $6a$ in	y	0	0	0	0	0	0	0	0	0	0	0
$R3c$	z	0	0	0	0	0	0	0	0	0	0	0
	B_{iso} (Å ²)	—	—	0.41(6)	2.27(28)	0.46(2)	1.10(2)	0.43(5)	0.50(4)	1.29(6)	1.75(5)*	2.08(6)*
O: $18e$ in	x	0.445(4)	0.448(4)	0.1158(9)	0.2412(28)	0.1137(2)	0.1224(3)	0.4438(2)	0.5548(2)	0.5497(3)	0.5455(2)	0.5438(3)
$R\bar{3}c$; $18b$	y	0	0	0.3426(16)	0.3905(33)	0.3420(4)	0.3473(4)	0	0	0	0	0
in $R3c$	z	1/4	1/4	0.0775(11)	0.0296(18)	0.0772(2)	0.0747(2)	1/4	1/4	1/4	1/4	1/4
	B_{iso} (Å ²)	—	—	0.93(4)	3.8(19)	0.80(1)	2.05(2)	1.03(4)	1.18(4)	2.61(6)	3.80(6)*	4.9(1)*

¹ X-ray powder diffraction data.² Neutron powder diffraction data.* Calculated from β_{ij} values given in the reference.

stable for CeGaO_3 in the whole temperature range under investigation. The structural parameters of CeGaO_3 at selected temperatures are listed in Table 34. Temperature dependencies of the lattice parameters and cell volume obtained in our study are shown in Figure 55.

The lattice parameters are very close to each other in the whole temperature range. Because of the anisotropy of the thermal expansion, three regions with different ratios of lattice parameters were identified (Figure 55). At low temperatures, the shape of the CeGaO_3 lattice is pseudo-tetragonal ($a_p \approx b_p > c_p$), but its crystal structure remains orthorhombic. With increasing temperature, the relationship of the lattice parameters smoothly changes to $a_p > b_p > c_p$ and above 600 K, it is $a_p > c_p > b_p$. As mentioned above, such cell parameter ratio observed in GdFeO_3 -type perovskites indicates a forthcoming phase transition to a rhombohedral structure. Such a transition was found in CeGaO_3 by means of DTA measurements performed in argon atmosphere (Vasylechko and Senyshyn, 2004). As can be seen in Figure 56, a reversible first-order phase transformation occurs at 1222 K with a temperature hysteresis of ± 7 K. This observation is in good agreement with the earlier reported transition temperature 1253 K in CeGaO_3 (Portnoj and Timofeeva, 1986).

The limitation of equipment used by Vasylechko and Senyshyn (2004) did not allow to collect diffraction data for cerium gallate above 1230 K. However, taking into account that HT modifications of LaGaO_3 and $\text{La}_{1-x}\text{Ce}_x\text{GaO}_3$ solid solutions (see below) adopt the rhombohedral LaAlO_3 -type structure, we may assume with confidence that the same type structure is inherent for the HT modification of CeGaO_3 .

3.2.3 Praseodymium gallate PrGaO_3

The first report about the crystal structure of PrGaO_3 was given by Ruggiero and Ferro (1954), where similar to lanthanum gallate, the 'ideal' perovskite-type structure has been reported. Later, Geller (1957) ascribed the GdFeO_3 structure at RT for praseodymium gallate, which was confirmed by Marezio et al. (1968). The interest in this material was renewed in 1990th because of its possible application as a substrate for HTSC films (Watts et al., 1989; O'Bryan et al., 1990; Sasaura et al., 1990a; Berkstresser et al., 1991; Miyazawa et al., 1993b; Han et al., 1994; Utke et al., 1997). Room- and high-temperature lattice parameters were measured at certain temperatures in the temperature range 300–1270 K and reported in these publications. Besides, some authors mentioned the existence of a possible HT phase transformations in PrGaO_3 . O'Bryan et al. (1990) claimed to observe a second-order transition at 1090 K using DTA and DSC methods. Based on X-ray diffraction experiments and other thermal studies, Sasaura and Miyazawa (1992) supposed the occurrence of a phase transition above 1670 K, presumably from orthorhombic to rhombohedral. Differential thermal analysis performed by Miyazawa et al. (1993b) did not confirm the existence of a second-order transition around 1090 K, which was reported earlier by O'Bryan et al. (1990), but it revealed a first-order-like transition at around 1850 K, very close to the melting temperature. First results on the low-temperature behaviour of PrGaO_3 were reported by Marti et al. (1994) and Podlesnyak et al. (1994). In their publications, lattice,

TABLE 34 Structural parameters of CeGaO₃ at different temperatures

Parameters		Stan et al. (2002) ¹	Vasylechko and Senyshyn (2004) ²	Vasylechko and Senyshyn (2004) ²	Vasylechko and Senyshyn (2004) ²	Vasylechko and Senyshyn (2004) ²
		<i>Pnma</i> (RT)	<i>Pbnm</i> (12 K)	<i>Pbnm</i> (RT)	<i>Pbnm</i> (573 K)	<i>Pbnm</i> (1173 K)
	<i>a</i> (Å)	5.484(1)	5.4856(3)	5.4909(1)	5.5034(6)	5.5406(3)
	<i>b</i> (Å)	7.747(1)	5.4840(3)	5.4856(1)	5.4950(4)	5.5229(3)
Atom: sites	<i>c</i> (Å)	5.490(1)	7.7332(2)	7.7480(2)	7.7727(8)	7.8230(5)
Ce, 4 <i>c</i>	<i>x</i>	0.0276(2)	−0.0050(8)	−0.0038(6)	−0.0061(10)	−0.0084(10)
	<i>y</i>	1/4	0.0285(4)	0.0275(2)	0.0250(4)	0.0188(7)
	<i>z</i>	0.9954(4)	1/4	1/4	1/4	1/4
	<i>B</i> _{iso} (Å ²)	—	0.11(5)	0.43(5)	0.82(4)	0.95(5)
Ga, 4 <i>b</i>	<i>x</i>	1/2	1/2	1/2	1/2	1/2
	<i>y</i>	0	0	0	0	0
	<i>z</i>	0	0	0	0	0
	<i>B</i> _{iso} (Å ²)	—	0.16(8)	0.6(2)	0.70(6)	1.19(9)
O1, 4 <i>c</i>	<i>x</i>	0.490(2)	0.086(5)	0.075(3)	0.082(6)	0.025(11)
	<i>y</i>	1/4	0.489(5)	0.492(2)	0.508(7)	0.458(9)
	<i>z</i>	0.089(2)	1/4	1/4	1/4	1/4
	<i>B</i> _{iso} (Å ²)	—	0.43(2)	1.9(5)	1.6(6)	1.5(10)
O2, 8 <i>d</i>	<i>x</i>	0.281(3)	−0.282(6)	−0.287(3)	−0.289(9)	−0.304(6)
	<i>y</i>	0.032(1)	0.288(6)	0.277(3)	0.294(9)	0.256(9)
	<i>z</i>	0.728(3)	0.040(2)	0.035(2)	0.023(6)	0.051(4)
	<i>B</i> _{iso} (Å ²)	—	0.43(2)	1.7(3)	1.7(5)	1.0(6)

¹ X-ray powder diffraction data.² Synchrotron powder diffraction data.

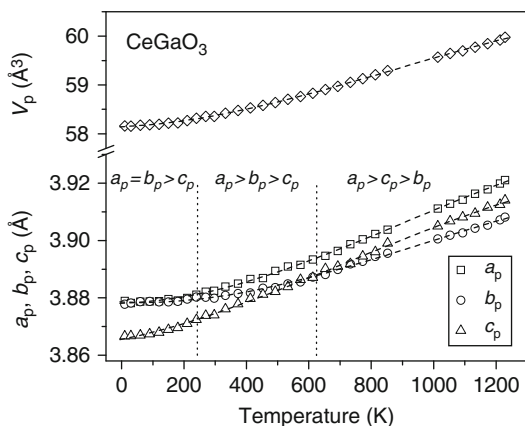


FIGURE 55 Normalized lattice parameters of CeGaO_3 at temperatures 12–1230 K (B) taken from Vasylechko and Senyshyn (2004). The dashed lines are polynomial fits: $a_p(T) = 3.8784(1) [1 + 1.33(3) \times 10^{-8}T^2 - 5.0(2) \times 10^{-12}T^3]$; $b_p(T) = 3.8780(2) [1 + 8.0(3) \times 10^{-9}T^2 - 2.3(3) \times 10^{-12}T^3]$; $c_p(T) = 3.8680(3) [1 + 1.89(6) \times 10^{-8}T^2 - 9.2(5) \times 10^{-12}T^3]$ for the temperature range 12–1230 K. The vertical dotted lines separate tentatively the regions with different ratios of the lattice parameters.

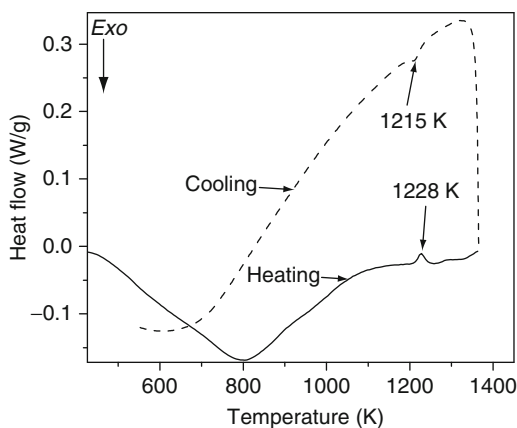


FIGURE 56 DTA data of CeGaO_3 measured on heating and cooling in argon atmosphere.

positional, and displacement parameters of atoms at 12 K and RT were refined based on *in situ* neutron powder diffraction data. A precise examination of the LT behaviour of PrGaO_3 over the temperature range 12–298 K has been carried out using the synchrotron radiation HRPD technique (Vasylechko et al., 2002b; Savvetskii et al., 2003b). Highly anisotropic and non-linear thermal expansion has been revealed in PrGaO_3 . The cell parameter c smoothly increases with temperature, whereas minima are observed at 64 and 166 K for the a and b parameter, respectively (Figure 57A–C). A deviation from the ‘normal’ behaviour is more pronounced for the b -parameter, for which the LT value at 12 K is higher than at

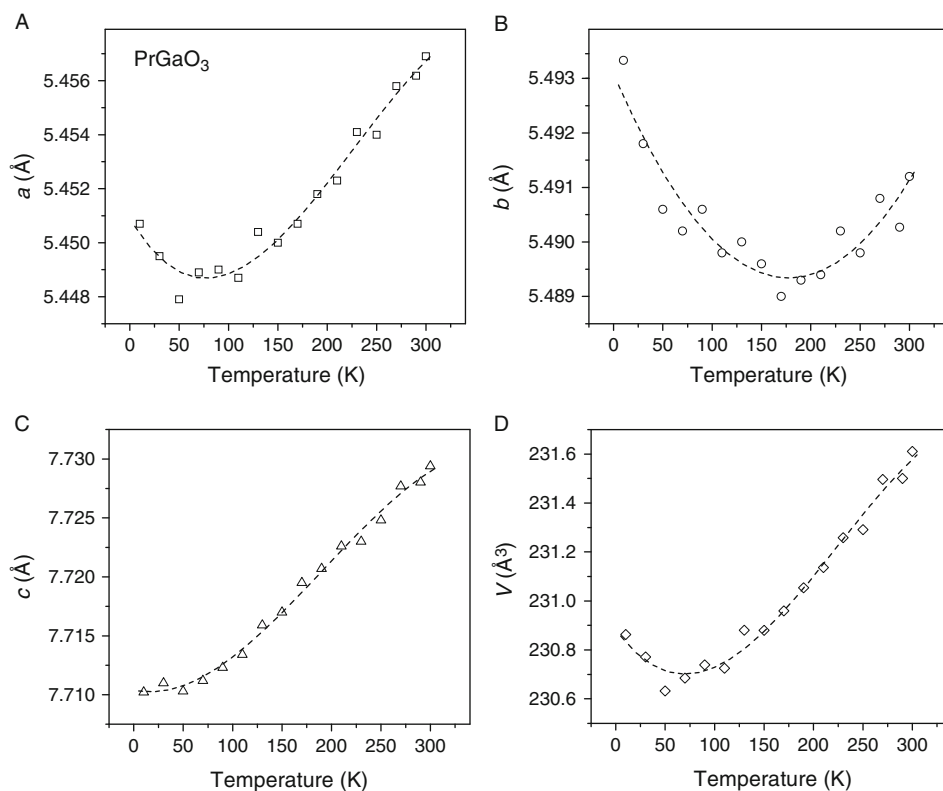


FIGURE 57 Temperature dependencies of lattice parameters (A–C) and cell volume (D) of PrGaO_3 over temperature range 12–300 K. The dashed lines are polynomial fits: $a_p(T) = 5.4509(5) (1 - 10(3) \times 10^{-6}T + 9(2) \times 10^{-8}T^2 - 1.3(4) \times 10^{-10}T^3)$; $b_p(T) = 5.4934(4) (1 - 10(2) \times 10^{-6}T + 4(1) \times 10^{-8}T^2 - 5(1) \times 10^{-11}T^3)$; $c_p(T) = 7.7098(3) (1 + 5.6(4) \times 10^{-8}T^2 - 9(1) \times 10^{-11}T^3)$ for the temperature range 12–300 K.

RT (Figure 57B, Table 35). Note that a similar value of the b -parameter at 12 K and RT was reported by Marti *et al.* (1994); however, the authors did not comment on this observation.

Similar to pure PrGaO_3 , anomalies in thermal expansion were observed in some praseodymium-containing solid solutions of the PrGaO_3 – RGaO_3 systems (see below). Furthermore, the amplitude of the negative thermal expansion in these solid solutions depends directly on the amount of praseodymium. Attempts to model this anomaly via semi-classical simulations (Senyshyn *et al.*, 2005b) were unsuccessful, which may confirm that electronic effects are involved. The separation of the experimental heat capacity into lattice and crystal field components has been found to be a promising approach to explain the negative thermal expansion in praseodymium gallate (Senyshyn *et al.*, 2007). The interaction between phonons and the crystal-field excitation of the ground multiplet of $4f$ elements is assumed to be the reason for the negative thermal expansion in praseodymium gallate. At LT, such interaction results in negative Grüneisen parameters, which increase

TABLE 35 Structural parameters of PrGaO₃ at different temperatures

	Parameters	Marti et al.	Marti et al.	Vasylechko et al.	Vasylechko	This work ⁴	This work ⁴	This work ⁴
		(1994) ¹	(1994) ¹	(2000c, 2005) ²	(2001) ³	12 K	573 K	1173 K
		12 K	298 K	RT	RT	12 K	573 K	1173 K
Atom: sites	<i>a</i> (Å)	5.4526(2)	5.4592(2)	5.4557(1)	5.45596(6)	5.45085(3)	5.46966(4)	5.50925(8)
	<i>b</i> (Å)	5.4947(2)	5.4929(2)	5.4901(1)	5.49035(5)	5.49349(3)	5.49614(4)	5.51976(8)
	<i>c</i> (Å)	7.7121(3)	7.7321(3)	7.7275(2)	7.72782(8)	7.71044(4)	7.74877(6)	7.8020(1)
Pr, 4c	<i>x</i>	−0.0065(9)	−0.0066(10)	−0.00742(2)	−0.0070(3)	−0.0075(3)	−0.0075(3)	−0.0068(5)
	<i>y</i>	−0.0386(4)	−0.0357(5)	0.03522(3)	0.0358(1)	0.0370(2)	0.0327(1)	0.0272(2)
	<i>z</i>	1/4	1/4	1/4	1/4	1/4	1/4	1/4
	<i>B</i> _{iso} (Å ²)	1.90(5)	0.54(5)	0.417(8)	1.07(2)	0.23(4)	1.02(1)	1.78(2)
Ga, 4b	<i>x</i>	1/2	1/2	1/2	1/2	1/2	1/2	1/2
	<i>y</i>	0	0	0	0	0	0	0
	<i>z</i>	0	0	0	0	0	0	0
	<i>B</i> _{iso} (Å ²)	1.50(3)	0.13(3)	0.30(2)	0.95(2)	0.25(7)	0.93(2)	1.37(3)
O1, 4c	<i>x</i>	0.0786(5)	0.0769(6)	0.0758(4)	0.089(3)	0.081(2)	0.080(2)	0.055(4)
	<i>y</i>	0.5164(4)	0.5152(4)	0.4848(4)	0.489(2)	0.477(2)	0.491(2)	0.486(3)
	<i>z</i>	1/4	1/4	1/4	1/4	1/4	1/4	1/4
	<i>B</i> _{iso} (Å ²)	1.66(5)	0.28(6)	0.48(3)	0.29	1.8(5)	1.5(3)	1.3(4)
O2, 8d	<i>x</i>	−0.2123(3)	0.7870(3)	−0.2868(2)	−0.291(2)	−0.295(2)	−0.301(2)	−0.279(4)
	<i>y</i>	0.2109(3)	0.2116(3)	0.2871(2)	0.300(2)	0.300(2)	0.293(2)	0.272(4)
	<i>z</i>	0.0419(2)	0.0420(3)	0.0404(2)	0.037(1)	0.0437(13)	0.0418(14)	0.052(2)
	<i>B</i> _{iso} (Å ²)	1.65(4)	0.30(4)	0.41(2)	0.29	2.6(4)	1.4(2)	2.2(3)

The space group is *Pbmm*.

¹ Neutron powder diffraction data.

² Single crystal synchrotron diffraction data.

³ X-ray powder diffraction data.

⁴ Synchrotron powder diffraction data.

smoothly and at temperatures above 160 K become zero within the experimental uncertainty. We note here that several structural anomalies observed in rare earth aluminates that were reported in the previous section, for example, the phase-transformations in the $\text{CeAlO}_3\text{--}\text{AlO}_3$ pseudo-binary system, the anomalous structural LT behaviour in erbium and thulium aluminates, and the negative thermal expansion of praseodymium gallate may all have the same origin.

Room- and high-temperature structural investigations of PrGaO_3 performed by means of single crystal and powder diffraction using synchrotron radiation have been reported by Vasylechko (2001), Vasylechko *et al.* (2000c, 2002b,c, 2005). For the structure determination, small single-domain crystals were extracted from a Czochralski grown boule. Single crystal diffraction data consisting of 6303 reflections have been collected using a Kappa-diffractometer equipped with a CCD-detector, located at beamline F1, synchrotron laboratory HASYLAB/DESY (Vasylechko *et al.*, 2000c). The analysis of the experimental data allowed for two competing structural models, either space group $Pbnm$ or $Pbn2_1$. The values of agreement factors and the anisotropic displacement parameters of the atoms support the centrosymmetric space group $Pbnm$, which has been chosen for the final description of PrGaO_3 at RT (Vasylechko *et al.*, 2000c, 2005). An *in situ* HT synchrotron powder diffraction study of PrGaO_3 revealed that the structure remains orthorhombic up to 1173 K. The temperature behaviour of the lattice parameters and the cell volume in the temperature range of 12–1173 K are given in Figure 58.

Similar to other GdFeO_3 -type perovskites, the cell parameters change non-linearly and anisotropically with temperature. Maximum and practically equal thermal expansion was observed along the a - and c -directions, whereas the thermal expansion along the b -axis is approximately half of that. Over the whole temperature range under investigation, the normalized lattice parameters of

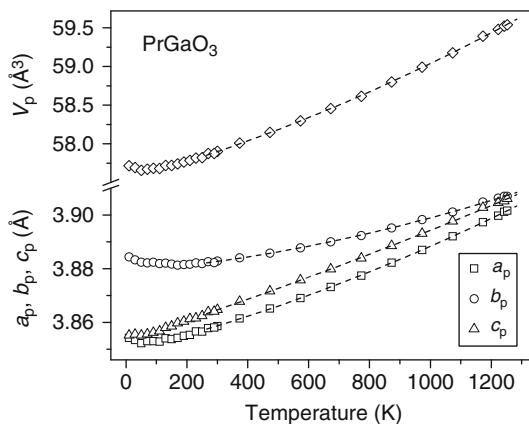


FIGURE 58 Behaviour of normalized lattice parameters and cell volume of PrGaO_3 between 12 and 1250 K. The dashed lines are polynomial fits: $a_p(T) = 3.8492(2) + 2.84(7) \times 10^{-5}T + 1.07(4) \times 10^{-7}T^2$; $b_p(T) = 3.8791(3) + 9.1(9) \times 10^{-6}T + 1.07(6) \times 10^{-8}T^2$; $c_p(T) = 3.8534(3) + 3.6(1) \times 10^{-5}T + 4.6(7) \times 10^{-9}T^2$ for the temperature range 270–1253 K.

PrGaO₃ are $b_p > c_p > a_p$. However, from extrapolating the lattice parameters, a different ratio may be predicted at higher temperatures, in particular $a_p > c_p > b_p$ above 1690 K. The latter happens in lanthanum and cerium gallates just before the $Pbnm-R\bar{3}c$ phase transformation. Therefore, one can expect that this kind of phase transformation occurs in PrGaO₃ at higher temperatures. As shown below, such a phase transition could be predicted near 1856 K.

Analysis of interatomic distances performed by Vasylechko et al. (2005) revealed that increasing temperature leads to a systematic increase of the eight shortest Pr–O bonds, whereas a reduction of the four longer Pr–O distances is observed. From the variation of the Pr–O interatomic distances with temperature, it was concluded that the CN 8 should be chosen for the Pr atoms in the temperature range 12–1000 K, whereas for temperatures above 1000 K, a CN 10 is more realistic. Pronounced anisotropic behaviour has also been observed for the Pr–Pr, Pr–Ga, and Ga–Ga distances. The thermal development of the Ga–Ga bonds reflects the well-known behaviour of the perovskite-like (pseudo-perovskite) lattice, defined as $a_{pc} = \sqrt{(a_0^2 + b_0^2)}/2$ and $c_{pc} = c_0/2$. Due to anisotropic thermal expansion, all Ga–Ga distances become equal near 894 K, hence the values of the pseudo-cubic parameters a_{pc} and c_{pc} also become equal. Nevertheless, the value of the shear angle $\gamma_{pc} = 2 \times \arctg(b_0/a_0)$ (89.81°) deviates from 90° at this temperature.

An almost linear increase of the average bond lengths (PrO)₈, (PrO)₉, (PrO)₁₀, (PrO)₁₂, as well as of the (OO)₈ average distances can be observed with increasing temperature, whereas the average (GaO)₆ distances practically do not change. Such non-uniform expansion of the Pr–O and Ga–O bonds in PrGaO₃ structure causes a decrease of the perovskite structural deformation with increasing temperature, which is also reflected in a steady increase of the observed tolerance factors (Vasylechko et al., 2005).

As it was mentioned above, the ratios of the cation–cation distances $(AB)_{\max}/(AB)_{\min}$ and the average distances $(AA)_6/(BB)_6$ reflects well the degree of deformation in the ABO₃ perovskite structures and can serve to predict the phase transformation in perovskites (Vasylechko et al., 2005). From the extrapolation of the temperature dependence of the (PrPr)₆/(GaGa)₆ average distance ratio, the transition from the orthorhombic to the rhombohedral structure in PrGaO₃ has been estimated to occur at 1856 K. This value agrees very well with the transition temperature of 1850 K detected using DTA (Sasaura et al., 1990a), as well as the value of 1855 K obtained from linear extrapolation of the phase transition temperatures in the La_{1-x}Pr_xGaO₃ solid solution (see below).

3.2.4 Neodymium gallate NdGaO₃

Similar to the rare earth gallates mentioned above, information available in the literature about real crystal structure of NdGaO₃ is contradictory. The discussion has started long time ago when first reports have appeared about perovskite-type neodymium gallate (Ruggiero and Ferro, 1954; Keith and Roy, 1954), where its structure has been described to be cubic. Geller (1957) attributed the crystal structure of NdGaO₃ to GdFeO₃-type structure. The same structural type has

later been used by [Marezio et al. \(1968\)](#) for the entire RGaO_3 series including neodymium gallate. [Brusset et al. \(1967a\)](#) mentioned the cubic structure for NdGaO_3 ($a = 3.86 \pm 0.02 \text{ \AA}$) in a first papers, whereas in another publication ([Brusset et al., 1967b](#)), the structure was reported to be orthorhombic and with the non-centrosymmetric space group $Pbn2_1$, based on the analysis of Patterson function for the cations. One should note that some Nd–O interatomic distances (2.13 and 2.20 \AA) reported in this paper were underestimated and considerably smaller than the sum of the Nd^{3+} and O^{2-} ionic radii. The same structural model was used by [Marti et al. \(1994\)](#). From neutron diffraction data, the authors refined lattice parameters and atomic positions of NdGaO_3 at 12 K and RT in the space group $Pbn2_1$. However, more detailed investigations of the structure using X-ray powder diffractometry ([Ubizskii et al., 1994](#)), Raman and IR spectroscopy ([Savytskii et al., 1997](#)), showed that NdGaO_3 adopts the space group $Pbnm$ at room temperature. Based on the results of X-ray single crystal diffraction and chemical etching experiments, [Marti et al. \(1996\)](#) confirmed the presence of an inversion centre in the NdGaO_3 structure and refined the structure in the centrosymmetric space group $Pbnm$. Based on constant wavelength powder neutron diffraction measurements, it was shown that neodymium gallate orders anti-ferromagnetically at temperatures below 1 K ([Marti et al., 1995](#)).

Neodymium gallate is stable over a wide temperature range without any pronounced discontinuity. Some authors ([O'Bryan et al., 1990](#); [Scheel et al., 1991](#)) described a second-order phase transition at 1120–1220 K that was detected using DTA technique. However, this was not confirmed by either HT X-ray studies ([Utke et al., 1997](#); [Sasaura et al., 1990b](#)) or calorimetric studies ([Miyazawa et al., 1993b](#)).

Studies of dielectric and magnetic properties performed by [Savytskii et al. \(1999\)](#) revealed an anomalous thermal behaviour of neodymium gallate around 180–200 K. In order to study this anomaly, a series of single crystal diffraction experiments using synchrotron radiation was performed at 100 K and RT ([Vasylechko et al., 1998, 2000d](#)). For this purpose, a small single-domain plate-like crystal was extracted from an NdGaO_3 boule grown by the Czochralski method. Sets of 14508 and 17654 Bragg reflections were collected at 100 and 293 K, respectively, using the Kappa-diffractometer at HASYLAB, beamline F1. Two different starting models were tested for both the LT and RT structure. However, the analyses of the results proved the centrosymmetric space group $Pbnm$ for the NdGaO_3 structure at either temperature. Owing to a large number of experimental observations and reasonable statistics, the centrosymmetric model was finally refined using an anharmonic approximation of thermal motions of cations. The analysis revealed that both LT and RT structures differ considerably in the character of the thermal motions of the atoms. Major differences occur in the B_{22} amplitude of the anisotropic displacement tensor of the cations, whereas other parameters remain almost constant. The observed anomalous behaviour indicates that the collective cation motion confined to (001) plane at LT. It was assumed that basically all thermal anomalies observed in the dielectric properties of NdGaO_3 near 200 K are related to a dramatic change in the thermal displacement parameters of the atoms.

LT studies using HRPD and synchrotron radiation ([Senyshyn et al., 2001](#); [Vasylechko et al., 2002b](#); [Savytskii et al., 2003b](#)) confirmed that neodymium gallate

is isostructural with GdFeO_3 in the temperature region 12–300 K and also revealed deviations from the ‘normal’ thermal behaviour of the lattice parameters (Figure 59). HT powder diffraction studies have been performed below 1173 K in Senyshyn et al. 2004a, and below 923 K in Chaix-Pluchery et al. (2005), which confirm the GdFeO_3 -type structure of NdGaO_3 at these temperatures. The structural parameters of NdGaO_3 at different temperatures are listed in Table 36, and the temperature behaviour of the lattice parameters are shown in Figures 59 and 60.

The LT dependencies of the a and c lattice parameter of NdGaO_3 show a classical increase with increasing temperature (Figure 59A and C), whereas for the b -lattice parameter, a ‘sigmoidal’ increase has been observed (Figure 59B). Raman studies of a single crystalline plate of NdGaO_3 show interaction of the A_g phonons and the crystal-field excitations of the $^4I_{9/2}$ ground multiplet of the Nd^{3+} ion, which are insufficient to induce a phase transformation in NdGaO_3 , but are strong enough to cause anomalies of the thermal expansion (Savytskii et al., 2003b). Similar to praseodymium gallate, semi-classical simulations have been performed by Senyshyn et al. 2004a, and they have been found incapable of

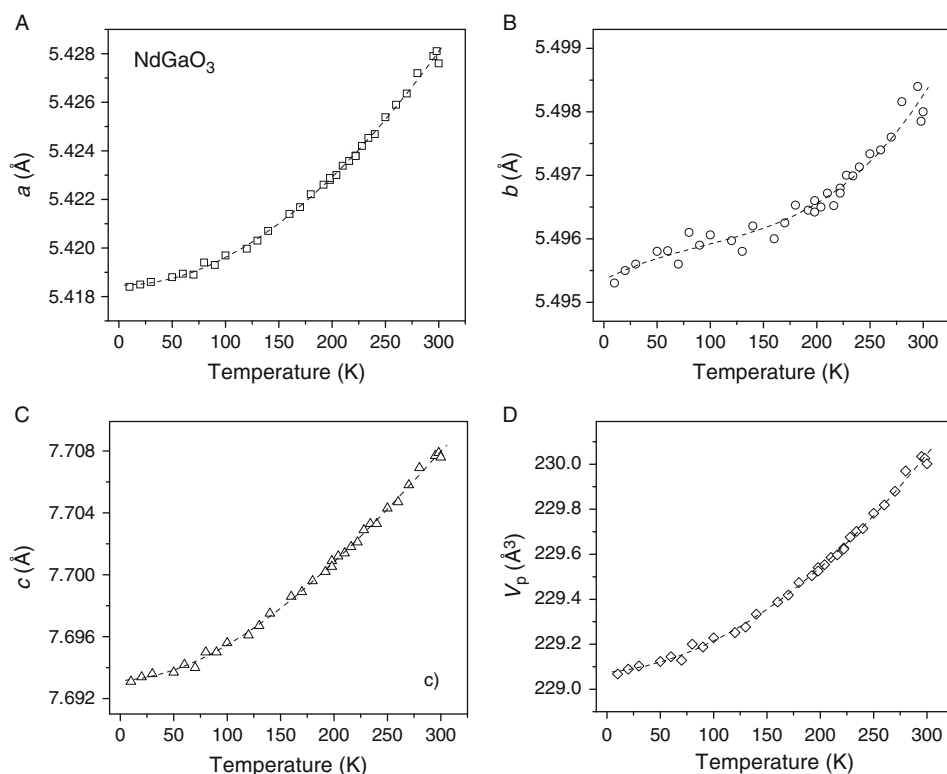


FIGURE 59 Behaviour of lattice parameters (A–C) and cell volume (D) of NdGaO_3 between 12 and 300 K. The dashed lines are polynomial fits: $a_p(T) = 5.41845(5) (1 + 2.23(9) \times 10^{-8}T^2 - 9(2) \times 10^{-12}T^3)$; $b_p(T) = 5.4954(2) (1 + 1.6(4) \times 10^{-6}T - 8.4(5) \times 10^{-9}T^2 + 3(1) \times 10^{-11}T^3)$; $c_p(T) = 7.69237(8) (1 + 3.13(9) \times 10^{-8}T^2 - 3.4(3) \times 10^{-11}T^3)$ for the temperature range 12–300 K.

TABLE 36 Crystallographic data for NdGaO₃ at different temperatures

	Parameters	Brusset et al. (1967b) ¹	Marti et al. (1994) ²	Marti et al. (1994) ²	Ubizskii et al. (1994) ¹	Marti et al. (1996) ²	Sanjuán et al. (1998) ¹	Vasylechko et al. (2000d) ³	Vasylechko et al. (2000d) ³	Savvtskii et al. (2003b) ⁴	Senyshyn et al. (2004a) ⁴	Senyshyn et al. (2004a) ⁴
		<i>Pbn</i> 2 ₁ (RT)	<i>Pbn</i> 2 ₁ (12 K)	<i>Pbn</i> 2 ₁ (RT)	<i>Pbnm</i> (RT)	<i>Pbnm</i> (RT)	<i>Pbnm</i> (RT)	<i>Pbnm</i> (100 K)	<i>Pbnm</i> (RT)	<i>Pbnm</i> (12 K)	<i>Pbnm</i> (573 K)	<i>Pbnm</i> (1173 K)
	<i>a</i> (Å)	5.44(2)	5.4245(2)	5.4333(2)	5.4276(1)	5.4332(2)	5.4264(1)	5.4176(2)	5.4276(1)	5.41842(2)	5.44332(6)	5.48349(8)
	<i>b</i> (Å)	5.50(2)	5.5016(2)	5.5036(2)	5.4979(1)	5.5034(2)	5.4958(1)	5.4952(2)	5.49790(9)	5.49534(2)	5.50500(6)	5.52418(8)
Atom: sites	<i>c</i> (Å)	7.71(2)	7.7018(3)	7.7157(3)	7.7078(2)	7.7155(3)	7.7060(1)	7.6871(3)	7.7078(1)	7.69311(3)	7.7296(1)	7.7832(1)
Nd: 4c in	<i>x</i>	−0.0039(4)	0.0100(4)	0.0094(4)	−0.0105(8)	0.0094(4)	−0.0091(2)	0.49087(2)	0.49092(4)	−0.0100(2)	−0.0078(4)	−0.0073(4)
<i>Pbnm</i> ; 4a	<i>y</i>	0.0013(16)	0.0434(3)	0.0418(3)	0.0414(4)	0.0421(2)	−0.0416(1)	0.04268(2)	0.04142(4)	0.0433(1)	0.0390(2)	0.0333(2)
in <i>Pbn</i> 2 ₁	<i>z</i>	0	0.25	0.25	1/4	1/4	1/4	1/4	1/4	1/4	1/4	1/4
	<i>B</i> _{iso} (Å ²)	0.75	−0.22(3)	0.02(4)	0.42(6)	−0.03(3)	0.17(2)	0.21(1)	0.42(2)	0.10(2)	0.99(3)	1.72(4)
Ga: 4b in	<i>x</i>	0.5076(7)	0.5034(22)	0.5048(19)	1/2	1/2	1/2	0	0	1/2	1/2	1/2
<i>Pbnm</i> ; 4a	<i>y</i>	0.0429(7)	−0.0040(22)	−0.0044(21)	0	0	0	0	0	0	0	0
in <i>Pbn</i> 2 ₁	<i>z</i>	0.2497(23)	0.5063(8)	0.5068(8)	0	0	0	1/2	1/2	0	0	0
	<i>B</i> _{iso} (Å ²)	0.26	0.06(4)	0.13(4)	0.49(11)	0.13(3)	0.30(2)	0.17(1)	0.31(2)	0.32(4)	0.66(5)	1.47(8)
O1: 4c in	<i>x</i>	0.472(25)	0.5829(4)	0.5825(5)	0.087(6)	0.9171(5)	0.0850(17)	0.0803(4)	0.0800(5)	0.088(2)	0.078(2)	0.069(3)
<i>Pbnm</i> ; 4a	<i>y</i>	−0.039(25)	−0.0187(4)	−0.0178(4)	0.486(5)	0.4820(4)	0.5211(15)	0.0181(3)	0.0174(5)	0.484(2)	0.492(2)	0.489(3)
in <i>Pbn</i> 2 ₁	<i>z</i>	0.031(25)	0.2660(9)	0.2640(11)	1/4	1/4	1/4	3/4	3/4	1/4	1/4	1/4
	<i>B</i> _{iso} (Å ²)	2.0	−0.02(3)	0.17(3)	0.7(4)	0.22(4)	0.61(10)	0.31(2)	0.46(3)	0.84(2)	1.0(4)	2.2(6)
O2: 8d in	<i>x</i>	0.274(25)	0.2874(13)	0.2853(13)	0.714(5)	0.2905(3)	0.7860(13)	0.7098(2)	0.7107(3)	−0.2947(13)	−0.292(2)	−0.289(3)
<i>Pbnm</i> ; 4a	<i>y</i>	0.308(25)	0.2881(14)	0.2889(16)	0.283(5)	0.2919(3)	0.2059(12)	0.2092(2)	0.2097(3)	0.2911(13)	0.292(2)	0.290(3)
in <i>Pbn</i> 2 ₁	<i>z</i>	0.317(25)	0.4668(12)	0.4679(13)	0.046(3)	0.4569(2)	0.0436(9)	0.5426(2)	0.5422(2)	0.0432(9)	0.039(2)	0.046(2)
	<i>B</i> _{iso} (Å ²)	2.0	−0.02(3)	0.17(3)	1.4(3)	0.19(4)	0.12(10)	0.33(2)	0.47(2)	0.84(2)	1.1(4)	2.3(5)
O3: 4a in	<i>x</i>	0.271(25)	0.2963(15)	0.2972(14)	−	−	−	−	−	−	−	−
<i>Pbn</i> 2 ₁	<i>y</i>	0.293(25)	0.2976(15)	0.2953(16)	−	−	−	−	−	−	−	−
	<i>z</i>	0.819(25)	0.0538(11)	0.0539(12)	−	−	−	−	−	−	−	−
	<i>B</i> _{iso} (Å ²)	2.0	−0.02(3)	0.17(3)	−	−	−	−	−	−	−	−

¹ X-ray powder diffraction data.² Neutron powder diffraction data.³ Synchrotron single crystal diffraction data.⁴ Synchrotron powder diffraction data.

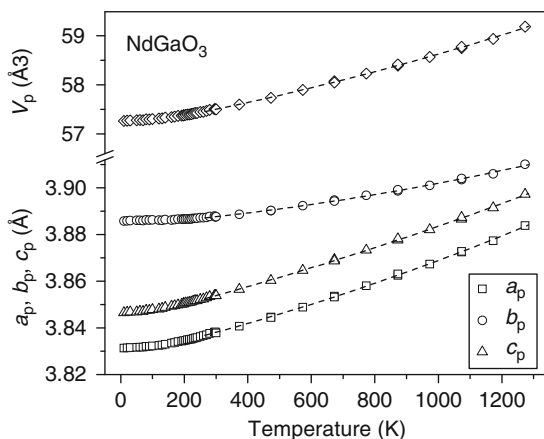


FIGURE 60 Behaviour of normalized lattice parameters and cell volume of NdGaO_3 between 12 and 1250 K. The dashed lines are polynomial fits: $a_p(T) = 3.8340(3) [1 + 1.42(5) \times 10^{-8}T^2 - 5.1(4) \times 10^{-12}T^3]$; $b_p(T) = 3.8860(2) [1 + 5.7(3) \times 10^{-9}T^2 - 1.6(2) \times 10^{-12}T^3]$; $c_p(T) = 3.8498(3) [1 + 1.43(5) \times 10^{-8}T^2 - 5.4(4) \times 10^{-12}T^3]$ for the temperature range 270–1273 K.

reproducing the ‘sigmoidal’ behaviour of NdGaO_3 lattice parameters together with anomalies of the thermal vibrations. This may indicate that electronic effects are involved on the non-classical behaviour.

The LT anomalies in the thermal behaviour of ErAlO_3 and TmAlO_3 mentioned above enable us to draw some parallels with perovskite-type praseodymium and neodymium gallates. Both pairs of elements, namely Pr and Nd, and Er and Tm, are the elements with an open f -shell, which splits under the influence of crystal field. Their corresponding electronic configurations (either Pr and Nd or Er and Tm) differ only by one electron in the $4f$ -shell. For PrGaO_3 and ErAlO_3 , negative thermal expansion has been reported, whereas for NdGaO_3 and TmAlO_3 , an unusual ‘sigmoidal’ behaviour of the lattice parameters occurs.

The temperature behaviour of interatomic distances in the NdGaO_3 structure is similar to the above-described behaviour in PrGaO_3 . The increase of eight shortest Nd–O bonds is accompanied with a decrease of four longer bonds (Vasylechko, 2005). The behaviour of the cation–cation distances also reflects a small decrease of the orthorhombic deformation of the perovskite structure with increasing temperature; however, the deformation is more pronounced than in PrGaO_3 . For instance, an equalization of the Ga–Ga distances in the NdGaO_3 structure is observed near 1200 K, which is about 300° higher than in praseodymium gallate. All average distances increase smoothly with rising temperature. From analysis of the thermal behaviour of all structural parameters, it was concluded that NdGaO_3 will remain orthorhombic up to its melting point (Vasylechko, 2005).

3.2.5 Samarium gallate, SmGaO_3 , and heavier rare earth gallates

As mentioned in the introduction of the current section, there are limited data about crystal structure parameters of rare earth gallates with rare earth elements heavier than neodymium. Only structural parameters of GdGaO_3 determined from X-ray

TABLE 37 Crystallographic data for RGaO_3 (R = Pm, Sm, Eu and Gd) perovskites at RT

Parameters		Guitel <i>et al.</i> (1976) ¹	Vasylechko <i>et al.</i> (2002b) ²	Senyshyn <i>et al.</i> (2005b) ³	Senyshyn <i>et al.</i> (2005b) ³	Senyshyn <i>et al.</i> (2005b) ^{3, 4}
		GdGaO ₃	SmGaO ₃	PmGaO ₃	SmGaO ₃	EuGaO ₃
Atom: sites	a (Å)	5.322	5.37809(5)	5.39663	5.37809(5)	5.351
	b (Å)	5.537	5.51661(6)	5.50777	5.51661(6)	5.528
	c (Å)	7.606	7.65501(8)	7.67771	7.65501(8)	7.628
R, 4c	x	0.98530(5)	−0.0131(3)	−0.01121	−0.0131(3)	−0.01377
	y	0.05933(5)	0.0498(2)	0.04765	0.0498(2)	0.05505
	z	1/4	1/4	1/4	1/4	1/4
	B_{iso} (Å ²)	0.455(8)	0.87(3)	—	—	—
Ga, 4b	x	0	1/2	1/2	1/2	1/2
	y	1/2	0	0	0	0
	z	0	0	0	0	0
	B_{iso} (Å ²)	0.42(2)	1.66(5)	—	—	—
O1, 4c	x	0.09502(85)	0.101(2)	0.08544	0.089(2)	0.09151
	y	0.47235(86)	0.448(2)	0.47598	0.474(2)	0.47295
	z	1/4	1/4	1/4	1/4	1/4
	B_{iso} (Å ²)	0.6(1)	1.08(9)	—	—	—
O ₂ , 8d	x	0.69999(57)	−0.318(2)	−0.29291	−0.295(2)	−0.29676
	y	0.29887(60)	0.277(2)	0.28676	0.288(2)	0.28957
	z	0.04913(47)	0.0349(13)	0.04473	0.0459(13)	0.04728
	B_{iso} (Å ²)	0.55(9)	1.08(9)	—	—	—

¹ X-ray single crystal diffraction data.² X-ray powder diffraction data.³ Lattice parameters and/or atomic positions deduced from interpolation.⁴ Lattice parameters from [Marezio *et al.* \(1968\)](#).

single crystal diffraction have been reported by [Guitel *et al.* \(1976\)](#) (Table 37). As a part of investigation of the LaGaO_3 – SmGaO_3 pseudo-binary system (see below), a sample with a nominal composition Sm_2O_3 : Ga_2O_3 has been prepared by [Vasylechko *et al.* \(2000b\)](#). X-ray phase analysis revealed ~57 wt.% of a perovskite phase, ~27 wt.% of a garnet phase, and ~16 wt.% of $\text{Sm}_4\text{Ga}_2\text{O}_9$. The lattice parameters of SmGaO_3 and $\text{Sm}_4\text{Ga}_2\text{O}_9$ have been found to be in good agreement with the literature data ([Marezio *et al.*, 1968](#); [Nicolas *et al.*, 1984](#); [Yamane *et al.*, 1995](#)), whereas for the garnet phase, a pronounced increase of the lattice parameter was observed compared with stoichiometric $\text{Sm}_3\text{Ga}_5\text{O}_{12}$ (12.512 and 12.434 Å, respectively). This can be explained by formation of the $\text{Sm}_3[\text{Sm}_x\text{Ga}_{2-x}]\text{Ga}_5\text{O}_{12}$ solid solution due to a partial substitution of hexacoordinated gallium by samarium ions. According to [Nicolas *et al.* \(1984\)](#), the lattice parameters of the garnet phase in Sm_2O_3 – Ga_2O_3 system vary between 12.432 and 12.500 Å, and the terminal composition of this solid solution is defined as $\text{Sm}_3[\text{Sm}_{0.245}\text{Ga}_{1.755}]\text{Ga}_5\text{O}_{12}$.

The relatively high amount of the perovskite phase in the sample enabled refinement of its crystal structure parameters from X-ray powder diffraction data (Vasylechko et al., 2002b). The obtained structural parameters of SmGaO_3 (Table 37) agree well with those of other RGaO_3 compounds as well as with data obtained for $\text{La}_{1-x}\text{Sm}_x\text{GaO}_3$ solid solutions (see below). For all other RGaO_3 perovskites with R heavier than gadolinium, only lattice parameters are reported in the literature. Therefore, for those compounds that could not be obtained via solid-state synthesis or from the melt, predicted structural parameters may be a useful alternative.

With this goal in mind (prediction of the perovskite structures), Woodward (1997a,b) developed program package POTATO, in which the bond-valence method established by Brown (1978) was combined with Glazer's notation of tilt distortions of perovskites (Glazer, 1972, 1975). However, the large amount of information required as input for calculations (bond distances, octahedral tilt system, as well as magnitudes of octahedra tilt angles) does not make this program easy to use, especially for prediction of novel perovskite materials. It prompted development of another program package that is capable of predicting crystal structures based only on the chemical composition of perovskites, which is known as SPuDS (Structure Prediction Diagnostic Software) (Lufaso and Woodward, 2001).

In order to reproduce structural peculiarities of rare earth gallates, we have simulated the lattice parameters of all RGaO_3 perovskites and compared them with the experimental lattice constants reported by Marezio et al. (1968). Both theoretical and experimental lattice parameters are shown in Figure 61. As it is obvious, the bond-valence model works well for a - and c -parameters, but it does not properly reproduce the experimental behaviour of the b -parameter, experimental values of which go through a maximum near the GdGaO_3 and TbGaO_3 compositions. Furthermore, this method does not reproduce the pseudo-tetragonality of CeGaO_3 nor does it reproduce the lattice parameter ratio $a > b$ of LaGaO_3 . The GII, calculated for different tilt systems, reveals

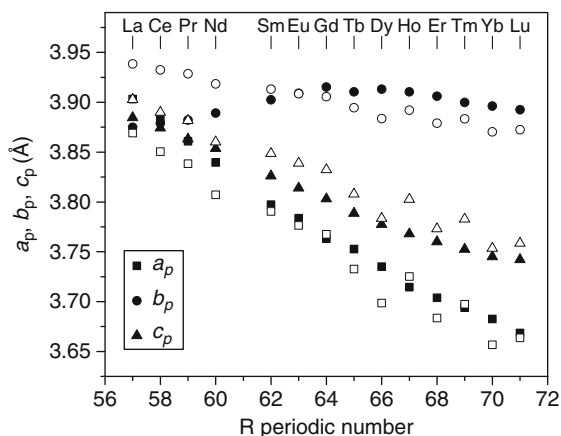


FIGURE 61 Normalized RT lattice parameters for different RGaO_3 perovskites versus atomic number of the rare earth metal. Solid points, experimental data (Marezio et al., 1968); open points, calculated by SPuDS.

minimum values for the $a^-a^-a^-$ tilt system (S.G. $R\bar{3}c$), and the SPuDS algorithm reproduces correctly the experimental lattice parameters for RGaO_3 ($R = \text{Gd-Lu}$).

In order to create structural input into semi-classical simulations of the compounds RGaO_3 ($R = \text{La, Ce, Pr, Nd, Pm, Sm, Eu, and Gd}$), [Senyshyn et al. \(2005b\)](#) estimated the atomic positions in PmGaO_3 , SmGaO_3 , and EuGaO_3 using an interpolation procedure of known structural RT data for rare earth gallates and their solid solutions (see [Section 3.3](#)). The resulting structural parameters for RGaO_3 ($R = \text{Pm, Sm, and Eu}$) are shown in [Table 37](#) together with experimental data for SmGaO_3 and GdGaO_3 .

3.3 Solid solutions based on RGaO_3 compounds

Due to possible application of RGaO_3 perovskites as substrates for HTSC and CMR epitaxial films, the crystal structures of $\text{R}_{1-x}\text{R}'_x\text{GaO}_3$ solid solutions in the $\text{RGaO}_3\text{-R}'\text{GaO}_3$ pseudo-binary systems were described quite often in the literature. Different ratios in the lattice parameters of lanthanum gallate and other RGaO_3 compounds provide a pathway towards obtaining structures with desired lattice parameters by varying the R/R' composition. In this case, materials with metrically tetragonal or even cubic structures could be obtained at certain compositions and temperatures.

Rare earth gallates can also form solid solutions with other RMO_3 perovskites ($M = \text{Al, Fe, Co, Ni, and Mn}$). The interaction of $\text{RGaO}_3\text{-RAIO}_3$ systems with La, Pr, and Nd has been already discussed in [Section 2.3](#). [Kharton et al. \(1997\)](#) mentioned the formation of a continuous solid solution in $\text{LaGaO}_3\text{-LaCoO}_3$ system for the entire range of concentrations. [Chandrasekaran and Azad \(2001\)](#) reported the existence of a solid solution with orthorhombic structure in the $\text{LaGaO}_3\text{-LaFeO}_3$ system. The RT and HT structural behaviour in this system has been investigated by [Mori et al. \(2004\)](#). It was shown that at RT, $\text{LaGa}_{1-x}\text{Fe}_x\text{O}_3$ displays an orthorhombic GdFeO_3 type structure, which transforms into a rhombohedral structure at higher temperatures. The temperature of the phase transition increases linearly with increasing Fe content. Structural parameters of RT and HT modifications of $\text{LaGa}_{1-x}\text{Fe}_x\text{O}_3$ samples with $x = 0.1, 0.25, \text{ and } 0.5$ were refined in space groups $Pbnm$ and $R\bar{3}c$ and given by [Mori et al. \(2004\)](#).

[Bombik et al. \(2005b\)](#) reported that a solid solution with orthorhombic perovskite structure exists in $\text{ErGaO}_3\text{-ErFeO}_3$ system. Crystal structure parameters were refined for $\text{ErFe}_{1-x}\text{Ga}_x\text{O}_3$ samples with $x = 0.03, 0.06, 0.10, \text{ and } 0.15$.

Crystal structures of selected $\text{RGa}_{0.5}\text{M}_{0.5}\text{O}_3$ compositions from the $\text{RGaO}_3\text{-RMO}_3$ systems ($R = \text{La and Nd}$; $M = \text{Mn, Fe, Co, and Ni}$) were studied by [Cussen et al. \(2001\)](#). It was shown that structures belong to the GdFeO_3 -type. No ordering of M-cations in the octahedral sites has been observed.

[Noginova et al. \(2001\)](#) have described the growth of $\text{LaGa}_{1-x}\text{Mn}_x\text{O}_3$ single crystals with $x = 0.005, 0.02, 0.1, \text{ and } 0.5$. No structural parameters were reported in this chapter. An A-cation-deficient perovskite solid solution $\text{La}_{0.9}\text{Ga}_{1-x}\text{Mn}_x\text{O}_y$ ($x = 0\text{-}1$) with rhombohedral structure has been prepared by [Polteva et al. \(2004\)](#). It was shown that the unit cell volume increases with the increasing Mn concentration in the range $x = 0\text{-}0.6$.

Since the discovery of high ionic conductivity in Sr- and Mg-doped LaGaO₃ (LSGM) and other rare earth gallates, a great number of publications have appeared in the literature devoted to different aspects of preparation and characterization of the materials. Aliovalent substitution of cations in the RGaO₃ structures led to the formation of oxygen-deficient R_{1-x}Sr_xGaO_{3-δ} and R_{1-x}Sr_xGa_{1-2x}Mg_{2x}O_{3-δ} compounds, which depending on the composition display different kinds of monoclinic, orthorhombic, rhombohedral, and cubic modifications of perovskite structure. As these materials are not the subject of the present chapter, the readers are referred for publications and reviews, in which structures of these and other substituted rare earth gallates are discussed (Slater et al., 1998a,b; Inaba et al., 2001; Vasylechko et al., 2003d; Yashima et al., 2003; Cheng and Navrotsky, 2004; Shibasaki et al., 2004; Guenter et al., 2005, Yan et al., 2005).

In Section 3.3.1, we summarize available structural information about crystal structures of perovskite-type solid solutions in RGaO₃-R'GaO₃ pseudo-binary systems. The literature data are supplemented by original data presented here for the first time.

3.3.1 LaGaO₃-RGaO₃ (R = Ce-Gd) systems

LaGaO₃ forms solid solutions with the gallates of Ce, Pr, Nd, Sm, Eu, and Gd (Sanjuán et al., 1998; Vasylechko et al., 1999b, 2000b, 2000e, 2000f; Berkowski et al., 2000, 2001; Vasylechko, 2001, 2005). Results of X-ray diffraction analysis and concentration dependencies of lattice parameters show continuous solid solution La_{1-x}R_xGaO₃ in the LaGaO₃-RGaO₃ (R = Ce, Pr, and Nd) pseudo-binary systems (Figure 62A-C). In the systems LaGaO₃-SmGaO₃, LaGaO₃-EuGaO₃, and LaGaO₃-GdGaO₃ (Figure 62D-F), the region of the perovskite phase existence is limited to 80, 60 and 50 at.% of Sm, Eu, and Gd, respectively.

With higher concentrations of the R-component, the formation of R₃Ga₅O₁₂, R₄Ga₂O₉, and (Gd_{1-x}La_x)₂O₃ phases prevails in these systems. The amounts of these phases depend directly on the concentration of Sm, Eu, or Gd. Accordingly, the relative amount of the perovskite phase decreases and no traces of perovskite phase could be detected in samples with nominal compositions Eu₂O₃:Ga₂O₃ and Gd₂O₃:Ga₂O₃. There is a good agreement between the lattice parameters of La_{1-x}Eu_xGaO₃ (0 ≤ x ≤ 0.6) and La_{1-x}Gd_xGaO₃ (0 ≤ x ≤ 0.5), obtained by arc melting and the cell parameters for EuGaO₃ and GdGaO₃ synthesized by thermal decomposition of Eu₃Ga₅O₁₂ and Gd₃Ga₅O₁₂ garnets at 1300 K and a pressure of 45 kbar (Marezio et al., 1968).

The substitution of lanthanum by other rare earth elements in La_{1-x}R_xGaO₃ solid solution leads to a systematic decrease of the cell volume caused by the decrease of the average rare earth ionic radius (the lanthanide contraction). As it was mentioned before, the relationship between lattice parameters varies in the isostructural RGaO₃ perovskites from $a_p > c_p > b_p$ in LaGaO₃ to $a_p > b_p > c_p$ in CeGaO₃ and to $b_p > c_p > a_p$ in other rare earth gallates, RGaO₃. Therefore, in La_{1-x}R_xGaO₃ solid solutions, the lattice parameters *a* and *c* decrease with the increase of R content, whereas the *b* parameter remains almost constant or even increases (Figure 62). Hence, the characteristic feature of the crystal structure of solid solutions existing in the LaGaO₃-RGaO₃ pseudo-binary system is the

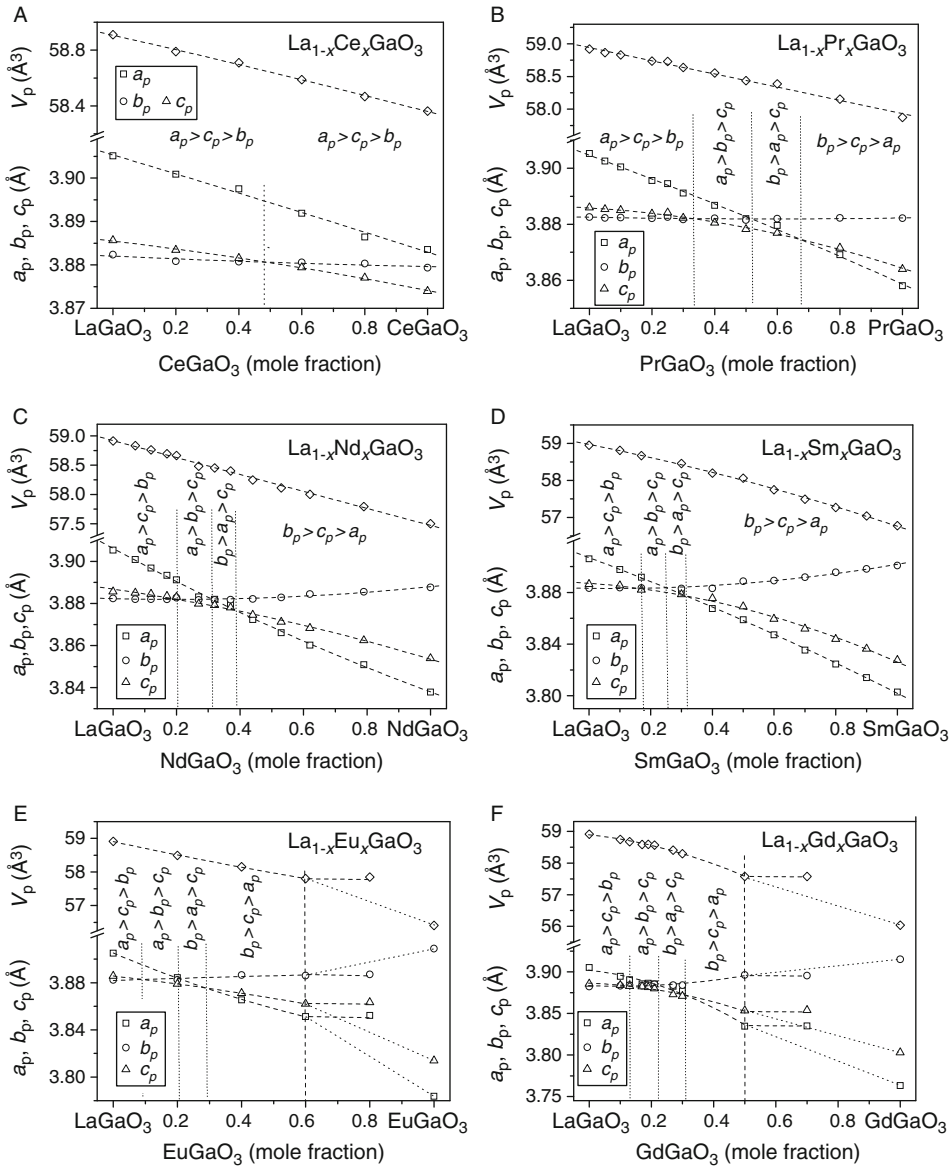


FIGURE 62 RT concentration dependencies of normalized lattice parameters in $\text{La}_{1-x}\text{R}_x\text{GaO}_3$ (R = Ce, Pr, Nd, Sm, Eu, Gd) solid solutions. Lattice parameters for EuGaO_3 and GdGaO_3 are from [Marezio et al. \(1968\)](#). The vertical dotted lines separate the regions with different ratios of the lattice parameters. The dashed lines are polynomial fits: (A) $\text{La}_{1-x}\text{Ce}_x\text{GaO}_3$ ($x = 0.0-1.0$) $a_p(x) = 3.9053(8) - 2.2(4) \times 10^{-2} \times x + 7(1) \times 10^{-4} \times x^2$; $b_p(x) = 3.8820(4) - 3(1) \times 10^{-3} \times x + 9(2) \times 10^{-4} \times x^2$; $c_p(x) = 3.8855(2) - 9(1) \times 10^{-3} \times x - 2.7(9) \times 10^{-3} \times x^2$; (B) $\text{La}_{1-x}\text{Pr}_x\text{GaO}_3$ ($x = 0.0-1.0$) $a_p(x) = 3.9047(5) - 4.2(3) \times 10^{-2} \times x - 5(3) \times 10^{-3} \times x^2$; $b_p(x) = 3.8825(2) - 2.2(6) \times 10^{-3} \times x + 1.9(5) \times 10^{-3} \times x^2$; $c_p(x) = 3.8858(3) - 6(2) \times 10^{-3} \times x - 1.5(2) \times 10^{-2} \times x^2$; (C) $\text{La}_{1-x}\text{Nd}_x\text{GaO}_3$ ($x = 0.0-1.0$) $a_p(x) = 3.9062(7) - 8.1(3) \times 10^{-2} \times x - 1.3(3) \times 10^{-2} \times x^2$; $b_p(x) = 3.8823(3) - 4(1) \times 10^{-3} \times x + 9(1) \times 10^{-3} \times x^2$;

presence of four regions with different relations of the a_p , b_p , and c_p lattice parameters. For some $\text{La}_{1-x}\text{R}_x\text{GaO}_3$ solid solutions, nearly the same lattice parameters have been observed at certain compositions (Figure 62B–F). The shapes of the unit cells are very close to tetragonal or cubic, but the crystal structures are orthorhombic. Using the HRPD technique in conjunction with SR led to resolving very weak splitting of Bragg reflections as well as confirmed orthorhombic distortions in these compounds (Vasylechko et al., 2001a, 2001b). Concentration dependencies of interatomic distances in $\text{La}_{1-x}\text{R}_x\text{GaO}_3$ solid solutions (see, e.g., Figure 63A–F) show a continuous change between LaGaO_3 and RGaO_3 structures as well as a systematic increase of the structural deformation when the R content increases. The latter is also detected as the increase of the interatomic distances ratio, the decrease of observed tolerance factors, and the increase of bond strain within the polyhedra (Vasylechko, 2005).

An increasing deformation of $\text{La}_{1-x}\text{R}_x\text{GaO}_3$ perovskite structure when La is substituted by other rare earth cations leads to a shift of the $Pbnm-R\bar{3}c$ phase transformation from 420 K in lanthanum gallate towards higher temperatures. Transition temperatures of the respective transformation in $\text{La}_{1-x}\text{R}_x\text{GaO}_3$ increase linearly with the concentration of R-cations, for example, 1 at.% substitution of La by Ce, Pr, Nd, Sm, or Gd increases the temperature of the $Pbnm-R\bar{3}c$ transformation by 8, 14, 21, 27, and 38 K, respectively (Vasylechko et al., 2001a; Vasylechko, 2005). The relationship between the temperature of structural phase transformations and the deformation of the perovskite structure will be discussed in Section 3.4.

Figure 64 represents examples of the thermal behaviour of $\text{La}_{1-x}\text{R}_x\text{GaO}_3$ solid solutions. The thermal variations of the lattice parameters are shown for $\text{La}_{0.9}\text{Gd}_{0.1}\text{GaO}_3$ (Senyshyn et al., 2002), $\text{La}_{0.4}\text{Ce}_{0.6}\text{GaO}_3$, and $\text{La}_{0.4}\text{Pr}_{0.6}\text{GaO}_3$ (Vasylechko, 2005) where the phase transformations occur at 800, 960, and 1200 K, respectively (Figure 64A–C). For samples with nominal compositions $\text{La}_{0.2}\text{Pr}_{0.8}\text{GaO}_3$, $\text{La}_{0.63}\text{Nd}_{0.37}\text{GaO}_3$, $\text{La}_{0.6}\text{Sm}_{0.4}\text{GaO}_3$, and $\text{La}_{0.6}\text{Eu}_{0.4}\text{GaO}_3$, the crystal structure remains orthorhombic in the temperature range 298–1250 K (Figure 64D–G). A pronounced anisotropy of the thermal expansion has been observed for all studied $\text{La}_{1-x}\text{R}_x\text{GaO}_3$ solid solutions. Similar to lanthanum and cerium gallates, in the vicinity of the phase transitions, the lattice parameters are $a_p > c_p > b_p$ for $\text{La}_{0.9}\text{Gd}_{0.1}\text{GaO}_3$, $\text{La}_{0.4}\text{Ce}_{0.6}\text{GaO}_3$, and $\text{La}_{0.4}\text{Pr}_{0.6}\text{GaO}_3$ (Figure 64A–C). Solid solutions of $\text{La}_{0.2}\text{Pr}_{0.8}\text{GaO}_3$ and $\text{La}_{0.63}\text{Nd}_{0.37}\text{GaO}_3$ (Figure 64D and E) have parameters $a_p > c_p > b_p$. Therefore, one can expect the $Pbnm-R\bar{3}c$ transformation in these materials to occur above 1250 K.

The thermal behaviour of the structural parameters of $\text{La}_{0.4}\text{Pr}_{0.6}\text{GaO}_3$ and $\text{La}_{0.2}\text{Pr}_{0.8}\text{GaO}_3$ solid solutions (Figure 64C and D) has been studied both by

$$c_p(x) = 3.8868(5) - 2.2(3) \times 10^{-3} \times x - 1.2(3) \times 10^{-3} \times x^2; \text{ (D) } \text{La}_{1-x}\text{Sm}_x\text{GaO}_3 \text{ (} x = 0.0\text{--}1.0) a_p(x) = 3.907(1) - 9.0(5) \times 10^{-2} \times x - 1.5(5) \times 10^{-2} \times x^2; b_p(x) = 3.8832(9) - 3(1) \times 10^{-3} \times x + 2.2(4) \times 10^{-2} \times x^2; c_p(x) = 3.887(1) - 1.7(5) \times 10^{-2} \times x - 4.4(5) \times 10^{-2} \times x^2; \text{ (E) } \text{La}_{1-x}\text{Eu}_x\text{GaO}_3 \text{ (} x = 0.0\text{--}0.6) a_p(x) = 3.9053(6) - 1.15(5) \times 10^{-1} \times x + 4.1(8) \times 10^{-2} \times x^2; b_p(x) = 3.882(2) - 1.0(4) \times 10^{-2} \times x - 3.2(6) \times 10^{-3} \times x^2; c_p(x) = 3.88566(3) - 3.08(3) \times 10^{-2} \times x - 1.41(4) \times 10^{-2} \times x^2; \text{ (F) } \text{La}_{1-x}\text{Gd}_x\text{GaO}_3 \text{ (} x = 0.0\text{--}0.5) a_p(x) = 3.902(3) - 4(3) \times 10^{-2} \times x - 1.8(5) \times 10^{-1} \times x^2; b_p(x) = 3.883(1) - 1.4(9) \times 10^{-2} \times x - 8(2) \times 10^{-2} \times x^2; c_p(x) = 3.887(1) - 1.3(8) \times 10^{-2} \times x - 1.1(2) \times 10^{-1} \times x^2.$$

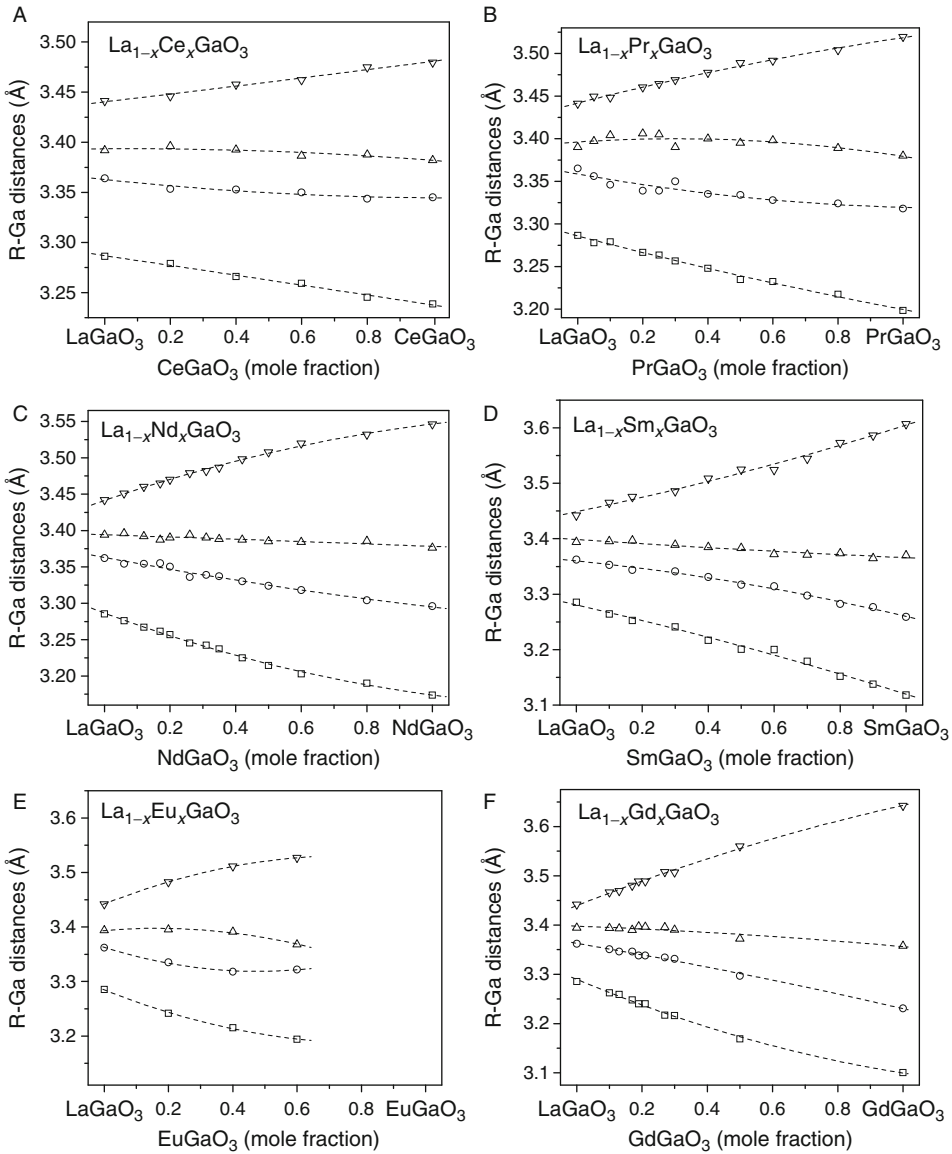


FIGURE 63 RT concentration dependencies of interatomic distances R–Ga in $\text{La}_{1-x}\text{R}_x\text{GaO}_3$ (R=Ce, Pr, Nd, Sm, Eu, Gd) solid solutions.

neutron powder diffraction (Aleksiyko *et al.*, 2001) and by HRPD and SR (Senyshyn *et al.*, 2003; Vasylechko, 2005). Similar as in praseodymium gallate, structural anomalies (negative thermal expansion) have been observed in both Pr-containing solid solutions. The degree of the negative thermal expansion depends on the praseodymium content, that is the anomaly decreases with increasing lanthanum content and disappears in lanthanum gallate. Refined structural

parameters of $\text{La}_{1-x}\text{R}_x\text{GaO}_3$ solid solutions at RT, as well as their LT and HT modifications are collected in Tables 38–45.

Based on the results of *in situ* diffraction studies, the high-temperature behaviour of phase relations in $\text{LaGaO}_3\text{--RGaO}_3$ pseudo-binary systems has been reconstructed (Vasylechko et al., 2001b, Senyshyn et al., 2003, 2004a). As shown in Figure 65, in $\text{LaGaO}_3\text{--NdGaO}_3$ system at 1073 K, a solid solution with the GdFeO_3 structure is limited to $0.3 < x \leq 1$, whereas in the region $0 < x < 0.3$,

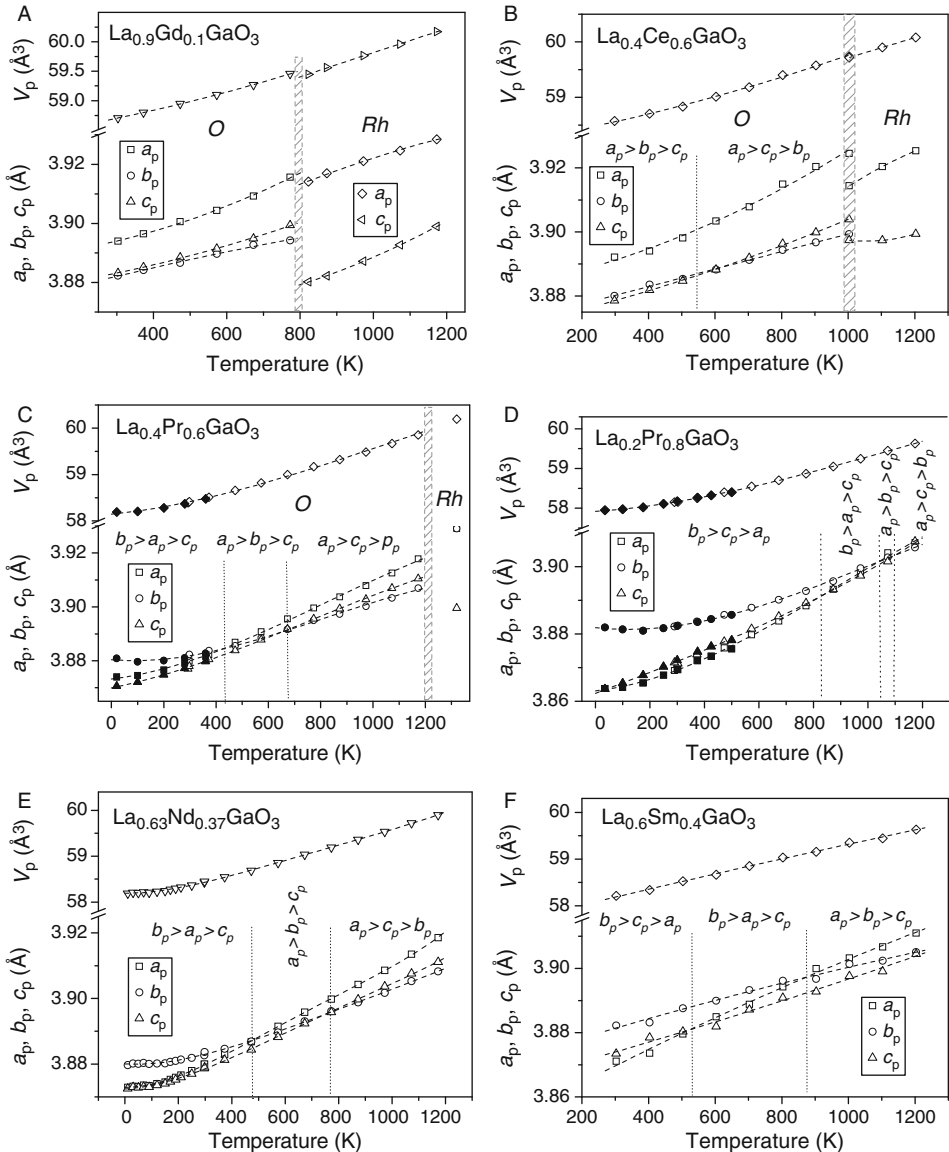


FIGURE 64 Continued

the rhombohedral phase is stable. This is in contrast to the situation at RT, where continuous solid solutions with the GdFeO_3 structure have been observed in the whole range of concentrations (see Figure 63). The existence of a solid solution with the pseudo-cubic shape of an orthorhombic unit cell $a_p = b_p = c_p$ is shifted to a region with higher amount of neodymium.

From *in situ* powder diffraction, DTA/DSC data, and melting temperatures reported in the literature, phase diagrams of the $\text{LaGaO}_3\text{-RGaO}_3$ ($R = \text{Ce, Pr, Nd, and Sm}$) pseudo-binary systems have been constructed (Figure 66A–D).

3.3.2 $\text{LaGaO}_3\text{-RGaO}_3$ ($R = \text{Tb-Er and Y}$) systems

Phase behaviours in the $\text{LaGaO}_3\text{-RGaO}_3$ systems with heavy lanthanides ($R = \text{Tb-Er}$) and yttrium differ considerably from those observed in systems with $R = \text{Ce-Gd}$. The extent of $\text{La}_{1-x}\text{R}_x\text{GaO}_3$ ($R = \text{Tb, Dy, Ho, Er, and Y}$) solid solutions does not exceed $x = 0.06$ (Figure 67A–E). Starting with $x = 0.05\text{--}0.10$, traces of a garnet phase with $(\text{R}_{1-x}\text{La}_x)_3\text{Ga}_5\text{O}_{12}$ compositions appear in the $(1-x)\text{LaGaO}_3\text{-xRGaO}_3$ systems. The amount of garnet phases increases with increasing R content and reaches 25–30 wt.% for samples containing 0.30–0.40 molar fractions of RGaO_3 . The lattice parameters of the perovskite phases in these samples are independent of these compositional changes (Figure 67). This together with the results of our X-ray phase analysis indicates that the limit of the existence of $\text{La}_{1-x}\text{R}_x\text{GaO}_3$ ($R = \text{Tb-Er and Y}$) solid solutions varies between 0.06–0.02 atomic fractions of R-component. Narrow homogeneity regions of the perovskite-type solid solutions in $\text{LaGaO}_3\text{-RGaO}_3$ ($R = \text{Tb-Er and Y}$) have been confirmed by DTA examinations of $\text{La}_{0.95}\text{Ho}_{0.05}\text{GaO}_3$, $\text{La}_{0.95}\text{Er}_{0.05}\text{GaO}_3$, and $\text{La}_{0.95}\text{Y}_{0.05}\text{GaO}_3$. The DTA studies revealed structural phase transformations at 628, 540, and 530 K respectively. Assuming a linear dependence of the $P6mm\text{-}R\bar{3}c$ phase transition temperature on the average radius of R-cation (see Section 3.4), the R^{3+} content in these samples can be estimated to be ca. 5, 3, and 2 at.%, respectively.

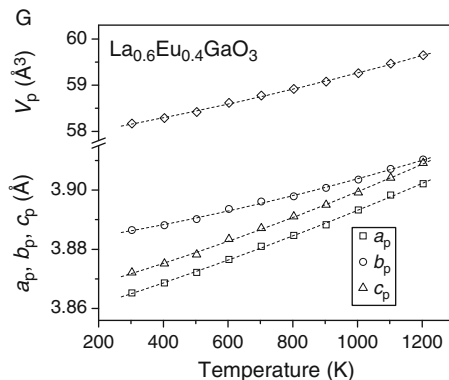


FIGURE 64 Thermal behaviour of lattice parameters and cell volumes for selected $\text{La}_{1-x}\text{R}_x\text{GaO}_3$ solid solutions. Solid points are from neutron powder diffraction (Aleksiyko *et al.*, 2001), open points are from HRPD and SR. The letters O and Rh designate orthorhombic and rhombohedral phases, respectively. The shaded areas correspond to two-phase regions. The vertical dotted lines separate the regions with different ratios of the lattice parameters.

TABLE 38 Structural parameters of $\text{La}_{1-x}\text{Ce}_x\text{GaO}_3$ solid solutions (S.G. $Pbnm$) at RT and HT

	Parameters	$\text{La}_{0.8}\text{Ce}_{0.2}$		$\text{La}_{0.6}\text{Ce}_{0.4}$	$\text{La}_{0.4}\text{Ce}_{0.6}$	$\text{La}_{0.2}\text{Ce}_{0.8}$	$\text{La}_{0.4}\text{Ce}_{0.6}$	
		$Pbnm$ (RT ¹)	$Pbnm$ (RT ¹)	$Pbnm$ (RT ¹)	$Pbnm$ (RT ¹)	$Pbnm$ (503 K ²)	$Pbnm$ (903 K ²)	$R\bar{3}c$ (1203 K ²)
	a (Å)	5.51425(5)	5.51079(5)	5.5029(1)	5.4965(1)	5.5127(2)	5.5446(2)	5.5512(1)
	b (Å)	5.48790(5)	5.48929(6)	5.4878(1)	5.4864(1)	5.4947(2)	5.5111(2)	–
Atom: sites	c (Å)	7.76510(8)	7.76410(9)	7.7591(2)	7.7540(2)	7.7695(3)	7.8001(2)	13.5079(5)
La(Ce): 4c in $Pbnm$; 6c in $R\bar{3}c$	x	–0.0045(2)	–0.0037(2)	–0.0037(6)	–0.0046(5)	–0.0057(8)	–0.0050(10)	0
	y	0.0190(1)	0.0227(1)	0.0221(3)	0.0256(2)	0.0222(4)	0.0158(6)	0
	z	1/4	1/4	1/4	1/4	1/4	1/4	1/4
	B_{iso} (Å ²)	0.91(1)	0.83(1)	0.77(3)	0.79(2)	0.79(3)	1.15(8)	1.37(7)
Ga: 4b in $Pbnm$; 6b in $R\bar{3}c$	x	1/2	1/2	1/2	1/2	1/2	1/2	0
	y	0	0	0	0	0	0	0
	z	0	0	0	0	0	0	0
	B_{iso} (Å ²)	0.96(2)	0.98(2)	0.85(5)	0.68(4)	0.70(5)	1.1(2)	0.86(12)
O1: 4c in $Pbnm$; 18e in $R\bar{3}c$	x	0.0611(12)	0.0614(13)	0.079(3)	0.080(3)	0.068(4)	0.035(6)	0.564(2)
	y	0.4993(12)	0.5002(12)	0.4863	0.510(3)	0.479(6)	0.484(8)	0
	z	1/4	1/4	1/4	1/4	1/4	1/4	1/4
	B_{iso} (Å ²)	0.9(2)	1.5(2)	2.1(5)	1.8(5)	1.5(6)	1.4(8)	1.4(3)
O2: 8d in $Pbnm$	x	–0.2802(14)	–0.269(2)	–0.279(3)	–0.281(4)	–0.284(5)	–0.298(4)	–
	y	0.2803(15)	0.2900(14)	0.284(3)	0.271(4)	0.270(6)	0.298(5)	–
	z	0.0331(8)	0.0424(8)	0.048(2)	0.043(2)	0.047(2)	0.043(3)	–
	B_{iso} (Å ²)	1.14(13)	0.93(11)	2.0(3)	2.1(3)	1.4(4)	2.5(6)	–

¹ X-ray powder diffraction data (Vasylechko, 2005).² Synchrotron powder diffraction data (this work).

TABLE 39 Structural parameters of $\text{La}_{1-x}\text{Pr}_x\text{GaO}_3$ solid solution at RT

	Parameters	$\text{La}_{0.95}\text{Pr}_{0.05}$ ¹	$\text{La}_{0.9}\text{Pr}_{0.1}$ ¹	$\text{La}_{0.2}\text{Pr}_{0.2}$ ¹	$\text{La}_{0.75}\text{Pr}_{0.25}$ ¹	$\text{La}_{0.7}\text{Pr}_{0.3}$ ¹	$\text{La}_{0.6}\text{Pr}_{0.4}$ ¹	$\text{La}_{0.5}\text{Pr}_{0.5}$ ¹	$\text{La}_{0.4}\text{Pr}_{0.6}$ ¹	$\text{La}_{0.8}\text{Pr}_{0.2}$ ¹	$\text{La}_{0.8}\text{Pr}_{0.2}$ ²
	<i>a</i> (Å)	5.51902(6)	5.51604(8)	5.50922(8)	5.50758(7)	5.50290(6)	5.49674(6)	5.48989(8)	5.48657(8)	5.47179(6)	5.4724
	<i>b</i> (Å)	5.49034(7)	5.49052(8)	5.49010(9)	5.49085(8)	5.48952(7)	5.49016(7)	5.48931(7)	5.48993(7)	5.49032(5)	5.4906
Atom: sites	<i>c</i> (Å)	7.7707(1)	7.7700(1)	7.7674(1)	7.7682(1)	7.7645(1)	7.7610(1)	7.75648(8)	7.7538(1)	7.74309(9)	7.7444
La(Pr): 4c	<i>x</i>	−0.0046(3)	−0.0064(3)	−0.0075(2)	−0.0073(3)	−0.0044(3)	−0.0072(3)	−0.0068(3)	−0.0079(2)	−0.0073(3)	−0.0069
	<i>y</i>	0.0192(1)	0.0189(2)	0.0216(1)	0.0224(2)	0.0237(1)	0.0256(2)	0.0284(2)	0.0289(1)	0.0320(2)	0.0308
	<i>z</i>	1/4	1/4	1/4	1/4	1/4	1/4	1/4	1/4	1/4	1/4
	<i>B</i> _{iso} (Å ²)	1.02(2)	1.13(3)	0.96(3)	0.85(3)	0.87(2)	1.05(3)	0.84(3)	1.10(3)	0.77(3)	–
Ga, 4b	<i>x</i>	1/2	1/2	1/2	1/2	1/2	1/2	1/2	1/2	1/2	1/2
	<i>y</i>	0	0	0	0	0	0	0	0	0	0
	<i>z</i>	0	0	0	0	0	0	0	0	0	0
	<i>B</i> _{iso} (Å ²)	0.94(2)	1.02(2)	0.94(2)	0.98(3)	0.81(2)	1.02(2)	0.76(2)	0.94(3)	0.79(9)	–
O1, 4c	<i>x</i>	0.068(3)	0.046(2)	0.061(3)	0.061(4)	0.065(3)	0.069(4)	0.060(4)	0.066(4)	0.078(4)	0.0748
	<i>y</i>	0.498(2)	0.500(2)	0.501(2)	0.491(3)	0.504(2)	0.491(2)	0.487(2)	0.493(2)	0.486(2)	0.4842
	<i>z</i>	1/4	1/4	1/4	1/4	1/4	1/4	1/4	1/4	1/4	1/4
	<i>B</i> _{iso} (Å ²)	1.5(4)	1.4(2)	1.3(2)	1.3(1)	1.4(2)	1.18(14)	1.28(12)	1.2(3)	1.1(4)	–
O2, 8d	<i>x</i>	−0.278(2)	−0.297(2)	−0.298(2)	−0.286(3)	−0.289(2)	−0.292(3)	−0.276(3)	−0.288(3)	−0.281(3)	−0.2841
	<i>y</i>	0.268(2)	0.275(2)	0.269(3)	0.274(4)	0.279(2)	0.299(3)	0.270(3)	0.295(3)	0.288(2)	0.2843
	<i>z</i>	0.0378(12)	0.0424(14)	0.034(2)	0.034(2)	0.034(2)	0.028(2)	0.040(2)	0.027(2)	0.039(2)	0.0397
	<i>B</i> _{iso} (Å ²)	1.1(2)	1.0(4)	1.3(3)	1.2(3)	1.4(4)	1.4(3)	1.8(4)	1.0(2)	1.4(2)	–

¹ X-ray powder diffraction data (Vasylechko, 2001).² Neutron powder diffraction data (Aleksiyko et al., 2001).

TABLE 40 Parameters of LT and HT structures of $\text{La}_{1-x}\text{Pr}_x\text{GaO}_3$ solid solution (S.G. $Pbnm$ and $R\bar{3}c$)

Parameter	$\text{La}_{0.4}\text{Pr}_{0.6}$	$\text{La}_{0.4}\text{Pr}_{0.6}$	$\text{La}_{0.4}\text{Pr}_{0.6}$	$\text{La}_{0.2}\text{Pr}_{0.8}$	$\text{La}_{0.2}\text{Pr}_{0.8}$	$\text{La}_{0.2}\text{Pr}_{0.8}$	$\text{La}_{0.2}\text{Pr}_{0.8}$	$\text{La}_{0.2}\text{Pr}_{0.8}$	$\text{La}_{0.2}\text{Pr}_{0.8}$	$\text{La}_{0.5}\text{Pr}_{0.5}$	$\text{La}_{0.4}\text{Pr}_{0.6}$	$\text{La}_{0.4}\text{Pr}_{0.6}$
	$Pbnm$ (20 K) ¹	$Pbnm$ (100 K) ¹	$Pbnm$ (360 K) ¹	$Pbnm$ (35 K) ¹	$Pbnm$ (100 K) ¹	$Pbnm$ (175 K) ¹	$Pbnm$ (375 K) ¹	$Pbnm$ (500 K) ¹	$Pbnm$ (1070 K) ²	$Pbnm$ (1070 K) ²	$R\bar{3}c$ (1320 K) ²	
a (Å)	5.4787	5.4794	5.4894	5.4642	5.4647	5.4666	5.4759	5.4809	5.5368(2)	5.5395(1)	5.55315(9)	
b (Å)	5.4874	5.4866	5.4911	5.4899	5.4891	5.4885	5.4922	5.4952	5.5199(2)	5.5248(1)	–	
Atom: sites	c (Å)	7.7411	7.7441	7.7596	7.7272	7.7307	7.7355	7.7494	7.7563	7.8140(3)	7.8203(1)	13.4996(3)
La(Pr): 4c in $Pbnm$; 6c in $R\bar{3}c$	x	–0.0073	–0.0074	–0.0078	–0.0079	–0.0068	–0.0071	–0.0073	–0.0072	–0.003(2)	–0.0052(4)	0
	y	0.0293	0.0288	0.0262	0.0335	0.0333	0.0327	0.0298	0.0289	0.0181(9)	0.0187(2)	0
	z	1/4	1/4	1/4	1/4	1/4	1/4	1/4	1/4	1/4	1/4	1/4
	B_{iso} (Å ²)	–	–	–	–	–	–	–	–	1.54(14)	1.66(7)	1.73(5)
Ga: 4b in $Pbnm$; 6b in $R\bar{3}c$	x	1/2	1/2	1/2	1/2	1/2	1/2	1/2	1/2	1/2	1/2	0
	y	0	0	0	0	0	0	0	0	0	0	0
	z	0	0	0	0	0	0	0	0	0	0	0
	B_{iso} (Å ²)	–	–	–	–	–	–	–	–	1.4(3)	1.32(14)	1.78(8)
O1: 4c in $Pbnm$; 18e in $R\bar{3}c$	x	0.074	0.0729	0.0709	0.0765	0.0760	0.0754	0.0746	0.0736	0.093(10)	0.097(3)	0.567(2)
	y	0.4871	0.4874	0.4885	0.4854	0.4848	0.4858	0.4859	0.4866	0.473(11)	0.488(3)	0
	z	1/4	1/4	1/4	1/4	1/4	1/4	1/4	1/4	1/4	1/4	1/4
	B_{iso} (Å ²)	–	–	–	–	–	–	–	–	3.0(19)	2.0(8)	2.7(4)
O2: 8d in $Pbnm$	x	–0.2824	–0.2827	–0.2811	–0.2856	–0.2852	–0.2849	–0.2842	–0.2836	–0.296(10)	–0.288(3)	–
	y	0.2820	0.2821	0.2810	0.2849	0.2850	0.2847	0.2839	0.2834	0.293(10)	0.281(3)	–
	z	0.0390	0.0382	0.0387	0.0397	0.0397	0.03967	0.0392	0.0393	0.041(6)	0.034(2)	–
	B_{iso} (Å ²)	–	–	–	–	–	–	–	–	4.5(15)	1.8(8)	–

¹ Neutron powder diffraction data (Aleksiyko et al., 2001).² X-ray synchrotron powder diffraction data (Vasylychko, 2005).

TABLE 41 Crystal structure of $\text{La}_{1-x}\text{Nd}_x\text{GaO}_3$ solid solution at RT (Vasylychko et al., 2000e, f; Berkowski et al., 2000)

	Parameters	$\text{La}_{0.93}\text{Nd}_{0.07}$	$\text{La}_{0.88}\text{Nd}_{0.12}$	$\text{La}_{0.83}\text{Nd}_{0.17}$	$\text{La}_{0.8}\text{Nd}_{0.2}$	$\text{La}_{0.73}\text{Nd}_{0.27}$	$\text{La}_{0.68}\text{Nd}_{0.32}$	$\text{La}_{0.63}\text{Nd}_{0.37}$	$\text{La}_{0.56}\text{Nd}_{0.44}$	$\text{La}_{0.47}\text{Nd}_{0.53}$	$\text{La}_{0.38}\text{Nd}_{0.62}$	$\text{La}_0\text{Nd}_{0.79}$
	a (Å)	5.51667(6)	5.51092(7)	5.50600(8)	5.50279(8)	5.4916(1)	5.4899(1)	5.48650(9)	5.4764(1)	5.46754(7)	5.45934(8)	5.44594(7)
	b (Å)	5.49006(7)	5.49041(7)	5.48987(8)	5.49054(8)	5.48956(8)	5.48958(9)	5.48968(8)	5.49016(8)	5.49118(6)	5.49363(8)	5.49503(7)
Atom: sites	c (Å)	7.77003(9)	7.76891(9)	7.7665(1)	7.7663(1)	7.7596(1)	7.7584(1)	7.7558(1)	7.7491(1)	7.74241(9)	7.73660(9)	7.72501(9)
La(Nd): 4c	x	-0.0046(3)	-0.0042(2)	-0.0035(4)	-0.0045(3)	-0.0063(3)	-0.0056(3)	-0.0054(3)	-0.0065(3)	0.0067(3)	-0.0066(2)	-0.0088(2)
	y	0.0195(1)	0.0216(2)	0.0227(2)	0.0238(2)	0.0262(2)	0.0267(2)	0.0278(2)	0.0305(1)	0.0327(1)	0.0352(1)	0.0376(1)
	z	1/4	1/4	1/4	1/4	1/4	1/4	1/4	1/4	1/4	1/4	1/4
	B_{iso} (Å ²)	0.60(3)	0.66(3)	0.85(3)	0.79(3)	0.78(3)	0.91(4)	0.61(4)	0.80(4)	0.61(3)	0.74(5)	0.84(1)
Ga, 4b	x	1/2	1/2	1/2	1/2	1/2	1/2	1/2	1/2	1/2	1/2	1/2
	y	0	0	0	0	0	0	0	0	0	0	0
	z	0	0	0	0	0	0	0	0	0	0	0
	B_{iso} (Å ²)	0.56(7)	0.62(8)	0.75(2)	0.64(2)	0.88(2)	0.90(2)	0.64(2)	0.79(3)	0.60(3)	0.67(5)	0.75(3)
O1, 4c	x	0.068(2)	0.070(3)	0.063(2)	0.074(2)	0.074(3)	0.058(2)	0.081(2)	0.071(4)	0.072(4)	0.071(3)	0.069(3)
	y	0.499(2)	0.497(2)	0.497(2)	0.496(2)	0.498(2)	0.496(2)	0.493(2)	0.492(2)	0.498(2)	0.488(2)	0.471(2)
	z	1/4	1/4	1/4	1/4	1/4	1/4	1/4	1/4	1/4	1/4	1/4
	B_{iso} (Å ²)	0.8(2)	1.3(3)	0.7(3)	1.1(3)	1.9(4)	0.8(3)	0.8(3)	0.9(3)	0.7(4)	1.4(4)	1.4(3)
O2, 8d	x	-0.284(2)	-0.277(2)	-0.291(2)	-0.280(2)	-0.284(3)	-0.288(3)	-0.280(3)	-0.281(3)	-0.297(3)	-0.274(2)	-0.291(2)
	y	0.276(2)	0.274(2)	0.273(2)	0.280(2)	0.275(3)	0.290(2)	0.280(2)	0.286(3)	0.284(2)	0.2898(13)	0.294(2)
	z	0.0402(11)	0.0371(12)	0.0363(14)	0.0407(11)	0.034(2)	0.0404(14)	0.0419(15)	0.030(2)	0.035(2)	0.0376(11)	0.034(2)
	B_{iso} (Å ²)	1.2(2)	0.9(2)	1.3(2)	0.9(2)	1.1(2)	0.9(2)	0.7(2)	0.9(2)	1.0(2)	1.1(3)	0.97(13)

Structural parameters for $\text{La}_{1-x}\text{Nd}_x\text{GaO}_3$ ($x = 0.1, 0.2, 0.4, 0.6,$ and 0.75) are also published in Sanjuán et al. (1998).

TABLE 42 Crystal structure of $\text{La}_{1-x}\text{Sm}_x\text{GaO}_3$ solid solutions at RT (Vasylechko et al., 2000b, 2001a)

Parameters		$\text{La}_{0.9}\text{Sm}_{0.1}$	$\text{La}_{0.83}\text{Sm}_{0.17}$	$\text{La}_{0.7}\text{Sm}_{0.3}$	$\text{La}_{0.6}\text{Sm}_{0.4}$	$\text{La}_{0.5}\text{Sm}_{0.5}$	$\text{La}_{0.4}\text{Sm}_{0.6}$	$\text{La}_{0.3}\text{Sm}_{0.7}$	$\text{La}_{0.2}\text{Sm}_{0.8}$	$\text{La}_{0.1}\text{Sm}_{0.9}$
	a (Å)	5.51186(4)	5.5023(1)	5.4911(1)	5.4731(2)	5.45640(8)	5.44398(4)	5.42464(4)	5.40867(3)	5.39354(3)
	b (Å)	5.49240(4)	5.49200(7)	5.4925(1)	5.4931(1)	5.49771(7)	5.50007(4)	5.50373(4)	5.50906(4)	5.51254(4)
Atom: sites	c (Å)	7.76996(6)	7.7658(1)	7.7555(1)	7.7516(2)	7.7351(1)	7.72224(7)	7.70388(6)	7.68781(5)	7.67198(5)
La(Sm):	x	-0.0063(2)	-0.0062(2)	-0.0061(2)	-0.0063(3)	-0.0070(4)	-0.0064(3)	-0.0085(2)	-0.0103(2)	-0.0101(2)
4c	y	0.02236(8)	0.02481(9)	0.0272(1)	0.0327(1)	0.0365(2)	0.0361(1)	0.0415(1)	0.0467(1)	0.0496(1)
	z	1/4	1/4	1/4	1/4	1/4	1/4	1/4	1/4	1/4
	B_{iso} (Å ²)	0.77(1)	0.80(3)	0.81(2)	0.76(2)	0.81(2)	0.73(2)	0.83(2)	0.68(1)	0.66(2)
Ga, 4b	x	1/2	1/2	1/2	1/2	1/2	1/2	1/2	1/2	1/2
	y	0	0	0	0	0	0	0	0	0
	z	0	0	0	0	0	0	0	0	0
	B_{iso} (Å ²)	0.85(1)	0.83(2)	0.90(3)	0.86(2)	0.90(4)	0.87(5)	0.96(3)	0.89(3)	0.91(3)
O1, 4c	x	0.0669(11)	0.0652(15)	0.067(2)	0.053(2)	0.067(2)	0.0674(15)	0.0600(15)	0.0982(13)	0.0735(12)
	y	0.4962(10)	0.4872(11)	0.4746(14)	0.4935(12)	0.4873(13)	0.4874(12)	0.4884(12)	0.4798(12)	0.4741(11)
	z	1/4	1/4	1/4	1/4	1/4	1/4	1/4	1/4	1/4
	B_{iso} (Å ²)	1.3(3)	1.5(2)	1.6(4)	1.14(12)	0.9(2)	1.3(3)	1.0(2)	0.94(4)	1.1(5)
O2, 8d	x	-0.2749(12)	-0.2775(15)	-0.272(2)	-0.278(2)	-0.287(2)	-0.272(2)	-0.2770(13)	-0.2999(10)	-0.2950(11)
	y	0.2724(13)	0.2881(14)	0.298(2)	0.287(2)	0.292(2)	0.2913(12)	0.2894(11)	0.2842(11)	0.2864(11)
	z	0.0389(6)	0.0434(8)	0.0402(9)	0.0352(12)	0.0362(11)	0.0471(9)	0.0302(9)	0.0400(8)	0.0368(7)
	B_{iso} (Å ²)	0.95(9)	1.15(12)	0.9(3)	1.08(14)	0.95(13)	1.0(3)	1.1(3)	0.94(15)	1.3(3)

TABLE 43 Parameters of orthorhombic (S.G. $Pbnm$) and rhombohedral (S.G. $R\bar{3}c$) modifications of $La_{1-x}R_xGaO_3$ ($R = Nd, Sm$) solid solutions at different temperatures, refined from synchrotron powder diffraction data

	Parameter	Savytskii	Vasylechko	Vasylechko	Vasylechko	Vasylechko	Vasylechko	This work	This work	This work	This work
		et al. (2003)	et al. (2001b)	et al. (2001b)	et al. (2001b)	et al. (2001b)	et al. (2001a)				
		$La_{0.63}Nd_{0.37}$	$La_{0.63}Nd_{0.37}$	$La_{0.63}Nd_{0.37}$	$La_{0.73}Nd_{0.27}$	$La_{0.73}Nd_{0.27}$	$La_{0.9}Sm_{0.1}$	$La_{0.6}Sm_{0.4}$	$La_{0.6}Sm_{0.4}$	$La_{0.6}Sm_{0.4}$	$La_{0.6}Sm_{0.4}$
		$Pbnm$						$Pbnm$			$Pbnm$
		$Pbnm$ (10 K)	$Pbnm$ (RT)	(1040 K)	$Pbnm$ (RT)	$R\bar{3}c$ (1140 K)	$R\bar{3}c$ (1040 K)	$Pbnm$ (RT)	(503 K)	$Pbnm$ (903 K)	$Pbnm$ (1203 K)
	a (Å)	5.47707(4)	5.48707(2)	5.53562(7)	5.49308(3)	5.55232(6)	5.55513(6)	5.4745(5)	5.4869(4)	5.5153(4)	5.5310(3)
	b (Å)	5.48670(4)	5.49099(2)	5.52336(7)	5.490458(3)	–	–	5.4903(4)	5.4980(4)	5.5108(3)	5.5226(4)
Atom: sites	c (Å)	7.74500(7)	7.75738(3)	7.8174(1)	7.76158 (4)	13.4806(2)	13.4919(2)	7.7468(7)	7.7603(7)	7.7855(3)	7.8089(5)
La(R): 4c in	x	–0.0065(4)	–0.0064(4)	–0.0058(13)	–0.0056(5)	0	0	–0.0095(8)	–0.0123(7)	–0.002(2)	–0.0074(13)
$Pbnm$; 6c in	y	0.0276(2)	0.0294(2)	0.0168(8)	0.0280(3)	0	0	0.0339(4)	0.0320(5)	0.0260(6)	0.0228(7)
$R\bar{3}c$	z	1/4	1/4	1/4	1/4	1/4	1/4	1/4	1/4	1/4	1/4
	B_{iso} (Å ²)	0.10(5)	0.25(2)	0.98(10)	0.66(5)	1.8(4)	2.11(11)	0.73(4)	0.86(5)	1.04(5)	1.13(6)
Ga: 4b in	x	1/2	1/2	1/2	1/2	0	0	1/2	1/2	1/2	1/2
$Pbnm$; 6b in	y	0	0	0	0	0	0	0	0	0	0
$R\bar{3}c$	z	0	0	0	0	0	0	0	0	0	0
	B_{iso} (Å ²)	0.40(7)	0.68(5)	1.4(2)	1.40(7)	1.1(5)	1.5(2)	0.55(7)	0.84(9)	1.06(9)	1.17(10)
O1: 4c in	x	0.076(3)	0.097(4)	0.080(11)	0.098(4)	0.559(8)	0.560(4)	0.065(8)	0.078(14)	0.060(8)	0.060(9)
$Pbnm$; 18e	y	0.499(2)	0.476(3)	0.467(11)	0.494(4)	0	0	0.464(8)	0.479(8)	0.471(9)	0.495(10)
in $R\bar{3}c$	z	1/4	1/4	1/4	1/4	1/4	1/4	1/4	1/4	1/4	1/4
	B_{iso} (Å ²)	0.669	0.53	2.5(5)	0.79	3.9(21)	4.9(13)	1.9(10)	0.8(16)	1.1(10)	1.3(12)
O2: 8d in	x	–0.294(2)	–0.279(3)	–0.283(10)	–0.279(4)	–	–	–0.290(10)	–0.312(9)	–0.301(12)	–0.310(10)
$Pbnm$	y	0.283(2)	0.286(2)	0.282(10)	0.273(4)	–	–	0.294(9)	0.287(10)	0.304(14)	0.316(11)
	z	0.0452(15)	0.038(2)	0.039(7)	0.040(2)	–	–	0.020(7)	0.004(7)	0.011(7)	0.011(8)
	B_{iso} (Å ²)	0.669	0.53	2.5(5)	0.79	–	–	2.1(6)	0.9(11)	1.8(6)	1.3(15)

TABLE 44 Structural parameters of $\text{La}_{1-x}\text{Eu}_x\text{GaO}_3$ solid solution at RT and HT (S.G. *Pbnm*)

	Parameters	$\text{La}_{0.8}\text{Eu}_{0.2}$	$\text{La}_{0.6}\text{Eu}_{0.4}$	$\text{La}_{0.4}\text{Eu}_{0.6}$	$\text{La}_{0.6}\text{Eu}_{0.4}$		
		RT ¹	RT ¹	RT ¹	503 K ²	903 K ²	1203 K ²
	a (Å)	5.4929(1)	5.4668(1)	5.4466(2)	5.4759(2)	5.4988(3)	5.5184(3)
	b (Å)	5.4898(1)	5.49640(9)	5.4957(2)	5.5012(2)	5.5165(3)	5.5299(2)
Atom: Sites	c (Å)	7.7577(1)	7.7420(2)	7.7242(2)	7.7559(3)	7.7900(4)	7.8182(4)
La(Eu): 4c	x	-0.0067(2)	-0.0082(3)	-0.0059(13)	-0.0069(11)	-0.0087(12)	-0.0090(13)
	y	0.0269(1)	0.0330(1)	0.0370(5)	0.0316(4)	0.0277(6)	0.0225(7)
	z	1/4	1/4	1/4	1/4	1/4	1/4
	B_{iso} (Å ²)	0.71(1)	0.73(2)	0.77(8)	0.81(4)	1.08(6)	1.15(6)
Ga: 4b	x	1/2	1/2	1/2	1/2	1/2	1/2
	y	0	0	0	0	0	0
	z	0	0	0	0	0	0
	B_{iso} (Å ²)	0.70(2)	0.69(2)	0.80(11)	0.59(7)	0.87(10)	1.26(10)
O1: 4c	x	0.0563(14)	0.0661(12)	0.0661(12)	0.099(8)	0.083(8)	0.072(13)
	y	0.5006(10)	0.4912(11)	0.4912(11)	0.486(6)	0.450(10)	0.472(13)
	z	1/4	1/4	1/4	1/4	1/4	1/4
	B_{iso} (Å ²)	2.0(2)	1.1(2)	3.0(7)	1.4(10)	2.4(12)	2.7(22)
O2: 8d	x	-0.295(2)	-0.2892(12)	-0.2892(12)	-0.297(6)	-0.300(8)	-0.295(9)
	y	0.284(2)	0.2746(14)	0.2746(14)	0.286(6)	0.285(9)	0.277(11)
	z	0.0281(9)	0.0314(8)	0.0314(8)	0.037(5)	0.036(7)	0.046(7)
	B_{iso} (Å ²)	1.00(11)	1.70(10)	1.7(4)	0.8(7)	1.2(8)	1.4(12)

¹ X-ray powder diffraction data (Vasylechko, 2005).² Synchrotron powder diffraction data (this work).

TABLE 45 Crystal structure of La_{1-x}Gd_xGaO₃ solid solution at RT and HT (S.G. *Pbnm* and *R3c*)

	Parameters	La _{0.9} Gd _{0.1}	La _{0.87} Gd _{0.13}	La _{0.83} Gd _{0.17}	La _{0.81} Gd _{0.19}	La _{0.79} Gd _{0.21}	La _{0.73} Gd _{0.27}	La _{0.7} Gd _{0.3}	La _{0.5} Gd _{0.5}	La _{0.9} Gd _{0.1}		
		<i>Pbnm</i> (RT) ¹	<i>Pbnm</i> (RT) ¹	<i>Pbnm</i> (RT) ¹	<i>Pbnm</i> (RT) ¹	<i>Pbnm</i> (RT) ¹	<i>Pbnm</i> (RT) ¹	<i>Pbnm</i> (RT) ¹	<i>Pbnm</i> (RT) ¹	<i>Pbnm</i> (RT) ¹	<i>Pbnm</i> (773 K) ²	<i>R3c</i> (823 K) ²
	<i>a</i> (Å)	5.5081(1)	5.5024(2)	5.4962(5)	5.4964(4)	5.4957(3)	5.4891(7)	5.4658(4)	5.4244(2)	5.5372(2)	5.5354(2)	5.5557(2)
	<i>b</i> (Å)	5.4922(1)	5.4927(2)	5.4925(4)	5.4938(3)	5.4946(3)	5.4934(4)	5.4929(4)	5.5101(2)	5.5073(3)	—	—
Atom: sites	<i>c</i> (Å)	7.7687(2)	7.7663(3)	7.7648(5)	7.7624(5)	7.7605(3)	7.7510(5)	7.7637(5)	7.7057(3)	7.7987(4)	13.4415(8)	13.5063(6)
La(Gd): 4c in <i>Pbnm</i> ; 6c in <i>R3c</i>	<i>x</i>	-0.0047(4)	-0.0063(3)	-0.0049(6)	-0.0053(5)	-0.0048(5)	-0.0065(7)	-0.0064(11)	-0.0085(4)	-0.004(3)	0	0
	<i>y</i>	0.0228(2)	0.0235(2)	0.0259(2)	0.0278(2)	0.0275(2)	0.0307(2)	0.0314(3)	0.0425(2)	0.0211(10)	0	0
	<i>z</i>	1/4	1/4	1/4	1/4	1/4	1/4	1/4	1/4	1/4	1/4	1/4
	<i>B</i> _{iso} (Å ²)	0.80(3)	0.68(4)	0.91(8)	0.86(6)	0.68(5)	0.86(8)	0.96(3)	0.80(5)	1.05(11)	1.63(13)	1.72(10)
Ga: 4b in <i>Pbnm</i> ; 6b in <i>R3c</i>	<i>x</i>	1/2	1/2	1/2	1/2	1/2	1/2	1/2	1/2	1/2	0	0
	<i>y</i>	0	0	0	0	0	0	0	0	0	0	0
	<i>z</i>	0	0	0	0	0	0	0	0	0	0	0
	<i>B</i> _{iso} (Å ²)	0.79(3)	0.7(2)	1.0(3)	0.86(4)	0.61(3)	0.87(4)	0.85(6)	0.77(11)	1.1(2)	1.6(2)	1.6(2)
O1: 4c in <i>Pbnm</i> ; 18e in <i>R3c</i>	<i>x</i>	0.063(2)	0.067(3)	0.061(3)	0.059(3)	0.057(4)	0.070(4)	0.075(4)	0.085(3)	0.073(9)	0.441 (6)	0.437(5)
	<i>y</i>	0.504(2)	0.491(2)	0.504(2)	0.505(2)	0.502(3)	0.508(3)	0.497(3)	0.488(2)	0.501(14)	0	0
	<i>z</i>	1/4	1/4	1/4	1/4	1/4	1/4	1/4	1/4	1/4	1/4	1/4
	<i>B</i> _{iso} (Å ²)	1.2(3)	1.7(4)	1.1(4)	1.0(5)	1.9(5)	1.3(5)	1.0(6)	1.1(4)	1.7(12)	3.0(14)	2.3(13)
O2: 8d in <i>Pbnm</i>	<i>x</i>	-0.293(2)	-0.304(2)	-0.288(4)	0.295(5)	0.298(3)	-0.301(4)	0.297(4)	-0.303(2)	-0.270(16)	—	—
	<i>y</i>	0.280(3)	0.274(3)	0.283(4)	-0.287(5)	-0.279(4)	0.295(4)	-0.283(4)	0.300(2)	0.270(16)	—	—
	<i>z</i>	0.0403(14)	0.027(2)	0.036(2)	0.040(2)	0.034(2)	0.035(2)	0.048(2)	0.049(2)	0.034(5)	—	—
	<i>B</i> _{iso} (Å ²)	1.4(2)	1.4(2)	1.5(2)	1.1(3)	1.1(3)	0.6(3)	1.1(3)	1.6(3)	1.7(7)	—	—

¹ X-ray powder diffraction data (Vasylechko et al., 1999b).² Synchrotron powder diffraction data (Senyshyn et al., 2002).

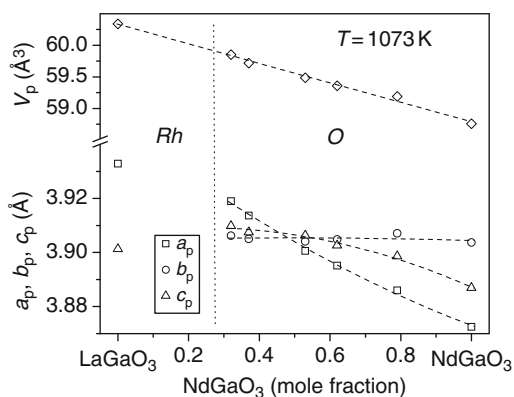


FIGURE 65 Concentration dependencies of the lattice parameters in $\text{La}_{1-x}\text{Nd}_x\text{GaO}_3$ solid solution at 1073 K (Vasylechko, 2005). The dashed lines are polynomial fits: $a_p(x) = 3.8536(4) - 1.3(5) \times 10^{-5} \times x + 1.0(2) \times 10^{-7} \times x^2$; $b_p(x) = 3.8842(2) - 3.0(3) \times 10^{-5} \times x + 8.3(9) \times 10^{-8} \times x^2$; $c_p(x) = 3.8544(3) + 2.1(5) \times 10^{-5} \times x + 5(1) \times 10^{-8} \times x^2$ for $0.3 < x \leq 1$.

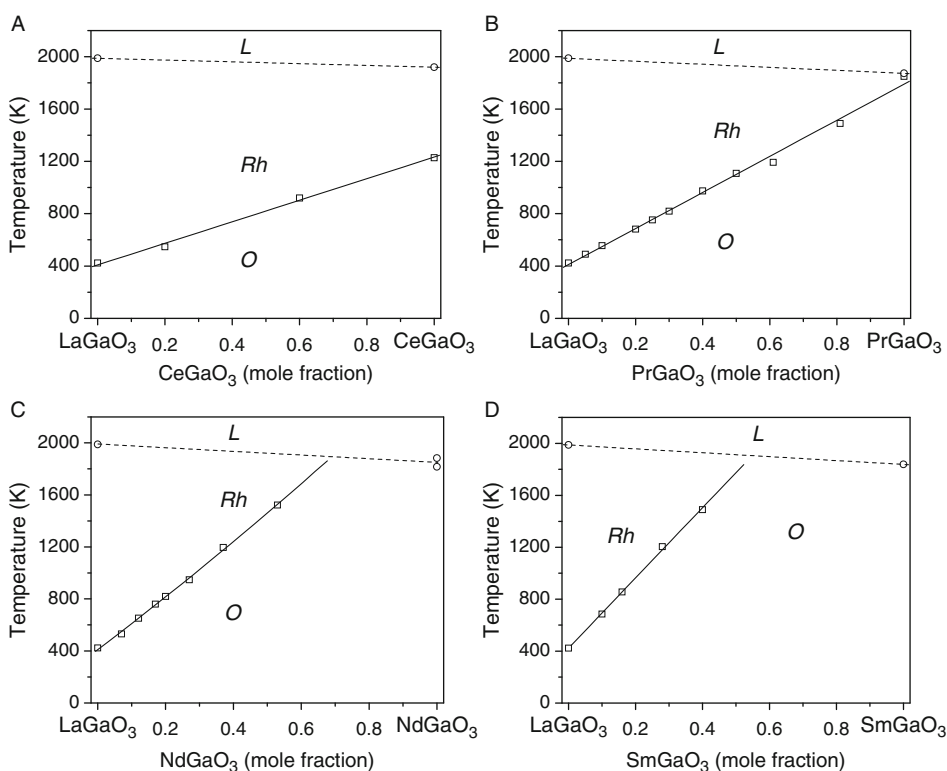


FIGURE 66 Phase diagrams of $\text{LaGaO}_3\text{-R GaO}_3$ ($R = \text{Ce, Pr, Nd, Sm}$) pseudobinary systems according to Vasylechko (2005). The letters L, Rh, and O designate liquid, rhombohedral, and orthorhombic phase fields, respectively. Linear fit of the critical temperatures in (A) $\text{La}_{1-x}\text{Ce}_x\text{GaO}_3$: $T_{\text{Rh-O}}(x) = 408(19) + 825(33) \times x$; (B) $\text{La}_{1-x}\text{Pr}_x\text{GaO}_3$: $T_{\text{Rh-O}}(x) = 411(15) + 1379(31) \times x$; (C) $\text{La}_{1-x}\text{Nd}_x\text{GaO}_3$: $T_{\text{Rh-O}}(x) = 406(18) + 2108(35) \times x$; (D) $\text{La}_{1-x}\text{Sm}_x\text{GaO}_3$: $T_{\text{Rh-O}}(x) = 424(13) + 2703(55) \times x$.

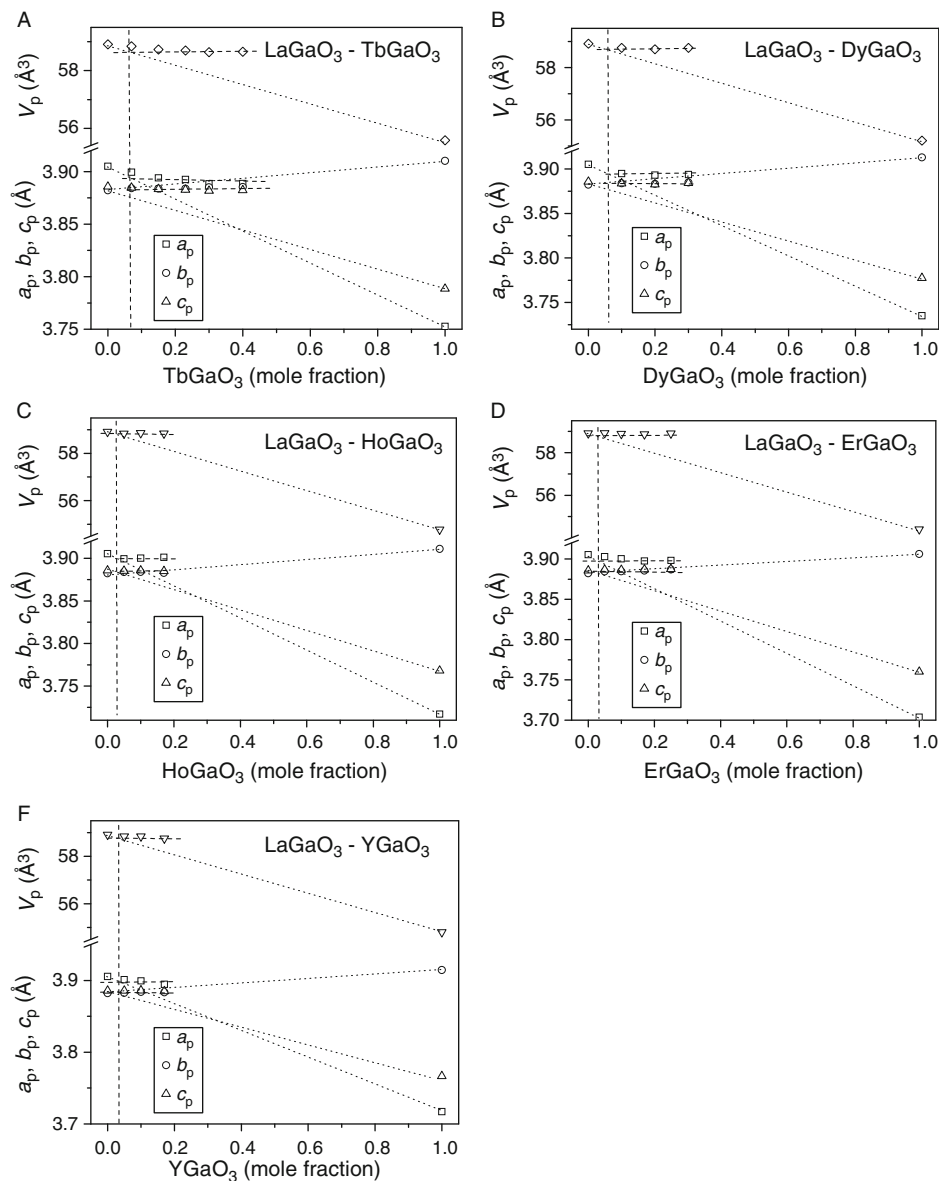


FIGURE 67 Normalized lattice parameters and cell volumes of samples in $\text{LaGaO}_3\text{-RGaO}_3$ ($R = \text{Tb, Dy, Ho, Er, Y}$) systems (Vasylechko, 2005). Lattice parameters of TbGaO_3 , DyGaO_3 , YGaO_3 , HoGaO_3 , and ErGaO_3 are from Marezio *et al.* (1968).

3.3.3 $\text{NdGaO}_3\text{-RGaO}_3$ ($R = \text{Pr-Gd}$) and $\text{PrGaO}_3\text{-RGaO}_3$ ($R = \text{Sm-Gd}$) systems

Data about phases and structural behaviour of $\text{PrGaO}_3\text{-RGaO}_3$ and $\text{NdGaO}_3\text{-RGaO}_3$ are limited. Dabkowska *et al.* (1993) and Aleksiyko *et al.* (2001) described the growth of $\text{Nd}_x\text{Pr}_{1-x}\text{GaO}_3$ and $\text{Nd}_x\text{Sm}_{1-x}\text{GaO}_3$ solid solution crystals.

TABLE 46 Structural parameters of Nd_{1-x}R_xGaO₃ (R = Pr, Sm, Eu, Gd) and Pr_{1-x}R_xGaO₃ (R = Sm, Eu, Gd) solid solutions

	Parameters	Nd _{0.75} Pr _{0.25}	Nd _{0.5} Pr _{0.5}	Nd _{0.25} Pr _{0.75}	Nd _{0.75} Sm _{0.25}	Nd _{0.5} Sm _{0.5}	Nd _{0.75} Sm _{0.25}		Nd _{0.5} Eu _{0.5}	Nd _{0.7} Gd _{0.3}	Pr _{0.5} Sm _{0.5}	Pr _{0.5} Eu _{0.5}	Pr _{0.7} Gd _{0.3}
		RT ¹	RT ¹	RT ¹	RT ¹	RT ¹	85 K ²	1173 K ²	RT ^{3#}	RT ^{3#}	RT ^{3#}	RT ^{3#}	RT ^{3#}
	<i>a</i> (Å)	5.43538(3)	5.44260(3)	5.44952(4)	5.41432(3)	5.40273(6)	5.4046(2)	5.46918(5)	5.38898(7)	5.39919(5)	5.41059(5)	5.39991(8)	5.41515(9)
	<i>b</i> (Å)	5.49590(3)	5.49397(3)	5.49245(4)	5.50183(3)	5.50661(5)	5.4971(2)	5.52593(6)	5.50924(7)	5.51199(4)	5.50076(5)	5.50677(8)	5.50717(9)
Atom: sites	<i>c</i> (Å)	7.71310(4)	7.71809(5)	7.72349(7)	7.69379(4)	7.68118(8)	7.6779(3)	7.76915(8)	7.6681(1)	7.68188(6)	7.68599(7)	7.6771(1)	7.6934(1)
R, 4c	<i>x</i>	-0.0087(2)	-0.0087(2)	-0.0073(3)	-0.0106(2)	-0.0107(3)	-0.0099(5)	-0.0079(6)	-0.0089(2)	-0.0104(2)	-0.0071(3)	-0.0078(4)	-0.0089(3)
	<i>y</i>	0.0414(1)	0.0392(1)	0.0379(1)	0.0450(1)	0.0467(2)	0.0458(3)	0.0362(2)	0.0485(1)	0.0474(1)	0.0433(1)	0.0457(2)	0.0446(1)
	<i>z</i>	1/4	1/4	1/4	1/4	1/4	1/4	1/4	1/4	1/4	1/4	1/4	1/4
	<i>B</i> _{iso} (Å ²)	0.52(2)	0.32(2)	0.29(2)	0.34(2)	0.48(3)	0.27(3)	1.19(2)	0.840(8)	0.85(1)	0.944(8)	0.79(1)	0.88(2)
Ga, 4b	<i>x</i>	1/2	1/2	1/2	1/2	1/2	1/2	1/2	1/2	1/2	1/2	1/2	1/2
	<i>y</i>	0	0	0	0	0	0	0	0	0	0	0	0
	<i>z</i>	0	0	0	0	0	0	0	0	0	0	0	0
	<i>B</i> _{iso} (Å ²)	0.89(5)	0.64(3)	0.58(3)	0.96(5)	0.55(4)	0.47(7)	0.55(4)	0.79(2)	0.71(3)	0.86(2)	0.71(3)	0.55(2)
O1, 4c	<i>x</i>	0.0860(15)	0.0796(15)	0.074(2)	0.0794(13)	0.094(3)	0.085(5)	0.085(3)	0.094(2)	0.085(2)	0.076(2)	0.081(2)	0.091(2)
	<i>y</i>	0.4771(13)	0.4793(13)	0.471(2)	0.4755(12)	0.463(3)	0.488(4)	0.482(3)	0.482(2)	0.4738(15)	0.4813(14)	0.467(2)	0.476(2)
	<i>z</i>	1/4	1/4	1/4	1/4	1/4	1/4	1/4	1/4	1/4	1/4	1/4	1/4
	<i>B</i> _{iso} (Å ²)	0.95(15)	0.86(12)	0.77(13)	0.68(12)	1.4(3)	0.6(5)	3.3(5)	0.7(2)	1.4(2)	0.26(13)	1.1(3)	1.6(2)
O2, 8d	<i>x</i>	-0.2866(12)	-0.2867(13)	-0.272(2)	-0.2878(11)	-0.292(2)	-0.289(4)	-0.291(2)	-0.2925(15)	-0.2975(11)	-0.2866(14)	-0.298(2)	-0.2876(15)
	<i>y</i>	0.2801(12)	0.2837(13)	0.279(2)	0.2811(11)	0.287(2)	0.295(3)	0.295(2)	0.2979(14)	0.2974(11)	0.2996(13)	0.299(2)	0.2903(14)
	<i>z</i>	0.0451(8)	0.0443(8)	0.0498(9)	0.0457(7)	0.0488(15)	0.045(3)	0.040(2)	0.0444(11)	0.0490(8)	0.0479(10)	0.0467(13)	0.0468(10)
	<i>B</i> _{iso} (Å ²)		0.86(12)	0.77(13)	0.68(12)	0.8(2)	0.2(3)	1.0(3)	0.70(13)	0.83(11)	0.82(12)	0.6(2)	0.72(15)

¹ X-ray powder diffraction data (Vasylechko et al., 2002d).² Synchrotron X-ray powder diffraction data (Senyshyn et al., 2004c).³ Synchrotron powder diffraction data (this work).

JCPDS – International Centre for Diffraction data, to be published.

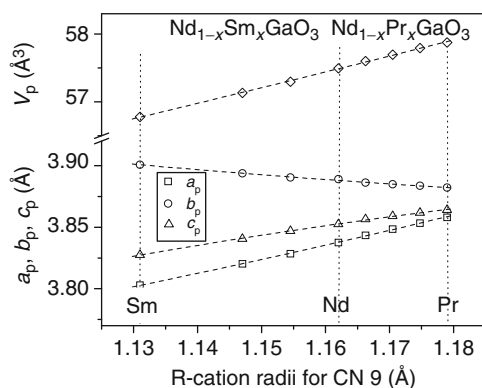


FIGURE 68 Lattice parameters of $\text{Nd}_{1-x}\text{Pr}_x\text{GaO}_3$ and $\text{Nd}_{1-x}\text{Sm}_x\text{GaO}_3$ solid solutions versus average radius of R-cation (Vasylechko *et al.*, 2002d).

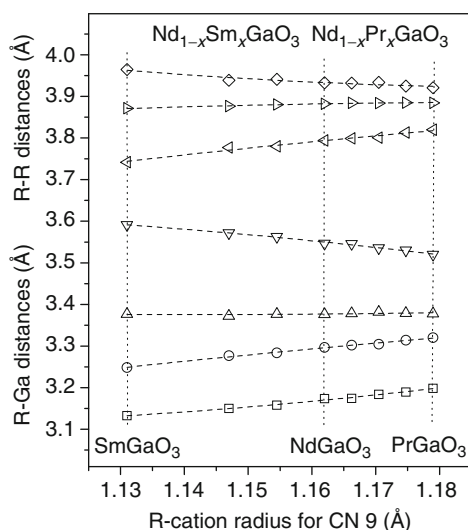


FIGURE 69 Interatomic distances R–R and R–Ga in $\text{Nd}_{1-x}\text{Pr}_x\text{GaO}_3$ and $\text{Nd}_{1-x}\text{Sm}_x\text{GaO}_3$ solid solutions versus average radius of R-cation (Vasylechko, 2005).

Structural peculiarities of solid solutions existing in NdGaO_3 – PrGaO_3 and NdGaO_3 – SmGaO_3 have been analysed by Vasylechko *et al.* (2002d). A continuous solid solution has been found in the NdGaO_3 – PrGaO_3 system, whereas the homogeneity range of the $\text{Nd}_{1-x}\text{Sm}_x\text{GaO}_3$ solid solution is limited to 75–80 at.% of Sm. The GdFeO_3 structure type is typical for all samples studied at RT. Structural parameters are listed in Table 46. Concentration dependencies of the lattice parameters and cell volumes in structures of $\text{Nd}_{1-x}\text{Pr}_x\text{GaO}_3$ and $\text{Nd}_{1-x}\text{Sm}_x\text{GaO}_3$ solid solutions are shown in Figure 68. In order to scale the lattices parameters for both systems, they are given as a function of the average rare earth cation radius $r(\text{R}^{3+})$ for CN 9.

The lattice parameters of $\text{Nd}_{1-x}\text{Pr}_x\text{GaO}_3$ and $\text{Nd}_{1-x}\text{Sm}_x\text{GaO}_3$ solid solutions change smoothly when the average rare earth ionic radius $r(\text{R}^{3+})$ varies from Sm

to Pr through Nd. An increase in $r(R^{3+})$ leads to an increase of the a and c lattice parameters and a decrease of the b lattice parameter. Simultaneously, the cell volume shows a characteristic linear behaviour in accordance with the Vegard's law. The structural data (Table 46) and the concentration dependencies of selected interatomic distances (Figure 69) confirm the decrease of the orthorhombic deformation in $Nd_{1-x}Pr_xGaO_3$ and $Nd_{1-x}Sm_xGaO_3$ solid solutions, when $r(R^{3+})$ increases. Increasing of tolerance factors results in a respective decrease of the $(R_{Ga})_{max}/(R_{Ga})_{min}$ and $(RR)_6/(GaGa)_6$ interatomic distances ratio, as well as bond-length distortions of polyhedra (Vasylechko et al., 2002d).

In order to broaden our knowledge about the structural properties of solid solutions in $NdGaO_3$ – $RGaO_3$ ($R = Eu$ and Gd) and $PrGaO_3$ – $RGaO_3$ ($R = Sm, Eu,$ and Gd) pseudo-binary systems, samples with nominal compositions $Nd_{0.5}R_{0.5}GaO_3$ and $Pr_{0.5}R_{0.5}GaO_3$ have been prepared by solid state reactions and subsequent arc melting (Basyuk and Vasylechko, unpublished data). X-ray phase analysis confirms pure perovskite phases in $Nd_{0.5}Eu_{0.5}GaO_3$, $Pr_{0.5}Sm_{0.5}GaO_3$, and $Pr_{0.5}Eu_{0.5}GaO_3$ specimens, whereas in the samples with nominal composition $Nd_{0.5}Gd_{0.5}GaO_3$ and $Pr_{0.5}Gd_{0.5}GaO_3$, a mixture of perovskite, garnet, and $R_4Ga_2O_9$ phases was detected. From the lattice parameters and cell volumes of the perovskite phases, it may be concluded that the extent of $R_{1-x}Gd_xGaO_3$ solid solutions in Pr and Nd systems does not exceed 0.4 and 0.5 mole fractions of Gd, respectively. Refined values of structural parameters for $Nd_{0.5}Eu_{0.5}GaO_3$, $Pr_{0.5}Sm_{0.5}GaO_3$, and $Pr_{0.5}Eu_{0.5}GaO_3$ are listed in Table 46.

Temperature-resolved structural studies of $Nd_{1-x}Sm_xGaO_3$ solid solutions are reported by Senyshyn et al. (2004c), where the thermal behaviour of $Nd_{0.75}Sm_{0.25}GaO_3$ has been studied in the temperature range 85–1200 K using HRPD and SR as well as theoretical simulations. Isostructural behaviour of $Nd_{0.75}Sm_{0.25}GaO_3$ to $GdFeO_3$ has been confirmed for the whole temperature region. Thermal dependencies of the lattice parameters and cell volume of $Nd_{0.75}Sm_{0.25}GaO_3$ are shown in Figure 70.

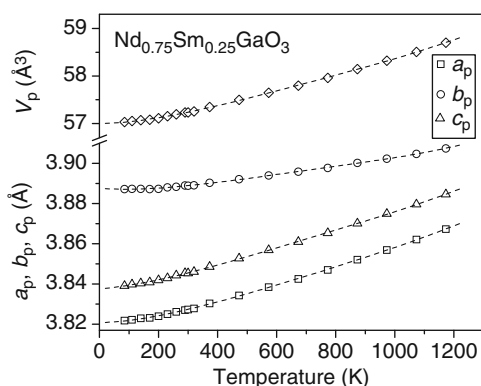


FIGURE 70 Thermal dependencies of the lattice parameters in $Nd_{0.75}Sm_{0.25}GaO_3$. The dashed lines are polynomial fits: $a_p(T) = 5.4040(2) + 1.26(4) \times 10^{-7}T - 1.14(8) \times 10^{-10}T^2 + 4.0(4) \times 10^{-14}T^3$; $b_p(T) = 5.4964(2) + 0.48(4) \times 10^{-7}T - 0.36(8) \times 10^{-10}T^2 + 1.2(4) \times 10^{-14}T^3$; $c_p(T) = 7.6738(3) + 0.87(6) \times 10^{-7}T - 0.7(1) \times 10^{-10}T^2 + 2.3(6) \times 10^{-14}T^3$ for the temperature range 85–1173 K.

3.4 Room temperature crystal structures of RGaO_3 and stoichiometric solid solutions: Patterns of consistence

As it was shown in a previous section, at RT, all rare earth gallates and their stoichiometric solid solutions have an orthorhombically distorted perovskite structure with different ratios of the normalized lattice parameters a_p , b_p , and c_p within the GdFeO_3 type. In LaGaO_3 , $a_p > c_p > b_p$; in CeGaO_3 , $a_p > b_p > c_p$, whereas in other rare earth gallates, this relationship is $b_p > c_p > a_p$. Normalized lattice parameters for all RGaO_3 perovskites and $\text{La}_{1-x}\text{R}_x\text{GaO}_3$ ($\text{R} = \text{Ce}–\text{Gd}$) and $\text{Nd}_{1-x}\text{R}_x\text{GaO}_3$ ($\text{R} = \text{Pr}$ and Sm) solid solutions are presented as a function of the R-cation radius in [Figure 71](#).

From the variation of the lattice parameters, two regions in the rare earth gallate systems (see [Figure 71A](#)) with ionic radii lying either between Lu and Tb(Gd) or between Tb(Gd) and La can be distinguished. For gallates that belong to the Lu–Tb(Gd) group, all of the lattice parameters increase with increasing rare earth ionic radius. In contrast, in the Tb(Gd)–La group, the increase of the a - and c -parameters is accompanied by a decreasing b parameter.

By analogy with the RFeO_3 ferrite series, [Marezio et al. \(1968\)](#) suggested that the anomalous behaviour of the b -parameter in the RGaO_3 family can be associated with anisotropic variations of the nearest R–O distances when the R-cation radius increases. As the size of the R-cation radius increases in the RFeO_3 series, the average R–O distances to the first nearest neighbour oxygen atoms increase, whereas the corresponding values for the second nearest neighbour oxygen atoms decrease. The first effect dominates from Lu to Gd and the b -parameter increases. The b unit cell dimension begins to decrease from Gd to La, which is explained by the second effect becoming dominant in this region ([Marezio et al., 1968, 1970](#)).

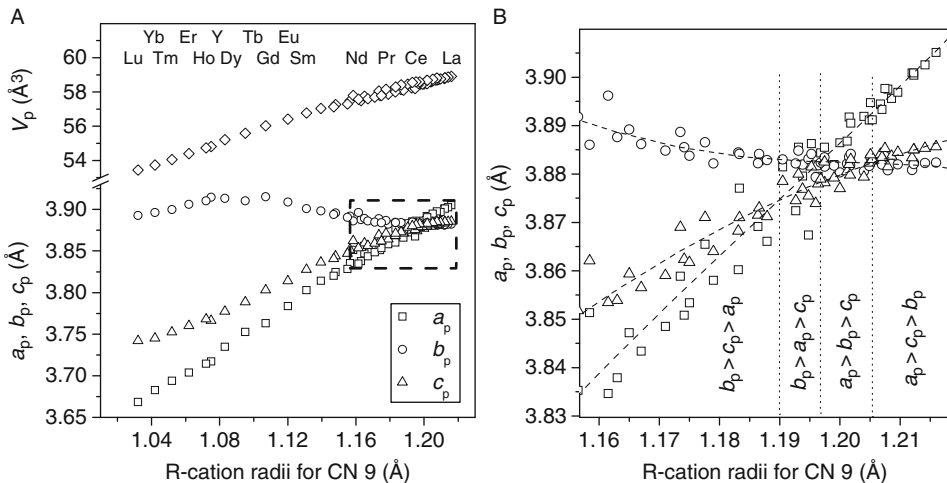


FIGURE 71 Lattice parameters of RGaO_3 phases and $\text{La}_{1-x}\text{R}_x\text{GaO}_3$, $\text{Nd}_{1-x}\text{R}_x\text{GaO}_3$ solid solutions as a function of the average ionic radius of the rare earth cation. Panel (B) is an expanded view of the region highlighted by a rectangular box in (A). Data for RGaO_3 ($\text{R} = \text{Sm}–\text{Lu}$, Y) are from [Marezio et al. \(1968\)](#). The vertical dotted lines separate regions with different ratios of the normalized lattice parameters. The dashed lines are guides for the eye.

The cell volumes increase steadily with increasing R-cation radius, although relative changes in the cell volumes are more pronounced for RGaO_3 perovskites with heavy lanthanides. The lattice parameters of solid solutions $\text{La}_{1-x}\text{R}_x\text{GaO}_3$ and $\text{Nd}_{1-x}\text{R}_x\text{GaO}_3$ are in good agreement with those of the pure RGaO_3 compounds (Figure 71B). An increase of $r(\text{R}^{3+})$ minimizes differences between a_p , b_p , and c_p and the difference practically disappears in CeGaO_3 . A further increase of $r(\text{R}^{3+})$ causes a change in the relationships between the perovskite lattice parameters. For most RGaO_3 compositions, the relationship is $b_p > c_p > a_p$, but for $\text{R}_{1-x}\text{R}'_x\text{GaO}_3$ with ionic radius larger than 1.19 Å, it may be $b_p > a_p > c_p$, $a_p > b_p > c_p$, or $a_p > c_p > b_p$ (Figure 71B).

The variations of individual interatomic distances in the crystal structures of La, Ce, Pr, Nd, Sm, and Gd gallates together with those in $\text{La}_{1-x}\text{R}_x\text{GaO}_3$ ($\text{R} = \text{Ce} - \text{Gd}$) and $\text{Nd}_{1-x}\text{R}_x\text{GaO}_3$ ($\text{R} = \text{Pr}$ and Sm) solid solutions are shown in Figure 72 as functions of the average rare earth ionic radius.

Interatomic distances R–Ga, R–R, Ga–Ga, and R–O show a tendency to merge when the rare earth cation radius $r(\text{R}^{3+})$ increases. The variation of R–O interatomic distances from GdGaO_3 to LaGaO_3 illustrates a redistribution due to the reduction of deformation of the perovskite cell and the impending transformation from the orthorhombic to rhombohedral structure. All RGaO_3 structures,

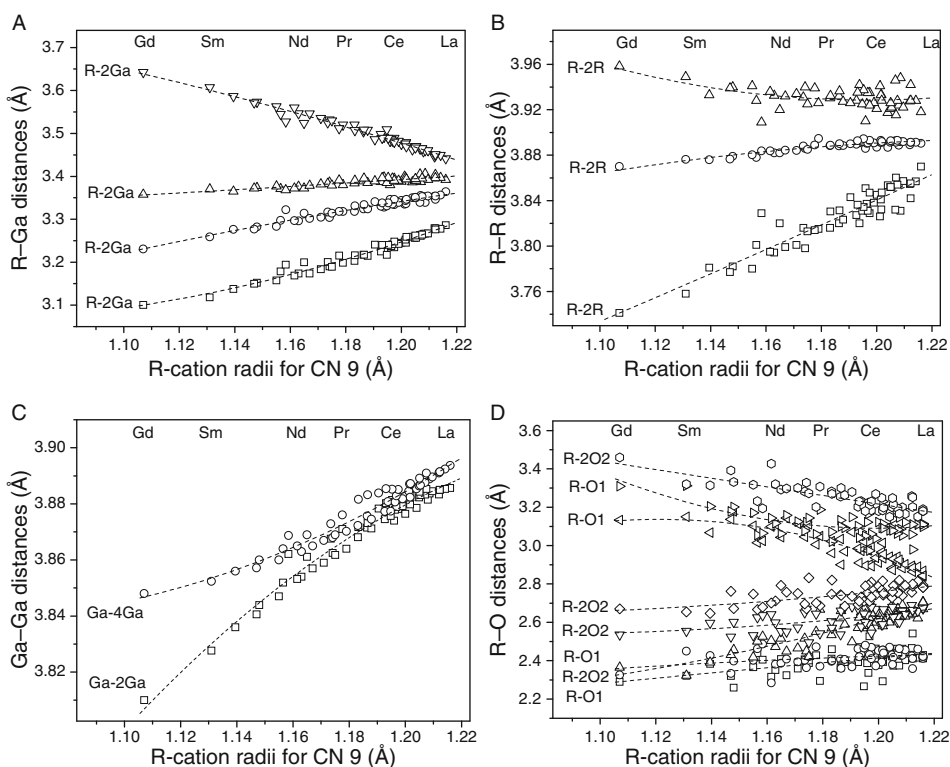


FIGURE 72 Interatomic distances R–Ga (A), R–R (B), Ga–Ga (C), and R–O (D) for RGaO_3 , $\text{La}_{1-x}\text{R}_x\text{GaO}_3$, and $\text{Nd}_{1-x}\text{R}_x\text{GaO}_3$ solid solutions as functions of the average ionic radius of the rare earth cation.

however, remain orthorhombic at RT, though the distribution of the 12 nearest R–O distances in LaGaO₃ and solid solutions with similar R-cation radius is close to the typical R–O bonding (3–6–3) in the rhombohedral perovskite. The lack of structural data for RGaO₃ perovskites with R-cations heavier than Gd does not allow to establish the relations between the interatomic distances and lattice parameter behaviour in the whole RGaO₃ series, similar to the picture given for rare earth ferrites by [Marezio *et al.* \(1968\)](#).

Similar to the above-described RAlO₃ aluminates ([Section 2.4](#)), the average interatomic distances (RR)₆, (RGa)₈, and (RO)_{8–12} in RGaO₃ perovskites increase with increasing $r(\text{R}^{3+})$ ([Figure 73](#)). Simultaneously, some shortenings of the mean distances (GaO)₆ and (OO)₈ occur in the structures of the RGaO₃ series. The observed shortening of interatomic bonds within the octahedra can be

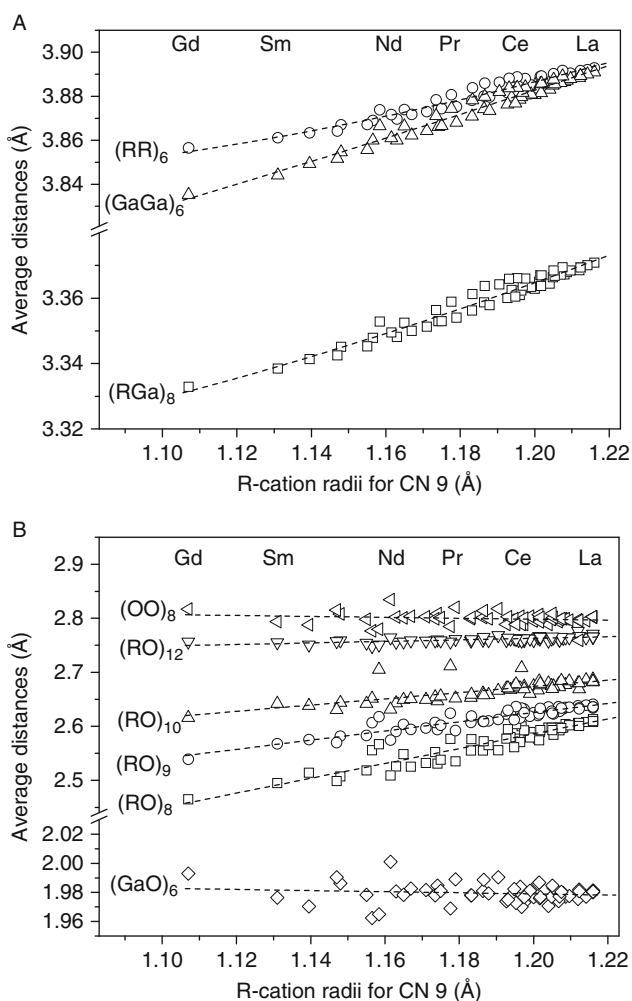


FIGURE 73 Mean interatomic distances (RR)₆, (RGa)₈, and (GaGa)₆ in panel (A) and (RO)_{8–12}, (GaO)₆, and (OO)₈ in panel (B) in RGaO₃ and R_{1-x}R_x'GaO₃ as functions of the average ionic radius of the rare earth cation.

explained by a densification of the crystal structure with increasing R^{3+} ionic radius, when the size of the R^{3+} cation approaches the effective radius of the oxygen anion.

The distribution of the interatomic distances in $RGaO_3$ and their solid solutions indicates a decreasing deformation of the perovskite structure from $GdGaO_3$ to $LaGaO_3$, which is also supported by the decrease of the average angles describing tilts of GaO_6 octahedra (Figure 74).

The perovskite structural deformation parameters, which are presented in Figure 75, show that the deformation steadily decreases in the series of rare earth gallates, when the average ionic radius of the R-cation increases. As one can see in Figure 75A and B, the systematic decrease of the $(RO)_{9-12}$, $(RGa)_8$, $(RR)_6$, and $(GaGa)_6$ bond strain is related to the increase of $r(R^{3+})$. No changes in the $(RO)_8$ and $(AlO)_6$ bond-length distortion is observed. The ratio of the cation/cation distances decreases in the $RGaO_3$ series (Figure 75C), whereas the observed tolerance factors systematically increase (Figure 75D).

3.5 Stability of the perovskite structure in rare earth gallates

$RGaO_3$ perovskites with R^{3+} ionic radii smaller than Nd (1.163 Å) could not be obtained by conventional synthesis routes. Therefore, $R_{1-x}R'_xGaO_3$ solid solutions have limited homogeneity ranges. The extent of solid solutions formed in $LaGaO_3$ – $RGaO_3$ pseudo-binary systems is shown as a function of the difference of the ionic radius between the end members $LaGaO_3$ and $RGaO_3$ (Figure 76). Continuous solid solutions $La_{1-x}R_xGaO_3$ are formed when $\Delta r < 0.06$ Å ($R = Ce$ – Nd). When $0.085 < \Delta r < 0.11$ Å, the homogeneity range of the solid solutions becomes limited to 0.5–0.8 atomic fractions of the R-component, and

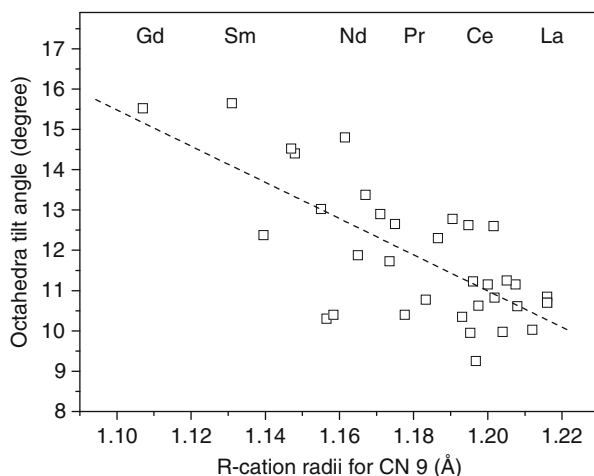


FIGURE 74 Mean octahedral tilt angles at RT in $RGaO_3$ and $R_{1-x}R'_xGaO_3$ versus average rare earth ionic radius. The values are calculated from the Ga–O1–Ga and Ga–O2–Ga interatomic angles in the corresponding structures.

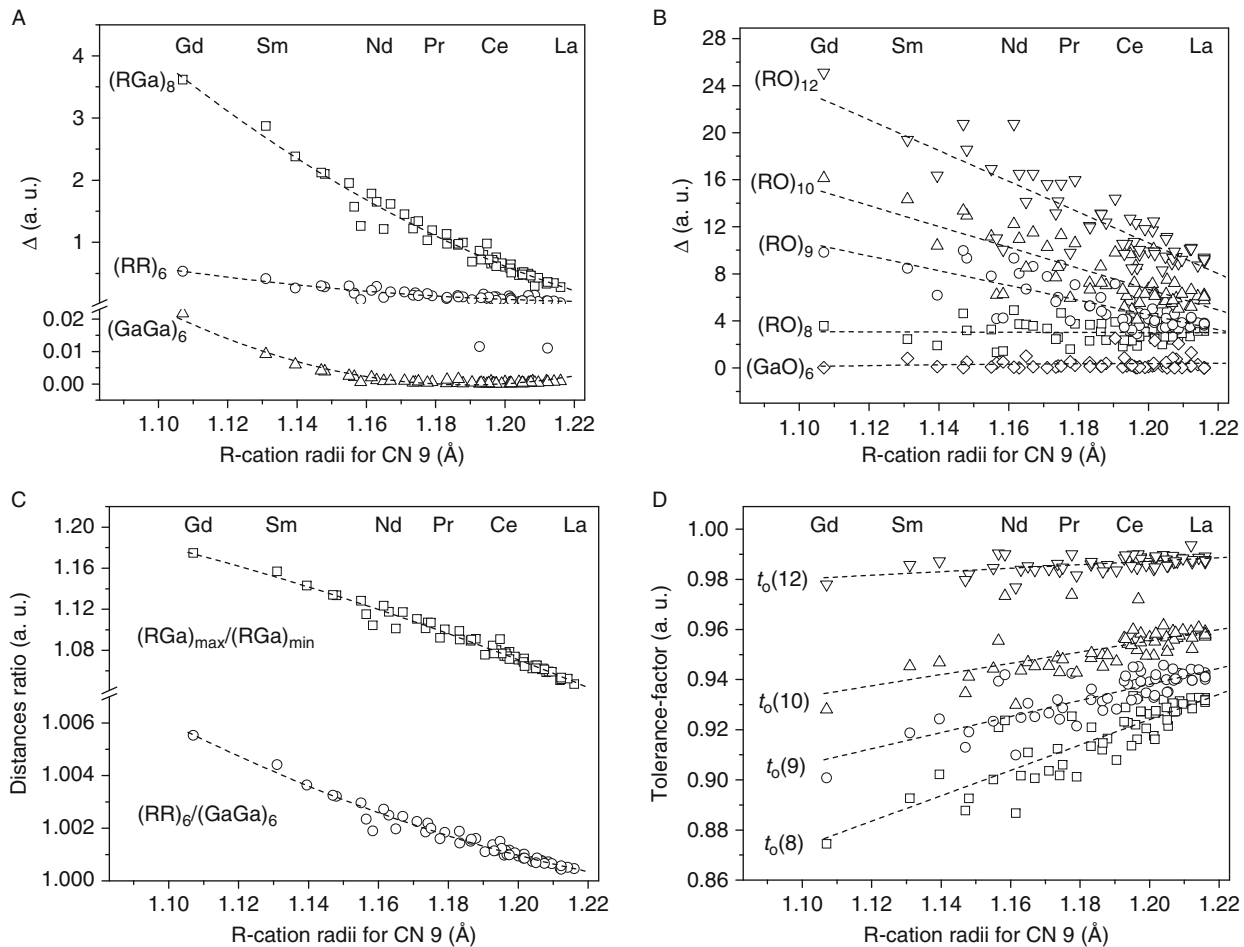


FIGURE 75 Degree of bond-strain (A–B), ratio of cation–cation distances (C), and observed tolerance factors (D) in the rare earth gallates as functions of the average ionic radius of the rare earth cation.

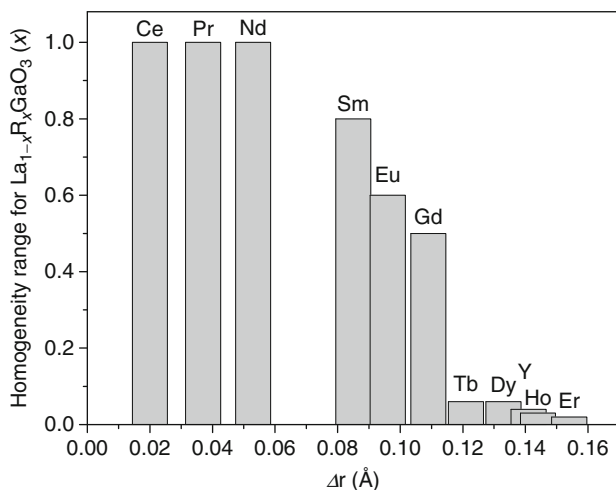


FIGURE 76 Plot of homogeneity ranges of perovskite-type solid solutions in $\text{La}_{1-x}\text{R}_x\text{GaO}_3$ pseudobinary systems versus the difference of the rare earth ionic radius $\Delta r = r(\text{La}) - r(\text{R})$.

when $\Delta r > 0.11 \text{ \AA}$ ($\text{R} = \text{Tb-Lu}$ and Y), substitution of the R-cation for La cannot exceed 0.02–0.06 mole fraction. There is not a smooth decrease in the homogeneity range: a rather sudden stop occurs between gadolinium and terbium. This stop points to two different mechanisms for the limited solubility of perovskites when $0.085 < \Delta r < 0.11 \text{ \AA}$ and when $\Delta r > 0.11 \text{ \AA}$.

It is well known that if a solute differs in its atomic size by more than 15% from the host, then limited or no solubility is likely (Hume-Rothery, 1955). Perovskite-type materials crystallize with close-packed structures, whose main feature is a presence of frameworks of tilted and distorted octahedra. Even minor substitutions on the A-site would lead to strained octahedral frameworks, and further increase may result in its destruction. Therefore, in perovskites, the conventional '15% limit' initially established for metals should be reduced to the level of 10% or even less. This agrees well with the observed value $\Delta r \approx 0.11 \text{ \AA}$. The analysis of the critical contents via the perovskite cell deformation reveals radius limitations at 1.213, 1.212, 1.210, 1.208, and 1.209 \AA corresponding to $x = 0.06, 0.06, 0.04, 0.03,$ and 0.02 for Er, Ho, Y, Dy, and Tb-containing $\text{La}_{1-x}\text{R}_x\text{GaO}_3$, respectively. Observed radii corresponding to limitations in solubility for different $\text{La}_{1-x}\text{R}_x\text{GaO}_3$ ($\text{R} = \text{Tb-Er}$ and Y) are very close to each other.

The diagram shown in Figure 76 cannot explain limited solid solubility in other $\text{R}\text{GaO}_3\text{-R}'\text{GaO}_3$ pseudo-binary systems. For instance, solid solutions of $\text{Nd}_{1-x}\text{Sm}_x\text{GaO}_3$ are limited when $x \approx 0.9$; for $\text{Pr}_{1-x}\text{Sm}_x\text{GaO}_3$, $\text{Pr}_{1-x}\text{Eu}_x\text{GaO}_3$, and $\text{Nd}_{1-x}\text{Eu}_x\text{GaO}_3$ solid solutions, it is already known that the limit is above $x \approx 0.5$, whereas for $\text{Pr}\text{GaO}_3\text{-Gd}\text{GaO}_3$ and $\text{Nd}\text{GaO}_3\text{-Gd}\text{GaO}_3$ systems, the limiting amount of gadolinium is less than 50 at.%. Moreover, the difficulties in obtaining RGaO_3 ($\text{R} = \text{Sm-Lu}$) at ambient pressure may be directly related to such limitations.

The average rare earth cationic radius is a measure of the structural deformation for an interlanthanide substitution in the RGaO_3 perovskite series. Therefore, an attempt to rephrase relevant discussions in terms of the average rare earth cationic radius has been made in [Senyshyn *et al.* \(2005b\)](#). A generalized stability diagram has been constructed ([Figure 77](#)), where R^{3+} radii corresponding to observed limitations in solubility for $\text{La}_{1-x}\text{Gd}_x\text{GaO}_3$, $\text{La}_{1-x}\text{Eu}_x\text{GaO}_3$, $\text{La}_{1-x}\text{Sm}_x\text{GaO}_3$, and $\text{Nd}_{1-x}\text{Sm}_x\text{GaO}_3$ solid solutions are presented by solid symbols as a function of Δr , whereas the open symbols illustrate the critical radii in the $\text{LaGaO}_3\text{--RGaO}_3$ ($\text{R} = \text{Tb--Er}$ and Y) systems. Radii corresponding to solubility limitations in $\text{LaGaO}_3\text{--RGaO}_3$ ($\text{R} = \text{Tb--Er}$ and Y) systems are nearly constant with the mean value of about $1.210(2) \text{ \AA}$, whereas for those in the $\text{LaGaO}_3\text{--RGaO}_3$ ($\text{R} = \text{Sm--Gd}$) and $\text{Nd}_{1-x}\text{Sm}_x\text{GaO}_3$ systems, a linear behaviour was observed.

Three regions can be distinguished in [Figure 77](#). In $\text{RGaO}_3\text{--R'GaO}_3$ pseudobinary systems with $\Delta r > 0.11 \text{ \AA}$, a continuous solid solution with perovskite structure is not formed due to the large difference in the rare earth cationic radii of the constituents; for RGaO_3 and solid solutions in $\text{RGaO}_3\text{--R'GaO}_3$ with average radius $r(\text{R}) < 1.128(3) + 0.32(3)\Delta r$, the perovskite structure is most probably not obtainable using a solid-state reaction synthesis, but the thermobaric technique can be used instead. Only compounds with $r(\text{R})$ and Δr fulfilling the following inequalities (also shown as the hashed region in [Figure 77](#)) may be obtained at ambient pressure in pure perovskite form:

$$r(\text{R}) > 1.128(3) + 0.32(3)\Delta r, \quad \Delta r < 0.11 \text{ \AA}$$

[Senyshyn *et al.* \(2005b\)](#) applied one more criterion, that is, the boundary (1.177 \AA) separating RGaO_3 and their solid solutions with and without first-order orthorhombic-to-rhombohedral phase transformation below their melting point, which

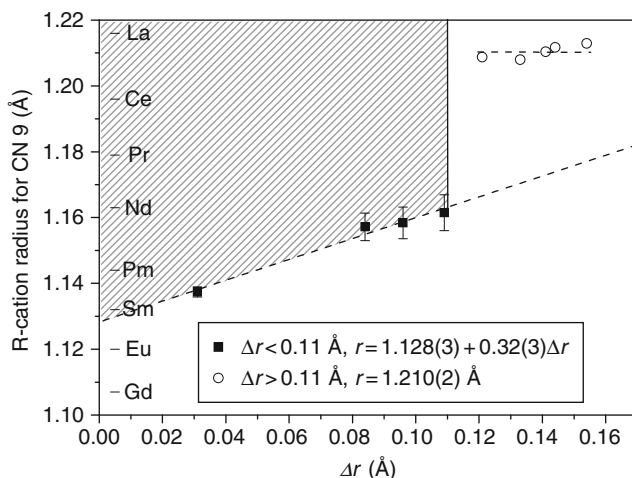


FIGURE 77 Generalized stability diagram for RGaO_3 and solid solutions in $\text{RGaO}_3\text{--R'GaO}_3$ pseudobinary systems. Δr is the difference of $r(\text{R})\text{--}r(\text{R}')$.

can lead to damaging or breaking of single crystals. The phase transformations occurring in RGaO_3 and their solid solutions are described in Chapter 243.

3.6 Phase transitions and thermal expansion

3.6.1 Phase diagram

In contrast to rare earth aluminates, only one type of the phase transformation, namely, $Pbnm-R\bar{3}c$ is observed in the corresponding gallates. In LaGaO_3 , this transition occurs at ca. 420 K; in cerium gallate, at 1228 K; and in PrGaO_3 , at about 1850 K. The same phase transformation occurs in $\text{La}_{1-x}\text{R}_x\text{GaO}_3$ solid solutions. With increasing R-content in $\text{La}_{1-x}\text{R}_x\text{GaO}_3$, the temperature of the $Pbnm-R\bar{3}c$ phase transition increases in the Ce–Pr–Nd–Sm–Gd–Ho–Er series (Figure 78A). The variation of the transition temperatures in RGaO_3 perovskites and their solid solutions shows linear behaviour (Figure 78B), when it is plotted versus the average rare earth ionic radius (Vasylechko et al., 2001a, 2002b).

From experimental data regarding the $Pbnm-R\bar{3}c$ phase transformation occurring in RGaO_3 and their solid solutions as well as other available data about the melting points of RGaO_3 (Nicolas et al., 1983; Mizuno and Yamada, 1985, 1988, 1989; Mizuno et al., 1985; Portnoj and Timofeeva, 1986; Bondar et al., 1988; Sasaura and Miyazawa, 1992; Miyazawa et al., 1993b), a generalized phase diagram may be constructed (Figure 79).

Melting and phase transformation temperatures were fitted by the linear functions of average rare earth ionic radius. The value of 1.177 Å has been determined from the intercept of two lines separating compositions with and without the $Pbnm-R\bar{3}c$ phase transformation below the melting point.

O'Bryan et al. (1990) proposed a set of criteria for good substrate materials. One of them is the absence of structural phase transitions not only in the

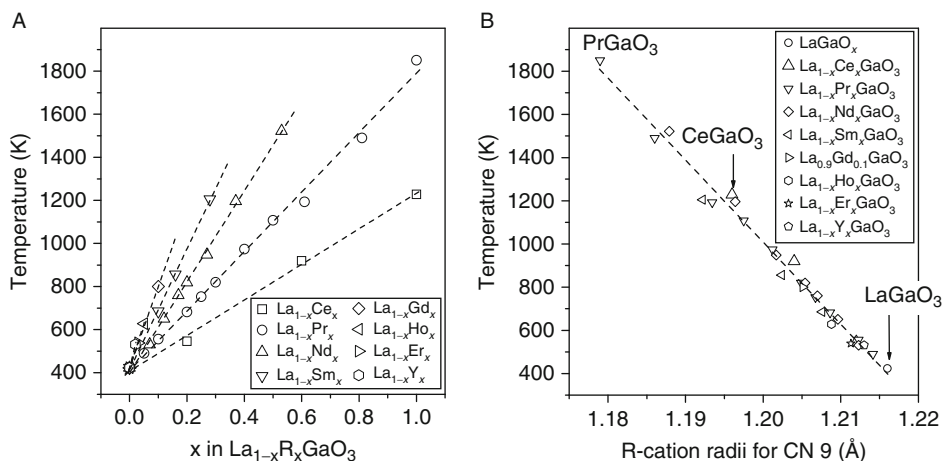


FIGURE 78 Orthorhombic-to-rhombohedral phase transition temperatures in RGaO_3 and $\text{La}_{1-x}\text{R}_x\text{GaO}_3$ solid solutions as functions of composition (A) and average R-cation radius (B).

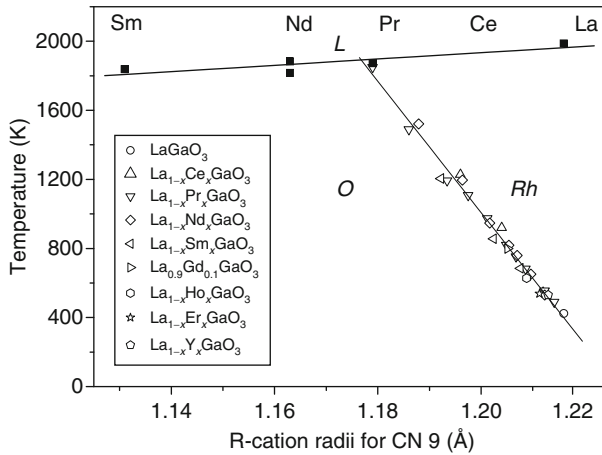


FIGURE 79 The generalized phase diagram of RGaO_3 and solid solutions of $\text{RGaO}_3\text{-R}'\text{GaO}_3$ pseudobinary systems. The letters L, O, and Rh designate liquid, orthorhombic, and rhombohedral phase fields, respectively. Linear fits of the observed critical temperatures: $T_{\text{O-Rh}}(r) = 47(1) \times 10^3 - 38.0(9) \times 10^3 \times r$; $T_{\text{L}}(r) = 0.3(7) \times 10^3 + 1.8(6) \times 10^3 \times r$.

temperature region of film deposition but also below the melting point of the substrate material in order to fully suppress the formation of micro-twins and reduce roughness of the substrate surface (Miyazawa, 1989). Detailed studies of RGaO_3 with respect to meeting the criteria by O'Bryan *et al.* were given by Senyshyn *et al.* (2005b). Thus, for those RGaO_3 and their solid solutions that have the average ionic radius in a ninefold coordination sphere greater than 1.177 \AA , the $P6mm\text{-}R\bar{3}c$ phase transition is expected to occur, resulting in strong tendency to twinning. Twin-free neodymium gallate was already described in the literature (Sasaura and Miyazawa, 1993), whereas to the best of our knowledge, twin-free LaGaO_3 , CeGaO_3 , or PrGaO_3 single crystals could not be obtained so far. Therefore, the stability diagram shown in Figure 77 has been redrawn (see Figure 80). A narrow region of RGaO_3 and solid solutions $\text{RR}'\text{GaO}_3$, with $r(\text{R})$ and Δr satisfying conditions $r(\text{R}) > 1.128(3) + 0.32(3)\Delta r$, $\Delta r < 0.11 \text{ \AA}$, and $r(\text{R}) < 1.177 \text{ \AA}$, may be used as a guide for selecting potential substrates.

3.6.2 Thermal expansion

The $P6mm\text{-}R\bar{3}c$ phase transformation which occurs in rare earth gallates is first order in nature, and in addition to chemical composition and temperature, it influences the thermal expansion. Thermal behaviour of the cell volume of RGaO_3 and some selected compositions of the $\text{La}_{1-x}\text{R}_x\text{GaO}_3$ ($\text{R} = \text{Ce-Gd}$) and $\text{Nd}_{1-x}\text{Sm}_x\text{GaO}_3$ systems is shown in Figure 81. HT structural data of lanthanum gallate were taken from Slater *et al.* (1998a) and Howard and Kennedy (1999). The observed cell dimensions were normalized to their RT values according to Eq. (7).

Neglecting LT structural anomalies that occur in praseodymium-containing gallates, in the whole temperature range 12–1200 K, the cell volumes increase

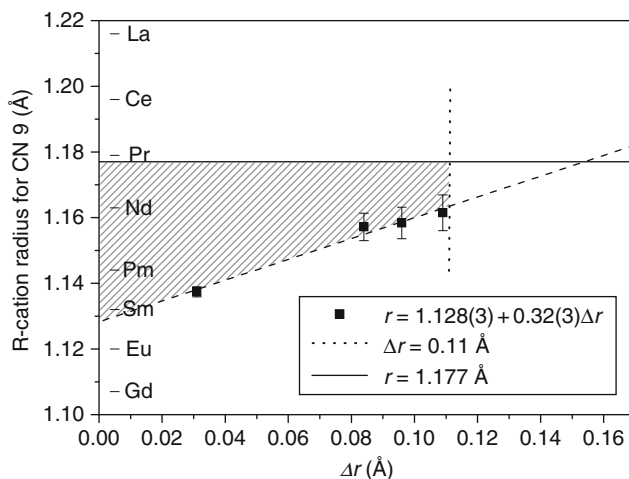


FIGURE 80 The generalized stability diagram of R GaO_3 and solid solutions of $\text{R GaO}_3\text{--R}'\text{GaO}_3$ pseudobinary systems. The hatched region indicates materials potentially suitable for twin-free substrates.

systematically in $\text{NdGaO}_3\text{--PrGaO}_3\text{--CeGaO}_3\text{--LaGaO}_3$, whereas the cell volumes for the respective $\text{La}_{1-x}\text{R}_x\text{GaO}_3$ ($\text{R} = \text{Ce}, \text{Pr}, \text{Nd}, \text{Sm}, \text{Gd}, \text{and Eu}$) and $\text{Nd}_{0.75}\text{Sm}_{0.25}\text{GaO}_3$ solid solutions have intermediate values in accordance with the average R-cation radius. The normalized cell volumes display almost identical temperature behaviour for all R GaO_3 compounds and their solid solutions (see Figure 81B).

The temperature behaviour of the lattice parameters in R GaO_3 as well as in some compositions of $\text{La}_{1-x}\text{R}_x\text{GaO}_3$ ($\text{R} = \text{Ce--Gd}$) and $\text{Nd}_{1-x}\text{Sm}_x\text{GaO}_3$ are shown in Figure 82A, C, and E. In contrast to similarities in the thermal evolution of the volume, discrepancies in the thermal expansion along different crystallographic directions are pronounced. The analysis of the thermal expansion reveals the largest elongation along the a (0.94–1.08% at 1200 K) and c (0.79–1.01% at 1200 K) directions in the orthorhombic lattice (Figure 82B and F). The elongation of the lattice in the b -direction (Figure 82D) is less pronounced (0.49–0.69%).

The linear thermal expansion coefficient α can be determined from the derivative of the temperature dependence of the cell dimension as $\alpha = \partial \ln\{L(T)\}/\partial T$. Here, $L(T)$ is the cell dimension at the corresponding temperature T . The volumetric TEC can be expressed via fundamental parameters, such as the Grüneisen parameter γ_v , the bulk modulus K , the molar volume V_m , the heat capacity C , phonon frequencies ω , and the internal energy U :

$$\alpha_v = \frac{1}{KV_m} \left(C_{\gamma_v} + \left(\frac{\partial \omega}{\partial T} \right)_v U \right) \quad (9)$$

At LT, the crystal behaves like a harmonic solid and the dependence of the phonon frequencies on temperature is negligibly small allowing one to ignore the

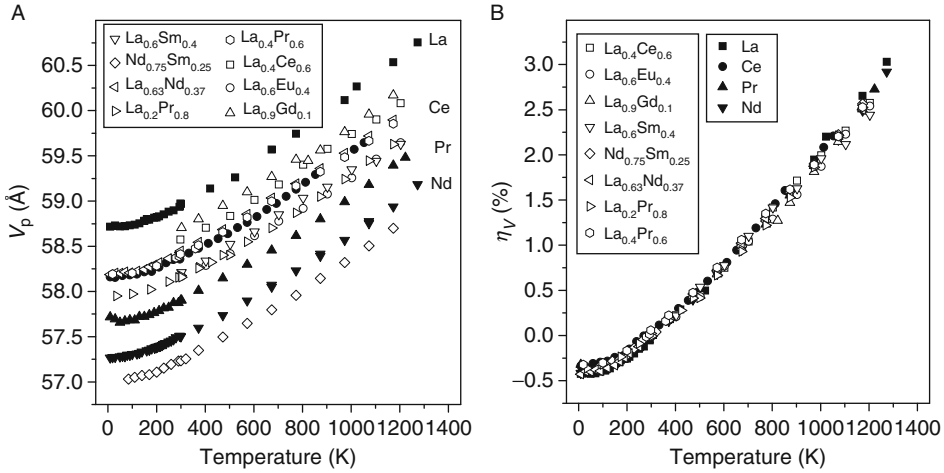


FIGURE 81 Thermal variation of cell volumes (A) and volumetric thermal expansion η (B) for RGaO_3 , $\text{La}_{1-x}\text{R}_x\text{GaO}_3$ ($\text{R}=\text{Ce-Gd}$), and $\text{Nd}_{0.75}\text{Sm}_{0.25}\text{GaO}_3$ solid solutions.

second term in Eq. (9). This is a principle of the quasi-harmonic approximation and its application leads to the following expression:

$$\alpha_V = \frac{\gamma_V \rho C_V}{K_T} = \frac{\gamma_V \rho C_P}{K_S}, \quad (10)$$

where γ_V is the Grüneisen parameter, ρ is the density of the material, K_T and K_S are isothermal and adiabatic bulk moduli, and C_V and C_P are the heat capacities at constant volume and pressure, respectively.

Senyshyn et al. (2005b) calculated the above-mentioned properties and determined the thermal expansion coefficient of rare earth gallates using a semi-classical approach. Ideal (X-ray) density, Grüneisen parameter, isohoric heat capacity C_V , bulk and shear moduli, and thermal expansion coefficient were calculated for RGaO_3 ($\text{R} = \text{La-Gd}$) at 300 K are listed in Table 47.

In most cases, phonon–phonon interactions dominate the thermal expansion coefficient α in a solid. The heat capacity and thermal expansion coefficient can be described by the sum of different contributions, for example, lattice, magnetic, electronic etc. Rare earth gallates are wide-band dielectrics, and above liquid helium temperature, they possess paramagnetism, therefore both electronic and magnetic contributions occurring in these materials can be neglected. However, thermal and magnetic properties of $4f$ -element containing materials display anomalies caused by interactions between crystal electric field and the electronic subsystem. Unfortunately, the approach employed by Senyshyn et al. (2005b) is not suitable to simulate such kinds of interactions, which are presumably the reasons for the LT anomalies in cerium and praseodymium containing aluminates as well as in the praseodymium containing gallates. Furthermore, the quasi-harmonic approximation is valid only at LT, which may be the reason for the

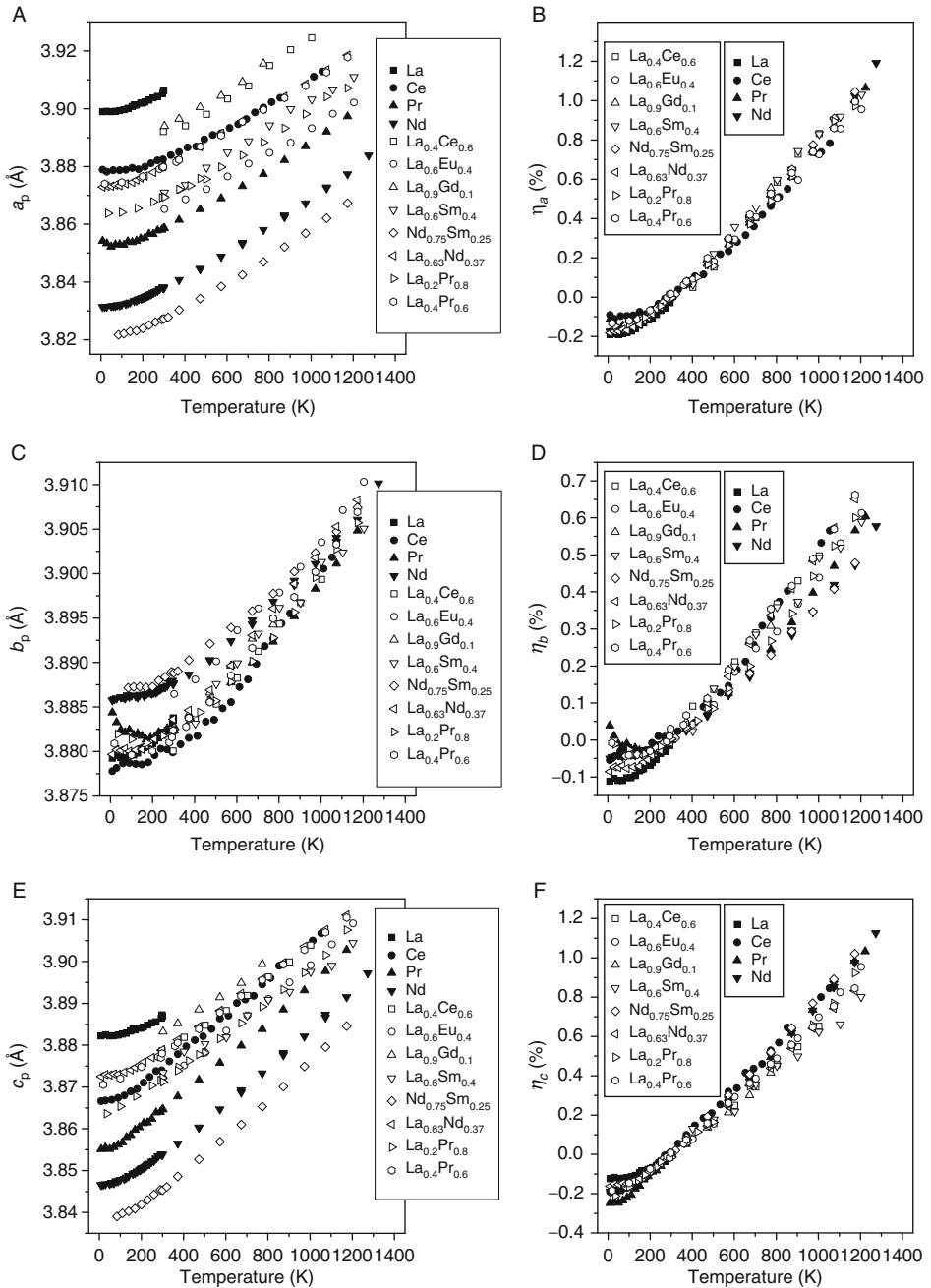


FIGURE 82 Thermal dependencies of lattice parameters (A, C, E) and their relative expansion (B, D, F) of orthorhombic rare earth gallates.

TABLE 47 Ideal (X-ray) density (ρ), Grüneisen parameter (γ_V), isohoric heat capacity (C_V , $Z = 4$), entropy (S), bulk (K_T) and shear (G_T) moduli, and volumetric thermal expansion coefficient (α_V) calculated for RGaO_3 ($R = \text{La-Gd}$) at 300 K using semi-classical approach (Senyshyn *et al.*, 2005b)

	ρ (g/cm ³)	γ_V (arb. units)	C_V (J/mole/K)	S (J/mole/K)	K_T (GPa)	G_T (GPa)	$\alpha_V \times 10^6$ (K ⁻¹)
LaGaO ₃	7.247	1.433	401.3	424.0	182.7	104.5	22.8
CeGaO ₃	7.364	1.408	399.4	417.3	186.4	104.1	22.2
PrGaO ₃	7.429	1.373	398.3	413.7	187.7	104.9	21.6
NdGaO ₃	7.564	1.317	397.3	411.0	188.7	105.8	21.0
PmGaO ₃	7.646	1.281	395.7	405.8	190.8	106.9	20.3
SmGaO ₃	7.843	1.235	394.7	403.8	192.2	107.7	19.9
EuGaO ₃	7.934	1.198	393.4	400.4	193.7	108.6	19.3
GdGaO ₃	8.143	1.177	392.1	397.3	195.8	109.6	19.2

slightly underestimated thermal expansion coefficients. Hence, in order to simulate structural properties at HT, other techniques should be applied, for example molecular dynamics simulations, that have been successfully used to predict HT/high-pressure structural behaviour of NdGaO₃ (Senyshyn *et al.*, 2004a) showing fair agreement with experimental data.

The experimentally observed temperature evolution of lattice parameters and cell volumes of rare earth gallates at LT displays a highly non-linear behaviour, whereas at temperatures above RT, it can be extrapolated linearly within little uncertainty. Thermal expansion coefficients are determined from the slope of the curve. The linear thermal expansion coefficients of RGaO_3 as well as for some compositions from $\text{La}_{1-x}\text{R}_x\text{GaO}_3$ ($R = \text{Ce-Gd}$) and $\text{Nd}_{1-x}\text{Sm}_x\text{GaO}_3$ systems are listed in Table 48 for different crystallographic directions and are shown in Figure 83 as functions of the average rare earth ionic radius. In the temperature range 300–1200 K, the linear thermal expansion coefficients of orthorhombic rare earth gallates lie within the limits $\alpha_a = (10.3\text{--}12.6) \times 10^{-6} \text{ K}^{-1}$, $\alpha_b = (5.3\text{--}7.7) \times 10^{-6} \text{ K}^{-1}$, and $\alpha_c = (9.3\text{--}11.65) \times 10^{-6} \text{ K}^{-1}$. Increasing rare earth ionic radius causes a weak reduction of α_c and, respectively, an increase of α_b , whereas α_a remains almost constant. The volumetric thermal expansion coefficient of orthorhombic gallates (Figure 83B) shows a weak decrease when the average ionic radii of the rare earth elements increases. Similar to aluminates, α_V of the rhombohedral structures is larger than that of the orthorhombic structures.

3.7 Dielectric properties of rare earth gallates

In contrast to rare earth aluminates, the microwave dielectric properties (dielectric permittivities and losses) of rare earth orthogallates were studied less. The relative dielectric permittivity in LaGaO₃ has been reported to be 25 (Sandstrom *et al.*, 1988), in PrGaO₃, ϵ_r is 24 (Sasaura *et al.*, 1990a), whereas in neodymium gallate, ϵ_r from 20 to 23 were given by different authors (Konaka *et al.*, 1991; Konopka and

TABLE 48 Thermal expansion coefficients of rare earth gallates (K^{-1})

Compound	Space group	Temperature (K)	$\alpha_a \times 10^6$	$\alpha_b \times 10^6$	$\alpha_c \times 10^6$	$\alpha_V \times 10^6$
LaGaO ₃	<i>Pbnm</i>	210–400	11.16	6.98	7.66	25.78
LaGaO ₃ ¹	<i>R-3c</i>	420–1200	8.49	–	15.30	32.62
CeGaO ₃	<i>Pbnm</i>	298–1200	10.35	7.69	11.04	29.32
PrGaO ₃	<i>Pbnm</i>	298–1200	11.26	6.25	11.13	29.21
NdGaO ₃	<i>Pbnm</i>	298–1200	11.94	5.62	11.34	29.06
NdGaO ₃ ²	<i>Pbnm</i>	301–923	11.3	2.3	9.1	22.7
NdGaO ₃ ³	<i>Pbnm</i>	298–1273	12.5	4.2	9.8	26.5
La _{0.4} Ce _{0.6} GaO ₃	<i>Pbnm</i>	298–1000	12.6	7.05	9.33	29.22
La _{0.4} Ce _{0.6} GaO ₃	<i>R-3c</i>	1000–1200	12.57	–	5.20	30.97
La _{0.2} Pr _{0.8} GaO ₃	<i>Pbnm</i>	298–1200	11.34	6.78	10.21	28.56
La _{0.4} Pr _{0.6} GaO ₃	<i>Pbnm</i>	298–1200	11.03	7.27	9.70	28.26
La _{0.63} Nd _{0.37} GaO ₃	<i>Pbnm</i>	298–1200	11.22	7.43	9.60	28.42
La _{0.6} Sm _{0.4} GaO ₃	<i>Pbnm</i>	298–1200	11.9	6.75	8.54	27.32
La _{0.6} Eu _{0.4} GaO ₃	<i>Pbnm</i>	298–1200	10.71	6.82	10.62	28.38
La _{0.9} Gd _{0.1} GaO ₃	<i>Pbnm</i>	298–800	11.57	6.78	8.68	28.13
La _{0.9} Gd _{0.1} GaO ₃	<i>R-3c</i>	800–1200	10.32	–	13.89	35.11
Nd _{0.75} Sm _{0.25} GaO ₃	<i>Pbnm</i>	298–1200	11.78	5.30	11.50	28.84

¹ Calculated from the lattice parameters given in Howard and Kennedy (1999).

² Data from Chaix-Pluchery et al. (2005).

³ Data from Sandiumenge et al. (1994).

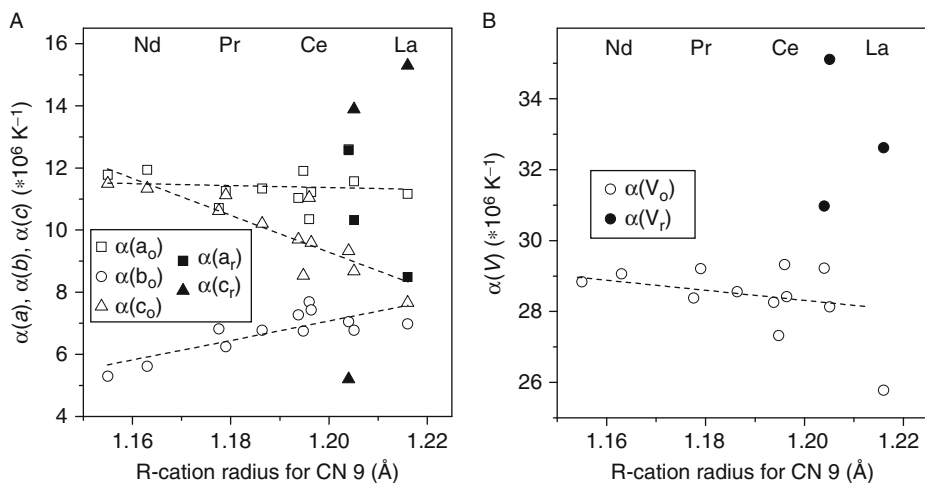


FIGURE 83 Components of the thermal expansion tensor (A) and volumetric thermal expansion coefficient (B) versus rare earth cation radius in rare earth gallates. The dashed lines are guides for the eye.

Wolff, 1992; Krupka *et al.*, 1994; Savytskii *et al.*, 1999; Kim *et al.*, 2002). Using a semi-classical approach and analytical form for an interatomic interactions, Senyshyn *et al.* (2005b) calculated the RT dielectric constants for RGaO_3 orthogallates with perovskite structure ($\text{R} = \text{La} - \text{Gd}$) being equal to 26.5 ($\text{R} = \text{La}$), 25.0 ($\text{R} = \text{Ce}$), 23.9 ($\text{R} = \text{Pr}$), 22.9 ($\text{R} = \text{Nd}$), 21.6 ($\text{R} = \text{Pm}$), 20.8 ($\text{R} = \text{Sm}$), 20.0 ($\text{R} = \text{Eu}$), and 19.2 ($\text{R} = \text{Gd}$). The obtained values are in good agreement with experimental data, whereas the dependence of ϵ_r for rare earth substitution is consistent with the behaviour of RTiNbO_6 (Sebastian *et al.*, 2001), RTiTaO_6 (Surendran *et al.*, 2002), and RAIO_3 (Cho *et al.*, 1999a).

Among all rare earth orthogallates with perovskite structure, the dielectric losses have been studied precisely only for neodymium gallate. At 6.5 GHz and temperatures above ca. 100 K, the $\tan\delta$ has been found to be about 10^{-4} , and further cooling results in an increase of $\tan\delta$ (7×10^{-4} at $T < 50$ K) (Konaka *et al.*, 1991). A similar trend was observed by Konopka and Wolff (1992) in the dielectric properties of NdGaO_3 at microwave frequencies from 4 to 40 GHz and at temperatures from 10 to 300 K. The authors suggested that collective interactions of Nd^{3+} magnetic moments and microwave fields are responsible for the increase of losses at LT. Krupka *et al.* (1994) observed an increase of $\tan\delta$ in NdGaO_3 upon cooling from ca. 6×10^{-4} at RT to ca. 10^{-3} at 70 K and no influence of an applied static magnetic field was observed.

The atomistic approach used by Senyshyn *et al.* (2005b) has been found inadequate to simulate anomalies of $\tan\delta$ observed in neodymium gallate, which could be the indicator of an electronic effects involved. A similar kind of a rather atypical behaviour of dielectric properties has been observed in Nd-doped YAlO_3 (Konaka *et al.*, 1991) and in NdSrGaO_4 (Konopka and Wolff, 1992; Konopka *et al.*, 1992). This could be attributed to intrinsic nature of Nd^{3+} .

Unfortunately, there is no information available on the dielectric losses of lanthanum and praseodymium gallates; however, the work performed by Sasaura *et al.* (1990a) and Dube *et al.* (1994) allows one to expect them to be reasonably low.

Recent progress in the field of wireless telecommunications has resulted in demand for temperature-stable materials ($t_f \approx 0$ ppm/K) with $\epsilon_r > 40$ and $Q \times f_r > 40000$. As has been mentioned in Section 2.6, compensation of t_f can be achieved by combining two compatible compounds with opposite t_f . Typical for rare earth perovskites, the temperature coefficient of the resonant frequency is negative, which makes them suitable to be used in combination with alkaline-earth titanates. For instance, for the orthorhombic perovskite calcium titanate CaTiO_3 , $\epsilon_r = 170$, $Q \times f_r = 3500$ GHz, and it has a high positive temperature coefficient of the resonant frequency ($t_f \approx +800$ ppm/K). This property makes pure CaTiO_3 useless for most applications. Combining CaTiO_3 with perovskite-type rare earth gallates may lead to the suppression of the large positive t_f and to the reduction of the dielectric loss ($\tan\delta$). Dielectric properties in $\text{LaGaO}_3\text{-CaTiO}_3$, $\text{La}_{0.50}\text{Nd}_{0.50}\text{GaO}_3\text{-CaTiO}_3$, $\text{NdGaO}_3\text{-CaTiO}_3$, and $\text{NdGaO}_3\text{-CaTiO}_3$ pseudo-binary systems were studied in Suvorov *et al.* (2001) and Nenasheva *et al.* (2003) and these are listed in Table 49. The ϵ_r increases with increasing content of calcium

TABLE 49 Dielectric properties of microwave dielectric materials based on RGaO_3

Composition	Sample, sintering conditions ¹	ϵ_r	$Q \times f$ (GHz)	f (GHz)	t_f (ppm/K)	Reference
LaGaO_3	single crystal	26.0	600 000	500	–	Sobolewski et al. (1991)
$(\text{LaGaO}_3)_{0.4}(\text{CaTiO}_3)_{0.6}$	1450/12	45	34 000	–	–20	Suvorov et al. (2001)
$(\text{LaGaO}_3)_{0.35}(\text{CaTiO}_3)_{0.65}$	1450/12	48	32 000	–	2	
$(\text{LaGaO}_3)_{0.3}(\text{CaTiO}_3)_{0.7}$	1450/12	52	27 000	–	40	
$(\text{LaGaO}_3)_{0.36}(\text{CaTiO}_3)_{0.64}$	–	46.5	48 000	8	–2.9	Nenasheva et al. (2003)
$(\text{LaGaO}_3)_{0.34}(\text{CaTiO}_3)_{0.66}$	–	47.5	46 000	8	3.6	
$(\text{La}_{0.50}\text{Nd}_{0.50}\text{GaO}_3)_{0.34}(\text{CaTiO}_3)_{0.66}$	–	43.6	43 000	8	–9.5	
$(\text{La}_{0.50}\text{Nd}_{0.50}\text{GaO}_3)_{0.33}(\text{CaTiO}_3)_{0.67}$	–	44.7	41 000	8	6.3	
$(\text{LaGaO}_3)_{0.3}(\text{CaTiO}_3)_{0.7}$	–	49.4	29 000	8	21.5	
NdGaO_3	–	22	85 000	–	–	Kim et al. (2002)
NdGaO_3	single crystal	21.9	44 000	18.5	183	Krupka et al. (1994)
$(\text{NdGaO}_3)_{0.4}(\text{CaTiO}_3)_{0.6}$	1450/12	44	30 000	–	–18	Suvorov et al. (2001)
$(\text{NdGaO}_3)_{0.35}(\text{CaTiO}_3)_{0.65}$	1450/12	45	38 000	–	1	
$(\text{NdGaO}_3)_{0.3}(\text{CaTiO}_3)_{0.7}$	1450/12	49	32 000	–	35	
$(\text{SmGaO}_3)_{0.4}(\text{CaTiO}_3)_{0.6}$	1450/12	42	35 000	–	–11	
$(\text{SmGaO}_3)_{0.35}(\text{CaTiO}_3)_{0.65}$	1450/12	45	34 000	–	1	
$(\text{SmGaO}_3)_{0.3}(\text{CaTiO}_3)_{0.7}$	1450/12	51	18 000	–	41	

¹ Sintering temperature (in K)/time (in hours).

titanate, which occurs at the expense of the high-quality factor $Q \times f_r$. It is now possible to prepare ceramics with a temperature-stable resonant frequency with $\varepsilon_r > 40$ and $Q \times f_r > 40\,000$.

ACKNOWLEDGEMENTS

The work was partially supported by the Ukrainian Ministry of Education and Sciences (via the Project 'Segnet'), the German Federal Ministry of Education and Research (BMBF project 03FU7DAR, WTZ Grant UKR-04/007), and the Grant-in-Aid program of the International Centre for Diffraction Data (ICDD Grant 01-06). We gratefully acknowledge the administrations support of HASYLAB/DESY (Hamburg, Germany), of the research reactor FRM-II (Garching n. Munich, Germany), and the Max-Planck Institute of Chemical Physics of Solids (MPI CPfS, Dresden, Germany) for kindly providing their unique research facilities. L. Vasylechko wishes to thank the Max-Planck Society for a research fellowship. A. Senyshyn gratefully acknowledges financial support from the German Academic Exchange Service (DAAD).

REFERENCES

- Abell, S., Harris, I. R., Cockayne, B., Lent, B. J. *Mater. Sci.* 1974, **9**, 527.
- Abu Safia, H. A. *Opt. Commun.* 1997, **139**, 212.
- Adylov, G. T., Voronov, G. V., Mansurova, E. P., Sigalov, L. M., Urazaeva, E. M. *Zh. Neorg. Khim.* 1988, **33**, 1062 (*in Russian*).
- Alain, P., Piriou, B. *Solid State Commun.* 1975, **17**, 35.
- Aleksiyko, R., Berkowski, M., Byszewski, P., Dabrowski, B., Diduszko, R., Fink-Finowicki, J., Vasylechko, L. O. *Cryst. Res. Technol.* 2001, **36**, 789.
- Alkebro, J., Begin-Colin, S., Mocellin, A., Warren, R. J. *Eur. Ceram. Soc.* 2000, **20**, 2169.
- Alkebro, J., Begin-Colin, S., Mocellin, A., Warren, R. J. *Solid State Chem.* 2002, **164**, 88.
- Allibert, M., Chatillon, C., Mareshal, J., Lissalde, F. J. *Cryst. Growth* 1974, **23**, 289.
- Altermatt, D., Brown, I. D. *Acta Crystallogr. A* 1987, **43**, 125.
- An, W. W., Miao, J. P., Zhang, Z. G. *Phys. B (Amsterdam, Neth.)* 2006, **382**, 262.
- Ananieva, G. V., Ivanov, A. O., Merkulyaeva, T. I., Mochalov, I. V. *Kristallografia (Crystallogr. Rep.)* 1978, **23**, 200 (*in Russian*).
- Ang, C., Yu, Z., Youn, H. J., Randall, C. A., Bhalla, A. S., Cross, L. E., Lanagan, M. *Appl. Phys. Lett.* 2003, **82**, 3734.
- Antic-Fidancev, E., Lemaitre-Blaise, M., Latroche, M., Porcher, P., Coutures, J., Coutures, J. P. *J. Alloys Compd.* 1997, **250**, 342.
- Arakcheeva, A. V., Pushcharovskii, D. Yu., Gekimyants, V. M., Popov, V. A., Lubman, G. U. *Crystallogr. Rep.* 1997, **42**, 46.
- Arsenev, P. A., Bienert, K. E., Potomkin, A. V. *Phys. Status Solidi A* 1975, **28**, 81.
- Arsenev, P. A., Kovba, L. M., Bagdasarov, Kh. S., Dzhurinskii, B. F., Potemkin, A. V., Pokrovskii, B. I., Spiridonov, F. M., Antonov, V. A., Ilyukhin, V. V. *Compounds of Rare Earth Elements. Systems with the Oxides of I-III Group Elements*, Nauka, Moscow, p.280, 1983 (*in Russian*).
- Badshaw, H., Iddles, D., Quinby, R., Reaney, I.-M. *J. Eur. Ceram. Soc.* 2003, **23**, 2435.
- Basyuk, T., Vasylechko, L. *Private communication*.
- Basyuk, T., Vasylechko, L., Syvorotka, I. I., Fedorchuk, A., Prots, Yu., Trots, D. *HASYLAB Ann. Rep.* 2007a, **1**, 795.
- Basyuk, T., Vasylechko, L., Syvorotka, I. I., Fedorchuk, A., Trots, D. *HASYLAB Ann. Rep.* 2007b, **1**, 733.
- Battle, P. D., Gibb, T. C., Jones, C. W., Studer, F. J. *Solid State Chem.* 1989, **78**, 281.
- Bdikin, I. K., Shmytko, I. M., Balbashov, A. M. *J. Appl. Crystallogr.* 1993, **26**, 71.
- Beach, D. B., Vallet, C. E., Paranthaman, M., Specht, E. D., Morell, J. S., Xue, Z. B. *Proc. Mater. Res. Soc. Symp.* 1998, **495**, 263.
- Belous, A. G., Ovchar, O. V., Valant, M., Suvorov, D. *Appl. Phys. Lett.* 2000, **77**, 1707.
- Belt, R. F., Uhrin, R. *Proc. SPIE* 1989, **1104**, 209.

- Benard, D. J., Walker, W. C. *Phys. Status Solidi* 1976, **18**, 717.
- Berkowski, M., Fink-Finowicki, J., Piekarczyk, W., Perchuć, L., Byszewski, P., Vasylechko, L. O., Savvitskii, D. I., Mazur, K., Sass, J., Kowalska, E., Kapuniak, J. J. *Cryst. Growth* 2000, **209**, 75.
- Berkowski, M., Fink-Finowicki, J., Byszewski, P., Diduszko, R., Kowalska, E., Aleksijko, R., Piekarczyk, W., Vasylechko, L. O., Savvitskij, D. I., Perchuć, L., Kapuniak, J. J. *Cryst. Growth* 2001, **222**, 194.
- Berkstresser, G. W., Valentino, A. J., Brandle, C. D. *J. Cryst. Growth* 1991, **109**, 457.
- Bertaut, F. *Acta Crystallogr. A* 1968, **24**, 217.
- Bertaut, F., Mareschal, J. *Compt. Rend.* 1963, **257**, 867.
- Bidaux, R., Meriel, P. J. *Phys. (Paris)* 1968, **29**, 220.
- Birgeneau, R. J., Kjems, J. K., Shirane, G., Van Uiter, L. G. *Phys. Rev. B* 1974, **10**, 2512.
- Bombik, A., Lesniewska, B., Mayer, J., Oles, A., Pacyna, A. W., Przewoznik, J. J. *Magn. Mater.* 1997, **168**, 139.
- Bombik, A., Böhm, H., Kusz, J., Pacyna, A. W., Wanklyn, B. M. *Solid State Commun.* 2005a, **134**, 277.
- Bombik, A., Lesniewska, B., Pacyna, A. W. *J. Magn. Mater.* 2005b, **285**, 11.
- Bondar, I. A., Toropov, N. A. *Bull. Acad. Sci. USSR, Div. Chem. Sci.* 1966, **2**, 195.
- Bondar, I. A., Vinogradova, N. V. *Izv. Akad. Nauk SSSR. Ser. Khim.* 1964, **5**, 785 (*in Russian*).
- Bondar, I. A., Koroleva, L. N., Bezruk, E. T. *Neorg. Mater. (Inorg. Mater.)* 1984, **20**(2), 257 (*in Russian*).
- Bondar, I. A., Degtyareva, V. Ya., Tseltin, P. A., Derbeneva, T. A., Mezentseva, L. P., Raikaya, L. N., Domanskii, A. I. *Zh. Neorg. Khim.* 1988, **33**(12), 3152 (*in Russian*).
- Bouvier, P., Kreisel, J. J. *Phys.: Condens. Matter* 2002, **14**, 3981.
- Brese, N. E., O'Keefe, M. *Acta Crystallogr. B* 1991, **47**, 192.
- Brown, I. D. *Chem. Soc. Rev.* 1978, **7**, 359.
- Brown, I. D., Altermatt, D. *Acta Crystallogr. B* 1985, **41**, 244.
- Brown, P. J., Nunez, V., Tasset, F., Forthyth, J. B. *Acta Crystallogr. A* 1992, **48**, 236.
- Brusset, H., Gillier-Pandraud, H., Berdot, J. L. *Bull. Soc. Chim. Fr.* 1967a, **4**, 1206.
- Brusset, H., Gillier-Pandraud, H., Berdot, J. L. *Bull. Soc. Chim. Fr.* 1967b, **8**, 2886.
- Brusset, H., Gillier-Pandraud, M. H., Saine, M. C. *Mater. Res. Bull.* 1975, **10**, 481.
- Budnikov, P. P., Kushakovskii, V. I., Belevantsev, V. S. *Dokl. Akad. Nauk SSSR* 1965, **165**, 1075 (*in Russian*); *Acad. Sci. USSR, Dokl. Chem.* **165**, 1177.
- Burbank, R. D. *J. Appl. Crystallogr.* 1970, **3**, 112.
- Carpenter, M. A., Howard, C. J., Kennedy, B. J., Knight, K. S. *Phys. Rev. B* 2005, **72**, 024118.
- Carruthers, J. R., Kokta, M., Barns, R. L., Crasso, M. J. *Cryst. Growth* 1973, **19**, 204.
- Chaix-Pluchery, O., Chenevier, B., Robles, J. J. *Appl. Phys. Lett.* 2005, **86**, 251911.
- Chakoumakos, B. C., Schlom, D. G., Urbanik, M., Luine, J. J. *Appl. Phys.* 1998, **83**, 1979.
- Chandrasekaran, A., Azad, A.-M. J. *Mater. Sci.* 2001, **36**, 4745.
- Cheng, H. H., Navrotsky, A. J. *Solid State Chem.* 2004, **177**, 126.
- Cho, S. Y., Kim, I. T., Hong, K. S. *J. Mater. Res.* 1999a, **14**, 114.
- Cho, S. Y., Hong, K. S., Ko, K. H. *Mater. Res. Bull.* 1999b, **34**, 511.
- Chval, J., Clement, D., Giba, J., Hybler, J., Loude, J.-F., Mares, J. A., Mihokova, E., Morel, C., Nejezchleb, K., Nikl, M., Vedda, A., Zaidi, H. *Nucl. Instrum. Methods Phys. Res., Sect. A* 2000, **443**, 331.
- Cockayne, B. J. *Less-Comm. Met.* 1985, **114**, 199.
- Cohen, E., Riseberg, L. A., Nordland, W. A., Burbank, R. D., Sherwood, R. C., van Uiter, L. G. *Phys. Rev.* 1969, **186**, 476.
- Coutures, J. P. *J. Am. Ceram. Soc.* 1985, **68**, 105.
- Coutures, J., Coutures, J. P. *J. Solid State Chem.* 1984, **52**, 95.
- Coutures, J., Nicolas, J., Antic, E., Schiffmacher, G., Coutures, J. P. *C. R. Seances Acad. Sci. Ser. II* 1983, **296**, 347.
- Cruciani, G., Matteucci, F., Dondi, M., Baldi, G., Barzanti, A. *Z. Kristallogr.* 2005, **220**, 930.
- Cussen, E. J., Rosseinsky, M. J., Battle, P. D., Burley, J. C., Spring, L. E., Vente, J. F., Blundell, S. J., Coldea, A. I., Singleton, J. J. *Am. Chem. Soc.* 2001, **123**, 1111.
- D'orio, M., Berlinger, W., Bednorz, J. G., Mueller, K. A. *J. Phys. C: Solid State Phys.* 1984, **17**, 2293.
- Dabkowska, H., Dabkowski, A., Greedan, J. E. *J. Cryst. Growth* 1993, **128**, 699.
- Dalziel, J. A. W., Welch, A. J. W. *Acta Crystallogr.* 1960, **13**, 956.

- De Rango, C., Tsoukaris, G., Zelwer, C. *Acta Crystallogr.* 1966, **20**, 590.
- Derighetti, B., Drumheller, J. E., Laves, F., Müller, K. A., Waldner, F. *Acta Crystallogr.* 1965, **18**, 557.
- Dernier, P. D., Maines, R. G. *Mater. Res. Bull.* 1971, **6**, 433.
- Diehl, R., Braundt, G. *Mater. Res. Bull.* 1975, **10**, 85.
- DiGiuseppe, M. A., Soled, S. L., Wenner, W. M., Macur, J. E. *J. Cryst. Growth* 1980, **49**, 746.
- du Boulay, D., Ishizawa, N., Maslen, E. N. *Acta Crystallogr. C* 2004, **60**, 120.
- Dube, D. C., Scheel, H. J., Reaney, I., Daglish, M., Setter, N. J. *Appl. Phys.* 1994, **75**, 4126.
- Egorov, V. M., Baikov, Yu. M., Kartenko, N. F., Melekh, B. T., Filin, Yu. N. *Phys. Solids State* 1998, **40**, 1911.
- Fahey, R. E., Strauss, A. J., Anderson, A. C. *J. Cryst. Growth* 1993, **128**, 672.
- Fay, H., Brandle, C. D. *Appl. Phys.* 1967, **38**, 3405.
- Fedulov, S. A., Venevtsev, Yu. N., Dzhiuchadze, D. F. *Kristallografia (Crystallogr. Rep.)* 1962, **7**, 408 (*in Russian*).
- Feng, M., Goodenough, J. B. *Eur. J. Solid State Inorg. Chem.* 1994, **31**, 663.
- Fesenko, E. G. *Perovskite Family and Ferroelectricity*. Moscow: Atomizdat, p. 248; 1972 (*in Russian*).
- Feteira, A., Sinclair, D. C., Lanagan, M. T. *J. Mater. Res.* 2005, **20**, 2391.
- Feteira, A., Sinclair, D. C., Lanagan, M. T. *J. Appl. Phys.* 2007, **101**, 064110.
- Fleury, P. A., Lazay, P. D., Van Uitert, L. G. *Phys. Rev. Lett.* 1974, **33**, 492.
- Fu, Q. X., Xu, X. Y., Peng, D. K., Liu, X. Q., Meng, G. Y. *J. Mater. Sci.* 2003, **38**, 2901.
- Fu, W. T., Ijdo, D. J. W. *J. Solid State Chem.* 2004, **177**, 2973.
- Fu, W. T., Ijdo, D. J. W. *J. Solid State Chem.* 2006, **179**, 2732.
- Fujii, H., Hidaka, M., Wanklyn, B. M. *Phase Transitions* 1999, **70**, 115.
- Garion, G., Wanklyn, B. M. *J. Cryst. Growth* 1967, **1**, 164.
- Geller, S. *J. Chem. Phys.* 1956, **24**, 1236.
- Geller, S. *Acta Crystallogr.* 1957, **10**, 243.
- Geller, S., Bala, V. B. *Acta Crystallogr.* 1956, **9**, 1019.
- Geller, S., Raccach, P. M. *Phys. Rev. B* 1970, **2**, 1167.
- Geller, S., Wood, E. A. *Acta Crystallogr.* 1956, **9**, 563.
- Geller, S., Curlander, P. J., Ruse, G. F. *Mater. Res. Bull.* 1974, **9**, 637.
- Geller, S., Jeffries, J. B., Curlander, P. J. *Acta Crystallogr. B* 1975, **31**, 2770.
- Giess, E. A., Sandstrom, R. L., Gallacher, W. J., Gupta, A., Shinde, S. L., Cook, R. F., Cooper, E. I., O'Sullivan, E. J. M., Roldan, J. M., Segmüller, A. P., Angilello, J. *IBM J. Res. Dev.* 1990, **34**, 916.
- Gilissen, R., Flipot, A. J., Lecocq, R. J. *Am. Ceram. Soc.* 1974, **57**, 274.
- Glazer, A. M. *Acta Crystallogr. B* 1972, **28**, 3384.
- Glazer, A. M. *Acta Crystallogr. A* 1975, **31**, 756.
- Glynn, T. J., Harley, R. T., Hayes, W., Rushworth, A. J., Smith, R. H. *J. Phys. C: Solid State Phys.* 1975, **8**, 126.
- Godina, N. A., Kohler, E. K. *Izv. Akad. Nauk SSSR* 1966, **1**, 24 (*in Russian*).
- Golub, A. M., Nedilko, S. A., Gozhdzhinskii, S. M. *Neorg. Mater. (Inorg. Mater.)* 1978, **14**, 1859 (*in Russian*).
- Goodenough, J. B. *Prog. Solid State Chem.* 1971, **5**, 145.
- Goodenough, J. B., Longo, J. M. *Landolt—Börnstein Tabellen, Neue Serie III/4a*. p. 126–314. Berlin: Springer-Verlag; 1970.
- Gorshunov, B. P., Kozlov, G. V., Sirotinsky, O. I., Chernyshev, I. M. *Sb. Kratk. Soobshch. Fiz. AN SSSR Fiz. Inst. P.N. Lebedeva (USSR)* 1991, **10**, 25 (*in Russian*).
- Gröbner, J., Lukas, H. L., Aldinger, F. *Z. Metallkd.* 1996, **87**, 268.
- Greshchikov, R. G., Popova, V. F., Shirvinskaya, A. K. *Glass Phys. Chem.* 2003, **2**, 194.
- Grishin, A. M., Gusakov, G. V., Mukhin, A. B., Starostyuk, N. Yu., Savitskii, D. I., Syvorotka, I. M. *JETP Lett.* 1993, **57**, 498.
- Guenter, M. M., Korte, C., Brunauer, G., Boysen, H., Lerch, M., Suard, E. Z. *Anorg. Allg. Chem.* 2005, **631**, 1277.
- Guenter, M. M., Lerch, M., Boysen, H., Toebbens, D., Suard, E., Baetz, C. *J. Phys. Chem. Solids* 2006, **67**, 1754.
- Guitel, J. C., Marezio, M., Mareschal, J. *Mater. Res. Bull.* 1976, **11**, 739.
- Guo, X., Sakurai, K. *J. Appl. Phys.* 2000a, **39**, 1230.

- Guo, X., Sakurai, K. J. Mater. Sci. Lett. 2000b, **19**, 451.
- Hammann, J., Ocio, M. Acta Crystallogr. A 1977, **33**, 975.
- Han, B., Neumayer, D. A., Schulz, D. L., Marks, T. J., Zhang, H., Dravid, V. P. Appl. Phys. Lett. 1992, **61**, 3047.
- Han, B., Neumayer, D. A., Marks, T. J., Rudman, D. A., Zhang, H., Dravid, V. P. Appl. Phys. Lett. 1993, **63**, 3639.
- Han, B., Neumayer, D. A., Schulz, D. L., Hinds, B. J., Marks, T. J. J. Vac. Sci. Technol. A 1994, **11**, 1431.
- Han, S. D., Kharkar, S. P., Taxak, V. B., Kumar, D., Park, Y.-Y. Mater. Sci. Eng., B 2006, **127**, 272.
- Harley, R. T. J. Phys. C: Solid State Phys. 1977, **10**, 205.
- Harley, R. T., Hayes, W., Perry, A. M., Smith, S. R. P. J. Phys. C: Solid State Phys. 1973, **6**, 2382.
- Hayward, S. A., Redfern, S. A. T., Salje, E. K. H. J. Phys.: Condens. Matter. 2002, **14**, 10131.
- Hayward, S. A., Morrison, F. D., Redfern, S. A. T., Salje, E. K. H., Scott, J. F., Knight, K. S., Tarantino, S., Glazer, A. M., Shuvaeva, V., Daniel, P., Zhang, M., Carpenter, M. A. Phys. Rev. B 2005, **72**, 54110.
- Henke, M., Perßon, J., Kück, S. J. Lumin. 2000, **87**, 1049.
- Hill, R. J., Jackson, I. Phys. Chem. Miner. 1990, **17**, 89.
- Hirahara, S., Fujikawa, N., Enami, S., Nishi, T. 1994 US Patent 5,356,844.
- Hollmann, E. K., Vendik, O. G., Zaitsev, A. G., Melekh, B. T. Supercond. Sci. Technol. 1994, **7**, 609.
- Howard, C. J., Kennedy, B. J. J. Phys.: Condens. Matter 1999, **11**, 3229.
- Howard, C. J., Kennedy, B. J., Chakoumakos, B. C. J. Phys.: Condens. Matter 2000, **12**, 349.
- Hreniak, D., Strek, W., Deren, A., Bednarkiewicz, A., Lukowiak, B. J. Alloys Compd. 2006, **408**, 828.
- Hsu, C.-S., Huang, C.-L. Mater. Res. Bull. 2001, **36**, 1939.
- Huang, C.-L., Chen, Y.-C. Mater. Res. Bull. 2002a, **37**, 563.
- Huang, C.-L., Chen, Y.-C. Jpn. J. Appl. Phys., Part 1 2002b, **41**, 1459.
- Huang, C.-L., Chen, Y.-C. J. Eur. Ceram. Soc. 2003, **23**, 167.
- Huang, C.-L., Chiang, K.-H. Mater. Res. Bull. 2002, **37**, 1941.
- Huang, C.-L., Hsu, C.-S. Mater. Res. Bull. 2001, **36**, 2677.
- Hughes, H. D., Iddles, M., Reaney, I. M. Appl. Phys. Lett. 2001, **79**, 2952.
- Hume-Rothery, W. Atomic Theory for Students of Metallurgy, 3rd Ed. p. 342. London: The Institute of Metals; 1995.
- Inaba, H., Hayashi, H., Suzuki, M. Solid State Ionics 2001, **144**, 99.
- ICSD—Inorganic Crystal Structure Database. Fachinformationszentrum (FIZ) Karlsruhe, Germany and National Institute of Standards and Technology (NIST), Version 2005–2 USA; USA; 2005.
- Ioffe, V. A., Leonov, A. I., Yanchevskaya, I. S. Fiz. Tverd. Tela (Sov. Phys. Solid State) 1962, **4**, 1788. (*in Russian*).
- Ishigaki, K., Seki, K., Nishimura, E., Watanabe, T., Yoshimura, M. J. Alloys Compd. 2006, **408**, 1177.
- Ishihara, N., Matsuda, H., Azmi Bin Bustam, M., Takita, Y. J. Am. Chem. Soc. 1994, **116**, 3801.
- Ishikawa, T., Takagi, H., Tatekawa, T., Tamura, H. 2002. US patent 6,380,115.
- Islam, M. S. Solid State Ionics 2002, **154**, 75.
- Jacob, K. T., Dasgupta, N., Näfe, H., Aldinger, F. J. Mater. Res. 2000, **15**, 2836.
- Jacob, M. V., Mazierska, J., Krupka, J. Trans. Mater. Res. Soc. Jpn. 2004, **29**, 1093.
- Jančar, B., Suvorov, D., Valant, M. J. Mater. Sci. Lett. 2001, **20**, 71.
- Jančar, B., Suvorov, D., Valant, M. Key Eng. Mater. 2002, **206–212**, 1289.
- Jančar, B., Suvorov, D., Valant, M., Drazic, G. J. Eur. Ceram. Soc. 2003, **23**, 1391.
- Jančar, B., Valant, M., Suvorov, D. Chem. Mater. 2004, **16**, 1075.
- Jones, D. M. Acta Crystallogr. B 2007, **63**, 69.
- Jourdan, M., Zakharov, A., Foerster, M., Adrian, H. J. Magn. Magn. Mater. 2004, **272**, 163.
- Kagawa, M., Suzuki, M., Mizoguchi, Y., Hirai, T., Syono, Y. J. Aerosol Sci. 1993, **24**, 349.
- Kagawa, M., Arimura, M., Nagano, M., Syono, Y. Adv. Sci. Technol. (Faeda, Italy, Surface Eng.) 1999, **20**, 241.
- Kajitani, M., Matsuda, M., Hoshikawa, A., Harjo, S., Kamiyama, T., Ishigaki, T., Izumi, F., Miyake, M. Chem. Mater. 2005, **17**, 4235.
- Kakihana, M., Okubo, T. J. Alloys Compd. 1998, **266**, 129.
- Kaminskii, A. A. Phys. Status Solidi A 1995, **148**, 9.
- Kanazawa, S., Ito, T., Yamada, K., Ohkubo, T., Nomoto, Y., Ishihara, T., Takita, Y. Surf. Coat. Technol. 2003, **169**, 508.

- Kanke, Y., Navrotsky, A. J. *J. Solid State Chem.* 1998, **141**, 424.
- Kapala, J. *J. Alloys Compd.* 2004, **373**, 179.
- Kaufherr, N., Mendelovici, L., Steinberg, M. J. *Less-Comm. Met.* 1985, **107**, 281.
- Kaufman, L., Hayes, F., Birnie, D. CALPHAD: Comput. Coupling Phase Diagrams Thermochem. 1981, **5**, 163.
- Kebin, L., Zhenzhong, Q., Xijun, L., Jingsheng, Z., Yuheng, Z. *Thin Solid Films* 1997, **304**, 389.
- Keith, M. L., Roy, R. *Am. Mineral.* 1954, **39**, 1.
- Kennedy, B. J., Vogt, T., Martin, C. D., Parise, J. B., Hriljac, J. A. *Chem. Mater.* 2002a, **14**, 2644.
- Kennedy, B. J., Howard, C. J., Prodjosantoso, A. K., Chakoumakos, B. C. *Appl. Phys.* 2002b, **74**(Suppl. 1), S1660.
- Key, T. S., Crist Jr., B. J. *Am. Ceram. Soc.* 2005, **88**, 191.
- Kharton, V. V., Viskup, A. P., Naumovich, E. N., Lapchuk, N. M. *Solid State Ionics* 1997, **104**, 67.
- Kim, Y. S. *Acta Crystallogr. B* 1968, **24**, 295.
- Kim, D. W., Kim, D. Y., Hong, K. S. *J. Mater. Res.* 2000, **15**, 1331.
- Kim, M.-H., Nahm, S., Choi, C.-H., Lee, H.-J., Park, H.-M. *Jpn. J. Appl. Phys., Part 1* 2002, **41**, 717.
- Kimura, K., Numazawa, T., Sato, M., Ikeya, T., Fukuda, T. *J. Appl. Phys.* 1995, **77**, 432.
- Kleptsyn, V., Guenrikhson, V., Bogunov, V. *J. Cryst. Growth* 1997, **171**, 109.
- Kobayashi, J., Tazoh, Y., Sasaura, M., Miyazawa, S. *J. Mater. Res.* 1991, **6**, 97.
- Konaka, T., Sato, M., Asano, H., Kubo, S. *J. Supercond.* 1991, **4**, 283.
- Konopka, J., Wolff, I. *IEEE Trans. Microwave Theor. Techn.* 1992, **40**, 2418.
- Konopka, J., Wolff, I., Lewandowski, S. J. *J. Appl. Phys.* 1992, **72**, 218.
- Koren, G., Gupta, A., Giess, E. A., Segmuller, A., Laibowitz, R. B. *Appl. Phys. Lett.* 1989, **54**, 1054.
- Kosola, A., Palvasaari, J., Putkonen, M., Niinisto, L. *Thin Solid Films* 2005, **479**, 152.
- Kotru, P. N., Razdan, A. K., Wanklyn, B. M. *J. Mater. Sci.* 1989, **24**, 793.
- Krupka, J., Geyer, R. G., Kuhn, M., Hinken, J. H. *IEEE Trans. Microwave Theor. Techn.* 1994, **42**, 1886.
- Krylov, V. S., Belova, I. L., Magunov, R. L., Kozlov, V. D., Kalinchenko, A. V., Krotilo, N. P. *Izv. Akad. Nauk SSSR. Neorg. Mater.* 1973, **9**, 1388 (*in Russian*).
- Kung, J., Rigden, S., Gwanmesia, G. *Phys. Earth Planet Inter.* 2000, **118**, 65.
- Kutty, T. R. N., Jayanthi, S. *Appl. Phys. Lett.* 2005, **86**, 122902.
- Kuz'min, M. D., Tishin, A. M. *J. Phys. D.: Appl. Phys.* 1991, **24**, 2039.
- Kuznetsova, T. F., Rat'ko, A. I., Bolotnikova, E. V., Poddenezhnyj, E. N. *Colloid J.* 2006, **68**, 457.
- Kyomen, T., Itoh, M. *J. Therm. Anal. Calorim.* 2002, **69**, 813.
- Lakiza, S. M., Lopato, L. M. *J. Am. Ceram. Soc.* 1997, **80**, 893.
- Lakiza, S., Fabricznaya, O., Wang, Ch., Zinkevich, M., Aldinger, F. *J. Eur. Ceram. Soc.* 2006, **26**, 233.
- Lehnert, H., Boysen, H., Dreier, P., Yu, Y. Z. *Kristallogr.* 2000a, **215**, 145.
- Lehnert, H., Boysen, H., Schneider, J., Frey, F., Hohlwein, D., Radaelli, P., Ehrenberg, H. Z. *Kristallogr.* 2000b, **215**, 536.
- Leonov, A. I. *Izv. Akad. Nauk SSSR, Otd. Khim. Nauk* 1963, **1**, 8 (*in Russian*).
- Leonov, A. I. High-temperature chemistry of cerium oxide compounds. Leningrad: Nauka, p. 199; 1970 (*in Russian*).
- Leonov, A. I., Andreeva, A. V., Shvaiko-Shvaikovskii, V. E., Keller, E. K. *Izv. Akad. Nauk SSSR. Neorg. Mater.* **2**, 517 (*in Russian*); *Inorg. Mater.* 1996, **2**, 446.
- Lerch, M., Boysen, H., Hansen, T. *J. Phys. Chem. Solids* 2001, **62**, 445.
- Levin, A. A. *Kristallografia (Crystallogr. Rep.)* 1992, **37**, 1020 (*in Russian*).
- Li, L., Tang, Z., Sun, W., Wang, P. *Phys. Chem. Glasses* 1997, **38**, 323.
- Li, L., Tang, Z., Sun, W., Wang, P. *Phys. Chem. Glasses* 1999, **40**, 126.
- Lim, D.-G., Kim, B. H., Kim, T.-G., Jung, H. J. *Mater. Res. Bull.* 1999, **34**, 1577.
- Liu, X. Q., Chen, X. M. *J. Eur. Ceram. Soc.* 2004, **24**, 1999.
- Liu, G., Wang, H., Makino, H., Ko, H. J., Hanada, T., Yao, T. *Appl. Surf. Sci.* 2002, **190**, 408.
- Liu, F. S., Liu, Q. L., Liang, J. K., Yang, L. T., Song, G. B., Luo, J., Rao, G. H. *J. Solid State Chem.* 2004, **177**, 1796.
- Lo, J.-R., Tseng, T.-Y. *Mater. Chem. Phys.* 1998, **56**, 56.
- Loutts, G. B., Warren, M., Taylor, R., Rachimov, R. R., Ries, H. R., Miller, G., Noginov, M. A., Curley, M., Noginova, N., Kuchtarev, N., Caulfield, H. J., Venkateswarlu, P. *Phys. Rev. B* 1998, **57**, 3706.

- Lufaso, M. W., Woodward, P. M. *Acta Crystallogr. B* 2001, **57**, 725.
- Lux, B. C., Clark, R. D., Salazar, A., Sveum, L. K., Krebs, M. A. *J. Am. Ceram. Soc.* 1993, **76**, 2669.
- Lybye, D., Poulsen, W. F., Mogensen, M. *Solid State Ionics* 2000, **128**, 91.
- Lyons, K. B., Birgeneau, R. J., Blount, E. I., Van Uitert, L. G. *Phys. Rev. B* 1975, **11**, 891.
- Lysenko, V. A., Voronin, G. F. *Vestn. Mosk. Univ., Ser. 2: Khim.* 1990, **31**, 30 (*in Russian*).
- Maier, A. A., Savinova, I. G. *Inorg. Mater.* 1996, **32**, 1078, *Neorg. Mater.* 1996, **32**, 1230 (*in Russian*).
- Makeev, Yu., Motornenko, A., Cherpak, N., Babiichuk, I., Kosmyna, M. *Tech. Phys. Lett.* 2002, **28**, 221.
- Mares, J. A., Pedrini, C., Moine, B., Blazek, K., Kvapil, J. *Chem. Phys. Lett.* 1993, **206**, 9.
- Mares, J. A., Nikl, M., Chval, J., Dafinei, I., Lecoq, P., Kvapi, J. *Chem. Phys. Lett.* 1995, **241**, 311.
- Mares, J. A., Nikl, M., Maly, P., Bartos, K., Nejezchleb, K., Blezek, K., Noteristefani, F., D'Ambrossio, C., Puertolas, D., Rosso, E. *Opt. Mater.* 2002, **19**, 117.
- Marezio, M., Remejka, J. P., Dernier, P. D. *Mater. Res. Bull.* 1966, **1**, 247.
- Marezio, M., Remeika, J. P., Dernier, P. D. *Inorg. Chem.* 1968, **7**, 1337.
- Marezio, M., Remeika, J. P., Dernier, P. D. *Acta Crystallogr. B* 1970, **26**, 2008.
- Marezio, M., Dernier, P., Remeika, P. J. *Solid State Chem.* 1972, **4**, 11.
- Marti, W., Fischer, P., Altorfer, F., Scheel, H. J., Tadin, M. J. *Phys.: Condens. Matter* 1994, **6**, 127.
- Marti, W., Medarde, M., Rozenkranz, S., Fischer, P., Furrer, A., Klemenz, C. *Phys. Rev. B* 1995, **52**, 4275.
- Marti, W., Fischer, P., Schefer, J., Kubel, F. Z. *Kristallogr.* 1996, **221**, 891.
- Mathur, S., Veith, M., Shen, H., Huefner, S., Jilavi, M. H. *Chem. Mater.* 2002, **14**, 568.
- Matkovskii, A. O., Savytskii, D. I., Sugak, D. Yu., Solskii, I. M., Vasylechko, L. O., Zhydachevskii, Ya. A., Mond, M., Petermann, K., Wallrafen, F. J. *Cryst. Growth* 2002, **241**, 455.
- Matraszek, A., Miller, M., Singheiser, L., Hilpert, K. J. *Am. Ceram. Soc.* 2003, **86**, 1911.
- Matsuda, M., Ohara, O., Murata, K., Ohara, S., Fukui, T., Miyake, M. *Electrochem. Solid-State Lett.* 2003, **6**, 140.
- Mazelsky, R., Kramer, W. E., Hopkins, R. H. J. *Cryst. Growth* 1968, **2**, 209.
- Mazierska, J., Krupka, J., Jacob, M. V., Ledenyov, D. *IEEE Trans. Microwave Theory Techn.: Microwave Symp. Digest* 2004, **3**, 1825.
- Minh, N. Q. *J. Am. Ceram. Soc.* 1993, **76**, 563.
- Miyazawa, S. *Appl. Phys. Lett.* 1989, **55**, 2230.
- Miyazawa, Y., Tushima, H., Morita, S. J. *Cryst. Growth* 1993a, **128**, 668.
- Miyazawa, S., Sasaura, M., Mukaida, M. J. *Cryst. Growth* 1993b, **128**, 704.
- Mizuno, M. *Yogio Kyokaishi. (J. Ceram. Soc. Jpn.)* 1979, **87**, 405.
- Mizuno, M., Noguchi, T. *Rep. Gov. Ind. Res. Inst. Nagoya* 1967, **16**, 171.
- Mizuno, M., Noguchi, T. *Yogio Kyokaishi (J. Ceram. Soc. Jpn.)* 1980, **88**, 322.
- Mizuno, M., Yamada, T. *Yogio Kyokaishi (J. Ceram. Soc. Jpn.)* 1985, **93**, 686.
- Mizuno, M., Yamada, T. *Yogio Kyokaishi (J. Ceram. Soc. Jpn.)* 1988, **96**, 54.
- Mizuno, M., Yamada, T. *Yogio Kyokaishi (J. Ceram. Soc. Jpn.)* 1989, **97**, 1334.
- Mizuno, M., Yamada, T. *Nagoya Kogio Gijutsu Shikensho Hokoku* 1992, **40(2)**, 389.
- Mizuno, M., Berjoan, M., Coutures, J. P., Foex, M. *Yogio Kyokaishi (J. Ceram. Soc. Jpn.)* 1974, **82**, 631.
- Mizuno, M., Yamada, T., Noguchi, T. *Yogio Kyokaishi (J. Ceram. Soc. Jpn.)* 1975, **83**, 90.
- Mizuno, M., Yamada, T., Noguchi, T. *Yogio Kyokaishi (J. Ceram. Soc. Jpn.)* 1977a, **85**, 24.
- Mizuno, M., Yamada, T., Noguchi, T. *Yogio Kyokaishi (J. Ceram. Soc. Jpn.)* 1977b, **85**, 90.
- Mizuno, M., Yamada, T., Noguchi, T. *Yogio Kyokaishi (J. Ceram. Soc. Jpn.)* 1977c, **85**, 374.
- Mizuno, M., Yamada, T., Noguchi, T. *Yogio Kyokaishi. (J. Ceram. Soc. Jpn.)* 1977d, **85**, 543.
- Mizuno, M., Yamada, T., Noguchi, T. *Yogio Kyokaishi (J. Ceram. Soc. Jpn.)* 1978, **86**, 359.
- Mizuno, M., Yamada, T., Ohtake, T. *Yogio Kyokaishi (J. Ceram. Soc. Jpn.)* 1985, **93**, 295.
- Mizusaki, J., Yasuda, I., Shimoyama, J., Yamauchi, S., Fueki, K. J. *Electrochem. Soc.* 1993, **140**, 467.
- Moeller, T., King, G. L. *J. Am. Chem. Soc.* 1953, **75**, 6060.
- Moon, J. H., Jang, H. M., Park, H. S., Shin, J. Y., Kim, H. S. *Jpn. J. Appl. Phys., Part 1* 1999, **38**, 6821.
- Morell, J. S., Xue, Z. B., Specht, E. D., Beach, D. B. *Mater. Res. Soc. Symp. Proc.* 1999, **547**, 309.
- Mori, K., Fukunaga, T., Shibata, K., Iwase, K., Harjo, S., Hoshikawa, A., Itoh, K., Kamiyama, T., Ishigaki, T. *Phys. B (Amsterdam, Netherlands)* 2004, **352**, 147.
- Morita, S., Watanabe, T., Funayama, M., Miyazawa, Y., Sekita, M. J. *Cryst. Growth* 1996, **166**, 370.
- Morozov, A. N., Morozova, O. Ya., Ponomarev, N. M., Knyazev, S. N. *Sverkhprovodimost: Fizika, Khimiya, Tekhnika* 1992, **5**, 388 (*in Russian*).

- Morozov, A. N., Morozova, O. Ya., Ponomarev, N. M. *Kristallografia* (Crystallogr. Rep.) 1993a, **38**, 149 (*in Russian*).
- Morozov, A. N., Morozova, O. Ya., Glukhov, K. Ya. *Kristallografia* (Crystallogr. Rep.) 1993b, **38**, 160 (*in Russian*).
- Moses, W. W., Derenzo, S. E., Fedorov, A., Korzhik, M., Gektin, A., Minkov, B., Aslanov, V. *IEEE Trans. Nucl. Sci.* 1995, **42**, 275.
- Moussa, S. M., Kennedy, B. J., Hunter, B. A., Howard, C. J., Vogt, T. J. *Phys.: Condens. Matter* 2001, **13**, 203.
- Moussa, S. M., Claridge, J. B., Rosseinsky, M. J., Clarke, S., Ibberson, R. M., Price, T., Iddles, D. M., Sinclair, D. C. *Appl. Phys. Lett.* 2003, **82**, 4537.
- Müller, K. A., Berlinger, W., Waldner, F. *Phys. Rev. Lett.* 1968, **21**, 814.
- Nakatsuka, A., Ohtaka, O., Arima, H., Nakayama, N., Mizota, T. *Acta Crystallogr. E* 2005, **61**, 148.
- Nenasheva, E. N., Mudraliubova, L. P., Kartenko, N. F. *J. Eur. Ceram. Soc.* 2003, **23**, 2443.
- Neuroth, G., Wallrafen, F. *J. Cryst. Growth* 1999, **198**, 435.
- Nicolas, J., Coutures, J., Coutures, J. P. *Rev. Int. Hautes Temp. Refract.* 1983, **20**, 129.
- Nicolas, J., Coutures, J., Coutures, J. P., Boudot, B. *J. Solid State Chem.* 1984, **52**, 101.
- Nieminen, M., Lehto, S., Niinisto, L. *J. Mater. Chem.* 2001, **11**, 2148.
- Nikl, M., Solovieva, N., Pejchal, J., Shim, J. B., Yoshikawa, A., Fukuda, T., Vedda, A., Martini, M., Yoon, D. H. *Appl. Phys. Lett.* 2004, **84**, 882.
- Noginov, M. A., Loutts, G. B., Jones, D. E., Turney, V. J., Rachimov, R. R., Herbert, L., Truong, A. *J. Appl. Phys.* 2002, **91**, 569.
- Noginova, N., Loutts, G. B., Gillman, E. S., Atsarkin, V. A., Verevkin, A. A. *Phys. Rev. B* 2001, **63**, 174414.
- Nordland, W. A., Van Uitert, L. G. *J. Phys. Chem. Solids* 1970, **31**, 1257.
- O'Bryan, H. M., Gallagher, P. K., Berkstresser, G. W., Brandle, C. D. *J. Mater. Res.* 1990, **5**, 183.
- Okada, S., Kudou, K., Izumi, K., Nakajima, K., Shishido, T. *Kokushikan Daigaku Rikogaku Kenkyusho Hokoku* (Bull. Sci. Eng. Res. Inst. Kokushikan University) 2004, **16**, 23.
- Okano, Y., Ikeya, T., Hoshikawa, K., Fukua, T. *J. Cryst. Growth* 1993, **131**, 616.
- Okazaki, H., Arakawa, A., Asahi, T., Oda, O., Aiki, K. *Solid-State Electron.* 1997, **41**, 263.
- Palacios, E., Bartolome, J., Luis, F. *Phys. Rev. B* 2003, **68**, 224425.
- Pawlak, D. A., Lukasiewicz, T., Carpenter, M., Malinowski, M., Diduszko, R., Kisielewski, J. *J. Cryst. Growth* 2005, **282**, 260.
- Pena, M. A., Fierro, J. L. *G. Chem. Rev.* 2001, **101**, 1981.
- Petrosyan, A. G., Shirinyan, G. O., Ovanesian, K. L., Pedrini, C., Dujardin, C. *J. Cryst. Growth* 1999, **198**, 492.
- Petrosyan, A. G., Shirinyan, G. O., Ovanesian, K. L., Pedrini, C., Dujardin, C., Garnier, N., Sowinski, S., Lecoq, P., Belsky, A. *Nucl. Instrum. Methods Phys. Res., Sect. A* 2002, **486**, 74.
- Petrosyan, A. G., Popova, V. F., Gusarov, V. V., Shirinyan, G. O., Pedrini, C., Lecoq, P. *J. Cryst. Growth* 2006, **293**, 74.
- Phase Equilibria Diagrams: Phase Diagrams for Ceramists. The American Ceramic Society 1994, **I–XI**.
- Podlesnyak, A., Rosenkranz, S., Fauth, F., Marti, W., Sheel, H. J., Furrer, A. *J. Phys.: Condens. Matter* 1994, **6**, 4099.
- Polini, R., Pamio, A., Traversa, E. *J. Eur. Ceram. Soc.* 2004, **24**, 1365.
- Polteva, T. V., Venskivskii, N. U., Kaleva, G. M., Mosunov, A. V., Prutchenko, S. G., Politova, E. D. *Inorg. Mater.* 2004, **40**, 80; *Neorg. Mater.* 2004, **10**, 90 (*in Russian*).
- Portnoj, K. I., Timofeeva, N. I. *Oxygen Compounds of Rare Earth Element*. Moscow: Metallurgiya; 1986 p.480 (*in Russian*).
- Pramanik, P. *Bull. Mater. Sci.* 1996, **19**, 957.
- Putnam, R. M., Navrotsky, A., Cordfunke, E. H. P., Huntelaar, M. E. *J. Chem. Thermodyn.* 2000, **32**, 911.
- Radhakrishna, P., Hamman, J., Ocio, M., Pari, P., Allain, J. *Solid State Commun.* 1981, **37**, 813.
- Ranløv, J., Nielsen, K. *J. Appl. Crystallogr.* 1995, **28**, 436.
- Rao, R. P. *J. Electrochem. Soc.* 1996, **143**, 189.
- Rao, G. H., Bärner, K., Brown, I. D. *J. Phys.: Condens. Matter* 1998, **10**, 757.
- Razdan, A. K., Bamzai, K. K., Hangloo, V., Kotru, P. N., Wanklyn, B. M. *J. Cryst. Growth* 2000, **219**, 40.
- Reid, A. F., Ringwood, A. E. *J. Geophys. Res.* 1975, **80**, 3363.

- Reller, A. *Philos. Mag.* 1993, **68**, 641.
- Robertson, J. *Rep. Prog. Phys.* 2006, **69**, 327–396.
- Rolin, M., Thanh, P. H. *Rev. Hautes Temp. Refract.* 1965, **2**, 182.
- Ross, N. L. *Phase Transitions* 1996, **58**, 27.
- Ross, N. L. *Phys. Chem. Miner.* 1998, **25**, 597.
- Ross, N. L., Zhao, J., Burt, J. B., Chaplin, T. D. *J. Phys.: Condens. Matter* 2004a, **16**, 5721.
- Ross, N. L., Zhao, J., Angel, R. J. *J. Solid State Chem.* 2004b, **177**, 3768.
- Ross, N. L., Zhao, J., Angel, R. J. *J. Solid State Chem.* 2004c, **177**, 1276.
- Roth, R. S. *J. Res. Natl. Bur. Stand.* 1957, **58**, 75.
- Roult, G., Pastuszak, R., Marchand, R., Laurent, Y. *Acta Crystallogr. C* 1983, **39**, 673.
- Ruggiero, A., and Ferro, R. *Atti della Accademia Nazionale dei Lincei, Classe di Scienze Fisiche, Matematiche Naturali: Rendiconti*; 1954, **8**, 48.
- Ruse, G. F., Geller, S. J. *Cryst. Growth* 1975, **29**, 305.
- Saitow, A., Yoshikawa, A., Horiuchi, H., Shishido, T., Fukuda, T., Tanaka, M., Mori, T., Sasaki, S. J. *Appl. Crystallogr.* 1998, **31**, 663.
- Sakurai, K., Guo, X. *Mater. Sci. Eng., A* 2001, **304–306**, 403.
- Salinas-Sanchez, A., Garcia-Munoz, J. L., Rodriguez-Carvajal, J., Saez-Puche, R., Martinez, J. J. *Solid State Chem.* 1992, **100**, 201.
- Samara, G. A. *J. Appl. Phys.* 1990, **68**, 4214.
- Sandiumenge, F., Dubs, C., Gömört, P., Gali, S. *Appl. Phys.* 1994, **75**, 5243.
- Sandstrom, R. L., Giess, E. A., Gallaher, W. J., Segmüller, A., Cooper, E. I., Chisholm, M. F., Gupta, A., Shinde, S., Laibowitz, R. B. *Appl. Phys. Lett.* 1988, **53**, 1874.
- Sanjuán, M. L., Orera, V. M., Merini, R. I., Blasco, J. J. *Phys.: Condens. Matter* 1998, **10**, 11687.
- Sasaki, S., Prewitt, C. T., Liebermann, R. C. *Am. Mineral.* 1983, **68**, 1189.
- Sasaura, M., Miyazawa, S. J. *Cryst. Growth* 1992, **123**, 126.
- Sasaura, M., Miyazawa, S. J. *Cryst. Growth* 1993, **131**, 413.
- Sasaura, M., Mukaida, M., Miyazawa, S. *Appl. Phys. Lett.* 1990a, **57**, 2728.
- Sasaura, M., Miyazawa, S., Mukaida, M. J. *Appl. Phys.* 1990b, **68**, 3643.
- Savytskii, D. I. *Crystal structure, orientation states and properties of rare earth gallates*. Ph.D. thesis. The Ivan Franko State Univ. of Lviv; 1997 p. 147 (*in Ukrainian*).
- Savytskii, D. I., Ubizskii, S. B., Vasylechko, L. O., Matkovskii, A. O., Syvorotka, I. M. *Crystallogr. Rep.* 1996, **41**, 859.
- Savytskii, D. I., Ubizskii, S. B., Vasylechko, L. O., Syvorotka, I. M., Matkovskii, A. O. *Acta Phys. Pol., A* 1997, **92**, 231.
- Savytskii, D. I., Ubizskii, S. B., Matkovskii, A. O., Suchocki, A., Bismayer, U., Pashkov, V. M., Borisov, V. N., Alexandrovskii, A. N., Soldatov, A. V. *Phase Transitions* 1999, **70**, 57.
- Savytskii, D. I., Vasylechko, L. O., Matkovskii, A. O., Solskii, I. M., Suchocki, A., Sugak, D. Yu., Wallrafen, F. J. *Cryst. Growth* 2000a, **209**, 874.
- Savytskii, D. I., Berkowski, M., Vasylechko, L. O., Fink-Finowicki, J., Matkovskii, A. O. *Cryst. Res. Technol.* 2000b, **35**, 53.
- Savytskii, D. I., Vasylechko, L. O., Berkowski, M., Fink-Finowicki, J., Aleksijko, R., Byszewski, P., Matkovskii, A. O. *Ferroelectrics* 2000c, **254**, 121.
- Savytskii, D., Senyshyn, A., Wieteska, K., Wierzchowski, W., Frukacz, Z., Bismayer, U., Vasylechko, L., Matkovskii, A. *Z. Kristallogr.* 2003a, **218**, 17.
- Savytskii, D., Vasylechko, L., Senyshyn, A., Matkovskii, A., Baehtz, C., Sanjuan, M. L., Bismayer, U., Berkowski, M. *Phys. Rev. B* 2003b, **68**, 024101.
- Scheel, H. J., Berkowski, M., Chabot, B. *Phys. C (Amsterdam, Neth.)* 1991, **185**, 2095.
- Schneider, S. J., Roth, R. S., Waring, J. L. *J. Res. Natl. Bur. Stand. A* 1961, **65**, 345.
- Schoonover, J. R., Saab, A., Bridgewater, J. S., Havrilla, G. J., Zugates, C. T., Treado, P. J. *Appl. Spectrosc.* 2000, **54**, 1362.
- Scott, J. F. *Phys. Rev.* 1969, **183**, 823.
- Sebastian, M. T., Solomon, S., Ratheesh, R., George, J., Mohanan, P. J. *Am. Ceram. Soc.* 2001, **84**, 1487.
- Sebastian, M. T., Axelsson, A.-K., McAlford, N. 2005. List of microwave dielectric resonator materials and their properties, <http://www.lsbu.ac.uk/dielectric-materials/>.
- Sekita, M., Miyazawa, Y., Morita, S., Sekiwa, H., Sato, Y. *Appl. Phys. Lett.* 1994, **65**, 2380.

- Sekita, M., Miyazawa, Y., Ishi, M. Appl. Phys. 1998, **83**, 7940.
- Selvam, M. P., Rao, K. J. Adv. Mater. 2000, **12**, 1621.
- Senyshyn, A., Vasylechko, L., Savytskii, D., Knapp, M., Baehetz, C., Bismayer, U., Berkowski, M., Matkovskii, A. HASYLAB Ann. Rep. 2001, **1**, 517.
- Senyshyn, A., Vasylechko, L., Savytskii, D., Baehetz, C., Knapp, M., Bismayer, U., Berkowski, M. HASYLAB Ann. Rep. 2002, **1**, 355.
- Senyshyn, A., Vasylechko, L., Knapp, M., Bismayer, U., Berkowski, M., Matkovskii, A. HASYLAB Ann. Rep. 2003, **1**, 503.
- Senyshyn, A., Vasylechko, L., Knapp, M., Bismayer, U., Berkowski, M., Matkovskii, A. J. Alloys Compd. 2004a, **382**, 84.
- Senyshyn, A. T., Vasylechko, L. O., Matkovskii, A. O. Bull. Lviv Polytech. Natl. Univ. Electronics 2004b, **514**, 130 (*in Ukrainian*).
- Senyshyn, A., Oganov, A. R., Vasylechko, L., Ehrenberg, H., Bismayer, U., Berkowski, M., Matkovskii, A. J. Phys.: Condens. Matter 2004c, **16**, 253.
- Senyshyn, A., Vasylechko, L., Trots, D., Knapp, M. HASYLAB Ann. Rep. 2005a, **1**, 433.
- Senyshyn, A., Ehrenberg, H., Vasylechko, L., Gale, J. D., Bismayer, U. J. Phys.: Condens. Matter 2005b, **17**, 6217.
- Senyshyn, A., Schnelle, W., Vasylechko, L., Ehrenberg, H., Berkowski, M. J. Phys.: Condens. Matter 2007, **19**, 156214.
- Shannon, R. D. J. Appl. Phys. 1993, **73**, 348.
- Shannon, R. D. Acta Crystallogr. A 1976, **32**, 751.
- Sharma, K. K., Kotru, P. N., Tandon, R. P., Wanklyn, B. M. J. Phys.: Condens. Matter 1998, **10**, 5277.
- Shelykh, A. I., Melekh, B. T. Phys. Solid State 2003, **45**, 238.
- Shelykh, A. I., Zhdanovich, N. S., Melekh, B. T., Kartenko, N. F., Filin, Yu. N., Prokofyev, A. V., Smirnov, I. A. Fiz. Tverd. Tela (Phys. Solid State) 1994, **36**, 817 (*in Russian*).
- Shevlin, S. A., Curioni, A., Andreoni, W. Phys. Rev. Lett. 2005, **94**, 146401.
- Shibasaki, T., Furuya, T., Wang, S., Hashimoto, T. Solid State Ionics 2004, **174**, 193.
- Shim, J. B., Yoshikawa, A., Nikl, M., Pejchal, J., Yoon, D.-H., Isshiki, M., Fukuda, T. Jpn. J. Appl. Phys., Part 1 2004, **43**, 7661.
- Shimada, T., Kakimoto, K. I., Ohsato, H. J. Eur. Ceram. Soc. 2005, **25**, 2901.
- Shirvinskaya, A. K., Popova, V. F. Dokl. Akad. Nauk SSSR 1977, **233**, 1110. (*in Russian*); Acad. Sci. USSR, Dokl. Chem. **233**, 242.
- Shishido, T., Tanaka, M., Horiuchi, H., Iwasaki, H., Toyota, N., Shindo, D., Fukuda, T. J. Alloys Compd. 1993, **192**, 84.
- Shishido, T., Nojima, S., Tanaka, M., Horiuchi, H., Fukuda, T. J. Alloys Compd. 1995a, **227**, 175.
- Shishido, T., Nakagawa, S., Yoshikawa, A., Horiuchi, H., Tanaka, M., Sasaki, T., Fukuda, T. Nippon Kagaku Kaishi (J. Chem. Soc. Jpn., Chem. and Industr. Chem.) 1995b, **9**, 697.
- Shishido, T., Sheng, Y. T., Horiuchi, H., Yoshikawa, A., Hosoya, S., Tozawa, S., Saito, A., Tanaka, M., Fukuda, T. Nippon Kagaku Kaishi (J. Chem. Soc. Jpn., Chem. and Industr. Chem.) 1996, **11**, 991.
- Shishido, T., Zheng, Y., Saito, A., Horiuchi, H., Okada, S., Kudou, K., Fukuda, T. J. Ceram. Soc. Jpn. 1997a, **105**, 681.
- Shishido, T., Zheng, Y., Saito, A., Horiuchi, H., Kudou, K., Okada, S., Fukuda, T. J. Alloys Compd. 1997b, **260**, 88.
- Shmurak, S. Z., Strukova, G. K., Shmyt'ko, I. M., Klassen, N. V., Kobelev, N. P., Derenzo, S. E., Weber, M. J. Nucl. Instrum. Methods Phys. Res., Sect. A 2005, **537**, 149.
- Shoup, S. S., Paranthaman, M., Goyal, A., Specht, E. D., Lee, D. F., Kroeger, D. M., Beach, D. B. J. Am. Ceram. Soc. 1998, **81**, 3019.
- Simon, R. W., Plan, C. E., Lee, A. E., Lee, G. S., Daly, K. P., Wire, M. S., Luine, J. A., Urbanik, M. Appl. Phys. Lett. 1988, **53**, 2677.
- Sinclair, W., Eggleton, R. A., Ringwood, A. E. Z. Kristallogr. 1979, **149**, 307.
- Sinha, A., Sharma, B. P., Gopalan, P. Electrochim. Acta 2006, **51**, 1184.
- Skowron, A., Huang, P., Petric, A. J. Solid State Chem. 1999, **143**, 202.
- Slater, P. R., Irvine, J. T. S., Ishihara, T., Takita, Y. J. Solid State Chem. 1998a, **139**, 135.
- Slater, P. R., Irvine, J. T. S., Ishihara, T., Takita, Y. Solid State Ionics 1998b, **107**, 319.

- Sobolewski, R., Gierlowski, P., Kula, W., Zarembinski, S., Lewandowski, S. J., Berkowski, M., Pajaczowska, A., Gorshunov, B. P., Lyudmirsky, D. B., Sirotinsky, O. I. IEEE Trans. Magnetics 1991, **27**, 876.
- Stan, M., Armstrong, T. J., Butt, D. P., Wallace, T. C., Park, Y. S., Haertling, C. L., Hartmann, T., Hanrahan, R. J. J. Am. Ceram. Soc. 2002, **85**, 2811.
- Stankus, S. V., Tyagel'sky, P. V. J. Cryst. Growth 1996, **167**, 165.
- Stoneham, A. M., Gavartin, J. L., Shluger, A. L. J. Phys.: Condens. Matter 2005, **17**, S2027.
- Sturge, M. D., Cohen, E., Van Uitert, L. G., Van Stapele, R. P. Phys. Rev. B 1975, **11**, 4768.
- Sun, P., Nakamura, T., Shan, Y. J., Inaguma, Y., Itoh, M., Kitamura, T. Jpn. J. Appl. Phys., Part 1, 1998, **37**, 5625.
- Surendran, K. P., Solomon, S., Varma, M. R., Mohanan, P., Sebastian, M. T. J. Mater. Res. 2002, **17**, 2561.
- Suvorov, D., Valant, M., Skapin, S., Kolar, D. J. Mater. Sci. 1998, **33**, 85.
- Suvorov, D., Valant, M., Jancar, B., Skapin, S. D. Acta Chim. Slov. 2001, **48**, 87.
- Takata, H., Iiduka, M., Notsu, Y., Harada, M. J. Alloys Compd. 2006, **408**, 1190.
- Tanaka, I., Kobashi, M., Kojima, H. J. Cryst. Growth 1993a, **128**, 680.
- Tanaka, M., Shishido, T., Horiuchi, H., Toyota, N., Shindo, T., Fukuda, T. J. Alloys Compd. 1993b, **192**, 87.
- Tas, A. C., Akinc, M. J. Am. Ceram. Soc. 1994, **77**, 2961.
- Taspinar, E., Tas, A. C. J. Am. Ceram. Soc. 1997, **80**, 133.
- Timofeeva, N. I., Timofeeva, E. N., Drozdova, L. N., Mordovin, O. A. Izv. Akad. Nauk SSSR, Neorg. Mater. 1969, **5**, 1742. (*in Russian*).
- Toropov, N. A., Kiseleva, T. P. Zh. Neorg. Khim. 1961, **6**(10), 2353 (*in Russian*); RUSS. J. Inorg. Chem. **6**, 1193.
- Toropov, N. A., Vasilieva, V. A. Dokl. Akad. Nauk SSSR 1963, **152**, 1379 (*in Russian*).
- Toropov, N. A., Bondar, I. A., Galakhov, F. Ya., Nikogosyan, Kh. S., Vinogradova, N. V. Izv. Akad. Nauk SSSR, Ser. Khim. 1964, **7**, 1158 (*in Russian*).
- Toropov, N. A., Barzakovskii, V. P., Lapin, V. V., Kurtseva, N. N. Handbook of Phase Diagrams of the Silicate Systems, vol. 1. Leningrad: Nauka; 1969. p. 882 (*in Russian*).
- Tozawa, S., Shishido, T., Tanaka, M., Sasaki, T., Chiba, T., Oishi, S., Machida, K., Kamegashira, N., Horiuchi, H., Nakajima, K. Gijutsu Gijutsu Kenkyu Hokoku (Techn. Rep. Inst. Met. Res. Tohoku University) 2003, **20**, 33 (*in Japanese*).
- Ubizskii, S. B., Vasylechko, L. O., Savytskii, D. I., Matkovskii, A. O., Syvorotka, I. M. Supercond. Sci. Technol. 1994, **7**, 766.
- Udalov, Yu. P. in: Galakhov, F. Ya., editor. Phase diagrams of the refractory oxide systems (*Diagrammy sostojanija sistem tugoplavkikh oksidov*), Issue 5, Binary systems, Part I. Leningrad: Nauka; 1985, pp. 116–171, Leningrad: Nauka; 1985. (*in Russian*).
- Udalov, Yu. P., Rakhmankulov, R. M., Chemekova, T. Yu., Belousova, O. L. Glass Phys. Chem. 2003, **29**, 200.
- Uecker, R., Reiche, P., Alex, V., Doerschel, J., Schalge, R. J. Cryst. Growth 1994, **137**, 278.
- Utke, I., Klemenz, C., Sheel, H. J., Nüesch, P. J. Cryst. Growth 1997, **174**, 813.
- Vasylechko, L. Visnyk Lviv Univ. Ser. Khim. 2001, **40**, 98 (*in Ukrainian*).
- Vasylechko, L. O. Crystal chemistry and phase transitions in complex oxides of rare earth elements with perovskite structure. Dr. Sci. Thesis. The Ivan Franko Natl. Univ. of Lviv, 2005, 343. (*in Ukrainian*).
- Vasylechko, L. O., Matkovskii, A. O. Bull. Lviv Polytech. Natl. Univ., Electronics 2004, **514**, 33 (*in Ukrainian*).
- Vasylechko, L. O., Senyshyn, A. T. Bull. Lviv Polytech. Natl. Univ., Electronics 2004, **513**, 3 (*in Ukrainian*).
- Vasylechko, L., Akselrud, L., Matkovskii, A., Sugak, D., Durygin, A., Frukacz, Z., Lukasiewicz, T. J. Alloys Compd. 1996, **242**, 18.
- Vasylechko, L., Akselrud, L., Morgenroth, W., Bismayer, U., Matkovskii, A., Savytskii, D. HASYLAB Ann. Rep. 1998, **1**, 555.
- Vasylechko, L., Matkovskii, A., Savytskii, D., Suchocki, A., Wallrafen, F. J. Alloys Compd. 1999a, **292**, 57.

- Vasylechko, L., Matkovskii, A., Suchocki, A., Savytskii, D., Syvorotka, I. J. *Alloys Compd.* 1999b, **286**, 213.
- Vasylechko, L., Savytskii, D., Schmidt, H., Bismayer, U., Matkovskii, A., Loutts, G., Paulmann, C. *HASYLAB Ann. Rep.* 2000a, **1**, 599.
- Vasylechko, L. O., Red'ko, N. A., Savytskii, D. I., Fadeev, S. V. *Bull. Lviv Polytech. Natl. Univ. Electronics* 2000b, **401**, 57 (*in Ukrainian*).
- Vasylechko, L., Savytskii, D., Schmidt, H., Bismayer, U., Matkovskii, A., Berkowski, M. *HASYLAB Ann. Rep.* 2000c, **1**, 615.
- Vasylechko, L., Akselrud, L., Morgenroth, W., Bismayer, U., Matkovskii, A., Savytskii, D. J. *Alloys Compd.* 2000d, **297**, 46.
- Vasylechko, L., Berkowski, M., Matkovski, A., Savytskii, D., Fink-Finowicki, J. *Mater. Res. Bull.* 2000e, **35**, 333.
- Vasylechko, L., Berkowski, M., Matkovskii, A., Piekarczyk, W., Savytskii, D. J. *Alloys Compd.* 2000f, **300–301**, 471.
- Vasylechko, L., Niewa, R., Borrmann, H., Knapp, M., Savytskii, D., Matkovskii, A., Bismayer, U., Berkowski, M. *Solid State Ionics* 2001a, **143**, 219.
- Vasylechko, L., Savytskii, D., Matkovskii, A., Berkowski, M., Knapp, M., Bismayer, U. J. *Alloys Compd.* 2001b, **328**, 264.
- Vasylechko, L., Niewa, R., Senyshyn, A., Pivak, Ye., Savytskii, D., Knapp, M., Baehtz, C. *HASYLAB Ann. Rep.* 2002a, **1**, 223.
- Vasylechko, L. O., Matkovskii, A. O., Savytskii, D. I., Berkowski, M., Bismayer, U., Solskii, I. M., Wallrafen, F. *Bull. Lviv Polytech. Natl. Univ. Electronics* 2002b, **459**, 61 (*in Ukrainian*).
- Vasylechko, L., Borrmann, H., Berkowski, M., Senyshyn, A., Savytskii, D., Knapp, M., Baehtz, C., Bismayer, U., Matkovskii, A. *HASYLAB Ann. Rep.* 2002c, **1**, 433.
- Vasylechko, L. O., Fadeev, S. V., Red'ko, N., Berkowski, M. *Bull. Lviv Polytech. Natl. Univ. Electronics* 2002d, **455**, 21 (*in Ukrainian*).
- Vasylechko, L., Matkovskii, A., Senyshyn, A., Savytskii, D., Knapp, M., Baehtz, C. *HASYLAB Ann. Rep.* 2003a, **1**, 251.
- Vasylechko, L., Fadeyev, S., Niewa, R., Schnelle, W., Knapp, M. *HASYLAB Ann. Rep.* 2003b, **1**, 399.
- Vasylechko, L., Fadyeev, S., Trots, D., Senyshyn, A., Niewa, R., Schnelle, W., Knapp, M. *HASYLAB Ann. Rep.* 2003c, **1**, 255.
- Vasylechko, L., Vashook, V., Savytskii, D., Senyshyn, A., Niewa, R., Knapp, M., Ullmann, H., Berkowski, M., Matkovskii, A., Bismayer, U. J. *Solid State Chem.* 2003d, **172(2)**, 396.
- Vasylechko, L., Senyshyn, A., Savytskii, D., Knapp, M., Baehtz, C., Bismayer, U. *HASYLAB Ann. Rep.* 2004a, **1**, 407.
- Vasylechko, L., Niewa, R., Senyshyn, A., Trots, D., Bismayer, U., Knapp, M., Baehtz, C., Fadyeev, S. *HASYLAB Ann. Rep.* 2004b, **1**, 323.
- Vasylechko, L., Pivak, Ye., Senyshyn, A., Savytskii, D., Berkowski, M., Borrmann, H., Knapp, M., Paulmann, C. J. *Solid State Chem.* 2005, **178**, 270.
- Vasylechko, L., Trots, D. M., Senyshyn, A., Lukasiewicz, T. *HASYLAB Ann. Rep.* 2006, **1**, 606.
- Vasylechko, L., Senyshyn, A., Trots, D. M. *HASYLAB Ann. Rep.* 2007a, **1**, 469.
- Vasylechko, L., Senyshyn, A., Trots, D., Niewa, R., Schnelle, W., Knapp, M. J. *Solid State Chem.* 2007b, **180**, 1277.
- Veith, M., Mathur, S., Lecerf, N., Bartz, K., Heintz, M., Huch, V. *Chem. Mater.* 2000, **12**, 271.
- Veith, M., Mathur, S., Shen, H., Lecerf, N., Huefner, S., Jilavi, M. H. *Chem. Mater.* 2001, **13**, 4041.
- Vidiasagar, K., Gopalakrishnan, J., Rao, C. N. R. J. *Solid State Chem.* 1985, **58**, 29.
- Vorotilova, L. S., Kviatkovskii, O. E., Levin, A. A., Shchegolev, B. F. *Fiz. Tverd. Tela (Phys. Solid State)* 1993, **35**, 285 (*in Russian*).
- Wang, Y., Liu, X., Yao, G.-D., Liebermann, R. C., Dudley, M. *Mater. Sci. Eng., A* 1991, **132**, 13.
- Wang, S. F., Hsu, Y. C., Chu, J. P., Wu, C. H. *Appl. Phys. Lett.* 2006, **88**, 042909.
- Wang, X., Yamada, H., Nishikubo, K., Xu, C. N. *Jpn. J. Appl. Phys., Part 1*, 2005, **44**, 961.
- Wanklyn, B. M., Midgley, D., Tanner, B. K. J. *Cryst. Growth* 1975, **29**, 281.
- Warshaw, I., Roy, R. J. *Am. Ceram. Soc.* 1959, **42**, 434.
- Watanabe, S., Hidaka, M., Yoshizawa, H., Wanklyn, B. M. *Phys. Status Solidi B* 2006, **243**, 424.
- Watts, B. E., Dabkowska, H., Wanklyn, B. M. J. *Cryst. Growth* 1989, **94**, 125.

- Woodward, P. M. *Acta Crystallogr. B* 1997a, **53**, 32.
- Woodward, P. M. *Acta Crystallogr. B* 1997b, **53**, 44.
- Wu, P., Pelton, D. J. *Alloys Compd.* 1992, **179**, 259.
- Wu, B., Zinkevich, M., Aldinger, F., Zhang, W. J. *Phys. Chem. Solids* 2007, **68**, 570.
- Yamaguchi, O., Sugiura, K., Mitsui, A., Shimizu, K. J. *Am. Ceram. Soc.* 1985, **68**, 44.
- Yamaguchi, I., Manabe, T., Sohma, M., Tsuchiya, T. *Phys. C (Amsterdam, Neth.)* 2002a, **382**, 269.
- Yamaguchi, I., Manabe, T., Sohma, M., Tsuchiya, T., Kumagai, T., Suzuki, S., Yamaguchi, Y., Watanabe, T., Mizuta, S. *Phys. C (Amsterdam, Neth.)* 2002b, **378–381**(Suppl. 2), 1227.
- Yamane, H., Ogawara, K., Omori, M., Hirai, T. J. *Am. Ceram. Soc.* 1995, **78**, 2385.
- Yan, B., Zhang, J., Liu, J., Liu, G. *Mater. Lett.* 2005, **59**, 3226.
- Yang, W. H., Hoy, D. S., Li, C. Z., Fan, H., Zhang, H. Y. *Solid State Commun.* 1990, **75**, 421.
- Yang, C. Y., Huang, Z. R., Yang, W. H., Ahou, Y. Q., Fung, K. K. *Acta Crystallogr. A* 1991, **47**, 703.
- Yashima, M., Nomura, K., Kageyama, H., Miyazaki, Y., Chitose, N., Adachi, K. *Chem. Phys. Lett.* 2003, **380**, 391.
- Yoshikawa, A., Saitow, A., Horiuchi, H., Shishido, T., Fukuda, T. J. *Alloys Compd.* 1998, **266**, 104.
- Young, A. P. J. *Phys. C: Solid State Phys.* 1975, **8**, 3158.
- Young, K. H., Strother, D. D. *Phys. C (Amsterdam, Netherlands)* 1993, **208**, 1.
- Yu, Y., Xie, S., Boysen, H. *Acta Phys. Sin.* 1993, **42**, 605.
- Zachariasen, W. H. *Acta Crystallogr.* 1949, **2**, 388.
- Zhang, Q., Saito, F. J. *Am. Ceram. Soc.* 2000, **83**, 439.
- Zhang, Y., Navrotsky, A. J. *Non-Cryst. Solids* 2004, **341**, 141.
- Zhang, Y., Navrotsky, A., Tangeman, J., Weber, J. K. R. J. *Phys.: Condens. Matter* 2003, **15**, 2343.
- Zhao, J., Ross, N. L., Angel, R. J. J. *Phys.: Condens. Matter* 2004a, **16**, 8763.
- Zhao, J., Ross, N. L., Angel, R. J. *Acta Crystallogr. B* 2004b, **60**, 263.
- Zhao, G., Zeng, X., Xia, C., Zhou, S., Li, S., Xu, J. J. *Cryst. Growth* 2004c, **267**, 522.
- Zhou, J.-S., Goodenough, J. B. *Phys. Rev. Lett.* 2005, **94**, 065501.
- Zinkevich, M., Geupel, S., Nitsche, H., Ahrens, M., Aldinger, F. J. *Phase Equilib. Diffus.* 2004, **25**, 437.
- Zinkevich, M., Geupel, S., Aldinger, F., Durygin, A., Saxena, S. K., Yang, M., Liu, Z.-K. *J. Phys. Chem. Solids* 2006, **67**, 1901.
- Zinoviev, S. Yu., Krzhizhanovskaya, V. A., Glushkova, V. B., Zharikov, E. V., Myzina, V. A. *Neorg. Mater. (Inorg. Mater.)* 1989, **25**, 785 (*in Russian*).

Luminescence of Polyoxometallolanthanoates and Photochemical Nano-Ring Formation

Toshihiro Yamase*

Contents	List of Symbols and Acronyms	298
	1. Introduction	299
	2. Energy transfer from O → M lmct to Ln ³⁺ Sites	301
	2.1 Polyoxometalates containing a single lanthanide cation	301
	2.2 Structures of polyoxometalates containing multiple Eu ³⁺ cations	304
	2.3 Crystal-field splitting and sensitized emission of Eu ³⁺	311
	2.4 Co-ordination of aqua and hydroxo ligands to Eu ³⁺	315
	2.5 Kinetics of the sensitized luminescence of Eu ³⁺	319
	2.6 Involvement of the O → M lmct triplet states in energy transfer	325
	3. Energy transfer among Ln ³⁺ Sites (FROM Tb ³⁺ TO Eu ³⁺)	328
	3.1 Luminescence spectra	328
	3.2 Luminescence decay dynamics	331
	3.3 Förster-Dexter-type energy transfer	333
	3.4 Decay of the O → M lmct triplet states and energy transfer	338
	4. Photochemical self-assembly of Ln ³⁺ -Containing Mo-Blue nano-rings	339
	4.1 Primary steps in the photoredox reaction with both proton and electron donors	339
	4.2 Photo-induced self-assembly of Mo-blue nano-rings	342
	4.3 Ln ³⁺ -induced modification to ellipsoidal Mo-blue rings	345
	4.4 Ln ³⁺ -induced modification of Mo-blue rings into Japanese rice-ball shape	347
	4.5 Ln ³⁺ -induced modification of Mo-blue rings into tube and chain structures	350

* Chemical Resources Laboratory, Tokyo Institute of Technology, R1-21, 4259 Nagatsuta, Midori-ku, Yokohama 226-8503 Japan
E-mail: tyamase@res.titech.ac.jp

5. Summary and Conclusions

Acknowledgements

References

352

354

354

List of Symbols and Acronyms

1	$\text{Na}_9[\text{Eu}(\text{W}_5\text{O}_{18})_2] \cdot 32\text{H}_2\text{O}$
1a	$[\text{Eu}(\text{W}_5\text{O}_{18})_2]^{9-}$
2	$\text{K}_{15}\text{H}_3[\text{Eu}_3(\text{H}_2\text{O})_3(\text{SbW}_9\text{O}_{33})(\text{W}_5\text{O}_{18})_3] \cdot 25.5\text{H}_2\text{O}$
2a	$[\text{Eu}_3(\text{H}_2\text{O})_3(\text{SbW}_9\text{O}_{33})(\text{W}_5\text{O}_{18})_3]^{18-}$
3	$\text{Na}_2\text{H}_{19}\{\text{Eu}_3\text{O}(\text{OH})_3(\text{H}_2\text{O})_3\}_2\text{Al}_2(\text{Nb}_6\text{O}_{19})_5 \cdot 47\text{H}_2\text{O}$
3a	$\{\text{Eu}_3\text{O}(\text{OH})_3(\text{H}_2\text{O})_3\}_2\text{Al}_2(\text{Nb}_6\text{O}_{19})_5\}^{21-}$
4	$[\text{NH}_4]_{12}\text{H}_2[\text{Eu}_4(\text{H}_2\text{O})_{16}(\text{MoO}_4)(\text{Mo}_7\text{O}_{24})_4] \cdot 13\text{H}_2\text{O}$
4a	$[\text{Eu}_4(\text{H}_2\text{O})_{16}(\text{MoO}_4)(\text{Mo}_7\text{O}_{24})_4]^{14-}$
5	$[\text{Eu}_2(\text{H}_2\text{O})_{12}][\text{Mo}_8\text{O}_{27}] \cdot 6\text{H}_2\text{O}$
5a	$[\text{Mo}_8\text{O}_{27}]^{6-}$
6	$\text{K}_2\text{H}_3\{[\text{Eu}(\text{H}_2\text{O})_8]_3[(\text{GeTi}_3\text{W}_9\text{O}_{37})_2\text{O}_3]\} \cdot 13\text{H}_2\text{O}$
6a	$[(\text{GeTi}_3\text{W}_9\text{O}_{37})_2\text{O}_3]^{14-}$
7	$[\text{Eu}(\text{H}_2\text{O})_8]_2[\text{V}_{10}\text{O}_{28}] \cdot 8\text{H}_2\text{O}$
8	$\text{K}_{15}\text{H}_3[\text{Tb}_{1.4}\text{Eu}_{1.6}(\text{H}_2\text{O})_3(\text{SbW}_9\text{O}_{33})(\text{W}_5\text{O}_{18})_3] \cdot 25.5\text{H}_2\text{O}$
9	$\text{Na}_7\text{H}_{19}\{[\text{Tb}_{4.3}\text{Eu}_{1.7}\text{O}_2(\text{OH})_6(\text{H}_2\text{O})_6\text{Al}_2(\text{Nb}_6\text{O}_{19})_5] \cdot 47\text{H}_2\text{O}$
10	$[\text{NH}_4]_{12}\text{H}_2[\text{Tb}_{3.1}\text{Eu}_{0.9}(\text{MoO}_4)(\text{H}_2\text{O})_{16}(\text{Mo}_7\text{O}_{24})_4] \cdot 13\text{H}_2\text{O}$
11	$[\text{PrNH}_3]_{24}[\text{Mo}_{28}^{\text{V}}\text{Mo}_{122}^{\text{VI}}\text{O}_{452}\text{H}_2(\text{H}_2\text{O})_{66}\{\text{La}(\text{H}_2\text{O})_5\}_2] \cdot 156 \pm 5\text{H}_2\text{O}$
11a	$[\text{Mo}_{28}^{\text{V}}\text{Mo}_{122}^{\text{VI}}\text{O}_{452}\text{H}_2(\text{H}_2\text{O})_{66}\{\text{La}(\text{H}_2\text{O})_5\}_2]^{24-}$
12	$[\text{NH}_3]_{14}[\text{Mo}_{24}^{\text{V}}\text{Mo}_{96}^{\text{VI}}\text{O}_{366}\text{H}_{14}(\text{H}_2\text{O})_{48}\{\text{La}(\text{H}_2\text{O})_5\}_6] \cdot 180 \pm 20\text{H}_2\text{O}$
12a	$[\text{Mo}_{24}^{\text{V}}\text{Mo}_{96}^{\text{VI}}\text{O}_{366}\text{H}_{14}(\text{H}_2\text{O})_{48}\{\text{La}(\text{H}_2\text{O})_5\}_6]^{14-}$
13	${}^i\text{PrNH}_3]_8[\text{Mo}_{28}^{\text{V}}\text{Mo}_{126}^{\text{VI}}\text{O}_{458}\text{H}_{12}(\text{H}_2\text{O})_{66}] \cdot 127\text{H}_2\text{O}$
13a	$[\text{Mo}_{28}^{\text{V}}\text{Mo}_{126}^{\text{VI}}\text{O}_{458}\text{H}_{12}(\text{H}_2\text{O})_{66}]^{8-}$
Φ	quantum yield of photoluminescence
Φ_{et}	quantum yield of overall energy transfer from $\text{O} \rightarrow \text{M}$ lmct to ${}^5\text{D}_0$ states
Φ_{triplet}	quantum yield of ${}^3\text{T}_{1\text{u}} \text{O} \rightarrow \text{M}$ lmct triplet emission
α	donor–acceptor interaction parameter
η_{rad}	ratio of radiation of the ${}^5\text{D}_0$ state of Eu^{3+} { $=k_{\text{rad}}/(k_{\text{rad}} + k_{\text{nr}})$ }
λ	wavelength of light
τ_{triplet}	exponential decay time of ${}^3\text{T}_{1\text{u}} \text{O} \rightarrow \text{M}$ lmct states
$\tau_{\text{H}_2\text{O}}^{-1}$	reciprocal lifetime in H_2O in $(\text{ms})^{-1}$
$\tau_{\text{D}_2\text{O}}^{-1}$	reciprocal lifetime in D_2O in $(\text{ms})^{-1}$
τ_{D}	intrinsic lifetime of donor
ω_1	central Mo–O–Mo bond angle of $\{\text{Mo}_{14}\}$ -typed framework
ω_2	central Mo–O–Mo bond angle of the half-moiety of $\{\text{Mo}_{14}\}$
ω_3	O–Mo–O bond angle for linking the above two central O atoms
a	hyperfine coupling constant in mT (militesla) unit
k_{ET}	nearest-neighbour energy-transfer rate between donor–acceptor pair

k_{nr}	non-radiative rate of the 5D_0 state of Eu^{3+}
k_{rad}	radiative rate of the 5D_0 state of Eu^{3+}
l_1	Mo–O bond distance (in Å unit) at central Mo–O–Mo linkage with ω_1
l_2	Mo–O bond distances (in Å unit) at the above Mo–O–Mo linkage with ω_2
lmct	ligand-to-metal charge transfer
n	number of aqua ligands in Ln^{3+} co-ordination sphere
n'	total number of aqua and hydroxo ligands in Ln^{3+} co-ordination sphere
n_A	density of acceptor (Eu^{3+})
r_{DA}	donor–acceptor separation (in Å)
s	6, 8, or 10 for multi-polar nature interactions
A	acceptor
CIDEP	chemically induced dynamic electron polarization
D	donor
D	ring diameter of nano-ring Mo-blue
DH	proton and electron donor
ESP	electron-spin polarization
J	inner quantum number (total angular momentum)
Ln^{3+}	trivalent lanthanide ion
R_0	critical radius for donor–acceptor energy transfer
Z	number of molecules in unit cell
$^3(O \rightarrow Mo \text{ lmct})$	$O \rightarrow Mo$ lmct excited triplet states
$^1(O \rightarrow Mo \text{ lmct})$	$O \rightarrow Mo$ lmct singlet state
3T	electron-spin triplet state
2D	electron-spin doublet state
Mo	Molybdenum
$\{Mo_2\}$ -linker	$[Mo(H_2O)O_2(\mu-O)Mo(H_2O)O_2]^{2+}$
$\{Mo_{14}\}$	$[(Mo_7O_{23})_2]^{10-}$
$\{Mo_{22}\}$	$[Mo_{22}O_{70}(H_2O)_{10}]^{10-}$
$\{Mo_{36}\}$	$[Mo_{36}O_{112}(H_2O)_{16}]^{8-}$
$\{Mo_{142}\}$	$[Mo_{142}O_{432}(OH)_{14}(H_2O)_{58}]^{26-}$, $[Mo_{28}^V Mo_{114}^{VI} O_{404}(OH)_{28}(H_2O)_{58}]^{12-}$
$\{Mo_{144}\}$	$Na_{24}[Mo_{144}O_{437}H_{14}(H_2O)_{56}] \cdot ca.250H_2O$
$\{Mo_{146}\}$	$Na_{22}[Mo_{146}O_{442}H_{14}(H_2O)_{58}] \cdot ca.250H_2O$
$\{Mo_{154}\}$	$[Mo_{154}O_{448}(OH)_{14}(H_2O)_{70}]^{14-}$, $[Mo_{28}^V Mo_{126}^{VI} O_{462}(H_2O)_{70}]^{28-}$
$\{Mo_{176}\}$	$[M_{176}O_{512}(OH)_{16}(H_2O)_{80}]^{16-}$

1. INTRODUCTION

In the recent past, polyoxometalate chemists have made many notable contributions to the general knowledge of the molecular design for construction of catalytic, electric, magnetic, electrochemical, photochemical, and biological materials (Hill, 1998; Pope and Müller, 2001; Yamase and Pope, 2002; Borrás-Alamenar

et al., 2003). In this chapter, we focus on the chemistry of polyoxolanthanoates, a special class of metal-oxide cluster compounds. Moreover, we put the emphasis on the understanding of the molecular mechanisms of energy transfer processes in metal-oxide phosphors. Indeed, this aspect remains often unclear, despite many investigations, mainly because the luminescence centres are insufficiently characterized. When several energy levels on acceptor such as a luminescent site overlap with $O \rightarrow M$ lmct in a metal-oxide phosphor doped with luminescent impurities, energy transfer from the $O \rightarrow M$ lmct excited states to these levels occurs and results in the sensitized luminescence of the acceptor. Such a process has been recognized for trivalent lanthanide ion (Ln^{3+}) in many non-molecular metal-oxides such as $\text{YVO}_4:\text{Eu}^{3+}$ (Bril and Wanmaker, 1964), $\text{CdNb}_2\text{O}_6:\text{Eu}^{3+}$ (Brittain and McAllister, 1985), $\text{La}_2\text{O}_3:\text{Ce}^{3+}$ (Blasse et al., 1991), and La_2MoO_8 (LaNbO_4 , NaGdO_2 , or NaYW_2O_6): Yb^{3+} , Er^{3+} (Sommerdijk and Bril, 1974). The dopant atoms in the metal-oxide lattice are located as single ions or aggregates at interstitial or/and host-metal sites, resulting in luminescence from a variety of dopant sites in the lattice, since it is difficult to control the nature of dopant sites during the preparation of the phosphor (Blasse and Grabmaier, 1994). On the other hand, polyoxometalates are stoichiometric compounds and provide structurally defined luminescent sites so that their characterization with respect to the crystal structure and local symmetry of the emitting centres is easy. One of the models used for rare-earth metal-oxide phosphors is decatungstoeuropate, $[\text{EuW}_{10}\text{O}_{36}]^{9-}$, first reported as its sodium salt in 1976 (Stillman and Thompson, 1976). Figure 1 shows the structure of $[\text{EuW}_{10}\text{O}_{36}]^{9-}$ ($=[\text{Eu}(\text{W}_5\text{O}_{18})_2]^{9-}$) indicating that four O atoms from the W_5O_{18} group [corresponding to one (W=O) lacunary ligand derived from $[\text{W}_6\text{O}_{19}]^{2-}$ with O_h -symmetric Lindqvist-type structure] of

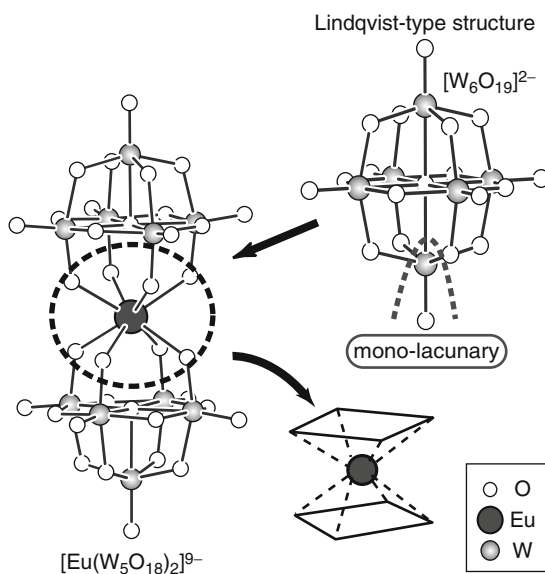


FIGURE 1 Structure of $[\text{Eu}(\text{W}_5\text{O}_{18})_2]^{9-}$. The W_5O_{18} group of the half anion corresponds to the mono-lacunary ligand derived from O_h -symmetrical $[\text{W}_6\text{O}_{19}]^{2-}$ with Lindqvist-type structure.

the half anion are bonded to the Eu atom, resulting in eightfold co-ordination with idealized D_{4d} symmetry. Thus, the generally termed 'polyoxometallolanthanoates' may be leaflet models for lanthanide-doped metal-oxide phosphors, although there yet seems to be no molecular model for the defect-operative up-conversion phosphors. The purpose of this chapter is to outline energy transfer processes in polyoxometallolanthanoates, particularly polyoxometalloeuropates as well as the Ln^{3+} -assisted photochemical synthesis of Mo-blue nano-rings. These Mo-blue species showing an extreme variety of complicated structures are $\text{Mo}^{\text{V}}/\text{Mo}^{\text{VI}}$ mixed-valence-typed polyoxomolybdates and favour the highly delocalized systems with characteristic dark-blue colour due to the inter-valence charge-transfer transitions. Lanthanide ions not only opened a novel method for the preparation of Mo-blue nano-ring derivatives but also provided a good tool for the mechanistic investigation of the self-assembly of Mo-blue nano-rings. Since the interaction between conducting electrons and paramagnetic Ln^{3+} ions contributes to the electronic structure of Mo-blue nano-ring derivatives, their Ln^{3+} -assisted design strongly contributes to both nano-science and nano-technology.

2. ENERGY TRANSFER FROM O \rightarrow M LMCT TO Ln^{3+} SITES

2.1 Polyoxometalates containing a single lanthanide cation

Earlier studies of energy-transfer processes in polyoxometallolanthanoates have been conducted for decatungstolanthanoates, $[\text{Ln}(\text{W}_5\text{O}_{18})_2]^{9-}$ (Stillman and Thompson, 1976; Blasse et al., 1981a,b; Ballardini et al., 1984b; Darwent et al., 1986; Sugeta and Yamase, 1993; Ozeki and Yamase, 1993). Table 1 shows quantum yields of Ln^{3+} emission induced by the O \rightarrow W lmct photoexcitation ($\lambda < 330$ nm) of $[\text{Ln}(\text{W}_5\text{O}_{18})_2]^{9-}$ ($\text{Ln} = \text{Sm}, \text{Tb}, \text{Dy}, \text{and Eu}$) solids. Decatungstoeuropate $[\text{Eu}(\text{W}_5\text{O}_{18})_2]^{9-}$ is the most luminescent among these compounds: low yields for the other decatungstolanthanoates are due to radiationless losses via charge-transfer $\text{Ln}^{4+}\text{-W}^{5+}$ states in Pr^{3+} and Tb^{3+} complexes and cross-relaxation based on the concentration quenching with a large critical distance (about 13 Å) in Sm^{3+} , Dy^{3+} , and Ho^{3+} complexes (Blasse et al., 1981a; Stillman and Thompson 1976). Interestingly, Gd^{3+} complex $[\text{Gd}(\text{W}_5\text{O}_{18})_2]^{9-}$ displays the broad green emission of the $[\text{W}_5\text{O}_{18}]^{6-}$ ligands, which is similar to the emission band of tungstate groups in non-molecular solids such as MgWO_4 and CdWO_4 (Blasse et al., 1981b). Analysis of the Eu^{3+} -luminescence in $\text{Na}_9[\text{Eu}(\text{W}_5\text{O}_{18})_2]\cdot 18\text{H}_2\text{O}$ based on the crystal

TABLE 1 Sensitized emission of Ln^{3+} for decatungstates

Decatungstate	Φ	
	4.2 K	300 K
$\text{Na}_9[\text{Sm}(\text{W}_5\text{O}_{18})_2]\cdot 18\text{H}_2\text{O}$	0.30	0.25
$\text{Na}_9[\text{Tb}(\text{W}_5\text{O}_{18})_2]\cdot 18\text{H}_2\text{O}$	0.05	0.01
$\text{Na}_9[\text{Dy}(\text{W}_5\text{O}_{18})_2]\cdot 18\text{H}_2\text{O}$	0.50	0.40
$\text{Na}_9[\text{Eu}(\text{W}_5\text{O}_{18})_2]\cdot 18\text{H}_2\text{O}$	0.90	0.80

structure of $\text{Na}_6\text{H}_2[\text{Ce}(\text{W}_5\text{O}_{18})_2] \cdot 30\text{H}_2\text{O}$ did not confirm the D_{4d} site symmetry of the metal ion evidenced for Ce^{4+} with square anti-prismatic CeO_8 co-ordination (Ibal et al., 1974): the number of components, for each of the ${}^5\text{D}_0 \rightarrow {}^7\text{F}_J$ ($J = 0-4$) transition disagreed with the prediction made on the basis of D_{4d} symmetry (zero ${}^5\text{D}_0 \rightarrow {}^7\text{F}_0$, two ${}^5\text{D}_0 \rightarrow {}^7\text{F}_1$, zero ${}^5\text{D}_0 \rightarrow {}^7\text{F}_2$, one ${}^5\text{D}_0 \rightarrow {}^7\text{F}_3$, and two ${}^5\text{D}_0 \rightarrow {}^7\text{F}_4$ lines). Thereafter, the crystal structure of $\text{Na}_9[\text{Eu}(\text{W}_5\text{O}_{18})_2] \cdot 32\text{H}_2\text{O}$ (1) revealed that the Eu^{3+} site in $[\text{Eu}(\text{W}_5\text{O}_{18})_2]^{9-}$ has C_{4v} and not D_{4d} symmetry (Sugeta and Yamase, 1993). Figure 2(A) and (B) shows the co-ordination geometries of Eu^{3+} and Ce^{4+} with selected inter-atomic distances (\AA) and bond angles ($^\circ$) for $\text{Na}_9[\text{Eu}(\text{W}_5\text{O}_{18})_2] \cdot 32\text{H}_2\text{O}$ and $\text{Na}_6\text{H}_2[\text{Ce}(\text{W}_5\text{O}_{18})_2] \cdot 30\text{H}_2\text{O}$, respectively. Figure 3 shows the sensitized photoluminescence spectrum of $\text{Na}_9[\text{Eu}(\text{W}_5\text{O}_{18})_2] \cdot 32\text{H}_2\text{O}$ at 4.2 K. Thus, the spectral pattern of photoluminescence recorded at 4.2 K, consisting in one ${}^5\text{D}_0 \rightarrow {}^7\text{F}_0$, two ${}^5\text{D}_0 \rightarrow {}^7\text{F}_1$, two ${}^5\text{D}_0 \rightarrow {}^7\text{F}_2$, two ${}^5\text{D}_0 \rightarrow {}^7\text{F}_3$, and four ${}^5\text{D}_0 \rightarrow {}^7\text{F}_4$ lines, with relative intensities of 1:50:17:5:27 is in good agreement with the C_{4v} site symmetry of square anti-prismatic EuO_8 co-ordination. The most notable result from the sensitized luminescence of $\text{Na}_9[\text{Eu}(\text{W}_5\text{O}_{18})_2] \cdot 32\text{H}_2\text{O}$ is that its quantum yield is large: 0.8, 0.9, and 1 at 300, 77, and 4.2 K, respectively (Blasse et al., 1981a; Ballardini et al., 1984a; Sugeta and Yamase, 1993).

Similarly, the sensitized luminescence of Eu^{3+} for potassium salts of $[\text{Eu}(\text{SiW}_{11}\text{O}_{39})_2]^{13-}$, $[\text{Eu}(\text{BW}_{11}\text{O}_{39})_2]^{15-}$, and $[\text{Eu}(\text{P}_2\text{W}_{17}\text{O}_{61})_2]^{17-}$ was investigated

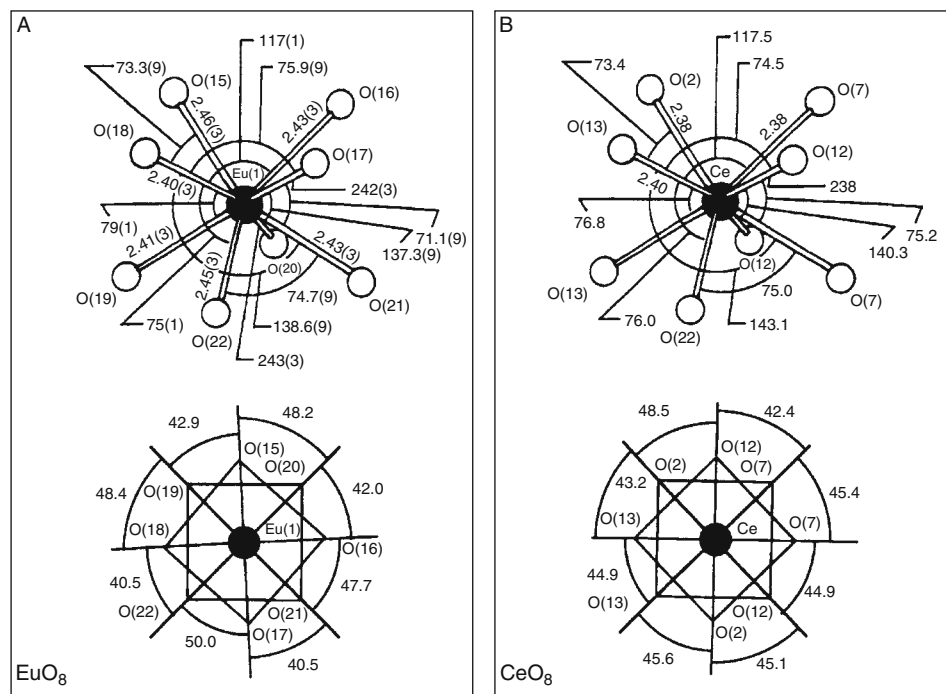


FIGURE 2 Co-ordination geometries of Eu^{3+} and Ce^{4+} with selected inter-atomic distances (\AA) and bond angles ($^\circ$) for $\text{Na}_9[\text{Eu}(\text{W}_5\text{O}_{18})_2] \cdot 32\text{H}_2\text{O}$ (A) and $\text{Na}_6\text{H}_2[\text{Ce}(\text{W}_5\text{O}_{18})_2] \cdot 30\text{H}_2\text{O}$ (B), respectively. The frameworks of EuO_8 and CeO_8 , projected on the square anti-prism square plane, are also represented. Figure is redrawn after Sugeta and Yamase (1993).

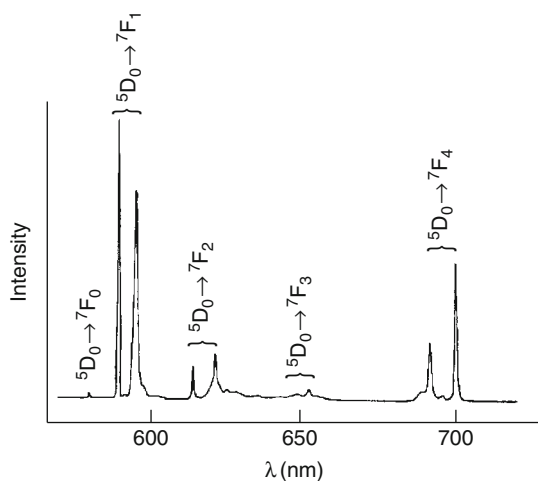


FIGURE 3 Sensitized-photoluminescence spectrum of $\text{Na}_9[\text{Eu}(\text{W}_5\text{O}_{18})_2] \cdot 32\text{H}_2\text{O}$ at 4.2 K. Figure is redrawn after [Sugeta and Yamase \(1993\)](#).

([Blasse et al., 1981b](#); [Ballardini et al., 1984a](#)) on the basis of the crystal structures of $\text{Cs}_{12}[\text{U}(\text{GeW}_{11}\text{O}_{39})_2] \cdot 13\text{--}14\text{H}_2\text{O}$ ([Tourné et al., 1980](#)) and $\text{K}_{16}[\text{Ce}(\text{P}_2\text{W}_{17}\text{O}_{61})_2] \cdot 50\text{H}_2\text{O}$ ([Molchanov et al., 1979](#)). Each anion, $[\text{SiW}_{11}\text{O}_{39}]^{8-}$, $[\text{BW}_{11}\text{O}_{39}]^{9-}$, and $[\text{P}_2\text{W}_{17}\text{O}_{61}]^{10-}$ is a monovacant ($\text{W}=\text{O}$) lacunary ligand derived from $[\text{SiW}_{12}\text{O}_{40}]^{4-}$, $[\text{BW}_{12}\text{O}_{40}]^{5-}$, and $[\text{P}_2\text{W}_{18}\text{O}_{62}]^{6-}$ known as α -Keggin (Si, B) and Wells-Dawson (P) structures, respectively, which are shown on [Figure 4A and B](#). The sensitized luminescence spectra are consistent with the C_{4v} symmetry of the distorted square anti-prismatic EuO_8 co-ordination site. Quantum yields decrease with the shift of the first absorption band of polyoxotungstate ligands to lower energy in the sequence $[\text{Eu}(\text{W}_5\text{O}_{18})_2]^{9-}$, $[\text{Eu}(\text{SiW}_{11}\text{O}_{39})_2]^{13-}$, and $[\text{Eu}(\text{P}_2\text{W}_{17}\text{O}_{61})_2]^{17-}$: the efficiency for the $[\text{Eu}(\text{SiW}_{11}\text{O}_{39})_2]^{13-}$ solids was estimated to be twofold lower than for $\text{Na}_9[\text{EuW}_{10}\text{O}_{36}] \cdot 32\text{H}_2\text{O}$ at 4.2 K, and the luminescence intensity for the $[\text{Eu}(\text{P}_2\text{W}_{17}\text{O}_{61})_2]^{17-}$ solid was extremely low even at 4.2 K, suggesting that the excitation energy of the $\text{O} \rightarrow \text{W}$ lmct band for this compound is quenched by the non-radiative transition within $[\text{P}_2\text{W}_{17}\text{O}_{61}]^{10-}$ ([Blasse et al., 1981b](#)). [Figure 4C](#) also shows the structure of Eu^{3+} -encrypted Preyssler complex, $[\text{EuP}_5\text{W}_{30}\text{O}_{110}]^{12-}$, which consists of a cyclic dehydrated condensation arrangement of five A-type hexa-vacant $[\text{PW}_6\text{O}_{26}]^{11-}$ fragments with D_{5h} symmetry. Solid samples of $\text{K}_{12}[\text{EuP}_5\text{W}_{30}\text{O}_{110}] \cdot 54\text{H}_2\text{O}$, prepared by substituting Eu^{3+} in $\text{K}_{12.5}\text{Na}_{1.5}[\text{NaP}_5\text{W}_{30}\text{O}_{110}] \cdot 15\text{H}_2\text{O}$, showed Eu^{3+} emission from two different sites (with decays of 0.29 and 0.40 ms for the ${}^5\text{D}_0$ level and 12 and 8 μs for the ${}^5\text{D}_1$ level at 4.3 K) upon direct excitation of the ${}^5\text{D}_{1,2} \leftarrow {}^7\text{F}_0$ transitions; these lifetimes are consistent with the co-ordination of two or three aqua ligands per Eu^{3+} ([Alizadeh et al., 1985](#); [Creaser et al., 1993](#); [Soderholm et al., 1995](#)). Interestingly, the excitation energy of the $\text{O} \rightarrow \text{W}$ lmct bands within the $[\text{P}_5\text{W}_{30}\text{O}_{110}]^{15-}$ ring is effectively quenched, resulting in a weakly sensitized luminescence for the inner Eu^{3+} ion. Such deactivation within the polyoxometalate ligands $[\text{P}_2\text{W}_{17}\text{O}_{61}]^{10-}$ and $[\text{PW}_6\text{O}_{26}]^{11-}$ is due to electron delocalization through the corner-shared $\text{W}-\text{O}-\text{W}$

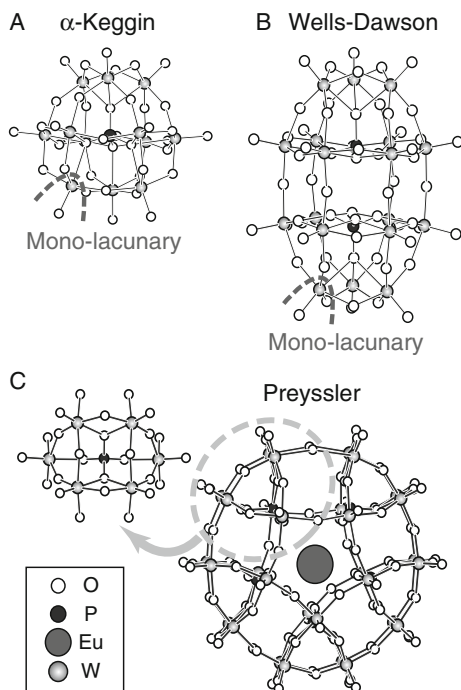


FIGURE 4 Structures of α -Keggin (A)-, Wells-Dawson (B)-, and Preyssler (C)-typed frameworks. Eu³⁺ is co-ordinated by oxygen atoms of mono-lacunary ligands for α -Keggin and Wells-Dawson frameworks, in contrast with the case of the Preyssler framework where Eu³⁺ is encapsulated in the centre of the anion.

bonds with bond angles larger than 150° which leads to a small cross-section for the excitation of the Eu³⁺ site, as discussed below.

2.2 Structures of polyoxometalates containing multiple Eu³⁺ cations

As exemplified above, photoexcitation of the O → M Imct bands of the polyoxometalloeuropates containing a single luminescent centre induces emission from both ⁵D₀ and ⁵D₁ excited states as a result of the intra-molecular transfer of the O → M Imct-band excitation energy. The narrow features of the intra-4f-electronic transitions are allowed due to mixing with vibrations and/or other electronic states of opposite parity. In addition to the single Eu³⁺-containing complex Na₉[Eu(W₅O₁₈)₂]·32H₂O (1), other polyoxometalloeuropates containing multiple Eu³⁺ centres such as K₁₅H₃[Eu₃(H₂O)₃(SbW₉O₃₃)(W₅O₁₈)₃]·25.5H₂O (2) (Yamase et al., 1990), Na₂H₁₉{[Eu₃O(OH)₃(H₂O)₃]₂Al₂(Nb₆O₁₉)₅}·47H₂O (3) (Ozeki et al., 1994), [NH₄]₁₂H₂[Eu₄(H₂O)₁₆(MoO₄)(Mo₇O₂₄)₄]·13H₂O (4) (Naruke and Yamase, 1991), [Eu₂(H₂O)₁₂][Mo₈O₂₇]·6H₂O (5) (Yamase and Naruke, 1991), and K₂H₃{[Eu(H₂O)₈]₃[(GeTi₃W₉O₃₇)₂O₃]}·13H₂O (6) (Sugeta and Yamase, 1997) were prepared for investigation of the aggregation motifs and of the sensitized emission of the Eu³⁺ centres in the oxide lattice. The polyoxometalate ligands in 2–6 affect the local co-ordination symmetry of the Eu³⁺ ions. In addition, they induce changes in

the Eu^{3+} -aggregates, leading to modification of the Eu^{3+} emission properties, such as spectrum pattern, lifetime, and yield of energy transfer from the $\text{O} \rightarrow \text{M}$ lmct states. The approximate co-ordination polyhedra around Eu^{3+} are square anti-prisms for **1** and **2**, a bicapped trigonal prism for **3**, and tricapped-trigonal prisms for **4–6**. The total numbers of aqua and hydroxo ligands co-ordinated to Eu^{3+} are 0, 2, 3, 4, 6, and 8 for **1–6**, respectively. The only observed luminescence upon excitation in the $\text{O} \rightarrow \text{M}$ lmct band of each complex was the ${}^5\text{D}_0$ (and ${}^5\text{D}_1$) \rightarrow ${}^7\text{F}_J$ ($J = 0-4$) emission with a single-exponential decay. The decay rate of the ${}^5\text{D}_0 \rightarrow {}^7\text{F}_J$ emission increases with the increasing number of aqua ligands co-ordinating the Eu^{3+} ion due to the weak vibronic coupling of the ${}^5\text{D}_0$ state with vibrational states of the high-frequency OH oscillators of the aqua ligand (Horrocks and Sudnick, 1979, 1981). The absence of broad $\text{O} \rightarrow \text{M}$ ($\text{M} = \text{W}, \text{Mo}$) lmct emission from the polyoxometalate ligands suggests that the energy transfer from these states

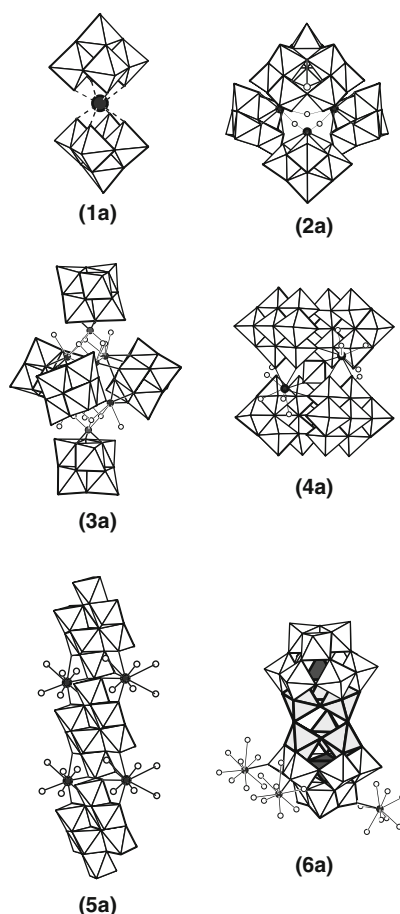


FIGURE 5 Structures of $[\text{Eu}(\text{W}_5\text{O}_{18})_2]^{9-}$ (**1a**), $[\text{Eu}_3(\text{H}_2\text{O})_3(\text{SbW}_9\text{O}_{33})(\text{W}_5\text{O}_{18})_3]^{18-}$ (**2a**), $[\{\text{Eu}_3\text{O}(\text{OH})_3(\text{H}_2\text{O})_3\}_2\text{Al}_2(\text{Nb}_6\text{O}_{19})_5]^{21-}$ (**3a**), $[\text{Eu}_4(\text{H}_2\text{O})_{16}(\text{MoO}_4)(\text{Mo}_7\text{O}_{24}/4)]^{14-}$ (**4a**), $[\text{Eu}_2(\text{H}_2\text{O})_{12}][\text{Mo}_8\text{O}_{27}]$ (**5a**), and $[\{\text{Eu}(\text{H}_2\text{O})_8\}_3][\{\text{GeTi}_3\text{W}_9\text{O}_{37}/2\text{O}_3\}]^{5-}$ (**6a**) as assemblies of linked MO_6 octahedra for **1–6**. Figure is redrawn after Yamase (1998).

to Eu^{3+} occurs with a much higher rate ($>10^6 \text{ s}^{-1}$) than the radiative process of the lmct states (Yamase and Sugeta, 1993).

Figure 5 shows the structures of six assemblies (1a–6a) of linked MO_6 octahedra in 1–6. As indicated above, the structure of the anion (1a) for 1 is distorted from its ideal D_{4d} symmetry in a way that the S_8 axis collinear with a C_4 axis is lost, and four terminal oxygen atoms in the W_5O_{18} group of the half anion are bonded to the Eu^{3+} ion, leading to a distorted square anti-prismatic eightfold co-ordination for Eu^{3+} (Figures 1 and 2). It is noteworthy that there is no aqua ligand co-ordinated to Eu^{3+} .

Figure 6 shows the details of the co-ordination motif of Eu^{3+} in 2a in which a central trinuclear $\text{Eu}_3(\text{H}_2\text{O})_3$ core with approximately C_{3v} point symmetry is linked tetrahedrally by three $[\text{W}_5\text{O}_{18}]^{6-}$ groups and one B- α -type $[\text{SbW}_9\text{O}_{33}]^{9-}$ anion. The $\text{SbW}_9\text{O}_{33}$ group is the trivalent Keggin-structured B- α -type ligand which contains a threefold co-ordinated Sb^{III} and three corner-sharing W_3O_{13} groups consisting in three edge-shared WO_6 octahedra. Each Eu^{3+} ion in the $\text{Eu}_3(\text{H}_2\text{O})_3$ ring achieves a distorted square anti-prismatic eightfold co-ordination by binding to four oxygen atoms from one W_5O_{18} group, two oxygen atoms from one $\text{SbW}_9\text{O}_{33}$ group, and two oxygen atoms from two aqua ligands.

Figure 7 shows the co-ordination motif of Eu^{3+} for 3a which consists in two $[\text{Eu}_3\text{O}(\text{OH})_3(\text{H}_2\text{O})_3]^{4+}$ clusters, two Al^{3+} cations, and five Lindqvist-type

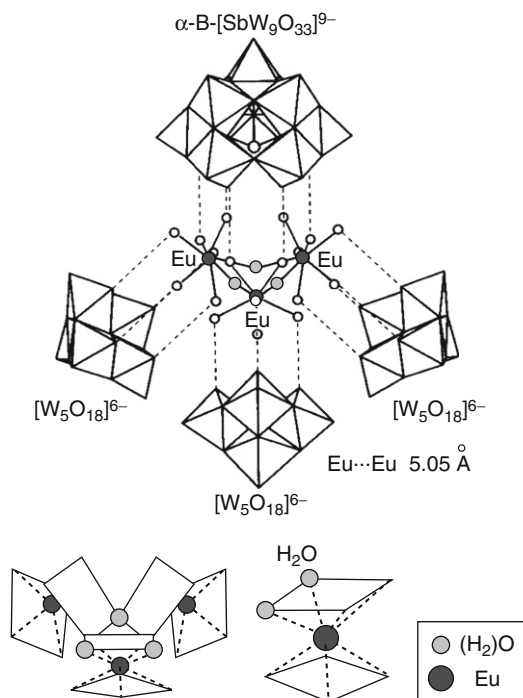


FIGURE 6 Co-ordination motif of Eu^{3+} (black circles) in $[\text{Eu}_3(\text{H}_2\text{O})_3(\text{SbW}_9\text{O}_{33})(\text{W}_5\text{O}_{18})_3]^{18-}$ (2a). Grey circles in the central $\text{Eu}_3(\text{H}_2\text{O})_3$ core represent O atoms of aqua ligands, and $\text{Eu}\cdots\text{Eu}$ distance of 5.05 Å indicates the averaged distance.

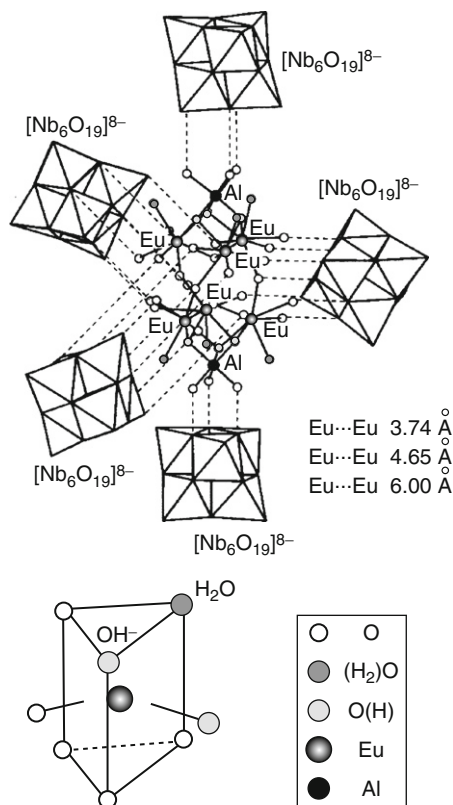


FIGURE 7 Co-ordination motif of Eu^{3+} (heavily dark circles) and Al^{3+} (black circles) in $\{[\text{Eu}_3\text{O}(\text{OH})_3(\text{H}_2\text{O})_3]_2\text{Al}_2(\text{Nb}_6\text{O}_{19})_5\}^{21-}$ (**3a**). dark grey, light grey, and white black circles represent O atoms of aqua O, hydroxo O, and niobate O, respectively. 3.74, 4.65, and 6.99 Å indicate averaged values for three kinds of $\text{Eu}\cdots\text{Eu}$ distances.

$[\text{Nb}_6\text{O}_{19}]^{8-}$ anions (Figure 1). In each $[\text{Eu}_3\text{O}(\text{OH})_3(\text{H}_2\text{O})_3]^{4+}$ cluster, the μ_3 -O atom is shared by three Eu^{3+} , and the hydroxo (OH^-) oxygen atom is shared by two Eu^{3+} and one Al^{3+} ions. Each Eu^{3+} ion exhibits the eightfold co-ordination geometry of a bicapped-trigonal prism, one trigonal face being defined by three oxygen atoms from $[\text{Nb}_6\text{O}_{19}]^{8-}$, OH^- , and aqua oxygen ligands, whereas the other trigonal face is defined by three oxygen atoms from two $[\text{Nb}_6\text{O}_{19}]^{8-}$ ligands (one oxygen for each) and one μ_3 -O ligand. Two approximately rectangular faces are capped each by an oxygen atom from $[\text{Nb}_6\text{O}_{19}]^{8-}$ and by another OH^- anion.

The co-ordination motif of Eu^{3+} ion in **4a** (Figure 8) consists in a central $[\text{Eu}_4(\text{MoO}_4)(\text{H}_2\text{O})_{16}]^{10+}$ unit and four $[\text{Mo}_7\text{O}_{24}]^{6-}$ ligands, with an overall D_{2d} symmetry. Each Eu^{3+} ion achieves approximate tricapped-trigonal-prismatic ninefold co-ordination by nine oxygen atoms; one oxygen atom stems from the central $[\text{MoO}_4]^{2-}$ tetrahedron, four oxygen atoms belong to three $[\text{Mo}_7\text{O}_{24}]^{6-}$ ligands (one, one, and two, respectively), and four oxygen atoms from four aqua ligands complete the co-ordination.

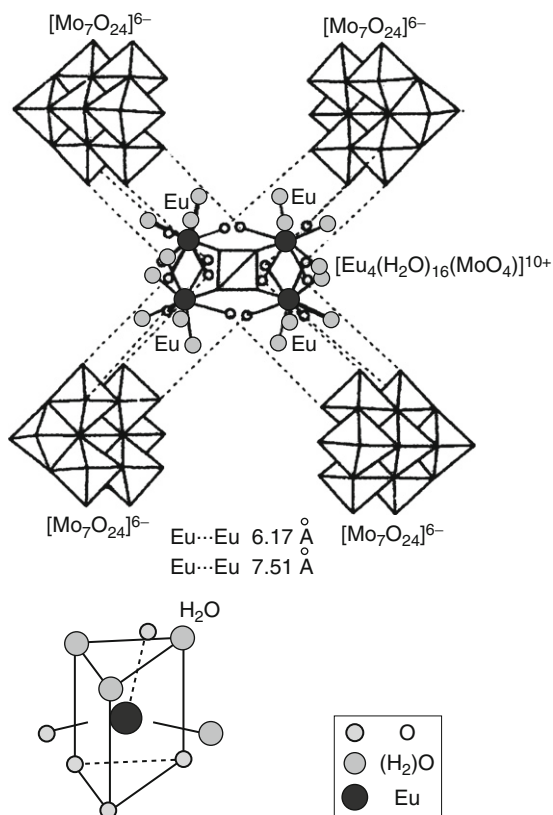


FIGURE 8 Co-ordination motif of Eu^{3+} (dark grey circles) in $[\text{Eu}_4(\text{H}_2\text{O})_{16}(\text{MoO}_4)(\text{Mo}_7\text{O}_{24})_4]^{14-}$ (**4a**). grey circles represent O atoms of aqua ligands, and 6.17 and 7.51 Å indicate averaged values for two kinds of $\text{Eu}\cdots\text{Eu}$ distances.

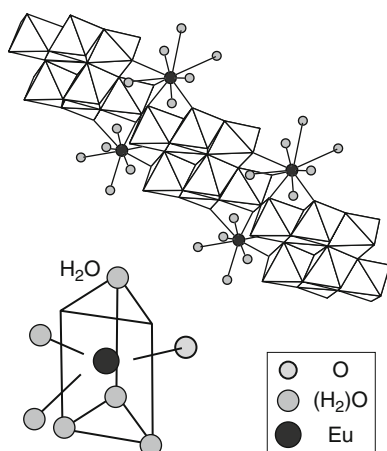


FIGURE 9 Co-ordination motif of Eu^{3+} (dark grey circles) in $[\text{Eu}_2(\text{H}_2\text{O})_{12}][\text{Mo}_8\text{O}_{27}]$ (**5a**). grey circles represent O atoms of aqua ligands.

The co-ordination motif of Eu^{3+} in **5a** (Figure 9) is isostructural with the anion in $[\text{NH}_4]_6[\text{Mo}_8\text{O}_{27}] \cdot 4\text{H}_2\text{O}$. The Eu^{3+} ion is linked by six aqua oxygen atoms, two oxygen atoms of the Mo_8O_{27} group, and one oxygen atom belonging to an MoO_6 octahedron of a neighbouring Mo_8O_{27} group, resulting in the formation of an infinite belt of the octamolybdate $\{[\text{Mo}_8\text{O}_{27}]^{6-}\}_\infty$ with approximate tricapped-trigonal-prismatic EuO_9 ninefold co-ordination geometry.

Figure 10 shows the co-ordination motif of Eu^{3+} in **6a** which is a double α -Keggin-structural compound, $[(\text{GeTi}_3\text{W}_9\text{O}_{37})_2\text{O}_3]^{14-}$; each Eu^{3+} site exhibits an approximate tricapped-trigonal-prismatic EuO_9 co-ordination geometry achieved by one terminal oxygen from $[(\text{GeTi}_3\text{W}_9\text{O}_{37})_2\text{O}_3]^{14-}$ and eight oxygen atoms from eight aqua ligands. The former is the capping atom of one of the trigonal faces.

The mean $\text{Eu}-\text{O}$ distances for Eu -polyoxometalate, -aqua (O_w), and -hydroxo (O_H) oxygen atoms for **1-6** are in the range of 2.4–2.5 Å. The $\text{Eu}-\text{O}-\text{M}$ bond angles can be classified into two categories: less than 130° and more than 140° . It should be noted that **2a** and **6a** possess distinguishably long mean $\text{Eu}-\text{O}_w$ distance (more than 2.6 Å) which suggests a decrease weakening in the interaction of the $^5\text{D}_0$ state with the vibrational states of the high-frequency $\text{O}_w\text{-H}$ oscillators as discussed below. Table 2 lists $\text{Eu}-\text{O}$ (and O_w or O_H) and $\text{Eu}-\text{O}-\text{M}$ bond angles together with the shortest $\text{Eu} \cdots \text{Eu}$ distances in the lattice.

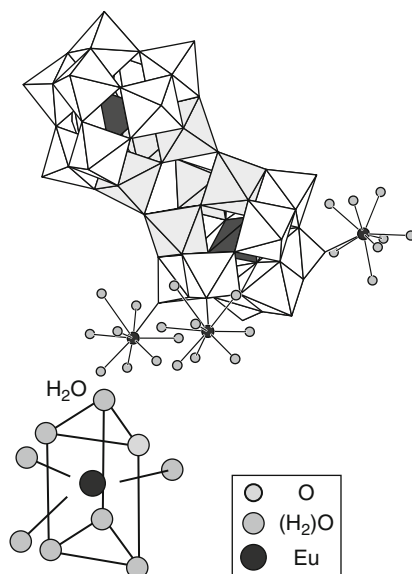


FIGURE 10 Co-ordination motif of Eu^{3+} (dark grey circles) in $\{[\text{Eu}(\text{H}_2\text{O})_8]_3[(\text{GeTi}_3\text{W}_9\text{O}_{37})_2\text{O}_3]\}^{5-}$ (**6a**). Grey circles represent O atoms of aqua ligands, and light grey octahedra and white tetrahedra indicate six TiO_6 octahedra in the centre of anion and two GeO_4 tetrahedra in the tri-lacunary $\text{GeW}_9\text{O}_{34}$ groups, respectively.

TABLE 2 Eu–O and the shortest Eu···Eu distances (in Å) and Eu–O–M bond angles (in degrees) for 1–6^a

	1	2	3	4	5	6
Eu–O	2.39(3)–2.46(3)	2.29(3)–2.51(3)	2.28(4)–2.51(3)	2.38(1)–2.48(2)	2.41(1)–2.58(1)	2.42(3)–2.43(3)
average value	2.43(1)		2.39(1)	2.43(1)	2.46(1)	2.43(1)
Eu–O _w			2.41(3)–2.54(3)	2.43(2)–2.59(2)	2.43(2)–2.61(1)	2.40(3)–2.59(3)
average value			2.48(2)	2.49(1)	2.48(1)	2.44(1)
average value		2.51(3)–2.64(3) 2.56(2)				2.59(3)–2.88(5) 2.78(3)
Eu–O _H			2.41(3)–2.54(3)			
average value			2.47(1)			
Eu···Eu	11.484(5)	5.015(5)	3.740(7)	6.158(2)	6.251(3)	7.631(3)
Eu–O–M	128(1)–132(1)	122(2)–127(2) 149(2)–153(2)	98(1)–106(1) ^b 140(2)–143(2) ^b	147(1)–157(8)	147(1)–158(1)	160(2)–171(1)

^a O_w, aqua oxygen; OH, hydroxo oxygen.^b In 3, the Eu–O–Nb bond angles of about 100° are for μ₃- and μ₄-atoms originated from bridging oxygen atoms in [Nb₆O₁₉]⁸⁻ ligands, and those of about 142° are for μ₃- and μ₂-atoms originated from terminal oxygen atoms.

2.3 Crystal-field splitting and sensitized emission of Eu^{3+}

The crystal-field splitting of the ${}^7\text{F}$ and ${}^5\text{D}$ Russell-Saunders terms can be unravelled from high-resolution emission spectra of both ${}^5\text{D}_0 \rightarrow {}^7\text{F}_j$ and ${}^5\text{D}_1 \rightarrow {}^7\text{F}_j$ transitions and excitation spectra of the ${}^5\text{D}_j (J = 0-2) \leftarrow {}^7\text{F}_j (J = 0 \text{ and } 1)$ transitions. In the case of **5** where C_1 symmetry predicted for the Eu^{3+} site, the predicted maximum number of components has been effectively observed for each transition. Energies for all the crystal-field sublevels of the ${}^7\text{F}_j (J = 0-4)$ and ${}^5\text{D}_j (J = 1-2)$ states are sketched in Figure 11 (Yamase and Naruke, 1991). The excitation spectrum of **5** recorded at 300 K by monitoring the ${}^5\text{D}_0 \rightarrow {}^7\text{F}_2$ emission also exhibits weak and broadened lines at 487.5, 511.2, and 555.5 nm which are due to a coupling of the ${}^7\text{F}_j (J = 0 \text{ and } 1)$ states with the Mo=O and Mo-O-Mo stretching vibration modes.

1-6 show the intense broad bands of the O \rightarrow M lmct absorption and the sharp lines corresponding to the transitions within the $4f^6$ shell of Eu^{3+} . Figure 12 gives typical examples of diffuse reflectance spectra for **3** and **6** at 300 K (Yamase et al., 1997). The optical absorption edges for the $[\text{Nb}_6\text{O}_{19}]^{8-}$ and $[(\text{GeTi}_3\text{W}_9\text{O}_{37})_2\text{O}_3]^{14-}$ ligands lie at 350 ± 10 nm and 380 ± 10 nm, respectively. Thus, the diffuse reflectance spectrum of **3** contains more lines corresponding to f-f transitions than that of **6**. For **3**, the ${}^5\text{D}_{0,1,2,3} \leftarrow {}^7\text{F}_0$ transitions occur at about 581, 527, 466, and 416 nm, respectively. Each line is accompanied by a satellite transition due to the population of the ${}^7\text{F}_1$ state, with a separation of about 300 cm^{-1} at 300 K; ${}^5\text{D}_{0,1,2,3} \leftarrow {}^7\text{F}_1$ transitions occur at about 590, 536, 473, and 420 nm, respectively. The sharp lines at 396, 384, 377, 363, and 320 nm may be assigned to the ${}^5\text{L}_{6,7,8,9}$ and ${}^5\text{H} \leftarrow {}^7\text{F}_0$ multiplet transitions, respectively (Ofelt, 1963). In **6**, the ${}^5\text{D}_{1,2} \leftarrow {}^7\text{F}_0$, ${}^5\text{D}_{1,2} \leftarrow {}^7\text{F}_1$, and ${}^5\text{L}_6 \leftarrow {}^7\text{F}_0$ lines appear at about 526, 466, 538, 472, and 395 nm, respectively. Figure 13 displays the low-resolution emission spectra of **3** and **6** at 4.2 K under excitation by the 248-nm light corresponding to the O \rightarrow Nb (or W) lmct bands; it also shows the high-resolution emission spectra of the ${}^5\text{D}_0 \rightarrow {}^7\text{F}_0$ transitions (Yamase et al., 1997). The ${}^5\text{D}_0 \rightarrow {}^7\text{F}_{0,1,2,3,4}$ lines are clearly visible in the range 580–710 nm. In **6**, the ${}^5\text{D}_1 \rightarrow {}^7\text{F}_{0,1,2,3}$ transitions are observed on the 4.2 K spectrum in the range 526–585 nm, whereas the weak ${}^5\text{D}_1 \rightarrow {}^7\text{F}_4$ transitions overlap with the strong ${}^5\text{D}_0 \rightarrow {}^7\text{F}_2$ transitions.

The relative intensities of the ${}^5\text{D}_0 \rightarrow {}^7\text{F}_j$ transitions at 4.2 K are listed in Table 3 for compounds **1-6** (Yamase et al., 1990; Naruke and Yamase, 1991; Yamase and Naruke, 1991; Sugeta and Yamase, 1993). The anhydrous Eu^{3+} site in **1** exhibits the highest intensity of the ${}^5\text{D}_0 \rightarrow {}^7\text{F}_1$ emission which appears as a doublet (Figure 2). Such a ${}^5\text{D}_0$ emission pattern is different from that of the hydrated Eu^{3+} site in **2-6**, for which the ${}^5\text{D}_0 \rightarrow {}^7\text{F}_2$ electric-dipole transition exhibits the highest intensity and features a multiplet structure. This implies that the presence of the aqua ligand in the first co-ordination sphere causes a dramatic increase in the magnitude of the hypersensitive ${}^5\text{D}_0 \rightarrow {}^7\text{F}_2$ transition. An increase in temperature resulted in no significant change in the relative intensity of the ${}^5\text{D}_0 \rightarrow {}^7\text{F}_j$ emission. The ${}^5\text{D}_1 \rightarrow {}^7\text{F}_{0,1,2,3}$ transitions for **6**, in which the relative intensity of the ${}^5\text{D}_1 \rightarrow {}^7\text{F}_1$ transition is the highest, have very weak intensities, and their integrated intensity is about 9% of the total ${}^5\text{D}_0 \rightarrow {}^7\text{F}_j$ emission at 4.2 K. In **3** where six

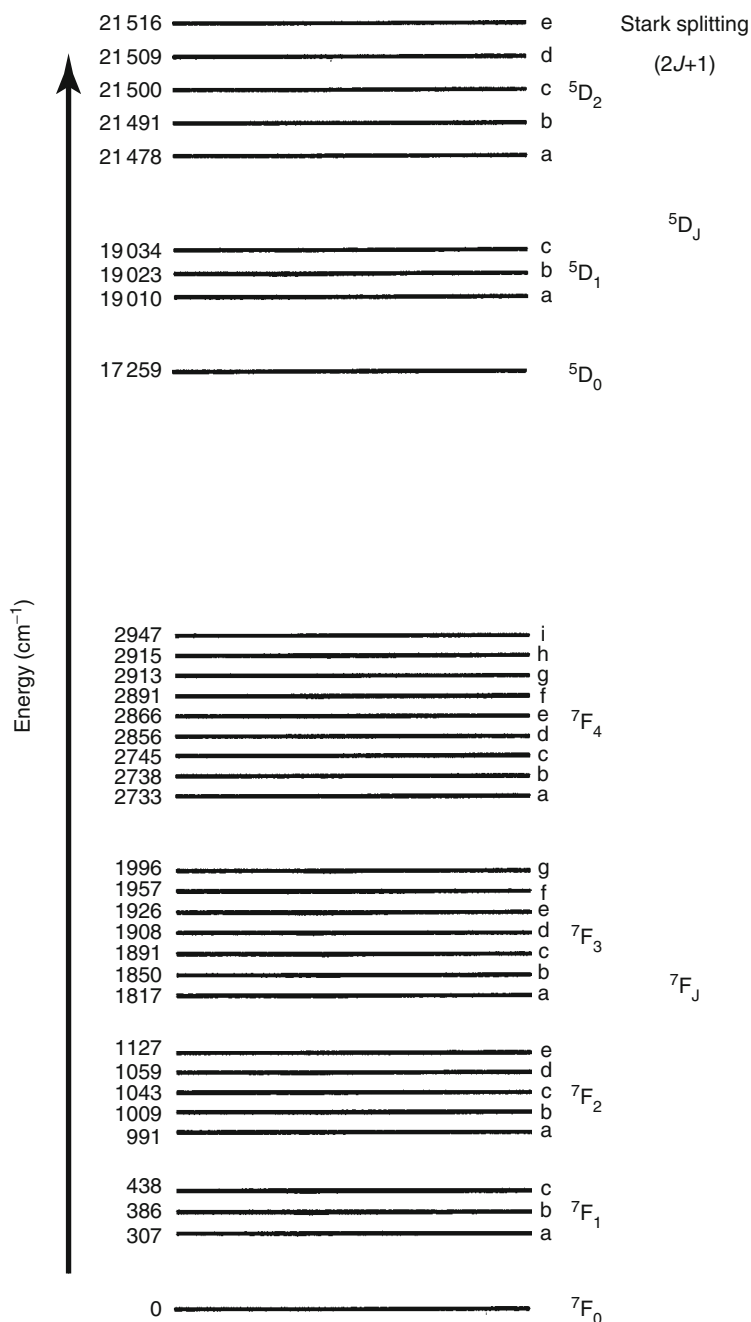


FIGURE 11 Energy-level diagram of the Stark splitting of 7F_J ($J = 0-4$) and 5D_J ($J = 0-2$) states of Eu^{3+} for 5. Figure is redrawn after Yamase and Naruke (1991).

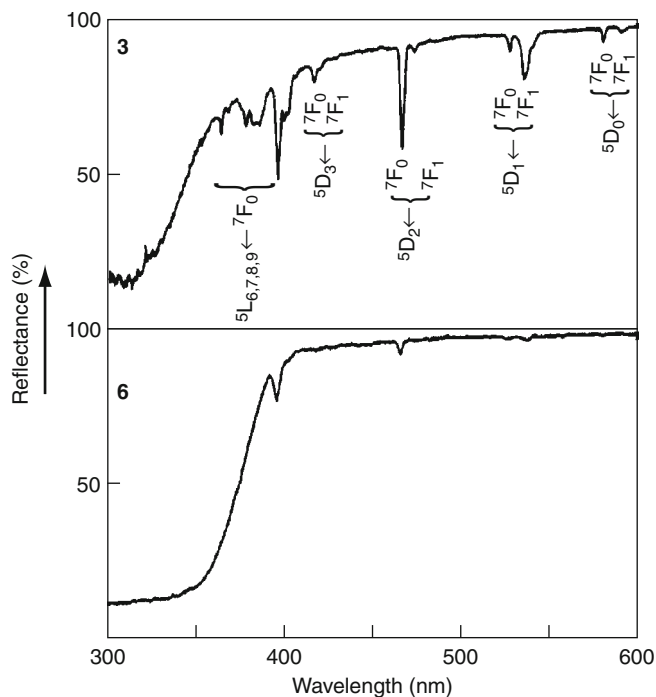
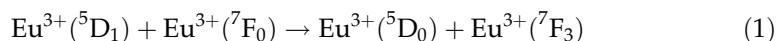


FIGURE 12 Diffuse reflectance spectra of **3** and **6** at 300 K. Figure is redrawn after Yamase et al. (1997).

crystallographically different Eu^{3+} sites exist, the observation of a broad asymmetric peak for the ${}^5\text{D}_0 \rightarrow {}^7\text{F}_0$ transition indicates that at least three Eu^{3+} sites (see inset in Figure 13) are responsible for the series of observed luminescence transitions, since the ${}^5\text{D}_0 \rightarrow {}^7\text{F}_0$ transition cannot be split by any crystal field. In contrast, an observable single ${}^5\text{D}_0 \rightarrow {}^7\text{F}_0$ peak at 579.6 nm for **6** (see inset in Figure 13) suggests that the two crystallographically different Eu^{3+} sites are almost equivalent spectroscopically. This is supported by the observation of three ${}^5\text{D}_0 \rightarrow {}^7\text{F}_1$ peaks, seven ${}^5\text{D}_0 \rightarrow {}^7\text{F}_3$ peaks, and nine ${}^5\text{D}_0 \rightarrow {}^7\text{F}_4$ peaks, in good agreement with a crystallographic site symmetry C_s or C_1 (Sugeta and Yamase, 1997; Yamase et al., 1997). Figure 14 shows the high-resolution emission spectra of the ${}^5\text{D}_0 \rightarrow {}^7\text{F}_3$ transition for **3** and **6**. The observable ${}^5\text{D}_0 \rightarrow {}^7\text{F}_3$ line at 646 nm in **3** corresponds to an energy difference ΔE (${}^7\text{F}_3 - {}^7\text{F}_0$) of about 1755 cm^{-1} , which is very close to the energy difference of about 1750 cm^{-1} between the ${}^5\text{D}_1$ and ${}^5\text{D}_0$ states (Yamase et al., 1997). In contrast, no ${}^5\text{D}_0 \rightarrow {}^7\text{F}_3$ line could be detected for **6** in the range 645–646 nm. Thus, the absence of ${}^5\text{D}_1 \rightarrow {}^7\text{F}_j$ emission for **3** (Figure 13) was attributed to the quenching of the higher level emission by cross-relaxation between the ${}^5\text{D}_1$ and ${}^7\text{F}_0$ states, as denoted by Eq. (1).



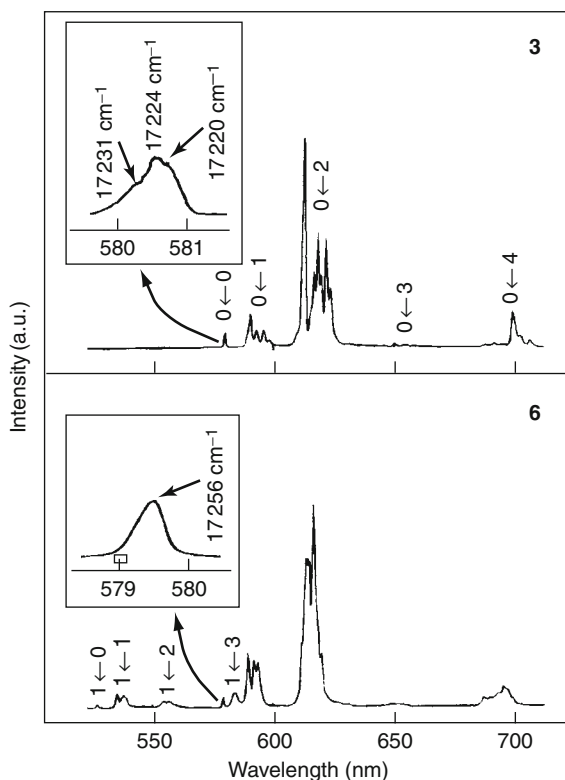


FIGURE 13 Emission spectra under the 248-nm light exposure of **3** and **6** at 4.2 K. Figure is redrawn after Yamase et al. (1997).

TABLE 3 Relative intensities of the ${}^5D_0 \rightarrow {}^7F_j$ emissions of Eu^{3+} at 4.2 K for **1–6**

Terminal level	1	2	3	4	5	6
7F_0	~0	2	1.3	1	~0	0.3
7F_1	50	18	9.9	13	15	17.2
7F_2	18	69	78.2	74	72	71.4
7F_3	5	3	1.0	1	2	1.0
7F_4	27	8	9.6	11	11	10.1

Relative intensities of the ${}^5D_0 \rightarrow {}^7F_j$ emissions for **4** were those at 77 K because of its degradation at 4.2 K.

The occurrence of such a cross-relaxation leads to the preponderance of the emission from 5D_0 .

Both the quantum yield (Φ) of the ${}^5D_0 \rightarrow {}^7F_j$ luminescence and the lifetime (τ) of the 5D_0 state under 248-nm photoexcitation at 4.2, 77, and 300 K are listed in Table 4 (Yamase et al., 1997). The temperature dependence of the Eu^{3+} emission intensity for compounds **1–6** upon excitation into the O \rightarrow M lmct bands is always larger than under the f–f bands excitation. The strong temperature dependence of

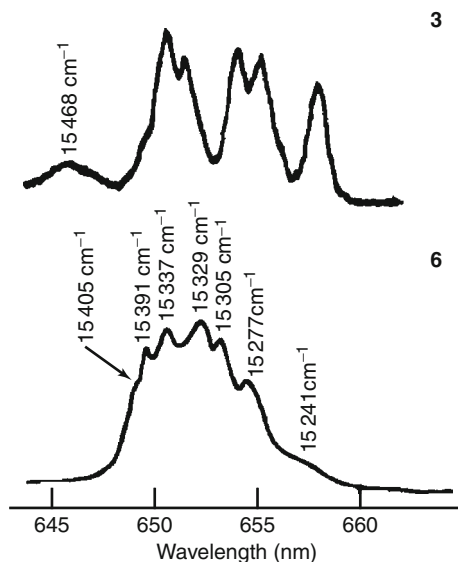


FIGURE 14 High-resolution emission spectra of the ${}^5D_0 \rightarrow {}^7F_3$ transition for **3** and **6** at 4.2 K. Figure is redrawn after Yamase et al. (1997).

the luminescence intensity under the $O \rightarrow M$ lmct excitation is associated with the thermal relaxation of the $O \rightarrow M$ lmct states competing with the energy transfer to Eu^{3+} in the lattice. On the other hand, the small temperature dependence of the luminescence intensity under the $f-f$ excitation reflects the absence of thermal expansion of the 5D_0 state, preventing non-radiative deactivation. The 5D_1 luminescence decay is similar for compounds **4–6** and strongly temperature-dependent [e.g., τ (4.2 K) = $14 \pm 2\ \mu\text{s}$ and τ (77 K) = $8 \pm 1\ \mu\text{s}$].

2.4 Co-ordination of aqua and hydroxo ligands to Eu^{3+}

Based on the linear plots of the reciprocal lifetimes of the 5D_0 state versus number (n) of aqua ligands in Eu^{3+} complexes for a variety of structurally well-characterized aminopolycarboxylatoeuropate complexes, a phenomenological method to estimate n in aqueous solutions was given at first with an uncertainty of 0.5 by

$$n = 1.05(\tau_{\text{H}_2\text{O}}^{-1} - \tau_{\text{D}_2\text{O}}^{-1}) \quad (2)$$

where $\tau_{\text{H}_2\text{O}}^{-1}$ and $\tau_{\text{D}_2\text{O}}^{-1}$ are the reciprocal experimental lifetimes in H_2O and D_2O solutions in $(\text{ms})^{-1}$, respectively (Horrocks and Sudnick, 1979, 1981). Thereafter, a refined equation in its simplest form with an uncertainty of 0.1 has been presented in Eq. (3), and has allowed the prediction of the number (q) of water molecules in the first co-ordination sphere of an Eu^{3+} complex in aqueous solution (Supkowski and Horrocks, 2002).

TABLE 4 Approximate co-ordination geometry (CG) around Eu^{3+} , average (TC) of the total charge of ligands bound to Eu^{3+} , total number (n') of aqua and hydroxo ligands bound to Eu^{3+} , ${}^5\text{D}_0 \rightarrow {}^7\text{F}_0$ energy (0–0 in cm^{-1}), and τ (in ms) and Φ of the ${}^5\text{D}_0 \rightarrow {}^7\text{F}_j$ emission upon O \rightarrow M lmct band excitation for **1–6**

	1	2	3	4	5	6
CG	sa ^a	sa	bt ^a	tt ^a	tt	tt
TC	12	9	7.3	6.5	3	4.7
n'	0	2	3	4	6	8
0–0	17212	17247	17231–17220	~17241	17259	17256
τ						
4.2 K	3.7	1.1 \pm 0.2	0.32 \pm 0.01	^b	0.16	0.15 \pm 0.01
77 K	3.3	1.1 \pm 0.2	0.31 \pm 0.01	0.24 \pm 0.02	0.17 \pm 0.01	0.14 \pm 0.01
300 K	2.8	1.1 \pm 0.2	0.31 \pm 0.02	0.20 \pm 0.01	0.17 \pm 0.01	0.14 \pm 0.01
Φ						
4.2 K	0.99	0.55	0.085 \pm 0.001	^b	0.034	(7 \pm 1) $\times 10^{-4}$
77 K	0.90	0.51	0.042 \pm 0.001	0.12	0.029	(2 \pm 1) $\times 10^{-4}$
300 K	0.80	0.25	0.009 \pm 0.001	0.07	0.013	

^a sa, square anti-prismatic; tt, tricapped-trigonal-prismatic; bt, bicapped trigonal prismatic.

^b Measurements at 4.2 K for **4** were not done because of its degradation.

$$q = 1.11(\tau_{\text{H}_2\text{O}}^{-1} - \tau_{\text{D}_2\text{O}}^{-1} - 0.31) \quad (3)$$

Since $\tau_{\text{D}_2\text{O}}$ corresponds to the lifetime of ${}^5\text{D}_0$ of the complex with $n = 0$, it is reasonable to use $\tau_{\text{D}_2\text{O}} = 3.7$ ms, the ${}^5\text{D}_0$ lifetime at 4.2 K for **1** (Sugeta and Yamase, 1993). The revised Eq. (3) was applied to **1–6** (at 4.2 K) solids with square anti-, bicapped trigonal-, and tricapped-trigonal-prismatic co-ordination geometries of Eu^{3+} . Table 4 lists the approximate co-ordination geometry, total number (n') of aqua and hydroxo ligands, total charge from ligands, and the ${}^5\text{D}_0 \rightarrow {}^7\text{F}_0$ energy (0–0 in cm^{-1}) for the Eu^{3+} sites of **1–6**. Figure 15 shows a plot of q values calculated by the difference ($\Delta\tau^{-1}$) in reciprocal ${}^5\text{D}_0$ lifetimes at 4.2 K between **2–6** and **1** versus the crystallographically determined number of aqua ligands in the first co-ordination spheres, n . The solid line in Figure 15A indicates the $q = n$ relationship [given by Eq. (3)] obtained for various aminopolycarboxylatoeuropate complexes (Supkowski and Horrocks, 2002). As shown in Figure 15A, q values for **2**, **3**, and **6** suggest n values of 0.5, 3, and 7 [Eq. (3)], respectively. Such a deviation from $q = n$ for **2** and **6** arises from the existence of elongated Eu– O_w distances which makes the Eu^{3+} – H_2O coupling per H_2O molecule weakened with, as a result, a low estimate of q : in **2**, the Eu– O_w distances of 2.51(3) – 2.64(3) Å [average 2.56(2) Å] for two O_w molecules are slightly longer than the average Eu– O_w distances [2.49 (1) and 2.48(1) Å] observed for **3–5** (Table 2), which results in estimating $q \approx 0.4$ (Figure 15B). Similarly, in **6**, one (capping) of eight O_w atoms is lying at a very long distance from the central Eu^{3+} atom, namely 2.59(3)–2.88(5) Å [average 2.78(3) Å] compared with other O_w atoms with Eu– O_w distances of 2.40(3)–2.59(3) Å

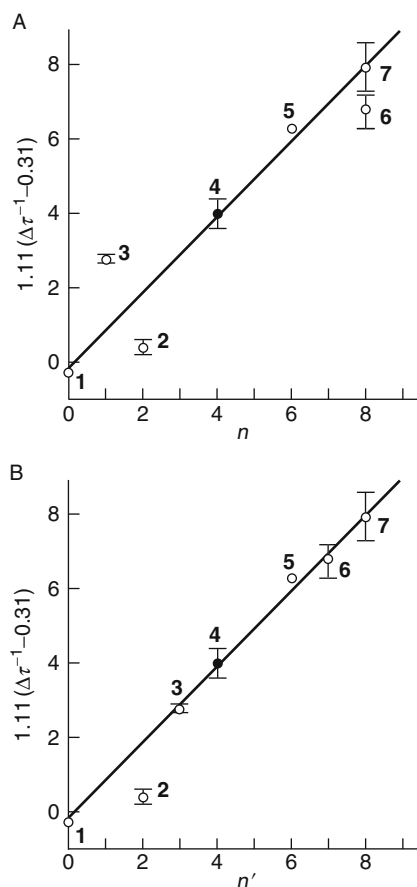


FIGURE 15 Plots of q values calculated by the difference ($\Delta\tau^{-1}$) in reciprocal 5D_0 lifetimes at 4.2 K between **2–6** and **1**, against number (n) of aqua ligands (A) and total number (n') of aqua and hydroxo ligands (B) in the first co-ordination spheres. A plot of q value of **4** at 4.2 K was replaced with the one at 77 K because of its degradation at 4.2 K.

[average 2.44(1) Å] (Figure 10), resulting in $q \approx 6.8$ (Figure 15B). Furthermore, a large deviation from $q = n$ for **3**, where two hydroxo ligands co-ordinate Eu^{3+} with Eu-O distances of 2.41(3)–2.54(3) Å [average 2.47(1) Å] (Figure 7 and Table 2), reveals a strong contribution of vibrational states of the high-frequency OH oscillators for two hydroxo ligands to the lifetime of 5D_0 as well as the case of aqua ligands. Although Eq. (3) should be used with care for the case of the long Eu-O_w distances of more than 2.6 Å, the $q = 1.11(\Delta\tau^{-1} - 0.31)$ value for the polyoxometalloyeuropate solids is sufficiently useful to predict the total number (n') of aqua and hydroxo ligands around Eu^{3+} (Figure 15B), irrespective of the co-ordination geometry of Eu^{3+} site, for compounds not amenable to study by single-crystal X-ray methods. As shown in Table 4, the Eu^{3+} site for high values (≥ 9) of the total charge of the ligands favours a square anti-prismatic geometry

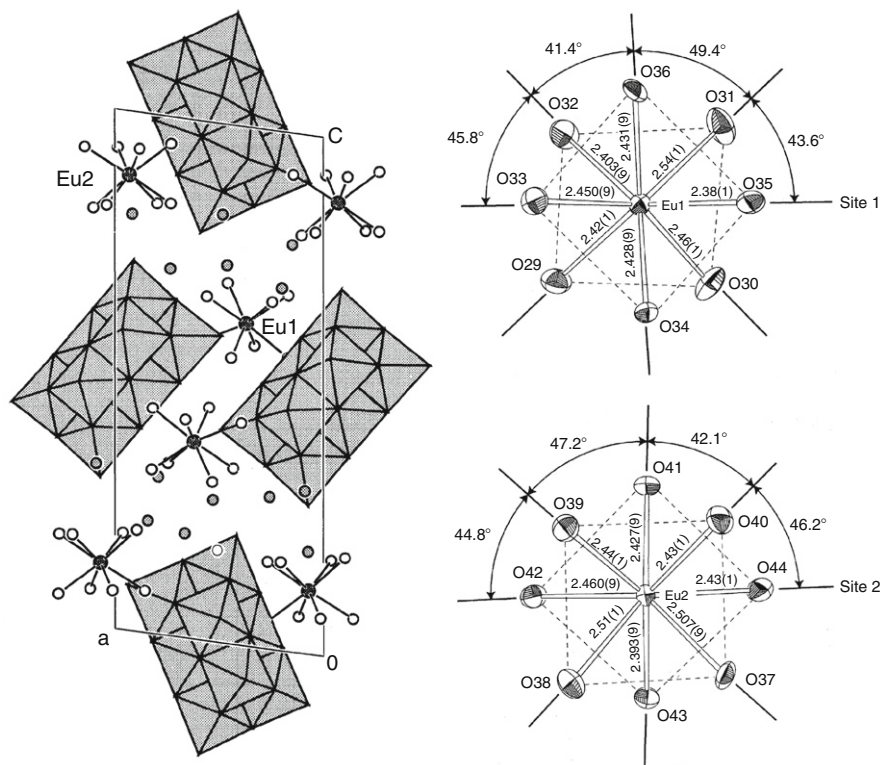


FIGURE 16 Crystal structure of $[\text{Eu}(\text{H}_2\text{O})_8]_2[\text{V}_{10}\text{O}_{28}] \cdot 8\text{H}_2\text{O}$ (**7**) and the co-ordination of eight aqua ligands (with $\text{Eu}-\text{O}_w$ distances of 2.34–2.54 Å) for two crystallographically different Eu sites of 1 and 2. Figure is redrawn after Yamase et al. (1998).

with $n \leq 2$, while lower charges (≤ 6.5) favour a tricapped-trigonal-prismatic geometry with $n \geq 4$. This could be explained by the contraction of the co-ordination sphere due to the nephelauxetic effect. However, in $[\text{Eu}(\text{H}_2\text{O})_8]_2[\text{V}_{10}\text{O}_{28}] \cdot 8\text{H}_2\text{O}$ (**7**), which exhibits no $\text{Eu}-\text{O}$ bonds involving the $[\text{V}_{10}\text{O}_{28}]^{6-}$ ligands, each Eu^{3+} ion is co-ordinated only by eight aqua ligands with a zero total charge in an approximate square anti-prismatic geometry (Yamase et al., 1999), suggesting that the co-ordination geometry of the Eu^{3+} site is not necessarily determined by the nephelauxetic effect. Figure 16 shows the crystal structure of **7** and the co-ordination of eight aqua ligands (with $\text{Eu}-\text{O}_w$ distances of 2.34–2.54 Å) for two crystallographically different Eu sites with approximately D_{4d} square anti-prismatic geometry. The low-resolution photoluminescence spectrum recorded at 4 K under excitation of the weak $^5\text{D}_1 \leftarrow ^7\text{F}_0$ absorption band at 525.6 nm is reproduced in Figure 17. It consists in zero $^5\text{D}_0 \rightarrow ^7\text{F}_0$, two $^5\text{D}_0 \rightarrow ^7\text{F}_1$, three $^5\text{D}_0 \rightarrow ^7\text{F}_2$, weak one $^5\text{D}_0 \rightarrow ^7\text{F}_3$, and four (two peaks and two shoulders) $^5\text{D}_0 \rightarrow ^7\text{F}_4$ transitions. We note that for **7**, the efficient excitation bands of Eu^{3+} are completely obscured by the intense and broad $\text{O} \rightarrow \text{V}$ charge transfer band of $[\text{V}_{10}\text{O}_{28}]^{6-}$ extending from the UV up to 500 nm.

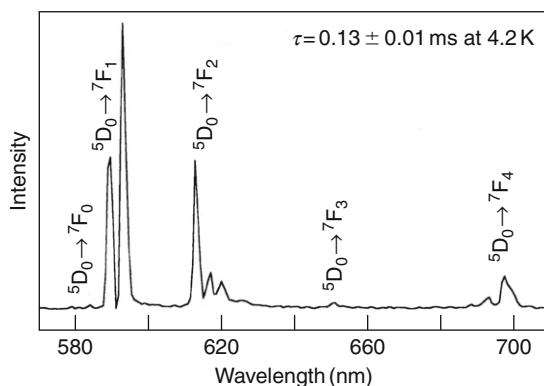


FIGURE 17 Low-resolution photoluminescence spectrum of **7** at 4.2 K under excitation of a weak ${}^5D_1 \leftarrow {}^7F_0$ absorption band. Figure is redrawn after Yamase et al. (1998).

The validity of $q = n'$ is confirmed by plotting q values (with $\tau_0 = 0.13 \pm 0.01$ ms at 4.2 K) against n' (Figure 15B).

The average value of Ln–O_w distances for the approximately square antiprismatic Ln³⁺ sites of lanthanide decavanadate decreases with increasing Ln atomic number: 2.45(4), 2.36(3), and 2.33(5) Å for [Eu(H₂O)₈]₂[V₁₀O₂₈]·8H₂O (Yamase et al., 1998), [Er(H₂O)₈]₂[V₁₀O₂₈]·9H₂O (Rivero et al., 1984), and [Yb(H₂O)₈]₂[V₁₀O₂₈]·8H₂O (Rivero et al., 1985), respectively, which is attributable to the lanthanide contraction of the ionic radius. Interestingly, [Nd(H₂O)₉]₂[V₁₀O₂₈]·10H₂O and [La(H₂O)₇]₂[V₁₀O₂₈]·6H₂O exhibit tricapped-trigonal-prismatic Nd(H₂O)₉ and LaO₂(H₂O)₇ sites (Saf'yanov and Belov, 1976; Saf'yanov et al., 1978). Other examples for the Eu³⁺ centres bound only to aqua ligands are tricapped-trigonal-prismatic Eu(H₂O)₉ sites in Eu(H₂O)₉(C₂H₅SO₄)₃ (Albertsson and Elding, 1977; Gerkin and Reppart, 1984) and [Eu(H₂O)₉][(BrO₃)₃] (Albertsson and Elding, 1977). High-resolution spectra of the ${}^5D_0 \rightarrow {}^7F_{1,2}$ emission observed under the ${}^5D_1 \leftarrow {}^7F_0$ excitation were carefully compared for 0.1 M EuCl₃ (aq) and crystals of [Eu(H₂O)₈]₂[V₁₀O₂₈]·8H₂O, Eu(C₂H₅SO₄)₃·9H₂O, and [Eu(H₂O)₉][(BrO₃)₃], in order to investigate the equilibrium between eight- and nine-co-ordinate Eu³⁺ (aq) species. Such a modelling of the 0.1 M EuCl₃ (aq) spectra showed that approximately two-thirds of Eu³⁺ ions exist as Eu(H₂O)₈³⁺ in aqueous solution (Tilkens et al., 2004).

2.5 Kinetics of the sensitized luminescence of Eu³⁺

The single exponential decay and its small dependence on temperature for the 5D_0 emission of Eu³⁺ in compounds **1–6** (Table 4) suggests that the energy migration between the Eu³⁺ sites at polyoxometalloyeuropate lattices is negligible, although the shortest Eu···Eu distance in **3** was 3.74 Å (Ozeki et al., 1994). The magnetic-dipole character of the ${}^5D_0 \rightarrow {}^7F_1$ transition implies the radiative rate of this transition to be almost independent of the Eu³⁺ chemical environment, as long as the mixing of electric-dipole character into this transition is small (Verweg et al.,

1988). Therefore, it is meaningful to use the ${}^5\text{D}_0 \rightarrow {}^7\text{F}_1$ magnetic-dipole transition as a standard in order to estimate the radiative rate for 1–6 (Blasse, 1991). We take 1 as a reference since it features an anhydrous Eu^{3+} site exhibiting a high quantum yield (~ 1.0). In addition, the ${}^5\text{D}_0 \rightarrow {}^7\text{F}_1$ transition has a sizeable intensity (Tables 1 and 4, Figure 3) and the optical absorption edge of the $\text{O} \rightarrow \text{W}$ lmct excitation band (~ 3.2 eV) is similar to the one of the other complexes. The radiative rate (k_{rad}) for Eu^{3+} in 1 amounts to $2.7 \times 10^2 \text{ s}^{-1}$ ($=1/3.7$ ms) at 4.2 K, and the ${}^5\text{D}_0 \rightarrow {}^7\text{F}_1$ transition represents 50% of the total emission intensity (Table 2). Therefore, the ${}^5\text{D}_0 \rightarrow {}^7\text{F}_1$ decay rate was evaluated to be $1.35 \times 10^2 \text{ s}^{-1}$. Thus, k_{rad} values for 2–6 were simply estimated from the relative intensities of the ${}^5\text{D}_0 \rightarrow {}^7\text{F}_1$ emission: for example, in 3, $k_{\text{rad}} = 1.4 \times 10^3$ ($=1.35 \times 10^2/0.099$) s^{-1} . Since the experimental decay rate constant of the emission for 3 was $(3.1 \pm 0.1) \times 10^3 \text{ s}^{-1}$ [$=1/(0.32 \pm 0.01)$ ms], we could estimate a non-radiative rate constant (k_{nr}) of $(1.7 \pm 0.1) \times 10^3$ and therefore the ratio (η_{rad}) of the ${}^5\text{D}_0$ radiative emission is 0.45 ± 0.01 . With these data, the yield (Φ_{et}) of the overall energy transfer from the $\text{O} \rightarrow \text{M}$ lmct state to the ${}^5\text{D}_0$ state (partially through the ${}^5\text{D}_1$ state) is calculated to be 0.18 ± 0.01 . Table 5 lists values of k_{rad} , k_{nr} , η_{rad} , and Φ_{et} at 4.2, 77, and 300 K for 1–6 (Yamase et al., 1997), which were obtained from the quantum yields (Φ) of the ${}^5\text{D}_0 \rightarrow {}^7\text{F}_j$ emission and emission decay rates ($1/\tau$) of the ${}^5\text{D}_0$ state under 248-nm light excitation (Table 4). The decrease in Φ_{et} with an increase in temperature was assigned to the d^1 hopping delocalization in the polyoxometalate ligand, which depends on the configuration of both $\text{M}-\text{O}-\text{M}$ and $\text{Eu}-\text{O}-\text{M}$ linkages (Yamase et al., 1990, 1997). The thermal deactivation of the $\text{O} \rightarrow \text{M}$ lmct states due to the d^1 hopping is based on the small disparity in the electronic configurations between the excited and ground states, which is reflected by the bond angles of the $\text{M}-\text{O}-\text{M}$ or $\text{Eu}-\text{O}-\text{M}$ linkage. Photoexcitation into the $\text{O} \rightarrow \text{M}$ lmct bands allows the hopping of the d^1 electron to the Eu^{3+} site through the $\text{Eu}-\text{O}-\text{M}$ linkage involving the 2p orbital of the bridging oxygen atom, provided the $\text{Eu}-\text{O}-\text{M}$ bond angles are about 150° , since the $f\pi$ - $p\pi$ - $d\pi$ orbital mixing on the $\text{Eu}-\text{O}-\text{M}$ linkage would be possible, similarly to the $d\pi$ - $p\pi$ - $d\pi$ orbital mixing observed for the corner-sharing MO_6 octahedra with similar $\text{M}-\text{O}-\text{M}$ bond angles (Yamase and Naruke, 1991; Yamase et al., 1997). The polyoxometalate ligands consisting of only edge-sharing MO_6 octahedra with $\text{M}-\text{O}-\text{M}$ bond angles of about 100° give a small temperature dependence of Φ_{et} (with its high value) due to the localization of the d^1 electron on the MO_6 octahedron, as exemplified by 1. An $\text{Eu}-\text{O}-\text{M}$ bond angle larger than 150° results in a strong temperature dependence of Φ_{et} for compounds 2–6 (Tables 2 and 5). The low value of Φ_{et} (0.24 ± 0.01 at 4.2 K) for 5 compared with 4 (0.48 ± 0.04 at 77 K) is ascribed to the additional factor of the small disparity between the excited and ground $\text{O} \rightarrow \text{M}$ lmct states, which arises from the nearly linear $\text{Mo}-\text{O}-\text{Mo}$ linkage [$179.9(1)^\circ$ with an $\text{Mo}-\text{O}$ distance of $1.88(1)$ Å, see Table 2] joining two γ - $[\text{Mo}_8\text{O}_{26}]^{4-}$ MoO_5 square-pyramids (Niven et al., 1991) through the twofold O atom (Yamase and Naruke, 1991). As described below, the quantum yield of the $\text{O} \rightarrow \text{M}$ lmct triplet luminescence for the highly symmetrical polyoxometalates with Lindqvist or Keggin structures is extremely small due to the small disparity between excited and ground state electronic configuration, as demonstrated in $[\text{NBu}_4]_2[\text{M}_6\text{O}_{19}]$ ($\text{M} = \text{W}$ and Mo) and $\text{K}_5[\text{BW}_{12}\text{O}_{40}] \cdot 15\text{H}_2\text{O}$

TABLE 5 Radiative rate (k_{rad} in s^{-1}), non-radiative rate (k_{nr} in s^{-1}), and ratio (η_{rad}) of radiation of the ${}^5\text{D}_0$ state of Eu^{3+} and quantum yield (Φ_{et}) of the overall energy transfer from O→M lmct states to the ${}^5\text{D}_0$ state (through the ${}^5\text{D}_1$ state in part) for **1–6**^a

	1	2	3	4	5	6
k_{rad}	2.7×10^2	7.5×10^2	1.4×10^3	1.1×10^3	9.0×10^2	7.9×10^2
k_{nr}						
4.2 K	~0	$(1.9 \pm 1.7) \times 10^2$	$(1.7 \pm 0.1) \times 10^3$		5.4×10^3	$(5.9 \pm 0.4) \times 10^3$
77 K	3×10	$(1.9 \pm 1.7) \times 10^2$	$(1.8 \pm 0.1) \times 10^3$	$(3.2 \pm 0.3) \times 10^3$	$(5.0 \pm 0.3) \times 10^3$	$(6.4 \pm 0.5) \times 10^3$
300 K	9×10	$(1.9 \pm 1.7) \times 10^2$	$(1.8 \pm 0.2) \times 10^3$	$(4.0 \pm 0.2) \times 10^3$	$(5.0 \pm 0.3) \times 10^3$	$(6.4 \pm 0.5) \times 10^3$
η_{rad}						
4.2 K	1.0	0.83 ± 0.15	0.45 ± 0.01		0.14 ± 0.01	0.15 ± 0.01
77 K	0.90	0.83 ± 0.15	0.43 ± 0.01	0.25 ± 0.02	0.15 ± 0.01	0.14 ± 0.01
300 K	0.75	0.83 ± 0.15	0.44 ± 0.03	0.21 ± 0.01	0.15 ± 0.01	0.14 ± 0.01
Φ_{et}						
4.2 K	1.0	0.69 ± 0.12	0.19 ± 0.01		0.24 ± 0.01	$(6 \pm 1) \times 10^{-3}$
77 K	1.0	0.64 ± 0.12	0.09 ± 0.01	0.48 ± 0.04	0.19 ± 0.01	$(2 \pm 1) \times 10^{-3}$
300 K	0.94	0.31 ± 0.06	0.02	0.33 ± 0.02	0.08 ± 0.01	

^a Since the relative intensities of ${}^5\text{D}_0 \rightarrow {}^7\text{F}_j$ emission were hardly changed with a variety of temperature, k_{rad} was evaluated to be independent of the temperature.

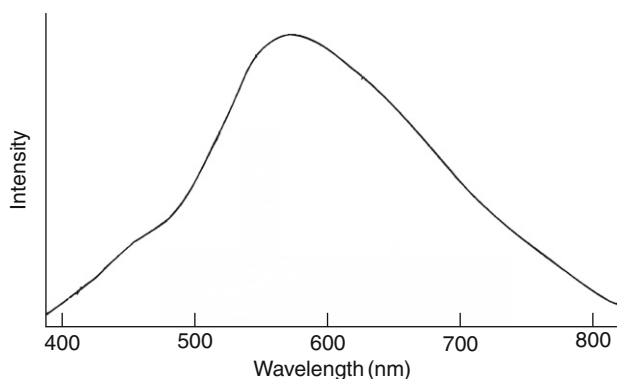


FIGURE 18 Green emission of the O \rightarrow W lmct triplet states under 248-nm light excitation of $\text{K}_9\text{H}_5[(\text{GeTi}_3\text{W}_9\text{O}_{37})_2\text{O}_3] \cdot 16\text{H}_2\text{O}$ at $T < 150$ K. Figure is redrawn after Yamase et al. (1997).

(Yamase and Sugeta, 1993). Both the extremely low value of $\Phi_{\text{et}} (\leq 6 \times 10^{-3})$ and the strong temperature dependence of the luminescence quantum yield (Table 5) for **6** are attributed to a strong temperature-dependent deactivation through the O \rightarrow M lmct states. In **6**, the condensed double Keggin structure for the $[(\text{GeTi}_3\text{W}_9\text{O}_{37})_2\text{O}_3]^{14-}$ component with approximate D_{3h} symmetry (Figure 10) involves large W–O–W, Ti–O–W, and Eu–O–W bond angles of more than 150° (viz Eu–O–W $\approx 165^\circ$, cf. Table 2), which results in a strong deactivation generated by the O \rightarrow M lmct states of $[(\text{GeTi}_3\text{W}_9\text{O}_{37})_2\text{O}_3]^{14-}$. This also leads to low values of both the quantum yield and the quenching temperature of the O \rightarrow M lmct triplet emission in $\text{K}_9\text{H}_5[(\text{GeTi}_3\text{W}_9\text{O}_{37})_2\text{O}_3] \cdot 16\text{H}_2\text{O}$ (Yamase et al., 1993; Sugeta and Yamase, 1997). Figure 18 shows a broad green emission peaking at 570 nm at low temperatures, $T < 150$ K, under 248-nm light excitation of $\text{K}_9\text{H}_5[(\text{GeTi}_3\text{W}_9\text{O}_{37})_2\text{O}_3] \cdot 16\text{H}_2\text{O}$ solid. The quantum yield of this emission from the O \rightarrow M lmct triplet states is extremely low, $(4.9 \pm 0.2) \times 10^{-3}$ at 4.2 K and $(1.0 \pm 0.1) \times 10^{-3}$ at 100 K. The corresponding luminescence decay shows two-exponential behaviour (due to two ${}^3\text{T}_{1u}$ triplet states), with associated lifetimes of 91 ± 6 and 140 ± 10 μs at 4.2 K and 10 ± 2 and 30 ± 4 μs at 100 K. Details are discussed in Section 2.6. On the other hand, a value (the energy transfer efficiency of $\Phi_{\text{et}} = 0.19 \pm 0.01$) observed for **3**, which contains the highly symmetrical $[\text{Nb}_6\text{O}_{19}]^{8-}$ ligands as shown in Figure 7) at 4.2 K is not as low as expected, compared with **6**, despite its strong temperature dependence of Φ_{et} (Table 5). This is associated with two factors. One is the distortion of the $[\text{Nb}_6\text{O}_{19}]^{8-}$ ligand co-ordinating Eu^{3+} in a heptadentate fashion, reducing the point symmetry of each $[\text{Nb}_6\text{O}_{19}]^{8-}$ ligands to C_{2v} , from the idealized O_h symmetry (Ozeki et al., 1994; Naruke and Yamase, 1996). The other is the slightly smaller bond angles (about 142°) of the Eu–O(μ_2)–Nb linkages compared with other polyoxometalloeuropates (Table 2).

TABLE 6 Emission and excitation maxima at 4.2 K, emission decay (τ_{triplet}) and quantum yield (Φ_{triplet}) of the O \rightarrow M lmct triplet emission for a variety of polyoxometalates

Complexes	Emission maximum (nm)	Excitation maximum (nm)	τ_{triplet}^a (μs)		Φ_{triplet}		
			4.2 K	77 K	4.2 K	77 K	300 K
$\text{K}_{5.5}\text{H}_{1.5}[\text{SbW}_6\text{O}_{24}] \cdot 6\text{H}_2\text{O}$	520	280	176 + 245	143 + 160	0.61	0.43	4.2×10^{-2}
$\text{Na}_5[\text{IMo}_6\text{O}_{24}] \cdot 3\text{H}_2\text{O}$	670	280, 330(sh)	133 + 246	110 + 189	2.6×10^{-2}	1.5×10^{-2}	
$\text{Na}_3\text{H}_6[\text{CrMo}_6\text{O}_{24}] \cdot 8\text{H}_2\text{O}^b$	703.0, 704.4	300, 400, 540	143	87	5.0×10^{-3}	1.0×10^{-3}	
$[\text{NH}_4]_3\text{H}_6[\text{FeMo}_6\text{O}_{24}] \cdot 7\text{H}_2\text{O}$	–	–	–	–	–	–	
$\text{K}_4\text{H}_5[\text{CoMo}_6\text{O}_{24}] \cdot 7\text{H}_2\text{O}$	–	–	–	–	–	–	
$\text{K}_6[\text{Mo}_7\text{O}_{24}] \cdot 4\text{H}_2\text{O}$	700	280, 350	169 + 209	142 + 190	9.4×10^{-2}	3.1×10^{-2}	7.0×10^{-4}
$[\text{NH}_4]_6[\text{Mo}_7\text{O}_{24}] \cdot 4\text{H}_2\text{O}$	700	–	6 + 17	6 + 15	1.9×10^{-2}	3.0×10^{-3}	
$\text{K}_5\text{H}_2[\text{SbMo}_6\text{O}_{24}] \cdot 7\text{H}_2\text{O}$	700	280, 355	97 + 140	92 + 172	3.5×10^{-2}	2.5×10^{-2}	
$\text{K}_5[\text{BW}_{12}\text{O}_{40}] \cdot 15\text{H}_2\text{O}$	520	–	134 + 185	105 + 140	4.0×10^{-4}	2.0×10^{-4}	
$\text{K}_5[\text{PTiW}_{11}\text{O}_{40}] \cdot 3\text{H}_2\text{O}$	560	285, 315(sh)	112 + 142	59 + 97	0.12	2.5×10^{-2}	
$\text{K}_7[\text{PTi}_2\text{W}_{10}\text{O}_{40}] \cdot 6\text{H}_2\text{O}$	580	280, 340(sh)	158 + 202	80	0.14	1.5×10^{-2}	
$\text{K}_3[\text{PMo}_{12}\text{O}_{40}] \cdot 44\text{H}_2\text{O}$	510	–	64 + 190	43 + 87	2.0×10^{-4}	1.0×10^{-4}	
$\text{A-}\beta\text{-Na}_8\text{H}[\text{PW}_9\text{O}_{34}] \cdot 24\text{H}_2\text{O}$	540	280, 310(sh)	113 + 173	133 + 171	0.14	0.11	

(continued)

TABLE 6 (continued)

Complexes	Emission maximum (nm)	Excitation maximum (nm)	τ_{triplet}^a (μs)		Φ_{triplet}		
			4.2 K	77 K	4.2 K	77 K	300 K
$\text{Cs}_4[\text{W}_{10}\text{O}_{32}] \cdot n\text{H}_2\text{O}$ ($n = 4$ or 5)	660	280, 360(sh)	203 + 306	157 + 217	6.4×10^{-2}	4.5×10^{-2}	
$[\text{NBu}_4]_2[\text{W}_6\text{O}_{19}]$	520	–	102 + 158	45 + 146	7.0×10^{-4}	1.0×10^{-4}	
$[\text{NBu}_4]_2[\text{Mo}_6\text{O}_{19}]$	530	–	107 + 250	88 + 159	1.0×10^{-4}	–	

^a A sum of two exponential decays is used. The accuracy for the τ_{triplet} values is within $\pm 15\%$ of each value.

^b R-line emission.

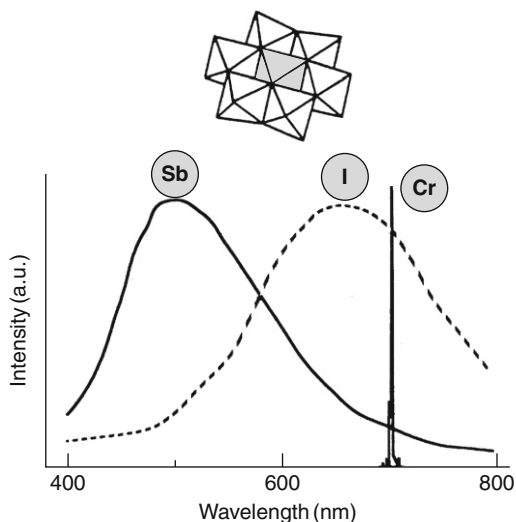


FIGURE 19 Structure of Anderson-type anion given by polyhedral representation and luminescence spectra observed under the $O \rightarrow M$ ($M = W$ or Mo) Imct-bands photoexcitation of three complexes, $K_{5.5}H_{1.5}[SbW_6O_{24}] \cdot 6H_2O$, $Na_5[IMo_6O_{24}] \cdot 3H_2O$, and $Na_3H_6[CrMo_6O_{24}] \cdot 8H_2O$. The grey octahedron in the anion structure indicates a central XO_6 ($X = Sb^{5+}, I^{7+}, Cr^{3+}$) octahedron. Figure is redrawn after Yamase (1998).

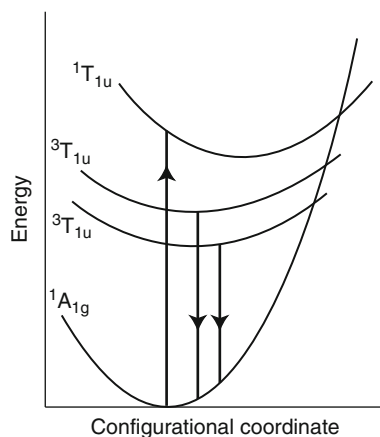


FIGURE 20 A schematic configuration co-ordinate model for the ${}^3T_{1u} \rightarrow {}^1A_{1g}$ emission of the polyoxometalates. Figure is redrawn after Yamase and Sugeta (1993).

2.6 Involvement of the $O \rightarrow M$ Imct triplet states in energy transfer

Table 6 lists emission and excitation maxima, lifetimes associated with the two exponential decays (τ_{triplet}), and quantum yields (Φ_{triplet}) of the ${}^3T_{1u} O \rightarrow M$ Imct triplet emission at 4.2 K for a variety of polyoxometalates (Yamase and Sugeta,

1993). One notes that the Φ_{et} value at 77 K (0.48 ± 0.04) for the edge-sharing MoO_6 octahedral polyoxomolybdoeuropate **4** is small compared with the same edge-sharing WO_6 octahedral polyoxotungstoeuropate **1** (Table 4). This difference could be explained by two factors: the deactivation of the $\text{O} \rightarrow \text{M}$ lmct states in part due to larger $\text{Eu}-\text{O}-\text{Mo}$ bond angles (of about 150°) and a smaller spin-orbit coupling in the MoO_6 octahedra (Yamase et al., 1997). The extent of the $\text{O} \rightarrow \text{M}$ lmct triplet energy transfer in polyoxometalate lattices has been investigated with three isostructural Anderson complexes $\text{K}_{5.5}\text{H}_{1.5}[\text{SbW}_6\text{O}_{24}] \cdot 6\text{H}_2\text{O}$, $\text{Na}_5[\text{IMo}_6\text{O}_{24}] \cdot 3\text{H}_2\text{O}$, and $\text{Na}_3\text{H}_6[\text{CrMo}_6\text{O}_{24}] \cdot 8\text{H}_2\text{O}$. Figure 19 shows the structure of the anions and the luminescence spectra observed under $\text{O} \rightarrow \text{M}$ ($=\text{W}$ or Mo) lmct photoexcitation. Such photoexcitation for the former two complexes leads to the broad ${}^3\text{T}_{1\text{u}} \rightarrow {}^1\text{A}_{1\text{g}}$ emission originating from the $\text{O} \rightarrow \text{M}$ lmct triplet states (Yamase and Sugeta, 1993). A schematic configuration co-ordinate model for this emission is shown in Figure 20 where the excited state parabola is offset relative to that of the ${}^1\text{A}_{1\text{g}}$ ground state due to the charge-transfer character of the transition. The emission behaviour of the polyoxometalates can be rationalized by two ${}^3\text{T}_{1\text{u}}$ triplet levels, $(t_{1\text{u}})^5(t_{2\text{g}})^1$ and $(t_{2\text{u}})^5(t_{2\text{g}})^1$, each of which is further split into four levels by spin-orbit coupling: $\text{A}_{1\text{u}}$, E_{u} , $\text{T}_{1\text{u}}$, and $\text{T}_{2\text{u}}$ (Blasse, 1980), which are considerably mixed (Van Oosterhout, 1977a, 1977b). The green emission of $\text{K}_{5.5}\text{H}_{1.5}[\text{SbW}_6\text{O}_{24}] \cdot 6\text{H}_2\text{O}$ is intense and observed even at room temperature (with $\Phi_{\text{triplet}} = 4.2 \times 10^{-4}$), in contrast to $\text{Na}_5[\text{IMo}_6\text{O}_{24}] \cdot 3\text{H}_2\text{O}$ which gives orange emission only at temperatures below 100 K. The small quantum yield of the emission for $\text{Na}_5[\text{IMo}_6\text{O}_{24}] \cdot 3\text{H}_2\text{O}$, compared with $\text{K}_{5.5}\text{H}_{1.5}[\text{SbW}_6\text{O}_{24}] \cdot 6\text{H}_2\text{O}$, is attributed to a smaller spin-orbit coupling in the former, with a resulting increase in the non-radiative ${}^1\text{T}_{1\text{u}} \rightarrow {}^1\text{A}_{1\text{g}}$ transition probability. On the other hand, $\text{Na}_3\text{H}_6[\text{CrMo}_6\text{O}_{24}] \cdot 8\text{H}_2\text{O}$, in which a central Cr^{3+} provides several energy levels within the $\text{O} \rightarrow \text{Mo}$ lmct emission bands, does not show any $\text{O} \rightarrow \text{Mo}$ lmct triplet emission, but instead sharp ${}^2\text{T}_{1\text{r}}$, ${}^2\text{E} \rightarrow {}^4\text{A}_2$ Cr^{3+} emission lines (Henderson and Inbusch, 1989), known as the R-lines with a single-exponential decay as a result of the energy transfer from the ${}^3\text{T}_{1\text{u}}$ $\text{O} \rightarrow \text{Mo}$ lmct states. If the energy transfer from the ${}^1\text{T}_{1\text{u}}$ $\text{O} \rightarrow \text{Mo}$ lmct states into Cr^{3+} were operative in this case, one would expect the co-existence of both $\text{O} \rightarrow \text{Mo}$ lmct triplet and Cr^{3+} luminescence, the rate of the inter-system crossing ${}^1\text{T}_{1\text{u}} \rightarrow {}^3\text{T}_{1\text{u}}$ being high enough to compete with the rate of the energy transfer. The rate of the energy transfer from the ${}^3\text{T}_{1\text{u}}$ $\text{O} \rightarrow \text{Mo}$ lmct states into Cr^{3+} in $\text{Na}_3\text{H}_6[\text{CrMo}_6\text{O}_{24}] \cdot 8\text{H}_2\text{O}$ was estimated to be larger than 10^6 s^{-1} ; otherwise, the $\text{O} \rightarrow \text{Mo}$ lmct triplet emission with a non-exponential long decay lasting several hundred microseconds at temperatures lower than 100 K should be observed. The same is true for the polyoxometallomanganates such as $\text{K}_6\text{Na}_2[\text{MnW}_6\text{O}_{24}] \cdot 12\text{H}_2\text{O}$, $\text{K}_6[\text{MnMo}_6\text{O}_{32}] \cdot 6\text{H}_2\text{O}$, and $\text{Na}_{12}[\text{Mn}(\text{Nb}_6\text{O}_{19})_2] \cdot 50\text{H}_2\text{O}$, in which intra-molecular energy transfer from the $\text{O} \rightarrow \text{M}$ ($=\text{W}$, Mo , or Nb) lmct triplet states into Mn^{4+} occurs, resulting in emission of the Mn^{4+} R-line only (Yamase et al., 1996). The $\text{O} \rightarrow \text{M}$ lmct triplet states were identified for the non-molecular oxides of transition metal ions with an empty d shell by ESR studies of the luminescent states in $\text{K}_2\text{Cr}_2\text{O}_7$, YVO_4 , and CaMoO_4 crystals at 1.2 K (van der Poel et al., 1984a, 1984b; Barendswaads and van der Waals, 1986; Barendswaads et al., 1989; Van Tol and van der Waals, 1992; Van Tol et al., 1992).

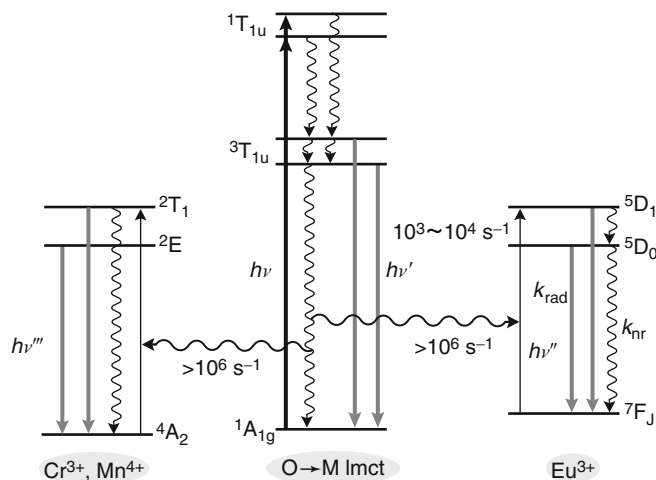


FIGURE 21 Scheme of the energy transfer processes from the O \rightarrow M Imct triplet states in both Anderson-typed polyoxometalates and polyoxometalloeuropates. Figure is redrawn after Yamase (1998).

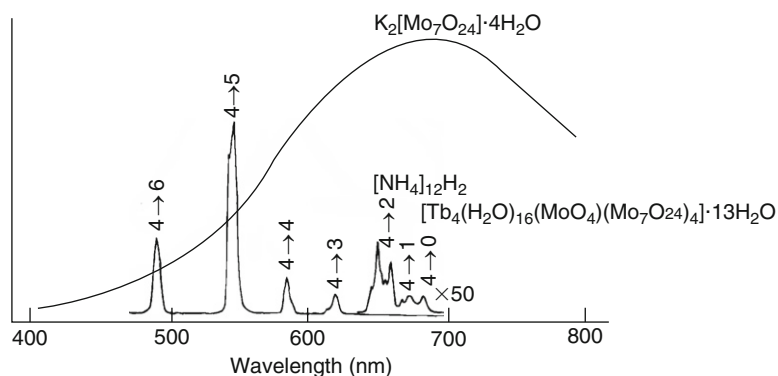


FIGURE 22 Luminescence spectra of $[\text{NH}_4]_{12}\text{H}_2[\text{Tb}_4(\text{H}_2\text{O})_{16}(\text{MoO}_4)(\text{Mo}_7\text{O}_{24})_4]\cdot 13\text{H}_2\text{O}$ and $\text{K}_2[\text{Mo}_7\text{O}_{24}]\cdot 4\text{H}_2\text{O}$ under O \rightarrow Mo Imct-band excitation at 77 and at 4.2 K, respectively. Figure is redrawn after Yamase et al. (1997).

Since the Eu (${}^5\text{D}_0 \rightarrow {}^7\text{F}_j$) transition energy is close to the energy of the ${}^2\text{T}_1$, ${}^2\text{E} \rightarrow {}^4\text{A}_2$ transitions of Cr^{3+} and Mn^{4+} , the emission properties for Anderson-typed complexes strongly support the involvement of the O \rightarrow M Imct triplet states in the energy transfer processes of the corresponding polyoxometalloeuropate lattices. Figure 21 shows the energy transfer processes for the O \rightarrow M Imct excitation in a variety of lattices.

For polyoxometalloboroates, the Tb^{3+} emission observed under O \rightarrow W Imct-band excitation is much stronger than under O \rightarrow Mo Imct-band excitation. This is also consistent with energy transfer occurring from the O \rightarrow M Imct

triplet states. The structures of the anions in $K_3Na_4H_2[Tb(W_5O_{18})_2] \cdot 20H_2O$ (Ozeki et al., 1992) and $[NH_4]_{12}H_2[Tb_4(H_2O)_{16}(MoO_4)(Mo_7O_{24})_4] \cdot 13H_2O$ are the same as for the corresponding Eu^{3+} complexes **1** and **4**, respectively. The photoluminescence spectra of the two terbate compounds are almost the same. A typical luminescence spectrum at 77 K under $O \rightarrow M$ lmct-band excitation for $[NH_4]_{12}H_2[Tb_4(H_2O)_{16}(MoO_4)(Mo_7O_{24})_4] \cdot 13H_2O$ is shown in Figure 22, where the emission spectrum of the $O \rightarrow Mo$ lmct triplet states of $K_6[Mo_7O_{24}] \cdot 4H_2O$ at 4.2 K is added for comparison with the $O \rightarrow W$ lmct triplet emission (Table 6 and Figures 18 and 19). The quantum yield of the $Tb^{3+} {}^5D_4 \rightarrow {}^7F_J$ ($J = 0-6$) emission under the $O \rightarrow M$ lmct-band excitation (at 300 nm) amounts to 0.05 at 77 K and 9×10^{-3} at 300 K for $K_3Na_4H_2[Tb(W_5O_{18})_2] \cdot 20H_2O$ (Ozeki and Yamase, 1993), whereas it is equal to 7×10^{-3} at 77 K and negligibly low at 300 K for $[NH_4]_{12}H_2[Tb_4(H_2O)_{16}(MoO_4)(Mo_7O_{24})_4] \cdot 13H_2O$ (Yamase et al., 1997). As shown in Figure 22, the spectral overlap between the broad orange emission (around 700 nm) of the $O \rightarrow Mo$ lmct triplet states and the f-f absorption (${}^5D_4 \leftarrow {}^7F_6$ transition at 486 nm) of Tb^{3+} is smaller than for the broad green emission ($\lambda_{max} \approx 520$ nm) of the $O \rightarrow W$ lmct triplet states for $K_9H_5[(GeTi_3W_9O_{37})_2O_3] \cdot 16H_2O$ in Figure 18 and $K_{5.5}H_{1.5}[SbW_6O_{24}] \cdot 6H_2O$ in Figure 19). Thus, energy transfer from the triplet states explains why $O \rightarrow W$ lmct photoexcitation provides a much higher yield of the Tb^{3+} emission compared with the $O \rightarrow Mo$ lmct photoexcitation (Yamase et al., 1997). It should be noted that the $O \rightarrow M$ lmct triplet states are reaction precursors for electron transfer to the $O \rightarrow M$ lmct excited states in a variety of polyoxometalates, from alkylammonium cations, alcohols, and carboxylic acids as electron donors, as established by the CIDEP technique for the photoredox reaction of $[V_4O_{12}]^{4-}$, $[Mo_7O_{24}]^{6-}$, and $[W_{10}O_{32}]^{4-}$ in solutions (Yamase and Ohtaka, 1994), as discussed below. Therefore, the $O \rightarrow M$ lmct triplet states participate in both electron transfer and energy transfer in the polyoxometalate lattices.

3. ENERGY TRANSFER AMONG Ln^{3+} SITES (FROM Tb^{3+} TO Eu^{3+})

3.1 Luminescence spectra

As discussed above, sensitized luminescence studies of polyoxometalloeuropates have provided the details of both the transfer and the relaxation of the excitation energy in the host lattices of Eu^{3+} -doped metal-oxide phosphors such as $Gd_2(WO_4)_3:Eu$, $Y_2WO_6:Eu$, $YNbO_4:Eu$, and $CaMoO_4:Eu$ (Blasse, 1966; Powell and Blasse, 1980). It should be remarked that the Eu -multinuclear polyoxometalloeuropates such as **2-4** exhibit a single-exponential decay of the 5D_0 emission with moderate values of the quantum yield, implying that the energy migration among Eu^{3+} sites due to exchange interaction is negligible (Yamase and Sugeta, 1993; Yamase et al., 1997; Yamase, 1998). Of particular interest is the investigation of the energy transport phenomena among lanthanide centres in the oxide lattices. This could be done by using mixed Ln^{3+} (Tb^{3+}/Eu^{3+})-containing polyoxometalate complexes based on the structures of **2-4**, $K_{15}H_3[Tb_{3-x}Eu_x(H_2O)_3(SbW_9O_{33})]$

(W₅O₁₈)₃·25.5H₂O, Na₇H₁₉{[Tb_{6-x}Eu_xO₂(OH)₆(H₂O)₆Al₂(Nb₆O₁₉)₅]·47H₂O, and [NH₄]₁₂H₂[Tb_{4-x}Eu_x(MoO₄)(H₂O)₁₆(Mo₇O₂₄)₄]·13H₂O (where $x = 0.9-1.7$), since the Tb/Eu-mixed complexes provide a favourable system for investigating the Tb³⁺ → Eu³⁺ energy transfer in the oxide lattices, where the emission lines of donor (Tb³⁺) and acceptor (Eu³⁺) are well separated and can be measured without much interference from each other. For these complexes, the ⁵D₀ state of Eu³⁺ builds up following excitation to Tb³⁺ (⁵D₄) with an accompanying emission of both the Tb³⁺ (⁵D₄) and Eu³⁺ (⁵D₀) ions, which provides strong evidence for the energy transfer from Tb³⁺ to Eu³⁺. A variety of the multiple Ln³⁺-containing polyoxometalates (Ln = Eu, Er, and Lu) with the same structural anions showed no significant change in the structure by the replacement of Eu³⁺ with other Ln³⁺, since the comparison of the crystallographic structure among three {[Ln₃O(OH)₃(H₂O)₃]₂Al₂(Nb₆O₁₉)₅}¹⁶⁻ (Ln=Eu, Er, and Lu) anions exhibited only a small change (within ~0.1 Å) in Ln···Ln distances due to the lanthanide contraction (Naruke and Yamase, 1996, 1997, 1998).

The sensitized emission of Tb³⁺ for three polyoxometalates as pure Tb complexes, K₁₅H₃[Tb₃(H₂O)₃(SbW₉O₃₃)(W₅O₁₈)₃]·25.5H₂O, Na₇H₁₉{[Tb₆O₂(OH)₆(H₂O)₆Al₂(Nb₆O₁₉)₅]·47H₂O, and [NH₄]₁₂H₂[Tb₄(MoO₄)(H₂O)₁₆(Mo₇O₂₄)₄]·13H₂O was investigated first (Yamase and Naruke, 1999). The luminescence spectra of these pure Tb complexes under 355-nm light irradiation consist of ⁵D₄ → ⁷F_{*J*} transition around 488, 545, 584, 624, 650, 668, and 682 nm for *J* = 6, 5, 4, 3, 2, 1, and 0 respectively, and the excitation spectra for the strongest ⁵D₄ → ⁷F₅ lines of the Tb³⁺ emission consist of ⁵D₄ ← ⁷F₆ lines (around 488 nm), composite ⁵D_{3,2} and ⁵L₁₀ ← ⁷F₆ lines (in the range 320–380 nm), and O → M (M = W, Nb, or Mo) lmct bands (at <330 nm). Emission and excitation spectra at 4.2 and 300 K for Na₇H₁₉{[Tb₆O₂(OH)₆(H₂O)₆Al₂(Nb₆O₁₉)₅]·47H₂O are exemplified in Figure 23. The relative intensity ratios of the f–f transitions for these three complexes hardly depend on temperature. In the excitation spectra of the pure Eu complexes, the ⁵D_{0,1,2,3} ← ⁷F₁ lines due to the thermal population of the ⁷F₁ state are more intense at temperatures $T \geq 77$ K with an accompanying reduction in the intensity of the ⁵D_{0,1,2,3} ← ⁷F₀ lines (Yamase et al., 1990, 1997). In contrast to the pure Eu complexes, none of excitation spectra of the pure Tb complexes exhibits hot lines (⁵D_{3,2} and ⁵L₁₀ ← ⁷F₅), since the large energy gap (about 2000 cm⁻¹) between the ⁷F₆ and ⁷F₅ states for Tb³⁺ compared with the energy difference (about 300–400 cm⁻¹) between the Eu(⁷F₀) and Eu(⁷F₁) states makes thermal population (at $T < 300$ K) of the ⁷F₅ state quite small (Figures 11 and 23).

We turn to the emission properties of K₁₅H₃[Tb_{1.4}Eu_{1.6}(H₂O)₃(SbW₉O₃₃)(W₅O₁₈)₃]·25.5H₂O (**8**), Na₇H₁₉{[Tb_{4.3}Eu_{1.7}O₂(OH)₆(H₂O)₆Al₂(Nb₆O₁₉)₅]·47H₂O (**9**), and [NH₄]₁₂H₂[Tb_{3.1}Eu_{0.9}(MoO₄)(H₂O)₁₆(Mo₇O₂₄)₄]·13H₂O (**10**) as the Tb/Eu-mixed polyoxometallolanthanoates. Compound **8** is regarded as a disordered mixture of Tb/Eu = 1/2 and 2/1, **9** as the one of Tb/Eu = 4/2 and 5/1, and **10** as the one of Tb/Eu = 3/1 and 4/0. Thereby, it is reasonable to assume that the energy transfer from Tb³⁺ to Eu³⁺ for **8–10** occurs exclusively at the shortest average Tb···Eu distance which is close to the shortest average Eu···Eu distance (5.05 Å for **8**, 3.76 Å for **9**, and 6.17 Å for **10**) for the corresponding pure Eu

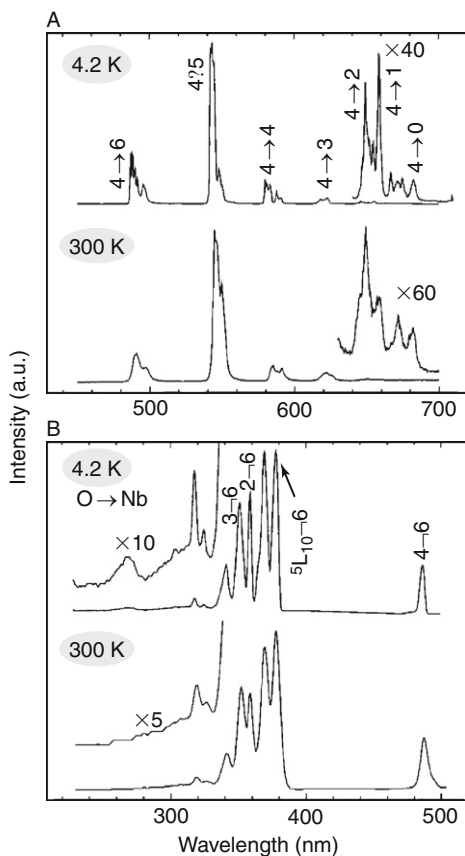


FIGURE 23 Luminescence (A) and excitation (B) spectra of $\text{Na}_7\text{H}_{19}[(\text{Tb}_6\text{O}_2(\text{OH})_6(\text{H}_2\text{O})_6)\text{Al}_2(\text{Nb}_6\text{O}_{19})_5] \cdot 47\text{H}_2\text{O}$ at 4.2 and 300 K. $4 \rightarrow J$ ($J=0-6$) and J ($J=2-4$) $\leftarrow 6$ transitions indicate ${}^5\text{D}_4 \rightarrow {}^7\text{F}_J$ and ${}^5\text{D}_J \leftarrow {}^7\text{F}_6$ for luminescence and excitation spectra, respectively. Figure is redrawn after Yamase and Naruke (1999).

complex (Figures 6–8), although it is difficult to distinguish between Tb and Eu by X-ray crystallography. Upon Tb^{3+} excitation (${}^5\text{D}_4 \leftarrow {}^7\text{F}_6$ transition) at 488 nm, the Tb/Eu-mixed complexes 8–10 exhibit transitions from both Tb^{3+} (${}^5\text{D}_4 \rightarrow {}^7\text{F}_J$, $J=5-0$) and Eu^{3+} (${}^5\text{D}_0 \rightarrow {}^7\text{F}_J$, $J=0-4$) in the spectral range 540–720 nm. ${}^5\text{D}_1 \rightarrow {}^7\text{F}_J$ lines of Eu^{3+} were observed under the 488-nm light exposure. Figure 24 exemplifies the excitation spectra of 8 at 4.2 and 300 K for the ${}^5\text{D}_4 \rightarrow {}^7\text{F}_5$ (A) and ${}^5\text{D}_0 \rightarrow {}^7\text{F}_2$ (B) emission. The excitation spectrum for the Eu^{3+} emission displays the contributions of both the $\text{O} \rightarrow \text{M}$ ($\text{M} = \text{W}, \text{Nb}, \text{or Mo}$) lmct states and the $f-f$ transitions of Tb^{3+} , in addition to direct $f-f$ transitions of Eu^{3+} (Figure 24B), whereas the excitation spectrum for the Tb^{3+} emission shows little contribution of the Eu^{3+} $f-f$ transitions (Figure 24A). This proves that the energy transfer occurs from Tb^{3+} to Eu^{3+} and not from Eu^{3+} to Tb^{3+} in the polyoxometallolanthanoate lattices. The 300-K excitation spectrum of the ${}^5\text{D}_0 \rightarrow {}^7\text{F}_2$ emission shows very weak

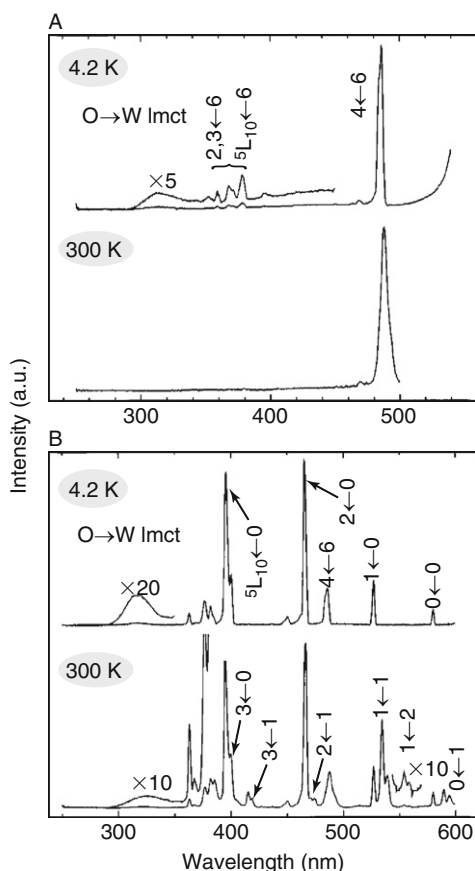


FIGURE 24 Excitation spectra of $\text{K}_{15}\text{H}_3[\text{Tb}_{1.4}\text{Eu}_{1.6}(\text{H}_2\text{O})_3(\text{SbW}_9\text{O}_{33})(\text{W}_5\text{O}_{18})_3] \cdot 25.5\text{H}_2\text{O}$ (**8**) at 4.2 and 300 K for the ${}^5\text{D}_4 \rightarrow {}^7\text{F}_5$ emission of Tb^{3+} (A) and the ${}^3\text{D}_0 \rightarrow {}^7\text{F}_2$ emission of Eu^{3+} (B). $J(=2-4) \leftarrow 6$ and $J(=0-3) \leftarrow J(=0-2)$ transitions indicate ${}^5\text{D}_J \leftarrow {}^7\text{F}_6$ of Tb^{3+} and ${}^5\text{D}_J \leftarrow {}^7\text{F}_J$ of Eu^{3+} , respectively. Figure is redrawn after Yamase and Naruke (1999).

${}^5\text{D}_1 \leftarrow {}^7\text{F}_2$ lines at 554 nm, the intensity of which is very small at $T \leq 200$ K, in addition to the ${}^5\text{D}_{0,1,2,3} \leftarrow {}^7\text{F}_1$ lines at 589.5 and 594.5, 534.0 and 539.0, 471.0 and 474.5, and 415.0 and 418.5 nm, respectively. The observation of the hot lines due to the population of the ${}^7\text{F}_2$ state is ascribed to the relatively small gap (about 1000 cm^{-1}) between the ${}^7\text{F}_2$ and ${}^7\text{F}_0$ states (Figure 11).

3.2 Luminescence decay dynamics

The decay patterns of the ${}^5\text{D}_4 \rightarrow {}^7\text{F}_J$ ($J = 5-0$) luminescence for $\text{K}_{15}\text{H}_3[\text{Tb}_3(\text{H}_2\text{O})_3(\text{SbW}_9\text{O}_{33})(\text{W}_5\text{O}_{18})_3] \cdot 25.5\text{H}_2\text{O}$ and $\text{Na}_7\text{H}_{19}[\text{Tb}_6\text{O}_2(\text{OH})_6(\text{H}_2\text{O})_6 \text{Al}_2(\text{Nb}_6\text{O}_{19})_5] \cdot 47\text{H}_2\text{O}$ are single exponentials at all temperatures, whereas the decay for $[\text{NH}_4]_{12}\text{H}_2[\text{Tb}_4(\text{MoO}_4)(\text{H}_2\text{O})_{16}(\text{Mo}_7\text{O}_{24})_4] \cdot 13\text{H}_2\text{O}$ is a single exponential at low temperatures ($T \leq 50$ K) but non-exponential at $T > 50$ K (Yamase and

Naruke, 1999; Yamase, 2001). The intrinsic lifetimes (τ_D) of the 5D_4 state for $K_{15}H_3[Tb_3(H_2O)_3(SbW_9O_{33})(W_5O_{18})_3] \cdot 25.5H_2O$, $Na_7H_{19}[[Tb_6O_2(OH)_6(H_2O)_6Al_2(Nb_6O_{19})_5] \cdot 47H_2O$, and $[NH_4]_{12}H_2[Tb_4(MoO_4)(H_2O)_{16}(Mo_7O_{24})_4] \cdot 13H_2O$ at $T < 50$ K are in the range 1.45–1.64, 0.63–0.73, and 0.46–0.50 ms, respectively. The lifetime for $K_{15}H_3[Tb_3(H_2O)_3(SbW_9O_{33})(W_5O_{18})_3] \cdot 25.5H_2O$ is slightly temperature dependent (e.g., $\tau_D = 1.59 \pm 0.05$, 1.42 ± 0.05 , and 1.30 ± 0.06 ms, at 4.2, 77, and 300 K, respectively), and the lifetime for $[NH_4]_{12}H_2[Tb_4(MoO_4)(H_2O)_{16}(Mo_7O_{24})_4] \cdot 13H_2O$ at $T > 50$ K strongly increases with non-exponentiality (Yamase and Naruke, 1999; Yamase, 2001). The decay behaviours for $K_{15}H_3[Tb_3(H_2O)_3(SbW_9O_{33})(W_5O_{18})_3] \cdot 25.5H_2O$ and $[NH_4]_{12}H_2[Tb_4(MoO_4)(H_2O)_{16}(Mo_7O_{24})_4] \cdot 13H_2O$ are associated with the non-radiative transition into the $Tb^{3+} \rightarrow W^{6+}$ (or Mo^{6+}) charge-transfer state, as demonstrated for the significant temperature dependence of the 5D_4 lifetime for $K_3Na_4H_2[Tb(W_5O_{18})_2] \cdot 20H_2O$ (with $\tau_D = 3.8, 2.7$, and 1.7 ms at 4.5, 77, and 300 K, respectively) in contrast to the almost temperature-independent lifetime for $Na_7H_{19}[[Tb_6O_2(OH)_6(H_2O)_6Al_2(Nb_6O_{19})_5] \cdot 47H_2O$ (Stuck and Fonger, 1976; Blasse et al., 1981; Ozeki and Yamase, 1993); τ_D values for $Na_7H_{19}[[Tb_6O_2(OH)_6(H_2O)_6Al_2(Nb_6O_{19})_5] \cdot 47H_2O$ and $[NH_4]_{12}H_2[Tb_4(MoO_4)(H_2O)_{16}(Mo_7O_{24})_4] \cdot 13H_2O$ are smaller than for $K_{15}H_3[Tb_3(H_2O)_3(SbW_9O_{33})(W_5O_{18})_3] \cdot 25.5H_2O$. The total number (n') of aqua and hydroxo ligands in the Tb^{3+} co-ordination sphere for $Na_7H_{19}[[Tb_6O_2(OH)_6(H_2O)_6Al_2(Nb_6O_{19})_5] \cdot 47H_2O$ ($n' = 3$) and $[NH_4]_{12}H_2[Tb_4(MoO_4)(H_2O)_{16}(Mo_7O_{24})_4] \cdot 13H_2O$ ($n' = 4$) is larger than for $K_{15}H_3[Tb_3(H_2O)_3(SbW_9O_{33})(W_5O_{18})_3] \cdot 25.5H_2O$ ($n' = 2$), as expected from the corresponding Eu^{3+} complexes (Table 4). Therefore, the variation of τ_D values for the Tb^{3+} complexes is explained by the radiationless deactivation of the 5D_4 state through weak coupling with the high-frequency OH oscillators of the aqua and hydroxo ligands, although the 5D_4 state of Tb^{3+} being approximately one OH-phonon energy (about 3000 cm^{-1}) higher than the 5D_0 state of Eu^{3+} is less effective for the deactivation by OH oscillators (Horrocks

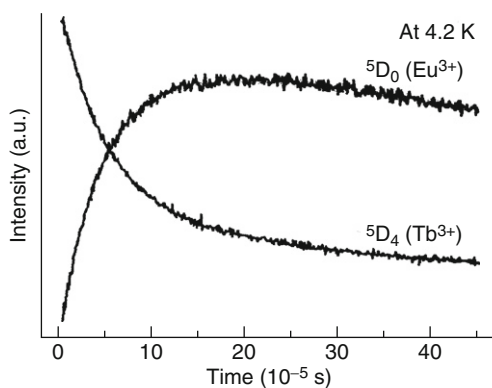


FIGURE 25 Decay curves of the $^5D_4 \rightarrow ^7F_5$ line of Tb^{3+} and the $^5D_0 \rightarrow ^7F_2$ line of Eu^{3+} for $K_{15}H_3[Tb_{1.4}Eu_{1.6}(H_2O)_3(SbW_9O_{33})(W_5O_{18})_3] \cdot 25.5H_2O$ (**8**) after pulsed excitation of the $^5D_4 \leftarrow ^7F_6$ transition of Tb^{3+} at 4.2 K. Figure is redrawn after Yamase (2001).

and Sudnick, 1979, 1981). While the three pure Tb complexes display single exponential decays of the Tb^{3+} emission (at $T < 50$ K for $[\text{NH}_4]_{12}\text{H}_2[\text{Tb}_4(\text{MoO}_4)(\text{H}_2\text{O})_{16}(\text{Mo}_7\text{O}_{24})_4] \cdot 13\text{H}_2\text{O}$), the Tb/Eu-mixed complexes **8–10** exhibit more complicated decay patterns. Figure 25 exemplifies the decay curves of the ${}^5\text{D}_4 \rightarrow {}^7\text{F}_5$ line of Tb^{3+} and the ${}^5\text{D}_0 \rightarrow {}^7\text{F}_2$ line of Eu^{3+} for **8** after pulsed excitation of the Tb (${}^5\text{D}_4 \leftarrow {}^7\text{F}_6$) transition (at 488 nm) at 4.2 K. The Eu^{3+} emission at 4.2 K shows a slow rise from zero to a maximum and then decays, which demonstrates the population of the $\text{Eu}({}^5\text{D}_0)$ state through energy transfer from the $\text{Tb}({}^5\text{D}_4)$ state. At longer duration after the excitation pulse, the decay of the $\text{Eu}({}^5\text{D}_0)$ state becomes a decreasing exponential function with an associated lifetime of 1.3 ± 0.1 ms, in agreement with the value (1.1 ± 0.2 ms) for the ${}^5\text{D}_0 \rightarrow {}^7\text{F}_1$ emission of Eu^{3+} in the pure complex **4** (Yamase et al., 1997). The decays of the ${}^5\text{D}_4$ state for the Tb/Eu-mixed complexes **8–10** are non-exponential at all temperatures and increase with an accompanying faster buildup of the $\text{Eu}({}^5\text{D}_0)$ population when the temperature increases. Figure 26 shows a semi-logarithmic representation of the luminescence decay for the ${}^5\text{D}_4 \rightarrow {}^7\text{F}_5$ emission of **8** under 488-nm excitation. The decay curves give the most convincing demonstration that the Tb–Eu transfer rate increases with increasing temperature.

3.3 Förster-Dexter-type energy transfer

The results of the luminescence decay for **8–10** were analysed in terms of the Förster-Dexter theory for multi-polar interaction between the donor (D) and the acceptor (A) (Yamase and Naruke, 1999). Since both the Tb–Tb transfer and the back transfer from Eu^{3+} to Tb^{3+} at 4.2 K are negligible, the intensity $[I(t)]$ of the Tb^{3+} emission after pulsed excitation can be described by the Inokuti–Hirayama

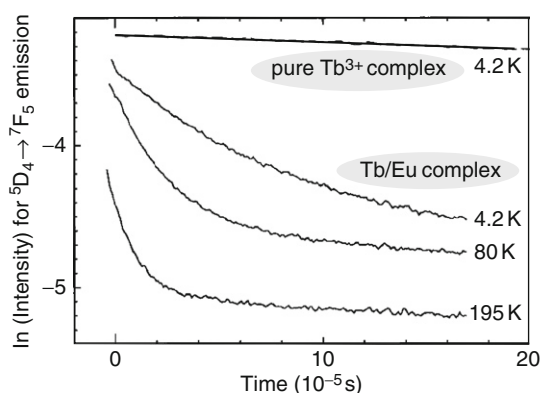


FIGURE 26 Semi-logarithmic decay curves of the ${}^5\text{D}_4 \rightarrow {}^7\text{F}_5$ line for $\text{K}_{15}\text{H}_3[\text{Tb}_3(\text{H}_2\text{O})_3(\text{SbW}_9\text{O}_{33})(\text{W}_5\text{O}_{18})_3] \cdot 25.5\text{H}_2\text{O}$ (as a pure Tb^{3+} complex) and $\text{K}_{15}\text{H}_3[\text{Tb}_{1.4}\text{Eu}_{1.6}(\text{H}_2\text{O})_3(\text{SbW}_9\text{O}_{33})(\text{W}_5\text{O}_{18})_3] \cdot 25.5\text{H}_2\text{O}$ (**8**) (as Tb/Eu-mixed complex) after 488-nm light pulse irradiation (corresponding to the ${}^5\text{D}_4 \leftarrow {}^7\text{F}_6$ transition of Tb^{3+}). Figure is redrawn after Yamase and Naruke (1999).

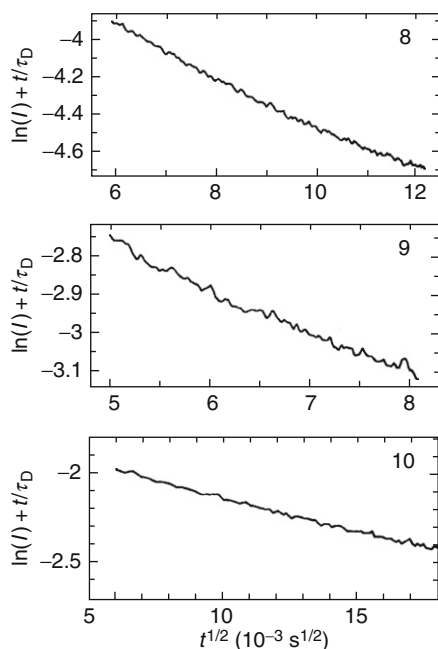


FIGURE 27 Plots of the ${}^5D_4 \rightarrow {}^7F_5$ emission decays of $K_{15}H_3[Tb_{1.4}Eu_{1.6}(H_2O)_3(SbW_9O_{33})(W_5O_{18})_3] \cdot 25.5H_2O$ (**8**), $Na_7H_{19}[(Tb_{4.3}Eu_{1.7}O_2(OH)_6(H_2O)_6Al_2(Nb_6O_{19})_5) \cdot 47H_2O$ (**9**), and $[NH_4]_{12}H_2[Tb_{3.1}Eu_{0.9}(MoO_4)(H_2O)_{16}(Mo_7O_{24})_4] \cdot 13H_2O$ (**10**) in the forms of $\ln I(t) + t/\tau_D$ against $t^{3/2}$ for $s = 6$, corresponding to an electric dipole–dipole interaction in Eq. (3). Figure is redrawn after Yamase (2001).

model (Förster, 1948; Dexter, 1953; Inokuti and Hirayama, 1965; Hegarty et al., 1981) as shown in Eq. (4),

$$\ln I(t) + \frac{t}{\tau_D} = -\left(\frac{4}{3}\right)\pi^{3/2}n_A r_{DA}^3 (k_{ET}t)^{3/s} \quad (4)$$

where n_A is the density of Eu^{3+} and k_{ET} is the nearest-neighbour transfer rate between a Tb–Eu pair for the Tb/Eu-mixed complexes with separation (in Å) of r_{DA} . Also, s is 6, 8, or 10 depending on the multi-polar nature of the Tb–Eu interaction, and τ_D ($=1.59 \pm 0.05$, 0.68 ± 0.05 , and 0.51 ± 0.05 ms for **8–10** at 4.2 K, respectively) is again the intrinsic lifetime (Yamase and Naruke, 1999; Yamase, 2001). Figure 27 shows plots of the ${}^5D_4 \rightarrow {}^7F_5$ emission decays of **8–10** in the forms of $\ln I(t) + t/\tau_D$ against $t^{3/2}$ for $s = 6$, corresponding to an electric dipole–dipole interaction. The approximate straight-line behaviour indicates that the above assumptions are correct and that the choice of $s = 6$ is valid. The effect of the lanthanide contraction on the inter-metallic distances in the isostructural complexes between pure Tb and Eu complexes is small, as implied by the small difference in mean Ln–O distances (2.42 and 2.43 Å) between $K_3Na_4H_2[TbW_{10}O_{36}] \cdot 20H_2O$ and $Na_9 [EuW_{10}O_{36}] \cdot 32H_2O$, respectively (Ozeki et al., 1992; Sugeta and Yamase, 1993; Ozeki and Yamase, 1994) and also by

the small change (within $\sim 0.1 \text{ \AA}$) in $\text{Ln}\cdots\text{Ln}$ distances among $\{[\text{Ln}_3\text{O}(\text{OH})_3(\text{H}_2\text{O})_3]_2\text{Al}_2(\text{Nb}_6\text{O}_{19})_5\}^{16-}$ ($\text{Ln} = \text{Eu}, \text{Er}, \text{and Lu}$) anions (Naruke and Yamase, 1996, 1997, 1998). Therefore, the r_{DA} value for the Tb/Eu-mixed complex is estimated to be close to the nearest averaged $\text{Eu}\cdots\text{Eu}$ distance for the pure Eu complex. Values for **8**, $n_{\text{A}} = 5.46 \times 10^{-4} \text{ ions \AA}^{-3}$ [$=1.6 \times 4/11680$, where 4 and 11680 are number (Z) of molecules in unit cell and cell volume (in \AA^3), respectively] (Yamase et al., 1990), $r_{\text{DA}} = 5.05 \text{ \AA}$, and the slope ($=110 \text{ s}^{-1/2}$) in Figure 27, provide $k_{\text{ET}} = (4.49 \pm 0.81) \times 10^4 \text{ s}^{-1}$. Thus, the donor–acceptor interaction parameter (α) is evaluated to be $(7.45 \pm 0.13) \times 10^8 \{=k_{\text{ET}} \cdot 5.05^6\} \text{ \AA}^6 \text{ s}^{-1}$, and also the critical radius (R_0) for the Tb–Eu energy transfer at which the probability of the energy transfer is the same as the one of the radiative decay of the donor ($=\text{Tb}^{3+}$) to be $10.3 \pm 0.2 \text{ \AA}$ [$=(\tau_{\text{D}}\alpha)^{1/6}$]. More distant neighbours as acceptors are positioned at the inter-molecular distance of 11.2 \AA in **8** (Yamase et al., 1990). Therefore, $R_0 = 10.3 \text{ \AA}$ for **8** indicates the predominance of intra-molecular energy transfer within a sphere with a radius of 10.3 \AA . In the case of **9**, the molecular structure of the pure Eu complex (Figure 7 and Table 2) shows five nearest neighbours as acceptors at average distances of 3.76 \AA (twice), 4.69 \AA (twice), and 6.00 \AA (once). For compound **10**, there are three nearest neighbours at average distances 6.16 \AA (twice) and 7.51 \AA (once). A similar treatment for the shortest average Tb \cdots Eu distance yields $k_{\text{ET}} = (4.68 \pm 0.90) \times 10^5 \text{ s}^{-1}$, $\alpha = (1.31 \pm 0.25) \times 10^9 \text{ \AA}^6 \text{ s}^{-1}$ ($=k_{\text{ET}} \cdot 3.76^6$), and $R_0 = 10.0 \pm 0.3 \text{ \AA}$ for **9** at 4.2 K, and $k_{\text{ET}} = (4.90 \pm 0.90) \times 10^3 \text{ s}^{-1}$, $\alpha = (2.70 \pm 0.51) \times 10^8 \text{ \AA}^6 \text{ s}^{-1}$ ($=k_{\text{ET}} \cdot 6.17^6$), and $R_0 = 7.2 \pm 0.5 \text{ \AA}$ for **10**. The R_0 values calculated for **9** and **10** indicate that the Tb-to-Eu energy transfer occurs almost within a central cavity of the molecule, if we consider the nearest neighbouring inter-molecular Tb \cdots Eu distances of 11.0 \AA (twice) for **9** (Ozeki et al., 1994) and 8.61 \AA for **10** (Naruke et al., 1991). The next nearest Tb \cdots Eu distances are 4.69 \AA in the central $[\text{Tb}_{4.3}\text{Eu}_{1.7}\text{O}_2(\text{OH})_6(\text{H}_2\text{O})_6]^{8+}$ core of **9** and 7.51 \AA in the central $[\text{Tb}_{3.1}\text{Eu}_{0.9}(\text{MoO}_4)(\text{H}_2\text{O})_{16}]^{10+}$ core of **10**. This allows us to estimate the rate of the electric dipole–dipole energy transfer to next nearest neighbours to be approximately $1/4$ [$=(3.76/4.69)^6$] and $3/10$ [$=(6.17/7.51)^6$] smaller than for the shortest average Tb \cdots Eu distances of 3.76 and 6.17 \AA for **9** and **10**, respectively. It is possible to fit the decay curves of the ${}^5\text{D}_4 \rightarrow {}^7\text{F}_5$ emission obtained at a variety of temperatures to Eq. (4) (with $s = 6$). Figure 28 shows plots of the calculated values of k_{ET} against temperature for **8–10**. As the temperature increases, these values increase and the effect is larger for **9**.

The basic requirement for a Förster–Dexter energy transfer is the spectral overlap between the donor emission spectrum and the acceptor absorption spectrum (Förster, 1948; Dexter, 1953). Figure 29 exemplifies the overlap between the emission spectrum of Tb^{3+} (left) and the excitation spectrum of Eu^{3+} (right) for **9**, data are estimated from spectra at 4.2 and 300 K. In Figure 29, the excitation lines due to the ${}^7\text{F}_1$ and ${}^7\text{F}_2$ states, which are involved in the energy transfer at high temperatures, are shaded. The widths at half height of the Tb^{3+} -emission lines are in the range of $40\text{--}100 \text{ cm}^{-1}$. At low temperatures $T < 100 \text{ K}$ for which the population of the ${}^7\text{F}_2$ state is negligible, the population of the ${}^7\text{F}_1$ manifold of Eu^{3+} is also low and the excitation transfer occurs mainly through the ${}^7\text{F}_0$ level. Therefore, it becomes evident that the condition for energy transfer is fulfilled

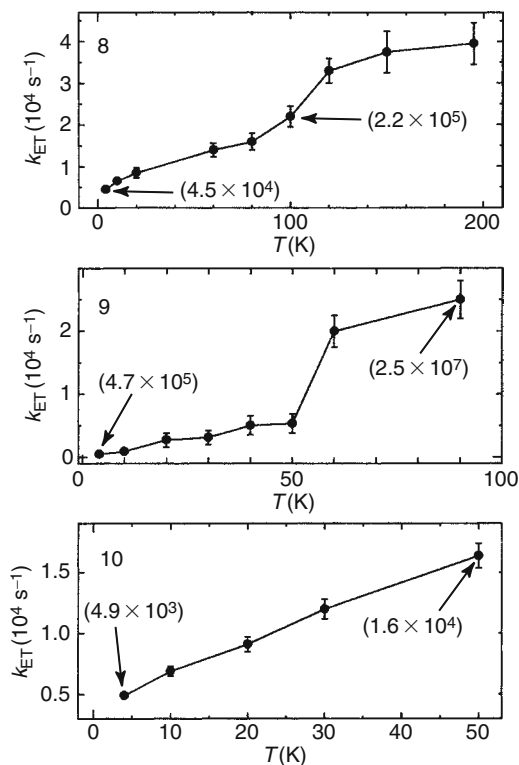


FIGURE 28 Plots of the calculated values of the nearest-neighbour transfer rate (k_{ET}) between a Tb–Eu pair for the Tb/Eu-mixed complexes against temperature for $\text{K}_{15}\text{H}_3[\text{Tb}_{1.4}\text{Eu}_{1.6}(\text{H}_2\text{O})_3(\text{SbW}_9\text{O}_{33})(\text{W}_5\text{O}_{18})_3] \cdot 25.5\text{H}_2\text{O}$ (**8**), $\text{Na}_7\text{H}_{19}[[\text{Tb}_{4.3}\text{Eu}_{1.7}\text{O}_2(\text{OH})_6(\text{H}_2\text{O})_6\text{Al}_2(\text{Nb}_6\text{O}_{19})_5] \cdot 47\text{H}_2\text{O}$ (**9**), and $[\text{NH}_4]_{12}\text{H}_2[\text{Tb}_{3.1}\text{Eu}_{0.9}(\text{MoO}_4)(\text{H}_2\text{O})_{16}(\text{Mo}_7\text{O}_{24})_4] \cdot 13\text{H}_2\text{O}$ (**10**). Figure is redrawn after Yamase (2001).

around 17150 cm^{-1} (583 nm), where the $^5\text{D}_4 \rightarrow ^7\text{F}_4$ line emission of Tb^{3+} around 17173 cm^{-1} overlaps with the $^5\text{D}_0 \leftarrow ^7\text{F}_0$ excitation of Eu^{3+} around 17241 cm^{-1} (see a light arrow in Figure 29, symbolizing the energy-transfer channel). A small energy mismatch (within 100 cm^{-1}) between the donor-emission and acceptor-excitation spectral lines implies the presence of the phonon-assisted energy transfer. At high temperatures, the transfer channels increase due to the thermal population of $^7\text{F}_1$ and $^7\text{F}_2$ states of Eu^{3+} , which results in an overlap between the $^5\text{D}_4 \rightarrow ^7\text{F}_5$ line emission and the $^5\text{D}_1 \leftarrow ^7\text{F}_1$ line excitation around 18600 cm^{-1} (and also the $^5\text{D}_1 \leftarrow ^7\text{F}_2$ line around 17900 cm^{-1} only at $T > 200\text{ K}$) with additional overlap of the $^5\text{D}_4 \rightarrow ^7\text{F}_4$ line emission with the $^5\text{D}_0 \leftarrow ^7\text{F}_1$ line excitation around 16960 cm^{-1} (see the heavy arrows as additional channels for energy transfer in Figure 29). This explains the large values of k_{ET} at high temperatures (Figure 28). An involvement of both the forbidden transition $^5\text{D}_0 \leftarrow ^7\text{F}_0$ and the magnetic dipole transition $^5\text{D}_0 \leftarrow ^7\text{F}_1$ in the Tb–Eu energy transfer process is associated with the low symmetry of Tb^{3+} and Eu^{3+} sites in **8–10**, where the LnO_8 and LnO_9

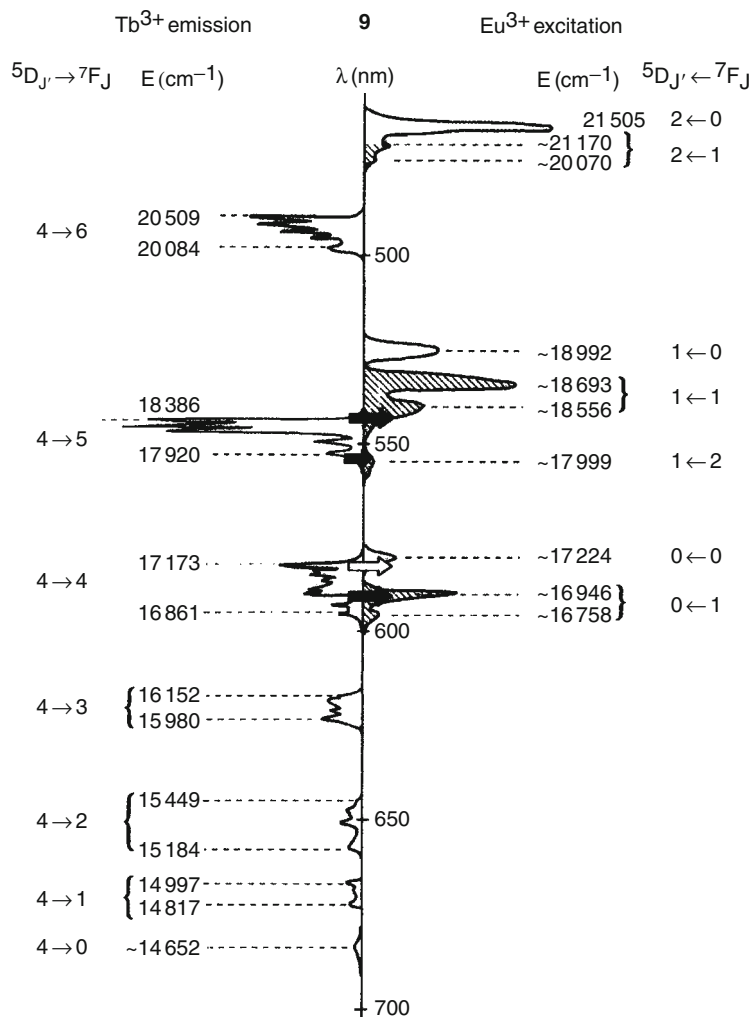


FIGURE 29 Overlap between the emission and excitation lines of Tb³⁺ (left) and Eu³⁺ (right). Photoexcitation of Na₇H₁₉[(Tb_{4.3}Eu_{1.7}O₂(OH)₆(H₂O)₆Al₂(Nb₆O₁₉)₅)·47H₂O (**9**) is done by the 488-nm light corresponding to the $5D_4 \leftarrow 7F_6$ transition. Channels for the Tb³⁺ → Eu³⁺ energy transfer are indicated by light and heavy arrows. Figure is redrawn after Yamase (2001).

polyhedra are of approximately C_{3v} , C_{1v} , and C_s symmetries, respectively (Figure 6–8) (Yamase et al., 1990; Naruke et al., 1991; Ozeki et al., 1994). Such low symmetries of the Eu³⁺ sites allow the $5D_0 \leftrightarrow 7F_J$ ($J = 0, 1$) transitions to have a non-vanishing electric-dipole transition probability with a resultant Förster-Dexter-type energy transfer arising from the electric dipole–dipole interaction. Thereby, the decay of Tb³⁺ emission in **8–10** is non-exponential, indicating that donor–donor transfer is much slower than donor–acceptor transfer, due to the disruption of the resonance energy transfer between Tb³⁺ ions probably through

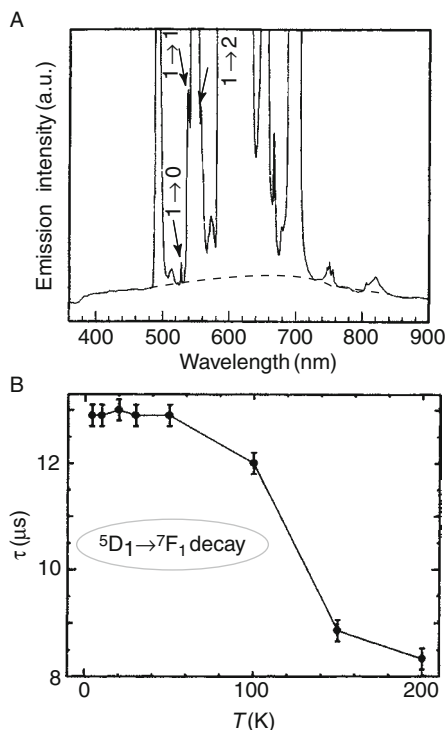


FIGURE 30 Luminescence spectrum (A) at 4.2 K and temperature dependence (B) of the exponential decays of the ${}^5D_1 \rightarrow {}^7F_1$ emission (around 536 nm) under 355-nm light excitation of the $O \rightarrow Mo$ lmct bands of $[NH_4]_{12}H_2[Tb_{3.1}Eu_{0.9}(MoO_4)(H_2O)_{16}(Mo_7O_{24})_4] \cdot 13H_2O$ (**10**). $1 \rightarrow J$ ($J=0-2$) and dotted line in (A) indicate ${}^5D_1 \rightarrow {}^7F_j$ emission of Eu^{3+} and the $O \rightarrow Mo$ lmct triplet emission, respectively. Figure is redrawn after Yamase (2001).

both aqua and hydroxo ligands (Blasse, 1990; Blasse and Brixner, 1990; Moret et al., 1990; Khawa et al., 1995). The lower crystal-field symmetry of **9** enhances the transition probabilities and broadens the excitation and emission lines. Since the widths of the Tb^{3+} -emission lines increase slightly increasing temperature below 100 K, the spectral overlap between the ${}^5D_4 \rightarrow {}^7F_4$ emission lines of Tb^{3+} and the ${}^5D_0 \leftarrow {}^7F_0$ excitation line of Eu^{3+} increases, with a resultant increase of the donor-acceptor transfer rate.

3.4 Decay of the $O \rightarrow M$ lmct triplet states and energy transfer

There is no ${}^5D_1 \rightarrow {}^7F_j$ emission under excitation of the $O \rightarrow M$ lmct states for **8**, **9**, and the corresponding pure Eu complexes (Yamase et al., 1990, 1997), probably due to non-radiative processes to 5D_0 via cross-relaxation [see Eq. (1)]. In contrast, ${}^5D_1 \rightarrow {}^7F_j$ emission is obtained for **10** and **4** (Naruke and Yamase, 1991). Figure 30A shows the ${}^5D_1 \rightarrow {}^7F_j$ transitions in addition to the ${}^5D_4 \rightarrow {}^7F_j$ and ${}^5D_0 \rightarrow {}^7F_j$ emission lines under 355-nm excitation ($O \rightarrow Mo$ lmct bands) of **10** at

4.2 K (Yamase, 2001). At this temperature, the ${}^5D_1 \rightarrow {}^7F_{0,1,2}$ lines around 526, 536, and 556 nm, respectively, have weak intensities. The decay of the ${}^5D_1 \rightarrow {}^7F_1$ emission is a single exponential function, and the lifetime (13 \rightarrow 8 μ s) of 5D_1 decreases with increasing temperature in the range 4.2 \rightarrow 200 K, as shown in Figure 30B where the exponential decay of the ${}^5D_1 \rightarrow {}^7F_1$ emission around 536 nm was measured as a function of the temperature. It is noteworthy that the 5D_1 lifetime for **10** is similar to that for the pure Eu complex **4** (Naruke and Yamase, 1991). Thus, the O \rightarrow M lmct excitation for the Tb/Eu-mixed complexes leads to the population of the 5D_4 state of Tb^{3+} and of both 5D_1 and 5D_0 states of Eu^{3+} , as a result of the Förster-Dexter resonance energy transfer through overlap between the broad O \rightarrow M lmct triplet emission band and the f-f absorption lines in the Tb/Eu-mixed polyoxometalate complexes. Figure 30A also shows the weak broad emission (peaking around 680 nm) of the O \rightarrow Mo lmct triplet states with approximately 1/280 of the intensity of the total f-f emissions of both Eu^{3+} and Tb^{3+} , the spectrum of which corresponds to the ${}^3T_{1u} \rightarrow {}^1A_{1g}$ transition of $[NH_4]_6[Mo_7O_{24}] \cdot 4H_2O$ (Table 6). Since the latter exhibits a bi-exponential decay lifetimes of 6 and 15 μ s at 4.2 K (Yamase and Sugeta, 1993), the approximately exponential decay (\sim 0.23 μ s) observed for the O \rightarrow Mo lmct triplet emission in **10** let us estimate the energy transfer rates from the O \rightarrow Mo lmct triplet states to $Tb^{3+}({}^5D_4)$ and $Eu^{3+}({}^5D_{0,1})$ states to be $4.3 \times 10^6 \text{ s}^{-1}$ [$=1/(0.23 \times 10^{-6}) - 1/(6 \times 10^{-6})$ or $1/(15 \times 10^{-6})$]. The calculated value is in good agreement with the value ($>10^6 \text{ s}^{-1}$) evaluated above for the energy transfer rate from the O \rightarrow M lmct triplet states to Eu^{3+} in the pure Eu complexes (Figure 21).

4. PHOTOCHEMICAL SELF-ASSEMBLY OF Ln^{3+} -CONTAINING MO-BLUE NANO-RINGS

The O \rightarrow M lmct triplet states are involved not only in energy transfer in polyoxometallolanthanoates but also in electron transfer for the photoredox reaction of the polyoxometalates with proton and electron donors (Yamase and Ohtaka, 1994; Yamase et al., 2003, 2005, 2006). This enabled us to propose a photochemical design of nano-ring Mo-blues by use of Ln^{3+} in a novel 'bottom-up' approach. Following the clarification of the primary steps of the photoredox reaction, nano-rings and nano-tubes based on Mo-blues have been successfully prepared by a photo-induced self-assembly reactions in solutions containing polyoxomolybdates, proton, electron donors, and Ln^{3+} .

4.1 Primary steps in the photoredox reaction with both proton and electron donors

CIDEP has been employed to investigate the primary steps of the solution photoredox reaction between polyoxomolybdates and both proton and electron donors (DH) such as alkylammonium cations, alcohols, and carboxylic acids (Yamase and Ohtaka, 1994; Yamase et al., 2003, 2005, 2006). Observation of emissive ESP signals of alkylamino radical cations, α -hydroxylalkyl radicals, and carboxylic acid

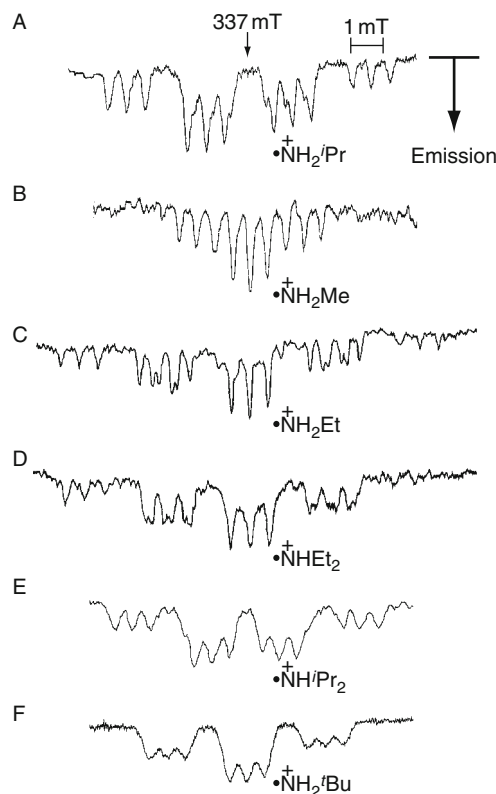


FIGURE 31 CIDEP spectra of amino radicals observed at 0.5 μs after 308-nm laser photolysis of $[\text{Mo}_7\text{O}_{24}]^{6-}$ /alkylammonium cations system in aqueous solutions at pH 5.4. The range of magnetic field for (B)–(F) is the same as for (A). $[\text{NH}_3^i\text{Pr}]^+$ (A), $[\text{NH}_3\text{Me}]^+$ (B), $[\text{NH}_3\text{Et}]^+$ (C), $[\text{NH}_2\text{Et}_2]^+$ (D), $[\text{NH}_2^i\text{Pr}_2]^+$ (E), and $[\text{NH}_2^t\text{Bu}]^+$ (F). Figure is redrawn after Yamase et al. (2003).

radicals for the photoredox reaction of polyoxomolybdates with alkylammonium cations, alcohols, and carboxylic acids, respectively reveals that the $\text{O} \rightarrow \text{Mo}$ lmct triplet states $^3(\text{O} \rightarrow \text{Mo} \text{lmct})$, produced by inter-system crossing from the excited $^1(\text{O} \rightarrow \text{Mo} \text{lmct})$ singlet states, are involved in the transfer of both proton and electron from alkylammonium cations, alcohols, and carboxylic acids to polyoxomolybdate anions. Such emissive ESP signals of the deprotonated one-electron oxidized donor radicals were also observed for polyoxo-tungstates and -vanadates (Yamase and Ohtaka, 1994). Figure 31 exemplifies the emissive CIDEP spectra of amino radicals observed 0.5 μs after laser photolysis of the $[\text{Mo}_7\text{O}_{24}]^{6-}$ /alkylammonium cation systems in aqueous solutions at pH 5.4. As in the case of the $[\text{Mo}_7\text{O}_{24}]^{6-}/[\text{NH}_3^i\text{Pr}]^+$ system, the emissive ESP (Figure 31a) generated at a sublevel ($^3T_+$) of $^3(\text{O} \rightarrow \text{Mo} \text{lmct})$ prior to the Boltzmann distribution is transferred to the daughter radical pair, $^3\{([\text{Mo}_7\text{O}_{24}\text{H}]^{6-}) \cdots \bullet^+\text{NH}_2\text{CHMe}_2\}_+$ (where subscript + indicates $m = 1$ as one of the magnetic triplet state sublevels characterized by $m = 1, 0, -1$) produced by the fast reaction with $[\text{PrNH}_3]^+$ to yield

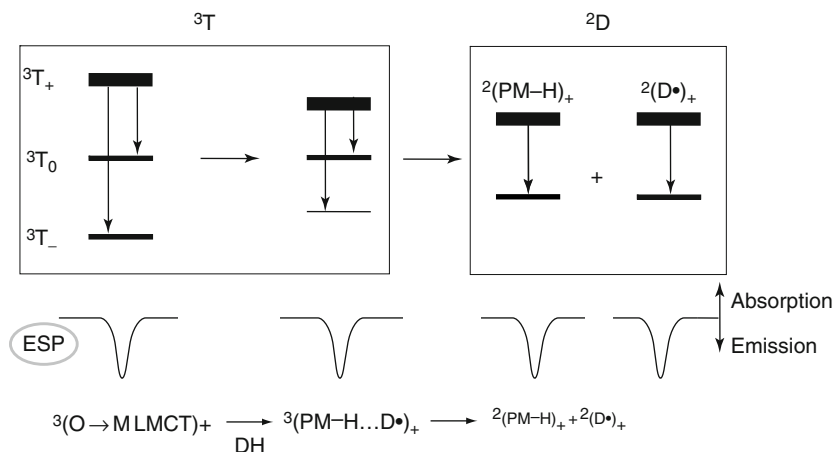
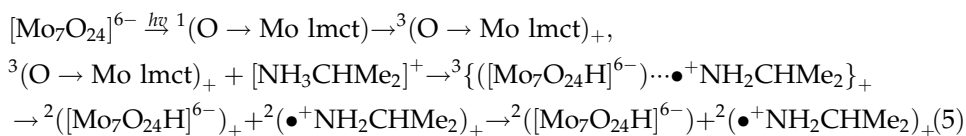


FIGURE 32 A typical change of ESP signals observed in the redox reaction between the $\text{O} \rightarrow \text{Mo}$ lmct triplet states ${}^3(\text{O} \rightarrow \text{Mo lmct})$ and proton and electron donors DH, which obey the spin angular momentum conservation. Widths of black lines indicate schematic extent of the Boltzmann distribution of radicals. Figure is redrawn after Yamase (2003).

two spin-polarized radicals ${}^2([\text{Mo}_7\text{O}_{24}\text{H}]^{6-})_+$ and ${}^2(\bullet^+\text{NH}_2\text{CHMe}_2)_+$ according to the conservation of spin angular momentum in the reaction steps. The spin-lattice relaxation of the former radical to the Boltzmann distribution is rapid enough to be terminated within sub-microseconds (Yamase, 2003). Figure 32 demonstrates a typical change in ESP signals observed in the redox reaction between ${}^3(\text{O} \rightarrow \text{Mo lmct})$ and DH which obey the spin angular momentum conservation. Equation (5) describes the primary reaction steps for generation and disappearance of the emissive ESP signal of $\bullet^+\text{NH}_2\text{CHMe}_2$ in the $[\text{Mo}_7\text{O}_{24}]^{6-}/[\text{iPrNH}_3]^+$ system to conserve overall spin angular momentum:



Similar emissive ESP signals around $g = 2.003$ are obtained for other $[\text{Mo}_7\text{O}_{24}]^{6-}$ /alkylammonium cation systems, such as MeNH_3^+ ($a_{\alpha\text{-H}(=\text{N-H})} = 0.50$ mT, $a_{\beta\text{-H}(=\text{C-H})} = 1.00$ mT, and $a_{\text{N}} = 0.50$ mT), EtNH_3^+ ($a_{\alpha\text{-H}(=\text{N-H})} = 2.25$ mT, $a_{\beta\text{-H}(=\text{C-H})} = 2.62$ mT, and $a_{\text{N}} = 0.54$ mT), Et_2NH_2^+ ($a_{\alpha\text{-H}(=\text{N-H})} = 0.13$ mT, $a_{\beta\text{-H}(=\text{C-H})} = 2.33$ mT, and $a_{\text{N}} = 0.55$ mT), ${}^i\text{Pr}_2\text{NH}_2^+$ ($a_{\alpha\text{-H}(=\text{N-H})} = 1.82$ mT, $a_{\beta\text{-H}(=\text{C-H})} = 2.29$ mT, and $a_{\text{N}} = 0.51$ mT), and ${}^t\text{BuNH}_3^+$ ($a_{\alpha\text{-H}(=\text{N-H})} = 2.15$ mT and $a_{\text{N}} = 0.50$ mT), as also shown in Figure 31B–F. Thus, all the alkylammonium cations acting as two-proton and -electron donors react with the ${}^3(\text{O} \rightarrow \text{Mo lmct})$ states of polyoxomolybdates to yield two-electron redox species under the photostationary state, as exemplified by the formation of NH_4^+ , acetone, propylene (as oxidation products of ${}^i\text{PrNH}_3^+$), and $[(\text{Mo}_7\text{O}_{23})_2]^{10-}$ ($\equiv[\text{Mo}_{14}]$) (as a reduction product of $[\text{Mo}_7\text{O}_{24}]^{6-}$)

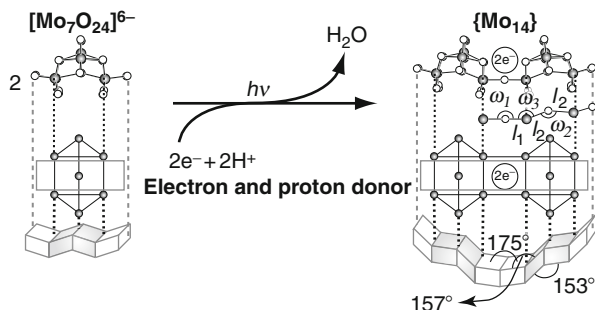


FIGURE 33 Two-electron photoreductive condensation of $[\text{Mo}_7\text{O}_{24}]^{6-}$ to *cis*-configured $[(\text{Mo}_7\text{O}_{23})_2]^{10-}$ ($\equiv\{\text{Mo}_{14}\}$) anion. Molecular curvature of $\{\text{Mo}_{14}\}$ is shown by Mo–O–Mo and O–Mo–O bond angles for the centre. Mo atoms are indicated by grey circles. Figure is redrawn after Yamase et al. (2005).

(Yamase et al., 1981; Yamase, 1991). Similar findings were reported for the primary steps in the $[\text{Mo}_{36}\text{O}_{112}(\text{H}_2\text{O})_{16}]^{8-}/[\text{PrNH}_3]^+$ system at pH 1.0.

4.2 Photo-induced self-assembly of Mo-blue nano-rings

As described above, photolysis of the $[\text{Mo}_7\text{O}_{24}]^{6-}$ /electron (and proton) donor system in aqueous solutions at pH 5–6 led to isolation of dimeric Mo-blue, $\{\text{Mo}_{14}\}$, which is a *cis*-configured two-electron reduced species with a molecular curvature of the –O–Mo–O–Mo–O– linkage (backbone framework) consisting in a central Mo–O–Mo bond angle $\omega_1 = 175^\circ$, a central Mo–O–Mo bond angle $\omega_2 = 153^\circ$ of the half-moiety, and an O–Mo–O bond angle $\omega_3 = 157^\circ$ for the linkage between these two centres (Yamase, 1991). Figure 33 shows a scheme for two-electron photoreductive condensation of $[\text{Mo}_7\text{O}_{24}]^{6-}$ to the *cis*-configured $\{\text{Mo}_{14}\}$ anion.

A variety of Mo-blues, the formation of which occurs upon the reduction of molybdates in strongly acidic aqueous solutions, were successfully characterized by Müller as condensed nano-rings of 28- and 32-electron species such as $[\text{Mo}_{154}\text{O}_{448}(\text{OH})_{14}(\text{H}_2\text{O})_{70}]^{14-}$ ($\{\text{Mo}_{154}\}$), $[\text{Mo}_{142}\text{O}_{432}(\text{OH})_{14}(\text{H}_2\text{O})_{58}]^{26-}$ ($\{\text{Mo}_{142}\}$), and $[\text{Mo}_{176}\text{O}_{512}(\text{OH})_{16}(\text{H}_2\text{O})_{80}]^{16-}$ ($\{\text{Mo}_{176}\}$). The $\{\text{Mo}_{154}\}$ and $\{\text{Mo}_{176}\}$ species appear as intact car-tire-shaped, rings with D_{7d} and D_{8d} symmetries, respectively, whereas $\{\text{Mo}_{142}\}$ is a deficient $\{\text{Mo}_{154}\}$ ring missing six $[\text{Mo}(\text{H}_2\text{O})\text{O}_2(\mu\text{-O})\text{Mo}(\text{H}_2\text{O})\text{O}_2]^{2+}$ units ($\equiv\{\text{Mo}_2\}$ -linker units) (Müller et al., 1999a, 1999b, 2001, 2004, Kögerler and Müller, 2002). Formation of similar $\{\text{Mo}_{154}\}$ and $\{\text{Mo}_{142}\}$ nano-rings has been also obtained by photolysis of aqueous solutions containing $[\text{Mo}_{36}\text{O}_{112}(\text{H}_2\text{O})_{16}]^{8-}$ ($\equiv\{\text{Mo}_{36}\}$) and alkylammonium cations as electron donors at pH = 1 and 2, respectively. They were characterized as $[\text{Mo}_{28}^{\text{V}}\text{Mo}_{126}^{\text{VI}}\text{O}_{462}(\text{H}_2\text{O})_{70}]^{28-}$ and $[\text{Mo}_{28}^{\text{V}}\text{Mo}_{114}^{\text{VI}}\text{O}_{404}(\text{OH})_{28}(\text{H}_2\text{O})_{58}]^{12-}$ (Yamase and Prokop, 2002; Yamase et al., 2003). Since $\{\text{Mo}_{36}\}$ incorporates two Mo_7O_{24} moieties in its centrosymmetric structure which occupy sevenfold pentagonal-bipyramidal MoO_7 sites (Krebs et al., 1991), it has been proposed that the degradative photoreductive

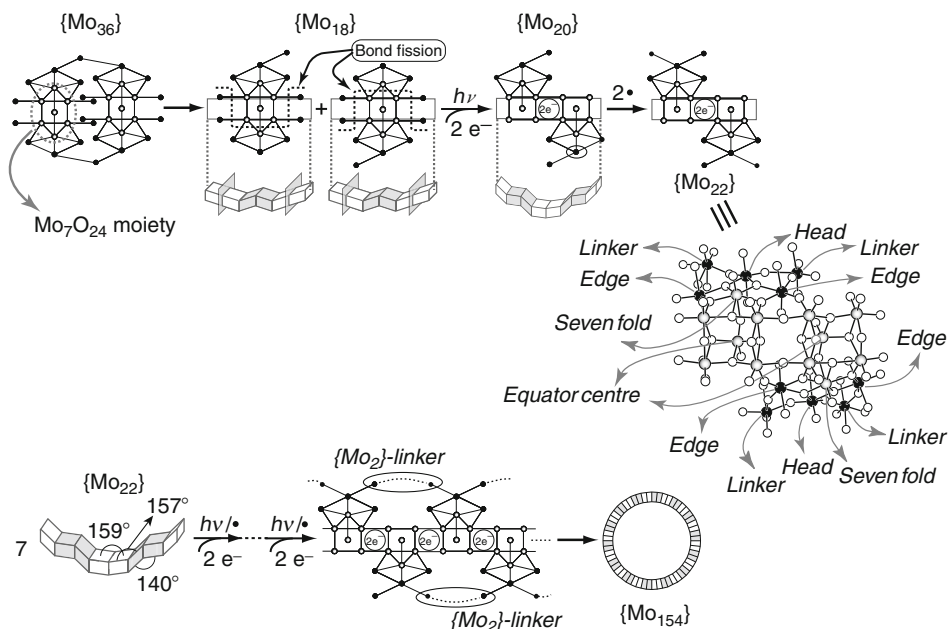


FIGURE 34 Proposed scheme of photo-induced self-assembly from {Mo₃₆} to {Mo₁₅₄} through the formation of {Mo₂₂} building blocks. *linker*, *head*, *sevenfold*, *edge*, *equator centre*, and {Mo₂}-*linker* are indicated for the identification of different types of Mo atoms. Mo atoms of {Mo₃₆} are indicated by grey (derived from Mo₇O₂₄ moieties) and black circles. Figure is redrawn after Yamase et al. (2005).

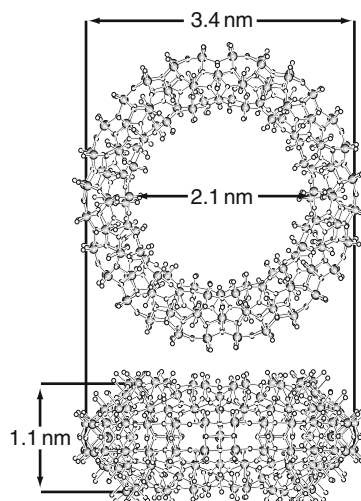


FIGURE 35 Structure of nano-sized {Mo₁₅₄} as an intact full ring with a car tire shape. Grey and white circles indicate Mo and O atoms, respectively.

condensation of the half molecules ($\{\text{Mo}_{18}\}$) proceeds with a mode similar to the $\{\text{Mo}_{14}\}$ formation. This results in the formation of a two-electron reduced building block, $[\text{Mo}_{22}\text{O}_{70}(\text{H}_2\text{O})_{10}]^{10-}$ ($\equiv\{\text{Mo}_{22}\}$) which undergoes successive two-electron-photoreductive condensations to form a cyclic heptamer $\{\text{Mo}_{154}\}$ (Yamase and Prokop, 2002; Yamase et al., 2003). The proposed scheme of photo-induced self-assembly to $\{\text{Mo}_{154}\}$ through the dehydrative condensations of $\{\text{Mo}_{22}\}$ is shown in Figure 34 where *linker*, *head*, *sevenfold*, *edge*, and $\{\text{Mo}_2\}$ -*linker* are indicated for identifying the different types of Mo atoms. Figure 35 exemplifies the structure of $\{\text{Mo}_{154}\}$ as an intact full ring. Each of the two inner rings (above and below the equator) consists in seven *head* MoO_6 octahedra (each of which is bonded to a *sevenfold* MoO_7 pentagonal bipyramid) and seven $\{\text{Mo}_2\}$ -*linker* units. The $\{\text{Mo}_{36}\}$ anion is a predominant species in aqueous solutions of isopolymolybdates at pH

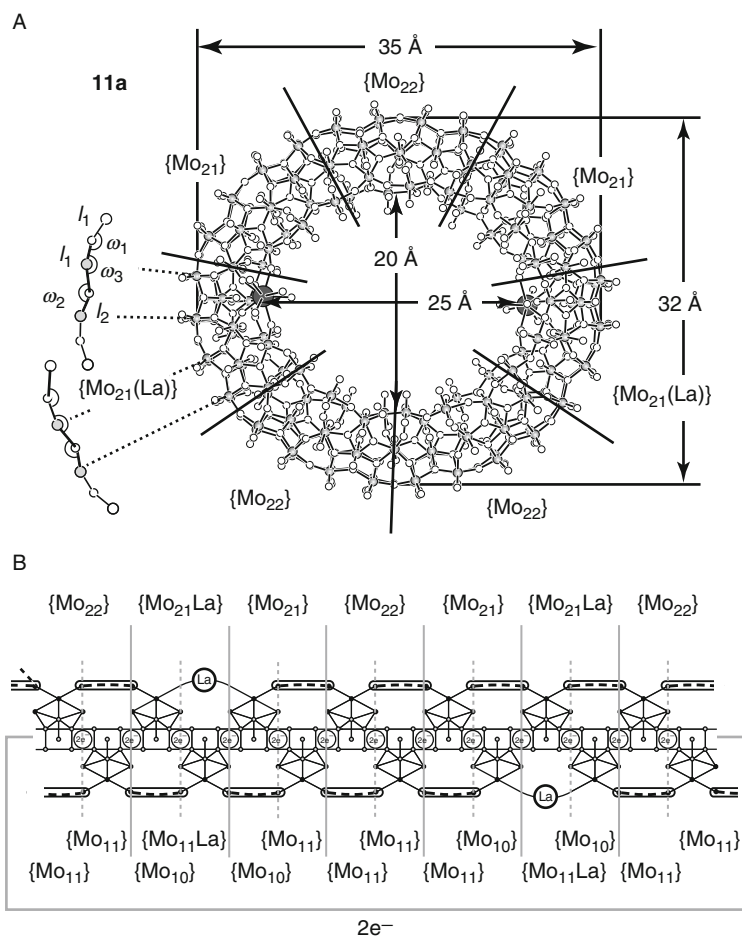


FIGURE 36 Nano-ring structure (A) and building-block sequence (B) of $[\text{Mo}_{28}^{\text{V}}\text{Mo}_{122}^{\text{VI}}\text{O}_{452}\text{H}_2(\text{H}_2\text{O})_{66}\{\text{La}(\text{H}_2\text{O})_5\}_2]^{24-}$ (**11a**). Figure is redrawn after Yamase et al. (2006).

≤ 2 , although a decrease of the solution acidity to pH 2 results in the defect structure of $\{\text{Mo}_{142}\}$. In addition, the photolysis of the $[\text{Mo}_7\text{O}_{24}]^{6-}$ /carboxylic acid systems at pH 3.4 where $\{\text{Mo}_{36}\}$ hardly exists but $\beta\text{-}[\text{Mo}_8\text{O}_{26}]^{4-}$ coexists (Aveston and Anacker, 1965; Griffith and Lesniak, 1969) led to the formation of a carboxylate-co-ordinated $\{\text{Mo}_{142}\}$ ring, $[\text{NH}_4]_{27}[\text{Me}_3\text{NH}]_3[\text{Mo}_{28}^{\text{V}}\text{Mo}_{114}^{\text{VI}}\text{O}_{429}\text{H}_{10}(\text{H}_2\text{O})_{49}(\text{CH}_3\text{CO}_2)_5(\text{C}_2\text{H}_5\text{CO}_2)] \cdot 150 \pm 10\text{H}_2\text{O}$ through the appearance of *sevenfold* pentagonal bipyramidal MoO_7 sites (Yamase et al., 2005).

4.3 Ln^{3+} -induced modification to ellipsoidal Mo-blue rings

Prolonged photolysis of aqueous solutions containing $[\text{Mo}_{36}\text{O}_{112}(\text{H}_2\text{O})_{16}]^{8-}$, $[\text{PrNH}_3]^+$, and LaCl_3 at pH 1.0 leads to the formation of $[\text{PrNH}_3]_{24}[\text{Mo}_{28}^{\text{V}}\text{Mo}_{122}^{\text{VI}}\text{O}_{452}\text{H}_2(\text{H}_2\text{O})_{66}\{\text{La}(\text{H}_2\text{O})_5\}_2] \cdot 156 \pm 5\text{H}_2\text{O}$ (**11**) crystals. Figure 36 shows the nano-ring structure (A) and the building-block sequence (B) of the anion (**11a**). The latter is ellipsoidal with an outer and inner ring diameters of approximately 35 and 25 Å, respectively, at its most elongated points, whereas the corresponding outer- and inner-ring diameters at its most compressed points are approximately 32 and 20 Å respectively. The $\text{La} \cdots \text{La}$ distance amounts to 25.22 Å and the ring sequence consists in $2\{\text{Mo}_{21}(\text{La})\}$, $2\{\text{Mo}_{21}\}$, and $3\{\text{Mo}_{22}\}$ building blocks. The formula $\{\text{Mo}_{21}(\text{La})\}$ means that a *linker* MoO_6 -octahedron in $\{\text{Mo}_{22}\}$ is replaced with an LaO_9 -distorted tricapped-trigonal prism and $\{\text{Mo}_{21}\}$ points to a *linker* MoO_6 -octahedron missing in $\{\text{Mo}_{22}\}$. In **11a**, two $\{\text{Mo}_2\}$ -linkers associated with the centrosymmetric relationship in intact $\{\text{Mo}_{154}\}$ ring are replaced by two distorted tricapped-trigonal-prismatic La^{3+} ions. As shown in Figure 37, each

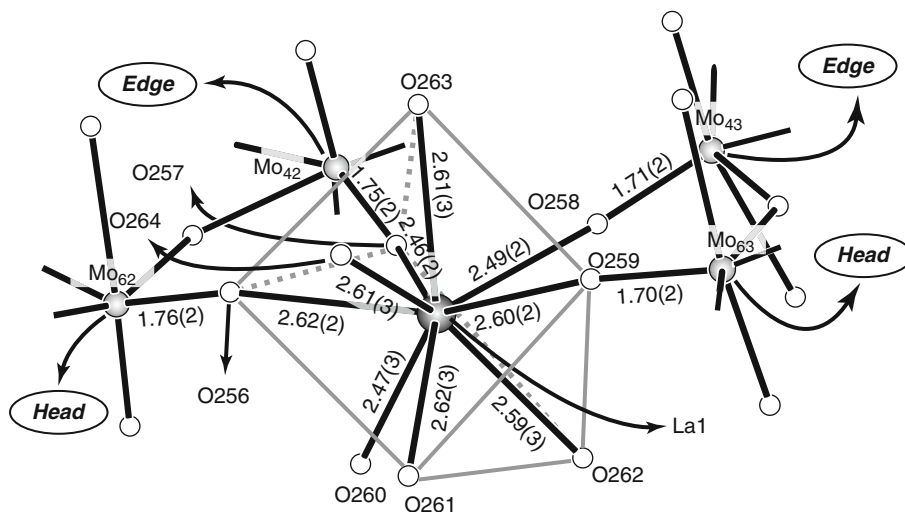


FIGURE 37 Structure of the LaO_9 site co-ordinated in the inner ring of **11a**. Grey line indicates the distorted tricapped-trigonal-prism co-ordination of the LaO_9 site. Figure is redrawn after Yamase et al. (2006).

Sub-block	ω_1	ω_2	ω_3	l_1	l_2	Hypothetical uniform ring diameter	
	/°			/Å		/Å	
{Mo ₁₁ (La)}	154–157 (156)	137–147 (142)	153–156 (155)	1.81–1.89 (1.87)	2.00–2.14 (2.07)	Decamer of {Mog(La)}	25
{Mo ₁₁ } and {Mo ₁₀ }	154–160 (158)	138–144 (141)	154–159 (158)	1.84–1.94 (1.90)	1.98–2.09 (2.05)	Tetradecamer of {Mo ₁₁ }	34

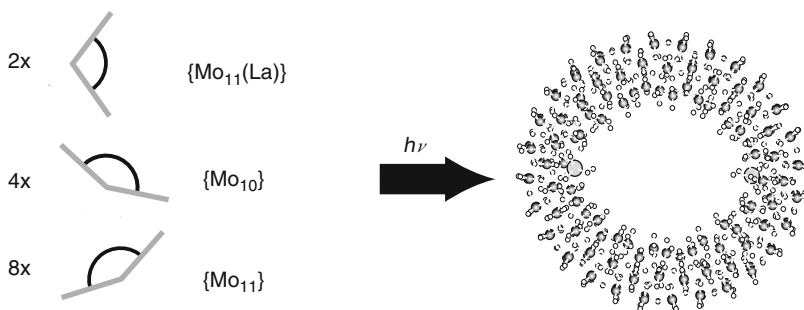
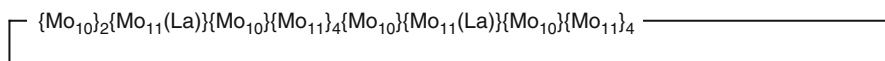


FIGURE 38 Molecular curvatures of three kinds of sub-building blocks ({Mo₁₁(La)}, {Mo₁₁}, and {Mo₁₀}) in **11a** ring, their sequence, and a scheme of cyclic dehydrative condensations to **11a**.

LaO₉ site in the inner ring consists in four two-co-ordinate oxygen atoms (1.70–1.76 Å of Mo–O bond lengths) from {Mo₁₅₀} anions and five aqua oxygen atoms with La–O bond distances of 2.46–2.62 Å. The ellipsoidal structure of **11a** results from a large molecular curvature of {Mo₂₁(La)} building blocks containing smaller and more electrophilic [La(H₂O)₅]³⁺ group compared with other building blocks such as {Mo₂₂} and {Mo₂₁}. By using Mo–O–Mo and O–Mo–O bond angles (ω_1 , ω_2 , and ω_3) and Mo–O bond distances (l_1 and l_2) for the incomplete double-cubane-type compartments above and below the equator (Figure 36), we can estimate the molecular curvature of these compartments for each building block (Yamase and Prokop, 2002). Figure 38 lists bond angles and bond lengths for the calculation of molecular curvatures of the sub-building blocks of {Mo₁₁(La)}, {Mo₁₁}, and {Mo₁₀}, as well as a schematic representation of **11a** as a 28-electron reduced species formed through successive 2-electron photoreductive condensations of 2-electron reduced building blocks, 2{Mo₂₁(La)}, 2{Mo₂₁}, and 3{Mo₂₂}, which could be divided into 2{Mo₁₁(La)}, 4{Mo₁₀}, and 8{Mo₁₁} sub-building-blocks. Values of ω_1 and ω_3 for the La³⁺-co-ordinating Mo₆O₂₃-related sub-building-block ({Mo₁₁(La)}) [ω_1 (154–157°, average 156°), ω_2 (137–147°, 142°), ω_3 (153–156°, 155°), l_1 (1.81–1.89 Å, 1.87 Å), and l_2 (2.00–2.14 Å, 2.07 Å)] are smaller than corresponding values [ω_1 (154–160°, 158°), ω_2 (138–144°, 141°), ω_3 (154–159°, 158°), l_1 (1.84–1.94 Å, 1.90 Å), and l_2 (1.98–2.09 Å, 2.05 Å)] for the {Mo₂}-linker

co-ordinating sub-building-blocks $\{\text{Mo}_{11}\}$ and $\{\text{Mo}_{10}\}$. If the building block consists of one kind of species, the above values of bond angles and bond lengths for each sub-building-block enable us to estimate the size of the ring made of uniform sub-building-blocks. Since the photoreductive cyclic condensation of the largely curved $\{\text{Mo}_{11}(\text{La})\}$ sub-building-blocks would proceed through missing MoO_6 -octahedral *linkers* for the $\text{Mo}-\text{O}-\text{La}$ linkage between La^{3+} and *head* Mo sites, thus, the photoreductive cyclic condensations of $\{\text{Mo}_{11}(\text{La})\}$ should be replaced by that of $\{\text{Mo}_9(\text{La})\}$ with almost the same molecular curvature as $\{\text{Mo}_{11}(\text{La})\}$ to yield a hypothetical 20-electron reduced $\{\text{Mo}_{90}(\text{La})_{10}\}$ ring with a diameter (D) of approximately 25 Å, where all the 10 $\{\text{Mo}_2\}$ -*linkers* in the inner rings (5 each above and below the outer ring) are substituted by La^{3+} cations, which correspond to the $\{\text{Mo}_{110}\}$ -pentameric ring of the $\{\text{Mo}_{22}\}$ building blocks. On the other hand, the photoreductive cyclic condensations of the other sub-building-blocks $\{\text{Mo}_{11}\}$ and $\{\text{Mo}_{10}\}$ would result in the formation of tetradecameric 28-electron reduced rings (for examples, $\{\text{Mo}_{154}\}$) with $D \approx 34$ Å, as discussed previously (Yamase and Prokop, 2002). As shown in Figure 38, thus, the 28-electron reduced ellipsoidal shape of **11a** is formed as a result of the photoreductive cyclic condensations between the two different molecular curved sub-building-blocks according to the sub-building-block sequence $\{\text{Mo}_{10}\}\{\text{Mo}_{11}(\text{La})\}\{\text{Mo}_{10}\}\{\text{Mo}_{11}\}_4$ $\{\text{Mo}_{10}\}\{\text{Mo}_{11}(\text{La})\}\{\text{Mo}_{10}\}\{\text{Mo}_{11}\}_4$ (corresponding to the ring sequence of building blocks $\{\text{Mo}_{21}(\text{La})\}\{\text{Mo}_{22}\}_2\{\text{Mo}_{21}(\text{La})\}\{\text{Mo}_{21}\}\{\text{Mo}_{22}\}\{\text{Mo}_{21}\}$). The same structural compounds were obtained for Y^{3+} -, Er^{3+} -, and Lu^{3+} -substituted species instead of La^{3+} .

4.4 Ln^{3+} -induced modification of Mo-blue rings into Japanese rice-ball shape

The photochemical manipulation of the ring shape with a combination of two kinds of sub-building-blocks having different molecular curvatures was also demonstrated for $[\text{Mo}_{120}\text{O}_{366}\text{H}_{14}(\text{H}_2\text{O})_{48}\{\text{La}(\text{H}_2\text{O})_5\}_6]^{4-}$. Prolonged photolysis of acidified solutions ($\text{pH} = 1.2$) containing $[\text{Mo}_7\text{O}_{24}]^{6-}$, $[p\text{-CH}_3\text{C}_6\text{H}_4\text{SO}_2]^-$ (*para*-toluenesulfinate), and LaCl_3 leads to formation of $[\text{NH}_3]_4[\text{Mo}_{24}^{\text{V}}\text{Mo}_{96}^{\text{VI}}\text{O}_{366}\text{H}_{14}(\text{H}_2\text{O})_{48}\{\text{La}(\text{H}_2\text{O})_5\}_6] \cdot 180 \pm 20\text{H}_2\text{O}$ (**12**) crystals (Yamase et al., 2006). Figure 39 shows the structure (A) and building-block sequence (B) of the anion (**12a**). The structure of **12a** is different from the one of **11a**, and resembles Japanese rice balls with an outer and inner ring diameter of approximately 30 and 17 Å, respectively. The same anion structure has been obtained by heating an aqueous solution containing Na_2MoO_4 , $\text{Pr}(\text{NO}_3)_3$, HCl , and hydrazinium dichloride at 70°C , yielding $[\text{Mo}_{120}\{\text{Pr}(\text{H}_2\text{O})_5\}_6\text{O}_{366}\text{H}_{12}(\text{H}_2\text{O})_{48}]^{6-}$ (Müller et al., 2001). Similarly, $[\{\text{Mo}_{128}\text{Eu}_4\text{O}_{388}\text{H}_{10}(\text{H}_2\text{O})_{81}\}_2]^{20-}$ has been isolated as an $\text{Eu}^{3+}/\text{H}^+$ mixed salt (Cronin et al., 2002). All of the six LaO_9 sites in **12a** are distorted tricapped-trigonal prisms, as in the case of **11a** (Figure 37). The $\text{La}\cdots\text{La}$ distances for the La_3 triangle in each of two inner rings are in the range 15.88–16.59 Å and the nearest $\text{La}\cdots\text{La}$ distances between the two inner rings are in the range 12.24–12.88 Å. The building-block sequence consists of six $\{\text{Mo}_{20}(\text{La})\}$ units. A 24-electron reduced species is produced through six successive 2-electron photo-reductions of 2-electron reduced building blocks $\{\text{Mo}_{20}(\text{La})\}$, which could be

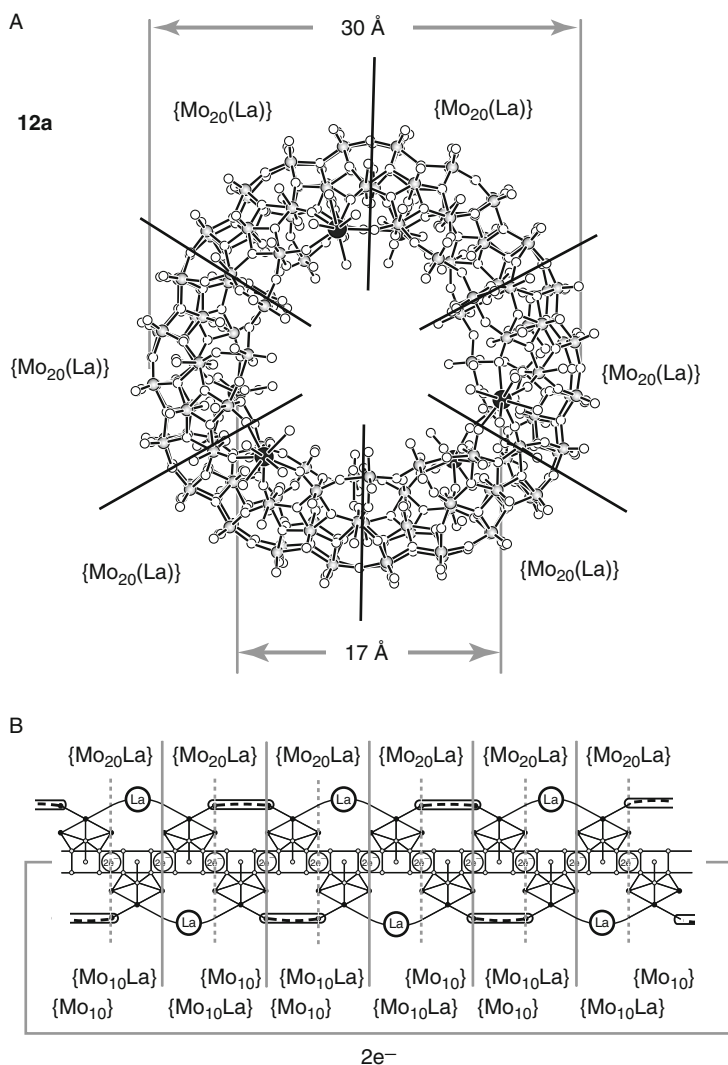


FIGURE 39 Nano-ring structure (A) and building-block sequence (B) of $[\text{Mo}_{24}^{\text{V}}\text{Mo}_{96}^{\text{VI}}\text{O}_{366}\text{H}_{14}(\text{H}_2\text{O})_{48}\{\text{La}(\text{H}_2\text{O})_5\}_6]^{4-}$ (**12a**). Figure is redrawn after Yamase et al. (2006).

divided into two sub-building-blocks, {Mo₁₀(La)} and {Mo₁₀} as the incomplete double-cubane-type Mo₆O₂₃-related moieties (Figure 39B). The molecular curvature of the {Mo₁₀(La)} sub-building-block is very similar to the one of the La³⁺-coordinate sub-building-block {Mo₁₁(La)} in **11a**, and is larger than that of {Mo₁₀}; on the other hand, the curvature of the latter is almost the similar to the one of {Mo₁₀} or {Mo₁₁} in **11a**. Figure 40 lists bond angles and bond lengths for the calculation of the molecular curvatures of the sub-building-blocks {Mo₁₀(La)} and {Mo₁₀}, and also shows a schematic representation of **12a** as a 24-electron reduced species

Sub-block	ω_1	ω_2	ω_3	l_1	l_2	Hypothetical uniform ring diameter	
	$^\circ$			\AA		\AA	
$\{\text{Mo}_{10}(\text{La})\}$	154–160 (157)	137–146 (142)	152–155 (154)	1.86–1.92 (1.90)	2.01–2.11 (2.06)	Decamer of $\{\text{Mo}_9(\text{La})\}$	24
$\{\text{Mo}_{10}\}$	157–161 (159)	137–140 (139)	154–158 (156)	1.83–1.95 (1.88)	1.98–2.10 (2.04)	Tetradecamer of $\{\text{Mo}_{11}\}$	32

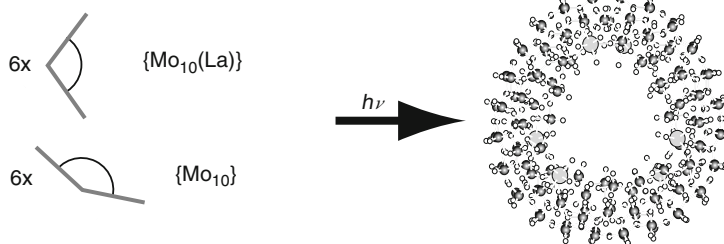
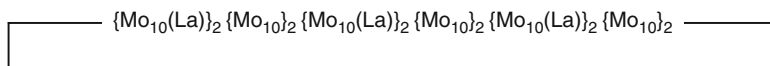


FIGURE 40 Molecular curvatures of two kinds of sub-building blocks ($\{\text{Mo}_{10}(\text{La})\}$ and $\{\text{Mo}_{10}\}$) in **12a** ring, their sequence, and a scheme of cyclic dehydrative condensations to **12a**.

formed through successive 2-electron photoreductive condensations of six 2-electron reduced building blocks, $\{\text{Mo}_{20}(\text{La})\}$, which could be divided into 6 $\{\text{Mo}_{10}(\text{La})\}$ and 6 $\{\text{Mo}_{10}\}$ sub-building-blocks. Values of ω_1 (154–160°, average 157°), ω_2 (137–146°, 142°), ω_3 (152–155°, 154°), l_1 (1.86–1.92 Å, 1.90 Å), and l_2 (2.01–2.11 Å, 2.06 Å) for $\{\text{Mo}_9(\text{La})\}$ predict the formation of the uniform ring as a cyclic decamer of the $\{\text{Mo}_{10}(\text{La})\}$ sub-building-blocks with $D \approx 24$ Å. Furthermore, the molecular curvature of $\{\text{Mo}_{10}\}$ ($\omega_1 = 157\text{--}161^\circ$, average 159° ; $\omega_2 = 137\text{--}140^\circ$, 139° ; $\omega_3 = 154\text{--}158^\circ$, 156° ; $l_1 = 1.83\text{--}1.95$ Å, 1.88 Å; and $l_2 = 1.98\text{--}2.10$ Å, 2.04 Å) let us predict the formation of the uniform ring (with $D \approx 32$ Å) consisting of 14 sub-building-blocks, corresponding to the cyclic heptamer (with $D \approx 34$ Å) of the $\{\text{Mo}_{22}\}$ building blocks. Thus, the 24-electron reduced Japanese rice-ball shape of **12a** results from 2-electron photoreductive cyclic hexameric condensations of 2-electron reduced $\{\text{Mo}_{20}(\text{La})\}$ building blocks which can be divided into $\{\text{Mo}_{10}(\text{La})\}$ and $\{\text{Mo}_{10}\}$ sub-building-blocks with different molecular curvatures (Figure 40), and having the sequence $\{\text{Mo}_{10}(\text{La})\}_2\{\text{Mo}_{10}\}_2\{\text{Mo}_{10}(\text{La})\}_2\{\text{Mo}_{10}\}_2\{\text{Mo}_{10}(\text{La})\}_2\{\text{Mo}_{10}\}_2$ (corresponding to the sequence of $\{\text{Mo}_{20}(\text{La})\}_6$ building blocks). The large number of incorporated La^{3+} ions in **12a** suggests that the anion may be produced under a high concentration ratio $[\text{La}^{3+}]/[\text{Mo}_{36}]$ compared to the case of **11a**. However, **11a** is formed when $[\text{La}^{3+}]/[\text{Mo}_{36}] = 2\text{--}7$, which is almost the same ratio range for the formation of **12a**, implying that the electron

(and proton) donor is also a controlling factor for both the ring shape and the ring size. In addition to the fact that **11** and **12** are formed at almost the same pH (pH 1), the co-ordination of La^{3+} to the inner rings in **11a** and **12a** is likely to occur through the $\text{La}^{3+} \subset \{\text{Mo}_{11}\}$ (or $\text{La}^{3+} \subset \{\text{Mo}_{10}\}$) precursor involved in the photochemical self-assembly rather than the $\text{La}^{3+} \subset \{\text{Mo}_{154}\}$ precursor after the formation of the $\{\text{Mo}_{154}\}$ full ring. The same structural compounds were obtained for Ce^{3+} -, Nd^{3+} -, and Sm^{3+} -substituted species instead of La^{3+} .

4.5 Ln^{3+} -induced modification of Mo-blue rings into tube and chain structures

Prolonged photolysis of aqueous solutions containing $[\text{Mo}_{36}\text{O}_{112}(\text{H}_2\text{O})_{16}]^{8-}$ (59 μmol), $[\text{PrNH}_3]^+$ (8.0 mmol), and LaCl_3 (22 μmol) in 76 ml H_2O at pH 1.0 leads to formation of $[\text{PrNH}_3]_8[\text{Mo}_{28}^{\text{V}}\text{Mo}_{126}^{\text{VI}}\text{O}_{458}\text{H}_{12}(\text{H}_2\text{O})_{66}] \cdot 127\text{H}_2\text{O}$ (**13**), the anion (**13a**) of which exhibits a nano-tube structure of $\{\text{Mo}_{154}\}$ rings. In **13a**, each inner ring contains a bis(μ -oxo)-linking $[\text{MoO}_2(\mu\text{-O})(\mu\text{-H}_2\text{O})\text{MoO}_2]^{2+}$ unit replacing one of seven $[\text{Mo}(\text{H}_2\text{O})\text{O}_2(\mu\text{-O})\text{Mo}(\text{H}_2\text{O})\text{O}_2]^{2+}$ $\{\text{Mo}_2\}$ -linker units. The neighbouring $\{\text{Mo}_{154}\}$ rings are connected by 6 Mo–O–Mo bridges between inner rings

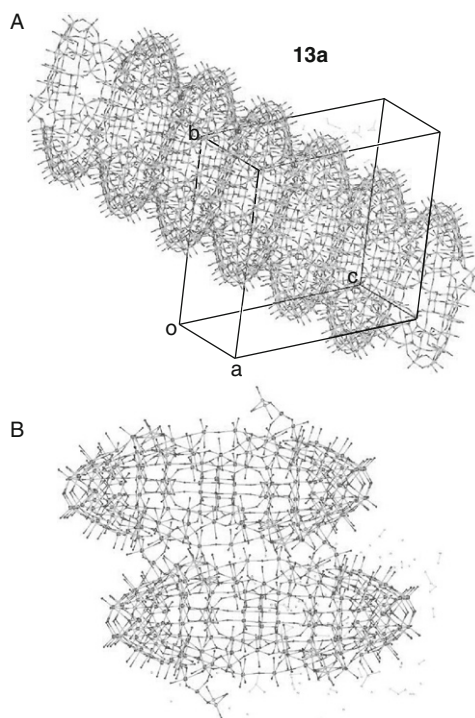


FIGURE 41 Structure of $\{[\text{Mo}_{28}^{\text{V}}\text{Mo}_{126}^{\text{VI}}\text{O}_{458}\text{H}_{12}(\text{H}_2\text{O})_{66}]^{8-}\}_{\infty}$ (**13a**) as a nano-tube of $\{\text{Mo}_{154}\}_{\infty}$. Packing (A) in unit cell and linkage (B) between the two $\{\text{Mo}_{154}\}$ nano-rings for **13a**. Figure is redrawn after Yamase et al. (2003).

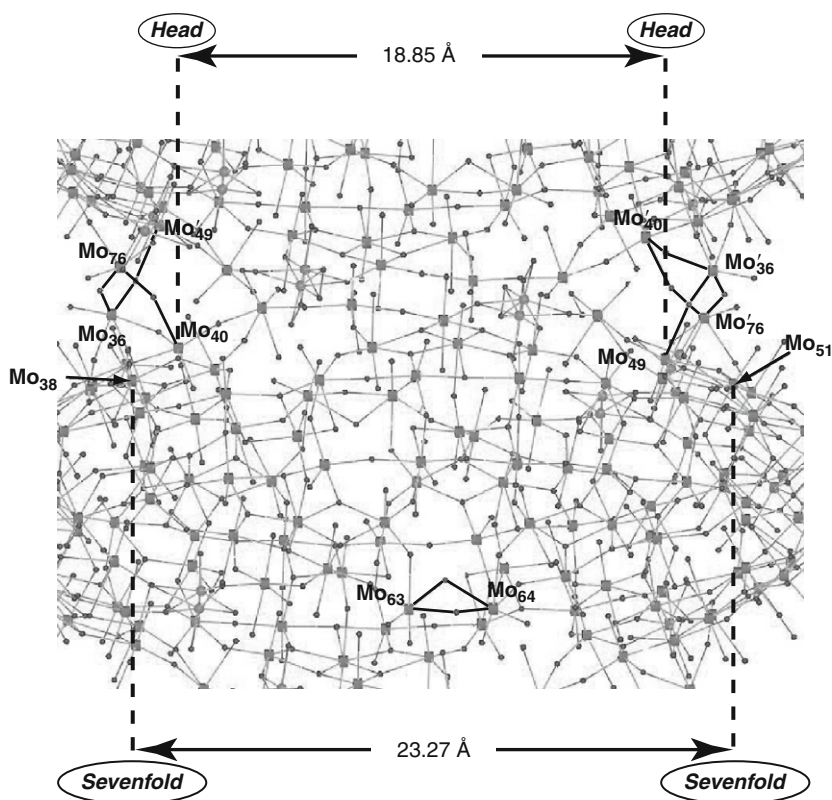


FIGURE 42 Linkage motif consisting of six Mo–O–Mo bonds between two $\{Mo_{154}\}$ rings. Figure is redrawn after Yamase et al. (2003).

consisting of 7 *head*- and 14 *linkers*- MoO_6 octahedra for each (Yamase et al., 2003). From the fact that the presence of La^{3+} in the reaction seems to be important for building the tubular structure, it is inferred that the connection between neighbouring $\{Mo_{154}\}$ units is favoured by the coexistence of La^{3+} . Figures 41 and 42 show the first nano-tube structure of **13a** and the linkage motif between two $\{Mo_{154}\}$ rings, respectively. As shown in Figure 42, two MoO_6 octahedral *heads* of Mo(40) and Mo(49) sites [with an $Mo(40)\cdots Mo(49)$ separation of 18.85 Å in the inner ring], which are edge-shared with seven-co-ordinate Mo(38) and Mo(51) sites [with an $Mo(38)\cdots Mo(51)$ separation of 23.27 Å], are corner-shared with two MoO_6 octahedral *linkers* [from Mo(76) and Mo(36') sites in the inner ring] belonging to the neighbouring ring molecule. Such MoO_6 octahedral *linkers* for the neighbouring ring are corner-shared with two MoO_6 octahedral *linkers* of Mo(36) and Mo(76') sites [with an $Mo(36)\cdots Mo(76')$ separation of 22.93 Å] which are also corner-shared with the two MoO_6 octahedral *heads* of Mo(49') and Mo(40') in the neighbouring ring, respectively. As a result, there exist six corner-sharing Mo–O–Mo bridges between the piled inner rings, with Mo–O bond distances equal to 2.33/1.74, 2.02/1.90, and 1.69/2.37 Å.

The linker motifs between the neighbouring rings for **13a** are quite different from that found in the chain structures of the deficient rings, $\text{Na}_{24}[\text{Mo}_{144}\text{O}_{437}\text{H}_{14}(\text{H}_2\text{O})_{56}] \cdot \text{ca.}250\text{H}_2\text{O}$ ($\{\text{Mo}_{144}\}$) and $\text{Na}_{22}[\text{Mo}_{146}\text{O}_{442}\text{H}_{14}(\text{H}_2\text{O})_{58}] \cdot \text{ca.}250\text{H}_2\text{O}$ ($\{\text{Mo}_{146}\}$): four Mo–O–Mo bridges consisting of two Mo(*head*)–O–Mo(*head*) and two Mo(*linker*)–O–Mo(*linker*) bonds at four adjacent MoO_6 octahedral sites in inner ring. Compounds $\{\text{Mo}_{144}\}$ and $\{\text{Mo}_{146}\}$ were thermally prepared from $\text{Na}_2\text{MoO}_4 \cdot 2\text{H}_2\text{O}/\text{Fe}/\text{HCl}$ and $\text{Na}_2\text{MoO}_4 \cdot 2\text{H}_2\text{O}/\text{Na}_2\text{S}_2\text{O}_4/\text{HCO}_2\text{H}/\text{HCl}$ systems, respectively (Müller et al., 1997, 1999c). In the structure of anion **13a** (Figure 42), one of seven $\{\text{Mo}_2\}$ -linker units in each inner ring is replaced by a bis(μ -oxo)-linked $[\text{MoO}_2(\mu\text{-O})(\mu\text{-H}_2\text{O})\text{MoO}_2]^{2+}$ unit [in 1.90/1.94 and 2.31/2.25 Å Mo–O distances between Mo(63) and Mo(64) linkers]. The Mo–O–Mo bonding motifs (2.02/1.90, 2.33/1.74, and 1.69/2.37 Å Mo–O bond distances) between the neighbouring inner rings indicate that the $\{\text{Mo}_{154}\}$ -based nano-tube structure results from both dehydrated condensation of terminal Mo–OH groups of *linkers* and the replacement of Mo– H_2O aqua ligands with terminal Mo=O groups (and vice versa) between *linker* and *head* in presence of La^{3+} . This indicates that the Ln^{3+} ions in the vicinity of the inner ring of the $\{\text{Mo}_{154}\}$ species act as traps for the water molecules liberated by both the condensation and replacement reactions. This is probably due to the high co-ordination number (8–12) of these ions and opens interesting perspective for the preparation of a variety of nano-tube isomers with chain or honeycomb structures. As shown above by the formation of ellipsoidal and Japanese rice-ball structures, the incorporation of the lanthanide cations into the inner rings supports the existence of the hypothetical $\text{La}^{3+} \subset \{\text{Mo}_{154}\}$ precursor in the formation of **13**.

5. SUMMARY AND CONCLUSIONS

By now, considerable insight has been gained into the intra-molecular energy transfer processes from the $\text{O} \rightarrow \text{M}$ ($=\text{Nb}, \text{V}, \text{Mo}, \text{W}$) lmct states (donor) to luminescent Ln^{3+} centres (acceptor) in polyoxometallolanthanoate complexes, which are leaflet models of lanthanide-doped metal-oxide phosphors. Local structures of lanthanide (mainly Eu^{3+} and Tb^{3+}) emission centres in the complex usually point to the co-ordination of aqua and hydroxo ligands in addition to metal-oxide oxo ligands, to a variety of co-ordination number and symmetry, and to the presence of aggregates. The cations surrounding the polyoxometallolanthanoates in the lattices contribute to the relaxation of the $\text{O} \rightarrow \text{M}$ lmct excitation energy due to the coupling with the O–M vibrational modes through interaction with the lattice oxygen atoms. The sensitized emission of Ln^{3+} in polyoxometallolanthanoates results from the energy transfer (with a rate larger than 10^6 s^{-1}) from two $\text{O} \rightarrow \text{M}$ lmct triplet levels through the singlet states along with a Förster-Dexter dipole–dipole type of coupling between the donor and the acceptor. Of particular importance is the localization of the $\text{O} \rightarrow \text{M}$ lmct triplet wave function on the MO_6 octahedron in the polyoxometalate ligands due to the electronic disparity between the ground and excited states, which is reflected by the bond angle of the M–O–M or Ln–O–M linkages: polyoxometalate ligands

having only edge-shared MO_6 octahedra with M-O-M bond angles of about 100° and Ln-O-M bond angles of about $100\text{--}130^\circ$ show a small temperature dependence of the energy transfer, whereas polyoxometalate ligands with M-O-M and Ln-O-M bond angles larger than 150° allow the d^1 -hopping delocalization in the ligands resulting in a decrease in the energy transfer with increasing temperature. The $\text{Tb}^{3+} \rightarrow \text{Eu}^{3+}$ energy transfer between different Ln^{3+} sites (LnO_8 or LnO_9) of low symmetry (C_1 and C_s) occurs through the overlap between the ${}^5\text{D}_4 \rightarrow {}^7\text{F}_4$ emission line of Tb^{3+} and the ${}^5\text{D}_0 \leftarrow {}^7\text{F}_0$ excitation line of Eu^{3+} : its rate increases with the shortening of the nearest $\text{Tb}\cdots\text{Eu}$ distance: 5×10^5 , 4×10^4 , and 5×10^3 s^{-1} for $\text{Tb}\cdots\text{Eu}$ distances of 3.8, 5.1, and 6.2 Å at 4.2 K. The rate of the $\text{Tb}^{3+} \rightarrow \text{Eu}^{3+}$ transfer increases with an increase in temperature due to an increase in transfer channels, that is larger overlap of the ${}^5\text{D}_4 \rightarrow {}^7\text{F}_4$ emission line with the ${}^5\text{D}_0 \leftarrow {}^7\text{F}_1$, ${}^5\text{D}_1 \leftarrow {}^7\text{F}_1$, and ${}^5\text{D}_0 \leftarrow {}^7\text{F}_2$ excitation lines, resulting from the thermal population of ${}^7\text{F}_1$ and ${}^7\text{F}_2$ states of Eu^{3+} . By a judicious combination of donors and acceptors in each system, more details should emerge from future studies concerning the contribution of the various reaction paths to the energy transfer from the $\text{O} \rightarrow \text{M}$ lmct triplet states in the lattices.

Radiative and non-radiative rates for various polyoxometalloyeuropates could be estimated from the large value (close to unity) of the quantum yield for the sensitized emission from the ${}^5\text{D}_0$ and ${}^5\text{D}_1$ states of Eu^{3+} in $\text{Na}_9[\text{Eu}(\text{W}_5\text{O}_{18})_2] \cdot 32\text{H}_2\text{O}$: the radiative rate for the ${}^5\text{D}_0 \rightarrow {}^7\text{F}_J$ ($J = 0\text{--}4$) transition ranges from 2.7×10^2 to 1.4×10^3 s^{-1} , and the non-radiative rate ($< 10^4$ s^{-1}) for the ${}^5\text{D}_0$ state increases with the total number of aqua and hydroxo ligands (for Eu-O distances smaller than 2.6 Å) bound to Eu^{3+} , due to the weak vibronic coupling with high-frequency OH oscillators. The co-ordination of aqua and hydroxo ligand with long $\text{Eu}\cdots\text{O}$ distances (2.6–2.9 Å) results in a drastic decrease in the non-radiative vibronic coupling process, which means that the empirical predictions of the number of aqua and hydroxo ligands co-ordinated around Eu^{3+} should be employed with care. In addition, $[\text{Eu}(\text{H}_2\text{O})_8]_2[\text{V}_{10}\text{O}_{28}] \cdot 8\text{H}_2\text{O}$ is a good model for unravelling the crystal field splitting of the Eu^{3+} octa-aqua cation. The subsequent analysis indicates that approximately two-thirds of the Eu^{3+} aqua cations in 0.1 M EuCl_3 (aq) exist as $[\text{Eu}(\text{H}_2\text{O})_8]^{3+}$, with square anti-prismatic co-ordination geometry.

The $\text{O} \rightarrow \text{M}$ lmct triplet states are involved not only in energy transfers in polyoxometalloylanthanoates but also in electron transfer during the photoredox reaction with proton and electron donors. This enables us to photochemically design nano-ring structural Mo-blues by the use of Ln^{3+} ions in a novel 'bottom-up' approach. The relevant structural manipulation can be varied systematically over a wide range in both size and shape. Since structures featuring nano-tubes, nano-chains, and ellipsoidal rings are promising from a viewpoint of nano-science and technology for the elaboration of electronic/magnetic devices and catalysts, further investigations concerning aiming at elucidating the mechanism of the photo-induced self-assembly of other structures appear worthwhile. The understanding of the aggregation process leading to a given class of polynuclear anionic metal-oxygen clusters is a great challenge. But such a knowledge would increase the degree of control of novel synthetic pathways for producing metal-oxide-based mesoscopic and colloidal materials with expected interesting properties

for material science. This is especially valid for polyoxometallolanthanoates which display a wide variety of structures with different symmetry and size.

ACKNOWLEDGEMENTS

This work was supported by Grants-in-Aid for Scientific Research, No. 17002006 from the Ministry of Education, Science, Sports, and Culture and CREST of JST.

REFERENCES

- Albertsson, J., Elding, I. *Acta Crystallogr.* 1977, **B33**, 1460.
- Alizadeh, M.H., Harmalker, S.P., Jeannin, Y., Martin-Frere, J., Pope, M.T. *J. Am. Chem. Soc.* 1985, **107**, 2662.
- Aveston, J., Anacker, E.W. *Inorg. Chem.* 1965, **3**, 735.
- Ballardini, R., Mulazzani, Q.G., Venturi, M., Bolletta, F., Balzani, V. *Inorg. Chem.* 1984a, **23**, 300.
- Ballardini, R., Chiorboli, Q.E., Balzani, V. *Inorg. Chim. Acta* 1984b, **96**, 323.
- Barendswaads, W., van der Waals, J.H. *Mol. Phys.* 1986, **59**, 337.
- Barendswaads, W., Van Tol, J., Weber, R.T., van der Waals, J.H. *Mol. Phys.* 1989, **67**, 651.
- Blasse, G. *J. Phys.* 1966, **45**, 2350.
- Blasse, G. *Struct. Bond.* (Berlin) 1980, **42**, 1.
- Blasse, G. *Inorg. Chim. Acta* 1990, **169**, 33.
- Blasse, G. *Eur. J. Solid State Inorg. Chem.* 1991, **t28**, 719.
- Blasse, G., Brixner, L.H. *Inorg. Chim. Acta* 1990, **169**, 25.
- Blasse, G., Grabmaier, B.C. *Luminescent Materials*, Berlin/Heidelberg: Springer-Verlag; 1994.
- Blasse, G., Dirksen, G.J., Zonnenevjlle, F. *Chem. Phys. Lett.* 1981a, **83**, 449.
- Blasse, G., Dirksen, G.J., Zonnenevjlle, F. *J. Inorg. Chem. Nucl. Chem.* 1981b, **43**, 2847.
- Blasse, G., Schipper, W., Hamelink, J.J. *Inorg. Chim. Acta* 1991, **189**, 77.
- Borrás-Alamenar, J.J., Coronado, E., Müller, A., Pope, M.T. *Polyoxometalate Molecular Science*, NATO Science Series, Dordrecht/Boston/London: Kluwer Academic Publishers; 2003.
- Bril, A., Wanmaker, W.L. *J. Electrochem. Soc.* 1964, **111**, 1363.
- Brittain, H.G., McAllister, W.A. *Spectrochim. Acta* 1985, **41A**, 1041.
- Creaser, I., Heckel, M.C., Neitz, R.J., Pope, M.T. *Inorg. Chem.* 1993, **32**, 1573.
- Cronin, L., Beugholt, C., Krickemeyer, K., Schmidtman, M., Bögge, H., Kögerler, P., Kim, T., Luong, K., Müller, A. *Angew. Chem. Int. Ed.* 2002, **41**, 2805.
- Darwent, J., Flint, C.D., O'Grady, P.J. *Chem. Phys. Lett.* 1986, **127**, 547.
- Dexter, D.L. *J. Chem. Phys.* 1953, **21**, 836.
- Förster, T. *Ann. Phys.* 1948, **2**, 55.
- Gerkin, R.E., Reppart, W.J. *Acta Crystallogr.* 1984, **C40**, 781.
- Griffith, W.P., Lesniak, P.J.B. *J. Chem. Soc. A* 1969, 1066.
- Hegarty, G.D., Huber, L., Yen, W.M. *Phys. Rev. B* 1981, **23**, 6271.
- Henderson, B., Inbusch, G.F. *Optical Spectroscopy of Inorganic Solids*, Clarendon: Oxford; 1989.
- Hill, C.L. *Chem. Rev.* 1998, **98**, 1.
- Horrocks, Jr., W. deW., Sudnick, D.R. *J. Am. Chem. Soc.* 1979, **101**, 334.
- Horrocks, Jr., W. deW., Sudnick, D.R. *Acc. Chem. Res.* 1981, **14**, 384.
- Ibal, J., Low, J.N., Weakley, T.J. *J. Chem. Soc. Dalton Trans.* 1974, 2021.
- Inokuti, H., Hirayama, F. *J. Chem. Phys.* 1965, **43**, 1978.
- Khawa, I.A., Parkes, C.C., McPherson, G.L. *Phys. Rev. B* 1995, **52**, 51.
- Kögerler, P., Müller, A. in: Yamase, T. Pope, M.T., editors. *Polyoxometalate Chemistry for Nano-Composite Design*, New York: Kluwer Academic/Plenum Publications; 2002, 1.
- Krebs, B., Stiller, S., Tytko, K.H., Mehmke, J. *Eur. J. Solid. State Inorg. Chem.* 1991, **28**, 883.
- Molchanov, V.I., Kazanskii, L.P., Torchenkova, E.A., Simonov, V.I. *Sov. Phys. Crystallogr.* 1979, **24**, 96.
- Moret, E., Bünzli, J.C., Schenk, K. *Inorg. Chim. Acta* 1990, **178**, 83.

- Müller, A., Kögerler, P., Dress, A.W.M. *Coord. Chem. Rev.* 2001, **222**, 193.
- Müller, A., Beugholt, C., Koop, M., Das, S.K., Schmidtmann, M.E., Bögge, H. *Z. Anorg. Allg. Chem.* 1999a, **625**, 1960.
- Müller, A., Krickenmeyer, E., Bögge, H., Schmidtmann, M.E., Beugholt, C., Das, S.K., Peters, F. *Chem. Eur. J.* 1999b, **5**, 1496.
- Müller, A., Das, S.K., Fedin, V.P., Krickenmeyer, E., Beugholt, C., Bögge, H., Schmidtmann, M.E., Hauptfleisch, B. *Z. Anorg. Allg. Chem.* 1999c, **625**, 1187.
- Müller, A., Krickenmeyer, E., Bögge, H., Schmidtmann, M.E., Peter, F., Mencke, C., Meyer, J. *Angew. Chem. Int. Ed.* 1997, **36**, 484.
- Müller, A., Beugholt, C., Bögge, H., Schmidtmann, M. *Inorg. Chem.* 2000, **39**, 3112.
- Müller, A., Das, S.K., Krickenmeyer, E., Kuhlmann, C. in: Sharples, J., editor., *Inorganic Synthesis*, New York: John Wiley & Sons; 2004, 191.
- Naruke, H., Yamase, T. *J. Lumin.* 1991, **50**, 55.
- Naruke, H., Yamase, T. *Acta Crystallogr.* 1996, **C52**, 2655.
- Naruke, H., Yamase, T. *J. Alloys Compd.* 1997, **255**, 183.
- Naruke, H., Yamase, T. *J. Alloys Compd.* 1998, **268**, 100.
- Naruke, H., Ozeki, T., Yamase, T. *Acta Crystallogr.* 1991, **C47**, 489.
- Niven, M.L., Cruywagen, J.J., Heyns, J.B. *J. Chem. Soc. Dalton Trans.* 1991, 2007.
- Ofelt, G.S. *J. Chem. Phys.* 1963, **38**, 2171.
- Ozeki, T., Yamase, T. *J. Alloys Compd.* 1993, **192**, 28.
- Ozeki, T., Yamase, T. *Acta Crystallogr.* 1994, **B50**, 128.
- Ozeki, T., Takahashi, M., Yamase, T. *Acta Crystallogr.* 1992, **C48**, 1370.
- Ozeki, T., Yamase, T., Naruke, H., Sasaki, Y. *Inorg. Chem.* 1994, **33**, 409.
- Pope, M.T., Müller, A. *Polyoxometallates: From Topology to Industrial Applications*, Dordrecht/Boston/London: Kluwer Academic Publishers; 2001.
- Powell, R.C., Blasse, G. *Struct. Bond.* 1980, **42**, 43.
- Rivero, B.E., Rigotti, G., Punte, G., Navaza, A. *Acta Crystallogr.* 1984, **C40**, 715.
- Rivero, B.E., Punte, G., Rigotti, G. *Acta Crystallogr.* 1985, **C41**, 817.
- Saf'yanov, Y.N., Belov, N.V. *Dokl. Akad. Nauk SSSR.* 1976, **227**, 112.
- Saf'yanov, Y.N., Kuz'min, E.A., Belov, N.V. *Dokl. Akad. Nauk SSSR.* 1978, **242**, 603.
- Soderholm, L., Liu, G.K., Muntntean, J., Malinsky, J., Antonio, M.R. *J. Phys. Chem.* 1995, **99**, 9611.
- Sommerdijk, J.L., Brill, A. *Philips Techn. Rev.* 1974, **34**, 24.
- Stillman, M.J., Thompson, A.J. *J. Chem. Soc. Dalton Trans.* 1976, 1138.
- Stuck, C.W., Fonger, W.H. *J. Chem. Phys.* 1976, **64**, 1784.
- Sugeta, M., Yamase, T. *Bull. Chem. Soc. Jpn.* 1993, **66**, 444.
- Sugeta, M., Yamase, T. *Acta Crystallogr.* 1997, **C53**, 1166.
- Supkowski, R.M., Horrocks, W.D., Jr. *Inorg. Chim. Acta* 2002, **340**, 44.
- Tilkens, L., Randall, K., Sun, J., Berry, M.T., May, P.S., Yamase, T. *J. Phys. Chem. A* 2004, **108**, 6624.
- Tourné, C.M., Tourné, G.F., Brianso, M.C. *Acta Crystallogr.* 1980, **B36**, 2012.
- van der Poel, W.A.J.A., Noort, M., Herbich, J., Coremans, C.J.M., van der Waals, J.H. *Chem. Phys. Lett.* 1984a, **103**, 245.
- van der Poel, W.A.J.A., Herbich, J., van der Waals, J.H. *Chem. Phys. Lett.* 1984b, **103**, 253.
- Van Oosterhout, A.B. *J. Chem. Phys.* 1977a, **67**, 2412.
- Van Oosterhout, A.B. *Phys. Status. Solidi A* 1977b, **41**, 601.
- Van Tol, J., van der Waals, J.H. *Mol. Phys.* 1992, **76**, 567.
- Van Tol, J., Van Hulst, J.A., van der Waals, J.H. *Mol. Phys.* 1992, **76**, 547.
- Verweg, J.W.M., Dirksen, G.J., Blasse, G. *J. Noncryst. Solids* 1988, **107**, 49.
- Yamase, T. *J. Chem. Soc. Dalton Trans.* 1991, 3055.
- Yamase, T. *Chem. Rev.* 1998, **98**, 307.
- Yamase, T. in: Pope, M.T., Müller, A., editors. *Polyoxometalate Chemistry*, Dordrecht: Kluwer Academic Publication; 2001, 187.
- Yamase, T. in: Borrís-Alamenar, J.J., Coronado, E., Pope, M.T., Müller, A., editors. *Polyoxometalate Molecular Science*, NATO science Series, Dordrecht: Kluwer Publishers; 2003, 201.
- Yamase, T., Naruke, H. *J. Chem. Soc. Dalton Trans.* 1991, 285.
- Yamase, T., Naruke, H. *J. Phys. Chem.* 1999, **42**, 8850.

- Yamase, T., Ohtaka, K. *J. Chem. Soc. Dalton Trans.* 1994, 2599.
- Yamase, T., Pope, M.T. *Polyoxometalate Chemistry for Nano-Composite Design*, New York: Kluwer Academic/Plenum Publications; 2002.
- Yamase, T., Prokop, P. *Angew. Chem. Int. Ed.* 2002, **37**, 466.
- Yamase, T., Sugeta, M. *J. Chem. Soc. Dalton Trans.* 1993, 759.
- Yamase, T., Sasaki, R., Ikawa, T. *J. Chem. Soc. Dalton Trans.* 1981, 628.
- Yamase, T., Naruke, H., Sasaki, Y. *J. Chem. Soc. Dalton Trans.* 1990, 1687.
- Yamase, T., Ozeki, T., Sakamoto, H., Nishiya, S., Yamamoto, A. *Bull. Chem. Soc. Jpn.* 1993, **66**, 103.
- Yamase, T., Kobayashi, T., Kettle, S.F.A. *J. Electrochem. Soc.* 1996, **143**, 1678.
- Yamase, T., Kobayashi, T., Sugeta, M., Naruke, H. *J. Phys. Chem.* 1997, **101**, 5046.
- Yamase, T., Naruke, H., San José Wéry, A.M., Kanaeko, M. *Chem. Lett.* 1998, 1281.
- Yamase, T., Prokop, P., Arai, Y. *J. Mol. Struct.* 2003, **656**, 107.
- Yamase, T., Yanao, Y., Ishikawa, E. *Langmuir* 2005, **21**, 7823.
- Yamase, T., Ishikawa, E., Abe, Y., Yano, Y. *J. Alloys Compd.* 2006, **408–412**, 693.

AUTHOR INDEX

- Abadli, L., see Krill, G. 40
 Abe, Y., see Yamase, T. 299, 301–306, 311–320, 322, 325–348, 350–351
 Abell, S. 119
 Abernathy, D., see Schüßler-Langeheine, C. 13
 Abrikosov, I.A., see Johansson, B. 18–19, 99
 Abrikosov, I.A., see Skorodumova, N.V. 49
 Abu Safia, H.A. 115
 Adachi, K., see Yashima, M. 249
 Adylov, G.T. 119
 Aerts, C.M. 33
 Ahou, Y.Q., see Yang, C.Y. 125
 Ahrens, M., see Zinkevich, M. 225, 227
 Ahuja, R. 14
 Ahuja, R., see Eriksson, O. 12–13, 18–19, 86
 Ahuja, R., see Skorodumova, N.V. 49
 Aiki, K., see Okazaki, H. 115
 Akai, H., see Crisan, V. 79
 Akinc, M. 117, 128
 Akselrud, L., see Vasylechko, L. 122, 129, 132, 138, 140, 142, 145–146, 148–150, 152, 155, 165, 168, 170, 173, 189, 191, 204, 206–208, 210, 213, 227–228, 230–232, 235, 237, 240–242, 245–247, 249, 251–253, 266–267, 275
 Alain, P. 142
 Alam, M.A., see Crowe, S.J. 13
 Alam, M.A., see Dugdale, S.B. 89
 Alam, M.A., see Fretwell, H.M. 13
 Alameda, J.M. 12
 Albers, R.C., see Eriksson, O. 12–13, 18–19, 86
 Albert, L., see Karnatak, R.C. 49
 Albertsson, J. 319
 Aldén, M., see Johansson, B. 18–19, 99
 Alder, B.J. 16
 Aldinger, F., see Lakiza, S. 118
 Aldinger, F., see Wu, B. 227
 Aldinger, F., see Zinkevich, M. 225, 227
 Aleksijko, R., see Berkowski, M. 228, 249
 Aleksijko, R., see Savvitskii, D.I. 125, 228, 230, 242, 282
 Aleksiyko, R., 228, 252, 254, 256, 264
 Alexandrovskii, A.N., see Savvitskii, D.I. 125, 228, 230, 242, 282
 Alizadeh, M.H. 303
 Alkebro, J. 123
 Allain, J., see Radhakrishna, P. 153, 162
 Allen, J.W. 68
 Allibert, M. 224–225
 Altermatt, D. 205
 Altorfer, F., see Marti, W. 230, 231, 233–235, 238–239, 242, 244
 Amadon, B. 29
 An, W.W. 124
 Anacker, E.W. 345
 Anacker, E.W., see Aveston, J. 345
 Ananieva, G.V. 125, 153, 155
 Andersen, O.K. 19, 23–24
 Andersen, O.K., see Anisimov, V.I. 19, 23, 28
 Anderson, P.W. 103–104
 Andreeva, A.V., see Leonov, A.I. 128, 170, 227
 Andreoni, W., see Shevlin, S.A. 224
 Andrews, A.B., see Joyce, J.J. 41
 Andrianov, A.V. 89–90, 95
 Ang, C. 216
 Angel, R.J. 128, 137, 145, 147, 157, 167
 Angel, R.J., see Ross, N.L. 145, 147, 157, 161, 167, 169
 Angel, R.J., see Zhao, J. 128, 137, 145
 Anisimov, V.I. 19–20, 23, 28
 Anisimov, V.I., see Harmon, B.N. 86
 Anisimov, V.I., see Lichtenstein, A.I. 19–20, 65
 Anisimov, V.I., see Zöfl, M.B. 29
 Antic, E., see Coutures, J. 224
 Antic-Fidancev, E. 22
 Antonio, M.R., see Soderholm, L. 303
 Antonov, V.A., see Arsenev, P.A. 120–121, 138, 161, 189
 Antonov, V.N. 20
 Antonov, V.N., see Oppeneer, P.M. 43
 Antropov, V.P., see Harmon, B.N. 86
 Aoki, H., see Takeda, N. 43
 Arai, Y., see Yamase, T. 299, 301–306, 311–320, 322, 325–348, 350–351
 Arakawa, A., see Okazaki, H. 115
 Arakcheeva, A.V. 230
 Arima, H., see Nakatsuka, A. 122, 126–127
 Arko, A.J., see Joyce, J.J. 41

- Arola, E. 6, 70–71, 74
 Arola, E., see Brown, S.D. 73–76
 Arsenev, P.A. 120–121, 138, 161, 189
 Aryasetiawan, F. 26–28
 Aryasetiawan, F., see Amadon, B. 29
 Aryasetiawan, F., see Anisimov, V.I. 19, 23, 28
 Asahi, T., see Okazaki, H. 115
 Asano, H., see Konaka, T. 222, 280, 282
 Aslanov, V., see Moses, W.W. 115
 Atsarkin, V.A., see Noginova, N. 248
 Auluck, S., see Ahuja, R. 14
 Aveston, J. 345
 Axelsson, A.-K., see Sebastian, M.T. 218–219, 223, 282
 Azad, A.-M., see Chandrasekaran, A. 248
- Babiichuk, I., see Makeev, Yu. 222
 Bacsá, W., see Degiorgi, L. 43
 Badrzadeh, S., see Dugdale, S.B. 89
 Badshaw, H. 220
 Baehz, C., see Savvytskii, D. 231–233, 237, 242–244
 Baehz, C., see Senyshyn, A. 152, 238, 242–244, 246, 248, 251–253, 262, 265, 267, 274, 276, 278, 280, 282
 Baehz, C., see Vasylechko, L. 122, 129, 132, 138, 140, 142, 145–146, 148–150, 152, 155, 165, 168, 170, 173, 189, 191, 204, 206–208, 210, 213, 227–228, 230–232, 235, 237, 240–242, 245–247, 249, 251–253, 266–267, 275
 Baer, Y., see Campagna, M. 64, 67–69
 Baer, Y., see Wuilloud, E. 49, 51
 Bagdasarov, Kh.S., see Arsenev, P.A. 120–121, 138, 161, 189
 Bähz, C., see Vasylechko, L.O. 228, 230–231, 237, 240, 242, 246–247, 249, 266–267, 275
 Balbashov, A.M., see Bdikin, I.K. 228
 Baldi, G., see Cruciani, G. 121
 Baltache, H., see Bouhemadou, A. 47
 Balzani, V. 301
 Balzani, V., see Ballardini, R. 301–303
 Bamzai, K.K., see Razdan, A.K. 122
 Banister, J.R. 86
 Barendswaads, W. 326
 Bärner, K., see Rao, G.H. 207
 Barns, R.L., see Carruthers, J.R. 224
 Bartlett, R.J., see Joyce, J.J. 41
 Bartolome, J., see Palacios, E. 138
 Bartos, K., see Mares, J.A. 115, 125
 Bart, K., see Veith, M. 124
 Barzanti, A.Z., see Cruciani, G. 121
 Bassani, F., see Andersen, O.K. 19, 23, 24
- Basyuk, T., 137, 166, 168, 170–172, 174–178, 182–184, 186, 267
 Battle, P.D. 182
 Battle, P.D., see Cussen, E.J. 248
 Bauer, E.D., see Kumar, R.S. 49
 Bayer, V., see Silva, J.L.F.D. 51
 Bdikin, I.K. 228
 Beach, D.B. 124
 Beach, D.B., see Morell, J.S. 228
 Beach, D.B., see Shoup, S.S. 124
 Becke, A.D.J. 16
 Bednorz, J.G., see D'Iorio, M. 133
 Begin-Colin, S., see Alkebro, J. 123
 Beiden, S.V. 58, 70
 Belevantsev, V.S., see Budnikov, P.P. 117–118
 Belous, A.G. 216
 Belov, N.V., see Saf'yanov, Y.N. 319
 Belova, I.L., see Krylov, V.S. 121
 Belsky, A., see Petrosyan, A.G. 119–121, 125, 191
 Belt, R.F. 228
 Benard, D.J. 133
 Benedict, U. 46
 Benedict, U., see Bihan, T.L. 46
 Benning, P.J., see Joyce, J.J. 41
 Berdot, J.L., see Brusset, H. 161, 163, 165, 183, 188, 242
 Berjoan, M., see Mizuno, M. 117, 120
 Berkowski, M. 115, 228, 242, 249
 Berkowski, M., see Aleksiyko, R. 228, 252, 254, 256, 264
 Berkowski, M., see Savvytskii, D. 231–233, 237, 242–244
 Berkowski, M., see Savvytskii, D.I. 125, 228, 230, 242, 282
 Berkowski, M., see Scheel, H.J. 115, 242
 Berkowski, M., see Senyshyn, A. 152, 238, 242–244, 246, 248, 251–253, 262, 265, 267, 274, 276, 278, 280, 282
 Berkowski, M., see Vasylechko, L. 122, 129, 132, 138, 140, 142, 145–146, 148–150, 152, 155, 165, 168, 170, 173, 189, 191, 204, 206–208, 210, 213, 227–228, 230–232, 235, 237, 240–242, 245–247, 249, 251–253, 266–267, 275
 Berkowski, M., see Vasylechko, L.O. 228, 230–231, 237, 240, 242, 246–247, 249, 266–267, 275
 Berkstresser, G.W. 229, 235
 Berkstresser, G.W., see O'Bryan, H.M. 138, 217, 229–230, 235, 242
 Berlinger, W., 126
 Berlinger, W., see D'Iorio, M. 133
 Berlinger, W., see Müller, K.A. 126
 Bertaut, F. 125, 229
 Beskrovnyi, A.I., see Andrianov, A.V. 89–90, 95
 Best, P.R.J. 82

- Beugholt, C., see Cronin, L. 347
 Beugholt, C., see Müller, A. 299, 352
 Bewleya, R.I., see Boothroyd, A.T. 49
 Bezruk, E.T., see Bondar, I.A. 224, 227, 275
 Bhalla, A.S., see Ang, C. 216
 Bianconi, A. 49, 51
 Bidaux, R. 148, 154
 Bienert, K.E., see Arsenev, P.A. 120–121, 138, 161, 189
 Biermann, S., see Amadon, B. 29
 Bihan, T.L. 46
 Bihlmayer, G., see Döbrich, K.M. 13
 Bihlmayer, G., see Kurz, P. 86–87
 Bihlmayer, G., see Turek, I. 87
 Bimberg, D., see Rinke, P. 27
 Birgeneau, R.J. 132
 Birgeneau, R.J., see Lyons, K.B. 132
 Birnie, D., see Kaufman, L. 120
 Bismayer, U., see Savytskii, D. 231–233, 237, 242–244
 Bismayer, U., see Savytskii, D.I. 125, 228, 230, 242, 282
 Bismayer, U., see Senyshyn, A. 152, 238, 242–244, 246, 248, 251–253, 262, 265, 267, 274, 276, 278, 280, 282
 Bismayer, U., see Vasylechko, L. 122, 129, 132, 138, 140, 142, 145–146, 148–150, 152, 155, 165, 168, 170, 173, 189, 191, 204, 206–208, 210, 213, 227–228, 230–232, 235, 237, 240–242, 245–247, 249, 251–253, 266–267, 275
 Bismayer, U., see Vasylechko, L.O. 228, 230–231, 237, 240, 242, 246–247, 249, 266–267, 275
 Blaha, P., see Mohn, P. 19
 Blasco, J., see Sanjuán, M.L. 230, 233, 244, 249, 258
 Blasse, G. 300–303, 320, 326, 328, 332, 338
 Blasse, G., see Powell, R.C. 328
 Blasse, G., see Verweg, J.W.M. 319
 Blezek, K., see Mares, J.A. 115, 125
 Blount, E.I., see Lyons, K.B. 132
 Blügel, S., see Döbrich, K.M. 13
 Blügel, S., see Kurz, P. 86–87
 Blügel, S., see Turek, I. 87
 Blume, M. 70, 72
 Blundell, S. 96
 Blundell, S.J., see Cussen, E.J. 248
 Blythe, R.I.R., see Joyce, J.J. 41
 Bögge, H., see Cronin, L. 347
 Bögge, H.Z., see Müller, A. 299, 352
 Bogunov, V., see Kleptsyn, V. 228
 Böhm, H., see Bombik, A. 148, 150–151, 158, 163, 248
 Bolletta, F., see Ballardini, R. 301–303
 Bolotnikova, E.V., see Kuznetsova, T.F. 124
 Bombik, A. 148, 150–151, 158, 163, 248
 Bondar, I.A. 224, 227, 275
 Bonville, P. 43
 Boothroyd, A.T. 49
 Boothroyd, A.T., see Gardiner, C.H. 51
 Boring, A.M. 49, 51
 Boring, A.M., see Eriksson, O. 12–13, 18–19, 86
 Boring, A.M., see Koelling, D.D. 14, 49, 51
 Borisov, V.N., see Savytskii, D.I. 125, 228, 230, 242, 282
 Borrás-Alamenar, J.J. 299
 Borrmann, H., see Vasylechko, L. 122, 129, 132, 138, 140, 142, 145–146, 148–150, 152, 155, 165, 168, 170, 173, 189, 191, 204, 206–208, 210, 213, 227–228, 230–232, 235, 237, 240–242, 245–247, 249, 251–253, 266–267, 275
 Bouchenoire, L., see Brown, S.D. 73–76
 Bouhemadou, A. 47
 Bouvier, P. 128, 135
 Boysen, H. 125, 230–231
 Boysen, H., see Lehnert, H. 126
 Boysen, H., see Lerch, M. 230–231
 Boysen, H., see Yu, Y. 125
 Brandle, C.D., see Berkstresser, G.W. 229, 235
 Brandle, C.D., see O'Bryan, H.M. 138, 217, 229–230, 235, 242
 Brese, N.E. 205
 Brianso, M.C., see Tourné, C.M. 303
 Bridgewater, J.S., see Schoonover, J.R. 231
 Bril, A. 300
 Bril, A., see Sommerdijk, J.L. 300
 Brittain, H.G. 300
 Brixner, L.H. 338
 Brixner, L.H., see Blasse, G. 300–303, 320, 326, 328, 332, 338
 Brooks, M.S.S., see Ahuja, R. 14
 Brooks, M.S.S., see Eriksson, O. 12–13, 18–19, 86
 Brown, I.D. 148, 205, 207, 247
 Brown, I.D., see Altermatt, D. 205
 Brown, I.D., see Rao, G.H. 207
 Brown, P.J. 151
 Brown, S.D. 73–76
 Bruno, E., see Staunton, J.B. 77–80, 82–83
 Brusset, H. 161, 163, 165, 183, 188, 242
 Buchanan, D.N.E., see Campagna, M. 64, 67–69
 Bucher, E., see Campagna, M. 64, 67–69
 Bucher, E., see Werner, A. 48
 Budnikov, P.P. 117–118
 Bünzli, J.C., see Moret, E. 338
 Burbank, R.D. 132
 Burbank, R.D., see Cohen, E. 132
 Burley, J.C., see Cussen, E.J. 248

- Burt, J.B., see Ross, N.L. 145, 147, 157, 161, 167, 169
- Buruzs, A., see Staunton, J.B. 77–80, 82–83
- Buschow, K.H.J., see Havinga, E.E. 43
- Butorin, S.M. 49, 51
- Byszewski, P., see Aleksiyko, R. 228, 252, 254, 256, 264
- Byszewski, P., see Berkowski, M. 228, 249
- Byszewski, P., see Savytskii, D.I. 125, 228, 230, 242, 282
- Cahn, R.W., see Kübler, J. 14, 17–18, 78
- Callcott, T.A., see Moewes, A. 49
- Calvert, L.D. 52
- Calvert, L.D., see Ono, S. 39
- Calvert, L.D., see Wang, B.Y. 39
- Campagna, M. 64, 67–69
- Can, J., see Vosko, S.H. 16
- Canfield, P.C., see Joyce, J.J. 41
- Canfield, P.C., see Robinson, R.A. 43
- Caro, P.E., see Karnatak, R.C. 49
- Carpenter, M., see Pawlak, D.A. 125
- Carpenter, M.A. 134–135
- Carrasco, J., see Loschen, C. 51
- Carruthers, J.R. 224
- Caulfield, H.J., see Loutts, G.B. 115
- Ceperley, D.M. 16
- Chabot, B., see Scheel, H.J. 115, 242
- Chainani, A. 67
- Chainani, A., see Ito, T. 67
- Chaix-Pluchery, O., see Carruthers, J.R. 224
- Chakoumakos, B.C. 126
- Chakoumakos, B.C., see Kennedy, B.J. 135, 182, 183
- Chandrasekaran, A. 248
- Chantis, A.N. 5, 27
- Chantis, A.N., see Larson, P. 20, 43
- Chaplin, T.D., see Ross, N.L. 145, 147, 157, 161, 167, 169
- Chatillon, C., see Allibert, M. 224–225
- Chatterjee, A., see Jayaraman, A. 7, 29, 39, 48
- Chen, X.M. 218
- Chen, X.M., see Liu, X.Q. 218
- Chenevier, B., see Carruthers, J.R. 224
- Cheng, H.H. 227, 249
- Cherpak, N., see Makeev, Yu. 222
- Chioncel, L., see Petukhov, A.G. 19
- Chiorboli, Q.E. 301
- Chiorboli, Q.E., see Ballardini, R. 301–303
- Chisholm, M.F., see Sandstrom, R.L. 280
- Chistiakov, O.D. 89
- Chitose, N., see Yashima, M. 249
- Cho, E.-J. 41
- Cho, S.Y. 227, 249
- Choi, C.-H., see Kim, M.-H. 282
- Chu, J.P., see Wang, S.F. 216
- Chung, J.-S., see Cho, E.-J. 41
- Chval, J. 189, 191
- Chval, J., see Mares, J.A. 125
- Claridge, J.B., see Moussa, S.M. 216
- Clark, R.D., see Lux, B.C. 123
- Clarke, S., see Moussa, S.M. 216
- Clement, D., see Chval, J. 189, 191
- Cockayne, B., see Abell, S. 119
- Cockayne, B.J. 119
- Cohen, E. 132
- Coldea, A.I., see Cussen, E.J. 248
- Collins, S.P. 70, 74
- Compagnini, G., see Degiorgi, L. 43
- Cooper, E.I., see Sandstrom, R.L. 280
- Cordfunke, E.H.P., see Putnam, R.M. 115, 120, 123
- Coremans, C.J.M., see van der Poel, W.A.J.A. 303
- Cornelius, A.L., see Kumar, R.S. 49
- Coronado, E., see Borrás-Alamenar, J.J. 299
- Coutures, J. 138, 142, 144, 150, 158–159, 189, 224
- Coutures, J., see Antic-Fidancev, E. 22
- Coutures, J., see Nicolas, J. 224–225, 227, 246, 275
- Coutures, J.P. 117, 138, 142, 144, 150, 158–159, 189, 224
- Coutures, J.P., see Antic-Fidancev, E. 22
- Coutures, J.P., see Coutures, J. 138, 142, 144, 150, 158–159, 189, 224
- Coutures, J.P., see Mizuno, M. 117, 120
- Coutures, J.P., see Nicolas, J. 224–225, 227, 246, 275
- Cowan, R.D. 20
- Cox, D.I. 104
- Cracknell, A.P. 89
- Crasso, M., see Carruthers, J.R. 224
- Creaser, I. 303
- Crisan, V. 79
- Crist Jr., B., see Key, T.S. 120
- Croft, M. 45
- Cronin, L. 347
- Cross, L.E., see Ang, C. 216
- Crowe, S.J. 13
- Cruciani, G. 121
- Cruywagen, J.J., see Niven, M.L. 320
- Curioni, A. 224
- Curioni, A., see Shevlin, S.A. 224
- Curley, M., see Loutts, G.B. 115
- Currie, D.B., see Boothroyd, A.T. 49
- Cussen, E.J. 248
- Czyzyk, M.T., see Anisimov, V.I. 19–20, 23, 28

- D'Ambrossio, C., see Mares, J.A. 115, 125
 Dabkowska, H. 227, 235, 264
 Dabkowska, H., see Watts, B.E. 235
 Dabkowski, A., see Dabkowska, H. 227, 264
 Dabrowski, B., see Aleksiyko, R. 228, 252, 254, 256, 264
 Dafinei, I., see Mares, J.A. 125
 Daly, K.P., see Simon, R.W. 222
 Dalziel, J.A.W. 148
 Däne, M., see Hughes, I.D. 6, 79, 86, 91, 94
 Däne, M., see Lüders, M. 5, 24, 79, 84, 97
 Darby, M.I. 97
 Darie, C., see Hassan, A.K. 12
 Darracq, S., see Bihan, T.L. 46
 Darwent, J. 301
 Das, M.P., see Temmerman, W.M. 4–5, 13–14, 21, 24–25, 36, 40–42, 45–46, 48, 53, 79, 81–82, 86
 Das, S.K., see Müller, A. 299, 352
 de Jonge, W.J.M., see Filip, A.T. 34
 de Jonge, W.J.M., see LeClair, P. 34
 De, M., see Ghosh, D.B. 37
 De, S.K., see Ghosh, D.B. 37
 Debray, D. 46
 Decker, D.L., see Debray, D. 46
 DeDominicis, C. 104
 Degiorgi, L. 43
 Degtyareva, V.Ya., see Bondar, I.A. 224, 227, 275
 Delin, A. 4, 18
 Delin, A., see Temmerman, W.M. 4–5, 13–14, 21, 24–25, 36, 40–42, 45–46, 48, 53, 79, 81–82, 86
 Delley, B., see Wuilloud, E. 49, 51
 Derbeneva, T.A., see Bondar, I.A. 224, 227, 275
 Derenzo, S.E., see Moses, W.W. 115
 Derenzo, S.E., see Shmurak, S.Z. 124
 Dernier, P. 138, 141, 143
 Dernier, P., see Marezio, M. 138, 141, 143
 Dernier, P.D. 228–230, 235, 242, 246–247, 249–250, 264, 268, 270
 Dernier, P.D., see Marezio, M. 228–230, 235, 242, 246–247, 249–250, 264, 268, 270
 Despault, J.G., see Ono, S. 39
 Devi, S.U., see Jayaraman, A. 7, 29, 39, 48
 Dexpert, H., see Karnatak, R.C. 49
 Dexter, D.L.J. 334–335
 Diduszko, R., see Aleksiyko, R. 228, 252, 254, 256, 264
 Diduszko, R., see Berkowski, M. 228, 249
 Diduszko, R., see Pawlak, D.A. 125
 Dimmock, J.O. 4
 D'Iorio, M. 133
 Dirksen, G.J. 301–303, 332
 Dirksen, G.J., see Blasse, G. 300–303, 320, 326, 328, 332, 338
 Dirksen, G.J., see Verweg, J.W.M. 319
 Diviš, M. 51
 Döbrich, K.M. 13
 Dobson, J.F., see Temmerman, W.M. 4–5, 13–14, 21, 24–25, 36, 40–42, 45–46, 48, 53, 79, 81–82, 86
 Domanskii, A.I., see Bondar, I.A. 224, 227, 275
 Dondi, M., see Cruciani, G. 121
 Dönni, A., see Li, D.X. 43
 Dönni, A., see Oyamada, A. 43
 Dowben, P.A., see Duan, C.-G. 20, 33
 Dreier, P., see Lehnert, H. 126
 Dreizler, R.M. 15, 21
 Dress, A.W.M., see Müller, A. 299, 352
 Duan, C.-G. 20, 33
 Dubs, C., see Sandiumenge, F. 281
 Duda, L.-C., see Butorin, S.M. 49, 51
 Dudley, M., see Wang, Y. 228–231
 Duffy, J.A., see Crowe, S.J. 13
 Dugdale, S.B. 89
 Dugdale, S.B., see Crowe, S.J. 13
 Dugdale, S.B., see Fretwell, H.M. 13
 Dujardin, C., see Petrosyan, A.G. 119–121, 125, 191
 Durygin, A., see Zinkevich, M. 225, 227
 Duthie, J.C. 4, 13, 18
 Dzhurinskii, B.F., see Arsenev, P.A. 120–121, 138, 161, 189
 Eastman, D.E., see Pollak, R.A. 67–68
 Ebert, H., see Brown, S.D. 73–76
 Ebert, H., see Crisan, V. 79
 Eccleston, R.S., see Boothroyd, A.T. 49
 Ederer, D.L., see Moewes, A. 49
 Eggleton, R.A. 122, 158, 169
 Eggleton, R.A., see Sinclair, W. 122, 158, 169
 Ehrenberg, H.Z., see Lehnert, H. 126
 Elding, I. 319
 Elding, I., see Albertsson, J. 319
 Entel, P., see Crisan, V. 79
 Eriksson, O. 12–13, 18–19, 86
 Eriksson, O., see Delin, A. 4, 18
 Eriksson, O., see Lebegue, S. 44, 65, 68–69
 Eriksson, O., see Svane, A. 18, 23, 29, 36, 38, 40–42, 44–49, 66, 99
 Eriksson, O., see Temmerman, W.M. 4–5, 13–14, 21, 24–25, 36, 40–42, 45–46, 48, 53, 79, 81–82, 86
 Ernst, A., see Hughes, I.D. 6, 79, 86, 91, 94
 Ernst, A., see Lüders, M. 5, 24, 79, 84, 97
 Erwin, R., see Robinson, R.A. 43
 Eschrig, H. 14, 19
 Eschrig, H., see Antonov, V.N. 20
 Eschrig, H., see Mohn, P. 19
 Eschrig, H., see Oppeneer, P.M. 43
 Esteva, J.-M., see Karnatak, R.C. 49
 Eur, J. 12

- Eyert, V. 18
 Eyring Jr., K.A.L., see Freeman, A.J. 4, 14, 24
 Eyring, L. 7–8, 29, 33, 39, 41, 49, 52–53
 Eyring, L., see Hulliger, F. 33, 43
 Eyring, L., see Jayaraman, A. 7, 29, 39, 48
 Eyring, L., see Sinha, S.K. 8
 Eyring, L., see Wachter, P. 41, 43
- Faber Jr, J., see Kern, S. 49
 Fabian, D.J., see Gyorffy, B.L. 6, 25, 77, 79–83, 103
 Fabrichnaya, O., see Lakiza, S. 118
 Fadeev, S.V., see Vasylechko, L.O. 228, 230–231, 237, 240, 242, 246–247, 249, 266–267, 275
 Fadeyev, S., see Vasylechko, L. 122, 129, 132, 138, 140, 142, 145–146, 148–150, 152, 155, 165, 168, 170, 173, 189, 191, 204, 206–208, 210, 213, 227–228, 230–232, 235, 237, 240–242, 245–247, 249, 251–253, 266–267, 275
 Faleev, S., see van Schilfgaarde, M. 27–28
 Fan, H., see Yang, W.H. 222
 Fanciulli, M., see Petit, L. 52–53, 56
 Fanciulli, M., see Scarel, G. 49, 53
 Fast, L., see Delin, A. 4, 18
 Fast, L., see Temmerman, W.M. 4–5, 13–14, 21, 24–25, 36, 40–42, 45–46, 48, 53, 79, 81–82, 86
 Faulkner, J.S. 25, 89
 Fauth, F., see Podlesnyak, A. 235
 Fedin, V.P., see Müller, A. 299, 352
 Fedorchuk, A., see Basyuk, T., 137, 166, 168, 170–172, 174–178, 182–184, 186, 267
 Fedorov, A., see Moses, W.W. 115
 Ferro, R. 228–229, 231, 235, 241
 Feynman, R.P. 80
 Fierro, J.L.G. 115
 Filin, Yu.N., see Shelykh, A.I. 128, 222
 Filip, A.T. 34
 Fink-Finowicki, J., see Aleksiyko, R. 228, 252, 254, 256, 264
 Fink-Finowicki, J., see Berkowski, M. 228, 249
 Fink-Finowicki, J., see Savvyskii, D.I. 125, 228, 230, 242, 282
 Fink-Finowicki, J., see Vasylechko, L. 122, 129, 132, 138, 140, 142, 145–146, 148–150, 152, 155, 165, 168, 170, 173, 189, 191, 204, 206–208, 210, 213, 227–228, 230–232, 235, 237, 240–242, 245–247, 249, 251–253, 266–267, 275
 Fischer, P., see Marti, W. 229–231, 233–235, 238–239, 242, 244
 Flint, C.D. 301
 Flint, C.D., see Darwent, J. 301
 Foex, M., see Mizuno, M. 117, 120
 Fonger, W.H., see Stuck, C.W. 332
 Förster, T. 334–335
- Fort, D., see Brown, S.D. 73–76
 Fort, D., see Wulff, M. 13, 51
 Forthyth, J.B., see Brown, P.J. 151
 Franceschi, E.J. 39
 Freeman, A.J. 4, 14, 24
 Freeman, A.J., see Dimmock, J.O. 4
 Freeman, A.J., see Pickett, W.E. 14
 Freeouf, J.L., see Pollak, R.A. 67–68
 Fretwell, H.M. 13
 Fretwell, H.M., see Dugdale, S.B. 89
 Frey, F., see Lehnert, H. 126
 Frukacz, Z., see Savvyskii, D. 231–233, 237, 242–244
 Fueki, K., see Mizusaki, J. 125
 Fujimori, A. 14
 Fujimori, A., see Cho, E.-J. 41
 Fukua, T., see Okano, Y. 125
 Fukuda, T., see Kimura, K. 115, 125
 Fukuda, T., see Nikl, M. 125, 191
 Fukuda, T., see Saitow, A. 186, 188
 Fukuda, T., see Shim, J.B. 125
 Fukuda, T., see Shishido, T. 122, 128, 149, 158, 227, 231–232
 Fukuda, T., see Yoshikawa, A. 138, 186–187
 Fukui, T., see Matsuda, M. 228
 Fukunaga, T., see Mori, K. 248
 Fulde, P., see Antonov, V.N. 20
 Fumi, F., see Andersen, O.K. 19, 23, 24
 Funayama, M., see Morita, S. 125, 189
 Fung, K.K., see Yang, C.Y. 125
 Furrer, A., see Marti, W. 229, 242
 Furrer, A., see Podlesnyak, A. 235
 Furuya, T., see Shibasaki, T. 229
- Gabe, E.J., see Wang, B.Y. 39
 Galakhov, F.Ya. 120–121
 Gali, S., see Sandiumenge, F. 281
 Gallagher, P.K., see O'Bryan, H.M. 138, 217, 229–230, 235, 242
 Gallaher, W.J., see Sandstrom, R.L. 280
 Ganduglia-Pirovano, M.V., see Silva, J.L.F.D. 51
 Garcia-Munoz, J.L., see Salinas-Sanchez, A. 207
 Gardiner, C.H. 51
 Gardiner, C.H., see Boothroyd, A.T. 49
 Gargano, A., see Bianconi, A. 49, 51
 Garnier, N., see Petrosyan, A.G. 119–121, 125, 191
 Gasgnier, M., see Karnatak, R.C. 49
 Gasiorowicz, S. 9
 Gaur, K.J. 53, 55
 Gavartin, J.L. 217
 Geballe, T.H.J. 34
 Gehring, G.A., see Beiden, S.V. 58, 70
 Gehring, G.A., see Langford, H.D. 4

- Gekimiyants, V.M., see Arakcheeva, A.V. 230
 Gektin, A., see Moses, W.W. 115
 Geller, S.J. 228
 George, J., see Sebastian, M.T. 218–219, 223, 282
 Georges, A. 28, 76, 103–104
 Georges, A., see Amadon, B. 29
 Gerkin, R.E. 319
 Gerward, L. 51
 Geupel, S., see Zinkevich, M. 225, 227
 Geyer, R.G., see Krupka, J. 282
 Ghosh, D.B. 37
 Giba, J., see Chval, J. 189, 191
 Gibb, T.C., see Battle, P.D. 182
 Gibbs, D. 70
 Giess, E.A., see Koren, G. 115
 Giess, E.A., see Sandstrom, R.L. 280
 Gillier-Pandraud, H., see Brusset, H. 161, 163, 165, 183, 188, 242
 Gillier-Pandraud, M.H., see Brusset, H. 161, 163, 165, 183, 188, 242
 Gillman, E.S., see Noginova, N. 248
 Ginatempo, B., see Staunton, J.B. 77–80, 82–83
 Gingerich, K.A. 52
 Giorgi, R., see Bianconi, A. 49, 51
 Givord, D., see Alameda, J.M. 12
 Glötzel, D., see Andersen, O.K. 19, 23, 24
 Glukhov, K.Ya. 230
 Glukhov, K.Ya., see Morozov, A.N. 230
 Glushkova, V.B., see Zinoviev, S.Yu. 225–226
 Godby, R.W. 27
 Gonis, A., see Gyorffy, B.L. 6, 25, 77, 79–83, 103
 Goodenough, J., see Zhou, J.-S. 193
 Goodenough, J.B. 193
 Gopalakrishnan, J., see Vidyasagar, K. 121
 Gopalan, P. 123
 Görnert, P., see Sandiumenge, F. 281
 Goto, T., see Oyamada, A. 43
 Gotsis, H.J. 20
 Goyal, A., see Shoup, S.S. 124
 Grabmaier, B.C. 300
 Grabmaier, B.C., see Blasse, G. 300–303, 320, 326, 328, 332, 338
 Greedan, J.E., see Dabkowska, H. 227, 264
 Griffith, W.P. 345
 Grigoriev, A.Y., see Schüßler-Langeheine, C. 13
 Gross, E.K.U. 15, 21
 Grübel, G., see Schüßler-Langeheine, C. 13
 Grush, M.M., see Moewes, A. 49
 Gschneidner Jr., K.A. 29–31
 Gschneidner Jr., K.A., see Eyring, L. 7–8, 29, 33, 39, 41, 49, 52–53
 Gschneidner Jr., K.A., see Hulliger, F. 33, 43
 Gschneidner Jr., K.A., see Jayaraman, A. 7, 29, 39, 48
 Gschneidner Jr., K.A., see Sinha, S.K. 8
 Gschneidner Jr., K.A., see Wachter, P. 41, 43
 Guenrikhson, V. 228
 Guenrikhson, V., see Kleptsyn, V. 228
 Gunnarsson, O. 17, 19, 26–27
 Gunnarsson, O., see Anisimov, V.I. 19, 23, 28
 Gunnarsson, O., see Aryasetiawan, F. 26–28
 Guo, J.-H., see Butorin, S.M. 49, 51
 Guo, X. 123
 Gupta, A., see Koren, G. 115
 Gupta, A., see Sandstrom, R.L. 280
 Gusarov, V.V., see Petrosyan, A.G. 119–121, 125, 191
 Gwanmesia, G. 122
 Gwanmesia, G., see Kung, J. 122
 Gyorffy, B.L. 6, 25, 77, 79–83, 103
 Gyorffy, B.L., see Arola, E. 6, 70–71, 74
 Gyorffy, B.L., see Johnson, D.D. 79, 81
 Györffy, B.L., see Lüders, M. 5, 24, 79, 84, 97
 Gyorffy, B.L., see Razee, S.S.A. 79
 Gyorffy, B.L., see Staunton, J. 25, 70, 77, 79, 82, 83, 85
 Gyorffy, B.L., see Staunton, J.B. 77–80, 82–83
 Gyorffy, B.L., see Stocks, G.M. 25, 79, 81–82
 Gyorffy, B.L., see Strange, P. 5, 9, 17, 39–40, 61, 70–71, 74, 82
 Gyorffy, B.L., see Szotek, Z. 13, 44–46, 53, 89
 Ha, J.K., see LeClair, P. 34
 Haasen, P., see Kübler, J. 14, 17–18, 78
 Haga, Y., see Li, D.X. 43
 Haga, Y., see Mori, N. 44
 Haman, D.R., see Andersen, P.W. 103–104
 Hamelink, J.J. 300, 320
 Hamelink, J.J., see Blasse, G. 300–303, 320, 326, 328, 332, 338
 Hamman, J., see Radhakrishna, P. 153, 162
 Hammann, J., see Bonville, P. 43
 Hanada, T., see Liu, G. 115
 Hangloo, V., see Razdan, A.K. 122
 Hansen, T., see Lerch, M. 230–231
 Hansen, T.J. 230–231
 Hanyu, T. 49
 Hao, X., see Moodera, J.S. 34
 Harjo, S., see Mori, K. 248
 Harmalker, S.P., see Alizadeh, M.H. 303
 Harmon, B.N. 86
 Harmon, B.N., see Schirber, J.E. 13–14
 Harris, I.R., see Abell, S. 119
 Hashi, K., see Li, D.X. 43
 Hashi, K., see Oyamada, A. 43
 Hashimoto, T., see Shibasaki, T. 229
 Hassan, A.K. 12
 Haule, K. 29
 Haule, K., see Kotliar, G. 28, 29

- Hauptfleisch, B.Z., see Müller, A. 299, 352
 Havinga, E.E. 43
 Havrilla, G.J., see Schoonover, J.R. 231
 Hayes, F. 120
 Hayes, F., see Kaufman, L. 120
 Heathman, S., see Bihan, T.L. 46
 Heaton, R.A. 22
 Heckel, M.C., see Creaser, I. 303
 Hedin, L. 16, 26
 Hedley, D.C.R., see Fretwell, H.M. 13
 Hegarty, G.D. 334
 Heinemann, M. 4, 86
 Heintz, M., see Veith, M. 124
 Held, K. 5, 28–29, 104
 Held, K., see McMahan, A.K. 29, 104
 Henderson, B. 326
 Henderson, G.F. 326
 Herbert, L., see Noginov, M.A. 115
 Herbich, J., see van der Poel, W.A.J.A. 303
 Hergert, W., see Hughes, I.D. 6, 79, 86, 91, 94
 Hergert, W., see Lüders, M. 5, 24, 79, 84, 97
 Hettler, M.H. 104
 Heyns, J.B., see Niven, M.L. 320
 Hidaka, M., see Watanabe, S. 133, 135
 Higuchi, T., see Chantis, A.N. 5, 27
 Hill, C.L. 299
 Hill, J.P. 70
 Hilpert, K., see Matraszek, A. 163
 Hinken, J., see Krupka, J. 282
 Hirai, T., see Yamane, H. 224, 246
 Hirayama, F., see Inokuti, H. 334
 Hirayama, F.J. 334
 Hirosaki, N. 52–53
 Hjortstam, O., see Eriksson, O. 12–13, 18–19, 86
 Hochheimer, H.D., see Werner, A. 48
 Hodges, J.A., see Bonville, P. 43
 Hoekstra, H.R. 52
 Hohenberg, P. 4, 15–16, 77
 Hohlwein, D., see Lehnert, H. 126
 Holland-Moritz, N.Z. 49
 Holland-Moritz, E., see Debray, D. 46
 Holtzberg, F., see Pollak, R.A. 67–68
 Holzapfel, W.B., see Benedict, U. 46
 Hong, K.S., see Cho, S.Y. 227, 249
 Hong, K.S., see Kim, D.W. 216
 Hopkins, R.H., see Mazelsky, R. 125, 145
 Hopkins, R.H.J. 125, 145
 Horiuchi, H., see Saitow, A. 186, 188
 Horiuchi, H., see Shishido, T. 122, 128, 149, 158, 227, 231–232
 Horiuchi, H., see Yoshikawa, A. 138, 186–187
 Horne, M. 36, 40
 Horne, M., see Aerts, C.M. 33
 Horne, M., see Arola, E. 6, 70–71, 74
 Horne, M., see Brown, S.D. 73–76
 Horne, M., see Svane, A. 18, 23, 29, 36, 38, 40–42, 44–49, 66, 99
 Horrocks, Jr., W. deW. 305, 315–316, 332
 Horrocks, Jr., W. deW., see Supkowski, R.M. 315–316
 Hoshikawa, A., see Mori, K. 248
 Hoshikawa, K., see Okano, Y. 125
 Hosoya, S., see Shishido, T. 122, 128, 149, 158, 227, 231–232
 Howard, C.J., see Carpenter, M.A. 134–135
 Howard, C.J., see Kennedy, B.J. 135, 182, 183
 Howard, C.J., see Moussa, S.M. 134
 Hoy, D.S., see Yang, W.H. 222
 Hriljac, J.A., see Kennedy, B.J. 135, 182, 183
 Hsu, Y.C., see Wang, S.F. 216
 Hu, M., see Kumar, R.S. 49
 Huang, Z.R., see Yang, C.Y. 125
 Hubbard, J. 19, 28, 65
 Huber, L. 334
 Huber, L., see Hegarty, G.D. 334
 Huch, V., see Veith, M. 124
 Hüfner, S., see Mathur, S. 124
 Hüfner, S., see Veith, M. 124
 Hüfner, S., see Freeman, A.J. 4, 14, 24
 Hughes, I.D. 6, 79, 86, 91, 94
 Hui, F.L., see Ono, S. 39
 Hulliger, F. 33, 43
 Hulliger, F., see Li, D.X. 43
 Hulliger, F., see Oyamada, A. 43
 Huntelaar, M.E., see Putnam, R.M. 115, 120, 123
 Hunter, B.A., see Moussa, S.M. 134
 Hybertsen, M.S. 27–28
 Hybler, J., see Chval, J. 189, 191
 Iandelli, A. 39, 43
 Ibal, J. 302
 Ibberson, R.M., see Moussa, S.M. 216
 Iddles, D., see Badshaw, H. 220
 Iddles, D.M., see Moussa, S.M. 216
 Ikawa, T., see Yamase, T. 299, 301–306, 311–320, 322, 325–348, 350–351
 Ikeya, T., see Kimura, K. 115, 125
 Ikeya, T., see Okano, Y. 125
 Illas, F., see Loschen, C. 51
 Ilyukhin, V.V., see Arsenev, P.A. 120–121, 138, 161, 189
 Imbert, P., see Bonville, P. 43
 Inbusch, G.F., see Henderson, B. 326
 Inokuti, H. 334
 Irvine, J.T.S., see Slater, P.R. 115, 230–234, 249, 276
 Ishi, M. 115
 Ishigaki, T., see Mori, K. 248
 Ishigaki, T., see Robinson, R.A. 43

- Ishihara, T., see Slater, P.R. 115, 230–234, 249, 276
 Ishii, H., see Hanyu, T. 49
 Ishii, T., see Hanyu, T. 49
 Ishikawa, E., see Yamase, T. 299, 301–306, 311–320, 322, 325–348, 350–351
 Isshiki, M., see Shim, J.B. 125
 Ito, T. 67
 Ito, T., see Chantis, A.N. 5, 27
 Itoh, K., see Mori, K. 248
 Itoh, M. 168, 191, 224
 Itoh, M., see Kyomen, T. 168, 191, 224
 Ivanov, A.O., see Ananieva, G.V. 125, 153, 155
 Iwasaki, H., see Shishido, T. 122, 128, 149, 158, 227, 231–232
 Iwase, K., see Mori, K. 248
 Izumi, K., see Okada, S. 128
- Jackson, C. 12–14
 Jacob, M.V., see Mazierska, J. 218
 Jang, H.M., see Moon, J.H. 217–218
 Jarrell, M., see Hettler, M.H. 104
 Jaswal, S.S., see Duan, C.-G. 20, 33
 Jayanthi, S. 216
 Jayanthi, S., see Kutty, T.R.N. 216
 Jayaraman, A. 7, 29, 39, 45, 48
 Jayaraman, A., see Werner, A. 48
 Jeannin, Y., see Alizadeh, M.H. 303
 Jéhanno, G.J., see Bonville, P. 43
 Jensen, J. 8, 60–62, 87
 Jepsen, O., see Andersen, O.K. 19, 23, 24
 Jilavi, M.H., see Mathur, S. 124
 Jilavi, M.H., see Veith, M. 124
 Jingsheng, Z., see Kebin, L. 115
 Johansson, B. 12–13, 18, 99
 Johansson, B., see Ahuja, R. 14
 Johansson, B., see Delin, A. 4, 18
 Johansson, B., see Eriksson, O. 12–13, 18–19, 86
 Johansson, B., see Skorodumova, N.V. 49
 Johansson, B., see Svane, A. 18, 23, 29, 36, 38, 40–42, 44–49, 66, 99
 Johansson, B., see Temmerman, W.M. 4–5, 13–14, 21, 24–25, 36, 40–42, 45–46, 48, 53, 79, 81–82, 86
 Johnson, D.D. 79, 81
 Johnson, D.D., see Crisan, V. 79
 Johnson, D.D., see Gyorffy, B.L. 6, 25, 77, 79–83, 103
 Johnson, D.D., see Ling, M.F. 79
 Johnson, D.D., see Staunton, J.B. 77–80, 82–83
 Jones, C.W., see Battle, P.D. 182
 Jones, D.E., see Noginov, M.A. 115
 Jones, D.W. 13
 Jones, D.W., see Young, R.C. 13
- Jones, R.O. 17
 Jordan, R.G., see Young, R.C. 13
 Joyce, J.J. 41
 Jung, H., see Lim, D.-G. 219
- Kagawa, M., see Takeda, N. 43
 Kageyama, H., see Yashima, M. 249
 Kaindl, G., see Döbrich, K.M. 13
 Kaindl, G., see Schüßler-Langeheine, C. 13
 Kakehashi, Y. 77, 103
 Kakimoto, K.I. 218
 Kakimoto, K.I., see Shimada, T. 218
 Kakizaki, A., see Cho, E.-J. 41
 Kaleva, G.M., see Polteva, T.V. 248
 Kalinchenko, A.V., see Krylov, V.S. 121
 Kamada, T., see Hanyu, T. 49
 Kamiyama, T., see Mori, K. 248
 Kamiyami, T., see Robinson, R.A. 43
 Kanchana, V., see Gerward, L. 51
 Kanchana, V., see Kumar, R.S. 49
 Kanchana, V., see Svane, A. 18, 23, 29, 36, 38, 40–42, 44–49, 66, 99
 Kanchana, V., see Vaitheeswaran, G. 36, 44
 Kaneta, Y.J., see Sakai, O. 29
 Kanke, Y. 120–121, 227
 Kapala, J.J. 227
 Kappler, J.P., see Krill, G. 40
 Kapuniak, J., see Berkowski, M. 228, 249
 Karnatak, R.C. 49
 Kartenko, N.F., see Nenasheva, E.N. 218–219, 282–283
 Kartenko, N.F., see Shelykh, A.I. 128, 222
 Kasuya, T. 11, 43
 Kasuya, T., see Cho, E.-J. 41
 Kasuya, T., see Li, D.X. 43
 Kato, H., see Cho, E.-J. 41
 Kato, H., see Hanyu, T. 49
 Katsnelson, M.I. 65
 Katsnelson, M.I., see Lebegue, S. 44, 65, 68–69
 Kaufherr, N. 128
 Kaufman, L. 120
 Kazanskii, L.P., see Molchanov, V.I. 303
 Kebin, L. 115
 Keeton, S.C. 89
 Keith, M.L. 121, 128, 222, 241
 Keller, E.K., see Leonov, A.I. 128, 170, 227
 Keller, J., see Zölfl, M.B. 29
 Kennedy, B.J. 135, 182, 183
 Kennedy, B.J., see Carpenter, M.A. 134–135
 Kennedy, B.J., see Moussa, S.M. 134
 Kern, S. 49
 Kettle, S.F.A., see Yamase, T. 299, 301–306, 311–320, 322, 325–348, 350–351
 Key, T.S. 120

- Kharton, V.V. 248
 Khawa, I.A. 338
 Khenata, R., see Bouhemadou, A. 47
 Kim, B.H., see Lim, D.-G. 219
 Kim, D.W. 216
 Kim, D.Y., see Kim, D.W. 216
 Kim, H.S., see Moon, J.H. 217–218
 Kim, I.T., see Cho, S.Y. 227, 249
 Kim, M.-H. 282
 Kim, T., see Cronin, L. 347
 Kim, T.-G., see Lim, D.-G. 219
 Kim, Y.S. 128
 Kimura, K. 115, 125
 Kimura, S., see Ufuktepe, Y. 69
 King, G.L. 228–229
 Kinoshita, T., see Ufuktepe, Y. 69
 Kiseleva, T.P. 117
 Kisielewski, J., see Pawlak, D.A. 125
 Kittel, C. 10–11
 Kjems, J.K., see Birgeneau, R.J. 132
 Klassen, N.V., see Shmurak, S.Z. 124
 Klemenz, C., see Marti, W. 229, 242
 Kleptsyn, V. 228
 Knapp, M., see Senyshyn, A. 152, 238, 242–244, 246, 248, 251–253, 262, 265, 267, 274, 276, 278, 280, 282
 Knapp, M., see Vasylechko, L. 122, 129, 132, 138, 140, 142, 145–146, 148–150, 152, 155, 165, 168, 170, 173, 189, 191, 204, 206–208, 210, 213, 227–228, 230–232, 235, 237, 240–242, 245–247, 249, 251–253, 266–267, 275
 Knight, K.S., see Carpenter, M.A. 134–135
 Knyazev, S.N., see Morozov, A.N. 228
 Ko, H.J., see Liu, G. 115
 Ko, K., see Cho, S.Y. 227, 249
 Kobayashi, J. 229–230
 Kobayashi, T., see Yamase, T. 299, 301–306, 311–320, 322, 325–348, 350–351
 Kobelev, N.P., see Shmurak, S.Z. 124
 Kocer, C.J., see Hirosaki, N. 52–53
 Ködderitzsch, D., see Lüders, M. 5, 24, 79, 84, 97
 Koelling, D.D. 14, 49, 51
 Koelling, D.D., see Pickett, W.E. 14
 Koelling, D.D., see Schirber, J.E. 13–14
 Koepernik, K., see Eschrig, H. 14, 19
 Kögerler, P. 342
 Kögerler, P., see Cronin, L. 347
 Koh, H., see Döbrich, K.M. 13
 Kohgi, M., see Robinson, R.A. 43
 Kohlhepp, J.T., see Filip, A.T. 34
 Kohlhepp, J.T., see LeClair, P. 34
 Kohn, W. 4, 15–16, 77, 79
 Kokta, M., see Carruthers, J.R. 224
 Komatsubara, T.J., see Sakon, T. 43
 Komatsubara, T.J., see Takeda, N. 43
 Konaka, T. 222, 280, 282
 Konopka, J. 222, 280, 282
 Kontrym-Sznajd, G., see Dugdale, S.B. 89
 Koop, M., see Müller, A. 299, 352
 Koopmans, B., see Filip, A.T. 34
 Koren, G. 115
 Koroleva, L.N., see Bondar, I.A. 224, 227, 275
 Korotin, M.A., see Anisimov, V.I. 19–20, 23, 28
 Korringa, J. 79
 Korzhik, M., see Moses, W.W. 115
 Kosarev, D.L., see Andrianov, A.V. 19, 23, 28
 Kosmyna, M., see Makeev, Yu. 222
 Kosola, A. 124
 Kotani, A., see Butorin, S.M. 49, 51
 Kotani, A., see Bianconi, A. 49, 51
 Kotani, A., see Ogasawara, H. 49, 51
 Kotani, A., see Tanaka, S. 49
 Kotani, A., see Ufuktepe, Y. 69
 Kotani, T. 5, 27–28
 Kotani, T., see van Schilfgaarde, M. 27–28
 Kotliar, G. 28–29
 Kotliar, G., see Georges, A. 28, 76, 103–104
 Kotliar, G., see Haule, K. 29
 Kotru, P.N. 122
 Kotru, P.N., see Razdan, A.K. 122
 Kotru, P.N., see Sharma, K.K. 220
 Kowalska, E., see Berkowski, M. 228, 249
 Kozlov, V.D., see Krylov, V.S. 121
 Kramer, E.J., see Kübler, J. 14, 17–18, 78
 Kramer, W.E. 125, 145
 Kramer, W.E., see Mazelsky, R. 125, 145
 Kraut, B.
 Krauth, W., see Georges, A. 28, 76, 103–104
 Krebs, B. 342
 Krebs, M.A., see Lux, B.C. 123
 Kreisel, J., see Bouvier, P. 128, 135
 Kresse, G., see Silva, J.L.F.D. 51
 Krickemeyer, K., see Cronin, L. 347
 Krickemeyer, E., see Müller, A. 299, 352
 Krill, G. 40
 Krishnamurthy, H.R., see Hettler, M.H. 104
 Kroeger, D.M., see Shoup, S.S. 124
 Krotilo, N.P., see Krylov, V.S. 121
 Krupka, J. 282
 Krupka, J., see Mazierska, J. 218
 Krutzen, B.C.H. 14
 Krylov, V.S. 121
 Krzhizhanovskaya, V.A., see Zinoviev, S. Yu 225–226
 Kubel, F.Z., see Marti, W. 230, 231, 234, 242, 244
 Kübler, J. 14, 17–18, 78
 Kübler, J., see Sticht, J. 14
 Kubo, S., see Konaka, T. 222, 280, 282
 Kuchtarev, N., see Loutts, G.B. 115
 Kudou, K., see Okada, S. 128

- Kudou, K., see Shishido, T. 122, 128, 149, 158, 227, 231–232
 Kudrnovský, J., see Turek, I. 87
 Kuhlmann, C., see Müller, A. 299, 352
 Kuhn, M., see Krupka, J. 282
 Kumagai, T., see Yamaguchi, I. 124
 Kumar, R.S. 49
 Kumigashira, H., see Chainani, A. 67
 Kumigashira, H., see Chantis, A.N. 5, 27
 Kumigashira, H., see Ufuktepe, Y. 69
 Kung, J. 122
 Kurz, P. 86–87
 Kushakovskii, V.I., see Budnikov, P.P. 117–118
 Kusz, J., see Bombik, A. 148, 150–151, 158, 163, 248
 Kutty, T.R.N. 216
 Kuz'min, E.A., see Saġ'yanov, Y.N. 319
 Kuz'min, M.D. 115
 Kuznetsova, T.F. 124
 Kvapi, J., see Mares, J.A. 125
 Kviatkovskii, O.E., see Vorotilova, L.S. 149
 Kyomen, T. 168, 191, 224

 Lægsgaard, J. 29
 Lægsgaard, J., see Svane, A. 18, 23, 29, 36, 38, 40–42, 44–49, 66, 99
 Laibowitz, R.B., see Koren, G. 115
 Laibowitz, R.B., see Sandstrom, R.L. 280
 Lakiza, S. 118
 Lakiza, S.M. 119
 Lal, H.B. 53, 55
 Lambrecht, W.R.L., see Larson, P. 20, 43
 Lanagan, M., see Ang, C. 216
 Landau, L.D. 103
 Lander, G.H., see Kern, S. 49
 Langford, H.D. 4
 Lapchuk, N.M., see Kharton, V.V. 248
 Larson, P. 20, 43
 Latroche, M., see Antic-Fidancev, E. 22
 Laurent, Y., see Roult, G. 138, 141
 Lebegue, S. 44, 65, 68–69
 Lecerf, N., see Veith, M. 124
 LeClair, P. 34
 LeClair, P., see Filip, A.T. 34
 Lecoq, P., see Mares, J.A. 125
 Lecoq, P., see Petrosyan, A.G. 119–121, 125, 191
 Ledenyov, D., see Mazierska, J. 218
 Lee, A.E., see Simon, R.W. 222
 Lee, D.F., see Shoup, S.S. 124
 Lee, G.S., see Simon, R.W. 222
 Lee, H.-J., see Kim, M.-H. 282
 Léger, J.M. 40, 46
 Leger, J.M., see Krill, G. 40
 Léger, J.M., see Vedel, I. 44

 Legvold, S., see Banister, J.R. 86
 Lehnert, H. 126
 Lehto, S. 228
 Lehto, S., see Nieminen, M. 228
 Lemaire, R., see Alameda, J.M. 12
 Lemaitre-Blaise, M., see Antic-Fidancev, E. 22
 Lent, B., see Abell, S. 119
 Leonov, A.I. 128, 170, 227
 Lerch, M. 230–231
 Lesniak, P.J.B. 345
 Lesniak, P.J.B., see Griffith, W.P. 345
 Lesniewska, B., see Bombik, A. 148, 150–151, 158, 163, 248
 Levin, A.A. 149
 Levin, A.A., see Vorotilova, L.S. 149
 Levy, L.P., see Hassan, A.K. 12
 Lewandowski, S.J. 222, 280, 282
 Lewandowski, S.J., see Konopka, J. 222, 280, 282
 Li, C.Z., see Yang, W.H. 222
 Li, D.X. 43
 Li, D.X., see Oyamada, A. 43
 Li, L. 117–118
 Li, S., see Zhao, G. 191
 Liang, J.K., see Liu, F.S. 224
 Lichtenstein, A.I. 19–20, 28, 65
 Lichtenstein, A.I., see Anisimov, V.I. 19, 23, 28
 Lichtenstein, A.I., see Harmon, B.N. 86
 Lichtenstein, A.I., see Lebegue, S. 44, 65, 68–69
 Lichtenstein, A.I., see Petukhov, A.G. 19
 Liebermann, R.C. 201, 204
 Liebermann, R.C., see Sasaki, S. 201, 204
 Liebermann, R.C., see Wang, Y. 228–231
 Lifschitz, E.M. 103
 Lifshitz, I.M. 89
 Lim, D.-G. 219
 Lin, C.C.J., see Pederson, M.R. 22
 Lindgren, I. 20
 Ling, M.F. 79
 Ling, M.F., see Staunton, J.B. 77–80, 82–83
 Lissalde, F., see Allibert, M. 224–225
 Lister, S.J.S., see Boothroyd, A.T. 49
 Lister, S.J.S., see Gardiner, C.H. 51
 Liu, F.S. 224
 Liu, G. 115
 Liu, G., see Yan, B. 249
 Liu, G.K., see Soderholm, L. 303
 Liu, J., see Yan, B. 249
 Liu, Q.L., see Liu, F.S. 224
 Liu, X., see Wang, Y. 228–231
 Liu, X.Q. 218
 Liu, Z.-K., see Zinkevich, M. 225, 227
 Lloyd, P. 82
 Lo, J.-R. 122
 Loewenhaupt, M., see Debray, D. 46
 Longinotti, L.D., see Campagna, M. 64, 67–69

- Lonzarich, G.G., see Wulff, M. 13, 51
 Loong, C.-K., see Kern, S. 49
 Lopato, L.M. 119
 Lopato, L.M., see Lakiza, S.M. 119
 Loriers, C., see Krill, G. 40
 Loschen, C. 51
 Loucks, T.L. 89
 Loude, J.-F., see Chval, J. 189, 191
 Louie, S.G. 27–28
 Loutts, G., see Vasylechko, L. 122, 129, 132, 138,
 140, 142, 145–146, 148–150, 152, 155, 165, 168,
 170, 173, 189, 191, 204, 206–208, 210, 213,
 227–228, 230–232, 235, 237, 240–242, 245–247,
 249, 251–253, 266–267, 275
 Loutts, G.B. 115
 Loutts, G.B., see Noginov, M.A. 115
 Loutts, G.B., see Noginova, N. 248
 Lovesey, S.W. 70, 74
 Low, J.N. 302
 Low, J.N., see Ibal, J. 302
 Lu, Q., see Alameda, J.M. 12
 Lubman, G.U., see Arakcheeva, A.V. 230
 Lüders, M. 5, 24, 79, 84, 97
 Lüders, M., see Hughes, I.D. 6, 79, 86, 91, 94
 Lufaso, M.W. 115, 192, 207, 247
 Luine, J., see Chakoumakos, B.C. 126
 Luine, J.A., see Simon, R.W. 222
 Luis, F. 138
 Luis, F., see Palacios, E. 138
 Lukasiewicz, T., see Pawlak, D.A. 125
 Lukasiewicz, T., see Vasylechko, L. 122, 129,
 132, 138, 140, 142, 145–146, 148–150, 152, 155,
 165, 168, 170, 173, 189, 191, 204, 206–208, 210,
 213, 227–228, 230–232, 235, 237, 240–242,
 245–247, 249, 251–253, 266–267, 275
 Lundqvist, B.L., see Skorodumova, N.V. 49
 Luo, J., see Liu, F.S. 224
 Luong, K., see Cronin, L. 347
 Lux, B.C. 123
 Lybye, D. 115
 Lynn, J.W., see Robinson, R.A. 43
 Lyons, K.B. 132
 Lysenko, V.A. 119, 120

 Mackintosh, A.K. 8, 60–62, 87
 Maegawa, S., see Oyamada, A. 43
 Magunov, R.L., see Krylov, V.S. 121
 Mahan, G.D. 26–27
 Maier, A.A. 119
 Major, Z., see Crowe, S.J. 13
 Makeev, Yu. 222
 Makino, H., see Liu, G. 115
 Malinowski, M., see Pawlak, D.A. 125
 Malinsky, J., see Soderholm, L. 303

 Maly, P., see Mares, J.A. 115, 125
 Manabe, T., see Yamaguchi, I. 124
 Mannix, D., see Brown, S.D. 73–76
 Mansurova, E.P., see Adylov, G.T. 119
 Marabelli, F. 49
 Marcelli, A., see Bianconi, A. 49, 51
 Marchand, R., see Roult, G. 138, 141
 Mares, J.A. 115, 125, 189
 Mares, J.A., see Chval, J. 189, 191
 Mareschal, J., see Bertaut, F. 125, 229
 Mareshal, J., see Allibert, M. 224–225
 Marezio, M. 138, 141, 143, 228–230, 235, 242,
 246–247, 249–250, 264, 268, 270
 Marianetti, C.A., see Kotliar, G. 28, 29
 Marti, W. 229–231, 233–235, 238, 239, 242, 244
 Marti, W., see Podlesnyak, A. 235
 Martin, C.D., see Kennedy, B.J. 135, 182, 183
 Martin, R.M. 15, 24–25
 Martinez, J., see Salinas-Sanchez, A. 207
 Martin-Frere, J., see Alizadeh, M.H. 303
 Martini, M., see Nikl, M. 125, 191
 Mathur, S. 124
 Mathur, S., see Veith, M. 124
 Matkovskii, A., see Savytskii, D. 231–233,
 237, 242–244
 Matkovskii, A., see Senyshyn, A. 152, 238,
 242–244, 246, 248, 251–253, 262, 265, 267,
 274, 276, 278, 280, 282
 Matkovskii, A., see Vasylechko, L. 122, 129, 132,
 138, 140, 142, 145–146, 148–150, 152, 155, 165,
 168, 170, 173, 189, 191, 204, 206–208, 210, 213,
 227–228, 230–232, 235, 237, 240–242, 245–247,
 249, 251–253, 266–267, 275
 Matkovskii, A.O. 122, 125, 129–130, 132, 142,
 150–151, 155, 206–208
 Matkovskii, A.O., see Savytskii, D.I. 125, 228,
 230, 242, 282
 Matkovskii, A.O., see Vasylechko, L.O. 228,
 230–231, 237, 240, 242, 246–247, 249,
 266–267, 275
 Matraszek, A. 163
 Matsuda, M. 228
 Matsumara, T., see Li, D.X. 43
 Matsumura, T., see Ufuktepe, Y. 69
 Mattenberger, K., see Bihan, T.L. 46
 Matteucci, F., see Cruciani, G. 121
 Mattocks, P.G. 13–14
 Mavromaras, A. 4, 18, 91
 Mayer, J., see Bombik, A. 148, 150–151,
 158, 163, 248
 Mazelsky, R. 125, 145
 Mazierska, J. 218
 Mazin, I.I. 20
 Mazin, I.I., see Petukhov, A.G. 19
 Mazumdar, C., see Schüsler-Langeheine, C. 13

- Mazur, K., see Berkowski, M. 228, 249
 McAlford, N. 218–219
 McAlford, N., see Sebastian, M.T. 218–219, 223, 282
 McAllister, W.A. 300
 McAllister, W.A., see Brittain, H.G. 300
 McGuire, T. 32
 McIntyre, G.J., see Gardiner, C.H. 51
 McKelvy, M.J., see Gardiner, C.H. 51
 McMahan, A.K. 29, 104
 McMahan, A.K., see Held, K. 5, 28–29, 104
 McMorrow, D.F. 70
 McPherson, G.L. 338
 McPherson, G.L., see Khawa, I.A. 338
 Medarde, M., see Marti, W. 229, 242
 Mehmke, J. 342
 Mehmke, J., see Krebs, B. 342
 Mei, W.N., see Duan, C.-G. 20, 33
 Meier, R., see Schüßler-Langeheine, C. 13
 Melekh, B.T., see Shelykh, A.I. 128, 222
 Melekh, B.T.J., see Prokofiev, A.V. 53, 55
 Mencke, C., see Müller, A. 299, 352
 Mendelovici, L. 128
 Mendelovici, L., see Kaufherr, N. 128
 Meng, R.L., see Werner, A. 48
 Meriel, P., see Bidaux, R. 148, 154
 Merini, R.I., see Sanjuán, M.L. 230, 233, 244, 249, 258
 Merkulyaeva, T.I., see Ananieva, G.V. 125, 153, 155
 Mermin, N.D. 77
 Meservey, R., see Moodera, J.S. 34
 Messiah, A. 81
 Meyer, J., see Müller, A. 299, 352
 Mezentseva, L.P., see Bondar, I.A. 224, 227, 275
 Miao, J.P., see An, W.W. 124
 Midgley, D., see Wanklyn, B.M. 122
 Mihokova, E., see Chval, J. 189, 191
 Miller, G., see Loutts, G.B. 115
 Miller, M., see Matraszek, A. 163
 Milstein, F. 95
 Min, B.L., see Freeman, A.J. 4, 14, 24
 Minh, N.Q.J. 115
 Minkov, B., see Moses, W.W. 115
 Mirone, A. 12
 Mitsui, A., see Yamaguchi, O. 120
 Miyahara, K., see Bianconi, A. 49, 51
 Miyahara, T., see Cho, E.-J. 41
 Miyahara, T., see Hanyu, T. 49
 Miyake, M., see Matsuda, M. 228
 Miyazaki, Y., see Yashima, M. 249
 Miyazawa, S. 228–229, 235, 242, 275–276
 Miyazawa, S., see Kobayashi, J. 229–230
 Miyazawa, S., see Sasaura, M. 115, 228–229, 235, 241–242, 275–276, 280, 282
 Miyazawa, S.J. 228, 235, 275–276
 Miyazawa, Y. 115, 125
 Miyazawa, Y., see Morita, S. 125, 189
 Miyazawa, Y., see Sekita, M. 115, 125
 Mizota, T., see Nakatsuka, A. 122, 126–127
 Mizuno, M. 117–120, 128, 138, 224–227, 230, 275
 Mizusaki, J. 125
 Mizuta, S., see Yamaguchi, I. 124
 Mocellin, A., see Alkebro, J. 123
 Mochalov, I.V., see Ananieva, G.V. 125, 153, 155
 Moeller, T. 228–229
 Moewes, A. 49
 Mogensen, M. 115
 Mogensen, M., see Lybye, D. 115
 Mohanan, P., see Sebastian, M.T. 218–219, 223, 282
 Mohn, P. 19
 Moine, B., see Mares, J.A. 125
 Molchanov, V.I. 303
 Mond, M., see Matkovskii, A.O. 125
 Moodera, J.S. 34
 Moon, J.H. 217–218
 Morel, C., see Chval, J. 189, 191
 Morell, J.S. 228
 Morell, J.S., see Beach, D.B. 124
 Moret, E. 338
 Morgenroth, W., see Vasylechko, L. 122, 129, 132, 138, 140, 142, 145–146, 148–150, 152, 155, 165, 168, 170, 173, 189, 191, 204, 206–208, 210, 213, 227–228, 230–232, 235, 237, 240–242, 245–247, 249, 251–253, 266–267, 275
 Mori, K. 248
 Mori, N. 44
 Mori, T., see Saitow, A. 186, 188
 Morita, S. 125, 189
 Morita, S., see Miyazawa, Y. 125
 Morita, S., see Sekita, M. 115, 125
 Moriya, T. 77
 Morozov, A.N. 228, 230, 233
 Morozova, O.Ya. 228, 230, 233
 Morozova, O.Ya., see Morozov, A.N. 228, 230, 233
 Moses, W.W. 115
 Mosunov, A.V., see Polteva, T.V. 248
 Motornenko, A., see Makeev, Yu. 222
 Moussa, S.M. 134, 216
 Movshovich, R., see Robinson, R.A. 43
 Mudraliubova, L.P. 218–219, 282–283
 Mudraliubova, L.P., see Nenasheva, E.N. 218–219, 282–283
 Müller, K.A., see D'Iorio, M. 133
 Mukaida, M. 115, 235, 241, 280, 282
 Mukaida, M., see Miyazawa, S. 228, 235, 242, 275
 Mukaida, M., see Sasaura, M. 115, 228–229, 235, 241–242, 275–276, 280, 282

- Mukaida, M.J. 228–229, 235, 242, 275–276
 Mulazzani, Q.G., see Ballardini, R. 301–303
 Müller, A. 299, 352
 Müller, A., see Borrás-Alamenar, J.J. 299
 Müller, A., see Cronin, L. 347
 Müller, A., see Kögerler, P. 342
 Müller, A., see Pope, M.T. 299
 Müller, A.P. 342, 347
 Müller, K.A. 126
 Muntntean, J., see Soderholm, L. 303
 Murata, K., see Matsuda, M. 228
 Myzina, V.A., see Zinoviev, S.Yu. 225–226
- Nahm, S., see Kim, M.-H. 282
 Naito, K., see Hanyu, T. 49
 Nakagawa, S., see Shishido, T. 122, 128, 149, 158, 227, 231–232
 Nakajima, K., see Okada, S. 128
 Nakatsuka, A. 122, 126–127
 Nakayama, N., see Nakatsuka, A. 122, 126–127
 Nakazawa, M., see Butorin, S.M. 49, 51
 Naruke, H. 304, 311, 320, 322, 329, 332–335, 337–339
 Naruke, H., see Ozeki, T. 304, 319, 322, 328, 334–335, 337
 Naruke, H., see Yamase, T. 299, 301–306, 311–320, 322, 325–348, 350–351
 Nath, K.G., see Ufuktepe, Y. 69
 Naumovich, E.N., see Kharton, V.V. 248
 Navaza, A., see Rivero, B.E. 319
 Navrotsky, A., see Kanke, Y. 120–121, 227
 Navrotsky, A., see Putnam, R.M. 115, 120, 123
 Navrotsky, A., see Zhang, Y. 124
 Navrotsky, A.J. 120–121, 124, 227, 249
 Neitz, R.J., see Creaser, I. 303
 Nejezchleb, K., see Chval, J. 189, 191
 Nejezchleb, K., see Mares, J.A. 115, 125
 Nekrasov, I.A., see Zöfl, M.B. 29
 Nenashaeva, E.N. 218–219, 282–283
 Neugebauer, J., see Rinke, P. 27
 Neuroth, G. 125
 Neyman, K.M., see Loschen, C. 51
 Nicholson, D.M., see Gyorffy, B.L. 6, 25, 77, 79–83, 103
 Nicholson, D.M., see Johnson, D.D. 79, 81
 Nicholson, D.M.C. 99
 Nicol, F., see Kumar, R.S. 49
 Nicolas, J. 224–225, 227, 246, 275
 Nicolas, J., see Coutures, J. 224
 Nielsen, K.J. 148, 150, 155, 157, 165
 Nieminen, M. 228
 Niewa, R., see Vasylechko, L. 122, 129, 132, 138, 140, 142, 145–146, 148–150, 152, 155, 165, 168, 170, 173, 189, 191, 204, 206–208, 210, 213, 227–228, 230–232, 235, 237, 240–242, 245–247, 249, 251–253, 266–267, 275
 Niinisto, L., see Kosola, A. 124
 Niinisto, L., see Nieminen, M. 228
 Nikl, M. 125, 191
 Nikl, M., see Chval, J. 189, 191
 Nikl, M., see Mares, J.A. 115, 125
 Nikl, M., see Shim, J.B. 125
 Nishikubo, K., see Wang, X. 122, 222
 Nishiya, S., see Yamase, T. 299, 301–306, 311–320, 322, 325–348, 350–351
 Nitsche, H., see Zinkevich, M. 225, 227
 Niven, M.L. 320
 Noailles, B.D.R.L.D., see Boothroyd, A.T. 49
 Noginov, M.A. 115
 Noginov, M.A., see Loutts, G.B. 115
 Noginova, N. 248
 Noginova, N., see Loutts, G.B. 115
 Noguchi, T. 117–120, 128, 138
 Noguchi, T., see Mizuno, M. 118–119
 Nojima, S., see Shishido, T. 122, 128, 149, 158, 227, 231–232
 Nomura, K., see Yashima, M. 249
 Noort, M., see van der Poel, W.A.J.A. 303
 Nordgren, J., see Butorin, S.M. 49, 51
 Nordland, W.A. 175, 183, 223–224
 Nordland, W.A., see Cohen, E. 132
 Nordström, L. 4, 18, 91
 Norman, M.R., see Freeman, A.J. 4, 14, 24
 Noteristefani, F., see Mares, J.A. 115, 125
 Novak, P., see Mohn, P. 19
 Nozieres, P. 104
 Numazawa, T., see Kimura, K. 115, 125
 Nunez, V., see Brown, P.J. 151
 Nusair, M., see Vosko, S.H. 16
- O'Bryan, H.M. 138, 217, 229–230, 235, 242
 O'Grady, P.J. 301
 O'Grady, P.J., see Darwent, J. 301
 O'Keefe, M., see Brese, N.E. 205
 Ocio, M., see Radhakrishna, P. 153, 162
 Oda, O., see Okazaki, H. 115
 Ofelt, G.S. 311
 Ogasawara, H. 49, 51
 Ogasawara, H., see Tanaka, S. 49
 Ogasawara, H., see Ufuktepe, Y. 69
 Ogata, S., see Hirosaki, N. 52–53
 Ogawara, K., see Yamane, H. 224, 246
 Oh, S.-J. 68
 Oh, S.-J., see Cho, E.-J. 41
 Ohara, O., see Matsuda, M. 228
 Ohara, S., see Matsuda, M. 228
 Ohsato, H., see Shimada, T. 218

- Ohsato, H.J. 218
 Ohtaka, O., see Nakatsuka, A. 122, 126–127
 Ohtake, T. 224–227, 230, 275
 Okada, K., see Bianconi, A. 49, 51
 Okada, K., see Ogasawara, H. 49, 51
 Okada, K., see Tanaka, S. 49
 Okada, S. 128
 Okada, S., see Shishido, T. 122, 128, 149, 158, 227, 231–232
 Okano, Y. 125
 Okayama, Y., see Mori, N. 44
 Okazaki, H. 115
 Olcese, G.L., see Iandelli, A. 39, 43
 Oles, A., see Bombik, A. 148, 150–151, 158, 163, 248
 Oliver, G.L., see Zunger, A. 5, 16, 20–22
 Olsen, J.S., see Gerward, L. 51
 Olson, C.G., see Joyce, J.J. 41
 Omori, M., see Yamane, H. 224, 246
 Ono, S. 39
 Oppeneer, P.M. 43
 Oppeneer, P.M., see Antonov, V.N. 20
 Orera, V.M., see Sanjuán, M.L. 230, 233, 244, 249, 258
 Ormeci, A., see Eriksson, O. 12–13, 18–19, 86
 Ostanin, S., see Staunton, J.B. 77–80, 82–83
 Ott, H.R. 43
 Oudovenko, V., see Haule, K. 29
 Oudovenko, V.S., see Kotliar, G. 28, 29
 Ovanesian, K.L., see Petrosyan, A.G. 119–121, 125, 191
 Ovchar, O.V., see Belous, A.G. 216
 Oyamada, A. 43
 Oyamada, A., see Li, D.X. 43
 Oyamada, A., see Sakon, T. 43
 Oyamada, A., see Takeda, N. 43
 Ozeki, T. 304, 319, 322, 328, 334–335, 337
 Ozeki, T., see Naruke, H. 304, 311, 320, 322, 329, 332–335, 337–339
 Ozeki, T., see Yamase, T. 299, 301–306, 311–320, 322, 325–348, 350–351
- Pacyna, A.W., see Bombik, A. 148, 150–151, 158, 163, 248
 Palacios, E. 138
 Palenzona, A.J. 43
 Palenzona, A.J., see Iandelli, A. 39, 43
 Palmer, S.B., see Alameda, J.M. 12
 Palmer, S.B., see Crowe, S.J. 13
 Palmer, S.B., see Fretwell, H.M. 13
 Palvasaari, J., see Kosola, A. 124
 Pamio, A. 227
 Pamio, A., see Polini, R. 227
 Paranthaman, M., see Beach, D.B. 124
 Paranthaman, M., see Shoup, S.S. 124
 Parcollet, O., see Kotliar, G. 28, 29
 Pari, P., see Radhakrishna, P. 153, 162
 Parise, J.B., see Kennedy, B.J. 135, 182, 183
 Park, H.-M., see Kim, M.-H. 282
 Park, H.S., see Moon, J.H. 217–218
 Parkes, C.C. 338
 Parkes, C.C., see Khawa, I.A. 338
 Pashkov, V.M., see Savvytskii, D.I. 125, 228, 230, 242, 282
 Pastuszak, R., see Roult, G. 138, 141
 Pattison, P., see Gardiner, C.H. 51
 Paulmann, C., see Vasylechko, L. 122, 129, 132, 138, 140, 142, 145–146, 148–150, 152, 155, 165, 168, 170, 173, 189, 191, 204, 206–208, 210, 213, 227–228, 230–232, 235, 237, 240–242, 245–247, 249, 251–253, 266–267, 275
 Pawlak, D.A. 125
 Pederson, M.R. 22
 Pedrini, C., see Mares, J.A. 125
 Pedrini, C., see Petrosyan, A.G. 119–121, 125, 191
 Pejchal, J., see Nikl, M. 125, 191
 Pejchal, J., see Shim, J.B. 125
 Pelton, D., see Wu, P. 120–121
 Pelton, D.J. 120–121
 Pena, M.A. 115
 Perčuĉ, L., see Berkowski, M. 228, 249
 Perdew, J.P. 5, 16, 20–22
 Perlov, A.Y., see Antonov, V.N. 20
 Perlov, A.Y., see Oppeneer, P.M. 43
 Persson, C., see Mohn, P. 19
 Peter, F., see Müller, A. 299, 352
 Petermann, K., see Matkovskii, A.O. 125
 Peterson, E., see Robinson, R.A. 43
 Petit, L. 52–53, 56
 Petit, L., see Gerward, L. 51
 Petit, L., see Svane, A. 18, 23, 29, 36, 38, 40–42, 44–49, 66, 99
 Petit, L., see Vaitheeswaran, G. 36, 44
 Petrosyan, A.G. 119–121, 125, 191
 Pettifor, D.G. 4, 13, 18
 Petukhov, A.G. 19
 Phariseau, P., see Gyorffy, B.L. 6, 25, 77, 79–83, 103
 Phariseau, P., see Stocks, G.M. 25, 79, 81–82
 Pickett, W.E. 14
 Piekarczyk, W., see Berkowski, M. 228, 249
 Piekarczyk, W., see Vasylechko, L. 122, 129, 132, 138, 140, 142, 145–146, 148–150, 152, 155, 165, 168, 170, 173, 189, 191, 204, 206–208, 210, 213, 227–228, 230–232, 235, 237, 240–242, 245–247, 249, 251–253, 266–267, 275

- Pindor, A.J., see Gyorffy, B.L. 6, 25, 77, 79–83, 103
- Pindor, A.J., see Staunton, J. 25, 70, 77, 79, 82, 83, 85
- Pinski, F.J., see Gyorffy, B.L. 6, 25, 77, 79–83, 103
- Pinski, F.J., see Johnson, D.D. 79, 81
- Piriou, B., see Alain, P. 142
- Pivak, Ye., see Vasylechko, L. 122, 129, 132, 138, 140, 142, 145–146, 148–150, 152, 155, 165, 168, 170, 173, 189, 191, 204, 206–208, 210, 213, 227–228, 230–232, 235, 237, 240–242, 245–247, 249, 251–253, 266–267, 275
- Plan, C.E., see Simon, R.W. 222
- Poddenezhnyj, E.N., see Kuznetsova, T.F. 124
- Podlesnyak, A. 235
- Poirier, D.M., see Joyce, J.J. 41
- Pokrovskii, B.L., see Arsenev, P.A. 120–121, 138, 161, 189
- Polini, R. 227
- Politova, E.D., see Polteva, T.V. 248
- Pollak, R.A. 67–68
- Polteva, T.V. 248
- Ponomarev, N.M., see Morozov, A.N. 228, 230, 233
- Pope, M.T. 299
- Pope, M.T., see Alizadeh, M.H. 303
- Pope, M.T., see Borrás-Alamenar, J.J. 299
- Pope, M.T., see Creaser, I. 303
- Popov, V.A., see Arakcheeva, A.V. 230
- Popova, V.F. 119
- Popova, V.F., see Petrosyan, A.G. 119–121, 125, 191
- Porcher, P., see Antic-Fidancev, E. 22
- Pornoj, K.I. 145, 173, 189, 235, 275
- Potemkin, A.V., see Arsenev, P.A. 120–121, 138, 161, 189
- Poulsen, W.F. 115
- Poulsen, W.F., see Lybye, D. 115
- Poulter, J., see Hughes, I.D. 6, 79, 86, 91, 94
- Powell, R.C. 328
- Pramanik, P. 123
- Prewitt, C.T. 201, 204
- Prewitt, C.T., see Sasaki, S. 201, 204
- Price, T., see Moussa, S.M. 216
- Prieto, J.E., see Döbrich, K.M. 13
- Prodjosantoso, A.K., see Kennedy, B.J. 135, 182, 183
- Prokofiev, A.V. 53, 55
- Prokofyev, A.V., see Shelykh, A.I. 128, 222
- Prokop, P., see Yamase, T. 299, 301–306, 311–320, 322, 325–348, 350–351
- Pruschke, T., see Hettler, M.H. 104
- Pruschke, T., see Zölfl, M.B. 29
- Prutchenko, S.G., see Polteva, T.V. 248
- Przewoznik, J., see Bombik, A. 148, 150–151, 158, 163, 248
- Puertolas, D., see Mares, J.A. 115, 125
- Punte, G., see Rivero, B.E. 319
- Purwanto, A., see Robinson, R.A. 43
- Pushcharovskii, D.Yu., see Arakcheeva, A.V. 230
- Putkonen, M., see Kosola, A. 124
- Putnam, R.M. 115, 120, 123
- Qteish, A., see Rinke, P. 27
- Quinby, R., see Badshaw, H. 220
- Rachimov, R.R., see Loutts, G.B. 115
- Rachimov, R.R., see Noginov, M.A. 115
- Radaelli, P., see Lehnert, H. 126
- Radhakrishna, P. 153, 162
- Raiskaya, L.N., see Bondar, I.A. 224, 227, 275
- Rajagopalan, M.J., see Vaitheeswaran, G. 36, 44
- Randall, C.A., see Ang, C. 216
- Randall, K., see Tilkens, L. 319
- Ranløv, J. 148, 150, 155, 157, 165
- Rao, C.N.R., see Vidyasagar, K. 121
- Rao, G.H. 207
- Rao, G.H., see Liu, F.S. 224
- Rao, K.J. 124
- Rao, R.P.J. 122
- Ratheesh, R., see Sebastian, M.T. 218–219, 223, 282
- Ravet, M.F., see Krill, G. 40
- Razdan, A.K. 122
- Razdan, A.K., see Kotru, P.N. 122
- Razee, S.S.A. 79
- Razee, S.S.A., see Staunton, J.B. 77–80, 82–83
- Reaney, I.-M., see Badshaw, H. 220
- Red'ko, N., see Vasylechko, L.O. 228, 230–231, 237, 240, 242, 246–247, 249, 266–267, 275
- Red'ko, N.A., see Vasylechko, L.O. 228, 230–231, 237, 240, 242, 246–247, 249, 266–267, 275
- Redon, A.M., see Vedel, I. 44
- Reid, A.F. 158, 169
- Reller, A. 114
- Remeika, J.P. 228–230, 235, 242, 246–247, 249–250, 264, 268, 270
- Remeika, J.P., see Marezio, M. 228–230, 235, 242, 246–247, 249–250, 264, 268, 270
- Remeika, P., see Marezio, M. 138, 141, 143
- Remeika, P.J. 138, 141, 143
- Remejka, J.P. 228
- Remejka, J.P., see Marezio, M. 228
- Reppart, W.J. 319
- Reppart, W.J., see Gerkin, R.E. 319
- Rhyne, J.J. 32

- Richter, M. 14
 Richter, M., see Eschrig, H. 14, 19
 Richter, M., see Schüßler-Langeheine, C. 13
 Ries, H.R., see Loutts, G.B. 115
 Rigden, S. 122
 Rigden, S., see Kung, J. 122
 Rigotti, G., see Rivero, B.E. 319
 Ringwood, A.E. 158, 169
 Ringwood, A.E.Z. 122, 158, 169
 Ringwood, A.E.Z., see Sinclair, W. 122, 158, 169
 Rinke, P. 27
 Riseberg, L.A., see Cohen, E. 132
 Rivero, B.E. 319
 Robertson, J. 216–217
 Robinson, L.B. 95
 Robinson, R.A. 43
 Robles, J., see Carruthers, J.R. 224
 Rodriguez-Carvajal, J., see Salinas-Sanchez, A. 207
 Rodriguez-Gonzalez, A., see Fretwell, H.M. 13
 Rolin, M. 117
 Rosengren, A. 18
 Rosenkranz, S., see Podlesnyak, A. 235
 Ross, N.L. 128, 137, 145, 147, 157, 161, 167, 169
 Ross, N.L., see Zhao, J. 128, 137, 145
 Rossat-Mignod, J., see Vedel, I. 44
 Rosseinsky, M.J., see Cussen, E.J. 248
 Rosseinsky, M.J., see Moussa, S.M. 216
 Rossnagel, K., see Döbrich, K.M. 13
 Rosso, E., see Mares, J.A. 115, 125
 Rostoker, N. 79
 Rotenberg, E., see Döbrich, K.M. 13
 Roth, R.S. 128
 Roth, R.S., see Schneider, S.J. 121, 224–226
 Roullet, G. 138, 141
 Roy, R. 121, 128, 222, 241
 Roy, R., see Keith, M.L. 121, 128, 222, 241
 Roy, R., see Warshaw, I. 119
 Rozenberg, M.J., see Georges, A. 28, 76, 103–104
 Rozenkranz, S., see Marti, W. 229, 242
 Ruban, A.V., see Johansson, B. 18–19, 99
 Ruderman, M.A. 11
 Rudigier, H. 43
 Ruggiero, A. 228–229, 231, 235, 241
 Ruse, G.F. 228
 Rusz, J. 51
- Saab, A., see Schoonover, J.R. 231
 Sabirianov, R.F., see Duan, C.-G. 20, 33
 Saez-Puche, R., see Salinas-Sanchez, A. 207
 Saf'yanov, Y.N. 319
 Sahnoun, M., see Bouhemadou, A. 47
 Saine, M.C., see Brusset, H. 161, 163, 165, 183, 188, 242
- Saito, A., see Shishido, T. 122, 128, 149, 158, 227, 231–232
 Saito, F., see Zhang, Q. 123
 Saito, F.J. 123
 Saitow, A. 186, 188
 Saitow, A., see Yoshikawa, A. 138, 186–187
 Sakai, O. 29
 Sakamoto, H., see Yamase, T. 299, 301–306, 311–320, 322, 325–348, 350–351
 Sakatsumi, S., see Takeda, N. 43
 Sakon, T. 43
 Sakurai, K. 123
 Salazar, A., see Lux, B.C. 123
 Salinas-Sanchez, A. 207
 Samara, G.A. 222
 San José Wéry, A.M., see Yamase, T. 299, 301–306, 311–320, 322, 325–348, 350–351
 Sandiumenge, F. 281
 Sandratsakii, L.M. 14
 Sandstrom, R.L. 280
 Sanjuán, M.L. 230, 233, 244, 249, 258
 Sanjuan, M.L., see Savytskii, D. 231–233, 237, 242–244
 Santi, G., see Svane, A. 18, 23, 29, 36, 38, 40–42, 44–49, 66, 99
 Santini, P., see Boothroyd, A.T. 49
 Sargolzaei, M., see Eschrig, H. 14, 19
 Sasaki, R., see Yamase, T. 299, 301–306, 311–320, 322, 325–348, 350–351
 Sasaki, S. 201, 204
 Sasaki, S., see Saitow, A. 186, 188
 Sasaki, T., see Shishido, T. 122, 128, 149, 158, 227, 231–232
 Sasaki, Y., see Ozeki, T. 304, 319, 322, 328, 334–335, 337
 Sasaura, M. 115, 228–229, 235, 241–242, 275–276, 280, 282
 Sasaura, M., see Kobayashi, J. 229–230
 Sasaura, M., see Miyazawa, S. 228, 235, 242, 275
 Sass, J., see Berkowski, M. 228, 249
 Sato, M., see Kimura, K. 115, 125
 Sato, M., see Konaka, T. 222, 280, 282
 Sato, N., see Sakon, T. 43
 Sato, N., see Takeda, N. 43
 Sato, N.K., see Chantis, A.N. 5, 27
 Sato, N.K., see Ito, T. 67
 Sato, T., see Chantis, A.N. 5, 27
 Sato, Y., see Sekita, M. 115, 125
 Sauer, J., see Silva, J.L.F.D. 51
 Savinova, I.G. 119
 Savinova, I.G., see Maier, A.A. 119
 Savrasov, S.Y., see Haule, K. 29
 Savrasov, S.Y., see Kotliar, G. 28, 29
 Savytskii, D. 231–233, 237, 242–244

- Savytskii, D., see Senyshyn, A. 152, 238, 242–244, 246, 248, 251–253, 262, 265, 267, 274, 276, 278, 280, 282
- Savytskii, D., see Vasylechko, L. 122, 129, 132, 138, 140, 142, 145–146, 148–150, 152, 155, 165, 168, 170, 173, 189, 191, 204, 206–208, 210, 213, 227–228, 230–232, 235, 237, 240–242, 245–247, 249, 251–253, 266–267, 275
- Savytskii, D.I. 125, 228, 230, 242, 282
- Savytskii, D.I., see Berkowski, M. 228, 249
- Savytskii, D.I., see Matkovskii, A.O. 125
- Savytskii, D.I., see Vasylechko, L.O. 228, 230–231, 237, 240, 242, 246–247, 249, 266–267, 275
- Sawatzky, G.A., see Anisimov, V.I. 19–20, 23, 28
- Saxena, S.K., see Zinkevich, M. 225, 227
- Scalettar, R.T., see Held, K. 5, 28–29, 104
- Scalettar, R.T., see McMahan, A.K. 29, 104
- Scarel, G. 49, 53
- Scarel, G., see Petit, L. 52–53, 56
- Scheel, H.J. 115, 242
- Scheel, H.J., see Marti, W. 230, 231, 233–235, 238–239, 242, 244
- Schefer, J., see Marti, W. 230, 231, 234, 242, 244
- Scheffler, M., see Rinke, P. 27
- Scheire, L. 25
- Scheire, L., see Gyorffy, B.L. 6, 25, 77, 79–83, 103
- Schenk, K., see Moret, E. 338
- Schiffmacher, G., see Coutures, J. 224
- Schipper, W. 300, 320
- Schipper, W., see Blasse, G. 300–303, 320, 326, 328, 332, 338
- Schirber, J.E. 13–14
- Schlom, D.G., see Chakoumakos, B.C. 126
- Schlüter, M., see Godby, R.W. 27
- Schmidt, F.A., see Schirber, J.E. 13–14
- Schmidt, H., see Vasylechko, L. 122, 129, 132, 138, 140, 142, 145–146, 148–150, 152, 155, 165, 168, 170, 173, 189, 191, 204, 206–208, 210, 213, 227–228, 230–232, 235, 237, 240–242, 245–247, 249, 251–253, 266–267, 275
- Schmidtman, M., see Cronin, L. 347
- Schmidtman, M., see Müller, A. 299, 352
- Schmidtman, M.E., see Müller, A. 299, 352
- Schneider, J., see Lehnert, H. 126
- Schneider, S.J. 121, 224–226
- Schneider, W.-D., see Wuilloud, E. 49, 51
- Schnelle, W., see Vasylechko, L. 122, 129, 132, 138, 140, 142, 145–146, 148–150, 152, 155, 165, 168, 170, 173, 189, 191, 204, 206–208, 210, 213, 227–228, 230–232, 235, 237, 240–242, 245–247, 249, 251–253, 266–267, 275
- Schoonover, J.R. 231
- Schüßler-Langeheine, C. 13
- Schwarz, K., see Mohn, P. 19
- Scott, J.F. 126, 132, 138
- Sebastian, M.T. 218–219, 223, 282
- Segmuller, A., see Koren, G. 115
- Segmüller, A., see Sandstrom, R.L. 280
- Sekita, M. 115, 125
- Sekita, M., see Morita, S. 125, 189
- Sekiwa, H., see Sekita, M. 115, 125
- Selvam, M.P. 124
- Senyshyn, A. 152, 238, 242–244, 246, 248, 251–253, 262, 265, 267, 274, 276, 278, 280, 282
- Senyshyn, A., see Savytskii, D. 231–233, 237, 242–244
- Senyshyn, A., see Vasylechko, L. 122, 129, 132, 138, 140, 142, 145–146, 148–150, 152, 155, 165, 168, 170, 173, 189, 191, 204, 206–208, 210, 213, 227–228, 230–232, 235, 237, 240–242, 245–247, 249, 251–253, 266–267, 275
- Senyshyn, A.T. 227, 232, 235–237
- Sham, L.J. 15, 27, 77
- Sham, L.J., see Godby, R.W. 27
- Shannon, R.D. 192, 223
- Sharma, B.P. 123
- Sharma, K.K. 220
- Shchegolev, B.F., see Vorotilova, L.S. 149
- Sheel, H.J., see Podlesnyak, A. 235
- Shelyakh, A.I., see Prokofiev, A.V. 53, 55
- Shilykh, A.I. 128, 222
- Shen, H., see Mathur, S. 124
- Shen, H., see Veith, M. 124
- Sheng, Y.T., see Shishido, T. 122, 128, 149, 158, 227, 231–232
- Sherwood, R.C., see Cohen, E. 132
- Shevlin, S.A. 224
- Shibasaki, T. 249
- Shibata, K., see Mori, K. 248
- Shida, H., see Li, D.X. 43
- Shim, J.B. 125
- Shim, J.B., see Nikl, M. 125, 191
- Shimada, T. 218
- Shimizu, K., see Yamaguchi, O. 120
- Shimoyama, J., see Mizusaki, J. 125
- Shimuzi, Y. 29
- Shin, J.Y., see Moon, J.H. 217–218
- Shin, S., see Chantis, A.N. 5, 27
- Shinde, S., see Sandstrom, R.L. 280
- Shindo, D., see Shishido, T. 122, 128, 149, 158, 227, 231–232
- Shirane, G., see Birgeneau, R.J. 132
- Shirinyan, G.O., see Petrosyan, A.G. 119–121, 125, 191
- Shirovani, I.
- Shirvinskaya, A.K. 119
- Shishido, T. 122, 128, 149, 158, 227, 231–232

- Shishido, T., see Okada, S. 128
 Shishido, T., see Saitow, A. 186, 188
 Shishido, T., see Yoshikawa, A. 138, 186–187
 Shluger, A.L.J. 217
 Shmurak, S.Z. 124
 Shmyt'ko, I.M., see Shmurak, S.Z. 124
 Shmytko, I.M., see Bdikin, I.K. 228
 Shoup, S.S. 124
 Shvaiko-Shvaikovskii, V.E., see Leonov, A.
 I. 128, 170, 227
 Sidorov, V.A.
 Sigalov, L.M., see Adylov, G.T. 119
 Silva, J.L.F.D. 51
 Simak, S.I., see Skorodumova, N.V. 49
 Simon, R.W. 222
 Simonov, V.I., see Molchanov, V.I. 303
 Sinclair, D.C., see Moussa, S.M. 216
 Sinclair, W. 122, 158, 169
 Singh, A.K., see Jayaraman, A. 7, 29, 39, 48
 Singh, D.J. 14
 Singheiser, L., see Matraszek, A. 163
 Singleton, J., see Cussen, E.J. 248
 Sinha, A. 123
 Sinha, S.K. 8
 Sinha, S.P. 12–13
 Sinha, S.P., see Skriver, H.L. 12–13, 17, 73
 Skorodumova, N.V. 49
 Skowron, A.
 Skriver, H.L. 12–13, 17, 73
 Skriver, H.L., see Johansson, B. 18–19, 99
 Skriver, H.L., see Wulff, M. 13, 51
 Slater, J.C. 24
 Slater, P.R. 115, 230–234, 249, 276
 Smirnov, I.A., see Shelykh, A.I. 128, 222
 Smitts, C.J.P., see Filip, A.T. 34
 Sobolewski, R. 283
 Soderholm, L. 303
 Söderlind, P., see Eriksson, O. 12–13, 18–19, 86
 Sohma, M., see Yamaguchi, I. 124
 Soldatov, A.V., see Savytskii, D. 231–233, 237,
 242–244
 Soldatov, A.V., see Savytskii, D.I. 125, 228,
 230, 242, 282
 Solomon, S., see Sebastian, M.T. 218–219,
 223, 282
 Solovieva, N., see Nikl, M. 125, 191
 Solovyev, I.V., see Anisimov, V.I. 19–20, 23, 28
 Solovyev, I.V., see Harmon, B.N. 86
 Solskii, I.M., see Matkovskii, A.O. 125
 Solskii, I.M., see Savytskii, D.I. 125, 228, 230,
 242, 282
 Solskii, I.M., see Vasylechko, L.O. 228, 230–231,
 237, 240, 242, 246–247, 249, 266–267, 275
 Sommerdijk, J.L. 300
 Sondhelm, S.A. 13
 Song, G.B., see Liu, F.S. 224
 Soven, P. 25, 81
 Sowinski, S., see Petrosyan, A.G. 119–121,
 125, 191
 Specht, E.D., see Beach, D.B. 124
 Specht, E.D., see Morell, J.S. 228
 Specht, E.D., see Shoup, S.S. 124
 Spedding, F.H., see Banister, J.R. 86
 Spiridonov, F.M., see Arsenev, P.A. 120–121,
 138, 161, 189
 Spring, L.E., see Cussen, E.J. 248
 Springelkamp, F.J. 14
 Stan, M. 225, 227, 231–232, 236
 Stankus, S.V. 119
 Starke, K., see Döbrich, K.M. 13
 Staunton, J. 25, 70, 77, 79, 82, 83, 85
 Staunton, J., see Gyorffy, B.L. 6, 25, 77, 79–83,
 103
 Staunton, J., see Strange, P. 5, 9, 17, 39–40, 61,
 70–71, 74, 82
 Staunton, J.B. 77–80, 82–83
 Staunton, J.B., see Crisan, V. 79
 Staunton, J.B., see Hughes, I.D. 6, 79, 86,
 91, 94
 Staunton, J.B., see Ling, M.F. 79
 Staunton, J.B., see Razee, S.S.A. 79
 Steinberg, M., see Kauffherr, N. 128
 Steinberg, M.J. 128
 Sterne, P.A. 14
 Sterne, P.A., see Temmerman, W.M. 4–5,
 13–14, 21, 24–25, 36, 40–42, 45–46, 48, 53, 79,
 81–82, 86
 Sticht, J. 14
 Stiller, S. 342
 Stiller, S., see Krebs, B. 342
 Stillman, M.J. 300, 301
 Stocks, G.M. 25, 79, 81–82
 Stocks, G.M., see Gyorffy, B.L. 6, 25, 77,
 79–83, 103
 Stocks, G.M., see Johnson, D.D. 79, 81
 Stocks, G.M., see Nicholson, D.M.C. 99
 Stocks, G.M., see Staunton, J. 25, 70, 77, 79, 82,
 83, 85
 Stocks, G.M., see Szotek, Z. 13, 44–46, 53, 89
 Stockton, S., see Brown, S.D. 73–76
 Stoneham, A.M. 217
 Stott, G.M., see Gyorffy, B.L. 6, 25, 77, 79–83, 103
 Stott, M.J. 82
 Strange, P. 5, 9, 17, 39–40, 61, 70–71, 74, 82
 Strange, P., see Aerts, C.M. 33
 Strange, P., see Arola, E. 6, 70–71, 74
 Strange, P., see Brown, S.D. 73–76
 Strange, P., see Horne, M. 36, 40
 Strange, P., see Svane, A. 18, 23, 29, 36, 38,
 40–42, 44–49, 66, 99

- Strange, P., see Temmerman, W.M. 4–5, 13–14, 21, 24–25, 36, 40–42, 45–46, 48, 53, 79, 81–82, 86
- Strobel, P., see Hassan, A.K. 12
- Strother, D.D. 115
- Strother, D.D., see Young, K.H. 115
- Strukova, G.K., see Shmurak, S.Z. 124
- Stuck, C.W. 332
- Studer, F., see Battle, P.D. 182
- Sturge, M.D. 133
- Suchocki, A., see Savvyskii, D.I. 125, 228, 230, 242, 282
- Suchocki, A., see Vasylechko, L. 122, 129, 132, 138, 140, 142, 145–146, 148–150, 152, 155, 165, 168, 170, 173, 189, 191, 204, 206–208, 210, 213, 227–228, 230–232, 235, 237, 240–242, 245–247, 249, 251–253, 266–267, 275
- Sudnick, D.R. 305, 315, 333
- Sudnick, D.R., see Horrocks Jr., W. deW. 305, 315–316, 332
- Suga, S., see Cho, E.-J. 41
- Sugak, D.Yu., see Matkovskii, A.O. 125
- Sugak, D. Yu., see Savvyskii, D.I. 125, 228, 230, 242, 282
- Sugeta, M. 301–302, 304, 306, 311, 313, 316, 322, 326, 328, 334, 339
- Sugeta, M., see Yamase, T. 299, 301–306, 311–320, 322, 325–348, 350–351
- Sugiura, K., see Yamaguchi, O. 120
- Sun, P. 217
- Sun, W., see Li, L. 117–118
- Supkowski, R.M. 315–316
- Surendran, K.P. 223, 282
- Sutter, C., see Schüsler-Langeheine, C. 13
- Suvorov, D. 218–220, 282–283
- Suvorov, D., see Belous, A.G. 216
- Suzuki, S., see Hanyu, T. 49
- Suzuki, S., see Yamaguchi, I. 124
- Suzuki, T., see Cho, E.-J. 41
- Suzuki, T., see Li, D.X. 43
- Suzuki, T., see Mori, N. 44
- Suzuki, T., see Oyamada, A. 43
- Suzuki, T., see Sakon, T. 43
- Suzuki, T., see Takeda, N. 43
- Suzuki, T., see Ufuktepe, Y. 69
- Svane, A. 18, 23, 29, 36, 38, 40–42, 44–49, 66, 99
- Svane, A., see Aerts, C.M. 33
- Svane, A., see Gerward, L. 51
- Svane, A., see Horne, M. 36, 40
- Svane, A., see Hughes, I.D. 6, 79, 86, 91, 94
- Svane, A., see Kumar, R.S. 49
- Svane, A., see Lebegue, S. 44, 65, 68–69
- Svane, A., see Lüders, M. 5, 24, 79, 84, 97
- Svane, A., see Petit, L. 52–53, 56
- Svane, A., see Scarel, G. 49, 53
- Svane, A., see Strange, P. 5, 9, 17, 39–40, 61, 70–71, 74, 82
- Svane, A., see Temmerman, W.M. 4–5, 13–14, 21, 24–25, 36, 40–42, 45–46, 48, 53, 79, 81–82, 86
- Svane, A., see Vaitheeswaran, G. 36, 44
- Sveum, L.K., see Lux, B.C. 123
- Swagten, H.J.M., see LeClair, P. 34
- Swagten, J.M., see Filip, A.T. 34
- Syassen, K. 48
- Syvorotka, I., see Vasylechko, L. 122, 129, 132, 138, 140, 142, 145–146, 148–150, 152, 155, 165, 168, 170, 173, 189, 191, 204, 206–208, 210, 213, 227–228, 230–232, 235, 237, 240–242, 245–247, 249, 251–253, 266–267, 275
- Syvorotka, I.I., see Basyuk, T., 137, 166, 168, 170–172, 174–178, 182–184, 186, 267
- Syvorotka, I.M., see Savvyskii, D.I. 125, 228, 230, 242, 282
- Szotek, W.M.T.Z., see Svane, A. 18, 23, 29, 36, 38, 40–42, 44–49, 66, 99
- Szotek, Z. 13, 44–46, 53, 89
- Szotek, Z., see Aerts, C.M. 33
- Szotek, Z., see Arola, E. 6, 70–71, 74
- Szotek, Z., see Beiden, S.V. 58, 70
- Szotek, Z., see Brown, S.D. 73–76
- Szotek, Z., see Horne, M. 36, 40
- Szotek, Z., see Hughes, I.D. 6, 79, 86, 91, 94
- Szotek, Z., see Lüders, M. 5, 24, 79, 84, 97
- Szotek, Z., see Nicholson, D.M.C. 99
- Szotek, Z., see Petit, L. 52–53, 56
- Szotek, Z., see Strange, P. 5, 9, 17, 39–40, 61, 70–71, 74, 82
- Szotek, Z., see Svane, A. 18, 23, 29, 36, 38, 40–42, 44–49, 66, 99
- Szotek, Z., see Temmerman, W.M. 4–5, 13–14, 21, 24–25, 36, 40–42, 45–46, 48, 53, 79, 81–82, 86
- Szunyogh, L., see Razez, S.S.A. 79
- Szunyogh, L., see Staunton, J.B. 77–80, 82–83
- Tadin, M., see Marti, W. 230, 231, 233–235, 238–239, 242, 244
- Tahvildar-Zadeh, A.N., see Hettler, M.H. 104
- Takahashi, H., see Mori, N. 44
- Takahashi, H.K.T., see Ito, T. 67
- Takahashi, M., see Ozeki, T. 304, 319, 322, 328, 334, 335, 337
- Takahashi, T., see Chantis, A.N. 5, 27
- Takahashi, T., see Ufuktepe, Y. 69
- Takata, H. 123
- Takeda, N. 43
- Takeda, N., see Sakon, T. 43
- Takeuchi, T., see Chantis, A.N. 5, 27

- Takita, Y., see Slater, P.R. 115, 230–234, 249, 276
- Tanaka, I. 125, 188
- Tanaka, K., see Takeda, N. 43
- Tanaka, M. 128, 130
- Tanaka, M., see Saitow, A. 186, 188
- Tanaka, M., see Shishido, T. 122, 128, 149, 158, 227, 231–232
- Tanaka, S. 49
- Tandon, R.P., see Sharma, K.K. 220
- Tang, Z., see Li, L. 117–118
- Tangeman, J., see Zhang, Y. 124
- Taniguchi, M., see Cho, E.-J. 41
- Tanner, B.K., see Wanklyn, B.M. 122
- Tas, A.C. 117, 123, 125, 128
- Taspinar, E. 123, 125
- Tasset, F., see Brown, P.J. 151
- Tasset, F.J., see Alameda, J.M. 12
- Taylor, J. 25
- Taylor, J.B., see Ono, S. 39
- Taylor, J.B., see Wang, B.Y. 39
- Taylor, K.N.R. 97
- Taylor, R., see Loutts, G.B. 115
- Tazoh, Y., see Kobayashi, J. 229–230
- Temmerman, W., see Lüders, M. 5, 24, 79, 84, 97
- Temmerman, W.M. 4–5, 13–14, 21, 24–25, 36, 40–42, 45–46, 48, 53, 79, 81–82, 86
- Temmerman, W.M., see Aerts, C.M. 33
- Temmerman, W.M., see Arola, E. 6, 70–71, 74
- Temmerman, W.M., see Beiden, S.V. 58, 70
- Temmerman, W.M., see Brown, S.D. 73–76
- Temmerman, W.M., see Horne, M. 36, 40
- Temmerman, W.M., see Langford, H.D. 4
- Temmerman, W.M., see Nicholson, D.M.C. 99
- Temmerman, W.M., see Petit, L. 52–53, 56
- Temmerman, W.M., see Stocks, G.M. 25, 79, 81–82
- Temmerman, W.M., see Strange, P. 5, 9, 17, 39–40, 61, 70–71, 74, 82
- Temmerman, W.M., see Svane, A. 18, 23, 29, 36, 38, 40–42, 44–49, 66, 99
- Temmerman, W.M., see Szotek, Z. 13, 44–46, 53, 89
- Teraoka, S., see Degiorgi, L. 43
- Thalmeier, A., see Antonov, V.N. 20
- Thanh, P.H. 117
- Thole, B.T., see Ogasawara, H. 49, 51
- Thompson, A.J., see Stillman, M.J. 300, 301
- Thompson, P., see Brown, S.D. 73–76
- Tilkens, L. 319
- Timofeeva, N.I. 117, 145, 173, 189, 235, 275
- Tishin, A.M. 115
- Tishin, A.M., see Kuz'min, M.D. 115
- Torchenkova, E.A., see Molchanov, V.I. 303
- Toropov, N.A. 117, 119, 121, 149, 150, 152
- Toropov, N.A., see Bondar, I.A. 224, 227, 275
- Torumba, D. 20
- Toshima, H. 125
- Toshima, H., see Miyazawa, Y. 125
- Tosi, M.P., see Andersen, O.K. 19, 23, 24
- Tourné, C.M. 303
- Tourné, G.F., see Tourné, C.M. 303
- Toyota, N., see Shishido, T. 122, 128, 149, 158, 227, 231–232
- Tozawa, S. 128
- Tozawa, S., see Shishido, T. 122, 128, 149, 158, 227, 231–232
- Traversa, E., see Polini, R. 227
- Traversa, E.J. 227
- Treado, P., see Schoonover, J.R. 231
- Trots, D., see Basyuk, T., 137, 166, 168, 170–172, 174–178, 182–184, 186, 267
- Trots, D., see Vasylechko, L. 122, 129, 132, 138, 140, 142, 145–146, 148–150, 152, 155, 165, 168, 170, 173, 189, 191, 204, 206–208, 210, 213, 227–228, 230–232, 235, 237, 240–242, 245–247, 249, 251–253, 266–267, 275
- Truong, A., see Noginov, M.A. 115
- Trygg, J. 19
- Trygg, J., see Eriksson, O. 12–13, 18–19, 86
- Trygg, J., see Svane, A. 18, 23, 29, 36, 38, 40–42, 44–49, 66, 99
- Tseltlin, P.A., see Bondar, I.A. 224, 227, 275
- Tseng, T.-Y. 122
- Tseng, T.-Y., see Lo, J.-R. 122
- Tsiok, O.B.
- Tsuchiya, T., see Yamaguchi, I. 124
- Tsybal, E.Y.J., see Duan, C.-G. 20, 33
- Turek, I. 87
- Turney, V.J., see Noginov, M.A. 115
- Tyagel'sky, P.V. 119
- Tytko, K.H. 342
- Tytko, K.H., see Krebs, B. 342
- Ubizskii, S.B. 228, 242, 244
- Ubizskii, S.B., see Savytskii, D.I. 125, 228, 230, 242, 282
- Udalov, Yu.P. 120–121, 226–227
- Udvardi, L., see Staunton, J.B. 77–80, 82–83
- Uecker, R. 228
- Ufuktepe, Y. 69
- Uhrin, R., see Belt, R.F. 228
- Ullmann, H., see Vasylechko, L. 122, 129, 132, 138, 140, 142, 145–146, 148–150, 152, 155, 165, 168, 170, 173, 189, 191, 204, 206–208, 210, 213, 227–228, 230–232, 235, 237, 240–242, 245–247, 249, 251–253, 266–267, 275
- Urzaeva, E.M., see Adylov, G.T. 119

- Urbanik, M., see Chakoumakos, B.C. 126
 Urbanik, M., see Simon, R.W. 222
 Utke, I. 230, 235, 242
- Vaitheeswaran, G. 36, 44
 Vaitheeswaran, G., see Gerward, L. 51
 Vaitheeswaran, G., see Kumar, R.S. 49
 Vaitheeswaran, G., see Svane, A. 18, 23, 29, 36, 38, 40–42, 44–49, 66, 99
 Valant, M., see Belous, A.G. 216
 Valentino, A.J., see Berkstresser, G.W. 229, 235
 Vallet, C.E., see Beach, D.B. 124
 van Daal, H.J., see Havinga, E.E. 43
 van de Vin, C.H., see LeClair, P. 34
 van der Poel, W.A.J.A. 303
 van der Waals, J.H. 326
 van der Waals, J.H., see Barendswaads, W. 326
 van der Waals, J.H., see van der Poel, W.A.J. A. 303
 van der Waals, J.H., see Van Tol, J. 326
 Van Hulst, J.A., see Van Tol, J. 326
 Van Oosterhout, A.B. 326
 van Schilfgaard, M. 27–28
 van Schilfgaard, M., see Larson, P. 20, 43
 Van Tol, J. 326
 Van Uitert, L.G. 175, 183, 223–224
 Van Uitert, L.G., see Birgeneau, R.J. 132
 Van Uitert, L.G., see Cohen, E. 132
 Van Uitert, L.G., see Lyons, K.B. 132
 Van Uitert, L.G., see Nordland, W.A. 175, 183, 223, 224
 Vashook, V., see Vasylechko, L. 122, 129, 132, 138, 140, 142, 145–146, 148–150, 152, 155, 165, 168, 170, 173, 189, 191, 204, 206–208, 210, 213, 227–228, 230–232, 235, 237, 240–242, 245–247, 249, 251–253, 266–267, 275
 Vasilechko, L.O., see Savvitskii, D.I. 125, 228, 230, 242, 282
 Vasilieva, V.A. 119, 121
 Vasylechko, L. 122, 129, 132, 138, 140, 142, 145–146, 148–150, 152, 155, 165, 167, 168, 170, 173, 189–191, 204, 206–208, 210, 213, 227–228, 230–233, 235, 237, 239–242, 245–247, 249, 251–253, 256, 266–267, 275
 Vasylechko, L., see Basyuk, T., 137, 166, 168, 170–172, 174–178, 182–184, 186, 267
 Vasylechko, L., see Savvitskii, D. 231–233, 237, 242–244
 Vasylechko, L., see Senyshyn, A. 152, 238, 242–244, 246, 248, 251–253, 262, 265, 267, 274, 276, 278, 280, 282
 Vasylechko, L.O. 122, 126–127, 129–132, 140–143, 147–148, 150–152, 154–156, 170, 178–180, 189–191, 204, 206–208, 213, 227–228, 230–232, 235–237, 239–242, 245–247, 249, 251–252, 255, 257, 261, 263–264, 266
 Vasylechko, L.O., see Aleksiyko, R. 228, 252, 254, 256, 264
 Vasylechko, L.O., see Berkowski, M. 228, 249
 Vasylechko, L.O., see Matkovskii, A.O. 125
 Vasylechko, L.O., see Savvitskii, D.I. 125, 228, 230, 242, 282
 Vedda, A., see Chval, J. 189, 191
 Vedda, A., see Nikl, M. 125, 191
 Vedel, I. 44
 Veith, M. 124
 Veith, M., see Mathur, S. 124
 Venkateswarlu, P., see Loutts, G.B. 115
 Venskovskii, N.U., see Polteva, T.V. 248
 Vente, J.F., see Cussen, E.J. 248
 Venturi, M., see Ballardini, R. 301–303
 Verevkin, A., see Noginova, N. 248
 Verweg, J.W.M. 319
 Vidyasagar, K. 121
 Vignale, G., see Temmerman, W.M. 4–5, 13–14, 21, 24–25, 36, 40–42, 45–46, 48, 53, 79, 81–82, 86
 Villars, P. 52
 Vinogradova, N.V., see Bondar, I.A. 224, 227, 275
 Viskup, A.P., see Kharton, V.V. 248
 Vogt, O., see Bihan, T.L. 46
 Vogt, O., see Vedel, I. 44
 Vogt, T., see Kennedy, B.J. 135, 182, 183
 Vogt, T., see Moussa, S.M. 134
 von Barth, U. 16
 Voronin, G.F. 119, 120
 Voronin, G.F., see Lysenko, V.A. 119, 120
 Voronov, G.V., see Adylov, G.T. 119
 Vorotilova, L.S. 149
 Vosko, S.H. 16
- Wachter, P. 41, 43, 49
 Wachter, P., see Degiorgi, L. 43
 Wadsworth, J.J., see Staunton, J. 25, 70, 77, 79, 82, 83, 85
 Waldner, F. 126
 Waldner, F., see Müller, K.A. 126
 Walker, W.C., see Benard, D.J. 133
 Wallrafen, F., see Matkovskii, A.O. 125
 Wallrafen, F., see Neuroth, G. 125
 Wallrafen, F., see Savvitskii, D.I. 125, 228, 230, 242, 282
 Wallrafen, F., see Vasylechko, L.O. 228, 230–231, 237, 240, 242, 246–247, 249, 266–267, 275
 Wallrafen, F.J. 125
 Wallrafen, F.J., see Matkovskii, A.O. 125
 Wang, B.Y. 39

- Wang, Ch., see Lakiza, S. 118
 Wang, H., see Liu, G. 115
 Wang, P., see Li, L. 117–118
 Wang, S., see Shibasaki, T. 229
 Wang, S.F. 216
 Wang, X. 122, 222
 Wang, Y. 16, 228–231
 Wang, Y., see Nicholson, D.M.C. 99
 Wanklyn, B.M. 122, 235
 Wanklyn, B.M., see Bombik, A. 148, 150–151, 158, 163, 248
 Wanklyn, B.M., see Kotru, P.N. 122
 Wanklyn, B.M., see Razdan, A.K. 122
 Wanklyn, B.M., see Sharma, K.K. 220
 Wanklyn, B.M., see Watanabe, S. 133, 135
 Wanklyn, B.M., see Watts, B.E. 235
 Wanmaker, W.L. 300
 Wanmaker, W.L., see Bril, A. 300
 Waring, J.L. 121, 224–226
 Waring, J.L., see Schneider, S.J. 121, 224–226
 Warren, M., see Loutts, G.B. 115
 Warren, R., see Alkebro, J. 123
 Warshaw, I. 119
 Wassdahl, N., see Butorin, S.M. 49, 51
 Watanabe, S. 133, 135
 Watanabe, T., see Morita, S. 125, 189
 Watanabe, T., see Yamaguchi, I. 124
 Watson, L.M., see Gyorffy, B.L. 6, 25, 77, 79–83, 103
 Watts, B.E. 235
 Weakley, T.J. 302
 Weakley, T.J., see Ibal, J. 302
 Weber, J.K.R., see Zhang, Y. 124
 Weber, M., see Shmurak, S.Z. 124
 Weber, R.T., see Barendswaads, W. 326
 Welch, A.J.W., see Dalziel, J.A.W. 148
 Werner, A. 48
 Werner, A., see Debray, D. 46
 Wertheim, G.K., see Campagna, M. 64, 67–69
 Weschke, E., see Schüßler-Langeheine, C. 13
 West, R.N., see Dugdale, S.B. 89
 Wierzchowski, W., see Savytskii, D. 231–233, 237, 242–244
 Wieteska, K., see Savytskii, D. 231–233, 237, 242–244
 Wilk, L., see Vosko, S.H. 16
 Wills, J.M., see Delin, A. 4, 18
 Wills, J.M., see Eriksson, O. 12–13, 18–19, 86
 Wills, J.M., see Temmerman, W.M. 4–5, 13–14, 21, 24–25, 36, 40–42, 45–46, 48, 53, 79, 81–82, 86
 Winkelkemper, M., see Rinke, P. 27
 Winter, H. 13, 25, 53, 79, 81
 Winter, H., see Arola, E. 6, 70–71, 74
 Winter, H., see Gyorffy, B.L. 6, 25, 77, 79–83, 103
 Winter, H., see Horne, M. 36, 40
 Winter, H., see Staunton, J. 25, 70, 77, 79, 82, 83, 85
 Winter, H., see Stocks, G.M. 25, 79, 81–82
 Winter, H., see Strange, P. 5, 9, 17, 39–40, 61, 70–71, 74, 82
 Winter, H., see Svane, A. 18, 23, 29, 36, 38, 40–42, 44–49, 66, 99
 Winter, H., see Temmerman, W.M. 4–5, 13–14, 21, 24–25, 36, 40–42, 45–46, 48, 53, 79, 81–82, 86
 Wire, M.S., see Simon, R.W. 222
 Wolff, I. 222, 280, 282
 Wolff, I., see Konopka, J. 222, 280, 282
 Wong, K.C. 89
 Wood, J.H., see Koelling, D.D. 14, 49, 51
 Woodward, P.M. 193, 247
 Woodward, P.M., see Lufaso, M.W. 115, 192, 207, 247
 Worledge, D.C. 34
 Wu, B. 227
 Wu, C.H., see Wang, S.F. 216
 Wu, P. 120–121
 Wuilloud, E. 49, 51
 Wulff, M. 13, 51
 Wyckoff, R.W.G. 33
 Xia, C., see Zhao, G. 191
 Xie, S. 125
 Xie, S., see Yu, Y. 125
 Xijun, L., see Kebin, L. 115
 Xu, C.N., see Wang, X. 122, 222
 Xu, J., see Zhao, G. 191
 Xue, Z.B., see Beach, D.B. 124
 Xue, Z.B., see Morell, J.S. 228
 Yacoubi, N., see Krill, G. 40
 Yamada, H., see Wang, X. 122, 222
 Yamada, T. 117–118, 128, 138, 224–227, 230, 275
 Yamada, T., see Mizuno, M. 117–118, 120, 128, 138, 224–227, 230, 275
 Yamaguchi, I. 124
 Yamaguchi, O. 120
 Yamaguchi, Y., see Yamaguchi, I. 124
 Yamamoto, A., see Yamase, T. 299, 301–306, 311–320, 322, 325–348, 350–351
 Yamane, H. 224, 246
 Yamase, T. 299, 301–306, 311–320, 322, 325–348, 350–351
 Yamase, T., see Naruke, H. 304, 311, 320, 322, 329, 332–335, 337–339
 Yamase, T., see Ozeki, T. 304, 319, 322, 328, 334, 335, 337

- Yamase, T., see Sugeta, M. 301–302, 304, 306, 311, 313, 316, 322, 326, 328, 334, 339
- Yamauchi, S., see Mizusaki, J. 125
- Yan, B. 249
- Yanagihara, M., see Hanyu, T. 49
- Yanao, Y., see Yamase, T. 299, 301–306, 311–320, 322, 325–348, 350–351
- Yang, C.Y. 125
- Yang, L.T., see Liu, F.S. 224
- Yang, M., see Zinkevich, M. 225, 227
- Yang, W.H. 222
- Yang, W.H., see Yang, C.Y. 125
- Yano, Y., see Yamase, T. 299, 301–306, 311–320, 322, 325–348, 350–351
- Yao, G.-D., see Wang, Y. 228–231
- Yao, T., see Liu, G. 115
- Yaresko, A.N., see Antonov, V.N. 20
- Yaresko, A.N., see Oppeneer, P.M. 43
- Yashima, M. 249
- Yasuda, I., see Mizusaki, J. 125
- Yen, W.M. 334
- Yen, W.M., see Hegarty, G.D. 334
- Yokoya, T., see Chantis, A.N. 5, 27
- Yoon, D.H., see Nikl, M. 125, 191
- Yoon, D.-H., see Shim, J.B. 125
- Yoshikawa, A. 138, 186–187
- Yoshikawa, A., see Nikl, M. 125, 191
- Yoshikawa, A., see Saitow, A. 186, 188
- Yoshikawa, A., see Shim, J.B. 125
- Yoshikawa, A., see Shishido, T. 122, 128, 149, 158, 227, 231–232
- Yoshizawa, H., see Watanabe, S. 133, 135
- Yosida, K. 11
- Youn, H.J., see Ang, C. 216
- Young, A.P. 132
- Young, K.H. 115
- Young, R.C. 13–14
- Yu, Y. 125
- Yu, Y.Z., see Lehnert, H. 126
- Yu, Z., see Ang, C. 216
- Yuheng, Z., see Kebin, L. 115
- Yuval, G., see Andersen, P.W. 103–104
- Zaanen, J., see Anisimov, V.I. 19, 23, 28
- Zaanen, J., see Lichtenstein, A.I. 19–20, 65
- Zachariassen, W.H. 128
- Zaidi, H., see Chval, J. 189, 191
- Zarychta, B., see Brown, S.D. 73–76
- Zawadowski, A. 104
- Zeng, X., see Zhao, G. 191
- Zhang, H.Y., see Yang, W.H. 222
- Zhang, J., see Yan, B. 249
- Zhang, Q. 123
- Zhang, W., see Wu, B. 227
- Zhang, Y. 124
- Zhang, Z.G., see An, W.W. 124
- Zhao, G. 191
- Zhao, J. 128, 137, 145, 147, 157, 167
- Zhao, J., see Ross, N.L. 145, 147, 157, 161, 167, 169
- Zharikov, E.V., see Zinoviev, S.Yu. 225–226
- Zhdanovich, N.S., see Shelykh, A.I. 128, 222
- Zheng, Y., see Shishido, T. 122, 128, 149, 158, 227, 231–232
- Zhenzhong, Q., see Kebin, L. 115
- Zhou, J.-S. 193
- Zhou, S., see Zhao, G. 191
- Zhydachevskii, Ya.A., see Matkovskii, A.O. 125
- Zimmer, H.G.
- Zinkevich, M. 225, 227
- Zinkevich, M., see Lakiza, S. 118
- Zinkevich, M., see Wu, B. 227
- Zinoviev, S.Yu. 225–226
- Zölfl, M.B. 29
- Zonnenevillage, F. 301–303, 332
- Zonnenevillage, F., see Blasse, G. 300–303, 320, 326, 328, 332, 338
- Zugates, C.T., see Schoonover, J.R. 231
- Zunger, A. 5, 16, 20–22
- Zwicknagl, G. 17

SUBJECT INDEX

- alloy analogy 75, 102
- aluminates, 113–284
- anomalous thermal expansion
 - rare earth aluminates, 207
 - DyAlO₃ 148
 - ErAlO₃ 150
 - GdAlO₃ 146
 - TbAlO₃ 148
 - TmAlO₃ 152
 - YAlO₃ 157
- rare earth gallates
 - La_{1-x}Pr_xGaO₃ 241
 - NdGaO₃ 243
 - PrGaO₃ 237
- anti-ferromagnetic structure 86
- aqua and hydroxo ligands 352–353
- atomic sphere approximation (ASA) 52

- band-like 4f-states 1–105
- band structure 53
 - Eu₂O₃ compounds 54
 - Gd₂O₃ compounds 54
 - Tb₂O₃ compounds 54
 - trivalent PrSb 37
- Bloch spectral function (BSF) 89
- bond lengths
 - rare earth aluminates 204
 - rare earth gallates 267

- CeAs compounds 44–45
- CeBi compounds 44–46
- CeN compounds 34–36, 45
- CeO₂ compounds 49, 51, 54
- Ce₂O₃ compounds 52
- CeP compounds 44–45
- cerium (Ce) element 7–8, 10, 31–32, 34–35, 97–98
- CeSb compounds 44–46
- CeS compounds 39, 45
- CeSe compounds 45–46
- CeTe compounds 45–46
- CeX compounds 36

- chemically induced dynamic electron
 - polarization (CIDEP) technique 328, 339–340
- coherent potential approximation (CPA) 25, 81–83, 103
- crystal structure
 - RAlO₃ 125
 - CeAlO₃ 128
 - DyAlO₃ 148
 - ErAlO₃ 150
 - EuAlO₃ 140
 - GdAlO₃ 144
 - HoAlO₃ 149
 - LaAlO₃ 125
 - LuAlO₃ 153
 - NdAlO₃ 138
 - PrAlO₃ 132
 - SeAlO₃ 158
 - SmAlO₃ 138
 - TbAlO₃ 148
 - TmAlO₃ 152
 - YAlO₃ 155
 - YbAlO₃ 153
 - RAl_{1-x}M_xO₃ solid solutions 161
 - RGaO₃ 228
 - CeGaO₃ 231
 - LaGaO₃ 229
 - NdGaO₃ 241
 - PrGaO₃ 235
 - RGaO₃ (R = Pm, Sm, Eu and Gd) 246
 - SmGaO₃ 245
 - RGa_{1-x}M_xO₃ solid solutions 248
 - R_{1-x}R'_xAlO₃ solid solutions
 - Ce_{1-x}La_xAlO₃ 170
 - Ce_{1-x}Nd_xAlO₃ 170
 - Ce_{1-x}Pr_xAlO₃ 171
 - Gd_{1-x}Lu_xAlO₃ 189
 - Gd_{1-x}Tb_xAlO₃ 189
 - La_{1-x}Er_xAlO₃ 166
 - La_{1-x}Eu_xAlO₃ 165
 - La_{1-x}Gd_xAlO₃ 165
 - La_{1-x}Nd_xAlO₃ 164
 - La_{1-x}Sm_xAlO₃ 166
 - La_{1-x}Tb_xAlO₃ 166

- crystal structure (*cont.*)
- $\text{La}_{1-x}\text{Y}_x\text{AlO}_3$ 166
 - $\text{Nd}_{1-x}\text{Dy}_x\text{AlO}_3$ 188
 - $\text{Nd}_{1-x}\text{Er}_x\text{AlO}_3$ 188
 - $\text{Nd}_{1-x}\text{Eu}_x\text{AlO}_3$ 188
 - $\text{Nd}_{1-x}\text{Sm}_x\text{AlO}_3$ 186
 - $\text{Nd}_{1-x}\text{Y}_x\text{AlO}_3$ 188
 - $\text{Pr}_{1-x}\text{Eu}_x\text{AlO}_3$ 183
 - $\text{Pr}_{1-x}\text{La}_x\text{AlO}_3$ 173
 - $\text{Pr}_{1-x}\text{Nd}_x\text{AlO}_3$ 173
 - $\text{Y}_{1-x}\text{Er}_x\text{AlO}_3$ 191
 - $\text{Y}_{1-x}\text{Lu}_x\text{AlO}_3$ 191
 - $\text{Y}_{1-x}\text{Yb}_x\text{AlO}_3$ 191
 - $\text{R}_{1-x}\text{R}'_x\text{GaO}_3$ solid solutions 248
 - $\text{La}_{1-x}\text{Ce}_x\text{GaO}_3$ 249
 - $\text{La}_{1-x}\text{Eu}_x\text{GaO}_3$ 249
 - $\text{La}_{1-x}\text{Gd}_x\text{GaO}_3$ 249
 - $\text{La}_{1-x}\text{Nd}_x\text{GaO}_3$ 253
 - $\text{La}_{1-x}\text{Pr}_x\text{GaO}_3$ 249
 - $\text{La}_{1-x}\text{R}_x\text{GaO}_3$ (R = Tb–Er, Y) 254
 - $\text{La}_{1-x}\text{Sm}_x\text{GaO}_3$ 249
 - $\text{Nd}_{1-x}\text{R}_x\text{GaO}_3$ (R = Pr, Sm, Eu, Gd) 264
 - $\text{Pr}_{1-x}\text{R}_x\text{GaO}_3$ (R = Sm, Eu, Gd) 265
- Curie temperature 78, 85
- Curie–Weiss type behaviour 78, 87
- decatingstoeuropate 300–301
- density functional theory (DFT) 4, 15, 20, 77
- density of states (DOS) 53
- Eu_2O_3 compounds 54
 - Gd_2O_3 compounds 54
 - heavy lanthanide, magnetic properties
 - for Ho 59
 - for Tb 59
 - pnictides
 - lanthanide nitrides 35
 - trivalent PrSb 37
 - trivalent SmAs 38
 - PrO_2 compounds 50
 - Tb_2O_3 compounds 54
- dichroism 73
- dielectric properties
- rare earth aluminates 216
 - rare earth gallates 280
- disordered local moment (DLM), spin fluctuations 98
- CPA role in 81–83
 - localized f-electrons 78
 - local moment 77
 - paramagnetic DLM state 83–86
 - standard model 77
- dynamical cluster approximation (DCA) 104
- dynamical fluctuations
- critical temperature 102
 - thermal fluctuations 102
- dynamical mean-field theory (DMFT) 5, 65, 76, 103
- Ce α - γ transition 29
 - Green's function 28
 - self-energy 28
 - spectral function 28
- DyN compounds 33–36
- dysprosium (Dy) element 7–8, 10, 31–32, 34–35
- electron-spin polarization (ESP) 339–341
- electron transfer 328
- electronic structure, 1–105
- energy transfer process 300
- energy transfer, Tb^{3+} to Eu^{3+} 353
- Förster-Dexter energy transfer
 - critical radius 335
 - crystal-field symmetry 338
 - donor-acceptor interaction parameter 335
 - electric dipole-dipole interaction 337
 - lanthanide contraction 334
 - luminescence 333
 - magnetic dipole transition 336
 - resonance energy transfer 337
 - spectral overlap 335
 - luminescence decay dynamics
 - aqua and hydroxo ligands 332–333
 - intrinsic lifetimes 332
 - luminescence spectra
 - energy gap 329
 - f-f transitions 329–330
 - lanthanide contraction 329
 - polyoxometalates 329
 - polyoxometalloeuropates 328
 - polyoxometalloylanthanoates 329–331
 - polyoxometalloyterbates 329
 - quantum yield 328
 - O \rightarrow M lmct triplet energy transfer
 - cross-relaxation 338
 - Förster-Dexter resonance energy transfer 339
 - lifetime 339
 - non-radiative processes 338
- ErAs compounds 27
- erbium (Er) element 7–8, 10, 27, 31–32, 34–35, 96
- ErN compounds 27, 34–36
- EuAs compounds 39
- EuBi compounds 39
- EuN compounds 35–36
- EuO compounds 46, 48
- Eu_2O_3 compounds 53
- Eu-pnictides 36, 38

- europium (Eu) element 7–8, 10, 31–32, 34–35
- EuSb compounds 39
- EuS compounds 39, 48
- EuX compounds 36

- 4f-band approach 4, 17
- 4f-core approach 4, 18
- 4f-states, character of, 1–105
- Fermi surface studies
 - Ce α - γ transition 14
 - of Dy and Ho 13
 - of Gd 13
 - of Gd-Y alloys 13
 - of Pr 13
 - of Tb 13
 - standard model 12–13
- finite temperature phase diagrams
 - spin fluctuations
 - CPA role in 81–83
 - localized f-electrons 78
 - local moment 77
 - paramagnetic DLM state 83–86
 - standard model 77
 - thermal fluctuations
 - dynamical fluctuations 76
 - spin fluctuations and valence fluctuations 75
 - valence fluctuations
 - alloy analogy 97
 - Ce phase diagram 101
 - critical temperature 101
 - delocalized f-state 97
 - discontinuities of total energy 102
 - equation of state of Ce 100
 - free energies, volume function 100
 - α - γ transition 97
 - localized f-state 97
 - local moments 97
 - phase transition 101
 - pV term discontinuities 102
 - total energies for Ce 98
 - total energy differences 98
 - total entropy discontinuities 102
 - transition pressure 98
 - volume collapse 98, 101
 - valence fluctuations
 - alloy analogy 97
 - Ce phase diagram 101
 - critical temperature 101
 - delocalized f-state 97
 - discontinuities of total energy 102
 - equation of state of Ce 100
 - free energies, volume function 100
 - α - γ transition 97
 - localized f-state 97
 - local moments 97
 - phase transition 101
 - pV term discontinuities 102
 - total energies for Ce 98
 - total energy differences 98
 - total entropy discontinuities 102
 - transition pressure 98
 - volume collapse 98, 101
- Förster-Dexter dipole–dipole type 352

- gadolinium (Gd) element 7–8, 10, 27, 31–32, 34–35, 60, 94–95
- gadolinium magnetic order
 - Bloch spectral function of 90–91
 - direct correlation function 91
 - Fermi surfaces 89
 - ferromagnetic structure 86
 - incommensurate magnetic structure 88
 - spin susceptibility 87–88, 92
- gallates, 113–284
- GdAs compounds 27
- Gd–Ho alloy 94
- GdN compounds 27, 33, 35–36
- Gd₂O₃ compounds 52–53
- GdS compounds 39
- Gd_{1–x}Dy_x 95
- Gd_{1–x}Er_x 95
- Gd_{1–x}Ho_x 95
- Gd_{1–x}Tb_x 95
- Gd_{1–x}Tm_x 95
- generalized gradient approximation (GGA) 16
- Green’s function 25–26, 28, 65, 89
- GW method 5
 - Green’s function 26
 - Hamiltonian 26
 - multiplet splittings 27
 - self-energy 26

- heavy-fermion behaviour 43
- heavy lanthanide metals 76
 - magnetic phase diagram
 - critical alloy concentrations 95
 - ferromagnetism and incommensurate ordering 95
 - magnetic ordering vectors 95–96
 - magnetic properties of 60–61
 - exchange splitting 58
 - hybridization 58
 - relativistic SIC-LSD 58
 - spin-orbit splitting 58
- holmium (Ho) element 7–8, 10, 31–32, 34–35, 96
- HoN compounds 34–36
- Ho₂O₃ compounds 52
- Hubbard U 19, 23, 69
- Hund’s rules 9, 57–58, 60, 64

- intermetallic YbAl₃ compound 49

- α -Keggin structures 304, 309–310
- Kondo resonance 104
- Korringa, Kohn, and Rostoker (KKR) formalism 79

- Landau theory of phase transitions 102
- lanthanide
 - Fermi surface studies 12–15
 - heavy fermion behaviour 6
 - lattice parameters 7
 - magnetic order 11

- lanthanide (*cont.*)
- magnetic properties
 - localized f electron states 8
 - magnetic moments 8, 10
 - spin-orbit coupling 9
 - standard model 8
 - valence 6
- lanthanide contraction 6, 97
- lanthanum (La) element 7-8, 10
- lattice distortion
- rare earth aluminates 198
 - rare earth gallates 247
- lattice parameters
- $RAlO_3$ and $R_{1-x}R'_xAlO_3$ solid solutions 161
 - $RGaO_3$ and $R_{1-x}R'_xGaO_3$ solid solutions 248
- ligand-to-metal charge-transfer states (lmct) 300
- light lanthanides, magnetic properties
- hybridization 63
 - neodymium 63
 - orbital magnetic moments 62
- local density approximation (LDA) 4, 15-16, 20, 86, 98
- local density approximation + Hubbard U (LDA+U) approach 5, 19-20, 23, 43, 51, 86
- local self-interaction-correction (LSIC) 77, 79, 86
- coherent potential approximation (CPA) 25
 - Green's functions 25
 - phase shift 24
- local spin density (LSD) 4, 15-16, 20
- localized 4f-states, 1-105
- lutetium (Lu) element 7-8, 10
-
- magnetic X-ray scattering (MXRS) 70
- metal-insulator Mott transition 104
- metal-oxide cluster compounds 300
- metal-oxide phosphors 300
- Mo-blue nano-rings 301
- building-block 345-349
 - molecular curvature 346-349
 - nano-tube 351-352
 - photochemical self-assembly 350
 - photo-induced self-assembly 344
 - building block 344
 - photolysis 342
 - photolysis 345, 347, 350
 - self-assembly
 - electron transfer 339
 - inter-system crossing 340
 - $O \rightarrow M$ lmct triplet states 339, 341
 - photolysis 340
 - molecular curvatures 349
 - monopnictides 42
- nano-ring formation 297-354
- nano-tubes 351-353
- NdN compounds 33, 35-36
- NdO₂ compounds 51
- Néel temperature 85
- neodymium (Nd) element 7-8, 10, 31-32, 34-35, 63
- nitrides 33
-
- octahedral tilt
- rare earth aluminates 197
 - rare earth gallates 247
- $O \rightarrow M$ energy transfer 352-353
- α -Keggin structure 309-310
 - aqua and hydroxo ligands
 - lifetime 315-316
 - nephelauxetic effect 318
 - polyoxometallopeuropate 317
 - chemically induced dynamic electron polarization (CIDEP) technique 328
 - configuration co-ordinate model 326
 - crystal-field splitting
 - luminescence and lifetime 314
 - $O \rightarrow M$ lmct 311-313
 - quantum yield 314-315
 - Eu^{3+} luminescence 301
 - f-f absorption 328
 - photoexcitation 304, 320, 326, 328
 - quantum yields 303, 320, 322, 326, 328
 - radiative rate 319-320, 353
 - sensitized luminescence kinetics
 - magnetic-dipole 319
 - non-radiative rate 320, 353
 - photoexcitation 320
 - polyoxometalate 320
 - quantum yields 320
 - radiative rate 320
 - vibronic coupling 305
- $O \rightarrow Mo$ lmct 341
- orbital magnetic moments 70
- magnetic properties
 - hybridization 63
 - neodymium 63
 - total energy of praseodymium, function of 58
- orbital polarization scheme 5
- Ce α - γ transition 18
 - orbital moment 18
 - volume collapse 18
- $O \rightarrow W$ lmct triplet states 322

- paramagnetic DLM state, spin fluctuations
 - direct correlation function 85
 - phase shifts 84
 - spin susceptibility 85
- perovskite structure types
 - $\bar{I}\bar{1}$ ($a^-b^-c^-$ tilt system) 200
 - $I2/m$ ($a^0b^-c^-$ tilt system) 200
 - $I4/mc\bar{m}$ ($a^0a^0c^-$ tilt system) 199
 - $Im\bar{m}a$ ($a^0b^-b^-$ tilt system) 198
 - $Pbnm$ ($a^+b^-b^-$ tilt system) 198
 - $Pm\bar{3}m$ ($a^0a^0a^0$ tilt system) 193
 - $R\bar{3}c$ ($a^-a^-a^-$ tilt system) 248
- phase diagrams
 - rare earth aluminates 207
 - CeAlO₃-LaAlO₃ 171
 - CeAlO₃-NdAlO₃ 171
 - CeAlO₃-PrAlO₃ 173
 - LaAlO₃-ErAlO₃ 166
 - LaAlO₃-EuAlO₃ 165
 - LaAlO₃-GdAlO₃ 165
 - LaAlO₃-NdAlO₃ 164
 - LaAlO₃-SmAlO₃ 166
 - LaAlO₃-TbAlO₃ 166
 - LaAlO₃-YAlO₃ 166
 - NdAlO₃-SmAlO₃ 188
 - PrAlO₃-LaAlO₃ 183
 - PrAlO₃-NdAlO₃ 183
 - rare earth gallates 275
 - homogeneity range 271
 - LaGaO₃-CeGaO₃ 263
 - LaGaO₃-NdGaO₃ 263
 - LaGaO₃-PrGaO₃ 263
 - LaGaO₃-SmGaO₃ 263
- phase formation and stability
 - rare earth aluminates 116
 - rare earth gallates 224, 271
- phase transitions
 - rare earth aluminates 207
 - CeAlO₃ 128
 - Ce_{1-x}La_xAlO₃ 170
 - Ce_{1-x}Nd_xAlO₃ 181
 - LaAlO₃ 126
 - La_{1-x}Er_xAlO₃ 166
 - La_{1-x}Eu_xAlO₃ 168
 - La_{1-x}Gd_xAlO₃ 165
 - La_{1-x}Nd_xAlO₃ 165
 - La_{1-x}Sm_xAlO₃ 166, 168
 - La_{1-x}Tb_xAlO₃ 166
 - La_{1-x}Y_xAlO₃ 166, 168
 - NdAlO₃ 138
 - Nd_{1-x}Sm_xAlO₃ 187
 - PrAlO₃ 132
 - Pr_{1-x}La_xAlO₃ 178
 - Pr_{1-x}Nd_xAlO₃ 175
 - SmAlO₃ 138
 - rare earth gallates 275
 - CeGaO₃ 235
 - LaGaO₃ 229
 - La_{1-x}Ce_xGaO₃ 251
 - La_{1-x}Er_xGaO₃ 254
 - La_{1-x}Gd_xGaO₃ 251
 - La_{1-x}Ho_xGaO₃ 254
 - La_{1-x}Nd_xGaO₃ 251
 - La_{1-x}Pr_xGaO₃ 241
 - La_{1-x}Sm_xGaO₃ 251
 - La_{1-x}Y_xGaO₃ 254
 - PrGaO₃ 241
- photoemission spectroscopy 63
- photoexcitation 304, 326, 328
- photo-induced self-assembly 343
- PmN compounds 35–36
- PmO₂ compounds 51
- polyoxolanthanoates 300–301
- polyoxometalates 299, 303–305, 320, 328–329, 352–353
- polyoxometalloeuropate 304, 317, 353
- polyoxometallolanthanoates 297–354
 - luminescence 297–354
- polyoxometaloterbates 327–328
- polyoxomolybdates 339
- polyoxomolybdoeuropate 326
- polyoxotungstate ligands 303
- polyoxotungstoeuropate 326
- PrAs compounds 46
- praseodymium (Pr) element 7–8, 10, 31–32, 34–35
- PrBi compounds 46
- Pr chalcogenides 47
- preparation methods
 - arc melting technique 122, 227
 - Bridgman technique 125
 - Czochralski technique 125, 228
 - decomposition and calcination hydroxides, cyanides, and nitrates 121
 - floating zone method 125, 228
 - flux methods 121, 228
 - glassy state 124
 - high pressure synthesis 122, 228
 - mechanical solid-state reaction 123
 - nanosized powders 123
 - polymer complex method 122
 - self-propagating combustion synthesis 123
 - solid state reactions 121, 228
 - spray pyrolysis technique 123
 - thin films 124, 228
- Preyssler structures 304
- PrN compounds 35–36
- PrO₂ compounds 49, 51, 54
- promethium (Pm) element 7–8, 10, 31–32, 34–35
- PrP compounds 46

- Pr pnictides 46
 PrSb compounds 46
 PrS compounds 46–47
 PrSe compounds 46–47
 PrTe compounds 46–47
 PrX compounds 36
- quantum yields 303, 320, 322, 326, 328, 353
- relativistic photon–electron interaction
 vertex 71
- Ruderman–Kittel–Kasuya–Yoshida (RKKY)
 interactions 8, 11, 77, 92
- samarium (Sm) element 7–8, 10, 31–32, 34–35
 self-interaction-corrected local spin density
 (SIC-LSD) 98
 – exchange-correlation function 21
 – localized electrons 20
 – self-interaction 20
 – valence 22
 self-interaction correction (SIC) 5, 70, 86
 sensitized luminescence 302–303, 319–325
 SmBi compounds 38
 Sm chalcogenides 40, 47
 SmN compounds 35–36
 Sm pnictides 38
 SmS compounds 46
 SmSe compounds 46–47
 SmTe compounds 46–47
 SmX compounds 36
 spectroscopy
 – asymmetry ratio, lanthanides Gd through to
 Tm 74–75
 – basic theory of X-ray scattering
 -- asymmetry ratio 73
 -- golden rule 70
 -- relativistic photon–electron interaction
 vertex 71
 -- X-ray scattering amplitude 71
 – heavy lanthanide metals 76
 – Hubbard-I approach
 -- atomic Hamiltonian 65
 -- multiplet structure 64
 -- self-energy 65–66
 -- SmAs and SmS 66
 -- standard model 64
 – localized f-states 64
 – multiplet structure 63
 – orbital moment 74, 76
 – relativistic SIC-LSD approach 70
 – spectral function
 -- divalent Sm 67
 -- divalent SmS 67
 -- of TmSe 69
 -- of trivalent in SmAs 66
 -- of trivalent Sm 66
 – spin moments 74, 76
 – valence 63
 spin-lattice relaxation 341
 spin magnetic moments 70
 – light lanthanides, magnetic properties 62
 -- hybridization 63
 -- neodymium 63
 – total energy of praseodymium, function
 of 58
 spin-orbit coupling 9, 17, 65, 79, 98
- TbN compounds 33–36
 TbO₂ compounds 49, 51, 54
 Tb₂O₃ compounds 52–53
 terbium (Tb) element 7–8, 10, 31–32, 34–35,
 60, 95
 thermal expansion
 – rare earth aluminates 207
 – rare earth gallates 276
 thermal expansion coefficient
 – rare earth aluminates 213
 – rare earth gallates 281
 thulium (Tm) element 7–8, 10, 31–32,
 34–35, 96
 Tm chalcogenides 40
 TmN compounds 34–36
 TmS compounds 69
 TmSe compounds 69
 TmTe compounds 69
 trivalent lanthanide ions, magnetic
 moments 10
- up-conversion phosphors 301
- valence transitions
 – band gap 48
 – B1 → B2 phase transition 44, 46, 48
 – B1 → B1 valence transitions 48
 – B1 (rocksalt) structure 44, 47–48
 – B2 (caesium chloride) structure 44, 47
 – cerium pnictides 44
 – chalcogenides 44, 46
 -- charge transfer and hybridization 39
 -- f–d overlap 33
 -- f–f overlap 33
 -- ionic picture 32
 -- lanthanide-sulphides 39
 -- mixed valence 41

- valence transitions (*cont.*)
 - monopnictides and monochalcogenides 32
 - NaCl structure 32, 39
 - spin-orbit coupling 40
 - valence balanced and unbalanced compounds 32–33
 - valence transition 40
 - cohesive energy of CeP 47
 - continuous transitions 44
 - critical point 46
 - delocalization transition 44
 - discontinuous transitions 44
 - dual character of 4f electrons 30
 - electronic and structural phase transitions 45–46
 - elemental lanthanides
 - equilibrium atomic sphere radii 32
 - lattice parameters 31
 - valence change 30
 - energy differences, different valence scenarios
 - for dioxides 50
 - for elemental lanthanides 31–32, 34
 - for lanthanide nitrides 34
 - for localized f-electrons 42
 - for SmX 41
 - for sulphides 31–32
 - equation of state, YbS 48
 - heavy fermion 29
 - ionic picture 29
 - isostructural transition 48
 - itinerant f-electrons 30, 44, 47
 - lanthanide oxides
 - A-type sesquioxide 56
 - bixbyite structure 52
 - charge transfer 53
 - conduction band 51
 - C-type sesquioxide 56
 - cubic Mn₂O₃ structure 52
 - delocalized f-electrons 52
 - dioxides RO₂ 49
 - energy gap 51
 - equilibrium volumes 51
 - exchange interaction 53
 - hybridization 53
 - insulators 53
 - intermediate valence 51
 - ionic picture 51
 - lanthanide contraction 52
 - La₂O₃ structure 52
 - localized f-electrons 52
 - oxidation energies 56
 - oxidation process 55
 - sesquioxides 49, 52
 - valence band 51
 - valence energy difference 52
 - lanthanide sesquioxides
 - band gaps 55
 - equilibrium volumes 53
 - localized f-electrons 30, 44, 46
 - pnictides 47
 - band gaps 33, 35
 - charge transfer and hybridization 33
 - electronegativity 38
 - f–d overlap 33, 36
 - ferromagnetic and anti-ferromagnetic order 33
 - f–f overlap 33, 36
 - f-occupancy 38
 - ionic picture 32
 - itinerant f-electrons 38
 - lanthanide contraction 37
 - lattice parameters, lanthanide nitrides 35
 - monopnictides and monochalcogenides 32
 - NaCl structure 32, 39
 - Na₂O₂ structure 39
 - narrow band gap insulators 34
 - NiAs structure 39
 - spin magnetic and orbital moments 34, 36
 - valence balanced and unbalanced compounds 32–33
 - samarium chalcogenides 47
 - soft anomaly in *pV*-curve 45, 48
 - spin-orbit coupling 48
 - transition pressures 44–48
 - valence changes 29
 - valence instability 48
 - ytterbium compounds
 - effective valence 42–43
 - elemental fcc Yb 42
 - heavy-fermion compounds 41, 43
 - intermediate valence 41, 43
 - intermetallics 42
 - mixed-valence 43
 - valence fluctuations 42
- Wells-Dawson structures 304
- YbAg compounds 42
- YbAl₂ compounds 42
- YbAl₃ compounds 42
- YbAs compounds 42–43
- YbAu compounds 42
- YbBi compounds 39, 42
- YbBiPt compounds 42
- YbCd compounds 42

- Yb chalcogenides 40, 48
YbIn compounds 42
YbIr compounds 42
YbN compounds 27, 34–36, 41–43
YbO compounds 42, 49
YbPb₃ compounds 42
YbP compounds 42–43
YbPd compounds 42
YbPd₃ compounds 42
Yb₃Pd compounds 42
Yb-prictides 36, 38
YbPo compounds 42
YbRh compounds 42
YbRu compounds 42
YbSb compounds 42–43
YbS compounds 39, 42
YbSe compounds 42
YbTe compounds 42
YbX compounds 36
YbZn compounds 42
ytterbium (Yb) element 7–8, 10, 31–32,
34–35